Mixed finite elements with independent strain interpolation for isotropic and orthotropic damage

Gabriel Barbat Vlad

Doctoral Degree in Civil Engineering

Thesis submitted as a compendium of publications

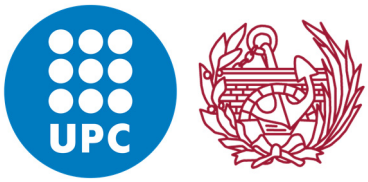

Technical University of Catalonia

Department of Civil and Environmental Engineering

Supervisors: Prof. Miguel Cervera

Prof. Michele Chiumenti

January 2021

To my mother and my father

And to all my family

The final test of a theory is its capacity

to solve the problems which originated it

George B. Dantzig

from *Linear Programming and Extensions* (1963)

Acknowledgements

I express my deep gratitude to my supervisors, Prof. Miguel Cervera and Prof. Michele Chiumenti, for their continuous guidance, constant support and sharing their expertise on numerical modelling and computational mechanics. They have been an endless source of enlightenment and encouragement during my Ph.D. studies. I am very thankful to have had the possibility to learn under your direction.

I am deeply grateful to Prof. Sergio Oller who supported and encouraged me over the course of many years. I thank as well all the professors in the department for giving thoughtful insight on many occasions.

The support provided by the Spanish Ministry of Education via the FPU program is gratefully acknowledged. The financial aid of the AGAUR via the FI program during the first months of my Ph.D. studies is also acknowledged.

I would like to thank as well all the members of the COMET team with whom I have worked during these years, for being always ready to provide technical assistance and creating a pleasant working environment.

I appreciate the chance of sharing a workplace and many great moments with my colleagues in the C1-102 office: Ester, Arnau, Laura, Alexis, Inocencio, Samuel, Domingo, Irene, Alejandro and Arnau (again). I hope that the photos on the walls remembering our time together will be respected and never removed.

I also would like to thank my colleagues from other offices for making the duration of the Ph.D. studies an unforgettable experience: Vicente, Tomas, Sungchul, Carlos (of whom there are many), Marc, Riccardo, Niccola, Raul, Oscar, Uxue, Xufei, Agustina, Anna, Mengjie, Simon, Manuel, Henning, Alejandro, Chiara, Simona, Jordi, Josei and many others. I especially thank Ruben for his disposition to help in bureaucratic and technical matters every time it was needed.

I thank the members of the team of professors of the Mechanics course, Alessandro and Cecilia, for sharing their experience in lecturing during these years.

I am grateful to the wonderful people in the Ph.D. management office, in particular Silvia, Rosa and Cesca, for their invaluable and quick aid during the whole process.

I could not have completed this work without the friendship and continuing support of Maria, Teresa, Marc and Carles. Special thanks to you for being present all the time.

I deeply appreciate the sincere support and kindness of my family during the completion of my Ph.D. studies. They have been strengthening my curiosity and my interest in science since I was a child. My deepest gratitude goes to my parents for their endless encouragement and love.

Abstract

The numerical modelling of fracture has been an active topic of research for over five decades. Most of the approaches employed rely on the use of the Finite Element Method, which has shown to be an effective and cost-efficient tool for solving many physical phenomena. However, the issue of the spurious dependency of the computed solution with the mesh orientation in cracking problems has raised a great concern since its early reports in the 1980s. This matter has proved to be a major challenge in computational solid mechanics; it affects numerous methods employed to solve the problem, in which the computed crack trajectories are spuriously dependent on the arrangement of the finite element (FE) mesh employed. When performing a structural analysis and, in particular, when computing localized failure, it is fundamental to use a reliable and mesh objective method to be able to trust the results produced by the FE code in terms of the fracture paths, bearing capacity, collapse mechanism and nonlinear responses.

In this doctoral thesis, the mixed ε/u strain/displacement finite element method is used together with multiple isotropic and orthotropic damage constitutive laws for the numerical modelling of quasi-brittle fracture with mesh objectivity. The independent interpolation of the strains increases the accuracy of the computed solution, guaranteeing the local convergence of the stress and strain fields. This feature is a crucial improvement over the standard FE formulation in solid mechanics where the strains are computed as local derivatives of the displacements and the local convergence of the resulting stresses and strains is not ensured. The enhanced precision provided by the mixed formulation in the area near the crack tip is decisive for obtaining unbiased numerical results with regard to the orientation of the FE mesh.

The strain-driven format of the mixed formulation enables to readily consider different constitutive laws defined in a stress-strain structure in the numerical simulations. The thesis includes the study of the effect of the material model employed in the resulting crack trajectories as well as the analysis of the relative performance of several isotropic and orthotropic damage behaviors in mode I, mode II, mode III and mixed mode fracture problems.

In this work specific isotropic and orthotropic damage laws are proposed for the numerical modelling of fracture under cyclic loading, which include tensile and compressive damage, stiffness recovery due to crack closure and reopening, as well as irreversible strains. Also, the capacity of the proposed model in reproducing the structural size effect is examined, which is an essential requirement for models aiming at computing quasi-brittle behavior.

In this thesis, a comprehensive comparison of the mixed FE formulation with other techniques employed for computing fracture, specifically the Extended Finite Element Method (XFEM) and the Phase-field model, is made, revealing the cost-efficiency of the proposed Mixed Finite Element Method for modelling quasi-brittle cracking with mesh objectivity. This allows to perform the analysis of real-scale structures, in 2D and 3D, with enhanced accuracy, demonstrating the applicability of this method in the engineering practice. The validation of the model is performed with an extensive comparison of computed results with existing experimental tests and numerical benchmarks. The capacity of the mixed formulation in reproducing force-displacement curves, crack trajectories and collapse mechanisms with enhanced accuracy is demonstrated in detail.

Resumen

La modelización numérica del fenómeno de la fractura ha sido un tema activo de investigación durante más de cinco décadas. La mayoría de las estrategias utilizadas se basan en el uso del Método de los Elementos Finitos, que ha demostrado ser una herramienta eficaz y computacionalmente eficiente para simular una gran variedad de fenómenos físicos. Sin embargo, la dependencia espuria de la solución calculada con la orientación de la malla en problemas de fisuración ha suscitado una gran preocupación de los investigadores desde los primeros informes al respecto en la década de 1980. Este problema ha demostrado ser un gran desafío de la mecánica computacional de sólidos; afecta a numerosos métodos empleados para resolver el problema, en los que la trayectoria de las fisuras calculada depende de forma espuria de la disposición de los elementos finitos en la malla utilizada. Al realizar un análisis estructural y, en particular, al calcular la localización de deformaciones, es fundamental poder utilizar un método fiable que asegure la objetividad con respecto a la malla para poder confiar en los resultados producidos por el código de elementos finitos en cuanto a trayectorias de fisuras, capacidad de carga, mecanismo de colapso y respuestas no lineales.

En esta tesis doctoral, el método de los elementos finitos mixtos ε/u deformación/desplazamiento es utilizado junto con varias leyes constitutivas de daño isótropo y ortótropo para la modelización numérica de la fractura cuasi-frágil de forma objetiva con respecto a la orientación de la malla. La interpolación independiente de las deformaciones aumenta la precisión de la solución calculada, garantizando la convergencia local de los campos de tensiones y deformaciones. Esta característica representa una mejora crucial con respecto a la formulación estándar de elementos finitos de la mecánica de sólidos, donde las deformaciones se calculan como derivadas locales de los desplazamientos y la convergencia local de las tensiones y deformaciones resultantes no está garantizada. La mayor precisión aportada por la formulación mixta en la zona cercana a la punta de la fisura es decisiva para obtener resultados numéricos que no presenten una dependencia espuria con la orientación de la malla de elementos finitos.

El formato expresado en función de la deformación de la formulación mixta permite considerar directamente diferentes leyes constitutivas que siguen una estructura tensión-deformación para su uso en las simulaciones numéricas. La tesis incluye el estudio del efecto que tiene la ley constitutiva utilizada en la trayectoria de las fisuras resultantes, así como el análisis del desempeño relativo de varias leyes de daño isótropas y ortótropas en problemas de fractura en modo I, modo II, modo III y modo mixto.

En este trabajo se proponen leyes de daño isótropo y ortótropo específicas para la modelización numérica de la fractura bajo carga cíclica, que incluyen daño a tracción y a compresión, recuperación de la rigidez por el cierre y reapertura de fisuras, así como deformaciones irreversibles. Además, se comprueba la capacidad del modelo propuesto para reproducir el efecto tamaño, que es un requisito esencial para los modelos que tengan como objetivo calcular el comportamiento cuasi-frágil de los materiales.

En la tesis se realiza una comparación exhaustiva de la formulación mixta de elementos finitos con otras técnicas que se utilizan para calcular el problema, específicamente el Método de los Elementos Finitos Extendidos (XFEM) y el modelo Phase-field, revelando la eficiencia computacional del Método de los Elementos Finitos Mixtos propuesto para modelizar la rotura cuasi-frágil de forma objetiva con respecto a la malla. Ello permite realizar el análisis de estructuras de tamaño real, en 2D y 3D, con mayor precisión, demostrando la aplicabilidad del método a problemas reales de ingeniería. La validación del modelo se realiza con una amplia comparación de resultados calculados con ensayos de laboratorio existentes y con simulaciones de casos teóricos de referencia. Se demuestra en detalle la capacidad de la formulación mixta para reproducir curvas fuerza-desplazamiento, trayectorias de fisuras y mecanismos de colapso con precisión mejorada.

Contents

Chapter 1

Introduction

1.1 Motivation

The Finite Element Method (FEM) has proved to be a reliable and effective tool for the numerical simulation of many physical problems. Among countless applications, it is regularly adopted for evaluating structural behavior in engineering practice. However, when modelling fracture in quasi-brittle materials, the standard displacement based finite element formulation of solid mechanics has the critical issue of producing crack paths spuriously dependent on the mesh alignment. Results computed with this approach cannot be trusted, as concerns regarding their quality arise. The calculation of the structural capacity and the determination of collapse mechanisms require an accurate method for performing the numerical simulation of localized failure, that needs to be able to produce mesh objective results.

Fracture has been analyzed using finite elements since the 1960s. A broad range of numerical models have been devised for its study. The issue of spurious mesh dependency, unambiguously reported since the 1980s, has shown to be a major challenge, requiring special attention. Many of the methods proposed have proved to suffer from spurious mesh dependent crack trajectories. Since then, several proposed methodologies have arisen as being able of producing mesh objective results. However, there exists no general consensus as to which method should be used, even though the physical problem being solved is the same. Also, numerous formulations and finite element (FE) codes show significant scatter when modelling the same problem.

The many methods proposed can be classified in two main categories according to the approach used to represent the crack in the problem. On the one hand, continuous approaches model fracture at constitutive level, as a degradation of the material. A softening damage or plasticity law is used to represent the nucleation and propagation of cracks in the body. This is the approach adopted in the standard smeared crack model, as well as in phase-field formulations, nonlocal damage models and many more. On the other hand, discontinuous methods explicitly introduce in the model the displacement or strain discontinuities generated by the crack in the structure. This was originally done by remeshing, although nowadays methods inserting the discontinuity in the solution through an enhancement of the FE formulation are preferred. This is the strategy followed

by the eXtended Finite Element Method (XFEM) or the Embedded Finite Element Method (EFEM) among others.

In the past, mixed finite element formulations have proved to have excellent capabilities in many numerical applications, within both fluid and solid mechanics. The ability of the u/p displacement/pressure FE for solving incompressibility in both situations is widely known. In particular, this FE formulation has also been used for the computational modelling of materials with isochoric plasticity. Mixed σ/u stress/displacement and ε/u strain/displacement FE formulations have also been considered, for computing strain localization problems with mesh objectivity. However, previous studies regarding mixed ε/u FE centered especially in the use of materials with softening plasticity.

Due to these reasons, the present doctoral thesis focuses on the computation of mesh objective results in localized failure problems with the mixed ε/u FE formulation together with isotropic and orthotropic damage constitutive laws.

1.2 Objectives

The main objective of the present doctoral thesis is the development, implementation in a FE code, validation and application of a model based on the mixed ε/u strain/displacement finite element formulation for the accurate and mesh objective numerical modelling of fracture in quasi-brittle materials with isotropic and orthotropic damage constitutive laws.

To achieve this primary objective, the following major objectives are addressed, organized in the corresponding topics:

- **State-of-the-art review.** To perform an exhaustive investigation of the existing publications on the numerical methods for the modelling of fracture.
- **Model.** To develop a numerical model for performing structural analyses and computing fracture based on the use of the mixed ε/u finite element formulation and damage constitutive laws.
- **Damage constitutive laws.** (i) To investigate the capacity of the mixed FE formulation for readily adopting a wide range of constitutive behaviors for modelling cracking. (ii) To assess the relative performance of the different material laws for computing crack trajectories in mode I, mode II, mode III and mixed mode fracture. (iii) To examine the role of the damage surface in the resulting fracture path.
- **Mesh objectivity.** (i) To assess the mesh objectivity of the proposed model based on the mixed ε/u FE formulation. For this, it is necessary to perform a study comparing the crack trajectories derived from computations of the same problem using several meshes with different finite element orientations. (ii) To compare the relative performance of the mixed FE model with respect to the standard displacement based formulation in this regard.
- **Validation.** To validate the proposed model with a comprehensive study of the ability of the mixed FE formulation in producing results comparable to those in the experimental tests and numerical benchmarks reported in the literature. Structural responses, crack trajectories, collapse mechanisms and force-displacement curves need to be accurately replicated.

- **Orthotropic damage.** (i) To explore the aptness of the mixed FE formulation for modelling cracking with orthotropic damage laws. (ii) To investigate the differences in the computed results between isotropic and orthotropic behavior. (iii) To examine the advantages of the use of the mixed formulation with respect to the standard one when computing orthotropic damage.
- **Cyclic loading.** (i) To develop and validate a damage constitutive law suitable for the numerical simulation of fracture under cyclic loading. For this, tensile and compressive damage, micro crack closure and reopening effects (MCR) as well as irreversible strains need to be considered. (ii) To assess its capacity in reproducing stiffness recovery in force-displacement curves and the effect of crack closure and reopening in the structure.
- **Structural size effect.** (i) To examine the ability of the proposed model in replicating the size effect behavior exhibited by quasi-brittle structures. (ii) To compare the computed results to existing experimental campaigns studying this phenomenon in terms of bearing capacity and post-peak behavior. (iii) To assess the capacity of the numerical model in reproducing Bazant's size effect law.
- **Critical appraisement.** To study the relative performance of the mixed FE model when compared to other existing numerical techniques devised to solve the problem of cracking. For this comparison, the Phase-field model (PFM) and the XFEM are selected, as they are currently popular representatives of the continuous and discontinuous approaches to fracture, respectively. The research should focus on the main differences in their formulation and discuss the principal assets and burdens ensuing from their application.
- **Engineering applications.** (i) To check the ability of the proposed mixed formulation in performing real-scale applications, in 2D and 3D, with computational efficiency. (ii) To assess the enhanced accuracy of the mixed ε/u formulation in terms of stresses and strains and its capacity of producing satisfactory results without the use of the extremely fine FE mesh densities required in regularized techniques.

1.3 Thesis outline

In this thesis, a model based on the mixed ε/u finite element formulation is developed and employed in the accurate numerical simulation of localized failure with mesh objectivity using isotropic and orthotropic damage constitutive laws. Chapter 2 provides the state-of-the-art review on the numerical modelling of cracks. The multiple approaches for computing cracking are presented, focusing on the main challenges that have been reported in the numerous articles and researches which have been critically examined. Chapter 3 offers an extensive comparison of the XFEM, the mixed FEM and the phase-field model for fracture. This comparative study comprises the principal differences of the continuous and discrete formulations of these methods as well as aspects related to their practical application. Their main assets and drawbacks are considered in relation to the challenges listed in the previous chapter. The study includes a set of numerical benchmarks where the performance of the three methods is contrasted. Chapter 4 summarizes the main scientific contributions of each of the articles incorporated in this thesis by compendium of publications. Chapter 5 closes with the conclusions of the thesis and proposes future research lines. Then the list of references is given and, finally, the articles included in this thesis by compendium of publications are provided.

1.4 Research dissemination

Publications in peer-reviewed international journals

This thesis is submitted as a compendium of the following publications:

- M. Cervera, G. B. Barbat and M. Chiumenti. **Finite element modelling of quasi-brittle cracks in 2D and 3D with enhanced strain accuracy.** *Computational Mechanics*, 60(5), 767–796 (2017).
  https://doi.org/10.1007/s00466-017-1438-8
- G. B. Barbat, M. Cervera and M. Chiumenti. **Appraisement of planar, bending and twisting cracks in 3D with isotropic and orthotropic damage models.** *International Journal of Fracture*, 210(1-2), 45–79 (2018).
  https://doi.org/10.1007/s10704-018-0261-3
- G. Vlachakis, M. Cervera, G. B. Barbat and S. Saloustros. **Out-of-plane seismic response and failure mechanism of masonry structures using finite elements with enhanced strain accuracy.** *Engineering Failure Analysis*, 97, 534–555, (2019).
  https://doi.org/10.1016/j.engfailanal.2019.01.017
- M. Cervera, G. B. Barbat and M. Chiumenti. **Architecture of a multi-crack model with full closing, reopening and sliding capabilities.** *Computational Mechanics*, 65, 1593-1620, (2020).
  https://doi.org/10.1007/s00466-020-01836-y
- G. B. Barbat, M. Cervera, M. Chiumenti and E. Espinoza. **Structural size effect: Experimental, theoretical and accurate computational assessment.** *Engineering Structures*, 213, 110555 (2020).
  https://doi.org/10.1016/j.engstruct.2020.110555

Presentations in international conferences

During the development of this thesis the ongoing work and results were presented in the following international conferences:

- M. Cervera, G. B. Barbat and M. Chiumenti. **FE modelling of quasi-brittle cracks in 2D and 3D with enhanced strain accuracy.** *XIV International Conference on Computational Plasticity, COMPLAS 2017, Barcelona, Spain, 5-7 September* (2017).
- G. B. Barbat, M. Cervera and M. Chiumenti. **Mixed finite elements for strain localization under monotonic, cyclic and dynamic loadings.** *6th European Conference on Computational Mechanics, ECCM 6, Glasgow, United Kingdom, 11-15 June* (2018).
- G. B. Barbat, M. Cervera and M. Chiumenti. **Mixed finite element modeling of quasi-brittle cracks under cyclic loading.** *VI International Conference on Computational Modeling of Fracture and Failure of Materials and Structures, CFRAC 2019, Braunschweig, Germany, 12-14 June* (2019).

Chapter 2

State of the art

This chapter critically reviews the different approaches that have been adopted over the last fifty years for the numerical modelling of cracks within the Finite Element Method (FEM). In this work, the distinction is made between the problem of fracture defined at continuum level and the corresponding discrete FE setting. The main challenges encountered by the different methods for computing cracking are analyzed.

2.1 Embedded, smeared and regularized cracks

2.1.1 Continuous setting

Figure 2.1 presents two alternative models for representing at the continuum level a crack S in a solid Ω. The discontinuity S splits the solid in two parts, denoted Ω^+ and Ω^-. Figure 2.2 shows the corresponding displacement and strain fields related to both approaches along a line normal to the fracture.

Figures 2.1a and 2.2a depict the representation of a *sharp crack*. A discontinuous jump w in the displacement field represents the fracture S occurring in the body. This results in a singularity appearing in the strain field at S.

Figures 2.1b and 2.2b exhibit the description of a *regularized crack*. In this approach, the jump w in the displacement field is regularized over a band of small, but finite, thickness b formed by two lines S^+ and S^- running parallel to S. Following this scheme, the ensuing displacement and strain fields in the solid Ω are continuous.

In the latter case, the regularization introduced avoids the development of sharp cracks. For this reason, the bandwidth b is also referred to as a "localization limiter". However, this approach also modifies the problem being solved. To preserve the consistency with respect to the original problem of fracture, the solution of the regularized problem needs to converge to the sharp one when the regularizing length diminishes, that is, for $b \to 0$.

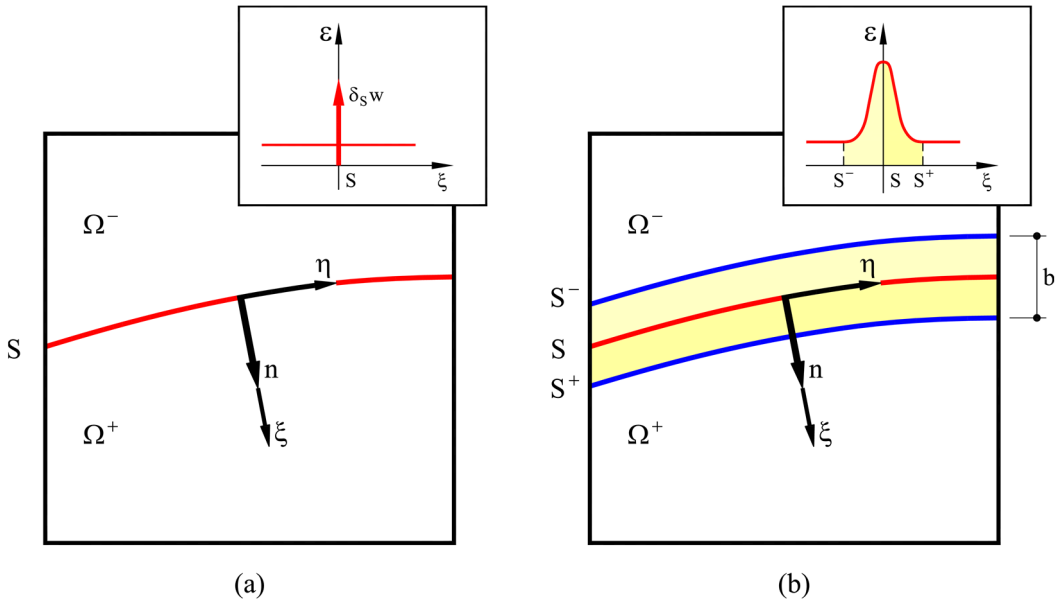

Figure 2.1: Depictions of (a) sharp and (b) regularized cracks in the continuous setting

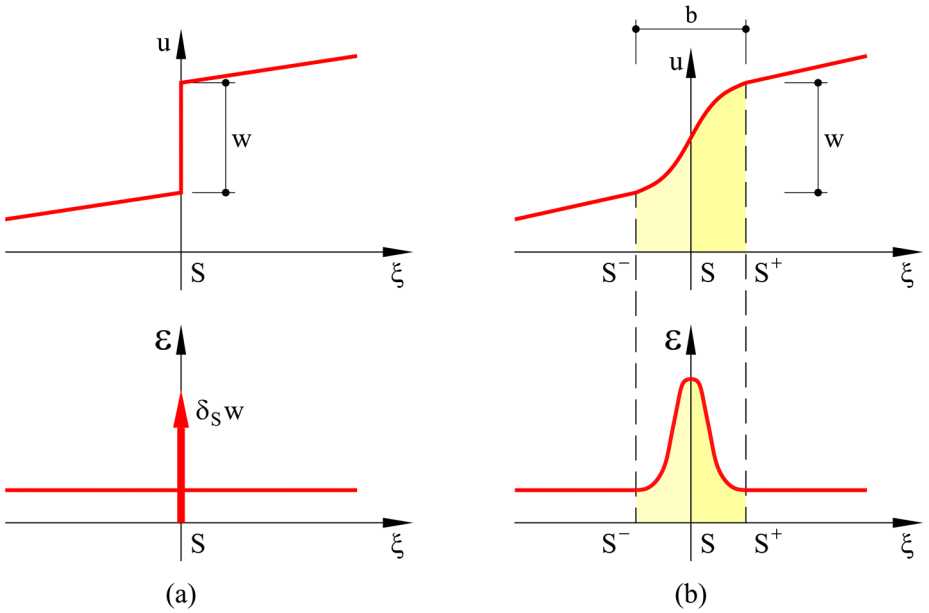

Figure 2.2: Depictions of (a) sharp and (b) regularized cracks in the continuous setting: (up) displacement and (bottom) strain fields

Both the sharp and the regularized continuum models follow behaviors based on the Fictitious Crack Model (FCM), presented by Hillerborg et al. in 1976 [1] and further detailed in references [2-5]. The FCM is an improved version from previous Cohesive Crack Models proposed by Dugdale [6] and Barenblatt [7-10]. Instead of considering that the crack causes an abrupt reduction of strength and stiffness, as in the original work of Rashid in 1968 [11], in the FCM a continuous degradation of the material is introduced, where the softening behavior is related to the fracture energy. Hillerborg's FCM follows a traction-jump format; Bazant and Oh in 1983 [12] proposed the *Crack Band Theory* (CBT) for fracture, an adaptation of the FCM, defined in terms of stress vs. strain.

2.1.2 Discrete setting

Figure 2.3 presents four alternative approaches adopted at the discrete level for computing the problem of fracture, derived from their continuum counterparts described in the previous section by introducing a finite element discretization in the body Ω. Figure 2.4 shows the resulting discrete displacement and strain fields.

Firstly, figures 2.3a and 2.4a depict the *embedded crack model*, generated from the continuum *sharp crack* setting. In this model, the formulation of the finite elements crossed by the crack S is devised to explicitly incorporate the discontinuity jump in the displacement field and the corresponding singularity arising in the strain field. This is the strategy followed by the Embedded Finite Element Method (EFEM), also referred to as the Strong Discontinuity Approach [13-16] and by the eXtended Finite Element Method (XFEM) [17-20].

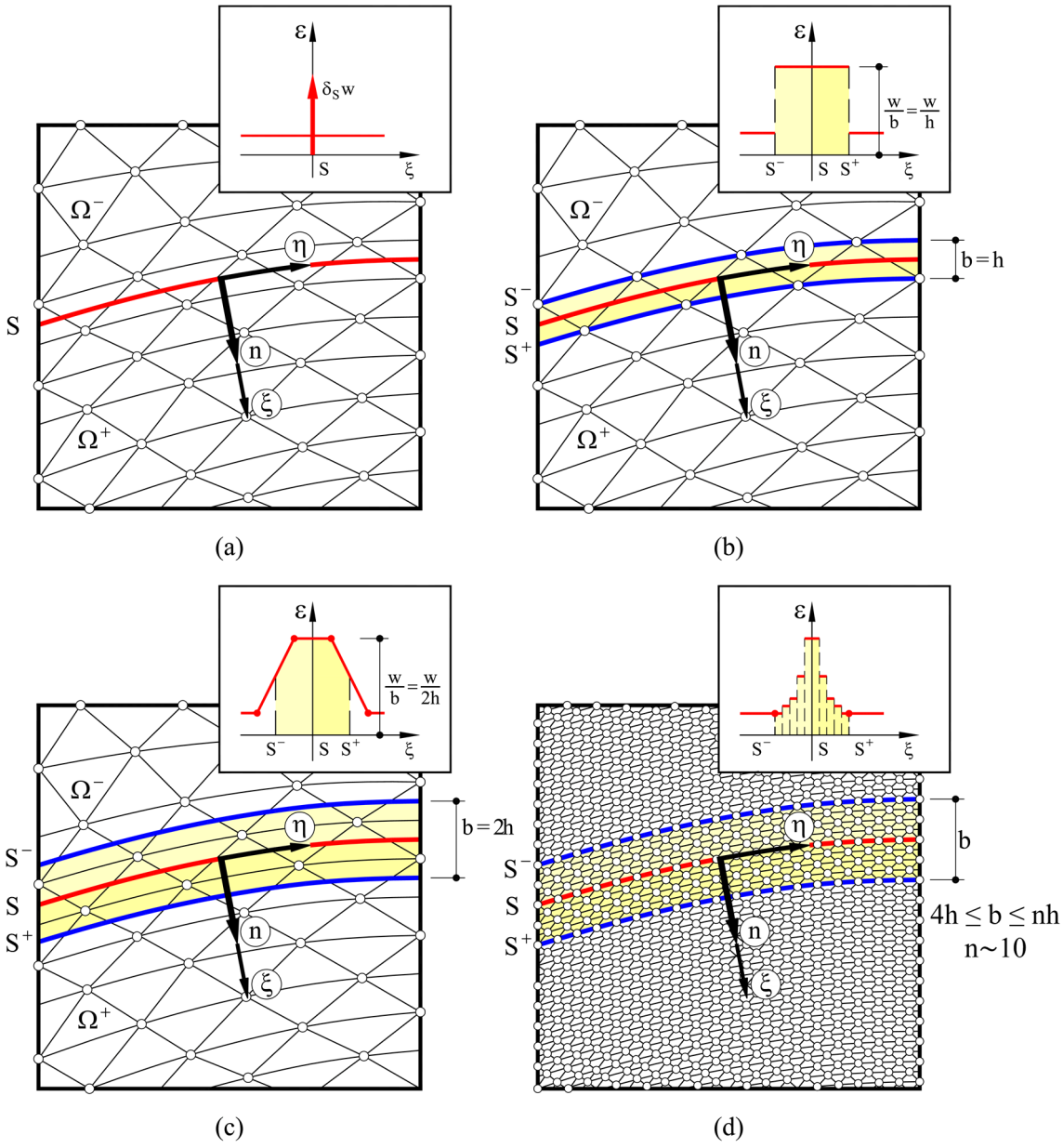

Figure 2.3: Depictions in the discrete setting of the (a) embedded crack model, (b) smeared crack model, (c) enhanced smeared crack model and (d) regularized crack model

Secondly, figures 2.3b and 2.4b introduce the *smeared crack model*, in which the discontinuity S is smeared over a band of finite elements of width $b = h$, h corresponding to the finite element size. This generates a continuous displacement field and a regular strain field in the body Ω. This strategy was first adopted by Rashid in 1968 [11] for analyzing prestressed concrete pressure vessels. The approach is simple to implement in nonlinear finite element codes. It uses the standard displacement based FE formulation from solid mechanics and it only requires the introduction of the desired stress vs. strain constitutive law [11, 12, 21, 22].

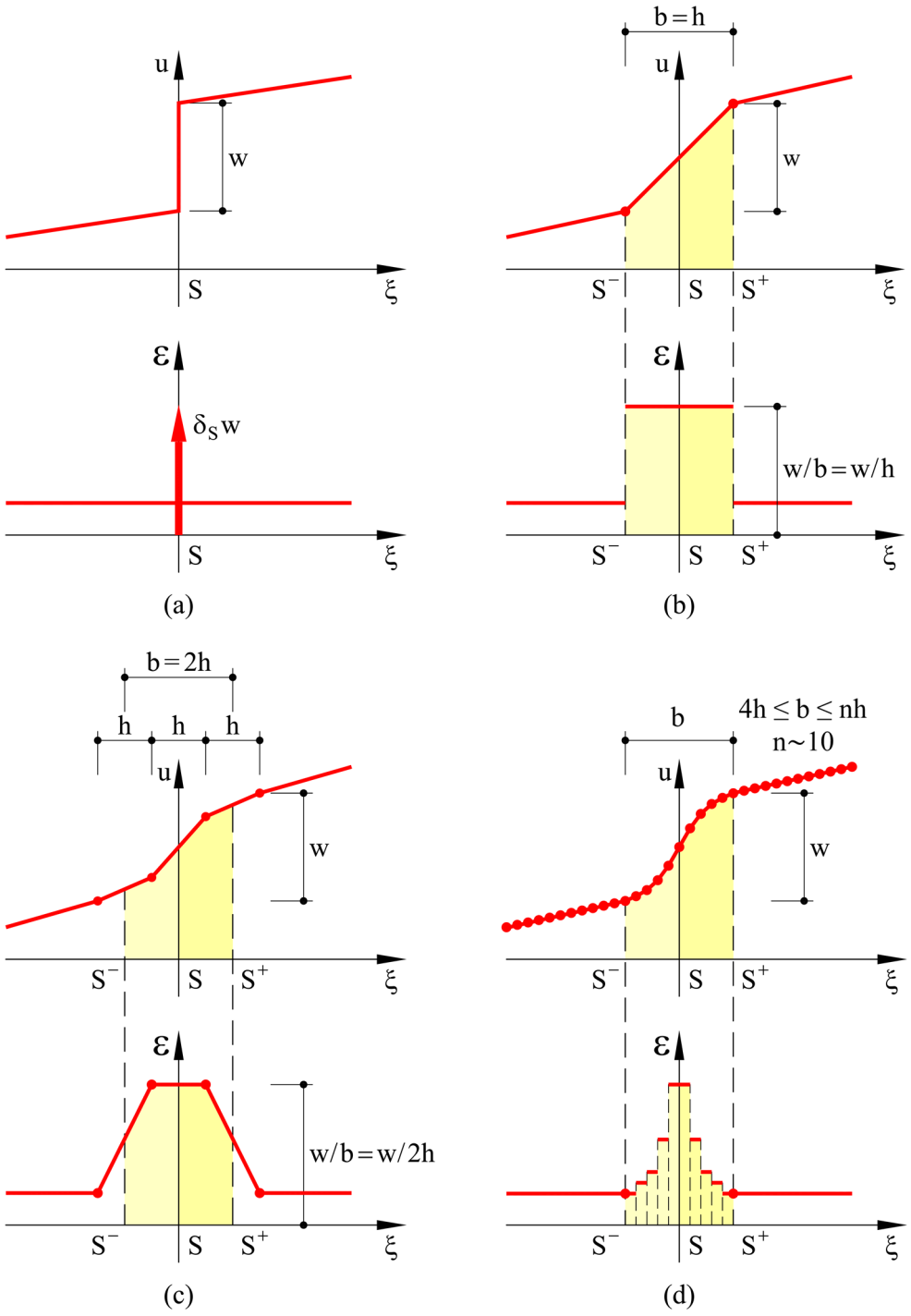

Figure 2.4: Depictions in the discrete setting of the (a) embedded crack model, (b) smeared crack model, (c) enhanced smeared crack model and (d) regularized crack model in terms of the (up) displacement and (bottom) strain fields

Within this framework, Bazant and Oh in 1983 [12] proposed the *Crack Band Theory* for fracture, in which the continuous softening behavior of the material law employed in the finite element analysis is accurately related to the fracture energy and the crack bandwidth $b = h$, allowing to obtain mesh size objective results.

Note that, following this approach, upon mesh refinement, the crack bandwidth tends to zero, $b = h \to 0$ and, therefore, the smeared crack band model converges to a sharp crack. Also, the Crack Band Theory allows to ensure the correct energy dissipation during the fracture process when the finite element size decreases. This method is used in many applications due to its simplicity and reasonable computational cost, which makes it suitable for large-scale analyses.

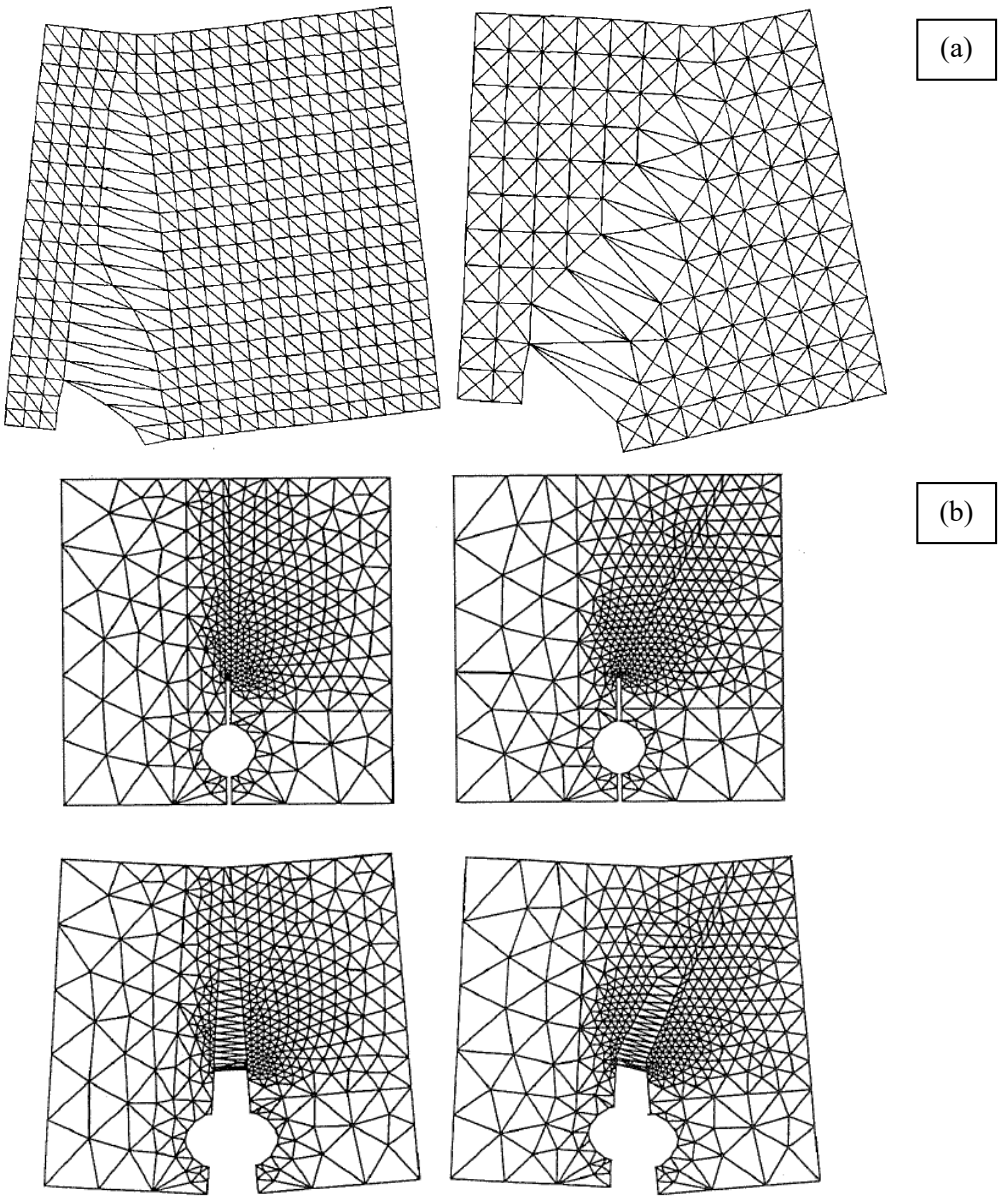

Figure 2.5: Computed crack trajectories of the same problem using different mesh orientations reported in references (a) [23] and (b) [24]

Unfortunately, results computed using the smeared crack model are affected by the issue of spurious mesh bias dependency; the crack trajectories are spuriously dependent on the orientation of the FE mesh employed. Cracks calculated with this technique tend to develop parallel to the boundaries of the elements introduced in the discrete setting to perform the calculation and,

consequently, the consistency with the physical problem of fracture is lost. Early reports of this issue, shown in Figure 2.5, can be found in references [22-25].

This lack of consistency between the problems at the continuum and discrete settings when computing fracture is provoked by the lack of local convergence of the stresses and strains in the standard displacement based FE formulation [26, 27]. Near quasi-singular points, such as in the vicinity of the tip of a crack, the norm of the error of the strains in the discrete FE solution, computed as the gradients of the displacements, becomes unbounded [28]. The path of the propagating crack is determined by the stress and strain fields, which are inaccurately computed at these critical locations, and their evaluation becomes irregularly dependent on the local discretization employed. The resulting trajectories are spuriously dependent on the FE mesh orientation bias [29]. Therefore, the issue of mesh bias dependency affecting the smeared crack model can be solved by enhancing the accuracy of the underlying FE formulation.

Thirdly, figures 2.3c and 2.4c show the *enhanced smeared crack model*. This method, proposed and developed by Cervera and coworkers [26, 27, 30-35] is based on the use of a mixed ε/u FE formulation. Under this approach, the strain field is no longer computed by local differentiation at element level; instead, strains are treated as additional primary unknowns of the problem, and are interpolated independently from the displacements. It can be observed in Figure 2.4c that both the displacement and the strains are linearly interpolated. Notably, the discrete strain field is continuous, in contrast to the standard displacement based FE formulation in solid mechanics, where the strains are inter-element discontinuous. This added degree of regularity in the strain definition enhances the order of convergence and the accuracy of the computed strain and stress fields. In particular, this FE formulation achieves local convergence of the discrete problem in terms of stress and strain, which is an essential feature in the region of the crack tip. Consequently, this approach, based on the use of the Mixed Finite Element Method (MFEM), allows to obtain mesh bias objective results. Using this approach, the crack is smeared over an effective bandwidth $b = 2h$, h corresponding to the element size.

Fourthly, figures 2.3d and 2.4d portray the *regularized crack model*. Following this strategy, the problem of fracture is modified at the continuum level to insert a length scale that acts as a localization limiter, avoiding the development of high displacement gradients and ensuring the regularity of the discrete problem. This "smoothing" of the FE solution amends the quasi-singular stress states that appear around the crack tip when using the standard FEM, preventing spurious mesh dependent results. The problem, at the continuum level, becomes regular and, therefore, the FE discretization employed can rely on inter-elemental discontinuous strains. As a result, this strategy demands the adoption of FE discretization resolutions able to represent the strain localization that occurs in the localizing band. For this reason, extremely fine meshes are required in regularized approaches, at least $4h \leq b \leq nh,\ n{\sim}10$, although, depending on the specific method used, much higher refinement levels are also regularly employed. This strategy has been followed by nonlocal [36-40], gradient-enhanced [41-46] and phase-field models [47-52].

The issue of the consistency between the physical phenomenon of fracture and the numerical simulations performed with regularized crack models was not conveniently addressed until phase-field models for brittle fracture were introduced. When nonlocal and gradient-enhanced models were initially proposed, the length scale was regarded as a material parameter, which was determined by the internal micro or mesostructures, and not as a regularizing length. Note that, under the former assumption, the correspondence with the problem of fracture is lost. Conversely, Phase-Field Models (PFM) are conceived as a regularized variational approach to brittle fracture [48, 53, 54] and, when the regularizing length tends to zero ($b \to 0$), the solution converges to the one corresponding to a sharp crack, in accordance with the Γ-convergence theorem [55, 56]. This feature, guaranteeing the consistency with the original problem, introduces a decisive

improvement in the PFM with respect to previous regularized models. In particular, the geometrically regularized phase-field model [56-70] can be mentioned, where it is proposed that the regularization length depends on the FE size, $5h \leq b \leq 10h$. Following this approach, the crack bandwidth b tends to zero upon mesh refinement.

2.2 The challenges of the numerical modelling of cracking

This section presents the most important aspects of the challenges addressed by the literature regarding the numerical modelling of cracking. The section is divided in three main categories: crack representation, crack propagation and strength and toughness.

2.2.1 Crack representation. Approximability

The first challenge considered in this work is the crack representation, concerning the ability of the discrete FE model to adequately reproduce the crack developing in the body.

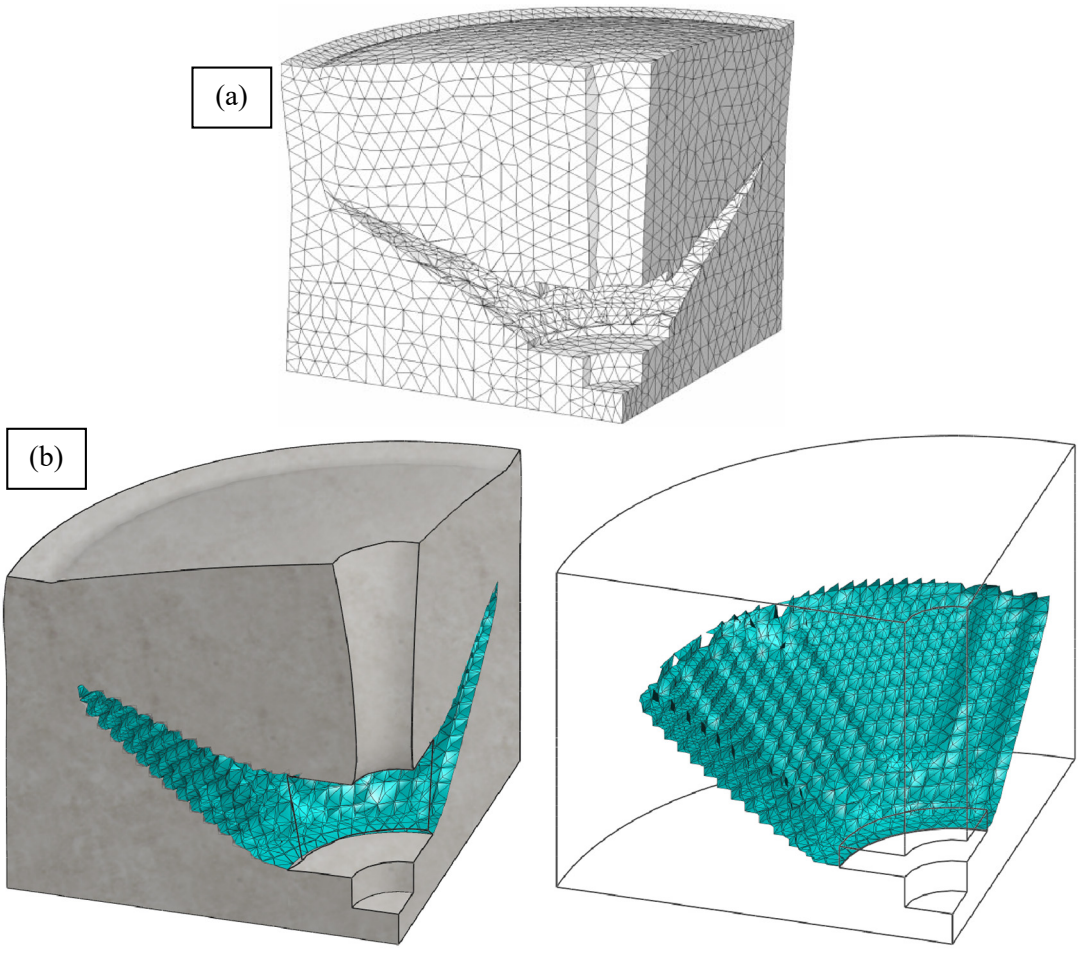

Figure 2.6: 3D simulation of a pull-out test using (a) the XFEM, taken from [71], and (b) the mixed FEM, taken from [72]

Different numerical models can generate realistic crack depictions. In Figure 2.6, the comparison of the results obtained in 3D simulations of the same pull-out test using the embedded crack model, XFEM [71], and the enhanced smeared crack model, the mixed FEM [72], is shown. Both

approaches require the post-processing of the direct output of the calculation to generate a suitable geometrical representation of the phenomenon of fracture.

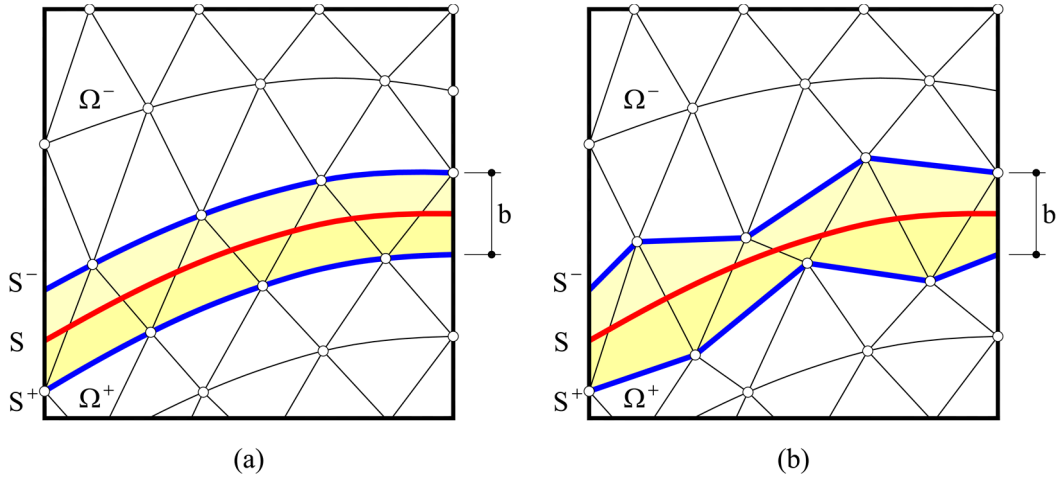

Figure 2.7: Numerical modelling of fracture with finite element boundaries oriented (a) parallel to the crack and (b) arbitrarily

The Finite Element Method relies on the use of interpolation functions to approximate the solution of the unknown fields inside the element. In cracking problems, the choice of the approximation space of the discrete displacements and strains deeply influences the performance of the method.

In references [23, 26, 27, 73, 74], the deficiencies of the standard displacement based finite element formulation of solid mechanics in reproducing separation modes in fracture problems are detailed. For example it is reported that, when using a mesh of standard linear triangles, resulting in a constant discrete approximation of the strain field throughout the FE, only in situations in which the boundaries of the element run parallel to the trajectory of the developing fracture, as in Figure 2.7a, can the ensuing strain and stress fields at the discontinuity S be approximated satisfactorily.

Contrariwise, when the FE boundaries have an arbitrary orientation and are not aligned with respect to the crack, as in Figure 2.7b, the discrete interpolation functions of this element cannot adequately represent the stress and strain fields at the fracture discontinuity. This is because in such case the localization bandwidth is not constant along the crack element-wise. Thus, a constant strain field cannot represent the discrete strain resulting at S from the separation of Ω^+ and Ω^-, that should be, at least, of linear precision. Similar limitations are reported for standard quadrilateral elements. This issue is not solved nor reduced through mesh refinement; it is related to the inability of the discrete strain field in standard linear elements for replicating separation modes [23, 26, 27, 73, 74].

The mixed ε/u FE formulation, which introduces a linear interpolation of the strain field, does not exhibit this problem, as it has been explained in references [26, 27]. This can be seen in Figure 2.8, where the capacity of the standard and mixed FEM for representing pure separation modes is examined. The arrows represent the computed directions of maximum principal strain arising at the crack band in a mode I fracture test. Only the mixed formulation can reproduce the correct strain field when the FE mesh employed is not well aligned with the crack. Contrariwise, it is shown in references [26, 27] that the low order standard formulation is only capable of properly reproducing separation modes in situations in which the crack develops parallel to the FE sides. This is also one of the reasons for the underlying error and the mesh biased results appearing in the discrete solution when using standard FE.

Despite employing elements that rely on a constant discrete approximation of the strain field, regularized crack methods are able of successfully reproducing displacement discontinuities by using a band extending over a large number of elements to represent the strain localization resulting from the separation of Ω^+ and Ω^-. In embedded crack models, the displacement interpolation is enriched by incorporating the discontinuity generated by the crack directly into the FE formulation [73, 74]. As it has been pointed out by Wu, the difference between the EFEM and XFEM is the level of precision of the enrichment introduced [75].

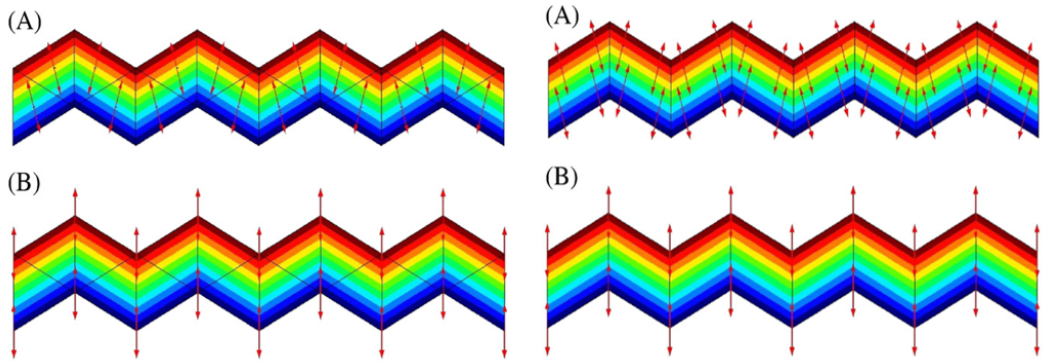

Figure 2.8: Standard (A) and mixed FEM (B) representation of separation modes in linear (left) triangles and (right) quadrilaterals [27]

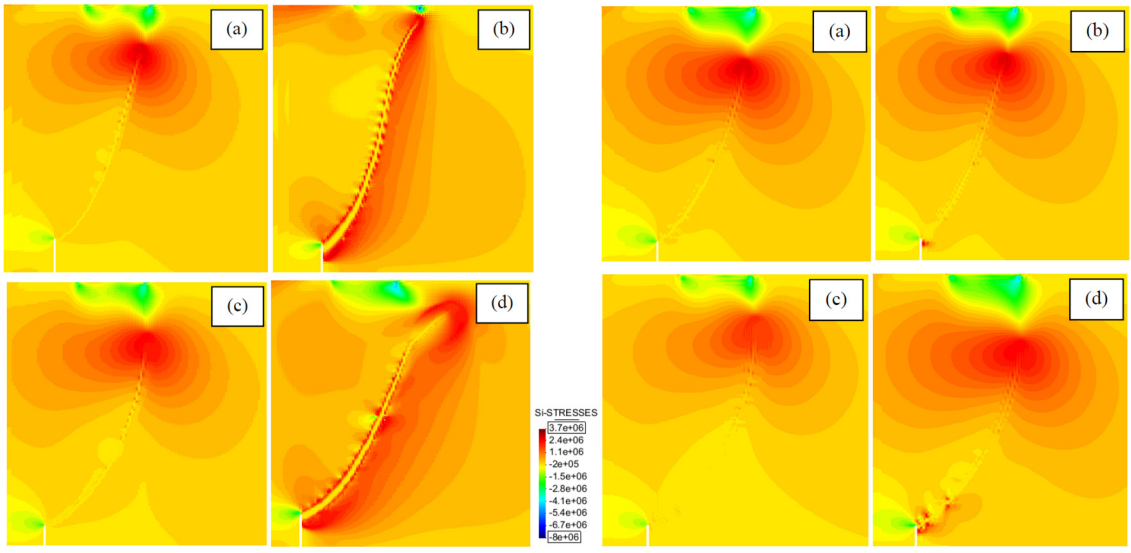

Figure 2.9: Contours of the major principal stress field in a mixed mode bending test computed with (left) standard FE and (right) mixed FE with different fracture criteria: (a) isotropic Rankine, (b) orthotropic Rankine, (c) isotropic Drucker–Prager and (d) orthotropic Drucker–Prager [32]

The deficient performance of the standard FE formulation for reproducing separation modes becomes particularly clear when used in conjunction with orthotropic crack models. As it can be seen in Figure 2.9, taken from a study performed in reference [32], which is included in the compendium, in such cases severe stress oscillations appear along the crack trajectory. This issue is caused again by the poor kinematic description of low order standard FE. The consequences related to the use of a meager approximation of the stress and strain field are magnified when using orthotropic constitutive laws: all the components of the stress field are not equally affected by the softening behavior sustained by the material. This leads to the development of spurious stress transfer across the open crack when the orientation of the remaining stress components is

inaccurately computed, such as in Figure 2.8. This fact made the use of orthotropic models impractical and caused their almost complete abandonment in favor of isotropic models for cracks [24, 32, 39, 73, 76]. As reported in reference [32], this issue is greatly alleviated by the inter-elemental continuity and enhanced accuracy of the stress and strain fields provided by the mixed FEM, so that practically no stress oscillations appear along the crack path when they are used together with orthotropic models, as can be seen in Figure 2.9.

2.2.2 Crack propagation. Uniqueness and mesh bias independence

A second challenge posed to numerical models of fracture is the crack propagation, that is, the ability of the discrete model to reproduce the onset and advance of the crack as well as determining the direction of progression of fracture. The correct resolution of these aspects is crucial in the computation of failure mechanisms and load carrying capacities when performing a structural analysis. The inability of many of the numerical models to produce physically realistic results due to the lack of mesh objectivity has attracted a lot of attention and promoted numerous research lines.

The physical problem of cracking has been examined from various approaches at the continuum level. Some of these are established on the basis of Griffith's theory of fracture, which proposes an energy based criterion for fracture propagation and regrettably does not determine the direction of progression of the crack. This second aspect has to be resolved as a separate ingredient of the problem [77, 78]. Neither does Griffith's theory incorporate a criterion for crack initiation. As reported in reference [78], these issues are inherited by many models following this approach.

Other methods rely on the use of a variety of stress-based criteria for determining the onset of fracture. In particular, for smeared crack models following this approach, the cohesive behavior of the material is defined so that the energy dissipated in the formation of the crack is objectively established, as proposed reference [12]. Thus, the model integrates both strength and energy criteria for the evolution of the crack behavior and works as a quasi-brittle version of Griffith's theory. The more recent geometrically regularized phase-field approach to fracture is based in the same energy conserving notions [56-70]. The Fictitious Crack Model [1-5] defined in terms of traction vs. separation laws involves as well an objective definition of energy dissipation, allowing the modelling of quasi-brittle failure.

The cohesive behavior of cracks can become quite complex, depending on the physical phenomena being numerically modelled in the simulations. The material exhibits a directional character in the gradual softening behavior in strength and stiffness, governing the tractions acting on the crack plane. Complex non-proportional loading situations can cause the sliding of the open crack and the development of shear stresses across the fracture plane. However, usually the material behavior can be simplified in monotonic loading through the introduction of isotropic models in the calculations. If cyclic loading is considered, the model needs to include crack closure and reopening capabilities, reproducing the stiffness recovery taking place during the phenomenon. The development of irreversible strains may become significant as well. All these characteristics are not always easily implementable in the numerical model [34].

In embedded crack models, material behaviors are defined using traction-separation laws, which are in many cases phenomenologically derived [4, 79-82]. Models employed in smeared and regularized models are commonly expressed in terms of stress vs. strain, with various levels of complexity [31, 32]. It has been recently shown in reference [34], included in the compendium, that orthotropic behavior, crack sliding, stiffness recovery due to crack closure and reopening and irreversible strains can be realistically considered in enhanced smeared crack models. By construction, most regularized crack models are limited to scalar damage and monotonic loading,

although promising advances are being made to consider more complex behaviors [83-85]. In references [86, 87] the relation between traction-based and stress-based models for representing the material behavior is addressed.

In addition to providing a criterion for initiation of cracking, the stress-based fracture models implicitly determine the direction of propagation of the crack, according to a generalization of Mohr's maximization postulate [88]. This idea is underlined in the investigations by Cervera and Wu on the subject [87, 89-91] as well as in those of Weihe and coworkers [92-94]. It follows that the direction of propagation of the crack is governed by the shape of the damage surface employed in the constitutive law of the material. Figure 2.10 shows the study reported in reference [32], included in the compendium, where different crack patterns are derived from the use of various cracking criteria in a cylindrical specimen subjected to mode III loading. In Figure 2.11, the fracture surface computed using an orthotropic Rankine damage model is compared to the real pattern obtained in a piece of chalk.

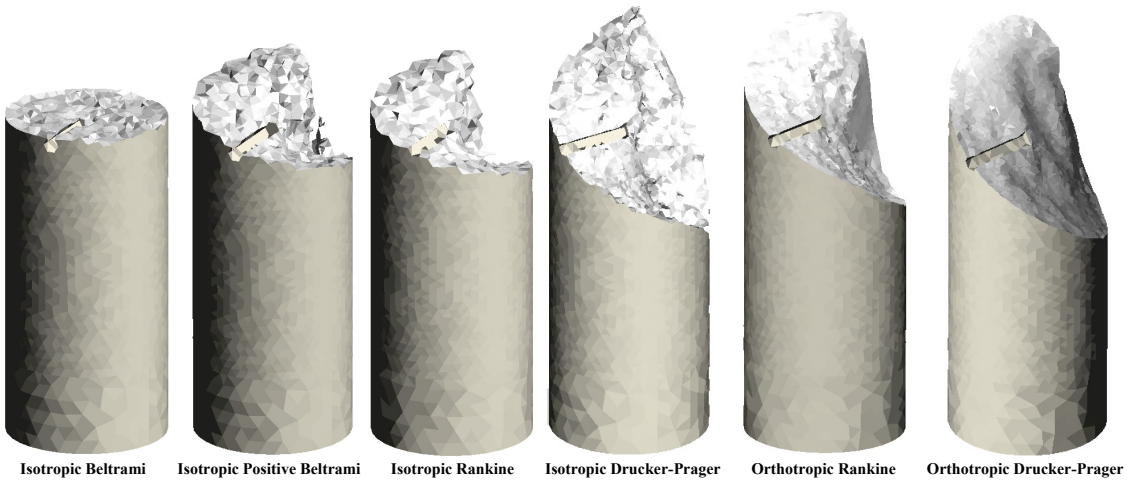

Figure 2.10: Crack surfaces computed with different cracking criteria in a cylindrical specimen subjected to mode III fracture using mixed FE [32]

Despite the fact that the direction of propagation of the crack is implicitly provided at the continuum level by the constitutive law, the lack of mesh objectivity of the standard FE formulation in solid mechanics critically pollutes the resulting discrete computed solution. This issue is originated by the absence of local convergence of the FE formulation in terms of stress and strain and poses a major challenge in both embedded and smeared models. The direction of advance of the fracture is controlled by the local stresses developing in the area of the crack tip, which are computed inaccurately in that region by the standard FE.

Given the nonlinear nature of the problem, introduced by the nonlinear material constitutive law, lack of uniqueness of the solution ensues in the discrete problem: many different results covering a wide variety of crack trajectories are able of reaching global convergence criteria. This, combined with the local discretization error of the standard FEM, results in the spurious dependency of the crack trajectory following from the computed FE model; the correspondence between the discrete and continuous problems is lost.

As is pointed out in reference [27, 35], even though linear order elements are usually employed, the use of higher order elements does not solve the problem of lack of local accuracy of the standard FEM. In situations involving strong displacement gradients and discontinuities such as in cracking, the higher order derivatives involved in the convergence estimates are not bounded either [27]. On the other hand, it has been verified that the mixed ε/u FE formulation has local convergence in terms of strain and stress [26, 27] and, therefore, is able of producing mesh objective results [30-35].

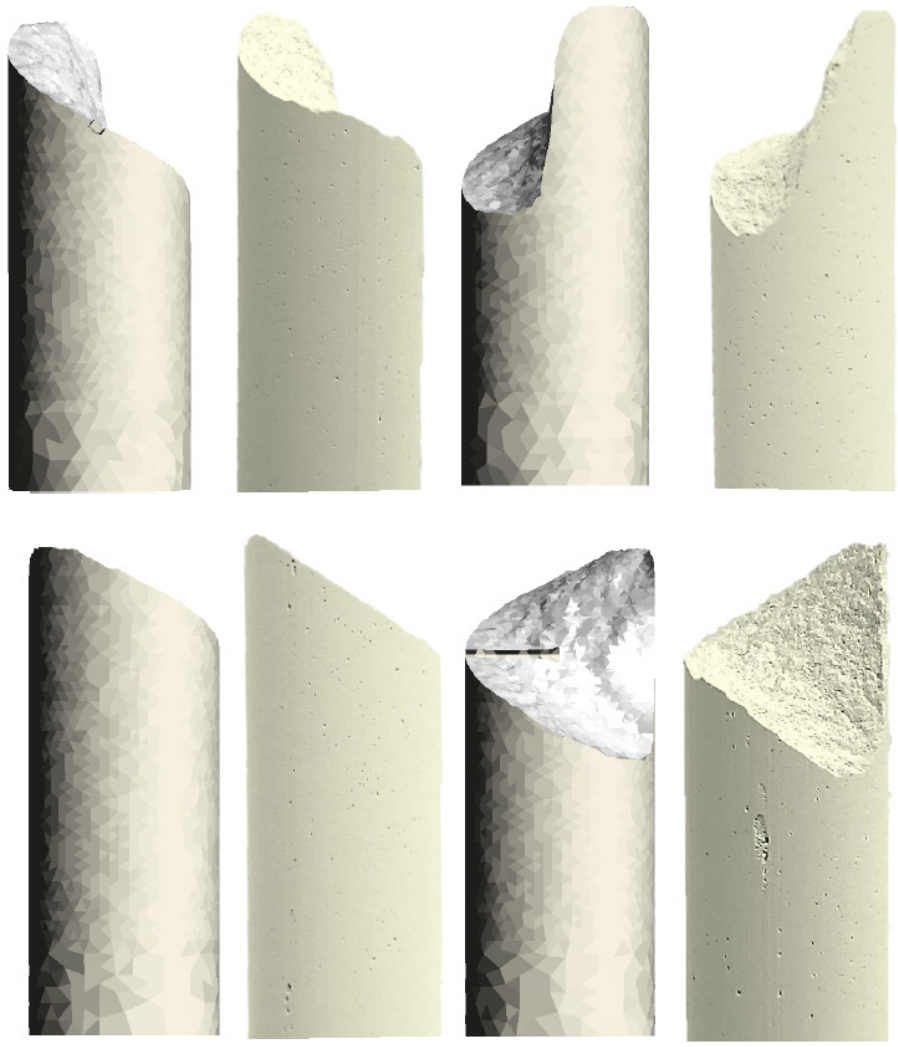

Figure 2.11: 3D simulation of a torsion test on a solid cylindrical specimen using mixed FE and an orthotropic Rankine damage model compared to the crack surface obtained in a piece of chalk [32]

Figure 2.12 shows a representative example, the computed stress field in the area of the tip of the notch in a linear elastic beam subjected to mixed mode bending for both standard and mixed FE. Visibly, the strain and stress fields become singular at the tip of the notch. When using the standard formulation, the computed solution is able of reaching global convergence criteria, but approximates very poorly the stresses in that area. This problem is not amenable through mesh refinement. As explained in reference [27], local error estimates are unbounded for the stresses and strains. Neither does the rounding of the tip of the notch resolve the issue; difficulties related to the lack of convergence of the FE solution will materialize as soon as the material behavior becomes nonlinear and a localized crack of width $b = h$ starts progressing through the FE mesh creating a singular stress field near its tip [27]. Conversely, the mixed formulation guarantees the local convergence of the strain and stress fields. Ensuingly, this method can produce reliable results in the area near the crack tip, which is a crucial aspect when computing fracture propagation.

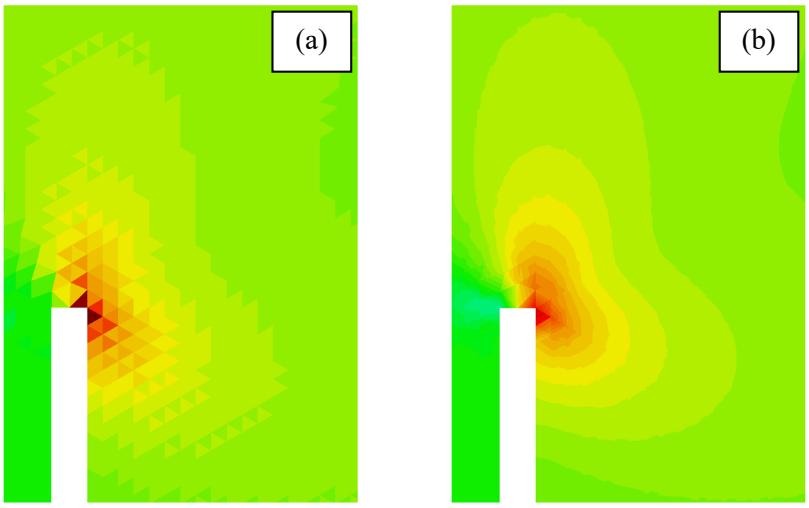

Figure 2.12: Contours of the major principal (elastic) stress field around the tip of a notch in a mixed mode bending test computed using triangular elements with the (a) standard and (b) mixed formulations

Figure 2.13 shows a mesh dependency study, taken from reference [33], which is included in the compendium, where the performance of the standard and mixed FE formulations are compared. It can be seen that the computed crack trajectory of the standard displacement based formulation is dependent on the orientation of the finite elements, while the mixed FE method produces mesh objective results for all the different FE alignments considered. Additional comparisons between the standard and the mixed formulations can be found in reference [35], also included in the compendium.

The issue of the spurious mesh bias arising from the lack of local convergence of the standard FE formulation is prevented when employing regularized crack models in which the problem of fracture is regularized at continuum level. The discrete FE model inherits the regularity introduced in the continuum setting; following this approach, the strong displacement gradients generating the lack of mesh objectivity are avoided while the resulting computed strain and stress fields are smoothed. This strategy presents the disadvantage of needing a refined level of FE resolution of the strain localization band, which requires the use of extremely fine meshes, especially when compared to the embedded and smeared methods.

In embedded crack models, the location and orientation of the crack needs to be a priori determined to insert the enriched discontinuity modes representing the fracture in the FE solution. For this, a criterion for crack propagation is introduced. However, if this criterion is defined exclusively in terms of the local stresses and strains computed at the tip of the crack, the lack of local convergence of the standard FEM pollutes the computation of the direction of advance of the crack, producing mesh dependent fracture paths. Also, as shown in Figure 2.14, the issue of lack of geometrical continuity of the resulting crack path appears. Spurious locking, lack of convergence of the global equilibrium problem and even spurious crack branching in the computed solution have been documented to appear in embedded crack models when the continuity of the crack path is not enforced [95-99]. For these reasons, the application of auxiliary crack tracking techniques is introduced in embedded crack models, despite the fact that, as mentioned in reference [27], “there is no variational justification for their use”. Tracking techniques are usually defined to include (i) a mesh objective criterion for deciding on the direction of crack propagation and (ii) an algorithm for imposing crack path continuity.

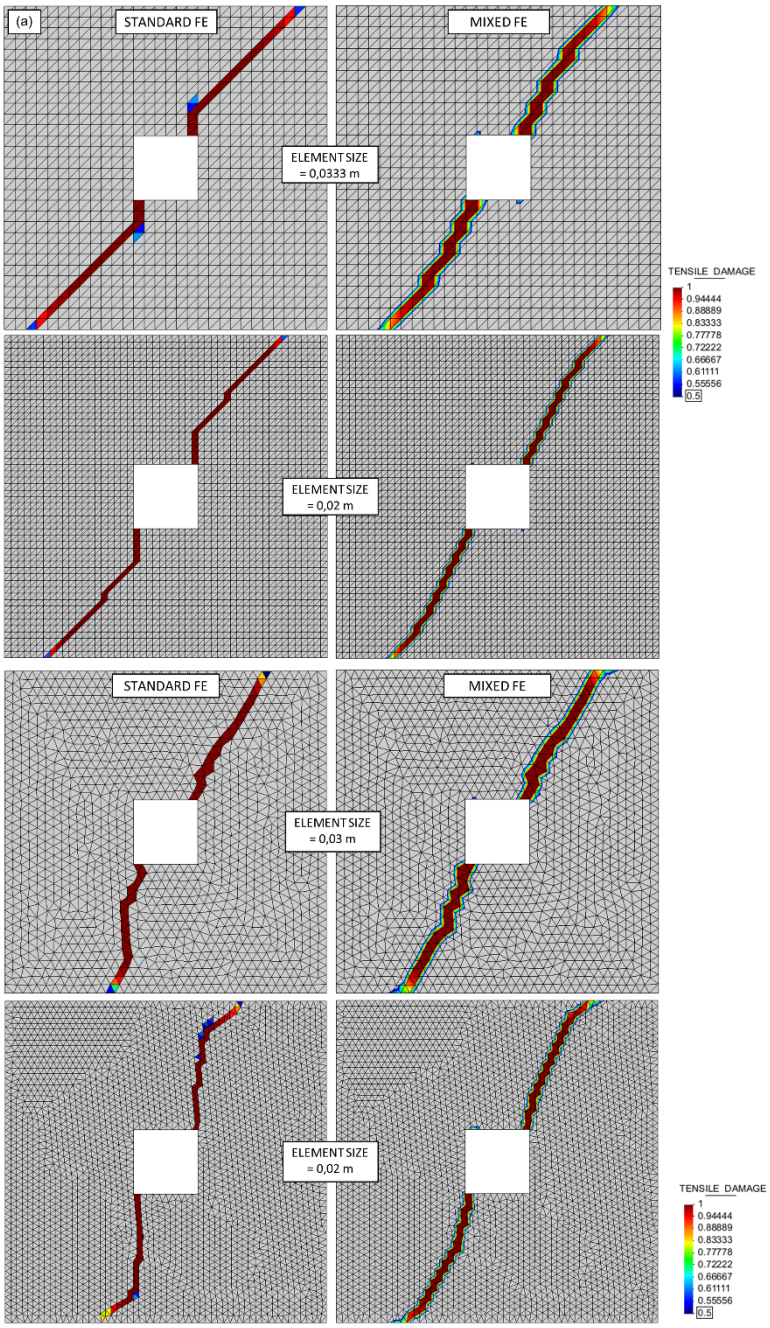

Figure 2.13: Mesh dependency study comparing crack trajectories computed with (left) standard FE and (right) mixed FE with varying element orientations and sizes [33]

On the one hand, embedded approaches such as the EFEM and the XFEM require the specification of an explicit criterion for the determination of the direction of crack progression to insert the discontinuity in the FE formulation [20, 95, 100-103]. This criterion needs to be defined so that the crack path is computed with mesh objectivity, not relying solely on the discrete local stress and strain field, affected by local discretization errors. Also, the criterion adopted is required to be consistently linked to the constitutive behavior of the material [28]. On the other hand, tracking techniques are employed to ensure crack path continuity in the FE solution [104]. Instead of inserting the discontinuity in the center of the FE, it is placed in such a way that it meets the discontinuity already present in neighboring elements [96], as shown in Figure 2.14. This alleviates the issues of spurious stress locking in the computed solution. After determining the direction of advance of the crack, tracking algorithms differentiate between the set of elements crossed by the discontinuity, where the nonlinear behavior of the material is allowed to take place,

from the set of FE which maintains a linear elastic behavior [27]. Therefore, these criteria for deciding on crack progression and location are over-imposed on the local constitutive law of the material.

In reference [102] it is shown that the EFEM produces spuriously mesh dependent results when no tracking method is used. Reference [102] also includes a comparison with a standard smeared crack model; it is exposed that both methods generate very similar mesh biased computations. Conversely, references [28, 29, 99, 105-107] expose that smeared crack models are able of achieving mesh objective results when tracking techniques are simultaneously implemented.

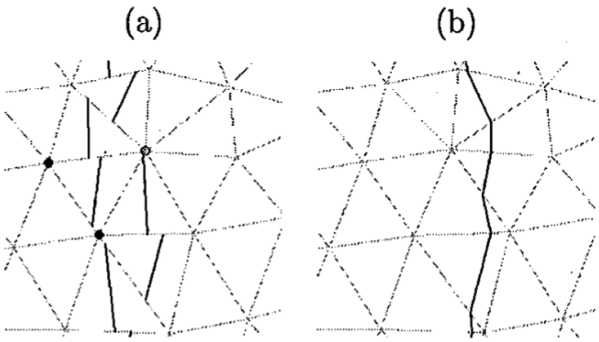

Figure 2.14: Crack pattern computed with an embedded model (a) without imposing crack path continuity and (b) enforcing it [96]

The use of tracking algorithms avoids the employment of purely local criteria for deciding on crack propagation and ensures mesh objectivity [104]. However, it presents some limitations, which need to be specifically resolved. For example, when considering a beam subjected to bending, the crack trajectory in many algorithms cannot develop past the neutral axis because most tracking methods introduce a criterion according to which the direction for fracture progress is perpendicular to the major principal stress [27, 108]. Also, they require special considerations to introduce the ability to model the phenomenon of branching in a physically meaningful way [27, 63].

2.2.3 Strength and fracture toughness. Structural size effect

Structural size effect refers to the phenomenon according to which the load capacity and the brittleness, once normalized with size, are comparably smaller in larger structures. This causes the behavior of real sized structures to deviate from laboratory observations performed on smaller specimens, which is a big concern in a wide range of engineering applications [109-114]. A more detailed overview of the phenomenon is presented in reference [35], included in the compendium of publications of this thesis.

Although many causes have been found for this phenomenon, it has been established that the main one, by far, is related to energetic aspects [115-120]. In quasi-brittle failure, the relation between the stored elastic energy in the structure and the energy engaged into the process of crack formation is not constant in geometrically similar specimens of varying sizes. Consequently, this phenomenon is fundamentally related to failure in softening materials and any model aiming to reproduce quasi-brittle cracking is required to be able to replicate structural size effect.

Bazant's size effect law describes the relationship between the load capacity of a structure and its size [109, 115, 119, 121]. It has been derived from both experimental observations and theoretical considerations. Its simplest form is

$$\sigma_{N_u} = B f_t \left(1 + \frac{L}{L_0}\right)^{-\frac{1}{2}} \tag{2.1}$$

where σ_{N_u} is the nominal strength, defined as

$$\sigma_{N_u} = c_n \frac{P_u}{Lt} \text{ (2D Scaling)}; \quad \sigma_{N_u} = c_n \frac{P_u}{L^2} \text{ (3D Scaling)} \tag{2.2}$$

with L being the characteristic size of the structure, t the thickness, P_u its load capacity, f_t the strength of the material and L_0 a reference structural size. B is a dimensionless parameter dependent on the geometry and boundary conditions of the specimen but not on its size and c_n is a dimensionless constant that may be arbitrarily selected.

Figure 2.15 displays the behavior exposed by Bazant's size effect law in Eq. (2.1). It shows how for small structures, with L/L_0 being much smaller than 1, the influence of structural size in the nominal strength disappears. In such case the load capacity is regulated by the tensile strength of the material and predictions based on limit analysis hold. For large structure, with the ratio L/L_0 being much larger than 1, the nominal strength becomes inversely proportional to the square root of the structural size. In such case, criteria based on fracture toughness and critical stress intensity factors, such as those used in Linear Elastic Fracture Mechanics (LEFM), are applicable. However, quasi-brittle fracture involves the whole range of intermediate size cases, from one type of failure to the other. Therefore, it is required to consider both the strength and the fracture toughness (or the fracture energy) in the nonlinear constitutive law of the material for accurately representing the behavior for all possible structural sizes.

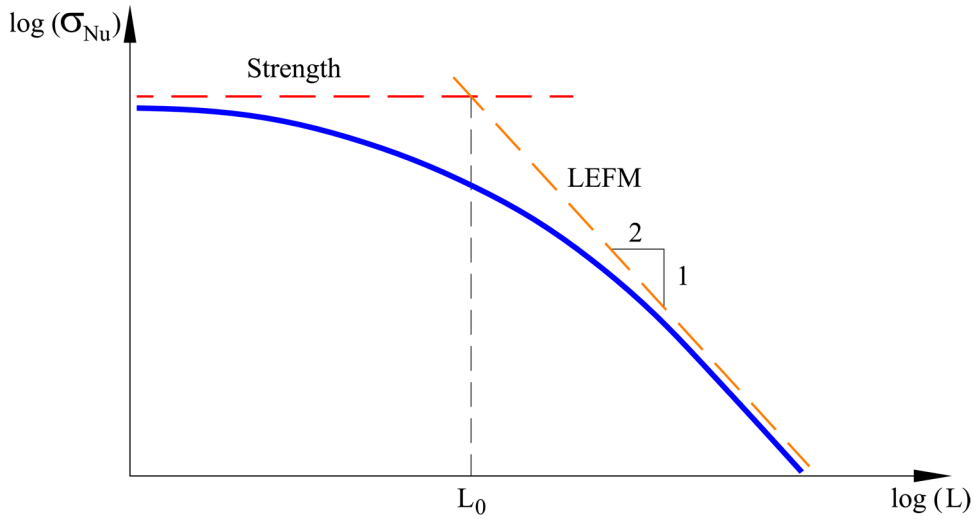

Figure 2.15: Bazant's size effect law

In this regard, reference [78] discusses on the fact that both the strength of the material and the fracture energy are essential ingredients for modelling fracture. Griffith's theory of fracture provides an energetic criterion for crack propagation and does not incorporate the strength. As mentioned in reference [78], numerous phase-field models, based on the regularization of Griffith's theory of fracture, inherit from this shortcoming and are unable to reproduce crack initiation, also called crack nucleation, which is a phenomenon governed by the strength of the material and requires the definition of a stress-based cracking criterion. Consequently, neither can

they replicate structural size effect and they are limited to brittle fracture. In reference [60] the successful numerical simulation of size effect with phase-field is reported, through the incorporation of a strength criterion in the model.

The dimensional analysis performed in reference [120] shows that, when softening materials are considered, the brittleness of the structural problem is dependent on its size. This is confirmed by experimental evidence. In Figure 2.16 is shown how, in force vs. displacement curves normalized with size, the nonlinear branch descends more rapidly and the dissipated energy is relatively smaller in larger structures. Failure takes place in a more brittle manner in larger structures while smaller ones behave in a more ductile way.

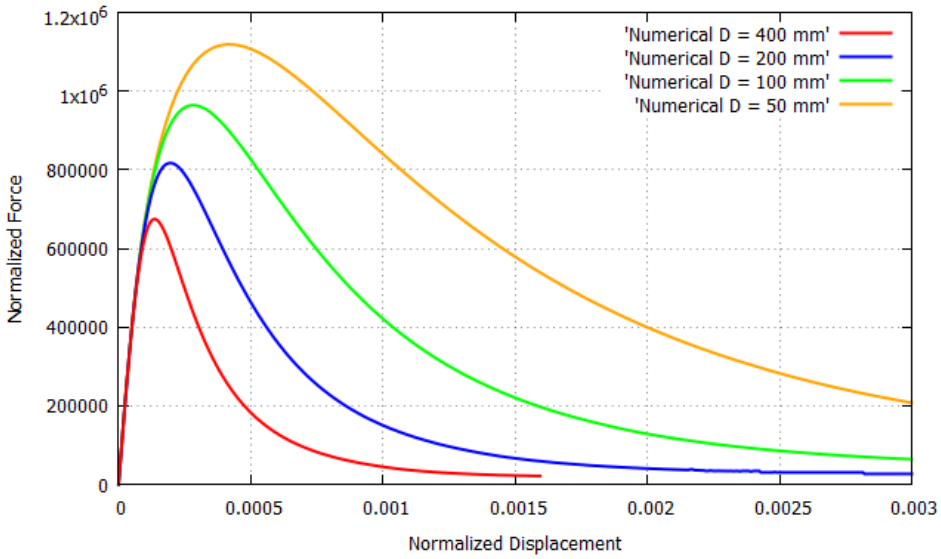

Figure 2.16: Force-displacement curves, normalized with size, of geometrically similar beams of varying depths *D*, from 50 mm to 400 mm, exhibiting size effect, computed with mixed FE [35]

In reference [120], the brittleness number Π_B is derived from the dimensional analysis. Π_B governs the nonlinear behavior of the structure and is equal to the ratio $L/\mathcal{L}$ of the characteristic size of the structure L to Irwin's material length $\mathcal{L} = EG_f/{f_t}^2$, where E is Young's modulus, f_t is the (tensile) strength and G_f is the fracture energy, that is, the energy dissipated per unit of area related to a crack developing in the material.

Modelling structural size effect requires the correct computation of the dissipated energy during the fracture process. Regarding the different alternatives of crack representation at the continuum level, when *sharp cracks* are considered, the total energy engaged in the development of the fracture is proportional to the resulting area of the crack surface. However, when considering *regularized cracks*, at continuous level, the energy dissipation is proportional to the volume of the localization band [86, 87]. Consequently, to guarantee the correspondence between the sharp and regularized approaches, in the latter the fracture energy per unit area, G_f, is regularized with the crack bandwidth b in the constitutive laws. This is equivalent to replacing G_f by the energy dissipated per unit volume $g_f = G_f/b$. In this manner, the brittleness of the original problem ensues

$$\Pi_B = \frac{L}{b} \cdot \frac{b}{\mathcal{L}} = \frac{L}{\mathcal{L}} \tag{2.3}$$

In the discrete FE problem, the embedded, smeared and regularized models need to be considered separately. In *embedded crack models,* the adopted traction-jump laws define the softening behavior in terms of the fracture energy of the material. Therefore, size effect is straightforwardly

considered. In *smeared crack models,* the regularization width b is defined according to the finite element mesh resolution; $b = \alpha h$, where h corresponds to the FE size and α is a constant dependent on the FE formulation. In standard FE $\alpha = 1$ while for mixed FE $\alpha = 2$. In either case the same brittleness number is obtained

$$\Pi_B = \frac{L}{\alpha h} \cdot \frac{\alpha h}{\mathcal{L}} = \frac{L}{\mathcal{L}} \tag{2.4}$$

confirming the consistency between the continuum and discrete problems in terms of fracture energy dissipation and verifying mesh size objectivity, in accordance to the Crack Band Theory introduced by Bazant and Oh [12].

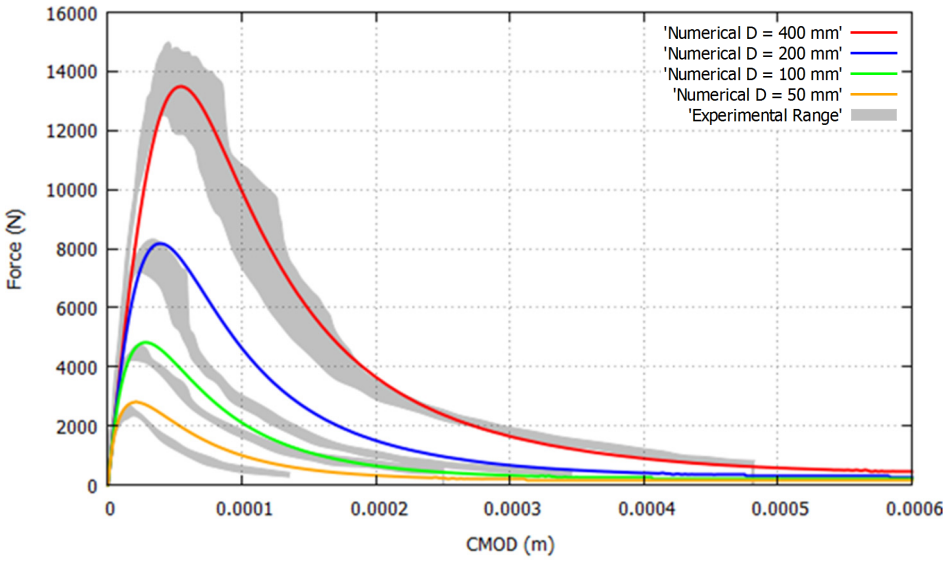

Figure 2.17: Structural size effect: Force-Crack Mouth Opening Displacement (CMOD) curves of geometrically similar notched beams computed with the mixed FEM [35]

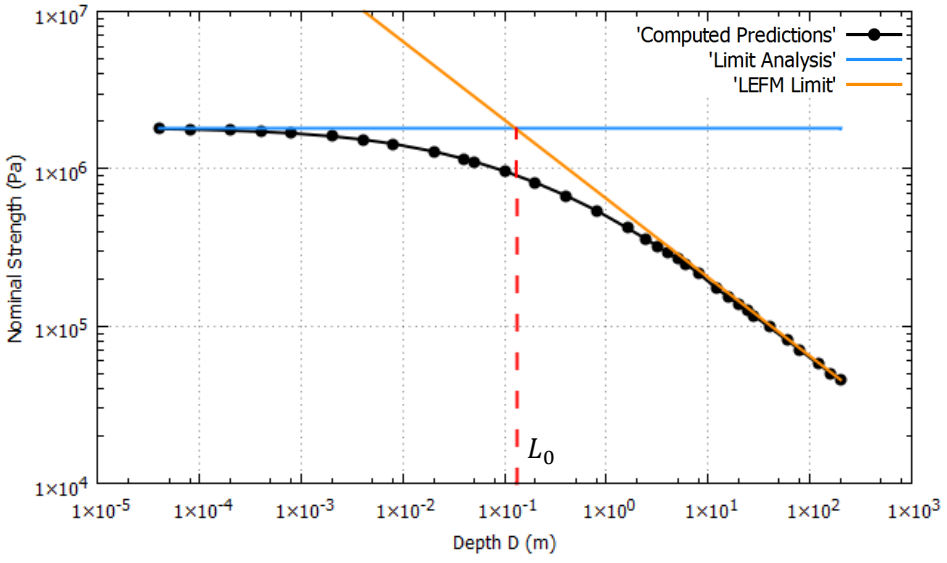

Figure 2.18: Computed predictions of the nominal strength vs. beam size for a series of geometrically similar notched beams using the mixed FEM [35]

In regularized crack models, two interpretations of the crack bandwidth b have been proposed. The length scale has been originally interpreted as a material property that acts as a localization limiter, so that the interpretation of Eq. (2.3) holds. In phase-field models b is introduced as a

regularizing length, so that Eq. (2.3) also applies. If this regularizing length is linked to the resolution of the mesh, then Eq. (2.4) can be considered. In any of the cases, size effect can be reproduced accurately.

Figure 2.17 shows an application of the enhanced smeared crack model reported in reference [35] in which the behavior of four geometrically similar notched beams with different sizes is numerically reproduced using the mixed FEM. It can be observed how the structural size effect displayed by the experimental test is matched remarkably well by the numerical results. Figure 2.18 exhibits how the computed nominal strengths of a series of geometrically similar beams with varying sizes follow Bazant's law over a wide range of structural sizes.

In the following sections, three numerical methods for modelling quasi-brittle fracture are examined in detail: (i) the XFEM, (ii) the mixed FEM and (iii) the Phase-field model, as representative techniques of the embedded, smeared and regularized crack models, respectively. They have been selected because of their outstanding merits.

2.3 XFEM

In the Extended Finite Element Method (XFEM), the standard displacement based FE formulation in solid mechanics is enriched, that is, extended, by introducing additional degrees of freedom and discontinuous interpolation functions to explicitly represent an embedded sharp crack in the discrete FE domain without the need of performing remeshing operations, which are difficult to implement and computationally burdensome.

The XFEM [17-20, 122] was proposed by Belytschko and coworkers at the end of the 20th century as an advance with respect to the previously existing discontinuous and embedded approaches. The strategy employed for enriching the FE solution, using functions satisfying the Partition of Unity property, was first introduced by Babuska and coworkers [123, 124] and was also applied in the so-called Generalized Finite Element Method (GFEM) [125-127]. Nowadays, there is general consensus that the GFEM and the XFEM are "basically identical" [128-133] and they are often referred to as the GFEM/XFEM.

First, sharp cracks were modelled in the discrete domain through a separation of the finite elements along their edges by doubling the nodes. Clough in 1962 [134] and Ngo and Scordelis in 1967 [135] analyzed pre-defined cracks, while Nilson in 1968 [136] was the first to evaluate fracture propagation according to a criterion set in terms of stress. Later, more involved remeshing approaches were proposed [137-140] where the crack is introduced by remeshing elements that are encountered along its trajectory. These approaches were found to be spuriously mesh dependent and, more importantly, involved a change in the mesh topology which increases their computational cost. Similarly, techniques considering the inclusion of cohesive interface elements [82, 141-145] representing the crack have been developed. However, all these techniques suffer from spurious mesh dependency unless a crack tracking technique or the smoothing of the FE solution is introduced [146, 147]. More details are given in the reviews of references [148, 149].

An improved technique proposed to consider sharp cracks is the Embedded Finite Element Method (EFEM), also referred to as the Strong Discontinuity Approach, in which the approximation of the displacement field is enriched to introduce the discontinuous displacements due to the crack in the discrete FE solution. Pioneering work by Ortiz at al. [13] was followed by Belytschko et al. [14] and others [15, 96, 150-153]. Reference [154] gives an extensive review of this topic. Similarly to the XFEM, the main advantage of the EFEM with respect to previous techniques is that no remeshing is required.

As generally used, the main difference between the EFEM with respect to the XFEM is the conformity of the extended displacement field. In Figure 2.19, a comparison regarding inter-elemental displacement continuity between conforming and non-conforming embedded formulations is shown. In the EFEM the extra degrees of freedom and correspondent static relations are introduced and established at element level; in this way, the additional unknowns may be locally condensed at the cost of inter-element displacement continuity [75]. Therefore, in practice, no supplementary nodal unknowns are introduced in the discrete FE problem to be solved. In the XFEM, the enrichment is introduced at nodal level and inter-elemental conformity of the enrichment functions is preserved. This results in additional degrees of freedom being added in the computed discrete FE problem. In references [75, 154-156] a comprehensive comparative study between the EFEM and the XFEM can be found. The enrichment used in the XFEM usually presents a better precision than the one used in EFEM for representing separation modes [75].

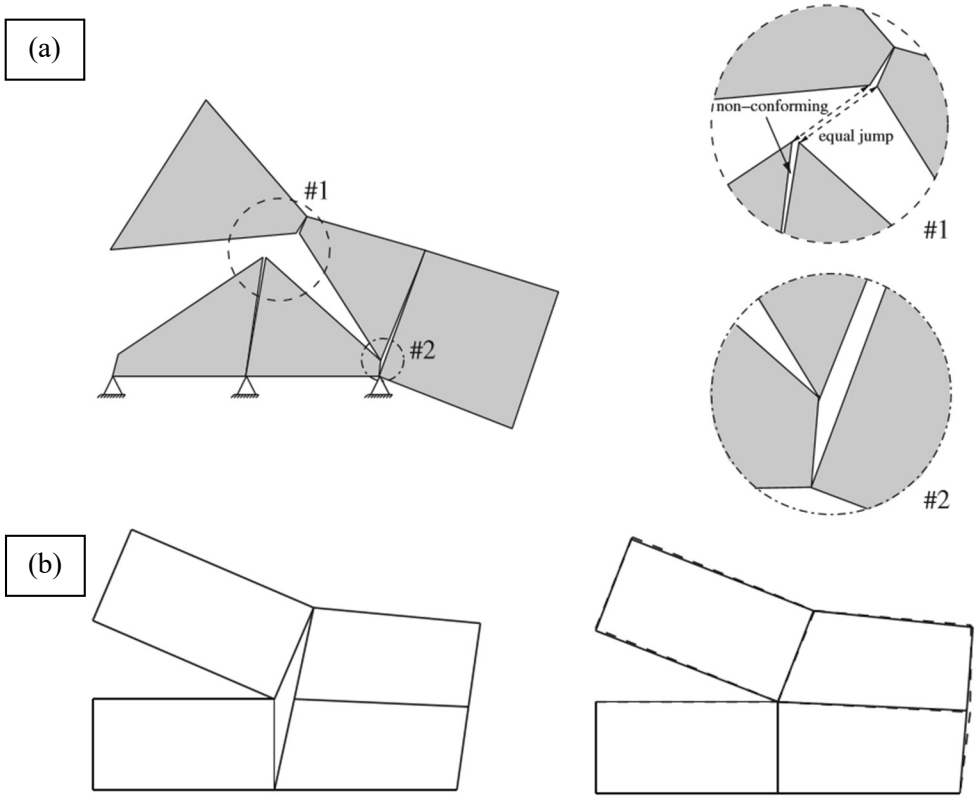

Figure 2.19: Non-conformity in the EFEM: (a) computed crack path with the EFEM, (b) comparison of non-conforming and conforming embedded formulations [156]

The implementation of embedded crack models requires the use of auxiliary crack tracking techniques to determine the location and orientation of the crack inside the domain. Several alternative strategies have been proposed, which can be seen in the review of reference [99]. However, these methods are established in a discretionary fashion, outside of the variational structure of the problem and violate the constitutive law of the material of the elements that are not crossed by the crack. The need of employing auxiliary crack tracking techniques is one of the largest drawbacks in the application of the XFEM.

Within the EFEM and XFEM frameworks, some approaches have proposed the representation of the displacement jump caused by the fracture in a regularized manner, considering regularized interpolation functions to represent the crack [157-160]. The resulting localization band introduced inside the FE solution has a width $b \leq h$, with b being treated as a numerical parameter

that needs to be selected. This strategy alleviates the numerical issues related to the use of discontinuous enrichment functions in embedded crack models.

In reference [75], Wu presented a unified framework that incorporated both the EFEM and the XFEM for modelling cohesive cracks. Using the variational multiscale method, a fine scale refinement containing the displacement jump across the crack is hierarchically added to the regular approximation of the displacement field. The difference between the EFEM and the XFEM lies in the approach adopted for constructing the discrete subspace for the fine scale.

The application of the XFEM to the problem of fracture is founded in two keystones: (i) the Partition of Unity property applied to locally enhance the FE approximation space so that conforming discontinuous displacements may be included only where the crack develops and (ii) the resulting variational form of the problem according to the embedded crack concept, which is able of accommodating Griffith's theory and quasi-brittle failure through the softening traction-separation law.

2.4 Mixed FEM

The mixed strain/displacement ε/u FE formulation follows the well-established framework of the smeared crack approach and the crack band theory. The discontinuous displacement caused by the crack is smeared across a band of small but finite thickness; this results in a localized but bounded strain field inside the crack band. Due to the enhanced accuracy of the mixed formulation in terms of strains and stresses, mesh-objective solutions are attained in quasi-brittle fracture. Following this approach, the setting of the problem of fracture in the continuum framework remains unaltered.

On the one hand, in the mixed ε/u FE formulation, in contrast to the standard displacement based FEM, the strain and the displacement fields are interpolated independently. This introduces a kinematical enhancement that allows to increase the order of convergence of the strain and stress fields and allows to achieve the mesh objectivity of the discrete FE solution, without the need of using auxiliary crack tracking techniques. On the other hand, the local format of the cracking problem is preserved, without introducing gradient or higher order terms in the constitutive law or regularizing terms in the variational form.

The use of a mixed FE formulation based on the Hellinger-Reissner variational principle [161-163], with both stresses and displacements as unknowns, was for the first time discussed in detail by Fraeijs de Veubeke in 1965 [164]. In the same year, Herrmann [165] proposed the use of a mixed FE formulation for incompressible and nearly incompressible materials with displacements and a variable depending on the pressure as primary unknowns. From 1968 onwards, the first numerical implementations and applications appeared [166-170], and the terms mixed finite element and mixed variational principle started being used for this approach [171-173].

The advantage of a mixed FE formulation over the irreducible one is that it allows increasing the order of convergence and, therefore, the accuracy of the fields selected as additional primary unknowns [174]. This feature is crucial in many applications where standard formulations have been proved to fail: incompressible and nearly-incompressible problems in computational solid [165, 175-178] and fluid [174, 175, 179-181] mechanics, shear locking in thin plates [182, 183] and shear and membrane locking in shells [167, 169, 170], to name just those better known.

With respect to quasi-brittle cracking, the adoption of a mixed strain/displacement FE formulation serves two purposes, one concerning crack initiation and propagation and the other regarding crack representation.

Following the smeared crack approach, the initiation and propagation of fracture is defined according to the stress-based criterion adopted in the constitutive law. The conformance to Griffith's theory is established during the nonlinear softening stage, which introduces the quasi-brittle behavior of the material, where the fracture energy of the crack needs to be objectively defined, in agreement with the crack band theory [12]. The capacity of the FE formulation to satisfactorily compute crack propagation depends crucially on the correct evaluation of the strain and stress field at the tip of the crack; the direction of crack progression is governed by the surface of the crack criterion adopted.

Regretfully, the standard FE formulation does not guarantee the local convergence of the stresses and strains in the area near the tip of the crack. This causes the spurious mesh dependency of the computed solution when the mesh is not appropriately aligned with the crack path. When using the mixed FEM, the order of convergence of the stress and strain fields is increased, and therefore the local convergence of the problem is ensured, which allows to achieve mesh objective results [26, 27]. Conversely, the PFM does not exhibit a spurious mesh dependency because the problem is regularized at continuum level, so that quasi-singular stress states never develop in the discrete FE problem.

Also, standard FE exhibit a poor capability for reproducing separation modes in a discrete smeared manner due to the inter-elemental discontinuity of the strains. Contrarily, mixed FE perform much better, as the underlying strain and stress fields are inter-element continuous. The use of mixed FE formulations allows to reconsider the use of orthotropic crack models, as the resulting discrete stress field is practically free from locking [32, 34].

As most of the nonlinear constitutive laws are defined in a strain-driven structure, in which the stress is evaluated in function of the strain, the adoption of a mixed strain/displacement formulation is more convenient than a stress/displacement one. The mixed ε/u FEM allows to readily adopt a large number of constitutive laws already established under this format [31, 32]. Symmetry of the formulation is ensured when the constitutive equation is introduced in secant form [31-33, 35].

The application of the mixed FEM to the problem of fracture is founded in two keystones: (i) setting the continuum variational form in terms of the strain and displacement fields, akin to the mixed Hellinger-Reissner principle, and (ii) the spatial regularization of the crack at the discrete level according to the smeared crack concept, ensuring the mesh size objectivity of the dissipated energy. The coupling of these two components constitutes a mixed FE formulation for quasi-brittle failure. It can naturally follow Griffith's theory of fracture, while being able to model crack nucleation. It includes as well a criterion for the direction of crack propagation through the underlying constitutive law.

2.5 Phase-field model

The phase-field model can be included, together with the nonlocal and gradient-enhanced models, in a broader family of regularized methods in which the *continuous statement of the problem* is modified so that the development of the strong displacement discontinuity caused by a sharp crack is avoided by transforming it into a band of finite thickness where the strains are highly localized but the regularity of the strain field is enforced. The resulting regularized continuous problem can

be discretized via a FE formulation which lacks inter-element continuity in the strains, while achieving mesh objectivity.

In nonlocal integral models [36-40, 184] the common continuum mechanics theory is altered by replacing a locally evaluated state variable, usually the strain field, by a nonlocal counterpart evaluated as a weighted integral average over a predefined spatial domain of finite diameter. This results in a smoothing of the strains driving the constitutive behavior, with intensity dependent on the range of the spatial averaging. Promoters of nonlocal models have claimed that this range is an internal length, a material property. A review of this topic is given by Bazant and Jirasek [185].

In gradient-enhanced models [41-46, 184], the common continuum mechanics formulation is altered by changing the definition of an originally locally defined variable, e.g. the equivalent strain, by its nonlocal counterpart, whose definition involves higher order derivatives (usually a Laplacean). The definition of the nonlocal variable may be either explicit, involving the Laplacean of the local variable, or implicit, involving the Laplacean of the nonlocal variable. In the latter, the method requires the solution of a Helmholtz-type boundary value problem. A length scale is required in the definition of the nonlocal variable for dimensional consistency. This length determines the width of the localization band in the regularized problem. Promoters of gradient-enhanced models have advocated that this length is an internal length, a material property.

Introducing a length scale that acts as a localization limiter in the continuum setting does regularize the problem, but this may cause a deviation from the physical problem of cracking. This accounts for the many inconsistencies found by the users of this type of models.

In reference [186] it was analytically proved and numerically shown that the nonlocal model proposed in reference [36] and the gradient-enhanced model of reference [41] produce non-physical results. Specifically, it was shown that in mode I fracture situations: (i) the (elastic) stress at the crack tip is not infinite, its value being dependent on the chosen material length; (ii) the maximum stress is not located at the crack tip but at a certain distance that changes according to the chosen material length; and (iii) the value of the maximum (elastic) stress is not infinite and also varies according to the material length employed. Consequently, in reference [186] it was proved that these methods predict damage initiation inside the specimen and not at the crack tip. Additionally, it was also shown that they produce incorrect crack trajectories, also dependent on the length scale.

In reference [43] another unintended consequence of introducing a localization limiter was reported: when using the gradient-enhanced formulation [41] the damage spreads out spuriously, and the pretension of a localization band for damage is very much lost. This effect has also been detected in the nonlocal integral model [187].

To avoid the aforementioned issues, several modifications of the original nonlocal and gradient-enhanced models have been proposed, reported and discussed in references [188-190]. These include evolving weighted averaging of the local and nonlocal variables [189, 191], the “over-nonlocal” approach, introducing an averaging with weights larger than one for the nonlocal variable and negative weights for the local one [188, 192] or evolving internal lengths dependent on the degradation of the material [43, 190, 193].

More recently, Phase-Field Models (PFM) for brittle fracture have been proposed and become widely employed [47-51, 194]. PFM are based on the regularization of Griffith’s theory of fracture, in which the sharp crack topology is regularized at the continuum level into a band of finite thickness by inserting in the statement of the problem a scalar phase-field variable as well as its gradient [64]. This scalar phase-field variable, ranging from 0 to 1, is related to the degradation of material and is easily identifiable with a scalar damage field. A length scale controlling the width of the regularization band is required in the definition of the regularized

problem for dimensional consistency. The evolution of the phase-field variable is computed through the introduction of an additional partial differential equation (PDE) in the problem.

The name *phase-field* comes from the original application for which the basis of the method was developed: multiphase problems regarding the creation, evolution, destruction and merging of interfaces (i.e. the boundaries of phases, regions with homogeneous physical properties that can be solid, fluid, etc.) in microstructures within computational material science. It was developed pursuing the idea of avoiding the difficulties resulting from the treatment of sharp interfaces and the use of models requiring to explicitly track these interfaces [195].

PFM were originally proposed as a regularized variational approach to brittle fracture [48, 53, 54]. A length scale parameter governing the width of the localization band is introduced in the continuum setting of the problem so that convergence to a sharp crack occurs when this length scale tends to zero, according to the Γ-convergence theorem [55, 56]. This property is the definitive advantage of PFM over previous regularized models.

Note that originally, in references [47, 49, 50], the length scale introduced in the model is understood as a numerical parameter involved in the mathematical regularization of the sharp crack. This length tends to zero for the diffuse crack to reach "Γ-convergence" to the original sharp crack [49]. However, this length is sometimes defined as an "intrinsic material parameter" [51, 196-198]; this approach misinterprets the original concept and is, as previously discussed, misleading, as it averts the consistency with the problem of fracture.

Lately, the geometrically regularized phase-field model, or phase-field regularized cohesive zone model (PF-CZM), has been introduced [57, 59, 60]. In this approach the incorporated length scale governs the localization bandwidth, but it has negligible effects on the computed global responses, as long as the regularized localization band can be resolved with a sufficiently fine spatial discretization [59]. Therefore, the length scale introduced in this method is a numerical parameter that can be set as small as deemed necessary. In FE analysis, the regularizing length is made dependent on the FE size, so that the crack bandwidth tends to zero upon mesh refinement, guaranteeing the consistency with the original problem. Reference [64] performs a sensitivity study of various phase-field models with respect the internal length scale where it is shown that only the PF-CZM among the ones considered is able to yield solutions independent of the regularizing lengths chosen.

The PFM is founded in two keystones: (i) the variational form of the problem of fracture, defined following Griffith's theory, and (ii) the spatial regularization of cracks, both established at the continuous level. In PF-CZM, the adoption of stress-based damage criteria in the constitutive law of the material provides a criterion for considering crack initiation and implicitly establishes the direction of propagation of cracking. This ingredient, lacking in Griffith's theory [77, 78], allows to introduce the quasi-brittle behavior of the fracture.

2.6 A 10-Point Checklist for modelling fracture

Considering the challenges that have been exposed and addressed by the literature regarding the FE simulation of cracking, the following ***10-Point Checklist***, to be verified by prospective numerical models of fracture, is proposed:

1. **Variational formulation in the continuous setting**
   The statement of the problem of cracking in the continuous setting should rely on a rigorous physical foundation and mathematical framework.

2. **Convergence of the FE formulation**
   Commonly, the regularity of the solution is assumed and the convergence of the FE formulation is verified at global level. When computing fracture, the regularity of the problem is lost and, thus, the local convergence is not guaranteed if the standard FE procedure is used. The FE formulation employed to calculate the problem needs to be designed to overcome this issue and reach convergence of the solution in terms of displacements, strains and stresses.
3. **Strength, toughness and energy dissipation**
   Fracture initiation and propagation depend on both the material strength and toughness. Consequently, numerical models are required to integrate stress and energy release rate criteria. The accurate modelling of structural size effect in quasi-brittle failure relies on the adequate blending of both.
4. **Criterion for direction of propagation**
   Griffith's theory of fracture does not include a criterion for the direction of propagation of cracking. Numerical models need to incorporate one, which can be either implicitly or explicitly defined. Its capability for reproducing cracking in a physically meaningful way needs to be assessed.
5. **Constitutive behavior generality**
   Numerical models for cracking should not be restricted to a few specific constitutive laws. They should be applicable to a wide range of materials and situations. Additionally to exhibiting a cohesive behavior, cracks may also be exposed to complex phenomena such as sliding as well as closure and reopening. In certain applications, the consideration of their nonlinear locally directional character may be required. The ability of the crack model to consider many different behaviors, and with a large degree of complexity, should be analyzed.
6. **Generality and implementation effort**
   The generality of the crack model should allow its application in conjunction with any interpolation basis (triangles, quadrilaterals, tetrahedra, hexahedra, prisms) with as few variations as possible. The implementation of element-dependent specific procedures for numerical integration, sampling or averaging is undesirable.
7. **Cost-efficiency**
   Different FE methods have different unknown variables in various sets of nodes, but they also require varying levels of mesh resolution. All these aspects influence the computational cost involved. Likewise, alternative FE formulations have different levels of accuracy and orders of convergence which determine their overall efficiency.
8. **Multiple, intersecting and branching cracks**
   Practical applications of fracture may often result in multiple, intersecting and/or branching cracks. Some models have considerable shortcomings in addressing these situations.
9. **Auxiliary tracking techniques**
   Many models rely on the use of auxiliary crack tracking techniques, introducing a significant restriction in their capabilities.
10. **Application in 3D**
    Engineering applications require crack models that can be employed in 3D problems. The smeared crack models implemented in commercial codes are routinely applied in 2D and 3D. A substitute model should be able to address the same type of applications.

Chapter 3

Comparative study of the XFEM, the Mixed FEM and the Phase-field model

This chapter contains a comparative investigation of the XFEM, the Mixed FEM and the Phase-field model for fracture. First, the continuum formulation, FE approximation and critical appraisal of the assets and drawbacks of each method are introduced. Then, the study is completed by presenting an exhaustive comparison of several numerical simulations obtained with these three approaches.

3.1 XFEM

In this section, the principal characteristics of the Improved-stable XFEM (Is-XFEM) developed by Wu and coworkers [63, 104, 199, 200] and used in the comparisons of this work, are laid out. The method follows the mathematical framework employed in the Strong Discontinuity Approach [16, 101, 201, 202]. Additional details are given in references [63, 75, 104, 199, 200].

Continuous formulation

Consider the domain Ω divided by a crack S in two parts, denoted Ω^+ and Ω^-, so that $\boldsymbol{u}^+$ and $\boldsymbol{u}^-$ are the displacement fields in their respective subdomain and $\breve{\boldsymbol{u}}$ is the relative displacement field of one part with respect to the other, as shown in Figure 3.1a

$$\breve{\boldsymbol{u}} = \boldsymbol{u}^+ - \boldsymbol{u}^- \tag{3.1}$$

The embedded crack S causes a discontinuity in the displacement field $\boldsymbol{u}$ that is explicitly considered

$$\boldsymbol{u} = \boldsymbol{u}^- + H_S \breve{\boldsymbol{u}} \tag{3.2}$$

where H_S is the Heaviside function which is equal to 0 in Ω^- and to 1 in Ω^+.

According to the variational multiscale method [203, 204], in Is-XFEM, the displacement field is reestablished as

$$\boldsymbol{u} = \bar{\boldsymbol{u}} + \tilde{\boldsymbol{u}} \tag{3.3}$$

where $\bar{\boldsymbol{u}}$ represents the coarse scale displacement field that satisfies the standard regularity conditions and $\tilde{\boldsymbol{u}}$ denotes the fine scale displacement field that incorporates the discontinuity caused by the crack S, as shown in Figure 3.1b. $\tilde{\boldsymbol{u}}$ can be further expressed as

$$\tilde{\boldsymbol{u}} = H_S \breve{\boldsymbol{u}} - \boldsymbol{u}' \tag{3.4}$$

where $\boldsymbol{u}'$ is the regular part of the fine scale, introduced so that $\tilde{\boldsymbol{u}}$ vanishes on the elemental boundaries, as shown in figures 3.1b and 3.1c. Note that $\bar{\boldsymbol{u}} - \boldsymbol{u}' = \boldsymbol{u}^-$.

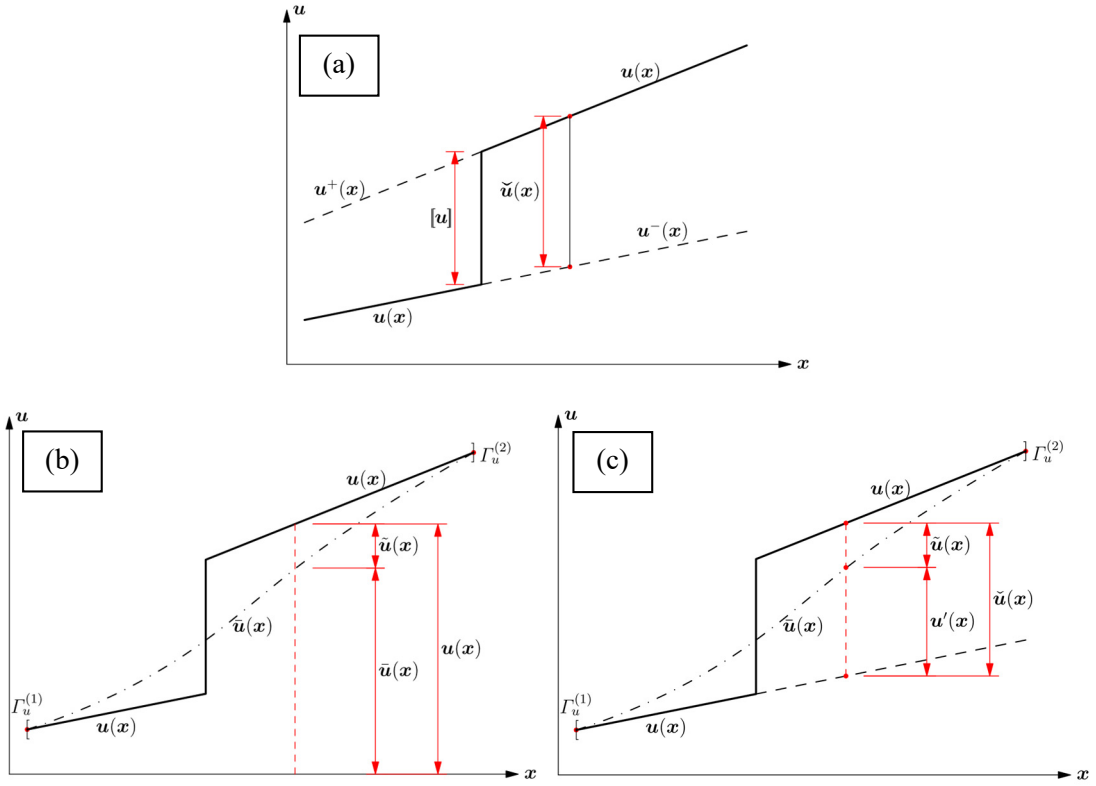

Figure 3.1: Strong discontinuity representing the crack in the continuous setting in Is-XFEM [75]

The strain field is obtained as the symmetric gradient of the displacements

$$\boldsymbol{\varepsilon} = \mathbf{S}\boldsymbol{u} \tag{3.5}$$

where $\mathbf{S}$ is the differential symmetric gradient operator. And, therefore

$$\boldsymbol{\varepsilon} = \bar{\boldsymbol{\varepsilon}} + \tilde{\boldsymbol{\varepsilon}} = \mathbf{S}\,\bar{\boldsymbol{u}} + \mathbf{S}\,\tilde{\boldsymbol{u}} = \mathbf{S}\,\bar{\boldsymbol{u}} + H_S \mathbf{S}\,\breve{\boldsymbol{u}} - \mathbf{S}\boldsymbol{u}' \tag{3.6}$$

Outside the crack, the material is assumed to have a linear elastic behavior, so the following constitutive law can be written in $\Omega \backslash S$:

$$\boldsymbol{\sigma} = \mathbf{D}_0 \boldsymbol{\varepsilon} \tag{3.7}$$

where $\mathbf{D}_0$ is the elastic constitutive matrix; $\boldsymbol{\sigma}$ and $\boldsymbol{\varepsilon}$ are the regular stress and strain fields in $\Omega \backslash S$.

The nonlinear behavior of the crack is introduced as a traction-separation law [63, 200]. Let $\boldsymbol{w}$ be the displacement jump at the crack, equal to $\breve{\boldsymbol{u}}$ evaluated at the discontinuity S, $\boldsymbol{w} = [\![\boldsymbol{u}]\!] = \breve{\boldsymbol{u}}(\boldsymbol{x} \in S)$

$$\boldsymbol{t} = \boldsymbol{E}_S \boldsymbol{w} = \phi \boldsymbol{E}_0 \boldsymbol{w} \tag{3.8}$$

where $\boldsymbol{E}_S$ and $\boldsymbol{E}_0$ are the secant and reference stiffness of the discontinuity, respectively, relating the displacement jump of the crack, $\boldsymbol{w}$, and the traction on the crack surface, $\boldsymbol{t}$. The *localized integrity variable* ϕ describes the cohesive behavior of the crack. ϕ is initially infinite, corresponding to an intact material. During the fracture process, ϕ monotonically decreases to zero as the crack opens.

The evolution of the localized integrity variable ϕ depends on the opening of the crack. A failure criterion, expressed in terms of the normal displacement jump across the crack w_n, is introduced

$$\mathbb{F}(w_n, \kappa) = w_n - \kappa = 0 \tag{3.9}$$

where κ is an equivalent displacement jump threshold. Its current value at time t is computed from the Kuhn-Tucker conditions, so that the irreversibility of the process is guaranteed

$$\kappa = \max\, w_n(\hat{t}) \quad \hat{t} \in [0, t] \tag{3.10}$$

The localized integrity variable ϕ can follow several evolution laws. In reference [63], both exponential and Cornelissen [79] softening functions, shown in Figure 3.2, are considered

$$\phi = \frac{f_t}{E}\frac{1}{\kappa}\exp\left(-\frac{f_t}{G_f}\kappa\right) \qquad Exponential \tag{3.11}$$

$$\phi = \frac{f_t}{E}\frac{1}{\kappa}\left[(1+\eta_1^3\tilde{\kappa}^3)\exp(-\eta_2\tilde{\kappa}) - \tilde{\kappa}(1+\eta_1^3)\exp(-\eta_2)\right] \qquad Cornelissen \tag{3.12}$$

where E is the initial elastic Young's modulus, f_t is the tensile strength and G_f is the fracture energy. The variable $\tilde{\kappa}$ is defined as $\tilde{\kappa} = \kappa f_t / (5.1361 G_f)$. The parameters considered in reference [63] for the Cornelissen softening law are $\eta_1 = 3.0$ and $\eta_2 = 6.93$.

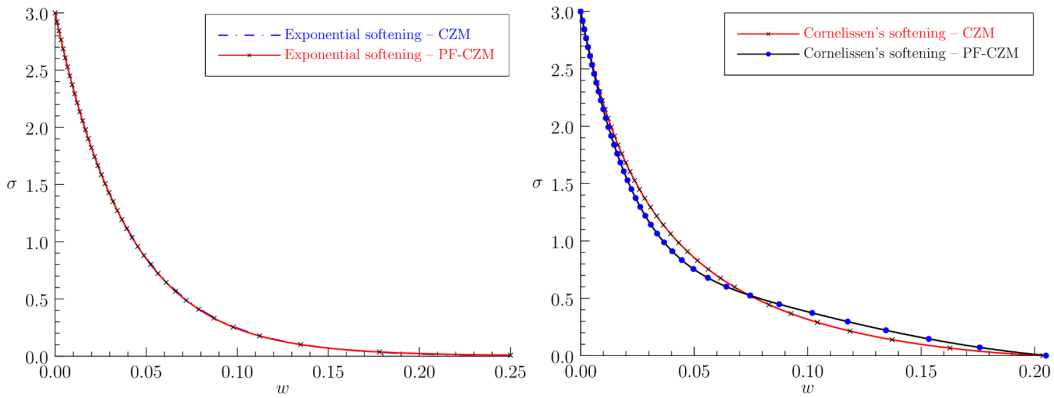

Figure 3.2: Constitutive behaviors considered for the XFEM and the PFM in reference [63]: (a) exponential and (b) Cornelissen softening laws, with $\boldsymbol{w} = \boldsymbol{\omega}$

Equilibrium is enforced as usual through the Cauchy momentum equation

$$\mathbf{S}^T \boldsymbol{\sigma} + \mathbf{f} = \mathbf{0} \tag{3.13}$$

where $\mathbf{S}^T$ is the differential divergence operator, adjoint to the $\mathbf{S}$ in Eq. (3.5), and $\mathbf{f}$ is the body forces vector.

From these considerations, the principle of virtual work is rewritten considering separately the work of the internal forces in $\Omega \backslash S$ and S in which Ω is divided

$$\int_{\Omega \backslash S} \delta \boldsymbol{\varepsilon}^T \boldsymbol{\sigma} \, \mathrm{d}\Omega + \int_S \delta \boldsymbol{w}^T \boldsymbol{t} \, \mathrm{d}S = \int_\Omega \delta \boldsymbol{u}^T \mathbf{f} \, \mathrm{d}\Omega + \int_{\Gamma_t} \delta \boldsymbol{u}^T \bar{\boldsymbol{t}} \, \mathrm{d}\Gamma \tag{3.14}$$

where $\bar{\boldsymbol{t}}$ is the vector of tractions acting on the boundary Γ_t of the domain.

FE approximation

The spatial domain is discretized into FE. The coarse/fine scale decomposition is adopted also in the FE spaces, so that the displacement $\boldsymbol{u}$ is approximated with a discrete interpolation $\hat{\boldsymbol{u}}$ defined as

$$\boldsymbol{u} \cong \hat{\boldsymbol{u}} = \boldsymbol{N}_u \boldsymbol{U} + \tilde{\boldsymbol{N}}_u \tilde{\boldsymbol{U}} \tag{3.15}$$

where $\boldsymbol{U}$ is the vector of the nodal displacements corresponding to the coarse scale and $\tilde{\boldsymbol{U}}$ is the vector of the nodal displacements of the fine scale. Note that the notation bar used in the previous subsection for the coarse scale is here dropped and only the curl used for the fine scale is retained. $\boldsymbol{N}_u$ and $\tilde{\boldsymbol{N}}_u$ are the matrices containing the interpolation functions adopted in the FE approximations. The coarse scale is interpolated on all the nodes of the domain, while the fine scale is interpolated only on the elements intersected by the crack S. Therefore, $\tilde{\boldsymbol{U}}$ are hierarchical enriched degrees of freedom representing the displacement jump caused by the crack.

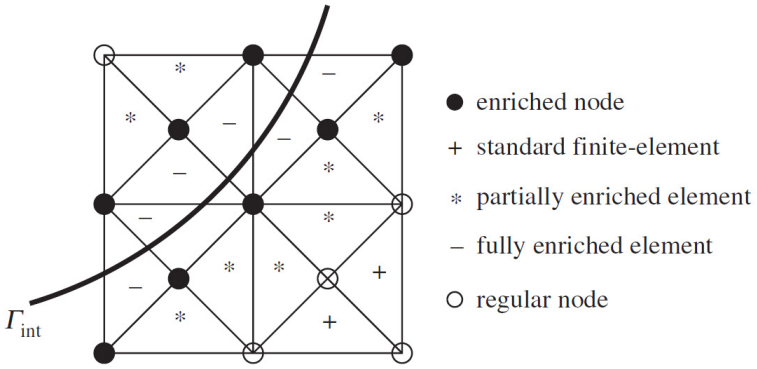

Figure 3.3: Crack path and enriched nodes in XFEM [205]

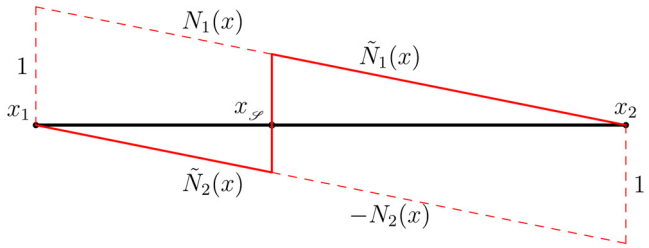

Figure 3.4: Interpolation functions for the coarse and fine scales employed [75]

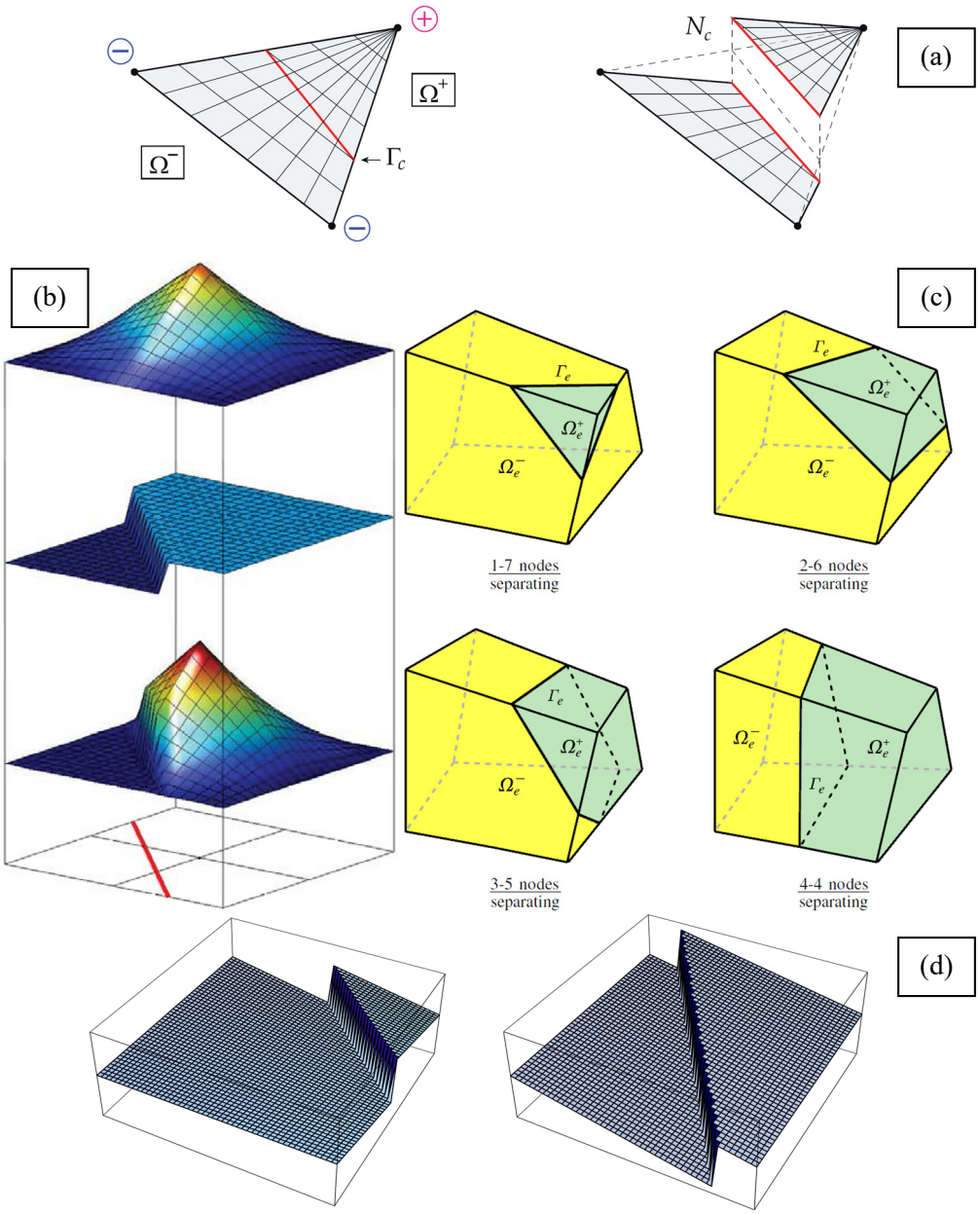

Figure 3.5: Embedding strong discontinuities in the discrete FE approximation: (a) [206], (b) [207], (c) [208] and (d) [102]

The enriched interpolation functions $\widetilde{N}_{u,j}$ incorporated in $\widetilde{\boldsymbol{N}}_u$ for the discretization of the fine scale are

$$\widetilde{N}_{u,j}(\boldsymbol{x}) = N_{u,j}(\boldsymbol{x})\theta_j(\boldsymbol{x}) \tag{3.16}$$

where $N_{u,j}$ are the standard linear shape functions which satisfy the partition of unity property [123, 124] and θ_j are the enrichment functions. References [128, 129, 209, 210] propose using

$$\theta_J(\boldsymbol{x}) = H_S(\boldsymbol{x}) - H_S(\boldsymbol{x}_J) \tag{3.17}$$

This corresponds to the Heaviside enrichment typically employed in the XFEM; the second term is added so that the enrichment functions may vanish at the nodes of the elements that are crossed by the crack, simplifying the implementation of the method.

To construct the interpolation functions, the nodes of a particular element located in Ω^+ and Ω^- need to be identified. That is, the crack has to be exactly located and oriented inside the element, as it can be seen in figures 3.3, 3.4 and 3.5.

The direct use of the Heaviside function for the enrichment causes the ill-conditioning of the problem when the crack trajectory gets too close to the elemental nodes. For this reason, in Is-XFEM, a stabilization term is added to the Heaviside functions used as enrichment [63]

$$\theta_J(\boldsymbol{x}) = H_S(\boldsymbol{x}) - c_s\varphi(\boldsymbol{x}) - (1 - c_s)H_S(\boldsymbol{x}_J); \quad \varphi(\boldsymbol{x}) = \sum_{j\in A^*} N_J(\boldsymbol{x})H_S(\boldsymbol{x}_J) \tag{3.18}$$

where the set A^* includes only the nodes in which the crack is embedded and $c_s \in [0,1]$ is a stabilization parameter. The case $c_s = 0$ corresponds to employing the Heaviside enrichment in Eq. (3.17). References [63, 199, 200] recommend the adoption of values for $c_s \in [0.01,0.1]$.

From Eq. (3.15), the following interpolation of the strain field $\boldsymbol{\varepsilon}$ is derived:

$$\boldsymbol{\varepsilon} \cong \hat{\boldsymbol{\varepsilon}} = \boldsymbol{B}_u\boldsymbol{U} + \widetilde{\boldsymbol{B}}_u\widetilde{\boldsymbol{U}} \tag{3.19}$$

where $\boldsymbol{B}_u$ is the regular compatibility matrix, $\boldsymbol{B}_u = \boldsymbol{S}\boldsymbol{N}_u$ and $\widetilde{\boldsymbol{B}}_u$ is the enriched compatibility matrix, consistent with the definition of the strain field $\boldsymbol{\varepsilon}$ in Eq. (3.6) and with the choice of the enrichment functions for the discrete displacement field. Note that, as shown in Figure 3.6, the matrix $\widetilde{\boldsymbol{B}}_u$ is discontinuous inside the element and, for this reason, specific sampling techniques need to be devised.

Introducing the FE approximation of Eqs. (3.15) and (3.19) in the weak form in Eq. (3.14) and splitting the discrete problem into standard and enriched degrees of freedom (or regular and fine scales), the following system of two equations is obtained:

$$\int_{\Omega\setminus S} \boldsymbol{B}_u^T\boldsymbol{\sigma}\,\mathrm{d}\Omega = \int_{\Omega} \boldsymbol{N}_u^T\mathbf{f}\,\mathrm{d}\Omega + \int_{\Gamma_t} \boldsymbol{N}_u^T\bar{\boldsymbol{t}}\,\mathrm{d}\Gamma \tag{3.20}$$

$$\int_{\Omega\setminus S} \widetilde{\boldsymbol{B}}_u^T\boldsymbol{\sigma}\,\mathrm{d}\Omega + \int_{S} \boldsymbol{N}_u^T\boldsymbol{t}\,\mathrm{d}S = \int_{\Omega} \widetilde{\boldsymbol{N}}_u^T\mathbf{f}\,\mathrm{d}\Omega + \int_{\Gamma_t} \widetilde{\boldsymbol{N}}_u^T\bar{\boldsymbol{t}}\,\mathrm{d}\Gamma \tag{3.21}$$

Introducing the constitutive relations (3.7) and (3.8) and operating, it results in

$$\int_{\Omega\setminus S} \boldsymbol{B}_u^T\mathbf{D}_0\boldsymbol{B}_u\boldsymbol{U}\,\mathrm{d}\Omega + \int_{\Omega\setminus S} \boldsymbol{B}_u^T\mathbf{D}_0\widetilde{\boldsymbol{B}}_u\widetilde{\boldsymbol{U}}\,\mathrm{d}\Omega = \int_{\Omega} \boldsymbol{N}_u^T\mathbf{f}\,\mathrm{d}\Omega + \int_{\Gamma_t} \boldsymbol{N}_u^T\bar{\boldsymbol{t}}\,\mathrm{d}\Gamma \tag{3.22}$$

$$\begin{aligned}\int_{\Omega\setminus S} \widetilde{\boldsymbol{B}}_u^T\mathbf{D}_0\boldsymbol{B}_u\boldsymbol{U}\,\mathrm{d}\Omega + \int_{\Omega\setminus S} \widetilde{\boldsymbol{B}}_u^T\mathbf{D}_0\widetilde{\boldsymbol{B}}_u^T\widetilde{\boldsymbol{U}}\,\mathrm{d}\Omega + \int_{S} \boldsymbol{N}_u^T\boldsymbol{E}_S\boldsymbol{N}_u\widetilde{\boldsymbol{U}}\,\mathrm{d}S \\ = \int_{\Omega} \widetilde{\boldsymbol{N}}_u^T\mathbf{f}\,\mathrm{d}\Omega + \int_{\Gamma_t} \widetilde{\boldsymbol{N}}_u^T\bar{\boldsymbol{t}}\,\mathrm{d}\Gamma\end{aligned} \tag{3.23}$$

and the following discrete FE formulation is obtained:

$$\begin{bmatrix}\boldsymbol{K}_{UU} & \boldsymbol{K}_{U\widetilde{U}} \\ \boldsymbol{K}_{\widetilde{U}U} & \boldsymbol{K}_{\widetilde{U}\widetilde{U}}\end{bmatrix}\begin{bmatrix}\boldsymbol{U} \\ \widetilde{\boldsymbol{U}}\end{bmatrix} = \begin{bmatrix}\boldsymbol{F} \\ \widetilde{\boldsymbol{F}}\end{bmatrix} \tag{3.24}$$

with

$$\boldsymbol{K}_{UU} = \int_{\Omega\setminus S} \boldsymbol{B}_u^T\mathbf{D}_0\boldsymbol{B}_u\,\mathrm{d}\Omega \tag{3.25}$$

$$\boldsymbol{K}_{\boldsymbol{U}\widetilde{\boldsymbol{U}}} = \int_{\Omega\setminus S} \boldsymbol{B}_u^T \mathbf{D}_0 \widetilde{\boldsymbol{B}}_u \, \mathrm{d}\Omega \tag{3.26}$$

$$\boldsymbol{K}_{\widetilde{\boldsymbol{U}}\boldsymbol{U}} = \int_{\Omega\setminus S} \widetilde{\boldsymbol{B}}_u^T \mathbf{D}_0 \boldsymbol{B}_u \, \mathrm{d}\Omega \tag{3.27}$$

$$\boldsymbol{K}_{\widetilde{\boldsymbol{U}}\widetilde{\boldsymbol{U}}} = \int_{\Omega\setminus S} \widetilde{\boldsymbol{B}}_u^T \mathbf{D}_0 \widetilde{\boldsymbol{B}}_u^T \, \mathrm{d}\Omega + \int_S \boldsymbol{N}_u^T \boldsymbol{E}_S \boldsymbol{N}_u \mathrm{d}S \tag{3.28}$$

$$\boldsymbol{F} = \int_\Omega \boldsymbol{N}_u^T \mathbf{f} \, \mathrm{d}\Omega + \int_{\Gamma_t} \boldsymbol{N}_u^T \bar{\boldsymbol{t}} \, \mathrm{d}\Gamma \tag{3.29}$$

$$\widetilde{\boldsymbol{F}} = \int_\Omega \widetilde{\boldsymbol{N}}_u^T \mathbf{f} \, \mathrm{d}\Omega + \int_{\Gamma_t} \widetilde{\boldsymbol{N}}_u^T \bar{\boldsymbol{t}} \, \mathrm{d}\Gamma \tag{3.30}$$

Note that the system in Eq. (3.24) is symmetric. This is a consequence of the variational consistency of the procedure followed.

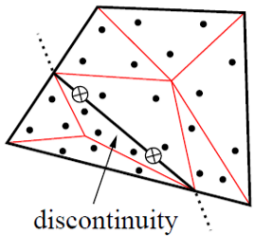

Figure 3.6: Integration scheme for a quadrilateral element crossed by a discontinuity [207]

Crack propagation and orientation criteria. Tracking algorithm

Instead of the local stress $\boldsymbol{\sigma}$, the Is-XFEM uses the following modified stress $\bar{\boldsymbol{\sigma}}_e$, computed as the average of the stresses over an element, to check *if crack propagation occurs*

$$\bar{\boldsymbol{\sigma}}_e = \frac{1}{V_e} \int_{\Omega_e} \boldsymbol{\sigma} \, \mathrm{d}\Omega \tag{3.31}$$

where V_e is the volume of element Ω_e. According to the Rankine criterion, a crack propagates into the element Ω_e if the major principal stress of $\bar{\boldsymbol{\sigma}}_e$ is larger than the material strength f_t. In such a case, the following adjusted nonlocal smoothed stress $\widetilde{\boldsymbol{\sigma}}_e$ is adopted to compute *the direction of crack propagation*

$$\widetilde{\boldsymbol{\sigma}}_e = \int_\Omega \varphi_0(r) \, \boldsymbol{\sigma} \, \mathrm{d}\Omega \approx \sum_{e=1}^{n_{V_e}} \varphi_0(r_e) \, V_e \, \bar{\boldsymbol{\sigma}}_e \tag{3.32}$$

with φ_0 being a weighting function depending on the distance r_e between the centroids of the element considered for crack propagation and neighboring ones

$$\varphi_0(r_e) = \exp\left(-\frac{r_e^2}{r_0^2}\right) \tag{3.33}$$

where r_0 is a numerical parameter to be defined. n_{V_e} denotes the number of elements e within a certain distance $r_e \leq 2.5 r_0$. In accordance to the Rankine criterion, the crack propagates

perpendicular to the major principal stress of $\tilde{\boldsymbol{\sigma}}_e$. The averaged nonlocal stress $\tilde{\boldsymbol{\sigma}}_e$ is not normalized, but this does not affect the resulting direction of advance of the crack.

The tracking algorithm adopted in references [63, 104] is based on element connections/graph. Crack propagation within elements is done following straight lines and intersecting discontinuities are not considered. More details can be seen in references [63, 104].

Appraisal

The major strong point of the XFEM with respect to previous discontinuous approaches is that it is able of explicitly modelling the strong discontinuity caused by the crack without the need of remeshing. The major frailty of the XFEM is that it requires the a priori knowledge of the location and orientation of the crack, therefore the necessity of employing auxiliary crack tracking techniques.

Assets

A1. Generality. The partition of unity concept upon which the XFEM is based in a robust and general numerical procedure that allows to introduce a conforming local enrichment of the approximation spaces. This makes the method attractive in many applications, including the numerical modelling of fracture.

A2. Strength, toughness and energy dissipation. The introduction of traction-separation laws, following the Fictitious Crack Model, in which both the strength and the fracture energy are included, allows to successfully represent softening quasi-brittle failure and structural size effect.

A3. No need of remeshing. The XFEM does not require the use of remeshing techniques to satisfactorily represent the discontinuity generated by a sharp crack in the displacement field.

A4. Reduced computational cost. In the XFEM, the number of degrees of freedom is only increased in the elements intersected by the crack; this affects only a very small part of the total number of nodes. Therefore, even if these additional degrees of freedom have to be assembled and solved at global level, the increase in the overall computational cost is small.

Drawbacks

D1. Constitutive behavior of cracks in terms of traction-separation laws. Instead of using the standard stress-strain models, methods representing sharp cracks, such as the XFEM, require to express the nonlinear constitutive law of the material in terms of the traction across the crack with respect to the displacement jump [89].

D2. Need for a criterion for the determination of the orientation of crack propagation. The insertion of the extended approximation space used by the XFEM requires the *a priori* determination of the location and orientation of the fracture. For this, a criterion for crack propagation needs to be introduced, consistent with the constitutive law employed. However, the local convergence of strain and stress fields cannot be guaranteed at the tip of the crack using the standard FEM. Thus, the criterion needs to be defined, in conjunction with a suitable crack tracking technique, such that mesh objective results are obtained. Therefore, this criterion is introduced in an ad hoc manner, and the local character of the original physical problem is lost.

D3. Need for specific analytical developments and numerical implementations. Handling discontinuities inside the finite element requires the development of specific sampling and integration schemes. Frequently, these need to be applied differently for each FE interpolation basis (triangles, quads, etc.) [18, 207, 211-218]. Also, implementation in 2D and 3D needs to be separately considered. This makes the development of the XFEM rather involved. As noted in

reference [219], "the implementation of customized integration schemes is possibly the most time-consuming part of an implementation of the XFEM". Different approaches have been proposed to alleviate these difficulties. The regularized XFEM, or REXFEM, presents the use of embedded but regularized discontinuities in the finite elements, avoiding the utilization of discontinuous interpolation functions [158, 220, 221]. In the so-called phantom node method [222-226], two overlapping elements are introduced, each representing the displacement field in one side of the FE domain intersected by the crack. This prevents as well using discontinuous interpolation functions for representing the crack.

D4. Multiple, intersecting and branching cracks. Although modelling these situations is possible using the XFEM [227-233], they require specific developments which are not straightforward to implement.

D5. Need for crack tracking techniques. Even if the displacement interpolation of the XFEM is conforming, a tracking technique is necessary to ensure the spatial continuity of the crack. Several alternatives have been proposed, using local, global and partial domain strategies. The elements crossed by the crack need to be labelled, as they are the only ones where the nonlinear cohesive softening behavior of the material may take place. As previously mentioned, the need and the use of these procedures lies outside the variational setting of the problem. Applying some tracking techniques in 3D problems is far from straightforward [63, 97, 234-236].

	Checklist for the XFEM	✓✓	✓	○	×	××
1	Variational formulation in the continuous setting				D1, D5	
2	Convergence of the FE formulation					D3,D4,D5
3	Strength, toughness and energy dissipation	A2				
4	Criterion for direction of propagation					D2, D5
5	Constitutive behavior generality					D1, D2, D5
6	Generality and implementation effort					D3, D4, D5
7	Cost-efficiency		A3, A4			D3, D4
8	Multiple, intersecting and branching cracks					D4
9	Auxiliary tracking techniques					D5
10	Application in 3D					D3, D4, D5

3.2 Mixed FEM

In the following, the mixed strain/displacement $\boldsymbol{\varepsilon/u}$ FE formulation is briefly introduced. The numerical model for fracture developed, implemented and employed in this doctoral thesis follows this methodology. Additional details can be found in references [26, 27, 31, 32, 34, 237, 238] and in the publications included in the compendium.

Continuous formulation

The *keystone of the Mixed FEM* is the formulation of the variational problem in terms of the strains $\boldsymbol{\varepsilon}$ and the displacements $\boldsymbol{u}$ as primary unknowns. First, the compatibility equation relates these two fields

$$\boldsymbol{\varepsilon} = \mathbf{S}\,\boldsymbol{u} \tag{3.34}$$

where $\mathbf{S}$ is the differential symmetric gradient operator. Secondly, the Cauchy momentum equation relates the stresses $\boldsymbol{\sigma}$ and the body forces $\mathbf{f}$

$$\mathbf{S}^T\boldsymbol{\sigma} + \mathbf{f} = \mathbf{0} \tag{3.35}$$

where $\mathbf{S}^T$ is the differential divergence operator, adjoint to the $\mathbf{S}$ in Eq. (3.34). And, thirdly, the constitutive equation connects the stress and strain vectors

$$\boldsymbol{\sigma} = \mathbf{D}\,\boldsymbol{\varepsilon} \tag{3.36}$$

where $\mathbf{D}$ is the (nonlinear) secant constitutive matrix. From thermodynamic considerations, $\mathbf{D}$ is symmetric and positive semidefinite.

Then, Eq. (3.34) is pre-multiplied by $\mathbf{D}$ and Eq. (3.36) is introduced into Eq. (3.35), resulting in the following system of PDEs, which corresponds to the strong form of the problem:

$$-\mathbf{D}\boldsymbol{\varepsilon} + \mathbf{D}\mathbf{S}\boldsymbol{u} = \mathbf{0} \tag{3.37}$$

$$\mathbf{S}^T(\mathbf{D}\boldsymbol{\varepsilon}) + \mathbf{f} = \mathbf{0} \tag{3.38}$$

The corresponding weak form of the mixed problem is obtained by: (i) multiplying Eq. (3.37) by a virtual strain vector, (ii) multiplying Eq. (3.38) by a virtual displacement vector, (iii) integrating both equations over the spatial domain, and (iv) applying the Divergence Theorem in the first term of Eq. (3.38). The resulting system of equations is

$$-\int_\Omega \delta\boldsymbol{\varepsilon}^T\mathbf{D}\boldsymbol{\varepsilon}\,\mathrm{d}\Omega + \int_\Omega \delta\boldsymbol{\varepsilon}^T\mathbf{D}\mathbf{S}\boldsymbol{u}\,\mathrm{d}\Omega = 0 \quad \forall\delta\boldsymbol{\varepsilon} \tag{3.39}$$

$$\int_\Omega (\mathbf{S}\delta\boldsymbol{u})^T(\mathbf{D}\boldsymbol{\varepsilon})\,\mathrm{d}\Omega = \int_\Omega \delta\boldsymbol{u}^T\mathbf{f}\,\mathrm{d}\Omega + \int_{\Gamma_t} \delta\boldsymbol{u}^T\bar{\boldsymbol{t}}\,\mathrm{d}\Gamma \quad \forall\delta\boldsymbol{u} \tag{3.40}$$

where the boundary Γ of the domain is divided in two parts: Γ_u, corresponding to the Dirichlet boundary condition and Γ_t corresponding to the Newmann boundary condition. The variational form of the problem consists in finding the displacement $\boldsymbol{u}$ and strain $\boldsymbol{\varepsilon}$ fields satisfying the system of Eqs. (3.39)-(3.40) and complying with the boundary condition $\boldsymbol{u} = \mathbf{0}$ in Γ_u, for the arbitrary virtual displacement vector $\delta\boldsymbol{u}$, which is also null on Γ_u, and the arbitrary virtual strain vector $\delta\boldsymbol{\varepsilon}$. Note that the problem is symmetric.

The *regularization keystone of the mixed FEM* follows the crack band model [12], and consists in the smearing of the sharp crack S over a band B of small, but finite, thickness b. The location and direction of propagation of the crack does not need to be a priori determined. It naturally follows from the constitutive behavior which, in this case, considering isotropic damage, corresponds to

$$\boldsymbol{\sigma} = \mathbf{D}(d)\,\boldsymbol{\varepsilon} = (1-d)\,\mathbf{D}_0\,\boldsymbol{\varepsilon} \tag{3.41}$$

where $\mathbf{D} = \mathbf{D}(d)$ is the secant constitutive matrix, written as a function of the internal scalar damage variable d that describes the degradation of the material and $\mathbf{D}_0$ is the initial elastic constitutive matrix. In an initially isotropic elastic material, $\mathbf{D}_0$ is defined in function of the undamaged elastic values of Young's modulus E and Poisson's ratio ν. The secant constitutive matrix is symmetric and positive semidefinite if $0 \leq d \leq 1$.

Cracks have an unquestionable locally directional character and orthotropic damage models have recently been re-assessed in relation with quasi-brittle failure in references [32, 34], included in the compendium, using the mixed FEM. However, an isotropic damage model is used in this part of the thesis in order to compare results obtained with the mixed FEM and corresponding simulations reported in the literature computed with the XFEM and the PFM. All the details on

the orthotropic damage constitutive laws employed with the proposed mixed FE formulation are given in references [32, 34].

The effective stress $\bar{\boldsymbol{\sigma}}$ is stipulated as $\bar{\boldsymbol{\sigma}} = \mathbf{D}_0\, \boldsymbol{\varepsilon}$, according to the hypothesis of strain equivalence. For the present comparison with the XFEM and the PFM, only tensile damage is considered. The Rankine fracture criterion for tension, whose surface is plotted in Figure 3.7a, is introduced as

$$\mathbb{F}\left(\bar{\sigma}_{eq}, r\right) = \bar{\sigma}_{eq}(\bar{\boldsymbol{\sigma}}) - r = \langle \bar{\sigma}_1 \rangle - r = 0 \tag{3.42}$$

where the major principal effective stress is taken as the equivalent effective stress, $\bar{\sigma}_{eq}(\bar{\boldsymbol{\sigma}}) = \langle \bar{\sigma}_1 \rangle$, and r is the current damage threshold. The initial value of the damage threshold is the tensile strength of the material f_t. The current value at time t of the damage threshold r is derived from the Kuhn-Tucker optimality and consistency conditions, to guarantee the positiveness of the dissipation and the irreversibility of damage

$$r = \max\left(f_t, \max \bar{\sigma}_{eq}(\hat{t})\right) \quad \hat{t} \in [0, t] \tag{3.43}$$

In this work, an exponential evolution law is considered for the internal damage variable d, shown in Figure 3.7b. Alternative functions can be used if deemed necessary. The requirement for these functions is that d grows monotonically from 0 to 1 as the damage threshold r progresses from f_t to infinity. Therefore

$$d = 1 - \frac{f_t}{r} \exp\left(-2H_d \frac{\langle r - f_t \rangle}{f_t}\right) \tag{3.44}$$

where H_d is the softening parameter controlling the material degradation rate.

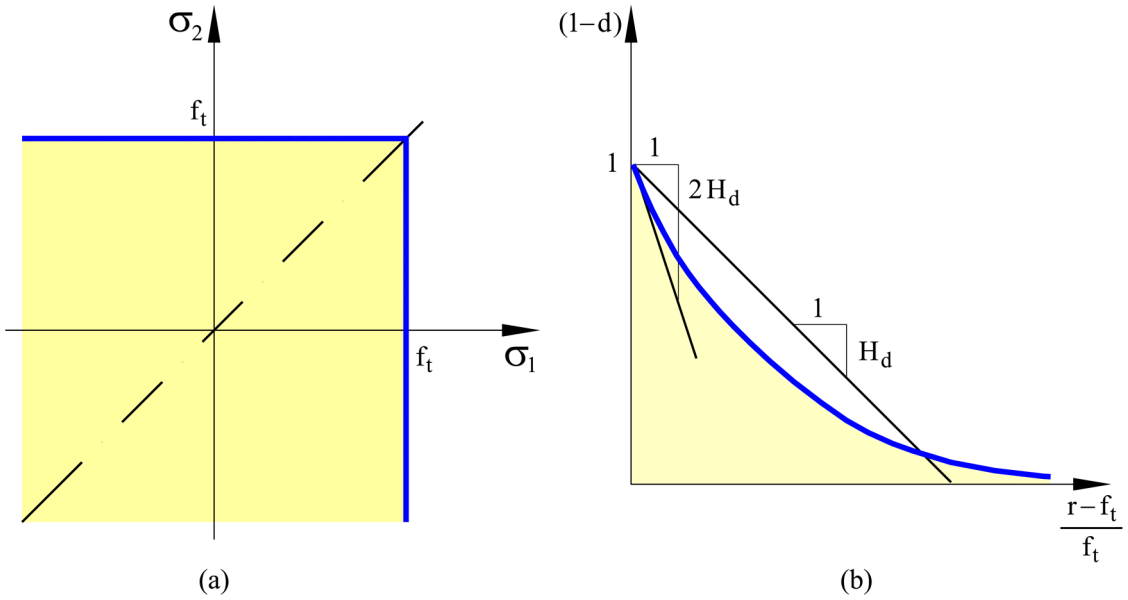

Figure 3.7: Rankine damage model: (a) damage surface and (b) softening function

In the crack band theory, H_d is related to the material properties through Irwin's material length $\mathcal{L} = EG_f/{f_t}^2$ and the crack bandwidth b

$$H_d = \frac{b}{2\mathcal{L} - b} \tag{3.45}$$

This approach allows to achieve mesh size independent results and to guarantee the correct energy dissipation when the crack progresses. Note that this is very similar to the uses in the

geometrically regularized PFM. In crack band theory, the crack bandwidth b is linked to the FE discretization: in mixed FE, $b = 2h$, h corresponding to the finite element size.

FE approximation

The discrete form of the mixed problem is obtained by discretizing the spatial domain Ω into non-intersecting FEs Ω_e, such that $\Omega = \cup\, \Omega_e$. The displacement $\boldsymbol{u}$ and the strain $\boldsymbol{\varepsilon}$ are substituted with discrete FE approximations $\widehat{\boldsymbol{u}}$ and $\hat{\boldsymbol{\varepsilon}}$ defined element-wise as

$$\boldsymbol{u} \cong \widehat{\boldsymbol{u}} = \boldsymbol{N}_u \boldsymbol{U} \tag{3.46}$$

$$\boldsymbol{\varepsilon} \cong \hat{\boldsymbol{\varepsilon}} = \boldsymbol{N}_\varepsilon \boldsymbol{E} \tag{3.47}$$

$\boldsymbol{U}$ and $\boldsymbol{E}$ are the vectors of the nodal values of the displacements and the strains. $\boldsymbol{N}_u$ and $\boldsymbol{N}_\varepsilon$ are the matrices composed of the interpolation functions adopted in the FE approximation.

When using mixed FE, the choice of the interpolation functions for the primary variables must satisfy the Inf-Sup stability condition, also known as the Ladyzhenskaya–Babuska–Brezzi (LBB) condition. Otherwise, the computed solution is unstable, presenting spurious oscillations in the displacement and strain fields [239-245].

The Inf-Sup condition is not fulfilled when equal order interpolation functions are used for $\boldsymbol{N}_u$ and $\boldsymbol{N}_\varepsilon$ [240, 241, 245]. To circumvent the strictness of this condition and to be able to use linear interpolation functions for both fields, a stabilization technique for the discrete mixed problem is required. The procedure employed in this work follows the Orthogonal Subscales Method, conceived within the Variational Multiscale Stabilization approach [203, 204, 246-250]. The process consists in replacing the FE approximation of the strain field in Eq. (3.47) with the following:

$$\boldsymbol{\varepsilon} \cong \hat{\boldsymbol{\varepsilon}} = \boldsymbol{N}_\varepsilon \boldsymbol{E} + \tau_\varepsilon (\boldsymbol{B}_u \boldsymbol{U} - \boldsymbol{N}_\varepsilon \boldsymbol{E}) = (1 - \tau_\varepsilon)\boldsymbol{N}_\varepsilon \boldsymbol{E} + \tau_\varepsilon \boldsymbol{B}_u \boldsymbol{U} \tag{3.48}$$

where τ_ε is a stabilization parameter such that $0 \leq \tau_\varepsilon \leq 1$ and $\boldsymbol{B}_u = \boldsymbol{S}\boldsymbol{N}_u$ is the standard compatibility matrix. Note that $\tau_\varepsilon = 0$ corresponds to the strain interpolation of the non-stabilized problem, while $\tau_\varepsilon = 1$ corresponds to the strain interpolation of the standard displacement based formulation. The stable interpolation is a blending of both. The values required for τ_ε are small but cannot be zero.

It is shown in references [26, 27, 249] that an optimal convergence rate of the problem is achieved by choosing $\tau_\varepsilon = c_\varepsilon\, h/L$, with c_ε being an arbitrary constant, L a reference size of the structure and h the FE size. In this work, $c_\varepsilon = 1$ is adopted.

Taking into consideration this stabilization procedure, the value of the crack bandwidth introduced in Eq. (3.45) is

$$b = (1 - \tau_\varepsilon)2h + \tau_\varepsilon h = (2 - \tau_\varepsilon)h \tag{3.49}$$

Introducing the FE approximations of Eqs. (3.46) and (3.48) into Eqs. (3.39)-(3.40) results in the following algebraic system of equations:

$$\begin{bmatrix} -\boldsymbol{M}_{\boldsymbol{\tau}} & \boldsymbol{G}_{\boldsymbol{\tau}} \\ \boldsymbol{G}_{\boldsymbol{\tau}}^T & \boldsymbol{K}_{\boldsymbol{\tau}} \end{bmatrix} \begin{bmatrix} \boldsymbol{E} \\ \boldsymbol{U} \end{bmatrix} = \begin{bmatrix} \boldsymbol{0} \\ \boldsymbol{F} \end{bmatrix} \tag{3.50}$$

where $[\boldsymbol{E} \quad \boldsymbol{U}]^T$ is the vector containing the nodal values of the unknowns of the problem, strains and displacements, and $\boldsymbol{M}_{\boldsymbol{\tau}} = (1 - \tau_\varepsilon)\boldsymbol{M}$, $\boldsymbol{G}_{\boldsymbol{\tau}} = (1 - \tau_\varepsilon)\boldsymbol{G}$ and $\boldsymbol{K}_{\boldsymbol{\tau}} = \tau_\varepsilon \boldsymbol{K}$. $\boldsymbol{M}$ is a mass like projection matrix, $\boldsymbol{G}$ is the discrete gradient matrix, $\boldsymbol{K}$ is a stiffness like matrix and $\boldsymbol{F}$ is the vector of external nodal forces:

$$\boldsymbol{M} = \int_{\Omega} \boldsymbol{N}_{\varepsilon}^{T} \mathbf{D} \boldsymbol{N}_{\varepsilon} \, \mathrm{d}\Omega \tag{3.51}$$

$$\boldsymbol{G} = \int_{\Omega} \boldsymbol{N}_{\varepsilon}^{T} \mathbf{D} \boldsymbol{B}_{u} \, \mathrm{d}\Omega \tag{3.52}$$

$$\boldsymbol{K} = \int_{\Omega} \boldsymbol{B}_{u}^{T} \mathbf{D} \boldsymbol{B}_{u} \, \mathrm{d}\Omega \tag{3.53}$$

$$\boldsymbol{F} = \int_{\Omega} \boldsymbol{N}_{u}^{T} \mathbf{f} \, \mathrm{d}\Omega + \int_{\Gamma_{\mathrm{t}}} \boldsymbol{N}_{u}^{T} \bar{\boldsymbol{t}} \, \mathrm{d}\Gamma \tag{3.54}$$

Appraisal

The major strong point of the Mixed FEM is that it constitutes an enhanced version of the standard smeared crack model based on the crack band theory, able to achieve mesh objective and convergent solutions. The weakest point is that it is not straightforwardly implementable in a standard FE code, although it fits well in a multiphysics platform.

Assets

A1. Rigorous physical fundamentals. The method is based on the mixed strain/displacement variational form of the nonlinear solid mechanics problem. It can accurately model quasi-brittle failure and follows Griffith's theory of fracture implemented through the crack band theory. It applies both to quasi-static as well as dynamic problems, in 2D or in 3D.

A2. Rigorous mathematical foundation. The adoption of a mixed formulation for the FE problem is soundly based, as it guarantees that the FE solution converges in quasi-singular situations.

A3. Generality of implementation. The strain/displacement ε/u FE formulation does not require any specific FE interpolation basis, so it can equally be used with triangles or quads, linear or quadratic. It does not necessitate any particular development to be implemented in 3D.

A4. Mesh bias and mesh size independence. Because the adopted mixed FE formulation has a better convergence rate than the standard FE one, convergence of the discrete nonlinear FE problem to the continuous solution can occur. Results of the FE problem are therefore mesh bias independent. The approach based on the crack band theory guarantees mesh size independence.

A5. Generality of the crack constitutive behavior. The mixed FEM can readily accommodate different suitable constitutive behaviors defined in stress vs. strain format. In the secant form here presented, isotropic and orthotropic damage models have been considered [32, 34], demonstrating that they do not yield identical solutions. Also, crack closing-reopening effects can be considered, as well as irreversible straining, both aspects essential when considering cyclic loading [34]. Figures 3.8 and 3.9 illustrate these remarkable features. Computational plasticity has been contemplated as well for the modelling of fracture [72, 237] and other strain localization problems [91, 251].

A6. Strength, toughness and energy dissipation. Both material strength and toughness are included in the material description, allowing to model quasi-brittle failure. Structural size effect is remarkably well reproduced [35].

A7. Branching and intersecting cracks. The Mixed FEM can handle branching and intersecting cracks as a matter of course if they spring in the solution of the specific problem [72].

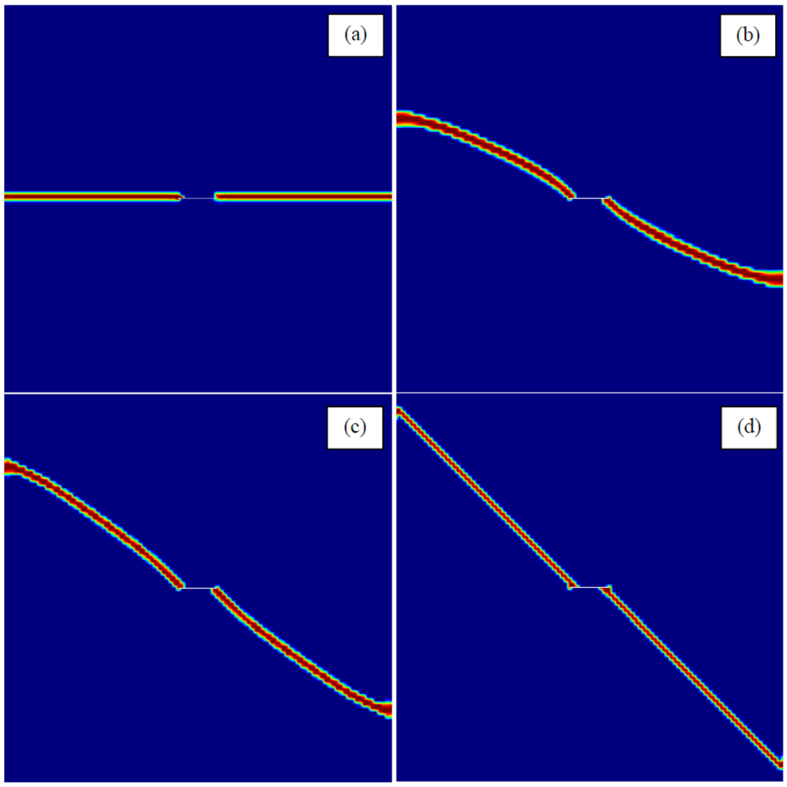

Figure 3.8: Damage contours of a cubic metal specimen subjected to monotonic shear loading using an isotropic Drucker-Prager model with different compressive vs. tensile strength ratios: (a) $f_c/f_t = 1$, (b) $f_c/f_t = 5$, (c) $f_c/f_t = 8$ and (d) $f_c/f_t = 100$, computed with mixed FE [34]

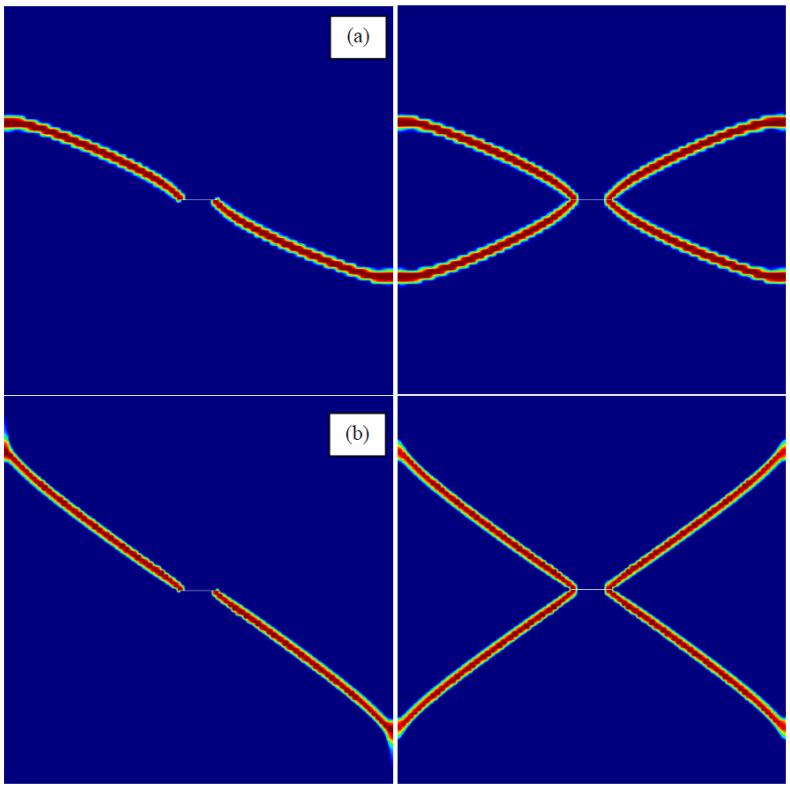

Figure 3.9: Damage contours of a cubic metal specimen subjected to (left) monotonic and (right) cyclic shear loading using (a) isotropic and (b) orthotropic Rankine models, computed with mixed FE [34]

A8. No crack tracking procedures are required. Griffith's theory for fracture consisted of a criterion for crack growth but did not address the prediction of the direction of progression of the crack [149, 194, 252, 253]. In the Mixed FEM, the direction of crack propagation is implicitly incorporated in the variational formulation through the constitutive model employed. When considering damage, crack directions naturally follow from the surface of the fracture criterion incorporated in the underlying model adopted.

A9. Computational efficiency. An apparent weak point of the Mixed FE formulation is the computational cost. The formulation requires the independent interpolation of strains and displacements and, thus, the number of nodal degrees of freedom is considerably increased with respect to the standard formulation. However, it needs to be considered that the mixed formulation has a higher convergence rate than standard FEM. This means that, for a given required bound of the discretization error, the mixed method requires *less* elements that the standard one. The difference is larger the smaller the required discretization error. For this reason, it can be shown [254] that, in practical applications, the mixed method is *less costly* that the standard one in terms of elements, degrees of freedom and CPU time.

Regarding the fineness that the Mixed FEM requires for cracking problems, the method smears the crack over a band of 2 elements, with bandwidth $b = 2h$, h corresponding to the mesh size. As shown in Figure 2.13, it can be used with the same mesh resolutions as the standard displacement based formulation. This involves meshes with fewer finite elements than those required by the PFM, *by several orders of magnitude*. Other strategies employed for reducing computational cost such as adaptive mesh refinement can be equally applied for both the MFEM and the PFM.

Drawbacks

D1. Implementation. Mixed FE formulations cannot be straightforwardly implemented in a standard FE code, as they require a multi-field structure.

	Checklist for the Mixed FEM	✓✓	✓	○	×	××
1	Variational formulation in the continuous setting	A1, A2				
2	Convergence of the FE formulation	A2				
3	Strength, toughness and energy dissipation	A6				
4	Criterion for direction of propagation	A2, A8				
5	Constitutive behavior generality	A3, A5				
6	Generality and implementation effort		A1, A3		D1	
7	Cost-efficiency			A9		
8	Multiple, intersecting and branching cracks	A7				
9	Auxiliary tracking techniques	A8				
10	Application in 3D		A1, A9			

3.3 Phase-field model

In this section, the geometrically regularized phase-field model, also known as the phase-field regularized cohesive zone model (PF-CZM), developed in references [56-70], and used in the numerical comparisons of this work, is briefly introduced. All the details on the method are given in the original references.

Continuous formulation

In the phase-field regularized cohesive zone model, the damage d that develops in the solid is treated as an additional field variable, together with the displacement field $\boldsymbol{u}$. Irreversibility of damage is properly enforced, so that damage cannot decrease.

The *variational keystone of the PFM* is Griffith's theory for fracture [53], which states that during the cracking process the body remains in equilibrium and, therefore, the principle of minimum energy holds. Consequently, in a closed system, the variation of the total energy when the crack develops is zero. Griffith also assumed that the formation of a crack involved a certain energy dissipation that must be accounted for in the process. The total energy of the system E_T is expressed as

$$E_T = W_\varepsilon + W_S - W_{ext} \tag{3.55}$$

where W_ε is the strain energy stored in the body, W_S is the energy dissipation required for the creation of the crack surface and W_{ext} is the work done by the external forces.

According to Griffith, the energy dissipated by the crack formation is proportional to the area of the developing fracture, A_S, through a material property, G_f, called the fracture energy, the dissipated fracture energy per unit of area [53], so that

$$W_S = G_f \int_S \mathrm{d}S = G_f A_S \tag{3.56}$$

For an elasto-damaging solid, the strain energy is

$$W_\varepsilon = \int_\Omega \Psi(d, \boldsymbol{\varepsilon})\, \mathrm{d}\Omega \tag{3.57}$$

with $\Psi(d, \boldsymbol{\varepsilon})$ being the strain energy density per unit of volume.

The work done by the external forces, the body forces $\mathbf{f}$ and the tractions $\bar{\boldsymbol{t}}$ acting on the corresponding boundary, Γ_t, has the standard expression

$$W_{ext} = \int_\Omega \boldsymbol{u}^T \mathbf{f}\, \mathrm{d}\Omega + \int_{\Gamma_t} \boldsymbol{u}^T \bar{\boldsymbol{t}}\, \mathrm{d}\Gamma \tag{3.58}$$

In equilibrium, the variation of the total energy E_T with respect to the crack growth a is zero [149]

$$\frac{\partial E_T}{\partial a} = 0 \tag{3.59}$$

From this, Griffith's criterion for fracture follows: a crack will develop in a body only if the release of stored elastic energy caused by its growth is greater than the energy required to create its surface [53, 252].

The *regularization keystone of the PFM* consists in the smoothing of the sharp crack S over a band B of small, but finite, thickness b, where the material is damaged, as shown in Figure 3.10. Consequently, the area of the crack A_S that appears in Eq. (3.56) is approximated as

$$A_S = \int_S \mathrm{d}S = \int_B \delta_s\, \mathrm{d}\Omega \approx \int_B \gamma(d, \nabla d)\, \mathrm{d}\Omega \tag{3.60}$$

so that the Dirac-delta δ_s describing the sharp crack is approximated with the crack surface density function $\gamma = \gamma(d, \nabla d)$, which is expressed in terms of the damage d and its gradient ∇d.

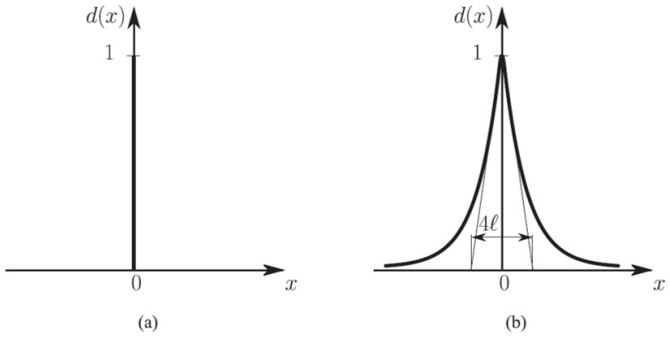

Figure 3.10: Representation of cracks using (a) embedded and (b) regularized models [255], with $b = 4l$

The gradient of the damage is inserted in the definition of γ to introduce the necessary regularity to the problem, as it can be seen in Figure 3.11.

The relation of the previous gradient-enhanced formulations with the phase-field models is evident [256-258]. The thickness b of the regularized crack is included in the expression of γ for dimensional consistency

$$\gamma(d, \nabla d) = \frac{1}{\pi}\left[\frac{1}{b}(2d - d^2) + b|\nabla d|^2\right] \tag{3.61}$$

Note that b is a regularizing length in a purely mathematical sense; it does not carry any material significance. In phase-field models, reducing the crack bandwidth b must ensure Γ-convergence to the sharp crack problem, as it can be seen in Figure 3.12 [56].

The strain energy density Ψ is written in terms of the strain $\boldsymbol{\varepsilon}$ and the damage index d as

$$\Psi(d, \boldsymbol{\varepsilon}) = \omega(d)\, \Psi_0(\boldsymbol{\varepsilon}) \tag{3.62}$$

where $\omega(d)$ is a monotonically decreasing function, ranging from 1 to 0, describing the degradation of the material in terms of the damage and $\Psi_0(\boldsymbol{\varepsilon})$ is the elastic strain energy of the material

$$\Psi_0(\boldsymbol{\varepsilon}) = \frac{1}{2}\boldsymbol{\varepsilon}^T \mathbf{D}_0\, \boldsymbol{\varepsilon} \tag{3.63}$$

where $\mathbf{D}_0$ is the elastic constitutive matrix. From this, the constitutive law is obtained as

$$\boldsymbol{\sigma} = \frac{\partial \Psi}{\partial \boldsymbol{\varepsilon}} = \omega(d)\frac{\partial \Psi_0}{\partial \boldsymbol{\varepsilon}} = \omega(d)\mathbf{D}_0\boldsymbol{\varepsilon} \tag{3.64}$$

Note that the conventional format of an isotropic damage model is recovered if the degradation function $\omega(d)$ is written as:

$$\omega(d) = (1 - d) \tag{3.65}$$

Instead, the geometrically regularized phase-field model adopts a generic degradation function

$$\omega(d) = \frac{(1-d)^p}{(1-d)^p + a_1 d\,(1 + a_2 d + a_3 d^2)} \tag{3.66}$$

As is detailed in references [56, 58], when choosing appropriate values for the exponent $p \geq 2$ and the parameters a_1, a_2 and a_3, the general softening function $\omega(d)$ in Eq. (3.66) adopts certain specific behaviors: linear, exponential, hyperbolic, etc., shown in Figure 3.13. Parameter a_1 is

proportional to the relation between Irwin's material length $\mathcal{L} = EG_f/{f_t}^2$ and the crack bandwidth b; parameters a_2 and a_3 are dependent on the tensile strength f_t and the fracture energy G_f.

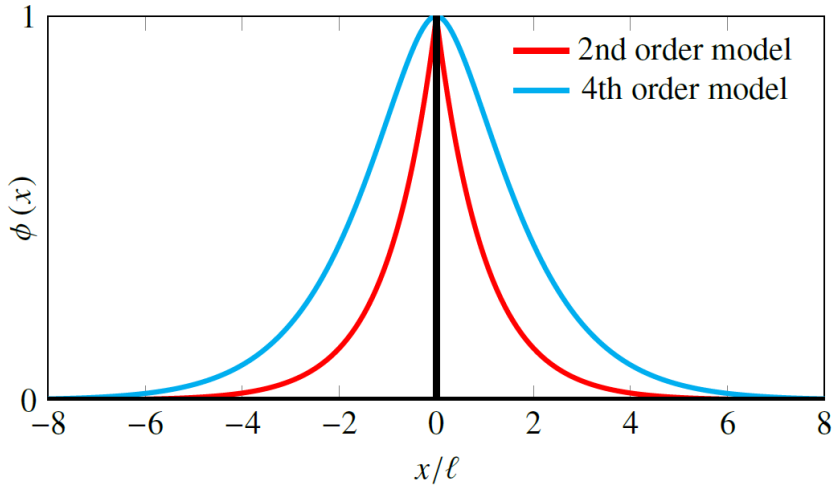

Figure 3.11: Damage profile of the 2nd and 4th order phase-field model [259], with $\boldsymbol{\phi(x)}$ being the phase-field variable identified with the damage $\boldsymbol{d(x)}$ and $\boldsymbol{b = 2l}$

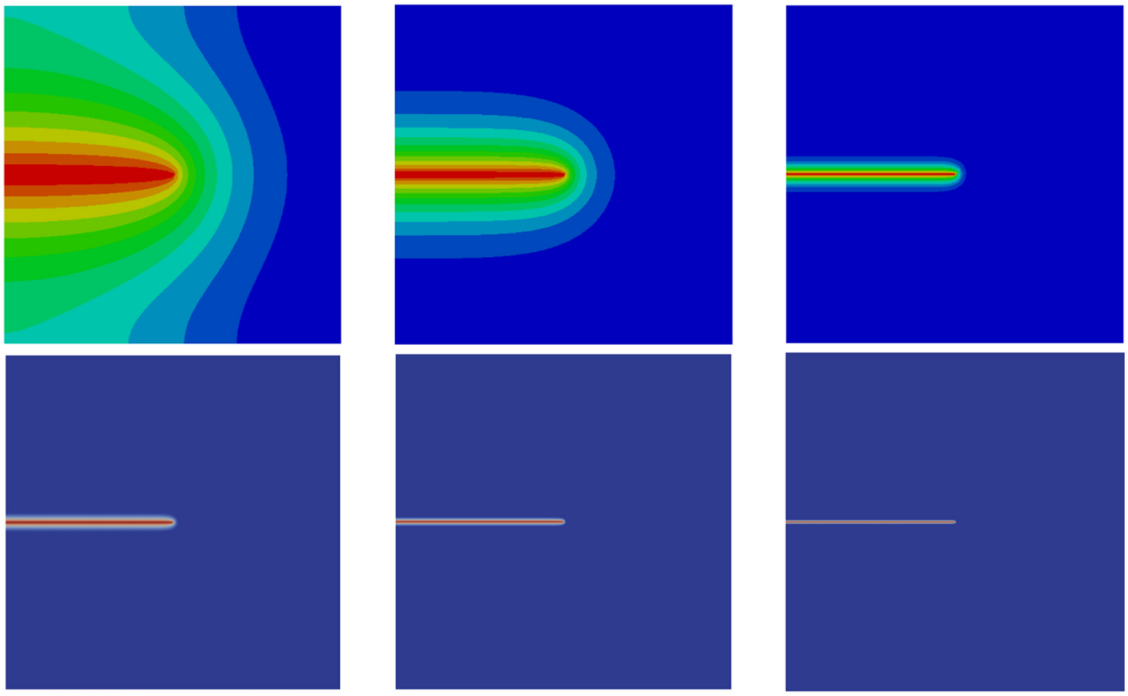

Figure 3.12: Γ-convergence: reducing the crack bandwidth in the phase-field model in reference [56]

The crack driving force Y, conjugate to the damage index, is

$$Y = -\frac{\partial \Psi(d, \boldsymbol{\varepsilon})}{\partial d} = -\frac{\partial \omega(d)}{\partial d}\Psi_0(\boldsymbol{\varepsilon}) \tag{3.67}$$

In PF-CZM, the crack driving force in Eq. (3.67) is substituted with the following:

$$Y = -\frac{\partial \omega(d)}{\partial d}\bar{Y}(\boldsymbol{\varepsilon}) \tag{3.68}$$

where $\bar{Y}$ is a modified reference energy defined in function of the equivalent effective stress $\bar{\sigma}_{eq}$, which allows to introduce an appropriate cracking criterion to define damage initiation and evolution

$$\bar{Y} = \frac{1}{2E}\bar{\sigma}_{eq}^2 \tag{3.69}$$

where E is the elastic Young modulus. Taking $\bar{\sigma}_{eq} = \langle \bar{\sigma}_1 \rangle$ corresponds to using the Rankine damage surface, $\bar{\sigma}_1$ being the maximum normal effective stress; the effective stress $\bar{\boldsymbol{\sigma}}$ is evaluated as $\bar{\boldsymbol{\sigma}} = \mathbf{D}_0\boldsymbol{\varepsilon}$. Other damage criteria may be adopted by changing the expression of $\bar{\sigma}_{eq}$ in terms of $\bar{\boldsymbol{\sigma}}$, as it can be seen in reference [260]. Note that Eq. (3.67), and the substitute Eq. (3.68), are strain-driven.

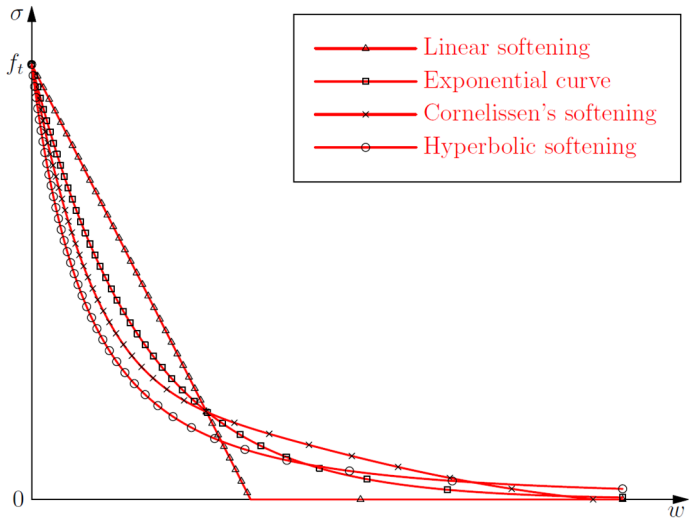

Figure 3.13: Softening laws adopted in phase-field simulations [56]

The damage flux vector $\boldsymbol{q}$ and the net damage supply per unit of volume r are defined as

$$\boldsymbol{q} = G_f \frac{\partial \gamma(d, \nabla d)}{\partial \nabla d} = \frac{2b}{\pi} G_f \nabla d \tag{3.70}$$

$$r = Y - G_f \frac{\partial \gamma(d, \nabla d)}{\partial d} = -\frac{\partial \omega(d)}{\partial d}\bar{Y}(\boldsymbol{\varepsilon}) - \frac{2}{\pi b} G_f (1 - d) \tag{3.71}$$

Using both the variational and the regularizing keystones, the expression of the total energy is rewritten as

$$E_T = \int_\Omega \omega(d)\Psi_0(\boldsymbol{\varepsilon})\, \mathrm{d}\Omega + G_f \int_B \gamma(d, \nabla d)\, \mathrm{d}\Omega - \int_\Omega \boldsymbol{u}^T \mathbf{f}\, \mathrm{d}\Omega - \int_{\Gamma_t} \boldsymbol{u}^T \bar{\boldsymbol{t}}\, \mathrm{d}\Gamma \tag{3.72}$$

and its minimization by applying Eq. (3.59) yields

$$\begin{aligned} \int_\Omega \delta\boldsymbol{\varepsilon}^T \underbrace{\omega(d)\frac{\partial \Psi_0(\boldsymbol{\varepsilon})}{\partial \boldsymbol{\varepsilon}}}_{=\boldsymbol{\sigma}} \mathrm{d}\Omega + \int_B \delta d \frac{\partial \omega(d)}{\partial d}\Psi_0(\boldsymbol{\varepsilon})\, \mathrm{d}\Omega + G_f \int_B \delta d \frac{\partial \gamma(d, \nabla d)}{\partial d}\mathrm{d}\Omega \\ + G_f \int_B \delta \nabla d \frac{\partial \gamma(d, \nabla d)}{\partial \nabla d}\mathrm{d}\Omega - \int_\Omega \delta \boldsymbol{u}^T \mathbf{f}\, \mathrm{d}\Omega - \int_{\Gamma_t} \delta \boldsymbol{u}^T \bar{\boldsymbol{t}}\, \mathrm{d}\Gamma = 0 \end{aligned} \tag{3.73}$$

Eq. (3.73) can then be split into a system of two equations, the first one corresponding to the classical Principle of Virtual Work, and the second one governing the evolution of damage

$$\int_{\Omega} \delta\boldsymbol{\varepsilon}^T \boldsymbol{\sigma}\, \mathrm{d}\Omega = \int_{\Omega} \delta\boldsymbol{u}^T \mathbf{f}\, \mathrm{d}\Omega + \int_{\Gamma_t} \delta\boldsymbol{u}^T \bar{\mathbf{t}}\, \mathrm{d}\Gamma \tag{3.74}$$

$$\int_{B} \nabla\delta d\ \boldsymbol{q}\, \mathrm{d}\Omega = \int_{B} \delta d\ r\, \mathrm{d}\Omega \tag{3.75}$$

where the divergence theorem has been applied to the term $\int_B\ \delta\nabla d\, \frac{\partial\gamma(d,\nabla d)}{\partial\nabla d}\, \mathrm{d}\Omega$.

The corresponding strong form of the problem is the following system:

$$\mathbf{S}^T\boldsymbol{\sigma} + \mathbf{f} = \mathbf{0} \tag{3.76}$$

$$\boldsymbol{G}^T\boldsymbol{q} + r = 0 \tag{3.77}$$

where $\boldsymbol{G}^T$ is the differential divergence operator.

FE approximation

Once the spatial domain is discretized into FE, the displacement $\boldsymbol{u}$ and damage d fields are approximated by independent interpolations $\hat{\boldsymbol{u}}$ and $\hat{d}$

$$\boldsymbol{u} \cong \hat{\boldsymbol{u}} = \boldsymbol{N}_u\boldsymbol{U} \tag{3.78}$$

$$d \cong \hat{d} = \boldsymbol{N}_d\boldsymbol{D} \tag{3.79}$$

where $\boldsymbol{U}$ and $\boldsymbol{D}$ are the vectors of the nodal values of the displacements and the damage in the whole domain, and $\boldsymbol{N}_u$ and $\boldsymbol{N}_d$ are the matrices containing the interpolation functions adopted in the FE approximations.

The following discrete approximations for the strain and the damage gradient fields ensue:

$$\boldsymbol{\varepsilon} \cong \hat{\boldsymbol{\varepsilon}} = \boldsymbol{B}_u\boldsymbol{U} \tag{3.80}$$

$$\nabla d \cong \nabla\hat{d} = \boldsymbol{B}_d\boldsymbol{D} \tag{3.81}$$

where $\boldsymbol{B}_d$ is the discrete gradient operator, defined as $\boldsymbol{B}_d = \mathbf{G}\boldsymbol{N}_d$.

Introducing the FE approximation in Eqs. (3.78), (3.79), (3.80) and (3.81) into the weak form in Eqs. (3.74)-(3.75) results in the following system of two equations:

$$\int_{\Omega} \boldsymbol{B}_u^T\boldsymbol{\sigma}\, \mathrm{d}\Omega = \int_{\Omega} \boldsymbol{N}_u^T\mathbf{f}\, \mathrm{d}\Omega + \int_{\Gamma_t} \boldsymbol{N}_u^T\bar{\mathbf{t}}\, \mathrm{d}\Gamma \tag{3.82}$$

$$\int_{B} \boldsymbol{N}_d^T\, r\, \mathrm{d}\Omega = \int_{B} \boldsymbol{B}_d^T\, \boldsymbol{q}\, \mathrm{d}\Omega \tag{3.83}$$

Several alternatives have been proposed for solving the nonlinear system of Eqs. (3.82)-(3.83), following an incremental procedure [62, 67]. For example, a staggered scheme may be used, so that the resulting algebraic system is

$$\begin{bmatrix} \boldsymbol{K}_{UU} & \mathbf{0} \\ \mathbf{0} & \boldsymbol{K}_{DD} \end{bmatrix} \begin{bmatrix} \Delta\boldsymbol{U} \\ \Delta\boldsymbol{D} \end{bmatrix} = \begin{bmatrix} \boldsymbol{r}_u \\ \boldsymbol{r}_d \end{bmatrix} \tag{3.84}$$

with

$$\boldsymbol{K_{UU}} = \int_{\Omega} \boldsymbol{B}_u^T \left(\frac{\partial \boldsymbol{\sigma}}{\partial \boldsymbol{\varepsilon}}\right) \boldsymbol{B}_u \, \mathrm{d}\Omega \tag{3.85}$$

$$\boldsymbol{K_{DD}} = \int_{B} \left(-\boldsymbol{N}_d^T \left(\frac{\partial r}{\partial d}\right) \boldsymbol{N}_d + \boldsymbol{B}_d^T \frac{2b}{\pi} G_f \boldsymbol{B}_d\right) \mathrm{d}\Omega \tag{3.86}$$

and $\boldsymbol{r}_u$ and $\boldsymbol{r}_d$ are the residuals related to Eqs. (3.82) and (3.83) respectively

$$\boldsymbol{r}_u = \int_{\Omega} \boldsymbol{N}_u^T \mathbf{f} \, \mathrm{d}\Omega + \int_{\Gamma_t} \boldsymbol{N}_u^T \bar{\boldsymbol{t}} \, \mathrm{d}\Gamma - \int_{\Omega} \boldsymbol{B}_u^T \boldsymbol{\sigma} \, \mathrm{d}\Omega \tag{3.87}$$

$$\boldsymbol{r}_d = \int_{B} \boldsymbol{N}_d^T \, r \, \mathrm{d}\Omega - \int_{B} \boldsymbol{B}_d^T \, \boldsymbol{q} \, \mathrm{d}\Omega \tag{3.88}$$

The off-diagonal terms have been removed in the system (3.84), neglecting the inter-field coupling, according to the discussion in references [56, 67]. Alternative approaches for computing the nonlinear problem have been proposed in [56, 62, 67].

Appraisal

The major strong point of the Phase-field Model with respect previous regularized approaches is that it is very rigorously founded in its two keystones: the variational formulation of the problem of fracture and the spatial regularization of the crack. The major weakness of the PFM is the extreme level of mesh resolution that it requires and its corresponding computational cost.

Assets

A1. Rigorous physical fundamentals. The method is based on the principle of minimum energy, resulting from the second law of thermodynamics, together with Griffith's theory of fracture. It applies both to quasi-static as well as dynamic problems, in 2D or in 3D.

A2. Rigorous mathematical foundation. The regularization of the sharp crack into a diffuse crack is soundly based, and this allows proving that the regularized problem converges to the original sharp one.

A3. Easiness of implementation. The PFM is easy to implement in any standard FE code, and especially in a multi-field FE code. It does not require any specific FE interpolation basis, so it can equally be used with triangles or quads, linear or quadratic. It does not require any particular development to be implemented in 3D.

A4. Mesh bias independence. Because the problem of fracture is regularized at continuous level, the corresponding discrete FE counterpart is able to produce mesh bias independent results without being affected by the lack of local convergence of the standard FE formulation.

A5. Strength, toughness and energy dissipation. PFM were originally devised to model brittle fracture but, as such, they could not incorporate the material strength, nor quasi-brittle failure. This serious drawback is overcome in more recent formulations incorporating the material strength, allowing to reproduce crack nucleation and quasi-brittle behavior [60, 78].

A6. Branching and intersecting cracks. PFM can handle branching and intersecting cracks as a matter of course if they spring in the solution of the specific problem.

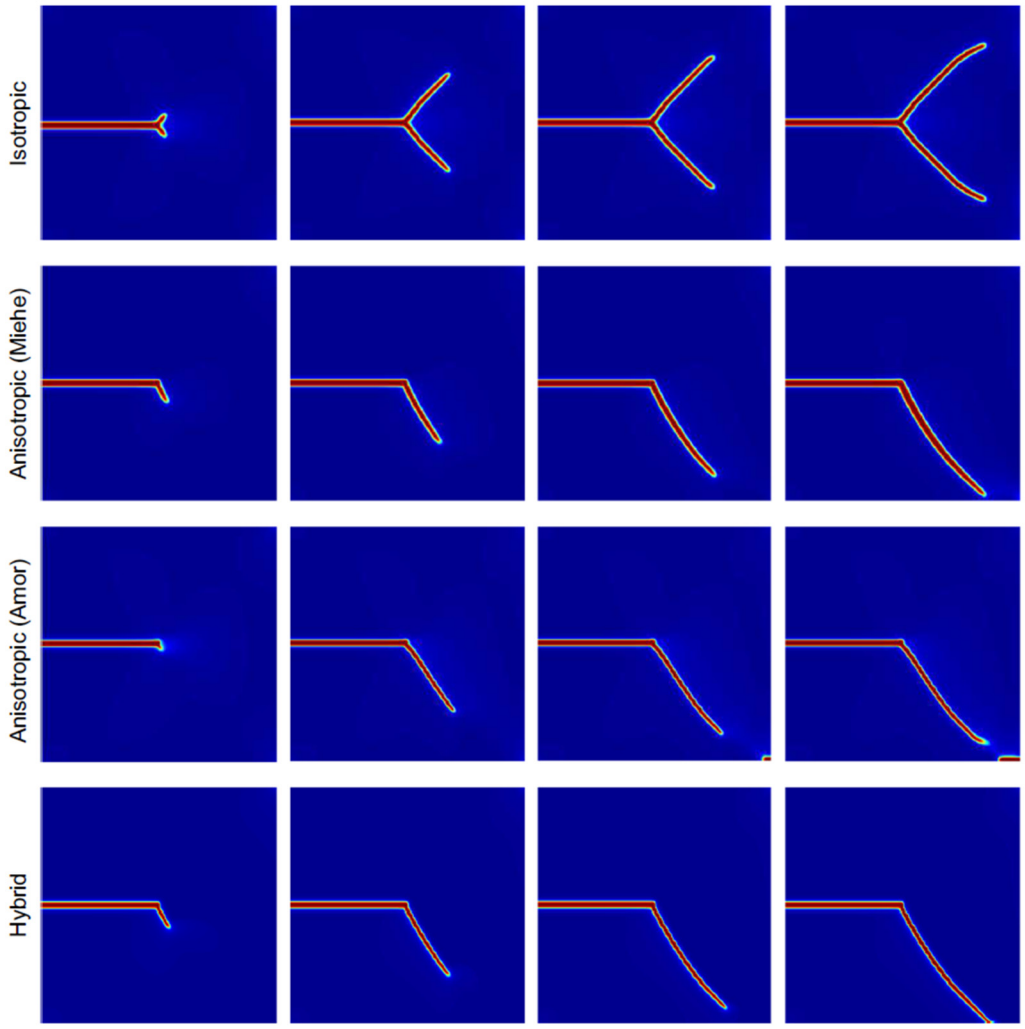

Figure 3.14: Comparison of damage contours obtained with isotropic, anisotropic and hybrid phase-field models, displayed in reference [262]

A7. No crack tracking procedures are required. Griffith's theory for fracture provides a criterion for crack growth but does not include the direction of propagation of the fracture [149, 194, 252, 253]. In PFM the direction of crack progression is implicitly incorporated in the variational formulation of the problem. Crack directions follow from the underlying constitutive model adopted, even if the corresponding damage surface is not always explicitly defined [78, 260]. Similarities can be found between the PFM formulation and the energy based crack tracking strategy in references [152, 261] where the path of the crack is chosen as the direction which minimizes the total mechanical energy.

A8. Allows for extensions of the crack constitutive behavior. The PFM represents the process of fracture using a scalar damage variable. In its original formulation, labeled "isotropic", the model does not discriminate tension from compression. Extensions have been made through the split of the strain energy density into different parts, such as positive and negative or volumetric and deviatoric, using the so-called "anisotropic" [49, 50, 263] or "hybrid" formulations [260, 262, 264]. This is a basic requirement to apply the model to materials such as concrete. Some of these developments are shown in Figure 3.14 [262].

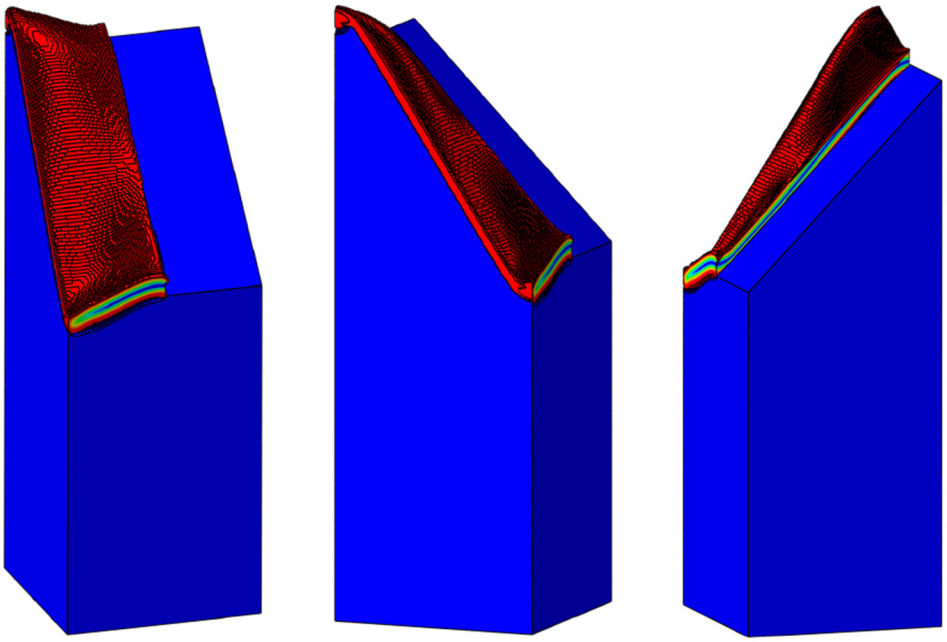

Figure 3.15: 3D mixed mode I and III fracture surface obtained with phase-field [70]

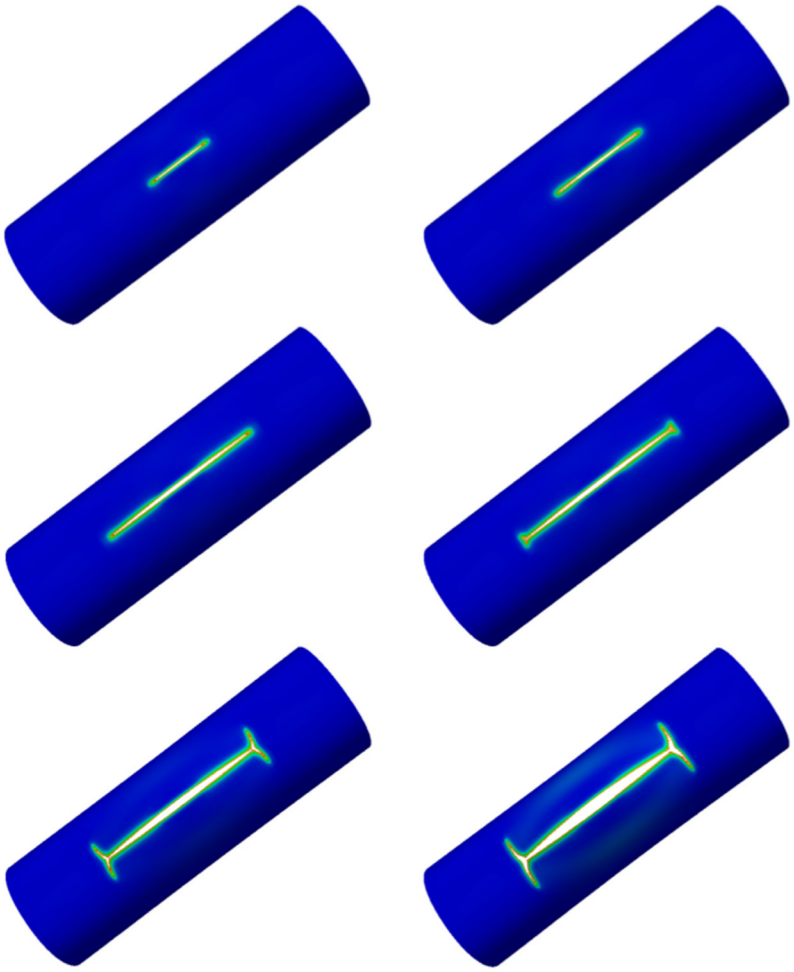

Figure 3.16: Cracking sequence of a hollow notched cylinder with tear straps under internal pressure computed with phase-field [269]

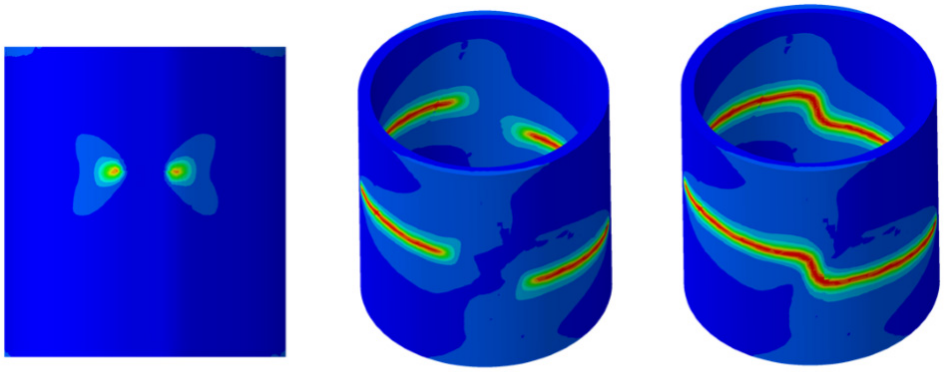

Figure 3.17: Crack propagation in a thick-walled cylinder computed with phase-field [270]

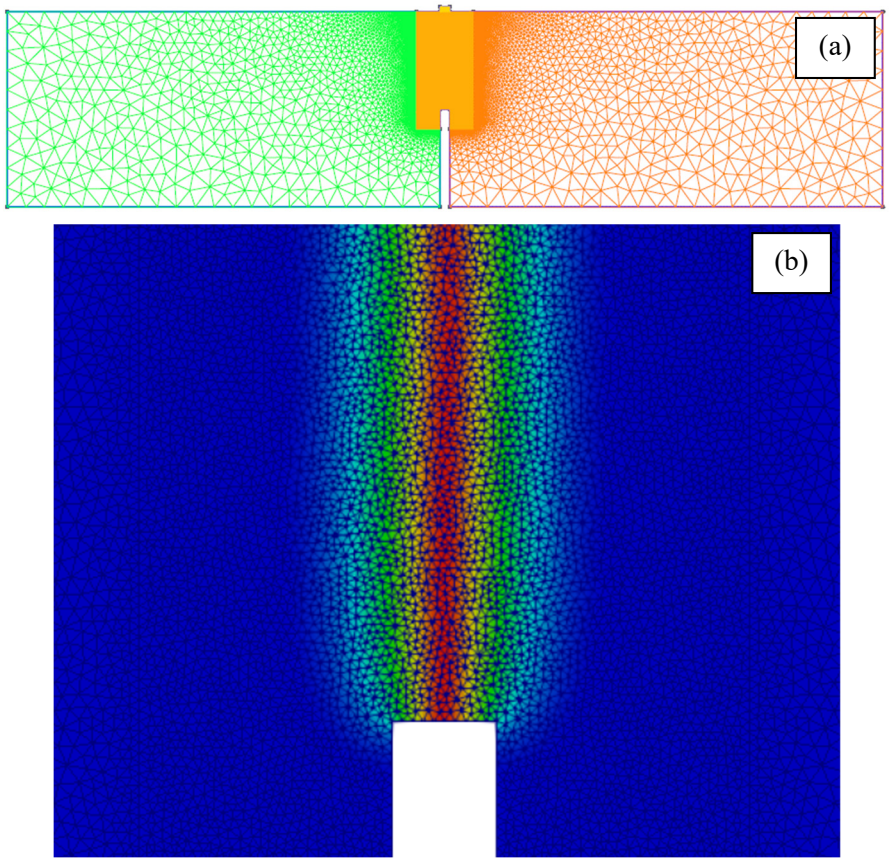

Figure 3.18: Mesh densities required in phase-field: three-point bending test of a notched beam: (a) model and (b) detail of the damage contour [63]

Drawbacks

D1. Generality with respect to constitutive behavior. From the original scalar isotropic damage model, the PFM has been extended to consider anisotropic brittle fracture [66, 83, 85, 265] including several damage mechanisms [84]. Effects such as irreversible straining and plasticity are also being considered [266, 267]. Stiffness recovery due to crack closure and reopening have not yet been included, even if it is possible [268]. Nonetheless, every development with regard to the constitutive behavior of the material requires the construction of a new version of the regularized variational formulation of the problem being solved. This process lacks the generality of the approach adopted in smeared crack models.

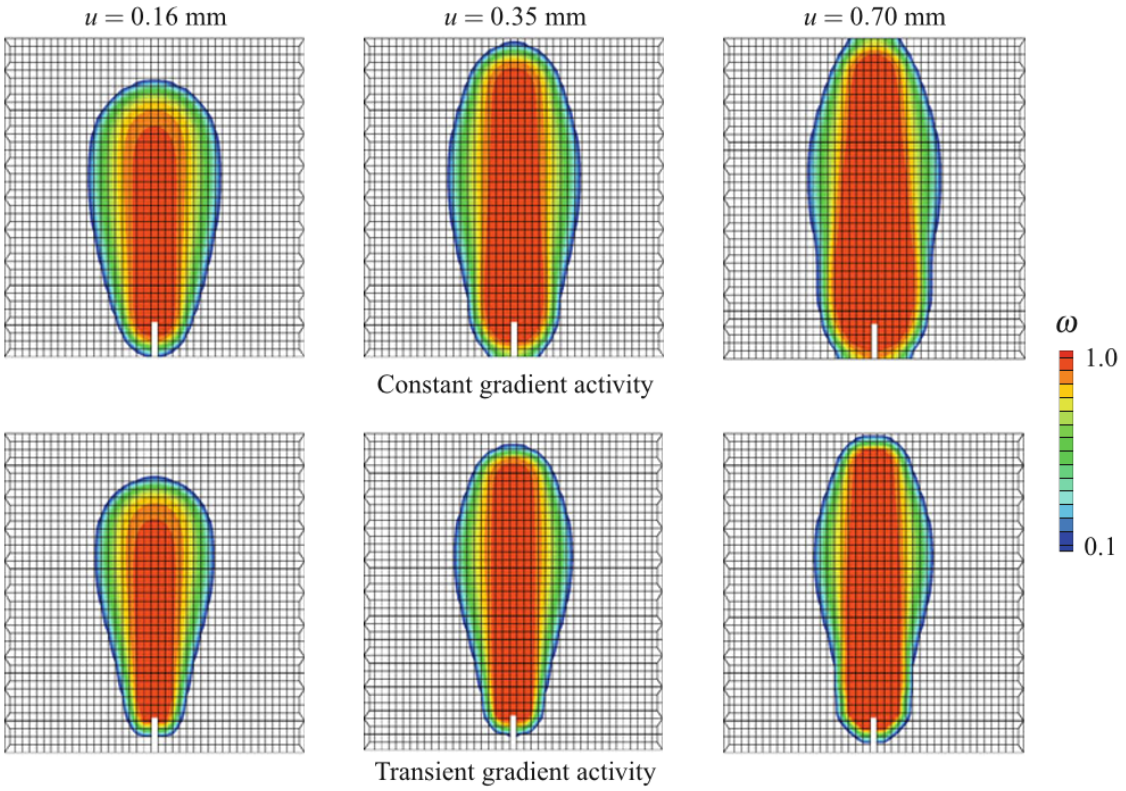

Figure 3.19: Mesh employed and evolution of the computed damage field in a four-point bending test using a gradient-enhanced damage model with (top) constant and (bottom) evolving length scale [46]

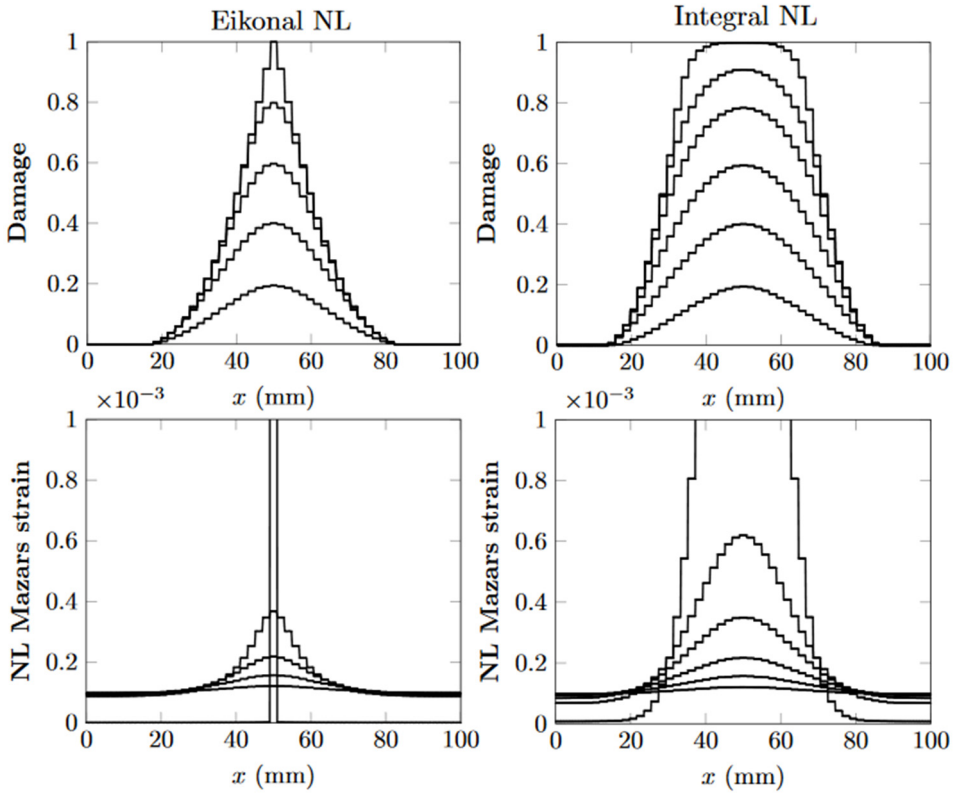

Figure 3.20: Damage and strain profiles of several nonlocal damage models, taken from [187]

D2. Extremely high computational cost. The weak point of the PFM is the computational cost. This method achieves mesh objectivity by regularizing the crack over a band of finite elements, with a minimum bandwidth $4h \leq b \leq nh;\ \ n{\sim}10$, h corresponding to the mesh size. In 2D this results in an increase of the number of elements required in the area where the crack develops by a factor of at least 16 to 100 times and in 3D the increment is by a factor of no less than 64 to 1000 with respect to the standard and mixed FE formulations.

This colossal computational cost prevents PFM from being used in engineering applications at the present. Figures 3.15, 3.16 and 3.17 show some of the very few 3D applications calculated so far [70, 269-275]. The prohibitively high computational cost involved justifies the quest for more cost-efficient alternative techniques. This issue has been addressed as well via the implementation of adaptive mesh refinement in references [50, 51, 276-279] and by computing the nodal phase-field variables only in a reduced sub-domain where damage develops rather than in the whole structure, as can be seen in Figure 3.18 [63].

The necessity of fine mesh densities is a common issue in methods introducing a high regularization of the localization band. Figure 3.19 shows a crack bandwidth extending over a large number of elements in a gradient-enhanced damage model. Figure 3.20 presents the discrete damage and strain profiles employed in simulations using several nonlocal damage models, which also require a large number of elements to represent strain localization in a regularized manner.

	Checklist for the PFM	✓✓	✓	○	×	××
1	Variational formulation in the continuous setting	A1, A2				
2	Convergence of the FE formulation		A4			
3	Strength, toughness and energy dissipation	A2, A5				
4	Criterion for direction of propagation	A4				
5	Constitutive behavior generality		A8		D1	
6	Generality and implementation effort		A1, A3			
7	Cost-efficiency					D2
8	Multiple, intersecting and branching cracks	A6				
9	Auxiliary tracking techniques	A7				
10	Application in 3D					D2

3.4 Numerical simulations of localized structural failure

In this section the numerical simulations reported in references [60, 63, 70] using the Is-XFEM and the PF-CZM are contrasted with corresponding results obtained with the mixed FE formulation proposed, implemented, validated and employed in this thesis. The study cases selected are some of the most popular in the community, having been considered many times for the validation of numerous numerical models. The objective of this section is to assess the comparative performance of the XFEM, the mixed FE approach and the PFM.

The mixed FE numerical simulations are computed with an enhanced version of the finite element code COMET [280]. Pre- and post-processing are performed with GID [281], developed at the International Center for Numerical Methods in Engineering (CIMNE). Convergence in each load step is reached when the ratio between the norm of residual forces and the norm of total external forces is lower than 10^{-3} %.

3.4.1 Wedge splitting test

In this section, the numerical analysis of a wedge splitting test reported in reference [282] is considered. In reference [282] multiple series of geometrically similar specimens of varying sizes are tested and numerically simulated using the Fictitious Crack Model. Other numerical simulations of these tests can be found in reference [283], where a gradient plasticity model is employed, in reference [71], which used the XFEM, in references [103, 284, 285], where the EFEM is considered, in reference [286], which used cohesive interface elements, and in reference [287], which used the peridynamic theory to model the crack propagation.

In the following study, the computations in reference [63], where a comparison of the results obtained with the Is-XFEM and the PF-CZM is made, are contrasted with corresponding simulations calculated with the mixed FEM. In this mode I fracture test the computed crack follows a straight trajectory. Therefore, this case is not used here to assess the mesh-objectivity of the examined FE formulations. However, it is employed as an initial reference test for comparing the three models in terms of the material nonlinear softening behavior. All the methods should converge to the same solution if the same properties and constitutive laws are employed. Note that the objective of this study is to compare the results with respect to the XFEM and the phase-field model solutions in reference [63] and not to reproduce the original experimental results. A comparison with the experiment can be found in reference [31], included in the compendium, where the mixed FEM has been already employed to replicate the wedge splitting test.

The geometry and boundary conditions of the test are shown in Figure 3.21. It is a specimen of dimensions 0.8 m x 0.8 m x 0.4 m with a vertical notch in the upper half. Two horizontal loads are applied close to the notch mouth. The same material properties as in reference [63] are considered and shown in Table 1. The simulation is performed under arc length control of the Crack Mouth Opening Displacement (CMOD) until it reaches 4 mm.

The simulation is performed in 2D under the plane strain assumption using a structured mesh of quadrilateral elements with a size of 1 cm, resulting in the 6,276 elements mesh shown in Figure 3.22. On the one hand, reference [63] used a similar FE size for the elements in the area where the crack develops in the corresponding simulations with the XFEM. On the other hand, for the phase-field computations a mesh size of 1 mm, 10 times smaller, was adopted in reference [63], which in 2D increases the number of elements employed in the simulation by a factor on the order of $10^2 = 100$.

Figure 3.23 shows the computed crack paths for the three methods examined in this work. Specifically, Figure 3.23a displays the trajectory obtained with the XFEM, while Figure 3.23c depicts the computed damage with the phase-field approach, both taken from reference [63], and Figure 3.23b exhibits the computed maximum principal strain with mixed FEs. In all the cases the fracture follows the same straight vertical line. In Figure 3.24 the force-displacement curves for the three methods are shown. The results for the XFEM and the PFM, which are almost overlapping, are taken from reference [63]. It can also be seen that the results produced by the mixed FE formulation are also practically the same. This shows that the constitutive laws used in the three methods are consistent with each other and are able of reproducing the same nonlinear cohesive behavior.

It should also be noted that the computational cost involved in each method to produce the same result is not the same. In particular, the computational cost involved in the phase-field method is much larger, as it requires a much finer FE mesh.

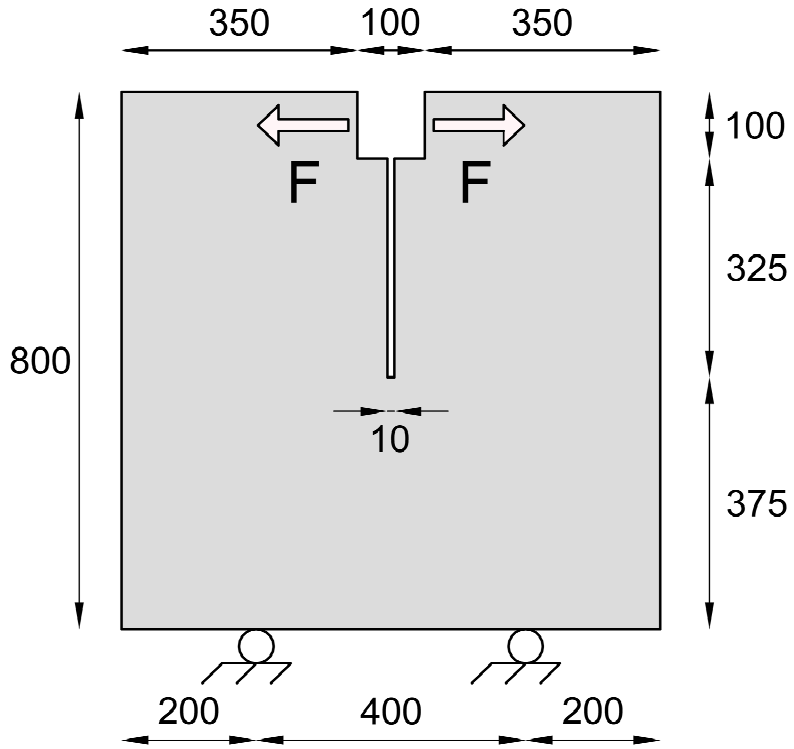

Figure 3.21: Geometry of the wedge splitting test (mm)

Young's Modulus	$28.3 \cdot 10^9$ Pa
Poisson's Ratio	0.18
Tensile Strength	$2.12 \cdot 10^6$ Pa
Tensile Fracture Energy	373 J/m2

Table 1: Material parameters of the wedge splitting test

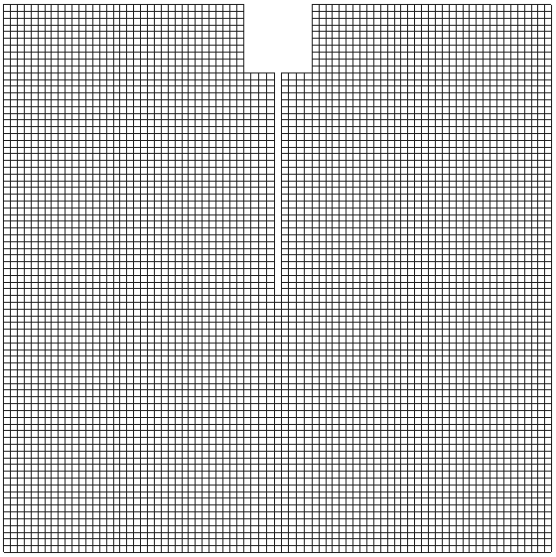

Figure 3.22: Mesh used for the wedge splitting test in the mixed FE simulation

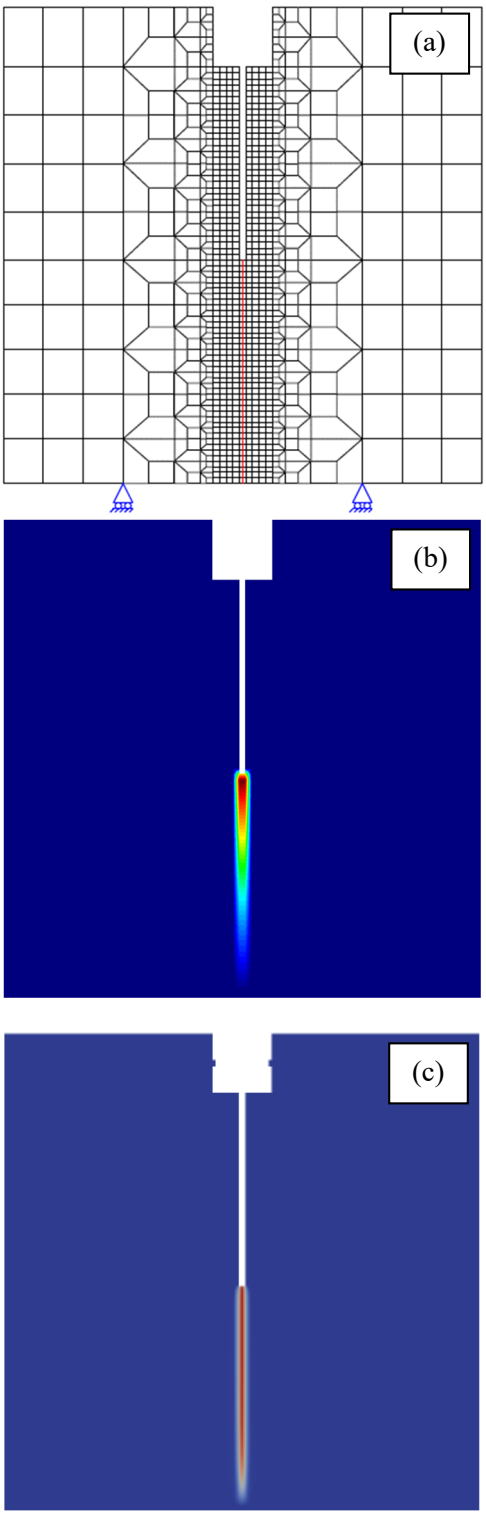

Figure 3.23: Computed crack paths in the wedge splitting test with: (a) the XFEM, (b) mixed FE and (c) phase-field, (a) and (c) taken from [63]

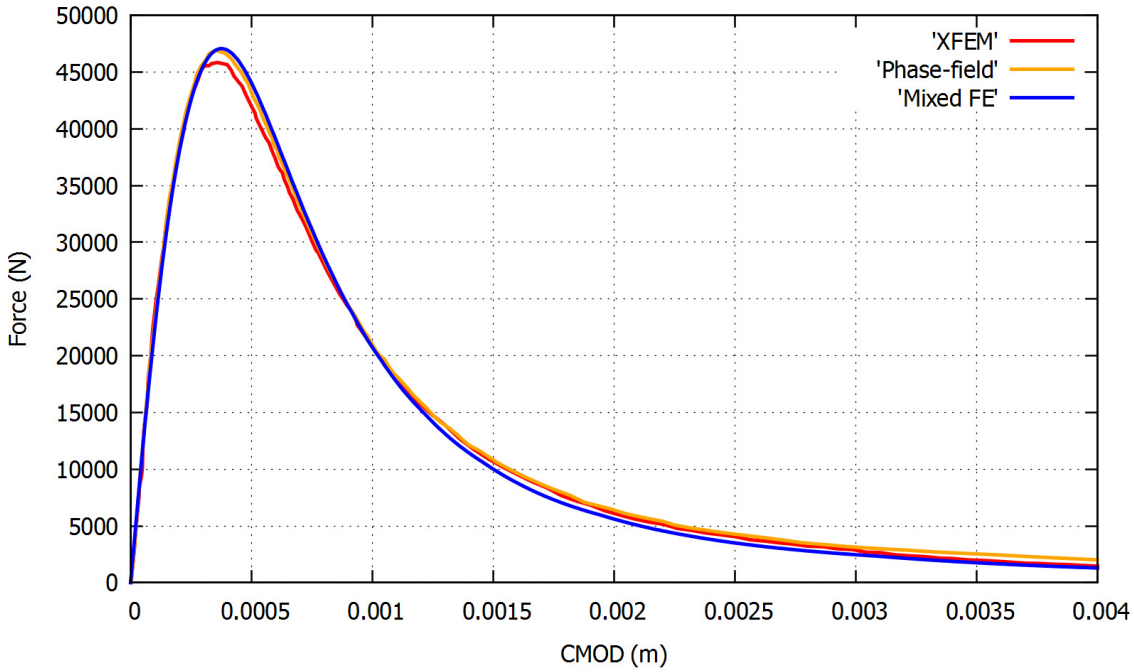

Figure 3.24: Force-CMOD curve of the wedge splitting test for the three methods considered

Mesh refinement analysis

The objective of this section is to assess the capacity of the mixed FE formulation of producing coherent results with different mesh sizes using both triangular and quadrilateral elements. For this, the simulation of the wedge splitting test is performed using the four different meshes detailed in Figure 3.25, where the FE size is taken as 10 mm and 3.33 mm both for triangles and quads. All these meshes, as well as all the other ones employed for the mixed FEM throughout this work, are much coarser than the ones customarily used in phase-field simulations.

In reference [63], the convergence analysis featured for the PFM compares meshes with elements of 1 mm and 0.5 mm. As displayed in Figure 3.25, in the mixed formulation the FE size can be set equal to the width of the notch, which is in this case of 1 cm. In the corresponding phase-field simulation in reference [63], the crack bandwidth b is taken as $10h$, h being the FE size, so that at least 1 mm elements are required.

The resulting maximum principal strain field, depicting the computed crack paths, is shown in Figure 3.26 for the four meshes, where it can be seen that the crack bandwidth is reduced when the mesh size decreases. In Figure 3.27 the force-CMOD curves obtained with the different meshes are assessed against each other. It can be examined, in Figure 3.27a, that the results derived from the quadrilateral elements are practically overlapping, while the ones computed with triangular elements in Figure 3.27b require a finer mesh to reach a perfectly converged solution. In Figure 3.27c it is verified that, when the FE size is reduced enough, both quadrilateral and triangular elements produce the same solution. It can be observed that suitable results can be reached with mixed FE without using the fine meshes required in the PFM.

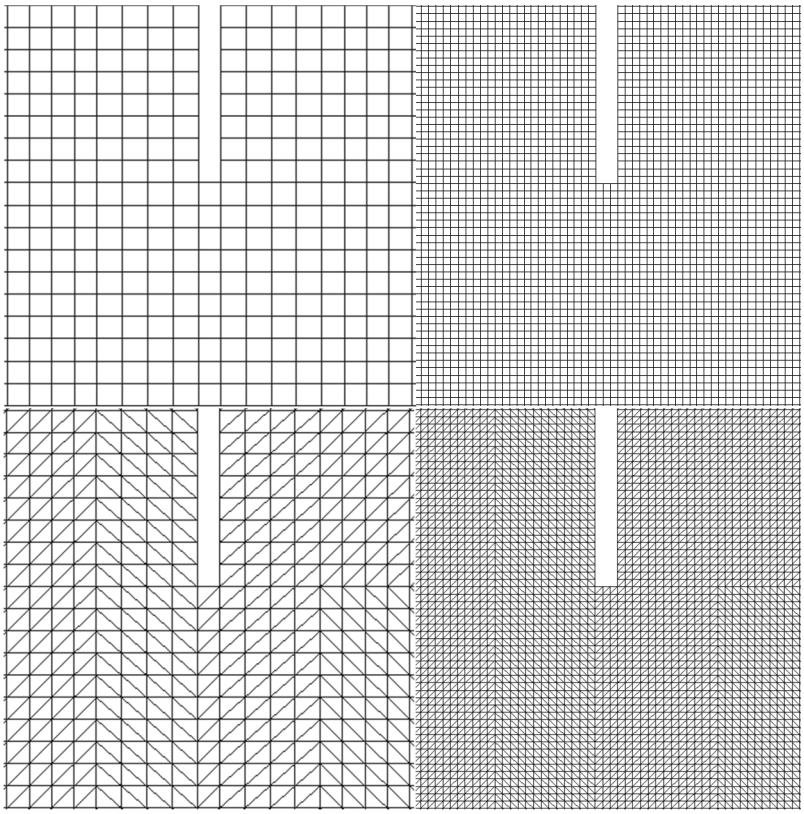

Figure 3.25: Detail of the meshes used for the convergence analysis around the tip of the notch: (up) quadrilateral and (bottom) triangular FE, using (left) h = 10 mm and (right) h = 3.33 mm

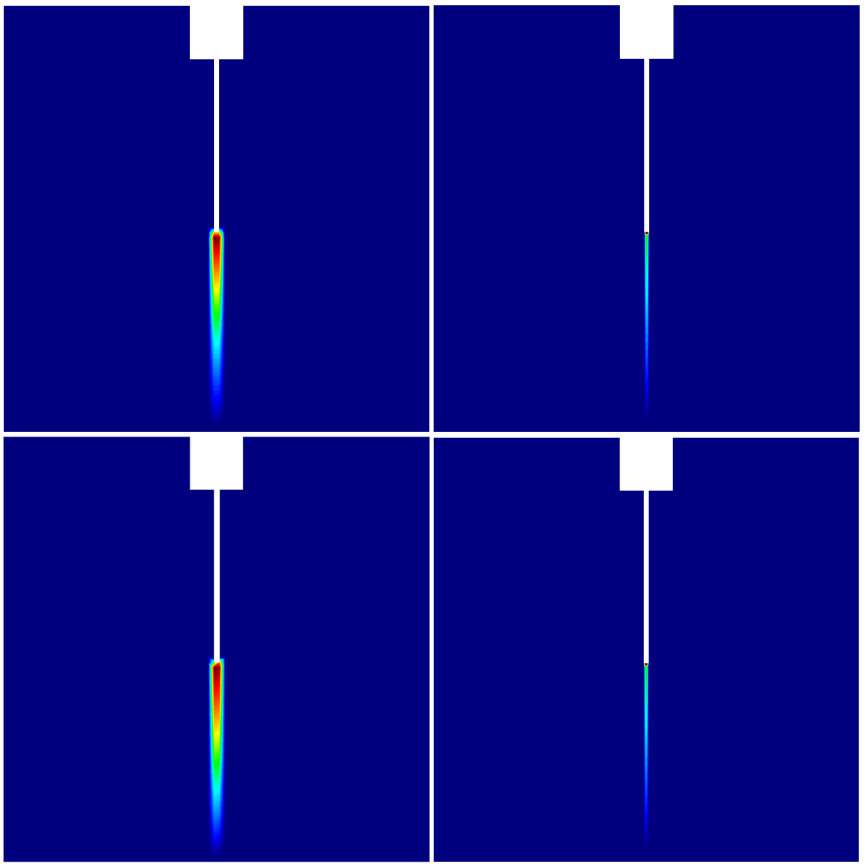

Figure 3.26: Mesh refinement analysis of the wedge splitting test: Computed crack paths with (up) quadrilateral and (bottom) triangular FE, using (left) h = 10 mm and (right) h = 3.33 mm

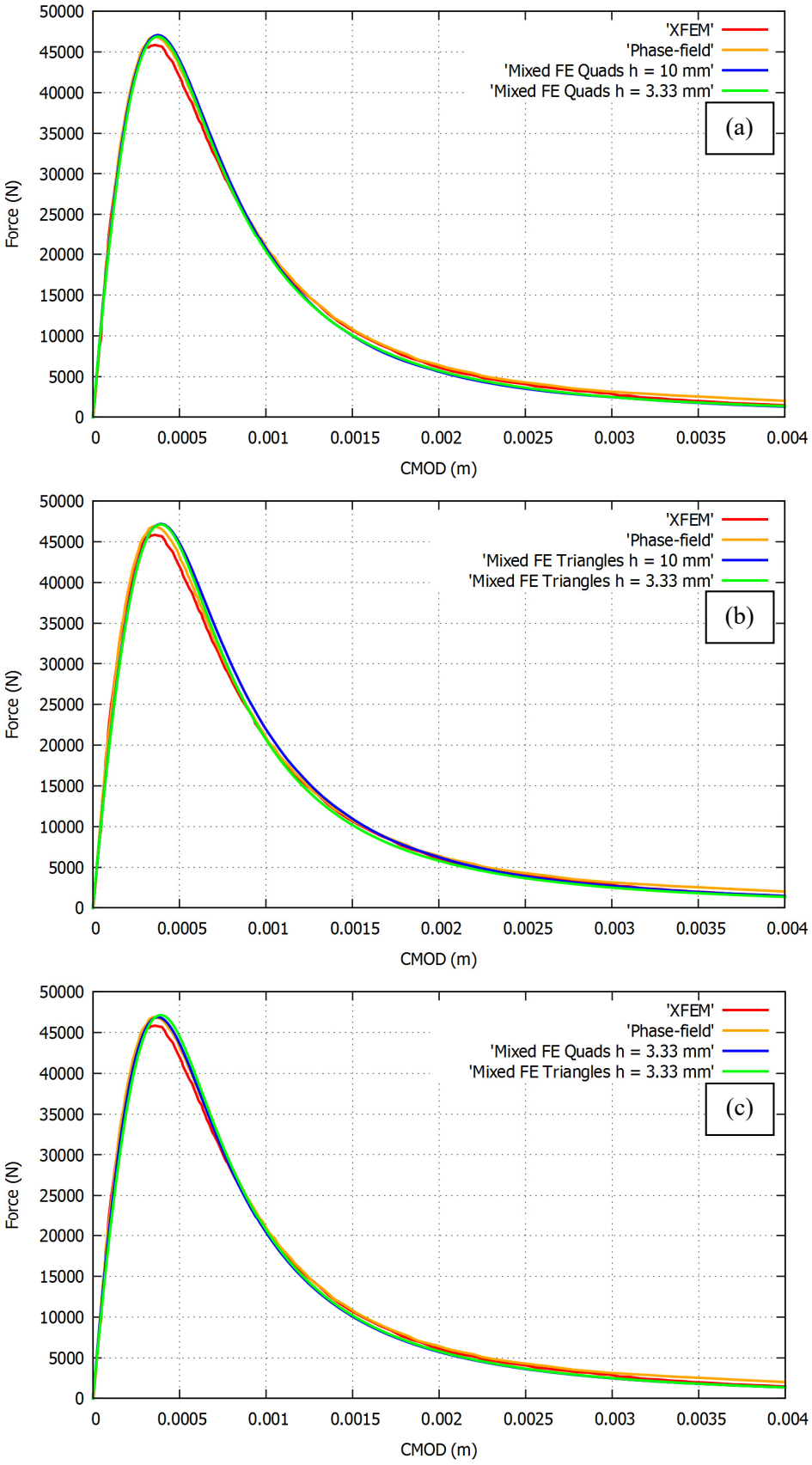

Figure 3.27: Mesh refinement analysis: Force-CMOD curve of the wedge splitting test for (a) quadrilateral elements, (b) triangular elements and (c) quadrilateral vs. triangular FE comparison

2D vs. 3D simulations

3D applications are scarce in phase-field literature due to the high computational cost involved and in the XFEM because of the additional implementation effort required. The generality and the affordable computational cost of mixed FE allows to readily perform the simulations in 3D.

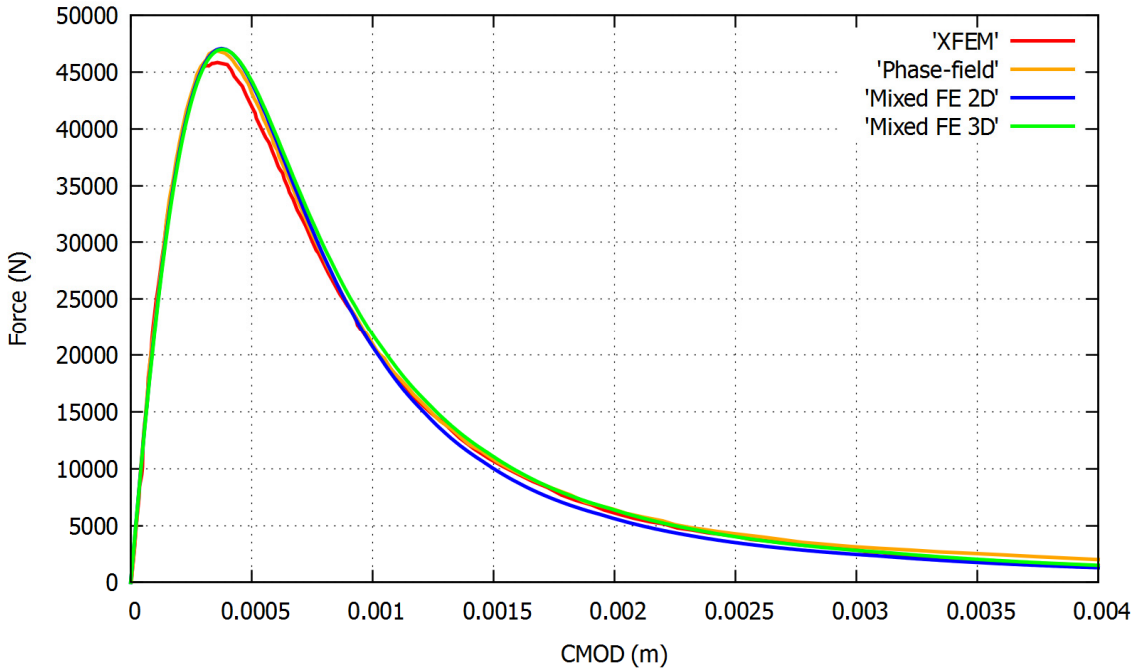

Figure 3.28: Force-CMOD curves of the wedge splitting test computed with mixed FE in 2D and 3D

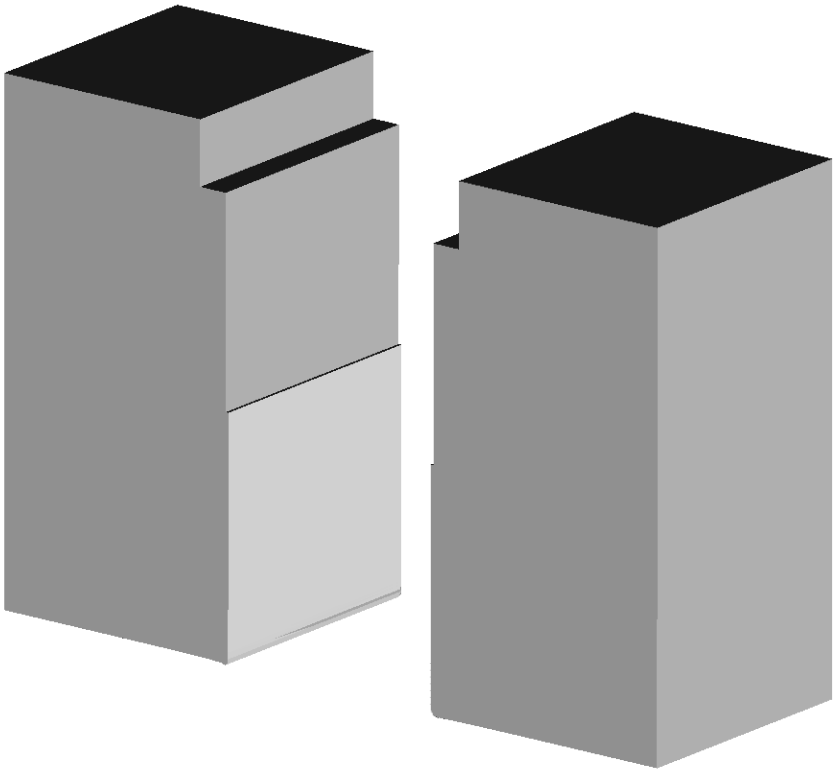

Figure 3.29: Computed crack surfaces of the wedge splitting test with mixed FE

With the intent of showing the capacity of the mixed FE method to accurately produce results in 3D, in this section the computations of the wedge splitting test obtained in 2D are compared with corresponding 3D simulations. The same material properties as in 2D, shown in Table 1, are employed in this case. The simulation is performed with a mesh of 6,276 hexahedral elements of 10 mm size and one element through the thickness.

The computed force-CMOD curves for the 2D and 3D analyses are shown in Figure 3.28. It can be seen that both results are very close to each other and also very similar to the XFEM and the phase-field method simulations in reference [63]. The crack surface obtained in the 3D simulation is shown in Figure 3.29.

3.4.2 Arrea and Ingraffea mixed mode bending test

In this section, the numerical simulation of the Arrea and Ingraffea experiment, reported in reference [288], is considered. Other numerical simulations of the tests can be found in references [22, 289], where a smeared crack model is employed; in reference [290], where the Fictitious Crack Model is considered; in references [96, 150], where a model with a transition from a continuous nonlocal formulation to a discontinuous embedded finite element method is proposed; in reference [291], which employed cohesive interface elements; in references [184, 292], where a nonlocal damage model is used; in references [16, 100, 293, 294], where the EFEM is applied; in reference [155], where the EFEM and the XFEM are compared; in reference [295], which compares rotating and fixed smeared crack models; in references [296, 297], where a meshfree method is introduced; in reference [298], where an approach coupling the finite element method and the discrete element method is proposed and in reference [299], where a model featuring a transition from a smeared crack damage model to the XFEM is used. Also, the numerical modelling of a beam with a similar geometry and boundary conditions, experimentally tested in reference [300], can be found in reference [300], which considered a lattice model, a method which introduces a network of 1D beam finite elements to model the 2D structure; in reference [42], where a gradient-enhanced damage model is used and in reference [301], which employed the XFEM to solve the problem.

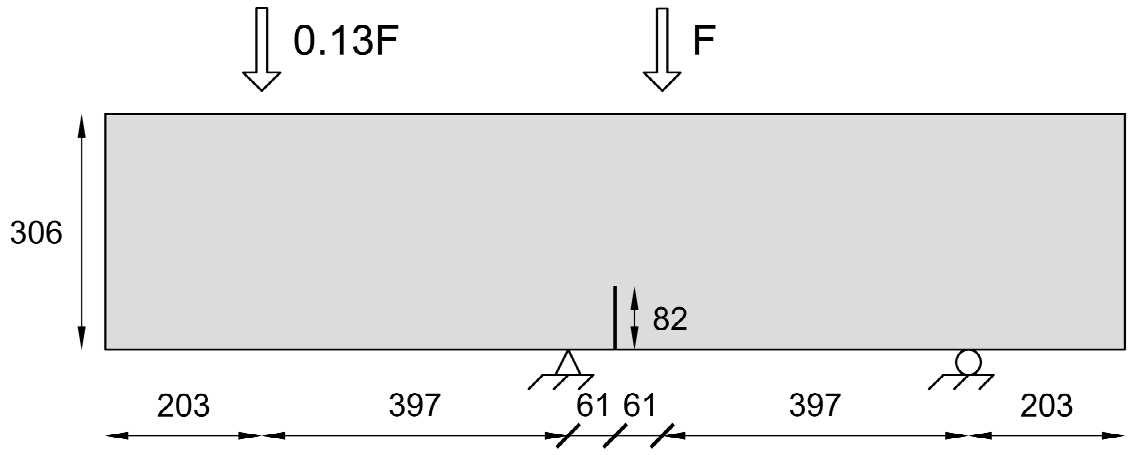

Figure 3.30: Geometry of the Arrea and Ingraffea mixed mode bending test (mm)

Young's Modulus	$28.8 \cdot 10^9$ Pa
Poisson's Ratio	0.18
Tensile Strength	$2.8 \cdot 10^6$ Pa
Tensile Fracture Energy	100 J/m^2

Table 2: Material parameters of the Arrea and Ingraffea test

In the following, the results obtained with the XFEM and the phase-field model in [63] are taken as references for the present comparison with the mixed FEM. The beam is subjected to four-point bending, so that the loading eventually leads to mixed mode fracture. Therefore, this example can be employed to assess the mesh objectivity in terms of crack trajectory of the three methods contrasted in this work. Also, it can be used to compare solutions obtained with alternative constitutive laws and study the effect that different damage surfaces have in the resulting crack trajectories.

The details of the geometry and boundary conditions of the experiment are given in Figure 3.30. The dimensions of the beam are 1.322 m x 0.306 m and the notch length is 82 mm. The thickness of the beam is 0.156 m and two eccentric loads F and 0.13F are applied.

The simulations are done under CMOD control. For comparison purposes, the same material properties as in reference [63], shown in Table 2, are used. Note that they were not chosen with the intent of reproducing the experiment but rather to compare the results of the XFEM and the PFM. A comparison between the mixed FE formulation and the experimental response can be found in reference [32], included in the compendium of publications.

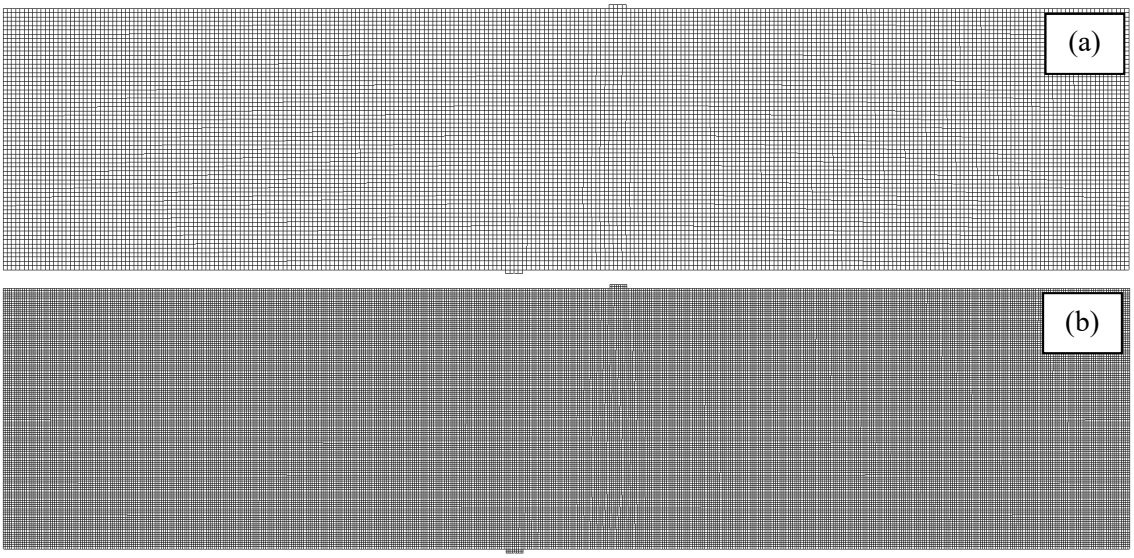

Figure 3.31: Meshes used for the Arrea and Ingraffea test in the mixed FE simulations with (a) h = 5 mm and (b) h = 2.5 mm

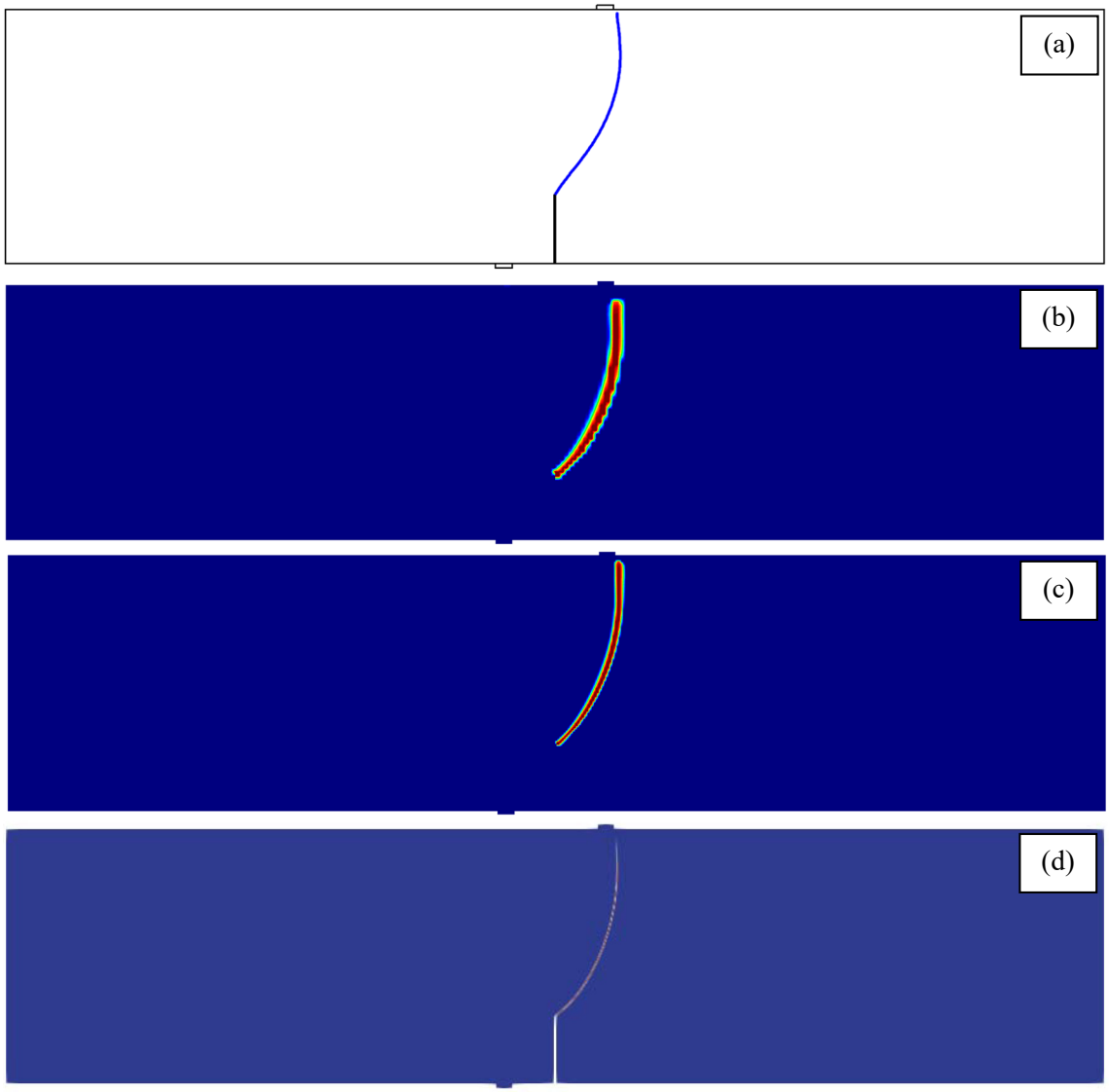

Figure 3.32: Comparison of the results of the Arrea and Ingraffea beam: (a) crack trajectory obtained with the XFEM and damage contours computed with (b) mixed FE using h = 5 mm, (c) mixed FE using h = 2.5 mm and (d) the phase-field model; (a) and (d) taken from [63]

The mixed FE simulations are performed under the plane stress hypothesis using quadrilateral elements of sizes 5 mm and 2.5 mm, which correspond to the sizes used for the XFEM simulations in reference [63] in the refined region where damage appears. This results in a mesh of 16,173 and 64,976 elements, respectively, shown in Figure 3.31. Again, the size of the elements used for the corresponding phase-field simulations in reference [63] is 10 times smaller, of 0.5 mm and 0.25 mm. This increases the number of elements as well as the number of degrees of freedom in 2D by a factor of approximately 100.

Figures 3.32b and 3.32c depict the computed damage contours of the Arrea and Ingraffea beam obtained with mixed FE. It can be seen that the path of the fracture, starting at the notch, turns upwards influenced by the mixed mode loading of the beam. It can be compared with computations using the XFEM and the PFM in figures 3.32a and 3.32d, taken from reference [63]. A detailed comparison of the crack trajectories is shown in Figure 3.33. The solutions obtained with the three methods are almost identical. In particular, it can be seen that the results from the phase-field model and the mixed FEM are practically the same. Note also that the computations

with mixed FE for both meshes are practically overlapping, showing that proper convergence is achieved.

Figure 3.34 shows the computed Force F vs. Crack Mouth Sliding Displacement (CMSD) curves with the three methods. It can be seen that they are very similar, even if they are not exactly the same. This is because, the simulations with the XFEM and the PFM were obtained in reference [63] using the Cornelissen softening curve [79] while for the mixed FEM exponential softening was considered. The Cornelissen softening law, defined in terms of crack opening, is used in reference [63] and yields a slightly different softening response than exponential decay.

The ability of the three methods to produce the same results is demonstrated again. This is remarkable as the difference in the computations performed with the three different methods for quasi-brittle cracking and with different FE codes is minimal.

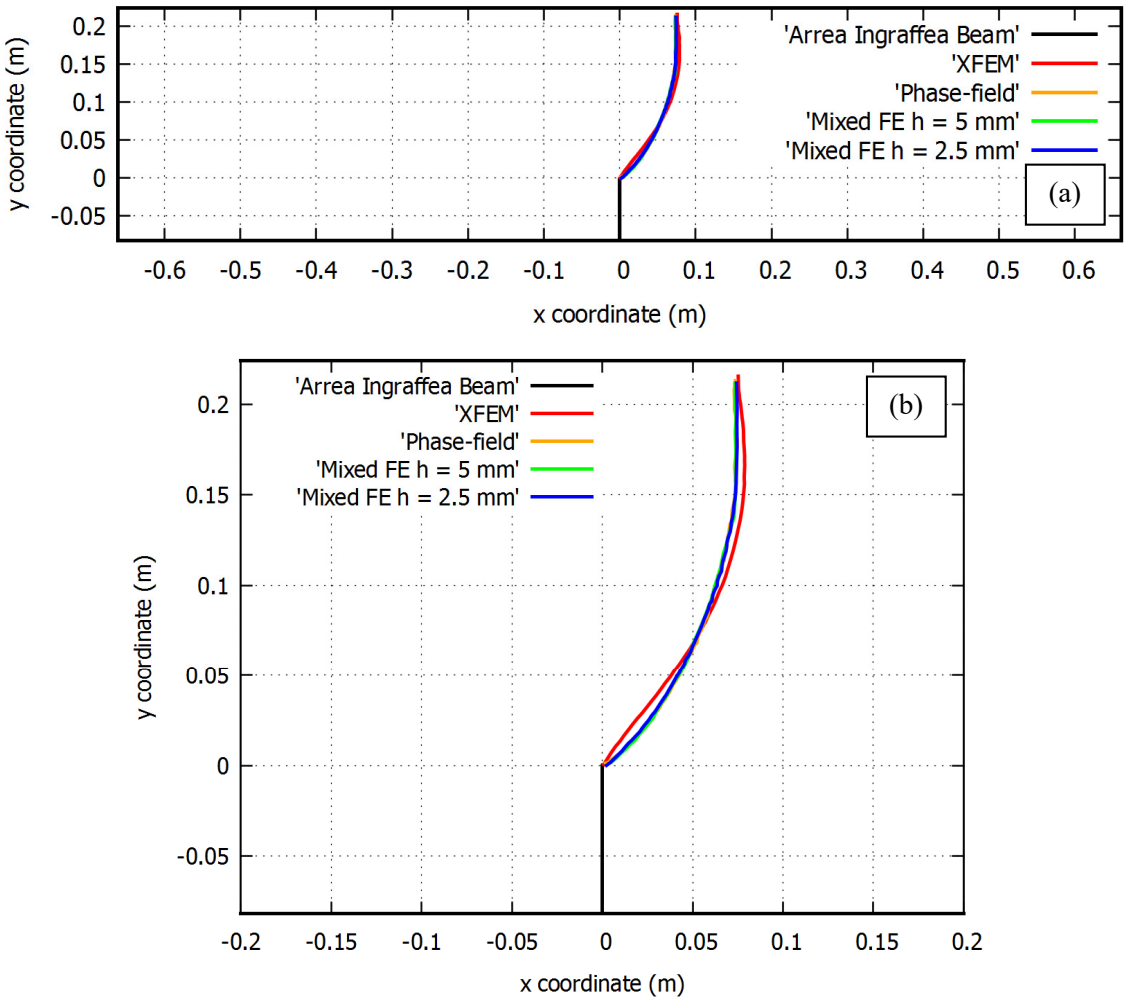

Figure 3.33: Comparison of the Arrea and Ingraffea beam crack trajectories (a) in the whole structure and (b) in detail

Note that while the phase-field model and the mixed FEM are able of producing practically the same results in terms of crack trajectory, the computed fracture path in the XFEM is slightly different. Interestingly, the results obtained with the two mesh sizes considered in reference [63] for the XFEM produce almost overlapping results. This small difference between the models is probably caused by a bias introduced by the crack tracking algorithm employed in the XFEM, while no procedures outside the variational form of the problem are implanted for the determination of the crack trajectory in mixed FE and the phase-field model.

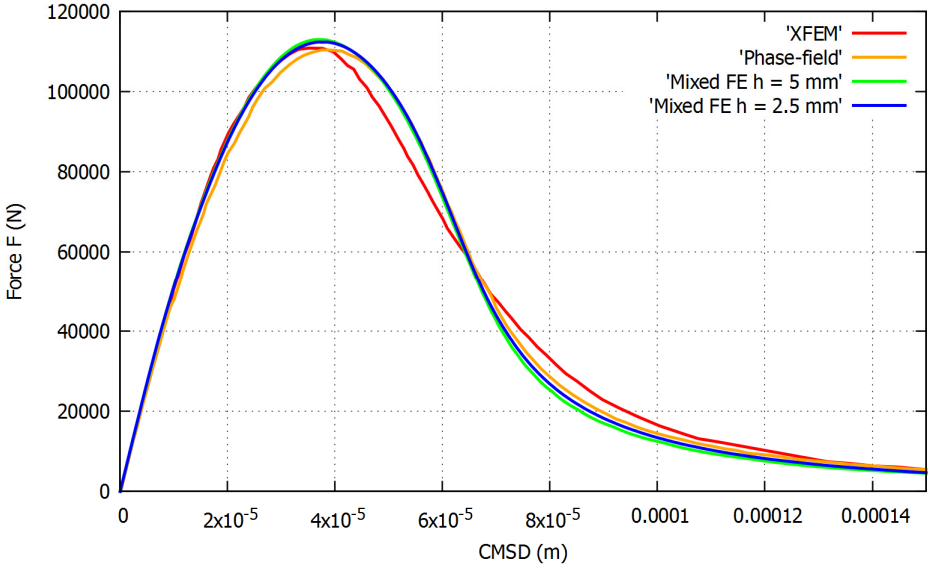

Figure 3.34: Computed Force F vs. CMSD curves of the Arrea and Ingraffea beam with the three methods considered

Comparison of the results obtained with different damage surfaces

The previous simulations of the mixed FEM were performed with an isotropic Rankine damage model, to maintain the consistency in the comparisons with the XFEM and phase-field results taken from reference [63]. However, as shown in references [32, 34], included in the compendium, mixed FE can be readily used in conjunction with different material laws defined in the traditional stress-strain format. This allows to study the effect that constitutive behaviors have on the crack trajectory.

Usually the XFEM employs exclusively the Rankine damage surface. This is because the XFEM requires the implementation of specific crack propagation criteria for each damage surface separately. For example, in reference [105] a tracking criterion consistent with the Mohr-Coulomb damage surface is developed. This differs from the mixed FE approach, as well as from the PF-CZM, were the direction of crack propagation is implicitly provided by the constitutive law and does not require tracking. Other studies, comparing the behavior of several damage criteria using mixed FE, are made in references [32, 34].

In this section, the Rankine, Positive Beltrami and Drucker-Prager surfaces, depicted in Figure 3.35 for plane stress, are considered. The same material properties given in Table 2 are used for all the cases. The compressive vs. tensile strength ratio for the Drucker-Prager criterion is taken as 10.

The computed damage contours are shown in Figure 3.36 and a detailed comparison of the crack trajectories is provided in Figure 3.37. On the one hand, it can be seen that the Rankine and Positive Beltrami criteria produce practically the same results. This is because their damage surfaces, portrayed in Figure 3.35, are the same in the traction-compression quadrant. On the other hand, the Drucker-Prager criterion produces a slightly more curved trajectory. In Figure 3.38, the corresponding force-CMSD results are provided. Again, the behavior of Rankine and Positive Beltrami is very similar, while a somewhat larger difference can be appreciated for the Drucker-Prager curve, which is caused by the deviation of the crack trajectory.

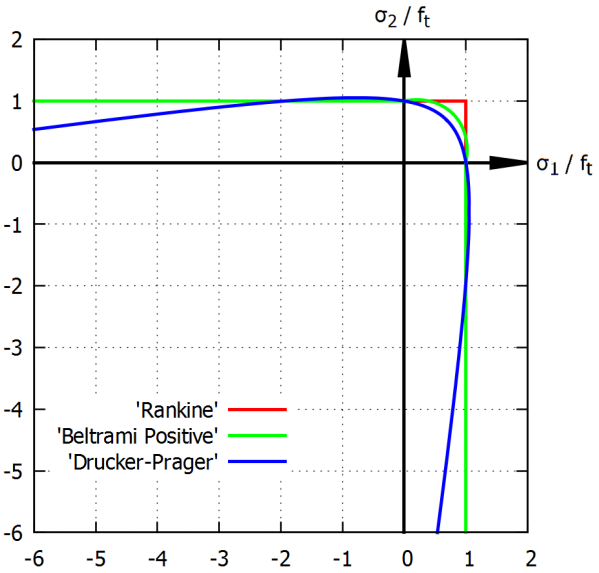

Figure 3.35: Rankine, Beltrami Positive and Drucker-Prager damage surfaces

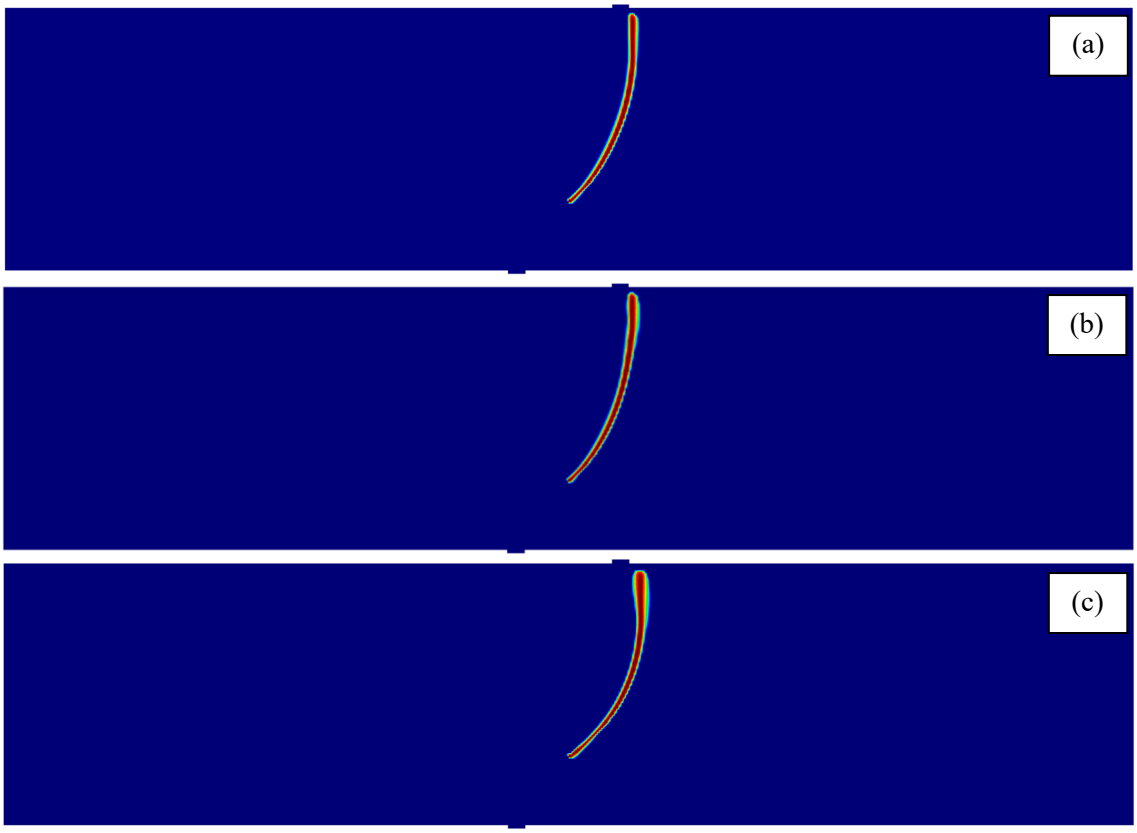

Figure 3.36: Damage contours computed with mixed FE of the Arrea Ingraffea beam using the (a) Rankine, (b) Positive Beltrami and (c) Drucker-Prager (fc/ft = 10) surfaces

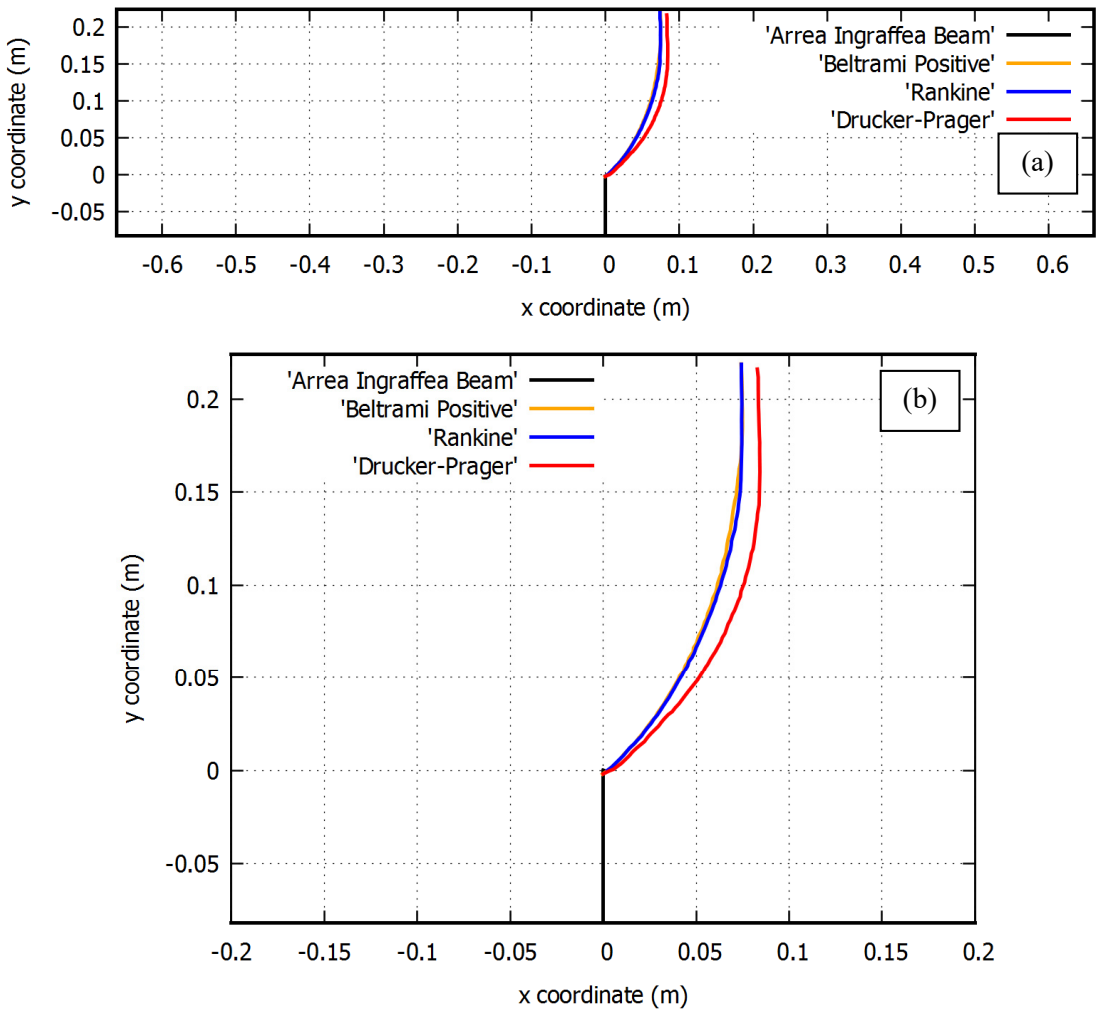

Figure 3.37: Comparison of the crack trajectories for the Rankine, Positive Beltrami and Drucker-Prager surfaces in the Arrea and Ingraffea beam (a) in the whole structure and (b) in detail

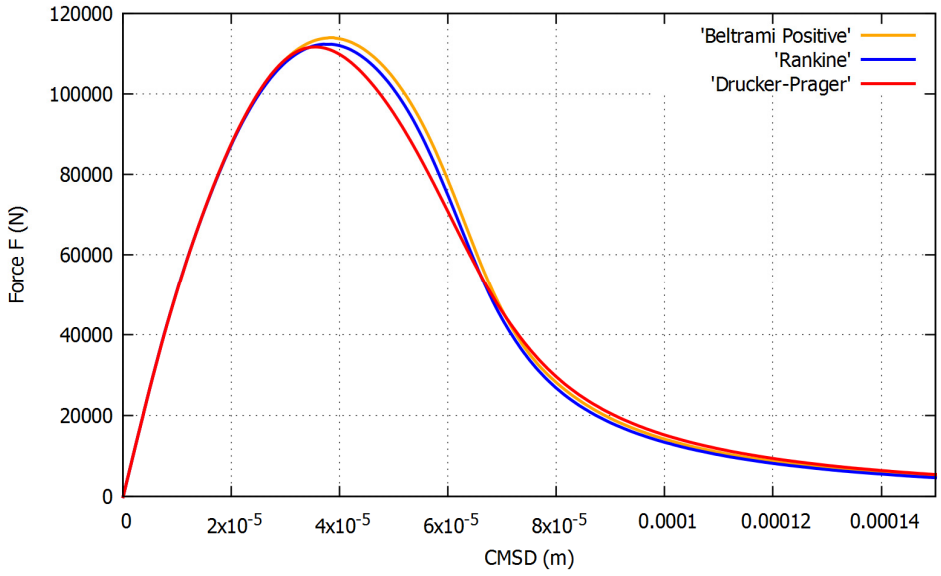

Figure 3.38: Computed Force F vs. CMSD curves of the Arrea and Ingraffea beam with the three damage surfaces considered

2D vs. 3D simulations

The generality and the affordable computational cost of mixed FE allows to produce the same results in 3D without any difficulty. In this section the computed results in 2D are contrasted to corresponding 3D simulations.

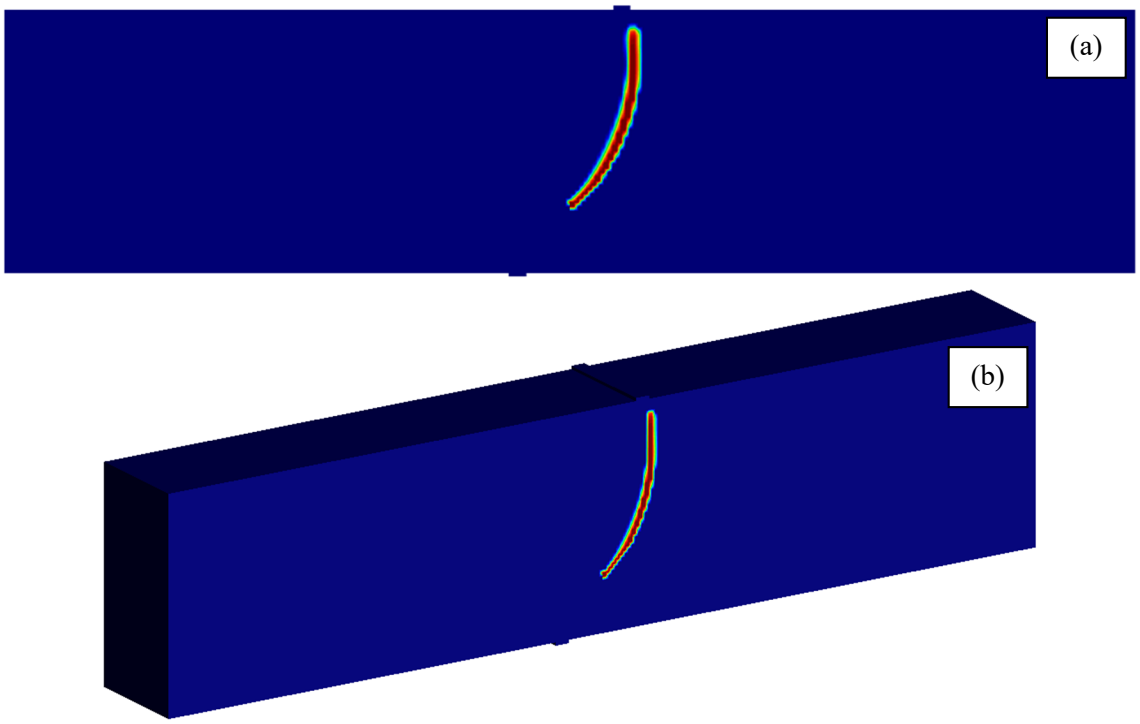

Figure 3.39: Damage contours of the 3D simulation of the Arrea and Ingraffea beam computed with mixed FE: (a) front view and (b) side view

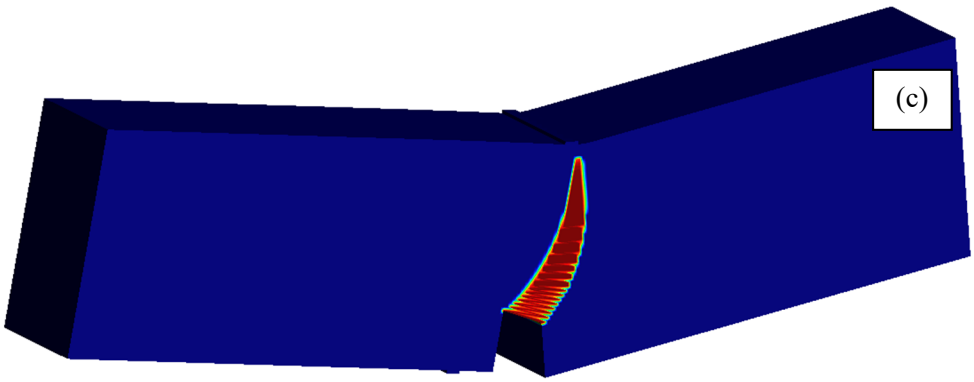

Figure 3.40: Damage contours of the 3D simulation of the Arrea and Ingraffea beam computed with mixed FE: (c) deformed shape (x 200)

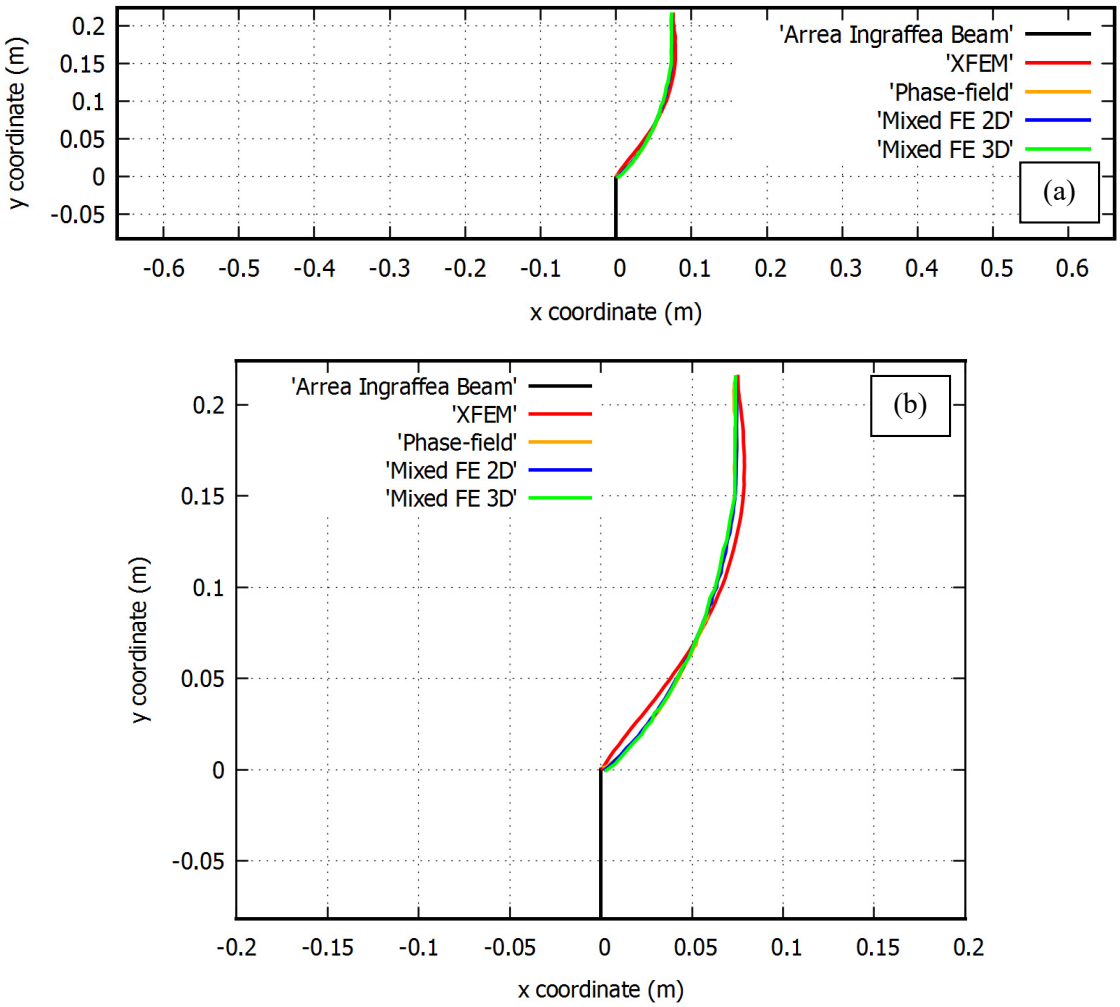

Figure 3.41: Comparison of the computed crack trajectories in 2D and 3D for the Arrea and Ingraffea beam with mixed FE (a) in the whole structure and (b) in detail

The same material properties of Table 2 are employed, and the 3D solution is obtained using a 16,173 hexahedral element mesh of 5 mm size and one element through the thickness.

Figures 3.39 and 3.40 show the computed damage contours in 3D simulations, comparable to the 2D results in figures 3.32b and 3.32c. A detailed comparison of the crack trajectories is provided in Figure 3.41. It can be seen that the 2D and 3D results are practically overlapping and are also almost the same as the phase-field results from reference [63] while the XFEM solution is, as previously mentioned, slightly different.

The computed Force F vs. CMSD curves in 2D and 3D are compared in Figure 3.42. They are almost coincident. It can be concluded that the plane stress hypothesis assumed for computing the beam in 2D is correct. The computed crack surface resulting from the 3D calculation is shown in Figure 3.43.

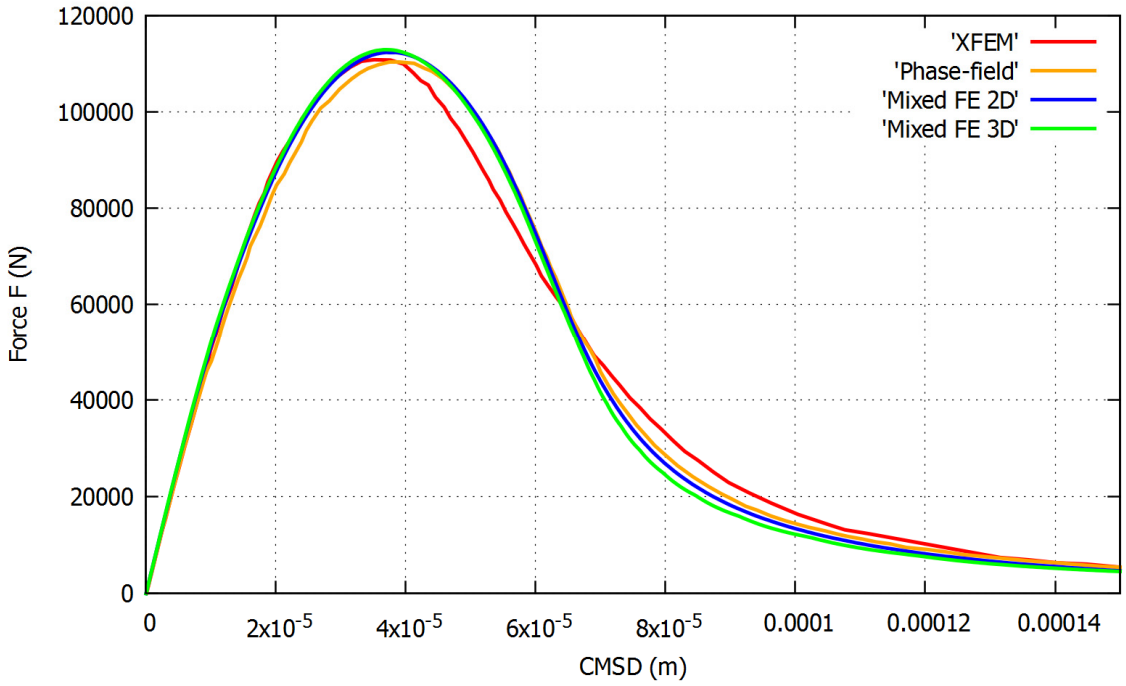

Figure 3.42: Comparison of the Force F vs. CMSD curves of the Arrea and Ingraffea beam computed with mixed FE in 2D and 3D

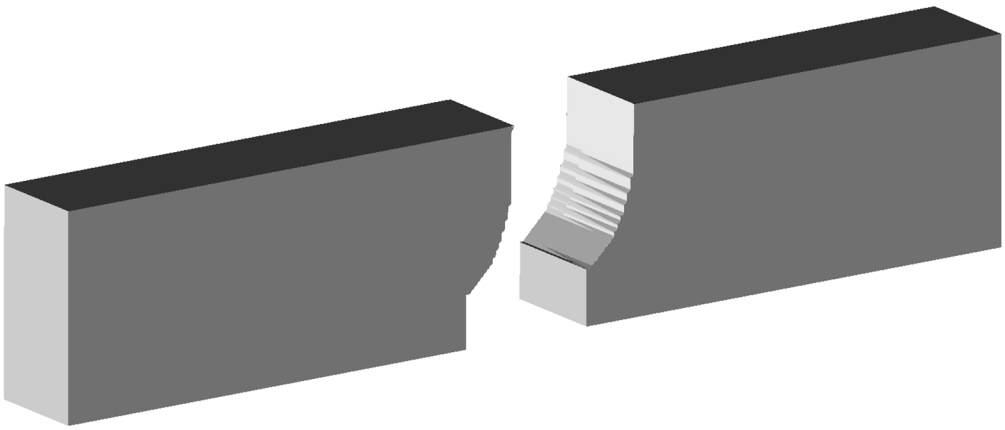

Figure 3.43: Computed crack surface of the Arrea and Ingraffea beam with mixed FE

3.4.3 Garcia-Alvarez beams

This section covers the numerical modelling of the Garcia-Alvarez experiments reported in reference [302], which also includes the computational modelling of the tests using interface elements. Other FEM simulations of the beams are given in reference [60] using the PF-CZM model, which are compared with mixed FE in this work. Note that in this case, no equivalent results with the Is-XFEM are available in the literature.

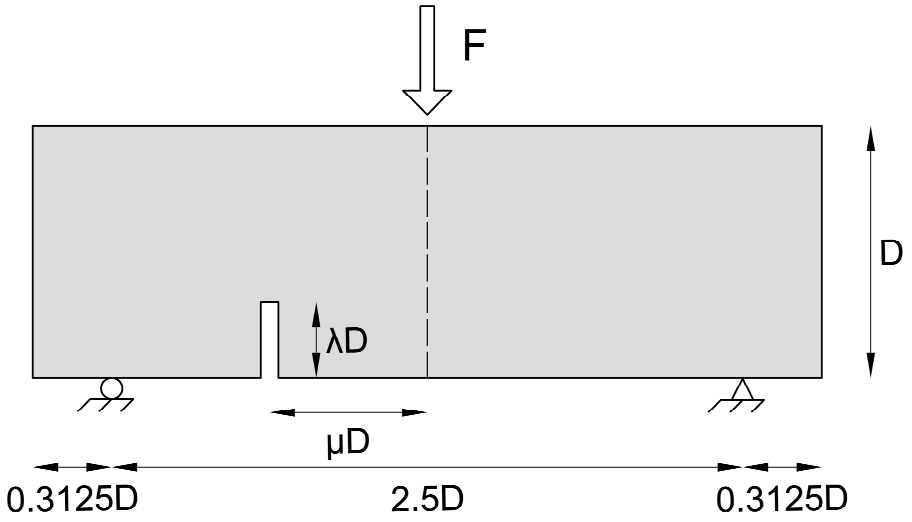

Figure 3.44: Geometry of the Garcia-Alvarez beams

Young's Modulus	$33.8 \cdot 10^9$ Pa
Poisson's Ratio	0.2
Tensile Strength	$3.5 \cdot 10^6$ Pa
Tensile Fracture Energy	80 J/m^2

Table 3: Material parameters of the Garcia-Alvarez beams

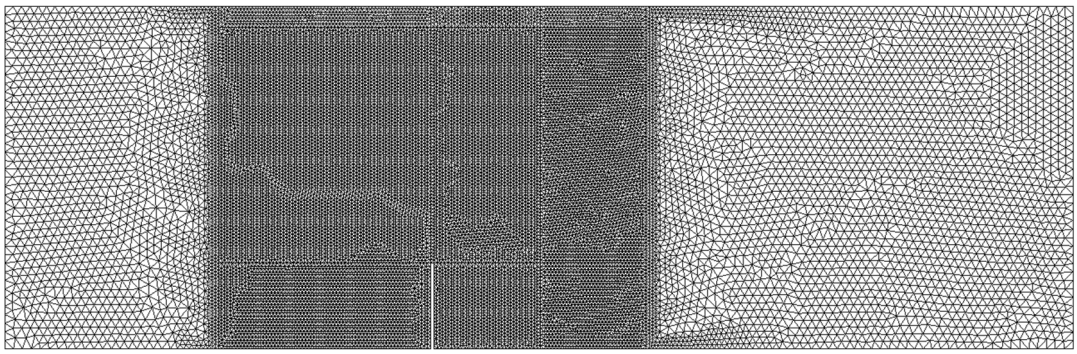

Figure 3.45: Mesh used for Garcia-Alvarez beams, eccentricity 0. 3125*D*, for the mixed FE simulations

In this experiment the phenomenon of structural size effect is studied. For this reason, geometrically similar beams with depths D of 80 mm, 160 mm and 320 mm are subjected to three-point bending. A constant span-to-depth ratio of 2.5 is considered. A notch of varying eccentricity is included, so that a mixed mode fracture develops. Specifically, notch eccentricities μD of $0.625D$, $0.3125D$ and $0.0D$ are introduced. In all the cases, the notch-to-depth ratio λ is 0.25 and the thickness of the beams is 50 mm. The details of the geometry can be examined in Figure 3.44. The material properties introduced are displayed in Table 3. The beams are subjected to a vertical force at the top midpoint and the numerical simulations are made under CMOD control.

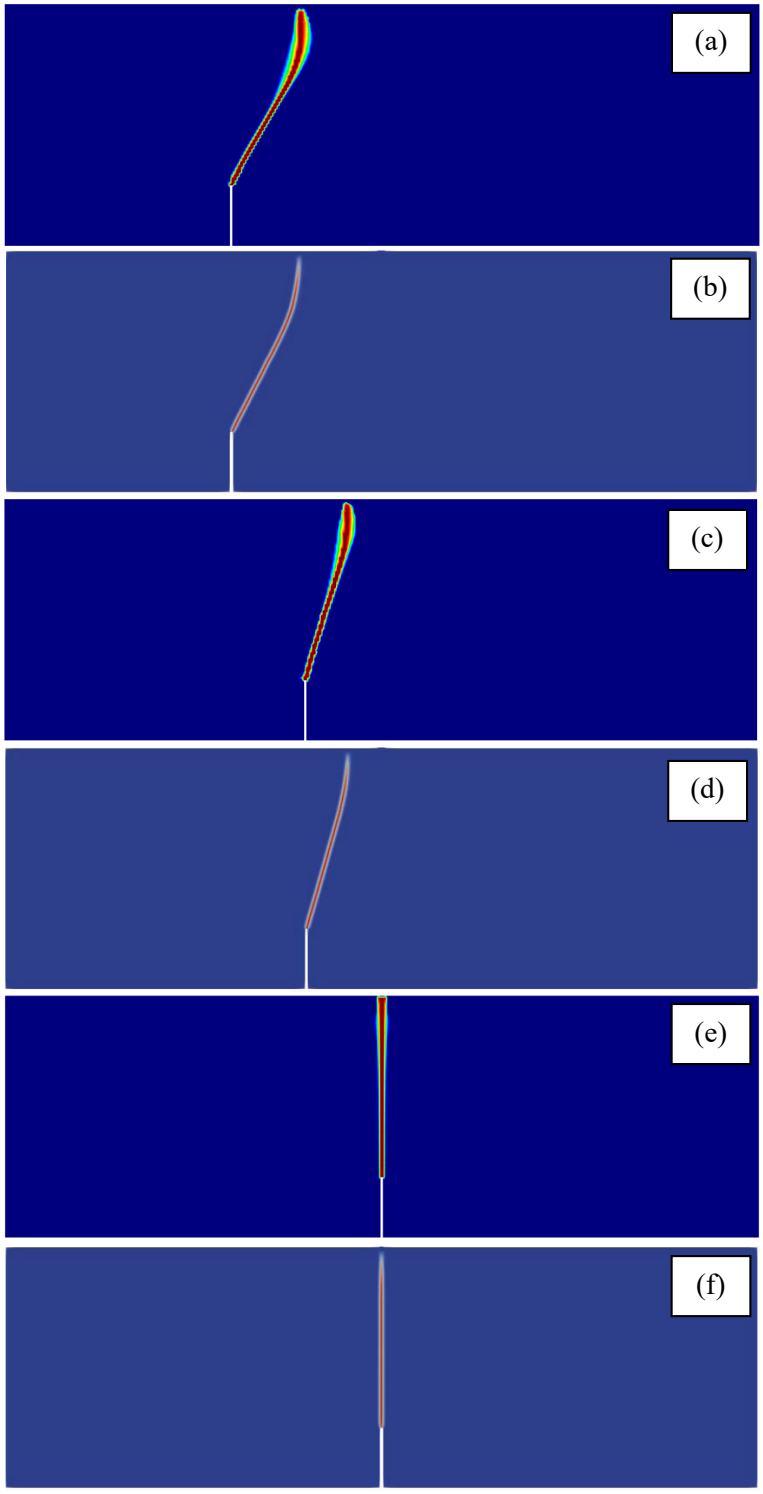

Figure 3.46: Comparison of the Garcia-Alvarez tests, $D = 160\ mm$ specimens, all three eccentricities: (a), (c) and (e) damage contours computed with mixed FE; (b), (d) and (f) damage contours captured with the phase-field method, taken from [60]

Only the medium-sized specimens, with depth $D = 160\ mm$, are considered in the present comparison, because these are the only cases for which reference [60] provided the computed crack trajectories with the phase-field model. The comparison between the original experimental results and the corresponding mixed FE simulations for all the beam sizes can be found in reference [35], which is included in the compendium of publications. There, the capacity of the mixed formulation in modelling the structural size effect phenomenon is demonstrated. Also, a

mesh independence study as well as a comparison between standard and mixed FE solutions are provided in reference [35] for this case.

The mixed FE simulations of the $0.3125D$ eccentricity case of this section have been made under the plane stress hypothesis using a mesh of 36,714 triangular elements, shown in Figure 3.45, which results from using a finite element size h of $10^{-2}D$ in the central area where damage develops. For the other eccentricity cases, the same FE size is used and similar meshes ensue. Note that in the results obtained with the PFM in reference [60] the thickness b of the regularized crack is equal to $10^{-2}D$ and that the finite element size is taken as $b = 10h$. This results in an element size of $10^{-3}D$, 10 times smaller.

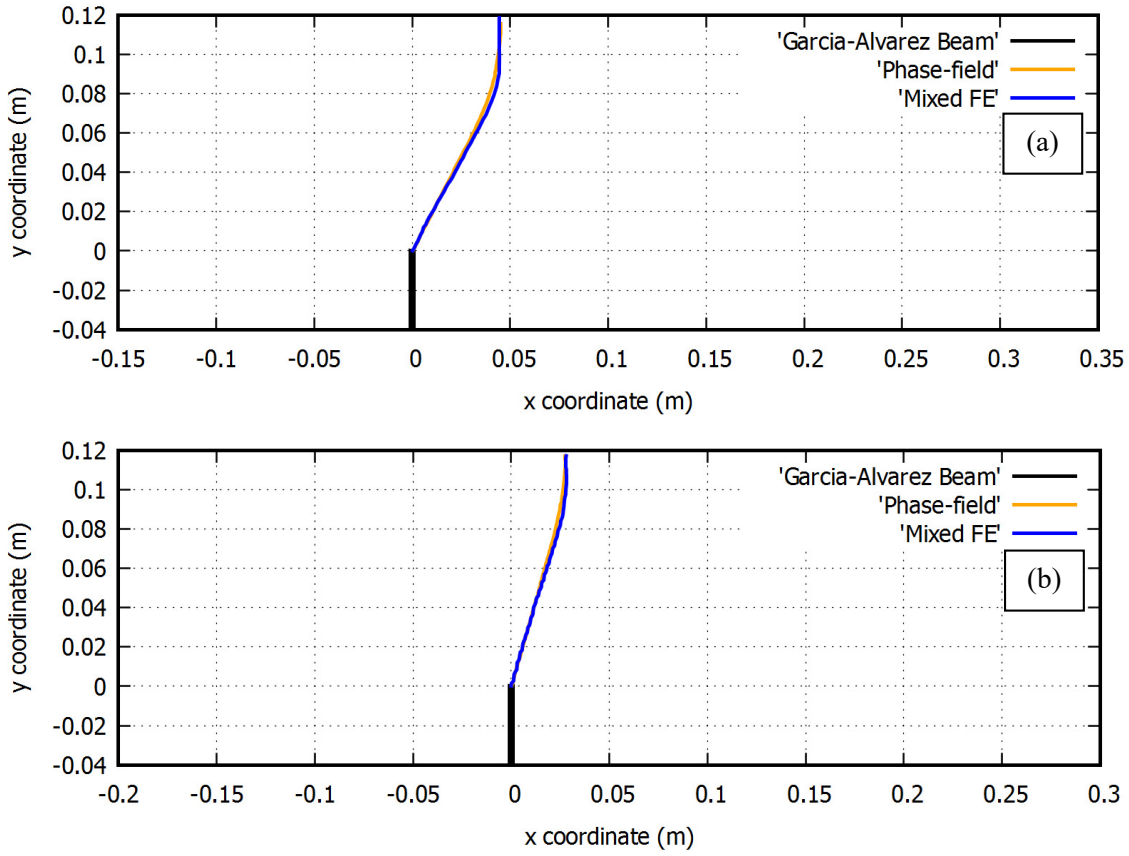

Figure 3.47: Detailed comparison of the computed crack trajectories of the Garcia-Alvarez tests, $D = 160\ mm$ for the (a) $0.625D$ and (b) $0.3125D$ eccentricities

In Figure 3.46 a comparison between the PFM and mixed FE results in terms of computed damage contours is shown. Specifically the medium-sized specimens with depth $D = 160\ mm$ and all three eccentricities are considered. It can be seen how the computed crack trajectories of the cases with notch eccentricities deviate towards the center of the beam while in the case without eccentricity the crack follows a vertical straight line. The results obtained with the two methods are very similar for all the cases. These computed crack trajectories are compared in detail in Figure 3.47. It can be observed that the results computed with the PFM and mixed FE are practically overlapping for all the eccentricities. The minimal difference existing between the solutions obtained with the phase-field model and mixed FE is remarkable. However, it must be pointed out that the phase-field method requires a much finer mesh density to achieve them.

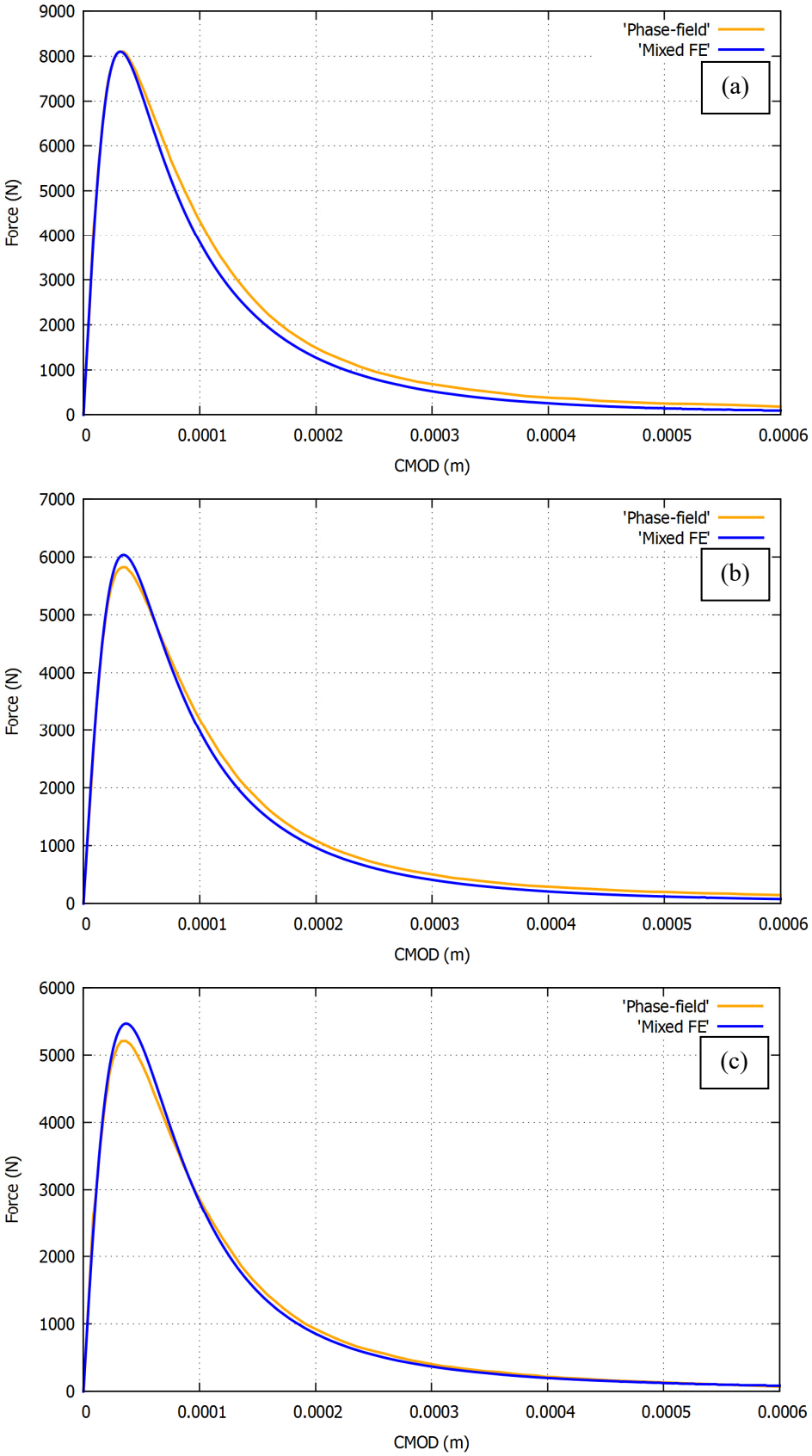

Figure 3.48: Comparison of the force-CMOD curves of the Garcia-Alvarez tests for a depth $D = 160\ mm$ with eccentricities (a) $0.625D$, (b) $0.3125D$ and (c) $0.0D$

Figure 3.48 compares the force-CMOD curves computed for the medium-sized specimens with depth $D = 160\ mm$ for the three eccentricities considered with the phase-field model and mixed FE. It can be seen that the results are not exactly the same for both methods. The small differences that can be seen are caused by the fact that reference [60] used a damage evolution law with Cornelissen softening to compute the phase-field results while exponential softening is considered here for mixed FE. This only causes minor differences in the computed force-CMOD curves. The resemblance between the results obtained with the two methods in terms of force-CMOD curves as well as crack trajectories, for all the eccentricities, using the same material properties, is noteworthy.

2D vs. 3D simulations

Once again, the corresponding 3D simulations are performed to evidence the capabilities of the mixed FE formulation for accurately producing 3D mesh objective results irrespective of the type of element employed.

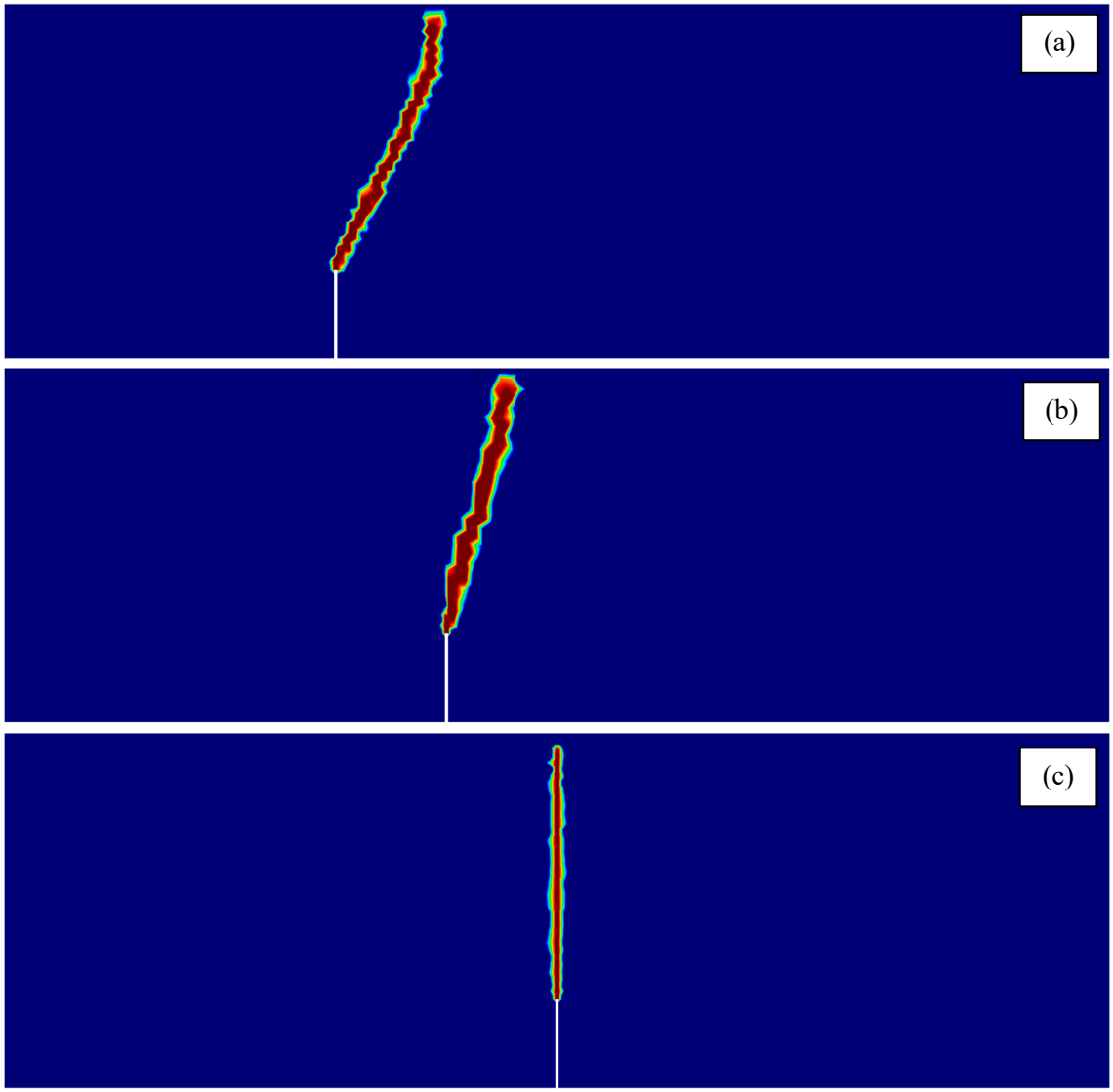

Figure 3.49: Damage contours, front view, from the 3D analyzes of the Garcia-Alvarez tests for a depth $D = 160\ mm$ with eccentricities (a) $0.625D$, (b) $0.3125D$ and (c) $0.0D$

The material properties are taken from Table 3. For this study, unstructured meshes of tetrahedral elements are used. For the case with eccentricity $0.625D$ the FE size is $1.875 \cdot 10^{-2}\ D = 3$ mm in the area where damage develops, resulting in a mesh with 35,149 nodes and 192,279 tetrahedral elements. In the case with an eccentricity of $0.3125D$ the FE size is $2.8125 \cdot 10^{-2}\ D = 4.5$ mm in the region where damage appears, and the corresponding FE mesh is of 7,666 nodes and 38,593 elements. And the case with no eccentricity has a FE size of $10^{-2}\ D = 1.6$ mm in the central region where the crack progresses, ensuing a 4,168 node and 18,546 element mesh.

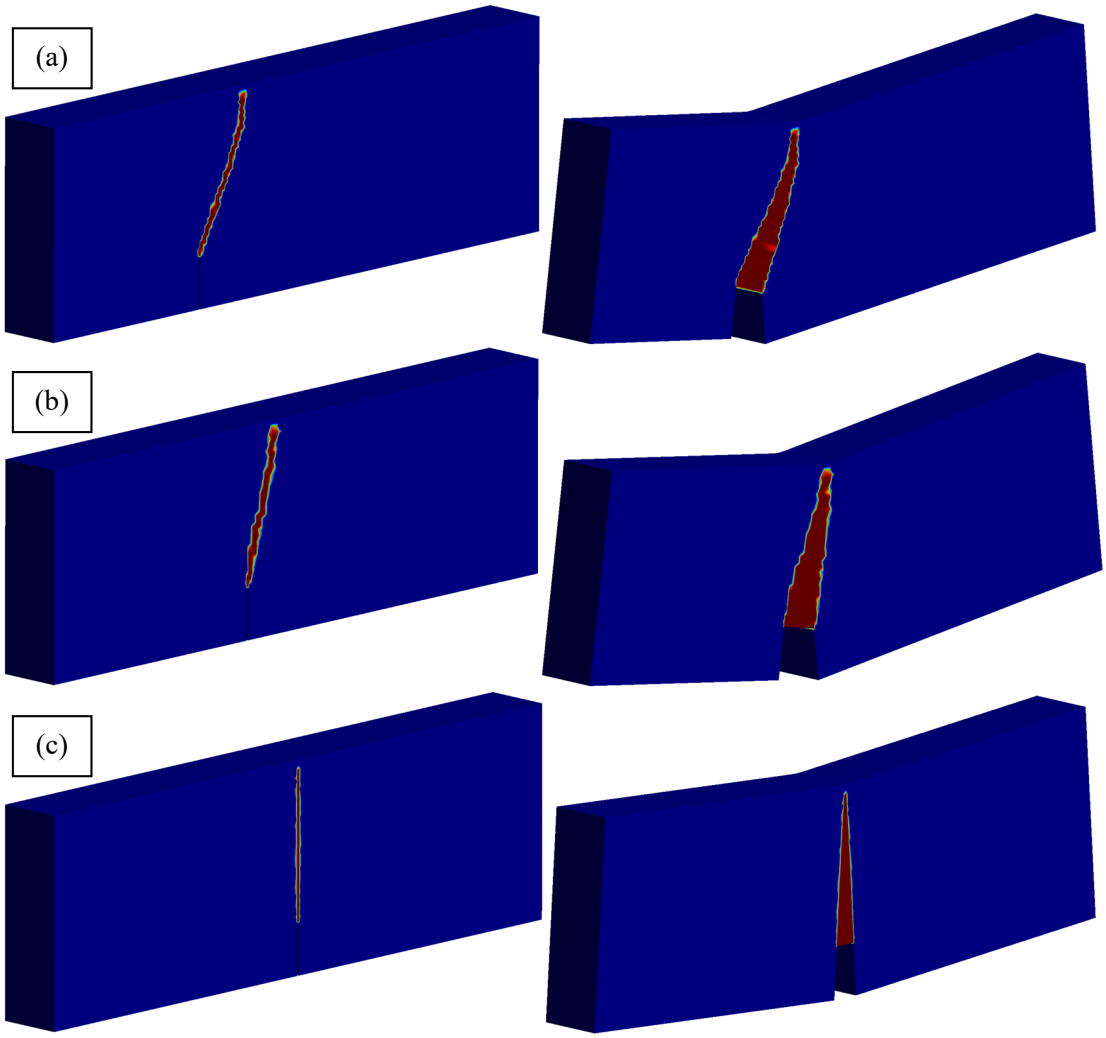

Figure 3.50: Damage contours: (left) lateral view and (right) deformed shape (x 50) from the 3D analyzes of the Garcia-Alvarez tests for a depth $D = 160\ mm$ with eccentricities of (a) $0.625D$, (b) $0.3125D$ and (c) $0.0D$

In Figure 3.49 the computed damage contours resulting from the 3D simulations are shown. They are to be compared with the corresponding 2D results in Figure 3.46. Figure 3.50 provides a lateral view of the 3D analyzes as well as the deformed shape (x 50) of the Garcia-Alvarez beams. A detailed comparison between the 2D and 3D crack trajectories is included in figures 3.51 and 3.52. Given the resolution of the unstructured meshes employed in the simulation, the results are optimal. Despite the coarse level of mesh refinement in 3D, the computed results practically match the 2D simulations obtained with the phase-field and mixed FE formulations and no trace of spurious mesh dependency can be appreciated, evidencing the accuracy of the mixed FE formulation.

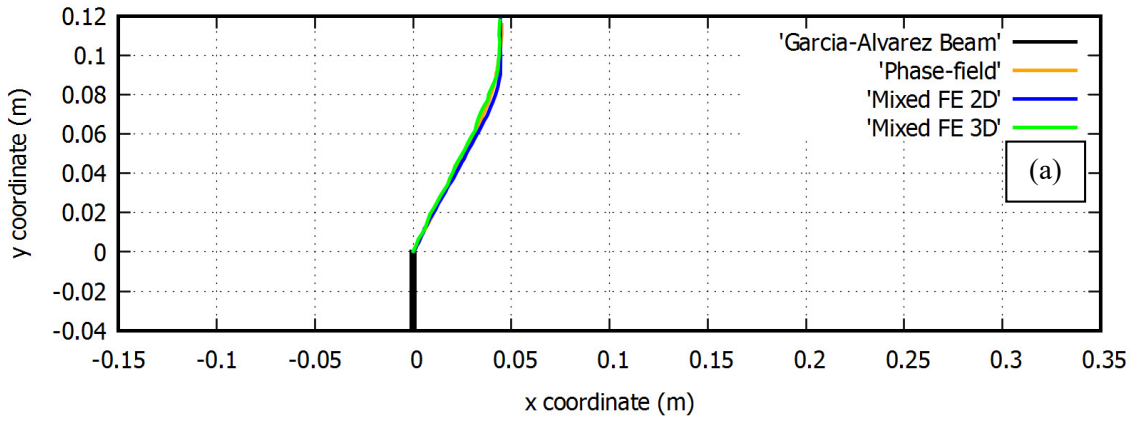

Figure 3.51: Comparison of the computed crack trajectories in 2D and 3D of the Garcia-Alvarez tests, $D = 160\ mm$ for the (a) 0.625D eccentricity

The resulting force-CMOD curves from the 3D analyses are contrasted in Figure 3.53 against the 2D counterparts previously exhibited. It can be seen that the 2D and 3D results are practically overlapping. It is inferred again that the plane stress hypothesis commonly assumed to perform the simulations of the beams is accurate enough. Figures 3.54 and 3.55 display the computed fracture surfaces obtained from the 3D calculations, where the fully unstructured mesh used in the simulation is observable. This shows the aptness of the mixed FE model to produce accurate 3D crack surfaces without spurious mesh dependency.

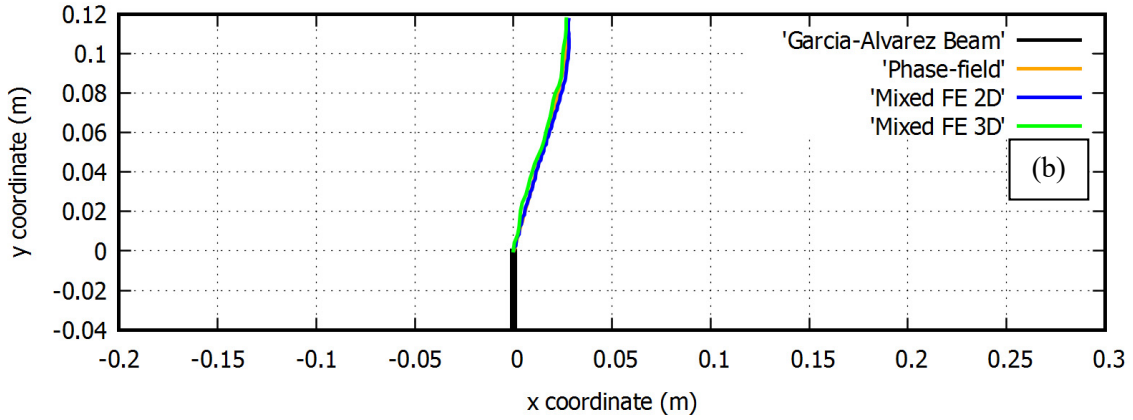

Figure 3.52: Comparison of the computed crack trajectories in 2D and 3D of the Garcia-Alvarez tests, $D = 160\ mm$ for the (b) 0.3125D eccentricity

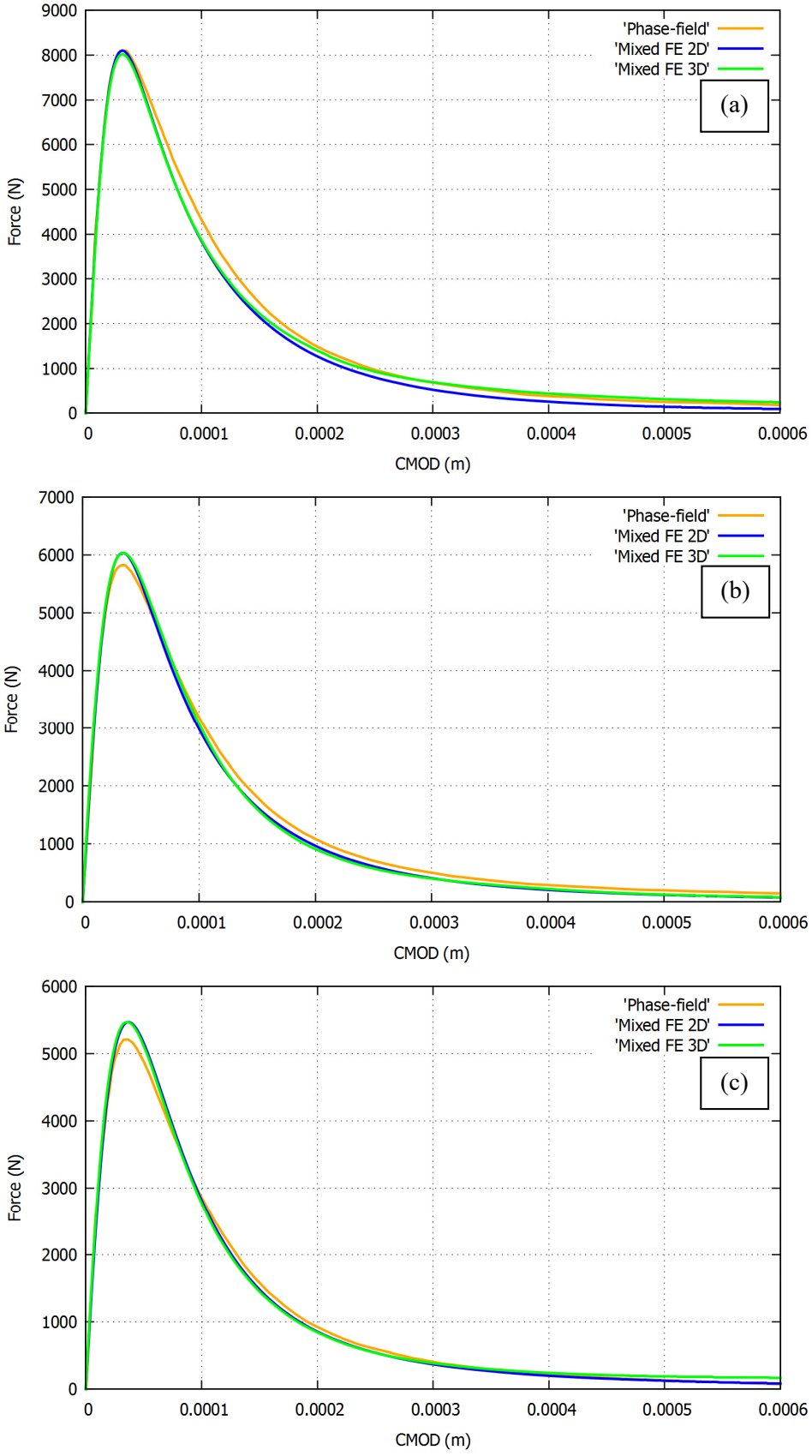

Figure 3.53: Comparison of the 2D and 3D computed force vs. CMOD curves of the Garcia-Alvarez beams for eccentricities (a) 0.625D (b) 0.3125*D* and (c) 0.0*D*

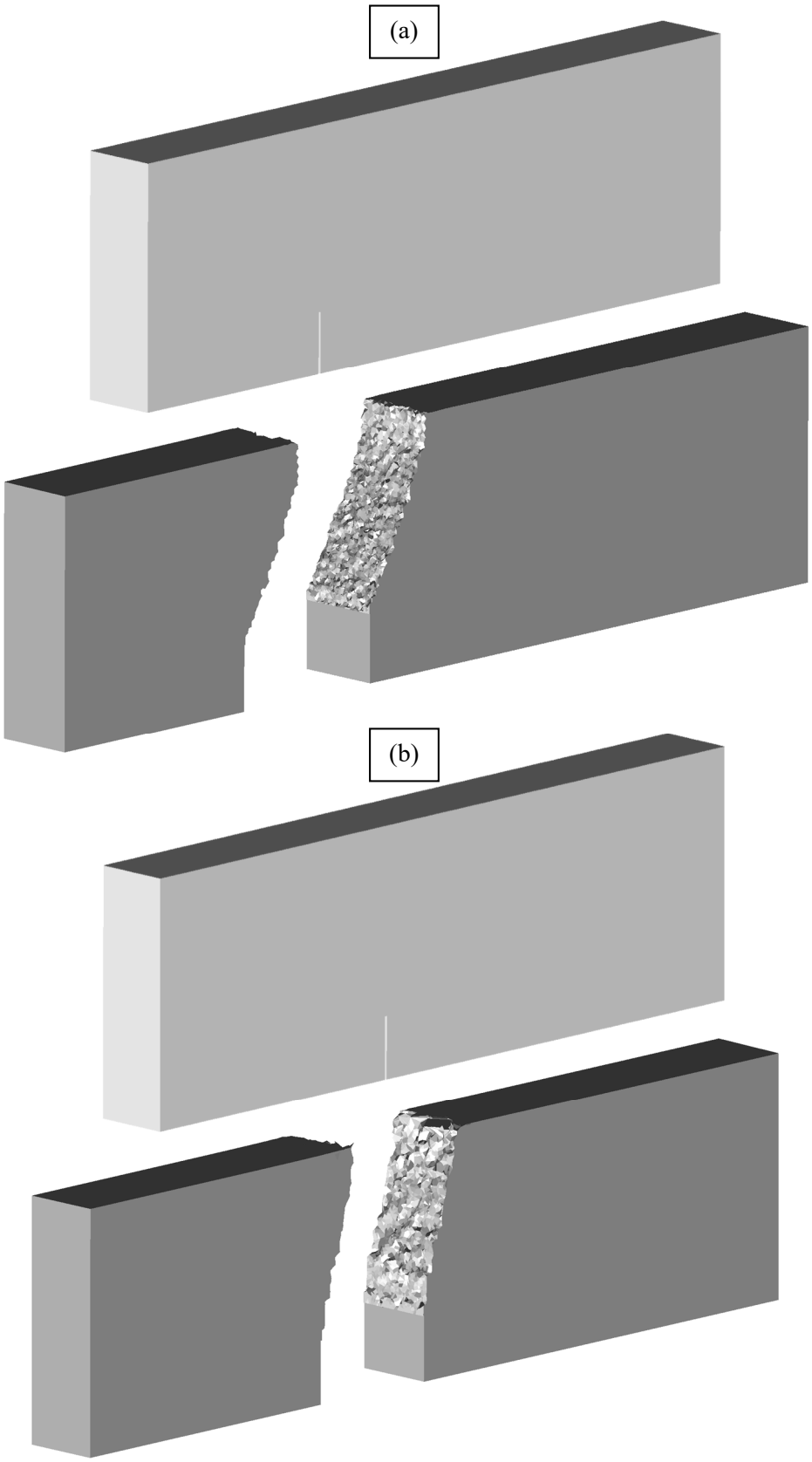

Figure 3.54: Computed crack surfaces of the Garcia-Alvarez beams, medium sizes, with eccentricities (a) 0.625*D* and (b) 0.3125*D*, using mixed FE

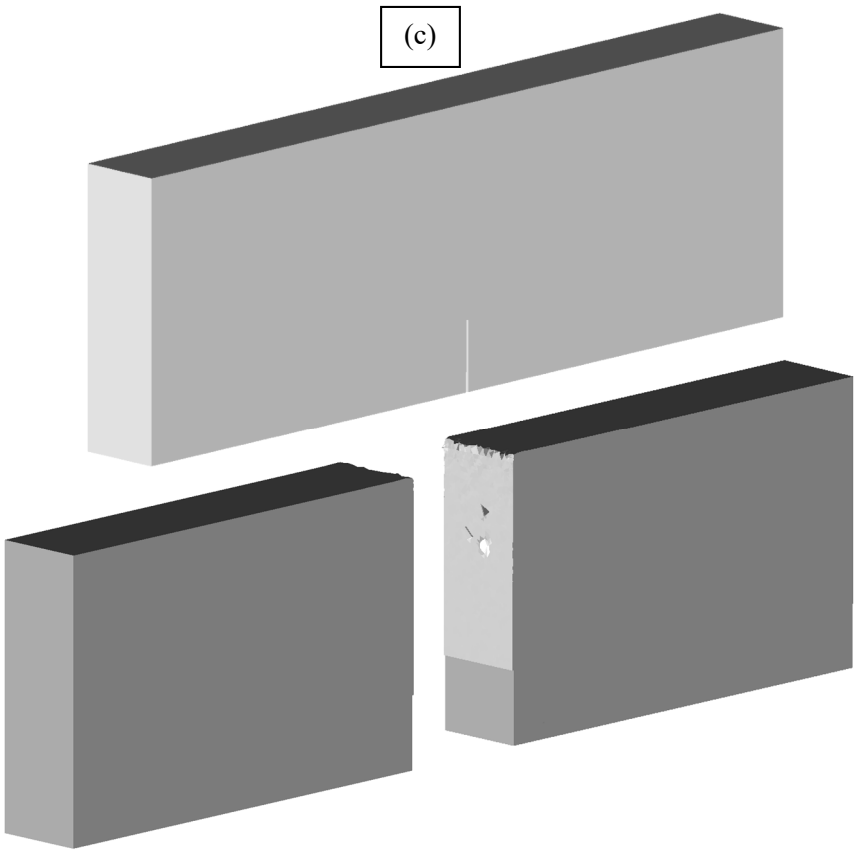

Figure 3.55: Computed crack surface of the Garcia-Alvarez beams, medium sizes, with eccentricity (c) 0.0*D*, using mixed FE

3.4.4 Koyna dam

In this section, the numerical simulation of a fracture propagating in the Koyna dam is considered.

An overview of the history of the dam, located in India, is given, for example, in reference [303]. After the beginning of the dam filling in 1962, the region, previously considered nearly nonseismic, started experiencing a serious increase in earthquake activity. In December 1967 a 6.5 magnitude earthquake caused some damage to the structure, raising the concern of the community. The seismic analysis of the Koyna dam has been performed many times, like for example in reference [303], which conducted a linear elastic FEM analysis; in references [304-312], where different smeared crack models are employed; in reference [313] which used the XFEM; and in reference [314], where the XFEM, a crack band model and a plasticity model are compared. Also, the quasi-static analysis of the dam overflow has become a reference benchmark in the community, as it can be seen for example in reference [315], where a comparison between linear elastic fracture mechanics (LEFM) and plasticity theories is made; in reference [295], which compares rotating and fixed smeared crack models; in reference [316], which also employed a smeared crack model; in references [96, 150], where a model with a transition from a continuous nonlocal formulation to a discontinuous embedded finite element method is proposed; in reference [299], where a model featuring a transition from a smeared crack damage model to the XFEM is used; in reference [317], which employed cohesive interface elements; and in reference [318], where the PFM is used to model fracture.

Again, the numerical results of reference [63] are taken here as reference for comparison with the XFEM and the PFM.

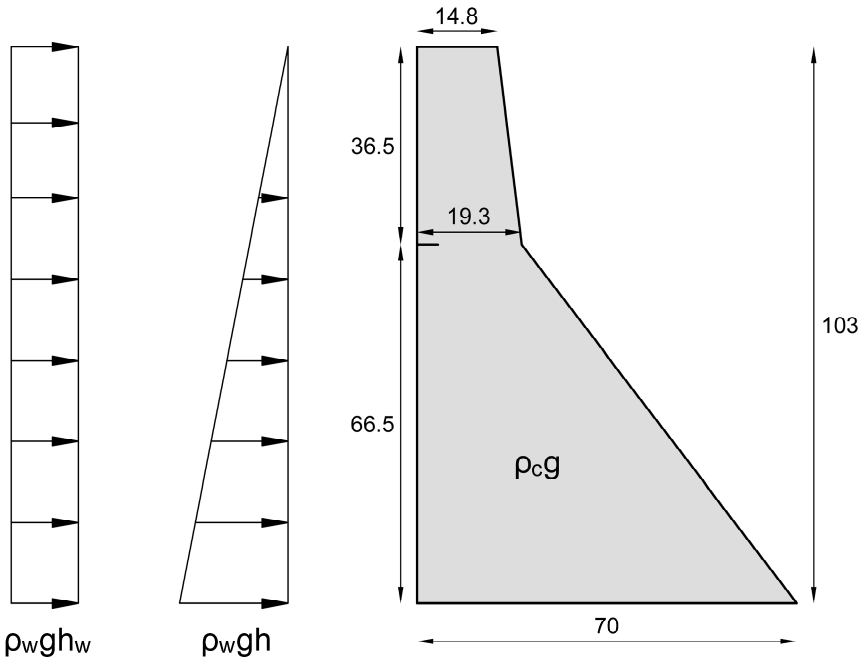

Figure 3.56: Geometry of the Koyna dam (m)

Young's Modulus	$25.0 \cdot 10^9$ Pa
Poisson's Ratio	0.2
Tensile Strength	$1.0 \cdot 10^6$ Pa
Tensile Fracture Energy	100 J/m^2
Concrete Density	2450 kg/m^3
Water Density	1000 kg/m^3

Table 4: Material parameters of the Koyna dam

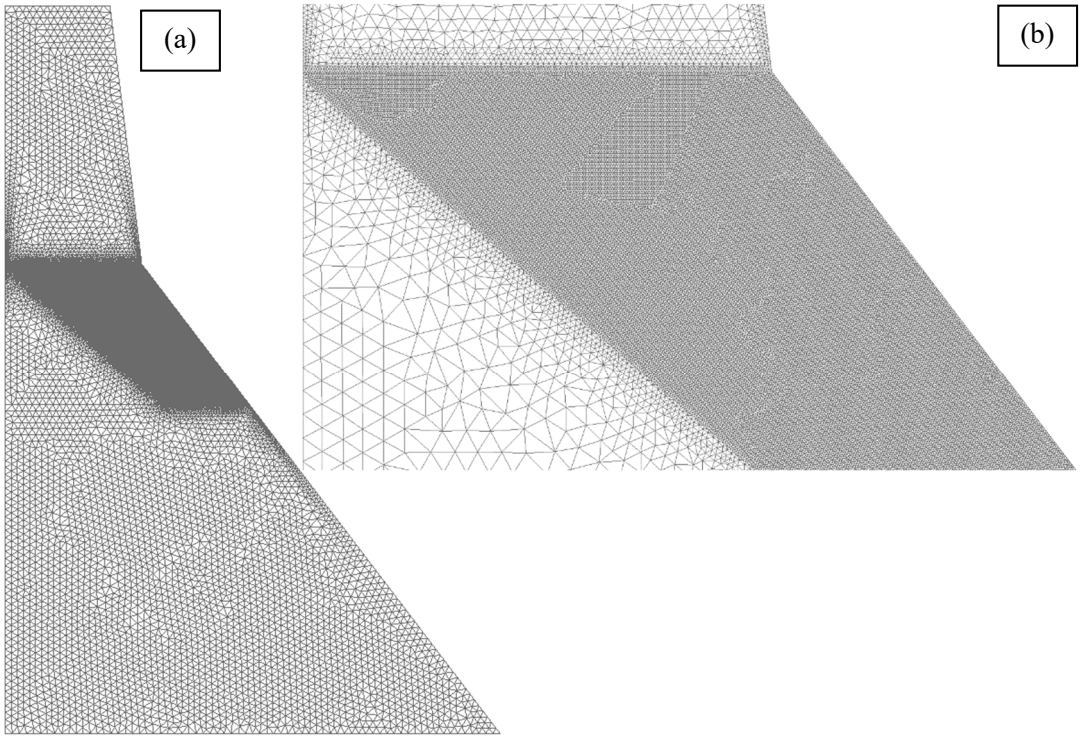

Figure 3.57: (a) Mesh used for the Koyna dam and (b) detail of the refined area

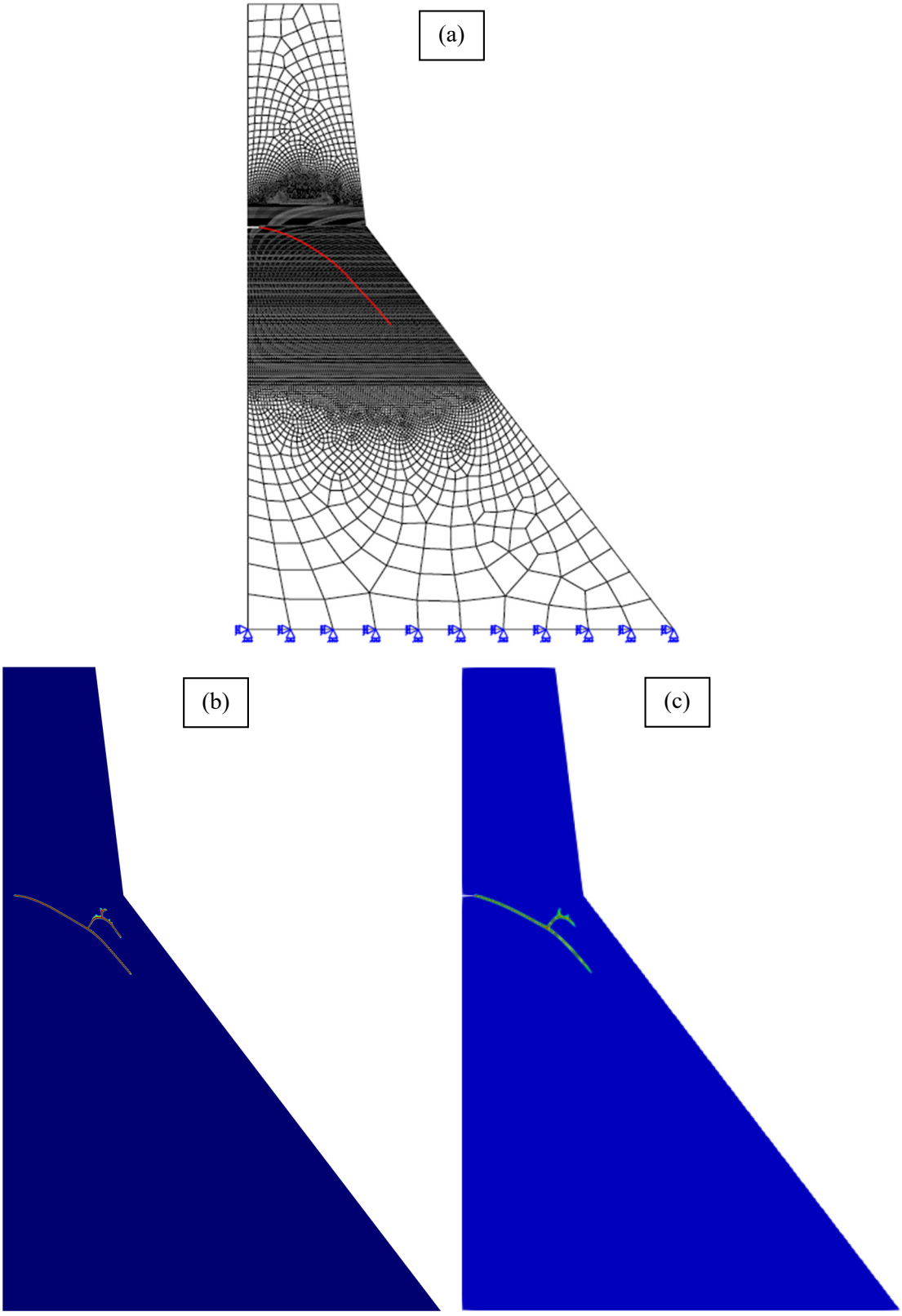

Figure 3.58: Comparison of the Koyna dam results: (a) crack trajectory obtained with the XFEM, (b) damage contour computed with mixed FE and (c) damage contour captured with the phase-field method, (a) and (c) taken from [63]

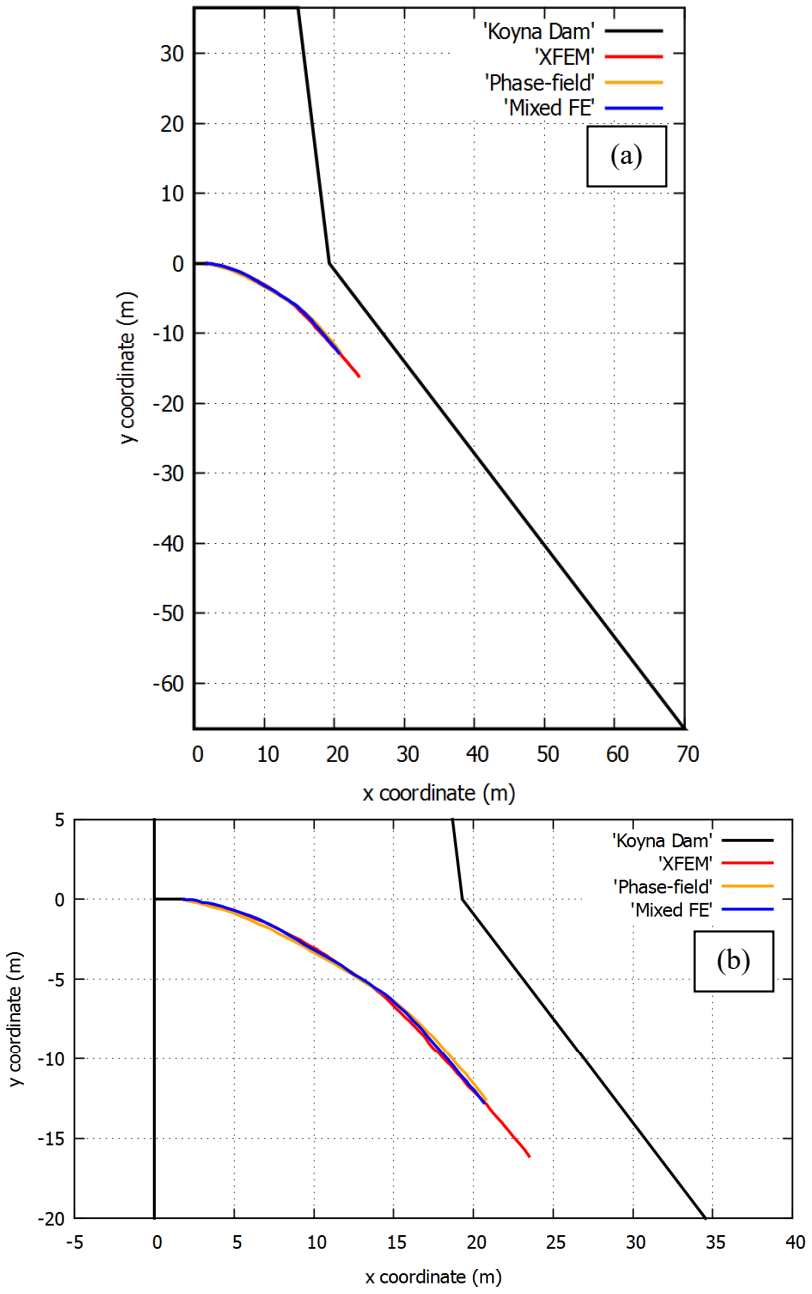

Figure 3.59: Comparison of the Koyna dam crack trajectories (a) in the whole structure and (b) in detail

The geometry of the Koyna dam is shown in Figure 3.56. It is a gravity dam made of concrete and has a height of 103 m. In the simulation, an initial crack of 1.93 m of length is located at a height of 66.5 m, representing the cracking that was discovered after the 1967 earthquake. The material parameters employed in the simulation are provided in Table 4.

The load in the dam is introduced in three stages: first the self-weight is applied, secondly the hydrostatic pressure corresponding to the full reservoir situation is imposed and, thirdly, a constant pressure corresponding to the dam overflow is assigned. Gravitational acceleration g is taken as 9.81 m/s^2. In the third stage, the applied load uniformly increases while the analysis is performed under arc length control of the horizontal displacement at the top of the dam until it reaches 75 mm.

The dam is computed using an unstructured mesh. Triangular elements of a size of 0.1 m are employed in the area where the crack develops and of 1 m in the rest, resulting in a 84,465 element mesh, shown in Figure 3.57. The notch width is set equal to zero. In reference [63], slightly larger FEs of size 0.3 m and 0.2 m are considered for the XFEM, while for the phase-field model 0.06 m and 0.04 m sized elements are employed in the refined area.

Figure 3.58 shows the results obtained with the mixed FE formulation compared with the XFEM and the PFM computations performed in reference [63]. It can be seen how the crack trajectory branches several times when using the mixed FEM and the PFM but that this phenomenon is not captured with the XFEM. The employed XFEM formulation does not have branching capabilities implemented. To be able to consider the phenomenon of branching when using the XFEM, it is necessary to include specific enrichment functions, integration schemes and crack tracking algorithms capable of handling multiple intersecting embedded discontinuities. The tracking algorithm must include a criterion indicating when branching occurs and the direction of propagation of the new cracks. All of this involves a significant additional effort when implementing the method. In contrast to the XFEM, branching in the PFM and the mixed FEM does not require special additional considerations. As a consequence of the inability of branching, the crack computed with the XFEM is longer, for the same imposed horizontal displacement at the top of the dam of 75 mm. Aside from this, a direct comparison of the main fracture path in Figure 3.59 shows that the three methods produce almost overlapping results in terms of the trajectory of the main crack.

Figure 3.60 shows the overflow height vs. top horizontal displacement curves of the Koyna dam with the three methods considered. It can be seen that the phase-field model and mixed FE produce practically the same results while the ones obtained with the XFEM are somewhat apart. This is likely due to the inability of the XFEM in capturing the branching of the crack. The computed results with phase-field and mixed FE are remarkably close and the overall phenomenon is well captured by both models.

Once again, after using equivalent materials laws and seeing that the obtained results are practically the same, it should be noted that the computational cost of the PFM is much larger than in the mixed FEM.

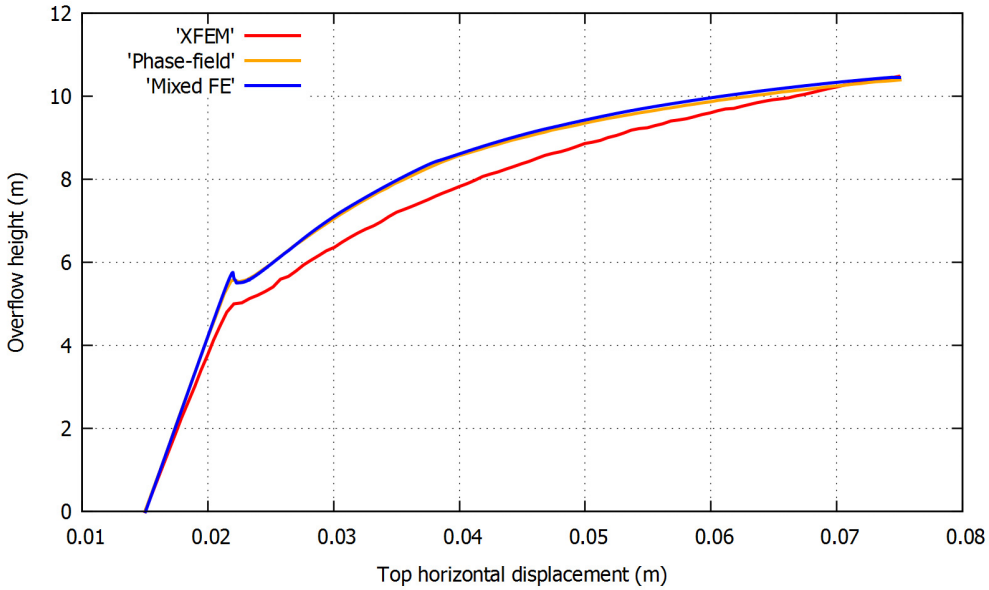

Figure 3.60: Computed overflow height vs. horizontal displacement at the top of the Koyna dam with the three methods considered

3.4.5 Buchholz skew notched beam

In this section, the numerical simulation of a skew notched beam subjected to three-point bending is considered. Computations with mixed FE for this case have already been presented in reference [31], included in the compendium, and they are here reexamined to compare them with the results recently obtained with the PF-CZM, reported in reference [70]. No corresponding simulations using the Is-XFEM are available in the literature so far.

This test, reported in reference [319], was carried out in a beam made of acrylic glass (PMMA). References [320, 321] performed the same experiment under cyclic loading to study fatigue crack growth. References [319-321] completed as well the numerical simulation of the test using the modified virtual crack closure integral (MVCCI) method. One member of the team who originally conducted the experiments is the coauthor of reference [322], which compares computations using the dual boundary element method (DBEM) and the MVCCI. This case has also been simulated in references [323-327], using the XFEM and in reference [328], where an eigenerosion approach to fracture is proposed.

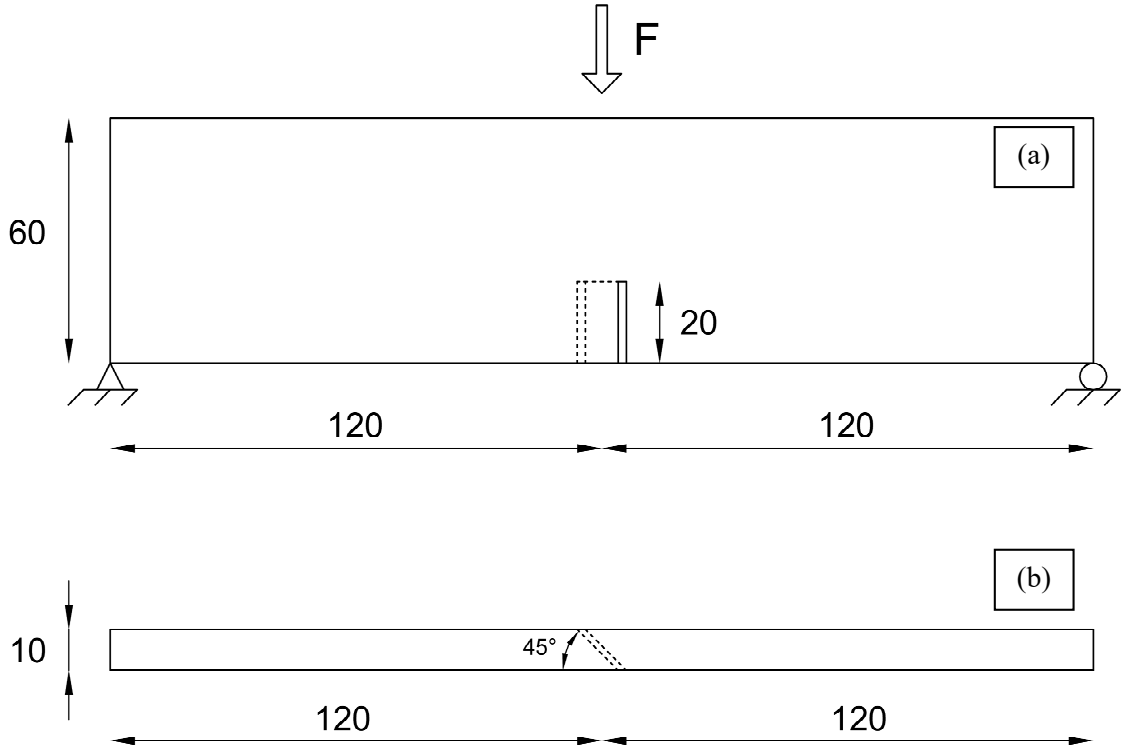

Figure 3.61: Geometry of the Buchholz skew notched beam (mm), (a) front view and (b) top view

Young's Modulus	$2.8 \cdot 10^9$ Pa
Poisson's Ratio	0.38
Tensile Strength	$2.0 \cdot 10^7$ Pa
Tensile Fracture Energy	500 J/m^2

Table 5: Material parameters of the Buchholz skew notched beam

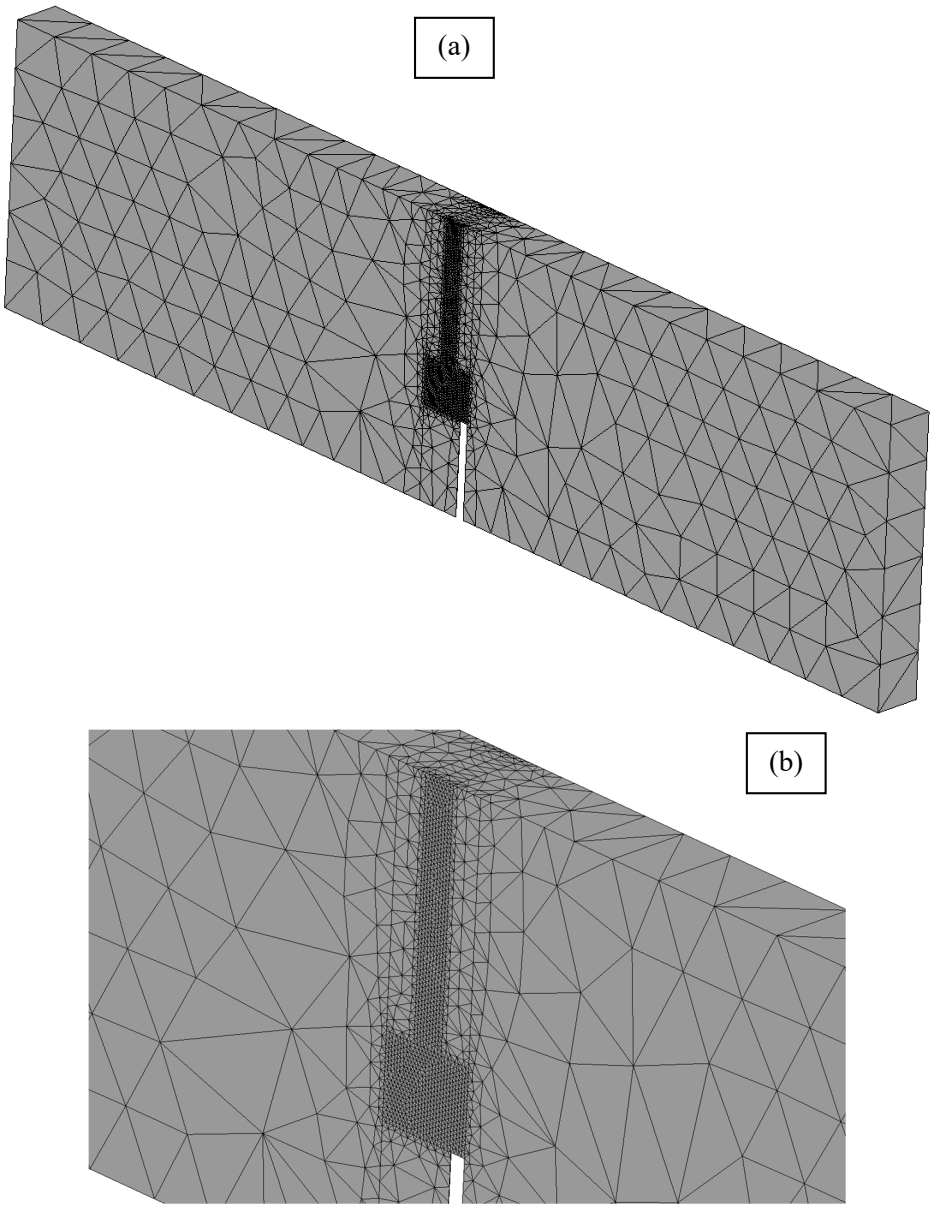

Figure 3.62: (a) Mesh used for the Buchholz skew notched beam and (b) detail of the refined area

Details of the geometry and boundary conditions of beam are shown in Figure 3.61. The beam has a span of 240 mm and a depth of 60 mm. Its thickness is 10 mm. The specimen has a notch of 20 mm x 2 mm with a deviation of 45º with respect to the surface of the specimen. The insertion of a skew notch causes the development of a twisting crack under mixed mode I and III fracture in the beam. For this reason, a 3D simulation is required. In the computations, the load is applied imposing increments of vertical displacement at the top midpoint of the beam. The material properties are shown in Table 5. The same material properties as in reference [70] are used to allow a direct comparison with the phase-field model. A comparison between the experiment and simulations obtained with mixed FE is available in reference [31].

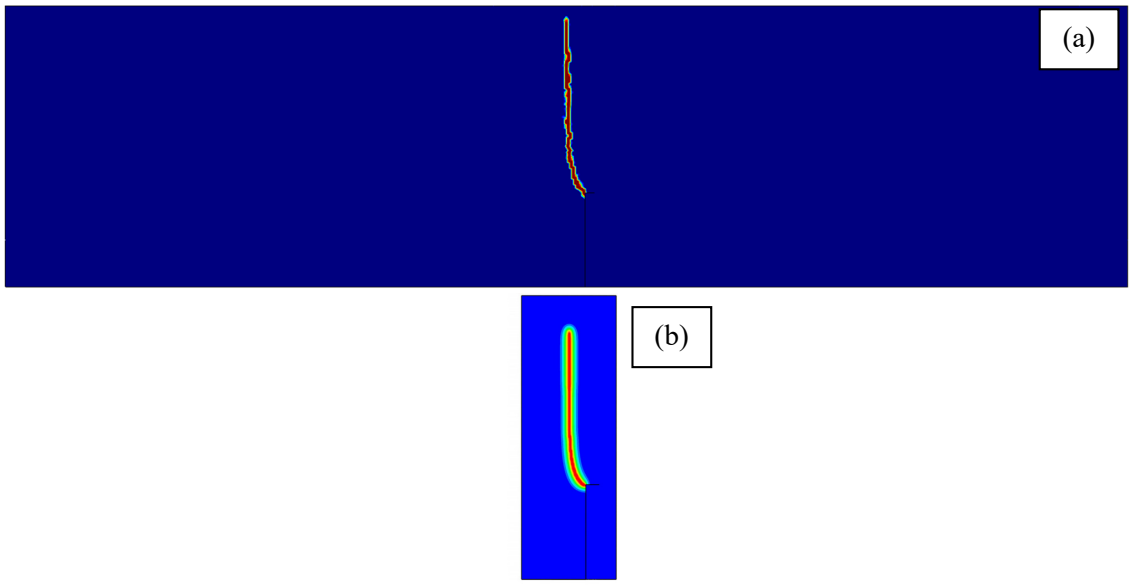

Figure 3.63: Damage contours of the Buchholz skew notched beam computed with (a) mixed FE and (b) phase-field, (b) taken from [70]

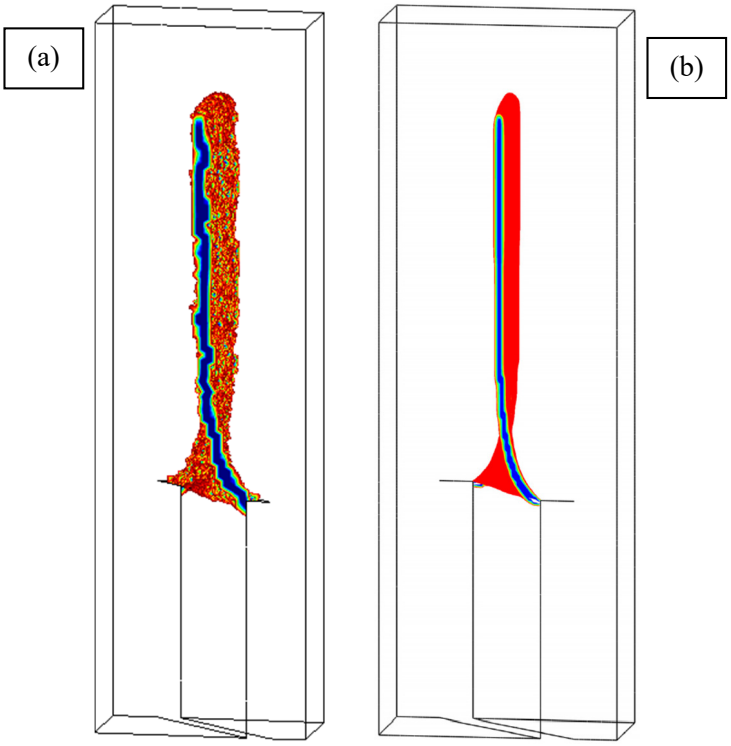

Figure 3.64: Computed damage profile of the Buchholz skew notched beam with (a) mixed FE and (b) phase-field, (b) taken from [70]

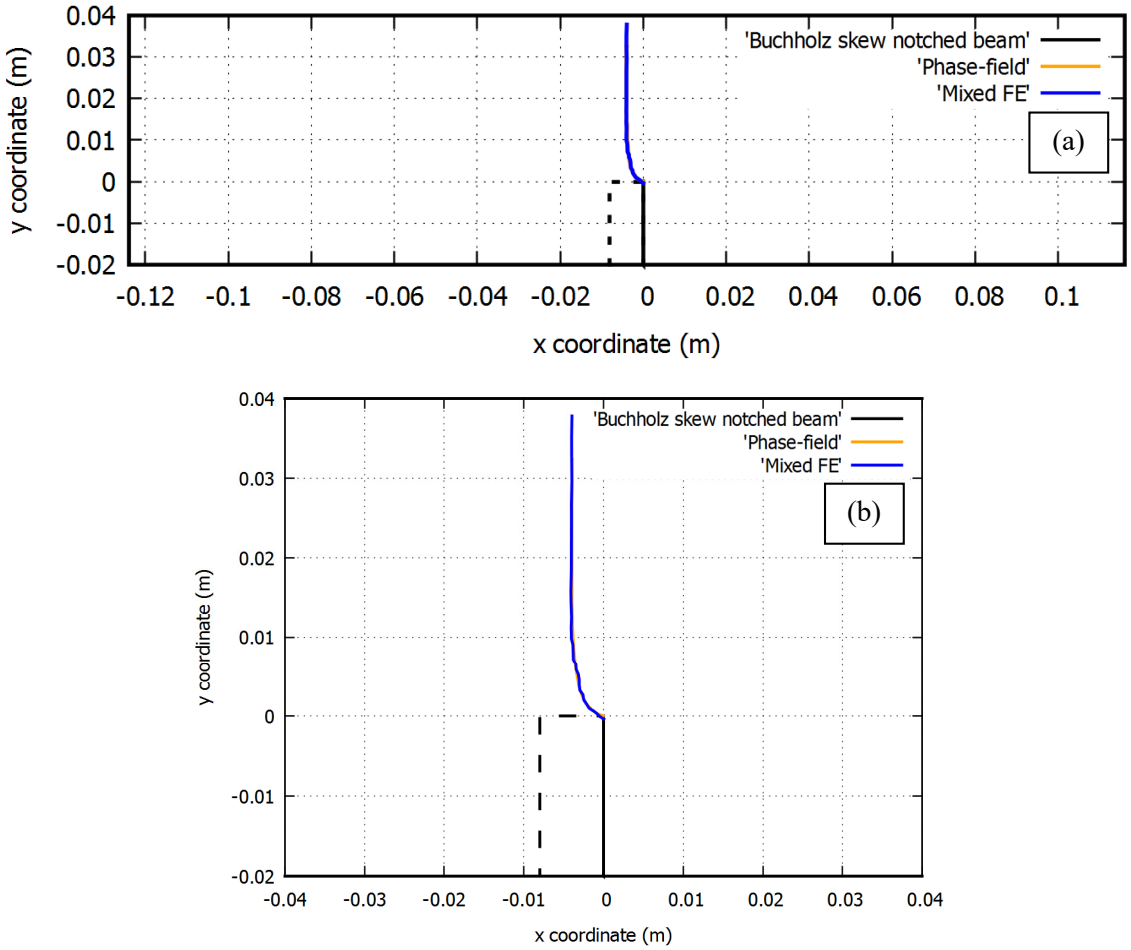

Figure 3.65: Comparison of the Buchholz skew notched beam crack trajectories (a) in the whole structure and (b) in detail

Figure 3.62 shows the 3D unstructured mesh used to perform the simulation with mixed FE. It is made of tetrahedral elements of 0.5 mm size in the central area where damage develops, resulting in a total of 49,221 nodes and 293,766 elements. Reference [70] solved the problem using a structured mesh with a FE size of 0.2 mm in the central part, which ensues in a total of 1,355,613 elements.

Figure 3.63 shows the computed damage contours obtained with the mixed FE formulation and with the phase-field model. It can be observed how the crack starts at the notch and deviates towards the center of the beam due to the mixed mode I and III loading conditions. A comparison of the computed damage profiles with both methods is presented in Figure 3.64. They are both able of producing the skew-symmetric and twisting pattern of the crack in agreement with the boundary conditions of the test. No sign of spurious mesh dependency can be appreciated in the results.

Figure 3.65 displays a detailed comparison of the computed crack trajectories from Figure 3.63. It can be seen how both methods produce practically the same results, even if the phase-field method produces a smoother solution. This is at the price of introducing a much finer mesh and solving a problem which requires a much larger computational cost. The computed crack resulting from the 3D calculation is shown in Figure 3.66. The detail of the unstructured mesh used to compute the problem can be perceived through the unsmooth fracture surface generated by the mixed FE method.

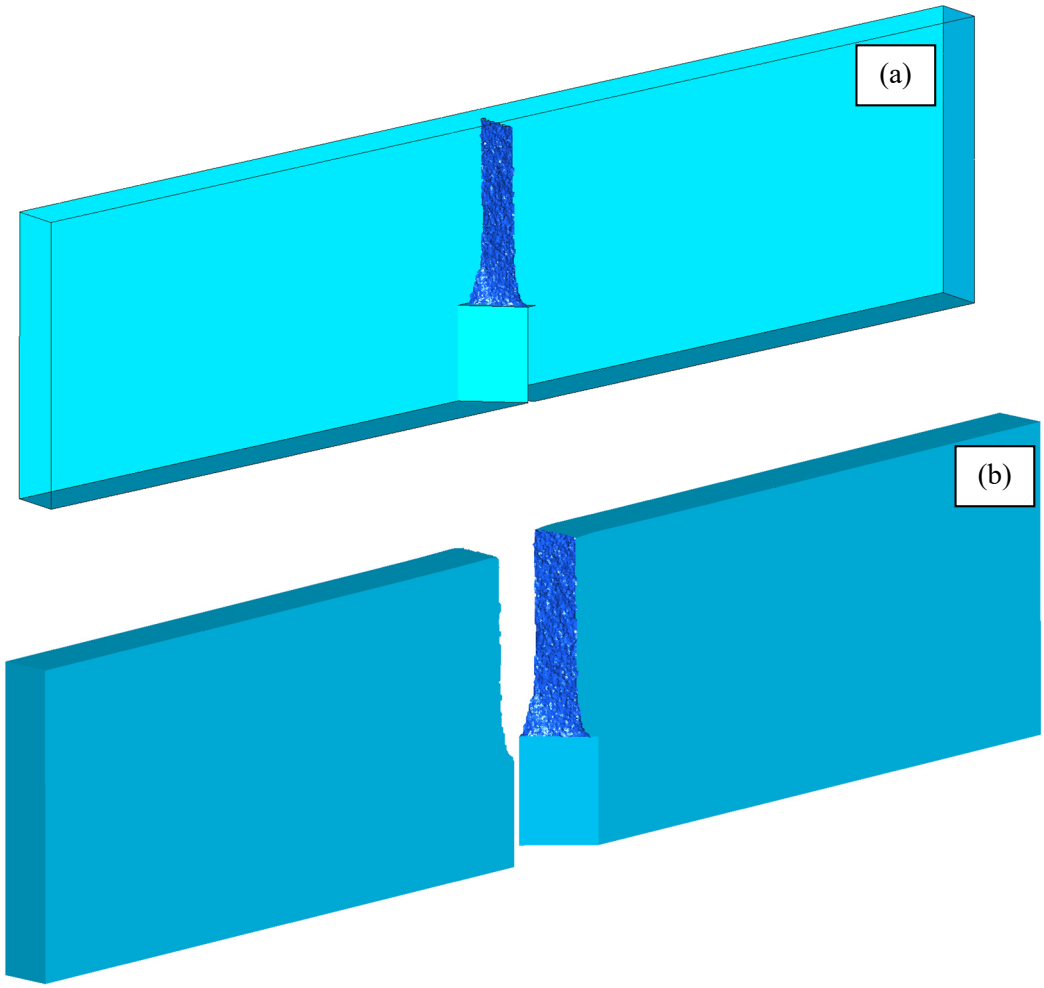

Figure 3.66: Computed crack surface of the Buchholz skew notched beam in (a) the whole structure and (b) the two separate pieces with mixed FE

3.5 Outlook

The XFEM, the MFEM and the PFM are the currently most promising methods used in computational failure mechanics of quasi-brittle materials. They are representatives of the embedded, smeared and regularized crack approaches, respectively.

From the independent appraisal of the XFEM, the MFEM and the PFM and the performance displayed in the numerical simulations, a comparative assessment is made herein using the 10-Point Checklist.

One salient observation is that all three methods get a double tick in modelling the physical aspects of *strength, toughness and energy dissipation*. The three also have the capacity of producing realistic failure mechanisms that are mesh objective. These are undoubtedly the main reasons for their adoption.

Notwithstanding, the XFEM presents shortcomings common to all methods in the embedded crack approaches.

	Checklist	XFEM	MFEM	PFM
1	Variational formulation in the continuous setting	×	✓✓	✓✓
2	Convergence of the FE formulation	××	✓✓	✓
3	Strength, toughness and energy dissipation	✓✓	✓✓	✓✓
4	Criterion for direction of propagation	××	✓✓	✓✓
5	Constitutive behavior generality	××	✓✓	×
6	Generality and implementation effort	××	✓	✓
7	Cost-efficiency	✓	○	××
8	Multiple, intersecting and branching cracks	××	✓✓	✓✓
9	Auxiliary tracking techniques	××	✓✓	✓✓
10	Application in 3D	××	✓	××

The MFEM and the PFM are the contestants for future developments, as they accomplish a double or single tick in many of the check points. In the above checklist, MFEM has several advantages, while not sporting any disqualifier.

On the one hand, the MFEM allows full generality regarding constitutive behavior. On the other hand, the PFM requires a degree of mesh resolution that makes it comparatively very expensive, especially for 3D applications.

The reason for these two features lays is the fundamental difference between the MFEM and the PFM. The PFM is conceived as a regularization of the problem of linear fracture at *continuous* level. The resolution to reproduce this regularity at discrete level requires very fine meshes, at least 4 to 10 elements across the crack and, in many cases, much finer. Also, usually only one isotropic damage index is represented by the phase-field, with very limited constitutive capabilities. Conversely, the MFEM is a fully general framework for solving the mechanical problem that enhances the accuracy of the discrete strain field and introduces the required regularity to solve fracture at *discrete* level. On the one side, the FE resolution needed for this is far fewer than for the PFM; on the other side, more involved constitutive behaviors such as orthotropic damage and irreversible strains can be considered straightforwardly.

The cost-efficiency issues of the MFEM and the PFM can be addressed by selectively and adaptively applying them in the relatively small parts of the structure where cracking is actually developing. Also, more general crack material behaviors are progressively being incorporated into the PFM, at the price of increasing its cost and complexity. For instance, introducing orthogonal damage requires the computation of three separate phase-field variables. These aspects highlight the relative advantage of the MFEM regarding the generality of the constitutive behavior and the cost-efficiency of the method.

Chapter 4

Mixed finite element modelling of fracture

Brief summary of the main scientific contributions of the publications included in the compendium

In this chapter, a brief summary indicating the main scientific contributions of each of the articles included in the compendium is given to highlight their relation to the main topics of the present thesis, aimed at the numerical modelling of fracture with a mixed strain/displacement ε/u finite element formulation and damage constitutive laws.

4.1 Finite element modelling of quasi-brittle cracks in 2D and 3D with enhanced accuracy

Article data

Title: Finite element modelling of quasi-brittle cracks in 2D and 3D with enhanced strain accuracy

Authors: M. Cervera, G.B. Barbat and M. Chiumenti

Journal: Computational Mechanics, 60(5), 767-796 (2017)

https://doi.org/10.1007/s00466-017-1438-8

Scientific contribution

After a brief introduction to the problem of FE modelling of cracking in quasi-brittle materials and to the main features of the mixed FE approach, this article presents the detailed derivation of the mixed ε/u finite element formulation in Voigt notation, ready-to-use for implementation in finite element codes. It includes the procedure for obtaining the strong and variational forms, the discrete FE equation in matrix format as well the stabilization procedure employed, based on the Variational Multiscale approach (VMS). This FE formulation is used in conjunction with an

isotropic damage model with exponential softening, written in strain-driven format, where both the Rankine and Drucker-Prager surfaces are employed as failure criteria. Then, the numerical simulation of six experimental tests reported in the literature are presented, with the objective of validating the proposed model and to demonstrate its aptness in 2D and 3D applications.

The computed results show the ability of the mixed FEM for modelling fracture in accordance with experimental evidence and without spurious mesh dependence in 2D and 3D. It is shown that the method can be used with any FE discretization: triangles, tetrahedra, quadrilaterals, hexahedra and prisms. The local isotropic damage law used together with the enhanced accuracy FE formulation is able of reproducing crack trajectories, failure mechanisms and force-displacement curves with mesh objectivity, without requiring to employ tracking algorithms and without introducing a strong regularization at the continuum level.

In addition, the convergence of the Mixed FE model in terms of the displacement and strain fields upon mesh refinement to a sharp crack is demonstrated. In particular, it is shown that the strain field, which is continuous, approximates the Dirac-delta function corresponding to the continuous level representation of a crack.

4.2 Appraisement of planar, bending and twisting cracks in 3D with isotropic and orthotropic damage models

Article data

Title: Appraisement of planar, bending and twisting cracks in 3D with isotropic and orthotropic damage models

Authors: G.B. Barbat, M. Cervera and M. Chiumenti

Journal: International Journal of Fracture, 210(1-2), 45–79 (2018)

https://doi.org/10.1007/s10704-018-0261-3

Scientific contribution

This paper introduces the use of orthotropic damage constitutive laws in the numerical modelling of quasi-brittle fracture with mixed finite elements. It focusses on the study of the performance of several damage laws, both isotropic and orthotropic, for computing fracture problems in mode I, mixed mode I and II and mode III loading. The effect of the damage criterion employed is assessed as well. For this, the Rankine, Beltrami, Positive Beltrami, Modified Beltrami and Drucker-Prager surfaces are considered as damage criteria. The investigation includes five sets of numerical simulations which are compared to theoretical or experimental results available in the literature. To show the capabilities of the model, all the computations, except for Willam's numerical test, are performed in 3D.

Results show that the mixed FEM is successful in incorporating orthotropic damage models. The inter-elemental strain continuity and enhanced accuracy of the mixed formulation alleviates to a great extent the spurious stress locking polluting computations performed with the standard displacement based FEM under orthotropic damage. This is confirmed in a comparative study investigating the relative performance of standard and mixed FE when orthotropic damage is introduced.

Computations exhibit the ability of the mixed FE model in reproducing planar, bending and twisting cracks using isotropic and orthotropic damage models in 3D. The solutions obtained are consistent with analytical derivations and experimental reports. The mesh objectivity achieved by the formulation allows to pose the problem of assessing the relative performance of several damage laws and studying the dependence of the ensuing fracture shape on the constitutive behavior employed. These type of investigations are prevented when using the standard FE formulation due to the spurious mesh dependence polluting the results obtained. Using the mixed FEM, the effect that the orthotropy and the damage criterion have in the computed crack surface is detailed. Depending on the actual problem being computed, important variations can be observed in the failure mechanisms and in the force-displacement curves derived from using different isotropic and orthotropic models, and in particular when the damage surface employed in the damage constitutive law is modified.

4.3 Out-of-plane seismic response and failure mechanism of masonry structures using finite elements with enhanced strain accuracy

Article data

Title: Out-of-plane seismic response and failure mechanism of masonry structures using finite elements with enhanced strain accuracy

Authors: G. Vlachakis, M. Cervera, G. B. Barbat and S. Saloustros

Journal: Engineering Failure Analysis, 97, 534–555, (2019)

https://doi.org/10.1016/j.engfailanal.2019.01.017

Scientific contribution

In this article, the mixed FEM is used for the accurate and mesh objective assessment of out-of-plane failure in unreinforced masonry structures. It includes the first application of the employed mixed FE formulation in real-scale structures.

Unreinforced masonry structures, which comprise a large part of the built cultural heritage, are particularly vulnerable to horizontal loading. During seismic events, they are prone to failure through the formation of out-of-plane mechanisms. However, the numerical assessment of this type of structures is still a challenging task because, among other aspects, results computed with standard finite elements lack mesh objectivity.

For this reason, this work assesses the performance of the mixed FEM for the numerical modelling of out-of-plane failure in masonry structures. The study includes the simulation of two real-scale masonry structures, one built with stones and the other one with bricks, which were submitted to shaking-table tests in a laboratory. An equivalent nonlinear static analysis is performed to evaluate the effect of the dynamic action. In the numerical model, the material is considered homogeneous and average properties are used to represent masonry. An isotropic Rankine damage constitutive law is selected to introduce the nonlinear behavior. The investigation includes an exhaustive comparison of the computed results with the damage pattern and collapse mechanism observed in the experiment, and examines as well the capability of the mixed FEM in predicting the load capacity of the structure. To show the superior performance of the mixed FE, corresponding

simulations using the standard displacement based FE formulation are also conducted and examined.

On the one hand, results obtained with the mixed FEM show good agreement with the experiments in terms of damage pattern, load capacity and collapse mechanism. The enhanced accuracy of the mixed formulation prevents the spurious mesh dependency in the resulting computations. On the other hand, the standard displacement based FEM produces solutions with mesh biased crack trajectories, a higher load carrying capacity and even, in one of the cases, a collapse mechanism different from the experimental one.

The article includes as well two additional benchmark numerical simulations, one for in-plane and the other for out-of-plane loading. For this study different meshes are selected, showing the mesh objectivity and the enhanced accuracy of the mixed FEM with respect to the standard formulation in strain localization problems. The standard formulation produces crack paths that are clearly biased by the orientation of the finite elements. Conversely, the mixed FEM predicts consistent fracture trajectories in all the cases, free of spurious mesh dependency, showing that it is a reliable technique for computing structural failure. This method allows to analyze the behavior of large structures with enhanced accuracy and mesh objectivity at a reasonable computational cost.

4.4 Architecture of a multi-crack model with full closing, reopening and sliding capabilities

Article data

Title: Architecture of a multi-crack model with full closing, reopening and sliding capabilities

Authors: M. Cervera, G. B. Barbat and M. Chiumenti

Journal: Computational Mechanics, 65, 1593-1620, (2020)

https://doi.org/10.1007/s00466-020-01836-y

Scientific contribution

This article focuses on the finite element modelling of cracking under cyclic loading. To achieve this goal, special constitutive laws have been designed, implemented and validated. The proposed material model considers tensile and compressive damage with parabolic-exponential softening, irreversible strains, stiffness recovery due to micro-crack closure-reopening effects (MCR) and sliding of open cracks (MCRS). Multi-cracking, the formation of multiple cracks in non-orthogonal directions caused by cyclic loading, is included. Two different versions of the damage model are devised: the first one is orthotropic and the second one is isotropic. Both the Rankine and Drucker-Prager damage criteria are considered. The model is used together with the mixed FEM, which produces mesh objective results in fracture problems with quasi-brittle materials and allows for the use of orthotropic damage laws.

First, the publication defines the features of the constitutive law proposed in this work for modelling cyclic loading. Then the formulation of both versions of the model, the isotropic and the orthotropic, are described. Afterwards, the performance of the proposed crack models is assessed at local level. Next, the simulations of (i) an experiment performed on a concrete beam

under mode I fracture and (ii) a numerical benchmark involving a metal specimen under pure shear and mixed mode I and II loadings are presented.

The computed results demonstrate the capacity of the proposed constitutive laws for modelling cracking under cyclic loading. The study of the model at local level demonstrates the need of providing a record of the directions in which cracks develop to represent MCR effects. It also exposes the requirement of introducing the sliding capabilities of cracks when considering stiffness recovery under shear cyclic loads. The behavior observed in experimental tests is appropriately reproduced. In the examples of application exhibited, the MCRS capabilities of the damage model are able to represent complex crack patterns originated under cyclic loading. Stiffness recovery due to crack closure in force-displacement curves, as well as the effect of crack closure and reopening in the structure are properly replicated.

Computations are performed both under monotonic and cyclic loading to assess the performance of the model in both situations. On the one hand, overlapping results are achieved in mode I and pure shear situations. On the other hand, in mixed mode fracture with non-proportional cyclic loading, differences arise from the effect of irreversible strains and crack sliding.

The mixed FE method allows the successful use of both the isotropic and orthotropic versions of the model, without the stress locking characteristic of the standard displacement based formulation, and to obtain results without spurious mesh dependency. It is shown again that different crack trajectories and force displacement curves are obtained when varying the damage surface employed or when orthotropic behavior instead of isotropic is considered.

4.5 Structural size effect: Experimental, theoretical and accurate computational assessment

Article data

Title: Structural size effect: Experimental, theoretical and accurate computational assessment

Authors: G. B. Barbat, M. Cervera, M. Chiumenti and E. Espinoza

Journal: Engineering Structures, 213, 110555 (2020).

https://doi.org/10.1016/j.engstruct.2020.110555

Scientific contribution

This article studies the structural size effect in fracture problems using the mixed finite element method. According to the introductory discussion on the subject, this phenomenon is intrinsically related to failure in quasi-brittle materials. In this type of materials, theoretical derivations and experimental observations show that the brittleness and load capacity of a structure are dependent on its size. Therefore, models aiming at the numerical analysis of fracture are required to correctly reproduce structural size effect.

First, the study identifies the features required in a constitutive law for reproducing the phenomenon. In this work, an isotropic Rankine damage model with exponential softening is used in all the cases. According to the works of Bazant and coworkers, the main source of structural size effect is the release of stored energy at the crack front during its propagation. Consequently, it is fundamental to enforce the correct dissipation of the fracture energy in the crack.

Next, the study shows the numerical simulation of several experimental campaigns where structural size effect is investigated. They involve the testing of several series of geometrically similar beams with varying dimensions, notched and unnotched, in mode I and mixed mode I and II loading. The mixed FEM is able of reproducing the reported collapse mechanisms, force-displacement curves and crack trajectories with enhanced accuracy for all the sizes, in 2D and 3D.

In addition, a mesh sensitivity study is carried out for both the standard and the mixed formulations. On the one hand, it is shown once again the absolute inability of the standard FEM in producing crack trajectories without a spurious mesh dependence on the FE orientation. Quadratic standard finite elements are examined as well, and they are nevertheless similarly unable of achieving mesh objective results. On the other hand, the capacity of the mixed FEM in obtaining consistent fracture paths irrespective of the mesh employed is verified.

Then, the relative weight of the statistical variability of the mechanical properties of the material in the overall size effect phenomenon is examined. A brief investigation verifies that in quasi-brittle failure the main source of size effect is related to energetic considerations and not statistical ones.

Eventually, the aptness of the proposed model in following Bazant's size effect law over a wide range of structural sizes is shown. The mixed FE formulation is able of producing the theoretical load capacities for the large and small scale limit cases in both notched and unnotched beams. As sizes vary, the model can satisfactorily recreate a smooth transition from one limit case to the other in the whole range of dimensions. It is shown that the computed results fit Bazant's size effect law over an extensive range of sizes with remarkable precision. Additionally, the numerical results are also able of reproducing with accuracy the expected changes in ductility and post-peak behavior originated by variations of structural size.

Chapter 5

Conclusions

5.1 Summary

The computation of mesh objective crack trajectories is a fundamental requirement in the nonlinear analysis of quasi-brittle fracture in order to confidently trust in the solutions provided by FE codes, especially during the structural evaluation process in engineering practice. This thesis focuses on the use of the mixed ε/u strain/displacement finite element for solving fracture problems with isotropic and orthotropic damage constitutive laws. The enhanced accuracy of the FE model eliminates the spurious mesh dependency observed in the standard displacement based FE approach when computing cracking.

The numerical simulation of fracture has been pursued by many researchers since the 1960s and attention to the problem of mesh biased results has been given since its early reports in the 1980s. This work has as a starting point the extensive review of the numerical methods proposed for modelling cracking. It emphasizes in the challenges met and in the developments made within the Finite Element Method due to its wide use and reputation in the computational mechanics community. Aspects regarding the physical problem of fracture, crack representation and propagation are discussed in detail. The causes and varied solutions found for the issue of spurious mesh dependency are examined. The inherent relation between structural size effect and quasi-brittle cracking is analyzed.

An extensive comparative examination of the XFEM, the mixed FEM and the phase-field model is performed, as they are deemed excellent representative techniques of the embedded, smeared and regularized crack approaches to the problem of fracture. The study centers on the main differences of these methods from several points of view: theoretical framework, formulation, implementation in FE codes and practical capabilities. The appraisal of the assets and drawbacks of these techniques is discussed in detail.

Existing results obtained with the XFEM and the phase-field approach are compared with corresponding computations performed with the model for fracture developed in this thesis based on the mixed FEM. All these methods produce excellent results without spurious mesh bias. The capacity of the mixed FE formulation to produce the same results as the phase-field technique

while requiring a much lower computational cost is shown. The computed crack trajectories produced by the XFEM show a dependency on the tracking criterion. Also, a specific implementation to model crack branching is required in the XFEM while this aspect is naturally solved by mixed FE and phase-field. Additionally, the ability of the mixed FE formulation in readily producing matching 2D and 3D results is shown. The capacity of the mixed FEM to straightforwardly accommodate different constitutive laws following a strain-driven format is demonstrated. The investigation evidences that the mixed FE formulation is free from most of the drawbacks present in alternative techniques for solving quasi-brittle cracking.

In this thesis, the ability of the Mixed Finite Element Method for performing structural analysis and computing localized failure with precision is demonstrated. Its generality, cost-efficiency and mesh objectivity allow to reproduce with accuracy experimental tests reported in the literature. It can include a wide variety of constitutive laws for the numerical modelling complex phenomena such as orthotropic damage, as well as stiffness recovery, irreversible strains and multi-cracking under cyclic loading. Its capacity for reproducing structural size effect has been verified. Ultimately, it has revealed its aptness for the computation of real-scale structures, showing positive prospects for its application in engineering practice.

5.2 Conclusions

In this doctoral thesis, a model based on the mixed ε/u strain/displacement finite element formulation for the accurate and mesh objective numerical modelling of fracture in quasi-brittle materials with isotropic and orthotropic damage constitutive laws is developed, implemented in a FE code, validated and employed in engineering applications.

The following conclusions can be drawn from the work presented in this thesis:

General conclusions on the numerical modelling of cracking

- The issue of the spurious mesh dependence of the computed solution with the mesh orientation cannot be ignored. FE formulations need to address it. When calculating structural responses, it is necessary to be able to trust the crack trajectories, collapse mechanisms, force-displacement curves and additional results obtained from a FE analysis.

- In quasi-brittle fracture, the issue of the spurious dependency of the computed crack trajectory with the FE mesh orientation arises from the discretization employed. The statement of the problem at the continuum level is not at the origin of the displayed mesh bias and its modification motivated by this reason is not required.

- The mixed FE model developed in this work as well as the XFEM and phase-field methods against which it is compared are all able of producing solutions with mesh objectivity. The assets and drawbacks of each one of these techniques are discussed in this thesis, considering the challenges of the numerical simulation of cracking identified in the state-of-the-art review and following the proposed *10-Point Checklist*. Mixed FE and the PFM are able of realistically modelling the problem of fracture without an explicit representation of the crack discontinuity and without the use of tracking techniques as done in the XFEM and in other models.

Conclusions on the constitutive models

- The strain-driven layout of the mixed formulation employed in this thesis allows to readily develop and implement different constitutive laws following the stress-strain format, while benefitting from the enhanced accuracy of the proposed FE method. Isotropic and orthotropic damage models, with a large number of damage surfaces, are considered for the successful numerical modelling of fracture.
- In quasi-brittle fracture, the constitutive law, in particular the damage surface, is a decisive factor in the determination of the crack trajectory, together with the geometry and boundary conditions of the structure.
- An isotropic damage law with the appropriate cracking criterion, i.e. Drucker-Prager, is able of reproducing with precision the results observed in mixed mode loading tests.
- The mixed FE formulation allows for the successful use of orthotropic damage models, a feature denied by the poor performance of the standard FE formulation. In many situations, isotropic and orthotropic damage models do not produce the same crack trajectories.
- Cyclic loading can be modelled with a proper damage constitutive law, such as the ones devised in this work, which include tensile and compressive damage, micro-crack closure/reopening effects and irreversible strains. The material models proposed are able of considering crack intersection, stiffness recovery in force-displacement curves and crack closure and reopening in the structure.
- A damage constitutive law featuring strength and fracture energy as nonlinear parameters is able to simulate the structural size effect phenomenon exhibited by quasi-brittle structures. Bazant's size effect law is followed with accuracy by the mixed FE model employed in this thesis.
- Following the approach proposed in Bazant's crack band model, mesh size objectivity is guaranteed through the regularization of the fracture energy with the FE size.

Conclusions on the results of the numerical simulations

- The mixed FE formulation and the phase-field model are definitively able of producing the same results. The mesh resolution required and the computational cost involved are much lower with the mixed FE technique.
- The computed crack trajectory with the XFEM is dependent on the tracking algorithm and the criterion of crack propagation introduced while in the mixed FEM and in the PFM the fracture path is implicitly determined by the damage surface employed. Also, if branching cracks are to be modelled, a specific implementation is required in the XFEM while this phenomenon naturally takes place in the other two techniques examined.
- The capacity of the mixed ε/u FE for obtaining mesh objective results has been demonstrated. This is due to its enhanced accuracy in terms of strains and stresses, a feature lacking in the standard displacement based formulation. Several investigations comparing the performance of the standard and mixed formulations show, on the one hand, the spurious dependence of standard FE with respect to the mesh employed and, on the other hand, the superior performance of mixed FE, which are capable of producing reliable and unbiased solutions.

- The ability of the mixed ε/u FE for reproducing a wide variety of reported experimental tests and numerical benchmarks in mode I, mode II, mode III and mixed mode fracture has been shown. The observed crack trajectories, force-displacement curves and collapse mechanisms are replicated with accuracy. Several existing experimental campaigns where structural size effect is studied have been reproduced, contributing to the validation of the model.
- The reasonable computational cost of the mixed FEM allows the computation of real-scale applications with mesh objectivity and enhanced accuracy.
- As evidenced by the results of this work, 3D applications with mixed FE do not require any specific development. The numerical cost of performing 3D simulations with this method is far more reasonable than with the phase-field model.

5.3 Main contributions

The research presented in this doctoral thesis includes the following original contributions:

- A model based on the mixed ε/u finite element formulation and the use of damage constitutive laws for the numerical simulation of fracture has been developed.
- A wide range of constitutive behaviors have been considered for the fracture model: isotropic and orthotropic damage with several cracking criteria. Specific material laws for cyclic loading which incorporate tensile and compressive damage, microcrack closure/reopening effects, as well as irreversible strains have been proposed.
- The mixed ε/u strain/displacement finite element formulation for damage has been implemented in the COMET code for the numerical modelling of cracking. This model shows a superior computational efficiency in the resolution of nonlinear problems in solid mechanics, producing mesh objective results with a fraction of the computational cost required in the phase-field method. Linear interpolation functions can be used for both unknown fields with the stabilization procedure employed, based on the Variational Multiscale Stabilization approach.
- The considered isotropic and orthotropic constitutive laws for monotonic and cyclic loading have been implemented in COMET, showing the capacity of the mixed ε/u FE formulation to be readily used in conjunction with different strain-driven constitutive laws.
- The simulation of many numerical benchmarks and existing experimental tests has been performed, showing the capacity of the model in producing mesh objective results and in accordance with the experiments. The aptness of the formulation for modelling mode I, mode II, mode III and mixed mode loading is shown. The capacity of the mixed FE model for computing real-scale applications has also been demonstrated. Several comparative studies between the standard and mixed FE formulation have been made, where the capacity of the latter in producing solutions without spurious mesh bias is evidenced.
- Special attention has been devoted to the study of the effect of the constitutive behavior and the damage surface employed in the ensuing crack trajectory. Also, the correspondence between the results of the 2D and 3D simulations obtained with the proposed model has been examined. In addition, the generality of the FE formulation has

been shown through its ability for being used together with any finite element interpolation: triangles, tetrahedra, quadrilaterals, hexahedra and prisms.

- Additionally, the capacity of the mixed formulation in modelling structural size effect, which is a phenomenon linked to quasi-brittle fracture, has been specifically studied. Its causes, which are related to energetic considerations, have been reascertained and verified.
- An extensive comparative study between the mixed FEM, the XFEM and the phase-field model for the numerical simulation of cracking is performed. The theoretical framework and formulation as well as aspects regarding their implementation in FE codes and their practical application have been examined.

5.4 Future research suggestions

In view of the capabilities that the mixed FE method has shown in the numerical modelling of fracture, promising achievements in the following applications can be expected:

- **Dynamics.** The use of the mixed FE formulation for addressing dynamic problems will certainly allow the determination of structural responses in seismic analyzes with enhanced accuracy. It will permit the simulation of complex phenomena such as branching due to inertia effects. Also, the aptness of the constitutive models developed for cyclic loading needs to be investigated when a dynamic analysis is performed.
- **Large strains.** The study of nonlinear solid mechanics problems with finite displacements and deformations will also benefit from the enhanced accuracy achievable with mixed FE. It will allow to consider geometrically nonlinear effects, such as buckling, with better precision.
- **Materials with orthotropic elasticity.** The inclusion in the numerical simulation of materials with orthotropic elastic properties may also be contemplated. In this way, elastic and damage-induced orthotropy may be considered concurrently using the mixed FEM.
- **Composite materials.** Applications involving the nonlinear analysis of composite structures with materials such as reinforced concrete will also benefit of the mesh objectivity attainable with the use of mixed FE.
- **Incompressibility.** The enhanced accuracy and aptness of the mixed ε/u finite element formulation for obtaining mesh objective results in cracking problems suggests the use of a three-field e/u/p deviatoric strain/displacement/pressure mixed FE for computing fracture in incompressible situations without spurious mesh dependency and with improved precision.

References

[1] A. Hillerborg, M. Modeer and P.-E. Petersson, "Analysis of crack formation and crack growth in concrete by means of fracture mechanics and finite elements," *Cement and Concrete Research,* vol. 6, no. 6, pp. 773-781, 1976.

[2] A. Hillerborg, A model for fracture analysis, Report TVBM-3005, Division of Building Materials, Lund Institute of Technology, Sweden, 1978.

[3] M. Modeer, A fracture mechanics approach to failure analyses of concrete materials, Report TVBM-1001, Division of Building Materials, University of Lund, Sweden, 1979.

[4] P.-E. Petersson, Crack growth and development of fracture zones in plain concrete and similar materials, Report TVBM-1006, Division of Building Materials, Lund Institute of Technology, Sweden, 1981.

[5] P.-J. Gustafsson, Fracture mechanics studies of non-yielding materials like concrete: modelling of tensile fracture and applied strength analyses, Report TVBM-1007, Division of Building Materials, Lund University, Sweden, 1985.

[6] D. Dugdale, "Yielding of steel sheets containing slits," *Journal of the Mechanics and Physics of Solids,* vol. 8, no. 2, pp. 100-104, 1960.

[7] G. Barenblatt, "On equilibrium cracks formed during brittle fracture. Fundamentals and hypotheses. Axisymmetrical cracks," *Prikladnaya Matematika i Mekhanika,* vol. 23, no. 3, pp. 434-444, 1959.

[8] G. Barenblatt, "On equilibrium cracks formed during brittle fracture. Straight cracks in flat plates," *Prikladnaya Matematika i Mekhanika,* vol. 23, no. 4, pp. 706-721, 1959.

[9] G. Barenblatt, "On equilibrium cracks formed during brittle fracture. Stability of isolated cracks. Relation with energy theories," *Prikladnaya Matematika i Mekhanika,* vol. 23, no. 5, pp. 892-900, 1959.

[10] G. Barenblatt, "The mathematical theory of equilibrium cracks in brittle fracture," *Advances in Applied Mechanics,* vol. 7, pp. 55-129, 1962.

[11] Y. Rashid, "Ultimate strength analysis of prestressed concrete pressure vessels," *Nuclear Engineering and Design,* vol. 7, no. 4, pp. 334-344, 1968.

[12] Z. Bazant and B. Oh, "Crack band theory for fracture of concrete," *Matériaux et Constructions,* vol. 16, no. 3, pp. 155-177, 1983.

[13] M. Ortiz, Y. Leroy and A. Needleman, "A finite element method for localized failure analysis," *Computer Methods in Applied Mechanics and Engineering,* vol. 61, no. 2, pp. 189-214, 1987.

[14] T. Belytschko, J. Fish and B. Engelmann, "A finite element with embedded localization zones," *Computer Methods in Applied Mechanics and Engineering,* vol. 70, no. 1, pp. 59-89, 1988.

[15] E. Dvorkin, A. Cuitino and G. Gioia, "Finite elements with displacement interpolated embedded localization lines insensitive to mesh size and distorsions," *International Journal for Numerical Methods in Engineering,* vol. 30, pp. 541-564, 1990.

[16] J. Oliver, A. Huespe, M. Pulido and E. Chaves, "From continuum mechanics to fracture mechanics: the strong discontinuity approach," *Engineering Fracture Mechanics,* vol. 69, pp. 113-136, 2002.

[17] T. Belytschko and T. Black, "Elastic crack growth in finite elements with minimal remeshing," *International Journal for Numerical Methods in Engineering,* vol. 45, pp. 601-620, 1999.

[18] N. Moes, J. Dolbow and T. Belytschko, "A finite element method for crack growth without remeshing," *International Journal for Numerical Methods in Engineering,* vol. 46, no. 1, pp. 131-150, 1999.

[19] J. Dolbow, N. Moes and T. Belytschko, "Discontinuous enrichment in finite elements with a partition of unity method," *Finite Elements in Analysis and Design,* vol. 36, no. 3-4, pp. 235-260, 2000.

[20] G. Meschke and P. Dumstorff, "Energy-based modeling of cohesive and cohesionless cracks via X-FEM," *Computer Methods in Applied Mechanics and Engineering,* vol. 196, pp. 2338-2357, 2007.

[21] R. de Borst and P. Nauta, "Non-orthogonal cracks in a smeared finite element model," *Engineering Computations,* vol. 2, pp. 35-46, 1985.

[22] J. Rots, P. Nauta, G. Kusters and J. Blauwendraad, "Smeared crack approach and fracture localization in concrete," *Heron,* vol. 30, pp. 1-48, 1985.

[23] J. Rots, "Computational modeling of concrete fracture," Ph.D. Thesis, Delft University of Technology, 1988.

[24] J. Oliver, M. Cervera, S. Oller and J. Lubliner, "Isotropic damage models and smeared crack analysis of concrete," *Proceedings: II International Conference on Computer Aided Analysis and Design of Concrete,* pp. 945-957, 1990.

[25] L. Sluys, "Wave propagation localisation and dispersion in softening solids," Ph.D. Thesis, Delft University of Technology, 1992.

[26] M. Cervera, M. Chiumenti and R. Codina, "Mixed stabilized finite element methods in nonlinear solid mechanics. Part I: Formulation," *Computer Methods in Applied Mechanics and Engineering,* vol. 199, no. 37-40, pp. 2559-2570, 2010.

[27] M. Cervera, M. Chiumenti and R. Codina, "Mixed stabilized finite element methods in nonlinear solid mechanics. Part II: Strain localization," *Computer Methods in Applied Mechanics and Engineering,* vol. 199, no. 37-40, pp. 2571-2589, 2010.

[28] M. Cervera and M. Chiumenti, "Smeared crack approach: back to the original track," *International Journal for Numerical and Analytical Methods in Geomechanics,* vol. 30, no. 12, pp. 1173-1199, 2006.

[29] M. Cervera and M. Chiumenti, "Mesh objective tensile cracking via a local continuum damage model and a crack tracking technique," *Computer Methods and Applied Mechanics in Engineering,* vol. 196, no. 1-3, pp. 304-320, 2006.

[30] M. Cervera, M. Chiumenti and R. Codina, "Mesh objective modeling of cracks using continuous linear strain and displacement interpolations," *International Journal for Numerical Methods in Engineering,* vol. 87, no. 10, pp. 962-987, 2011.

[31] M. Cervera, G. Barbat and M. Chiumenti, "Finite element modelling of quasi-brittle cracks in 2D and 3D with enhanced strain accuracy," *Computational Mechanics,* vol. 60, no. 5, pp. 767-796, 2017.

[32] G. Barbat, M. Cervera and M. Chiumenti, "Appraisement of planar, bending and twisting cracks in 3D with isotropic and orthotropic damage models," *International Journal of Fracture,* vol. 210, no. 1-2, pp. 45-79, 2018.

[33] G. Vlachakis, M. Cervera, G. Barbat and S. Saloustros, "Out-of-plane seismic response and failure mechanism of masonry structures using finite elements with enhanced strain accuracy," *Engineering Failure Analysis,* vol. 97, pp. 534-555, 2019.

[34] M. Cervera, G. Barbat and M. Chiumenti, "Architecture of a multi-crack model with full closing, reopening and sliding capabilities," *Computational Mechanics,* vol. 65, pp. 1593-1620, 2020.

[35] G. Barbat, M. Cervera, M. Chiumenti and E. Espinoza, "Structural size effect: Experimental, theoretical and accurate computational assessment," *Engineering Structures,* vol. 213, art. 110555, 2020.

[36] G. Pijaudier-Cabot and Z. Bazant, "Nonlocal damage theory," *Journal of Engineering Mechanics,* vol. 113, no. 10, pp. 1512-1533, 1987.

[37] Z. Bazant and G. Pijaudier-Cabot, "Nonlocal continum damage, localization instabilities and convergence," *Journal of Engineering Mechanics ,* no. 55, pp. 287-293, 1988.

[38] Z. Bazant and F.-B. Lin, "Nonlocal smeared cracking model for concrete fracture," *Journal of Structural Engineering,* vol. 114, no. 11, pp. 2493-2510, 1988.

[39] M. Jirasek and T. Zimmermann, "Rotating crack model with transition to scalar damage," *ASCE Journal of Engineering Mechanics,* vol. 124, no. 3, pp. 277-284, 1998.

[40] C. Giry, F. Dufour and J. Mazars, "Stress-based nonlocal damage model," *International Journal of Solids and Structures,* vol. 48, pp. 3431-3443, 2011.

[41] R. Peerlings, R. de Borst, W. Brekelmans and J. de Vree, "Gradient enhanced damage for quasi brittle materials," *International Journal for Numerical Methods in Engineering,* vol. 39, pp. 3391-3403, 1996.

[42] R. Peerlings, R. de Borst, W. Brekelmans and M. Geers, "Gradient-enhanced damage modelling of concrete fracture," *Mechanics of Cohesive-Frictional Materials ,* vol. 3, pp. 323-342, 1998.

[43] M. Geers, R. de Borst, W. Brekelmans and R. Peerlings, "Strain-based transient-gradient damage model for failure analyses," *Computer Methods in Applied Mechanics and Engineering,* vol. 160, pp. 133-153, 1998.

[44] M. Geers, R. de Borst, W. Brekelmans and R. Peerlings, "Validation and internal length scale determination for a gradient damage model: application to short glass-fibre-reinforced polypropylene," *International Journal of Solids and Structures,* vol. 36, pp. 2557-2583, 1999.

[45] C. Comi, "Computational modelling of gradient-enhanced damage in quasi-brittle materials," *Mechanics of Cohesive-Frictional Materials,* vol. 4, pp. 17-36, 1999.

[46] S. Saroukhani, R. Vafadari and A. Simone, "A simplifiend implementation of a gradient-enhanced damage model with transient length scale effects," *Computational Mechanics,* vol. 51, pp. 899-909, 2013.

[47] B. Bourdin, G. Francfort and J.-J. Marigo, "Numerical experiments in revisited brittle fracture," *Journal of the Mechanics and Physics of Solids,* vol. 48, no. 4, pp. 797-826, 2000.

[48] B. Bourdin, G. Francfort and J. Marigo, "The variational approach to fracture," *Journal of Elasticity,* vol. 91, pp. 5-148, 2008.

[49] C. Miehe, M. Hofacker and F. Welschinger, "A phase field model for rate-independent crack propagation: robust algorithmic implementation based on operator splits," *Computer Methods in Applied Mechanics and Engineering,* vol. 199, pp. 2765-2778, 2010.

[50] C. Miehe, F. Welschinger and M. Hofacker, "Thermodynamically consistent phase-field models of fracture: Variational principles and multi-field FE implementations," *International Journal for Numerical Methods in Engineering,* vol. 83, pp. 1273-1311, 2010.

[51] M. Borden, C. Verhoosel, M. Scott, T. Hughes and C. Landis, "A phase-field description of dynamic brittle fracture," *Computer Methods in Applied Mechanics and Engineering,* Vols. 217-220, pp. 77-95, 2012.

[52] C. Miehe, L.-M. Schänzel and H. Ulmer, "Phase field modeling of fracture in multi-physics problems. Part I. Balance of cracks surface and failure criteria for brittle crack propagation in thermo-elastic solids," *Computer Methods in Applied Mechanics and Engineering,* vol. 294, pp. 449-485, 2015.

[53] A. Griffith, "The phenomena of rupture and flow in solids," *Philosophical transactions of the Royal Society,* vol. CCXXI-A, pp. 163-198, 1920.

[54] A. Chambolle, G. Francfort and J.-J. Marigo, "Revisiting energy release rates in brittle fracture," *Journal of Nonlinear Science,* vol. 20, pp. 395-424, 2010.

[55] A. Braides, Approximation of free-discontinuity problems, Berlin: Springer, 1998.

[56] J.-Y. Wu, V. Nguyen, C. Nguyen, D. Sutula, S. Sinaie and S. Bordas, "Phase-field modeling of fracture," *Advances in Applied Mechanics,* vol. 53, pp. 1-183, 2020.

[57] J.-Y. Wu, "A unified phase-field theory for the mechanics of damage and quasi-brittle failure," *Journal of the Mechanics and Physics of Solids,* vol. 103, pp. 72-99, 2017.

[58] J.-Y. Wu, "A geometrically regularized gradient-damage model with energetic equivalence," *Computer Methods in Applied Mechanics and Engineering,* vol. 328, pp. 612-637, 2018.

[59] J.-Y. Wu and V. Nguyen, "A length scale insensitive phase-field damage model for brittle fracture," *Journal of the Mechanics and Physics of Solids,* vol. 119, pp. 20-42, 2018.

[60] D.-C. Feng and J.-Y. Wu, "Phase-field regularized cohesive zone model (CZM) and size effect of concrete," *Engineering Fracture Mechanics,* vol. 197, pp. 66-79, 2018.

[61] V. Nguyen and J.-Y. Wu, "Modeling dynamic fracture of solids with a phase-field regularized cohesive zone model," *Computer Methods in Applied Mechanics and Engineering,* vol. 340, pp. 1000-1022, 2018.

[62] J.-Y. Wu, "Robust numerical implementation of non-standard phase-field damage models for failure in solids," *Computer Methods in Applied Mechanics and Engineering,* vol. 340, pp. 767-797, 2018.

[63] J.-Y. Wu, J.-F. Qiu, V. Nguyen, T. Mandal and L.-J. Zhuang, "Computational modeling of localized failure in solids: XFEM vs PF-CZM," *Computer Methods in Applied Mechanics and Engineering,* vol. 345, pp. 618-643, 2019.

[64] T. Mandal, V. Nguyen and J.-Y. Wu, "Length scale and mesh bias sensitivity of phase-field models for brittle and cohesive fracture," *Engineering Fracture Mechanics,* vol. 217, art. 106532, 2019.

[65] Z.-J. Yang, B.-B. Li and J.-Y. Wu, "X-ray computed tomography images based phase-field modeling of mesoscopic failure in concrete," *Engineering Fracture Mechanics,* vol. 208, pp. 151-170, 2019.

[66] J.-Y. Wu, V. Nguyen, H. Zhou and Y. Huang, "A variationally consistent phase-field anisotropic damage model for fracture," *Computer Methods in Applied Mechanics and Engineering,* vol. 358, art. 112629, 2020.

[67] J.-Y. Wu, Y. Huang and V. Nguyen, "On the BFGS monolithic algorithm for the unified phase field damage theory," *Computer Methods in Applied Mechanics and Engineering,* vol. 360, art. 112704, 2020.

[68] J.-Y. Wu, T. Mandal and V. Nguyen, "A phase-field regularized cohesive zone model for hydrogen assisted cracking," *Computer Methods in Applied Mechanics and Engineering,* vol. 358, art. 112614, 2020.

[69] T. Mandal, V. Nguyen and J.-Y. Wu, "Evaluation of variational phase-field models for dynamic brittle fracture," *Engineering Fracture Mechanics,* vol. 235, art. 107169, 2020.

[70] J.-Y. Wu, Y. Huang, H. Zhou and V. Nguyen, "Three-dimensional phase-field modeling of mode I+II/III failure in solids," *Computer Methods in Applied Mechanics and Engineering,* vol. 373, art. 113537, 2020.

[71] P. Areias and T. Belytschko, "Analysis of three-dimensional crack initiation and propagation using the extended element method," *International Journal for Numerical Methods in Engineering,* vol. 63, pp. 760-788, 2005.

[72] L. Benedetti, M. Cervera and M. Chiumenti, "High-fidelity prediction of crack formation in 2D and 3D pullout tests," *Computers and Structures,* vol. 172, pp. 93-109, 2016.

[73] M. Jirasek and T. Zimmermann, "Analysis of rotating crack model," *Journal of Engineering Mechanics,* vol. 124, no. 8, pp. 842-851, 1998.

[74] M. Cervera, M. Chiumenti and D. Di Capua, "Benchmarking on bifurcation and localization in J2 plasticity for plane stress and plane strain conditions," *Computer Methods in Applied Mechanics and Engineering,* Vols. 241-244, pp. 206-224, 2012.

[75] J.-Y. Wu, "Unified analysis of enriched finite elements for modeling cohesive cracks," *Computer Methods in Applied Mechanics and Engineering,* vol. 200, no. 45-46, pp. 3031-3050, 2011.

[76] M. Cervera, "An orthotropic mesh corrected crack model," *Computer Methods and Applied Mechanics in Engineering,* vol. 197, no. 17-18, pp. 1603-1619, 2008.

[77] J. Vignollet, S. May, R. de Borst and C. Verhoosel, "Phase-field models for brittle and cohesive fracture," *Meccanica,* vol. 49, pp. 2587-2601, 2014.

[78] A. Kumar, B. Bourdin, G. Francfort and O. Lopez-Pamies, "Revisiting nucleation in the phase-field approach to brittle fracture," *Journal of the Mechanics and Physics of Solids,* vol. 142, art. 104027, 2020.

[79] H. Cornelissen, D. Hordijk and H. Reinhardt, "Experimental determination of crack softening characteristics of normalweight and lightweight concrete," *Heron,* vol. 31, no. 2, pp. 45-56, 1986.

[80] F. Wittmann, K. Rokugo, E. Bruhwiler, H. Mihashi and P. Simonin, "Fracture energy and strain softening of concrete as determined by means of compact tension specimens," *Materials and Structures,* vol. 21, pp. 21-32, 1988.

[81] G. Guinea, J. Planas and M. Elices, "A general fit for the softening curve of concrete," *Materials and Structures,* vol. 27, pp. 99-105, 1994.

[82] M. Ortiz and A. Pandolfi, "Finite-deformation irreversible cohesive elements for three-dimensional crack-propagation analysis," *International Journal for Numerical Methods in Engineering,* vol. 44, pp. 1267-1282, 1999.

[83] S. Teichtmeister, D. Kienle, F. Aldakheel and M.-A. Keip, "Phase field modeling of fracture in anisotropic brittle solids," *International Journal of Non-Linear Mechanics,* vol. 97, pp. 1-21, 2017.

[84] J. Bleyer and R. Alessi, "Phase-field modeling of anisotropic brittle fracture including several damage mechanisms," *Computer Methods in Applied Mechanics and Engineering,* vol. 336, pp. 213-236, 2018.

[85] B. Li and C. Maurini, "Crack kinking in a variational phase-field model of brittle fracture with strongly anisotropic surface energy," *Journal of the Mechanics and Physics of Solids,* vol. 125, pp. 502-522, 2019.

[86] M. Cervera and J.-Y. Wu, "On the conformity of strong, regularized, embedded and smeared discontinuity approaches for the modelling of localized failure in solids," *International Journal of Solids and Structures,* vol. 71, pp. 19-38, 2015.

[87] J.-Y. Wu and M. Cervera, "On the equivalence between traction- and stress-based approaches for the modeling of localized failure in solids," *Journal of the Mechanics and Physics of Solids,* vol. 82, pp. 137-163, 2015.

[88] O. Mohr, "Welche Umstande bedingen die Elastizitasgrenze und den Bruch eines Materials?," *Zeitschrift des Vereines Deutscher Ingenieure,* vol. 44, pp. 1524-1530, 1572-1577, 1900.

[89] J.-Y. Wu and M. Cervera, "A thermodynamically consistent plastic-damage framework for localized failure in quasi-brittle solids: Material model and strain localization analysis," *International Journal of Solids and Structures,* vol. 88, pp. 227-247, 2016.

[90] J.-Y. Wu and M. Cervera, "Strain localization of elastic-damaging frictional-cohesive materials: Analytical results and numerical verification," *Materials,* vol. 10, no. 4, art. 434, 2017.

[91] M. Cervera, J.-Y. Wu, M. Chiumenti and S. Kim, "Strain localization analysis of Hill's orthotropic elastoplasticity: Analytical results and numerical verification," *Computational Mechanics,* vol. 65, pp. 533-554, 2019.

[92] S. Weihe, F. Ohmenhauser and B. Kroplin, "A phenomenological approach to decompose geometrical and constitutive aspects of failure induced anisotropy," *Computational Materials Science,* vol. 13, no. 1-3, pp. 177-194, 1998.

[93] K. Keller, S. Weihe, T. Siegmund and B. Kroplin, "Generalized cohesive zone model: Incorporating triaxiality dependent failure mechanisms," *Computational Materials Science,* vol. 16, no. 1-4, pp. 267-274, 1999.

[94] F. Ohmenhauser, S. Weihe and B. Kroplin, "Algorithmic implementation of a generalized cohesive crack model," *Computational Materials Science,* vol. 16, no. 1-4, pp. 294-306, 1999.

[95] C. Feist, "A numerical model for cracking of plain concrete based on the strong discontinuity approach," Ph.D. thesis, University of Innsbruck, 2004.

[96] M. Jirasek and T. Zimmermann, "Embedded crack model. Part II: Combination with smeared cracks," *International Journal for Numerical Methods in Engineering,* vol. 50, pp. 1291-1305, 2001.

[97] R. Radulovic, O. Bruhns and J. Mosler, "Effective 3D failure simulations by combining the advantages of embedded Strong Discontinuity Approaches and classical interface elements," *Engineering Fracture Mechanics,* vol. 78, no. 12, pp. 2470-2485, 2011.

[98] J. Hernandez, J. Oliver, J. Cante and R. Weyler, "Numerical modeling of crack formation in powder forming processes," *International Journal of Solids and Structures,* vol. 48, no. 2, pp. 292-316, 2011.

[99] S. Saloustros, M. Cervera and L. Pela, "Challenges, tools and applications of tracking algorithms in the numerical modelling of cracks in concrete and masonry structures," *Archives of Computational Methods in Engineering,* vol. 26, pp. 961-1005, 2019.

[100] J. Oliver, A. Huespe, E. Samaniego and E. Chaves, "Continuum approach to the numerical simulation of material failure in concrete," *International Journal for Numerical and Analytical Methods in Geomechanics,* vol. 28, pp. 609-632, 2004.

[101] J. Oliver and A. Huespe, "Continuum approach to material failure in strong discontinuity settings," *Computer Methods in Applied Mechanics and Engineering,* vol. 193, pp. 3195-3220, 2004.

[102] J. Mosler and G. Meschke, "Embedded crack vs. smeared crack models: a comparison of elementwise discontinuous crack path approaches with emphasis on mesh bias," *Computer Methods in Applied Mechanics and Engineering,* vol. 193, no. 30-32, pp. 3351-3375, 2004.

[103] C. Feist and G. Hofstetter, "An embedded strong discontinuity model for cracking of plain concrete," *Computer Methods in Applied Mechanics and Engineering,* vol. 195, p. 7115–7138, 2006.

[104] J.-Y. Wu, F.-B. Li and S.-L. Xu, "Extended embedded finite elements with continuous displacement jumps for the modeling of localized failure in solids," *Computer Methods in Applied Mechanics and Engineering,* vol. 285, pp. 346-378, 2015.

[105] S. Saloustros, L. Pela and M. Cervera, "A crack-tracking technique for localized cohesive-frictional damage," *Engineering Fracture Mechanics,* vol. 150, pp. 96-114, 2015.

[106] S. Saloustros, L. Pela, M. Cervera and P. Roca, "Finite element modelling of internal and multiple localized cracks," *Computational Mechanics,* vol. 59, pp. 299-316, 2017.

[107] S. Saloustros, M. Cervera, L. Pela and P. Roca, "Tracking multi-directional intersecting cracks in masonry shear walls under cyclic loading," *Meccanica,* vol. 53, p. 1757–1776, 2018.

[108] M. Cervera, L. Pela, R. Clemente and P. Roca, "A crack-tracking technique for localized damage in quasi-brittle materials," *Engineering Fracture Mechanics,* vol. 77, no. 13, pp. 2431-2450, 2010.

[109] Z. Bazant and J. Planas, Fracture and size effect in concrete and other quasibrittle materials, Boca Raton: CRC Press, 1998.

[110] Z. Bazant, "Size effect," *International Journal of Solids and Structures,* vol. 37, pp. 69-80, 2000.

[111] Z. Bazant and Z. Guo, "Size effect on strength of floating sea ice under vertical line load," *Journal of Engineering Mechanics,* vol. 128, no. 3, pp. 254-263, 2002.

[112] Z. Bazant and G. Zi, "Size effect law and fracture mechanics of the triggering of dry snow slab avalanches," *Journal of Geophysical Research,* vol. 108, no. B2, 2003.

[113] ACI, Building code requirements for structural concrete (ACI 318-19), 2019.

[114] M. Rasoolinejad, A. Donmez and Z. Bazant, "Fracture and size effect suppression by mesh reinforcement of concrete and justification of empirical shrinkage and temperature reinforcement in design codes," *Journal of Engineering Mechanics,* vol. 146, no. 10, art. 04020120, 2020.

[115] Z. Bazant, "Fracture in concrete and reinforced concrete," in *Mechanics of Geomaterials*, 1985, pp. 259-303.

[116] Z. Bazant, J. Ozbolt and R. Eligehausen, "Fracture size effect: Review of evidence for concrete structures," *Journal of Structural Engineering,* vol. 120, no. 8, pp. 2377-2398, 1994.

[117] Z. Bazant and E.-P. Chen, "Scaling of structural failure," Sandia Report SAND96-2948, Albuquerque, New Mexico, 1997.

[118] Z. Bazant, "Size effect on structural strength: a review," *Archive of Applied Mechanics,* vol. 69, pp. 703-725, 1999.

[119] Z. Bazant, "Concrete fracture models: testing and practice," *Engineering Fracture Mechanics,* vol. 69, pp. 165-205, 2002.

[120] M. Cervera and M. Chiumenti, "Size effect and localization in J2 plasticity," *International Journal of Solids and Structures,* vol. 46, pp. 3301-3312, 2009.

[121] Z. Bazant and Q. Yu, "Universal size effect law and effect of crack depth on quasi-brittle structure strength," *Journal of Engineering Mechanics,* vol. 135, no. 2, pp. 78-84, 2009.

[122] N. Moes and T. Belytschko, "Extended finite element method for cohesive crack growth," *Engineering Fracture Mechanics,* vol. 69, pp. 813-833, 2002.

[123] J. Melenk and I. Babuska, "The partition of unity finite element method: basic theory and applications," *Computer Methods in Applied Mechanics and Engineering,* vol. 139, no. 1-4, pp. 289-314, 1996.

[124] I. Babuska and J. Melenk, "The partition of unity method," *International Journal for Numerical Methods in Engineering,* vol. 40, no. 4, pp. 727-758, 1997.

[125] T. Strouboulis, I. Babuska and K. Copps, "The design and analysis of the Generalized Finite Element Method," *Computer Methods in Applied Mechanics and Engineering,* vol. 181, pp. 43-69, 2000.

[126] C. Duarte, I. Babuska and J. Oden, "Generalized finite element methods for three-dimensional structural mechanics problems," *Computers and Structures,* vol. 77, no. 2, pp. 215-232, 2000.

[127] T. Strouboulis, K. Copps and I. Babuska, "The generalized finite element method," *Computer Methods in Applied Mechanics and Engineering,* vol. 190, no. 32-33, pp. 4081-4193, 2001.

[128] T. Belytschko, R. Gracie and G. Ventura, "A review of extended/generalized finite element methods for material modelling," *Modelling and Simulation in Materials Science and Engineering,* vol. 17, no. 4, art. 043001, 2009.

[129] T.-P. Fries and T. Belytschko, "The extended/generalized finite element method: an overview of the method and its applications," *International Journal for Numerical Methods in Engineering,* vol. 84, no. 3, pp. 253-304, 2010.

[130] D. Dias-da-Costa, J. Alfaiate, L. Sluys and E. Julio, "A comparative study on the modelling of discontinuous fracture by means of enriched nodal and element techniques and interface elements," *International Journal of Fracture,* vol. 161, pp. 97-119, 2010.

[131] I. Babuska and U. Banerjee, "Stable generalized finite element method (SGFEM)," *Computer Methods in Applied Mechanics and Engineering,* Vols. 201-204, pp. 91-111, 2011.

[132] N. Sukumar, J. Dolbow and N. Moes, "Extended finite element method in computational fracture mechanics: a retrospective examination," *International Journal of Fracture,* vol. 196, pp. 189-206, 2015.

[133] A. Egger, U. Pillai, K. Agathos, E. Kakouris, E. Chatzi, I. Aschroft and S. Triantafyllou, "Discrete and phase field methods for linear elastic fracture mechanics: A comparative study and state-of-the-art review," *Applied Sciences,* vol. 9, no. 12, art. 2436, 2019.

[134] R. Clough, "The stress distribution of Norfork Dam," *Structures and Materials Research,* vol. 100, no. 19, 1962.

[135] D. Ngo and A. Scordelis, "Finite element analysis of reinforced concrete beams," *American Concrete Institute Journal,* vol. 64, no. 3, pp. 152-163, 1967.

[136] A. Nilson, "Nonlinear analysis of reinforced concrete by the finite element method," *American Concrete Institute Journal,* vol. 65, no. 9, pp. 757-776, 1968.

[137] A. Ingraffea, "Discrete fracture propagation in rock: laboratory tests and finite element analysis," Ph.D. Thesis, University of Colorado, Boulder, 1977.

[138] V. Saouma, "Interactive finite element analysis of reinforced concrete: a fracture mechanics approach," Ph.D. Thesis, Cornell University, NY, 1981.

[139] M. Shephard, N. Yehia, G. Burd and T. Weidner, "Automatic crack propagation tracking," *Computers and Structures,* vol. 20, no. 1-3, pp. 211-223, 1985.

[140] P. Wawrzynek and A. Ingraffea, "Interactive finite element analysis of fracture processes: an integrated approach," *Theoretical and Applied Fracture Mechanics,* vol. 8, no. 2, pp. 137-150, 1987.

[141] X. Xu and A. Needleman, "Numerical simulations of fast crack growth in brittle solids," *Journal of the Mechanics and Physics of Solids,* vol. 42, no. 9, pp. 1397-1434, 1994.

[142] G. Camacho and M. Ortiz, "Computational modelling of impact damage in brittle materials," *International Journal of Solids and Structures,* vol. 33, no. 20-22, pp. 2899-2938, 1996.

[143] M. Tijssens, B. Sluys and E. van der Giessen, "Numerical simulation of quasi-brittle fracture using damaging cohesive surfaces," *European Journl of Mechanics - A/Solids,* vol. 19, no. 5, pp. 761-779, 2000.

[144] M. Falk, A. Needleman and J. Rice, "A critical evaluation of cohesive zone models of dynamic fracture," *Journal de Physique IV,* vol. 11, no. PR5, pp. 43-50, 2001.

[145] P. Zavattieri, "Modeling of crack propagation in thin-walled structures using a cohesive model for shell elements," *Journal of Applied Mechanics,* vol. 73, no. 6, pp. 948-958, 2006.

[146] N. Nourbakhshnia and G. Liu, "A quasi-static growth simulation based on the singular ES-FEM," *International Journal for Numerical Methods in Engineering,* vol. 88, no. 5, pp. 473-492, 2011.

[147] H. Nguyen-Xuan, G. Liu, N. Nourbakhshnia and L. Chen, "A novel singular ES-FEM for crack growth simulation," *Engineering Fracture Mechanics,* vol. 84, pp. 41-66, 2012.

[148] ACI Committee 446, "Finite element analysis of fracture in concrete structures: State-of-the-art (ACI 446.3R-97)," American Concrete Institute, 1997.

[149] T. Rabczuk, "Computational methods for fracture in brittle and quasi-brittle solids: State-of-the-art review and future perspectives," *ISRN Applied Mathematics,* vol. 2013, art. 849231, 2013.

[150] M. Jirasek and T. Zimmermann, "Embedded crack model: I. Basic formulation," *International Journal for Numerical Methods in Engineering,* vol. 50, pp. 1269-1290, 2001.

[151] M. Cervera, "A smeared-embedded mesh corrected damage model for tensile cracking," *International Journal for Numerical Methods in Engineering,* vol. 76, no. 12, pp. 1930-1954, 2008.

[152] Y. Zhang, R. Lackner, M. Zeiml and H. Mang, "Strong discontinuity embedded approach with standard SOS formulation: Element formulation, energy-based crack-tracking strategy, and validations," *Computer Methods in Applied Mechanics and Engineering,* vol. 287, pp. 335-366, 2015.

[153] Y. Zhang and X. Zhuang, "Cracking elements: a self-propagating strong discontinuity embedded approach for quasi-brittle fracture," *Finite Elements in Analysis and Design,* vol. 144, pp. 84-100, 2018.

[154] M. Jirasek, "Comparative study on finite elements with embedded discontinuities," *Computer Methods in Applied Mechanics and Engineering,* vol. 188, pp. 307-330, 2000.

[155] J. Oliver, A. Huespe and P. Sanchez, "A comparative study on finite elements for capturing strong discontinuities: E-FEM vs X-FEM," *Computer Methods in Applied Mechanics and Engineering,* vol. 195, no. 37-40, pp. 4732-4752, 2006.

[156] D. Dias-da-Costa, J. Alfaiate, L. Sluys, P. Areias and E. Julio, "An embedded formulation with conforming finite elements to capture strong discontinuities," *International Journal for Numerical Methods in Engineering,* vol. 93, no. 2, pp. 224-244, 2013.

[157] B. Patzak and M. Jirasek, "Process zone resolution by extended finite elements," *Engineering Fracture Mechanics,* vol. 70, no. 7-8, pp. 957-977, 2003.

[158] E. Benvenuti, "A regularized XFEM framework for embedded cohesive interfaces," *Computer Methods in Applied Mechanics and Engineering,* vol. 197, no. 49-50, pp. 4367-4378, 2008.

[159] E. Benvenuti, A. Tralli and G. Ventura, "A regularized XFEM model for the transition from continuous to discontinuous displacements," *International Journal for Numerical Methods in Engineering,* vol. 74, no. 6, pp. 911-944, 2008.

[160] E. Benvenuti, "Mesh-size-objective XFEM for regularized continuous–discontinuous transition," *Finite Elements in Analysis and Design,* vol. 47, no. 12, pp. 1326-1336, 2011.

[161] E. Hellinger, "Die allgemeinen Ansätze der Mechanik der Kontinua," in *Encyklopadie der mathematischen Wissenschaften*, vol. 4, Leipzig, Teubner, 1914, pp. 601-694.

[162] E. Reissner, "On a variational theorem in elasticity," *Journal of Mathematics and Physics,* vol. 29, no. 1-4, pp. 90-95, 1950.

[163] E. Reissner, "On a variational theorem for finite elastic deformations," *Journal of Mathematics and Physics,* vol. 32, no. 1-4, pp. 129-135, 1953.

[164] B. Fraeijs de Veubeke, "Displacement and equilibrium models in the finite element method," in *Stress Analysis, Ed. O.Z. Zienkiewicz and G. S. Holister*, London, Wiley, 1965, pp. 145-197.

[165] L. Herrmann, "Elasticity equations for incompressible and nearly incompressible materials by a variational theorem," *American Institute of Aeronautics and Astronautics Journal,* vol. 3, no. 10, pp. 1896-1900, 1965.

[166] R. Dunham and K. Pister, "A finite element application of the Hellinger-Reissner variational theorem," *Proceedings of the Second Conference on Matrix Methods in Structural Mechanics,* pp. 471-487, 1968.

[167] C. Prato, "A mixed finite element method for thin shell analysis," Ph.D. Thesis, Massachusetts Institute of Technology, 1968.

[168] L. Herrmann and D. Campbell, "A finite-element analysis for thin shells," *American Institute of Aeronautics and Astronautics Journal,* vol. 6, no. 10, pp. 1842-1847, 1968.

[169] C. Prato, "Shell finite element method via Reissner's principle," *International Journal of Solids and Structures,* vol. 5, pp. 1119-1133, 1969.

[170] L. Herrmann and W. Mason, "Mixed formulations for finite element shell analyses," *Conference on Computer Oriented Analysis of Shell Structures, Palo Alto, California,* 1970.

[171] R. Taylor, K. Pister and L. Herrmann, "On a variational theorem for incompressible and nearly-incompressible orthotropic elasticity," *International Journal of Solids and Structures,* vol. 4, pp. 875-883, 1968.

[172] T. Pian and P. Tong, "Basis of finite element methods for solid continua," *International Journal for Numerical Methods in Engineering,* vol. 1, pp. 3-28, 1969.

[173] O. Zienkiewicz, "Finite elements - The background story," in *Mathematics of Finite Elements and Applications*, New York, Academic Press, 1973, pp. 1-35.

[174] D. Misra and J. Nieber, "A comparative analysis of mixed finite element and conventional finite element methods for one-dimensional steady heterogeneous Darcy flow," in *Flow and Transport in Subsurface Environment*, Springer, 2018, pp. 141-187.

[175] D. Malkus and T. Hughes, "Mixed finite element methods - Reduced and selective integration methods: A unification of concepts," *Computer Methods in Applied Mechanics and Engineering,* vol. 15, no. 1, pp. 63-81, 1978.

[176] M. Chiumenti, Q. Valverde, C. Agelet de Saracibar and M. Cervera, "A stabilized formulation for incompressible elasticity using linear displacement and pressure interpolations," *Computer Methods and Applied Mechanics in Engineering,* vol. 191, no. 46, pp. 5253-5264, 2002.

[177] M. Chiumenti, Q. Valverde, C. Agelet de Saracibar and M. Cervera, "A stabilized formulation for incompressible plasticity using linear triangles and tetrahedra," *International Journal of Plasticity,* vol. 20, no. 8-9, pp. 1487-1504, 2004.

[178] M. Chiumenti, M. Cervera and R. Codina, "A mixed three-field FE formulation for stress accurate analysis including the incompressible limit," *Computer Methods and Applied Mechanics in Engineering,* vol. 286, pp. 1095-1116, 2015.

[179] J. Oden and L. Wellford, "Analysis of flow of viscous fluids by the finite-element method," *American Institute of Aeronautics and Astronautics,* vol. 10, no. 12, pp. 1590-1599, 1972.

[180] M. Kawahara and N. Takeuchi, "Mixed finite element method for analysis of viscoelastic fluid flow," *Computers and Fluids,* vol. 5, no. 1, pp. 33-45, 1977.

[181] M. Allen, R. Ewing and J. Koebbe, "Mixed finite element methods for computing groundwater velocities," *Numerical Methods for Partial Differential Equations,* vol. 3, pp. 195-207, 1985.

[182] L. Herrmann, "Finite-element bending analysis for plates," *Journal of the Engineering Mechanics Division,* vol. 93, no. 5, pp. 13-26, 1967.

[183] A. Poceski, Mixed Finite Element Method, Berlin: Springer-Verlag, 1992.

[184] M. Jirasek, "Nonlocal damage mechanics," *Revue Européenne de Génie Civil,* vol. 11, no. 7-8, pp. 993-1021, 2007.

[185] Z. Bazant and M. Jirasek, "Nonlocal integral formulations of plasticity and damage: Survey of progress," *Journal of Engineering Mechanics,* vol. 128, no. 11, pp. 1119-1149, 2002.

[186] A. Simone, H. Askes and L. Sluys, "Incorrect initiation and propagation of failure in non-local and gradient-enhanced media," *International Journal of Solids and Structures,* vol. 41, pp. 351-363, 2004.

[187] G. Rastiello, C. Giry, F. Gatuingt, F. Thierry and R. Desmorat, "Nonlocal damage formulation with evolving integral length: the eikonal nonlocal approach," in *Computational Modelling of Concrete Structures, Euro-C 2018*, Bad Hofgastein, Austria, 2018.

[188] G. Di Luzio and Z. Bazant, "Spectral analysis of localization in nonlocal and over-nonlocal materials with softening plasticity or damage," *International Journal of Solids and Structures,* vol. 42, pp. 6071-6100, 2005.

[189] G. Nguyen, "A damage model with evolving nonlocal interactions," *International Journal of Solids and Structures,* vol. 48, pp. 1544-1559, 2011.

[190] L. Poh and G. Sun, "Localizing gradient damage model with decreasing interactions," *International Journal for Numerical Methods in Engineering,* vol. 110, no. 6, pp. 503-522, 2017.

[191] Q. Bui, "Initiation of damage with implicit gradient-enhanced damage models," *International Journal of Solids and Structures,* vol. 47, pp. 2425-2435, 2010.

[192] L. Poh and S. Swaddiwudhipong, "Over-nonlocal gradient enhanced plastic-damage model for concrete," *International Journal of Solids and Structures,* vol. 46, no. 25-26, pp. 4369-4378, 2009.

[193] G. Pijaudier-Cabot, K. Haidar and J.-F. Dube, "Non-local damage model with evolving internal length," *International Journal for Numerical and Analytical Methods in Geomechanics,* vol. 28, no. 7-8, pp. 633-652, 2004.

[194] G. Francfort and J. Marigo, "Revisiting brittle fracture as an energy minimization problem," *Journal of the Mechanics and Physics of Solids,* vol. 48, no. 8, pp. 1319-1342, 1998.

[195] D. Cogswell, "A phase-field study of ternary multiphase microstructures," Ph.D. Thesis, Massachusetts Institute of Technology, 2010.

[196] C. Kuhn, A. Schluter and R. Muller, "On degradation functions in phase field fracture models," *Computational Materials Science,* vol. 108, pp. 374-384, 2015.

[197] T. Nguyen, J. Yvonnet, M. Bornert, C. Chateau, K. Sab, R. Romani and R. Le Roy, "On the choice of parameters in the phase field method for simulating crack initiation with experimental validation," *International Journal of Fracture,* vol. 197, pp. 213-226, 2016.

[198] E. Tanne, T. Li, B. Bourdin, J.-J. Marigo and C. Maurini, "Crack nucleation in variational phase-field models of brittle fracture," *Journal of the Mechanics and Physics of Solids,* vol. 110, pp. 80-99, 2018.

[199] J.-Y. Wu and F.-B. Li, "An improved stable X-FEM (Is-FEM) with a novel enrichment function for the computational modeling of cohesive cracks," *Computer Methods in Applied Mechanics and Engineering,* vol. 295, pp. 77-107, 2015.

[200] W. Li and J.-Y. Wu, "A consistent and efficient localized damage model for concrete," *International Journal of Damage Mechanics,* vol. 27, no. 4, pp. 541-567, 2018.

[201] J. Simo, J. Oliver and F. Armero, "An analysis of strong discontinuities induced by strain softening in rate-independnt inelastic solids," *Computational Mechanics,* vol. 12, pp. 277-296, 1993.

[202] J. Oliver, M. Cervera and O. Manzoli, "Strong discontinuities and continuum plasticity models: the strong discontinuity approach," *International Journal of Plasticity,* vol. 15, pp. 319-351, 1999.

[203] T. Hughes, "Multiscale phenomena: Green's function, Dirichlet-to-Neumann formulation, subgrid scale models, bubbles and the origins of stabilized methods," *Computer Methods in Applied Mechanics and Engineering,* vol. 127, no. 1-4, pp. 387-401, 1995.

[204] T. Hughes, G. Feijoo, L. Mazzei and J.-B. Quincy, "The variational multiscale method - a paradigm for computational mechanics," *Computer Methods in Applied Mechanics and Engineering,* vol. 166, no. 1-2, pp. 3-24, 1998.

[205] A. Vagbharathi and S. Gopalakrishnan, "An extended finite-element model coupled with level set method for analysis of growth of corrosion pits in metallic structures," *Proceedings of the Royal Society A: Mathematical, Physical and Engineering Sciences,* vol. 470, art. 20140001, 2004.

[206] F. Cazes, G. Meschke and M.-M. Zhou, "Strong discontinuity approaches: An algorithm for robust performance and comparative assessment of accuracy," *International Journal of Solids and Structures,* vol. 96, pp. 355-379, 2016.

[207] A. Simone, "Partition of unity-based discontinuous finite elements: GFEM, PUFEM, XFEM," *Revue Europeene de Genie Civil,* vol. 11, no. 7-8, pp. 1045-1068, 2007.

[208] F. Armero and J. Kim, "Three-dimensional finite elements with embedded strong discontinuities to model material failure in the infinitesimal range," *International Journal for Numerical Methods in Engineering,* vol. 91, no. 12, pp. 1291-1330, 2012.

[209] G. Zi and T. Belytschko, "New crack-tip elements for XFEM and applications to cohesive cracks," *International Journal for Numerical Methods in Engineering,* vol. 57, no. 15, pp. 2221-2240, 2003.

[210] P. Stapor, "Application of XFEM with shifted-basis approximation to computation of stress intensity factors," *Archive of Mechanical Engineering,* vol. 58, no. 4, pp. 467-483, 2011.

[211] N. Moes, A. Gravouil and T. Belytschko, "Non-planar 3D crack growth by the extended finite element and level sets - Part I: Mechanical model," *International Journal for Numerical Methods in Engineering,* vol. 53, pp. 2549-2568, 2002.

[212] A. Simone, "Partition of unity-based discontinuous elements for interface phenomena: computational issues," *Communications in Numerical Methods in Engineering,* vol. 20, pp. 465-478, 2004.

[213] E. Bechet, "Improved implementation and robustness study of the X-FEM for stress analysis around cracks," *International Journal of Numerical Methods in Engineering,* vol. 64, no. 8, pp. 1033-1056, 2005.

[214] G. Ventura, "On the elimination of quadrature subcells for discontinuous functions in the eXtended Finite-Element Method," *International Journal for Numerical Methods in Engineering,* vol. 66, pp. 761-795, 2006.

[215] D. Holdych, D. Noble and R. Secor, "Quadrature rules for triangular and tetrahedral elements with generalized functions," *International Journal for Numerical Methods in Engineering,* vol. 73, pp. 1310-1327, 2008.

[216] S. Bordas, T. Rabczuk, N. Hung, V. Nguyen, S. Natarajan, T. Bog, D. Quan and N. Hiep, "Strain smoothing in FEM and XFEM," *Computers and Structures,* vol. 88, no. 23-24, pp. 1419-1443, 2010.

[217] N. Vu-Bac, H. Nguyen-Xuan, L. Chen, S. Bordas, P. Kerfriden, R. Simpson, G. Liu and T. Rabczuk, "A node-based smoothed extended finite element method (NS-XFEM) for fracture analysis," *Computer Modeling in Engineering and Sciences,* vol. 73, no. 4, pp. 331-355, 2011.

[218] G. Ventura and E. Benvenuti, "Equivalent polynomials for quadrature in Heaviside function enriched elements," *International Journal for Numerical Methods in Engineering,* vol. 102, no. 3-4, pp. 688-710, 2015.

[219] T.-P. Fries, "Extended finite element methods (XFEM)," in *Encyclopedia of Continuum Mechanics*, Berlin, Heidelberg, Springer, 2018, pp. 1-10.

[220] E. Benvenuti and A. Tralli, "Simulation of finite-width process zone in concrete-like materials by means of a regularized extended finite element model," *Computational Mechanics,* vol. 50, pp. 479-497, 2012.

[221] E. Benvenuti, G. Ventura, N. Ponara and A. Tralli, "Variationally consistent eXtended FE model for 3D planar and curved imperfect interfaces," *Computer Methods in Applied Mechanics and Engineering,* vol. 267, pp. 434-457, 2013.

[222] A. Hansbo and P. Hansbo, "A finite element method for the simulation of strong and weak discontinuities in solid mechanics," *Computer Methods in Applied Mechanics and Engineering,* vol. 193, no. 33-35, pp. 3523-3540, 2004.

[223] J.-H. Song, P. Areias and T. Belytschko, "A method for dynamic crack and shear band propagation with phantom nodes," *International Journal for Numerical Methods in Engineering,* vol. 67, no. 6, pp. 868-893, 2006.

[224] T. Rabczuk, G. Zi, A. Gerstenberger and W. Wall, "A new crack tip element for the phantom-node method with arbitrary cohesive cracks," *International Journal for Numerical Methods in Engineering,* vol. 75, no. 5, pp. 577-599, 2008.

[225] T. Chau-Dinh, G. Zi, P.-S. Lee, T. Rabczuk and J.-H. Song, "Phantom-node method for shell models with arbitrary cracks," *Computers and Structures,* Vols. 92-93, pp. 242-256, 2012.

[226] N. Vu-Bac, H. Nguyen-Xuan, L. Chen, C. Lee, G. Zi, X. Zhuang, G. Liu and T. Rabczuk, "A phantom-node method with edge-based strain smoothing for linear elastic fracture mechanics," *Journal of Applied Mathematics,* vol. 2013, art. 978026, 2013.

[227] C. Daux, N. Moes, J. Dolbow, N. Sukumar and T. Belytschko, "Arbitrary branched and intersecting cracks with the extended finite element method," *International Journal for Numerical Methods in Engineering,* vol. 48, pp. 1741-1760, 2000.

[228] N. Sukumar, N. Moes, B. Moran and T. Belytschko, "Extended finite element method for three-dimensional crack modelling," *International Journal for Numerical Methods in Engineering,* vol. 48, no. 11, pp. 1549-1570, 2000.

[229] E. Budyn, G. Zi, N. Moes and T. Belytschko, "A method for multiple crack growth in brittle materials without remeshing," *International Journal for Numerical Methods in Engineering,* vol. 61, pp. 1741-1770, 2004.

[230] G. Zi, J. Song, E. Budyn, S. Lee and T. Belytschko, "A method for growing multiple cracks without remeshing and its application to fatigue crack growth," *Modelling and Simulation in Materials Science and Engineering,* vol. 12, no. 5, pp. 901-915, 2004.

[231] C. Richardson, J. Hegemann, E. Sifakis, J. Hellrung and J. Teran, "An XFEM method for modeling geometrically elaborate crack propagation in brittle materials," *International Journal for Numerical Methods in Engineering,* vol. 88, no. 10, p. 1042–1065, 2011.

[232] D. Xu, Z. Liu, X. Liu, Q. Zeng and Z. Zhuang, "Modeling of dynamic crack branching by enhanced extended finite element method," *Computational Mechanics,* vol. 54, pp. 489-502, 2014.

[233] J. Zhao, H. Tang and S. Xue, "Peridynamics versus XFEM: a comparative study for quasi-static crack problems," *Frontiers of Structural and Civil Engineering,* vol. 12, pp. 548-557, 2018.

[234] T. Gasser and G. Holapfel, "3D Crack propagation in unreinforced concrete. A two-step algorithm for tracking 3D crack paths," *Computer Methods in Applied Mechanics and Engineering,* vol. 195, no. 37-40, pp. 5198-5219, 2006.

[235] P. Jager, P. Steinmann and E. Kuhl, "Modeling three-dimensional crack propagation - A comparison of crack path tracking strategies," *International Journal for Numerical Methods in Engineering,* vol. 76, pp. 1328-1352, 2008.

[236] A. Ahmed, "eXtended Finite Element Method (XFEM) - Modeling arbitrary discontinuities and Failure analysis," Ph.D. Thesis, Universita degli Studi di Pavia, 2009.

[237] M. Cervera, M. Chiumenti, L. Benedetti and R. Codina, "Mixed stabilized finite element methods in nonlinear solid mechanics. Part III: Compressible and incompressible plasticity," *Computer Methods in Applied Mechanics and Engineering,* vol. 285, pp. 752-775, 2015.

[238] L. Benedetti, M. Cervera and M. Chiumenti, "3D modelling of twisting cracks under bending and torsion skew notched beams," *Engineering Fracture Mechanics,* vol. 176, pp. 235-256, 2017.

[239] O. Ladyzhenskaya, The mathematical theory of viscous incompressible flows, New York: Gordon and Breach, 1963.

[240] I. Babuska, "Error-bounds for finite element method," *Numerisch Mathematik,* vol. 16, pp. 322-333, 1971.

[241] F. Brezzi, "On the existence, uniqueness and approximation of saddle-point problems arising from lagrangian multipliers," *ESAIM: Mathematical Modelling and Numerical Analysis - Modélisation Mathématique et Analyse Numérique,* vol. 8, no. R2, pp. 129-151, 1974.

[242] I. Babuska, J. Oden and J. Lee, "Mixed-hybrid finite element approximations of second-order elliptic boundary-value problems," *Computer Methods in Applied Mechanics and Engineering,* vol. 11, pp. 175-206, 1977.

[243] F. Brezzi and K. Bathe, "A discourse on the stability conditions for mixed finite element formulations," *Computer Methods in Applied Mechanics and Engineering,* vol. 82, pp. 27-59, 1990.

[244] F. Brezzi and M. Fortin, Mixed and hybrid finite element methods, New York: Springer, 1991.

[245] D. Boffi, F. Brezzi and M. Fortin, Mixed finite element methods and applications, Berlin: Springer, 2013.

[246] R. Codina, "Stabilization of incompressibility and convection through orthogonal sub-scales in finite element methods," *Computer Methods in Applied Mechanics and Engineering ,* vol. 190, pp. 1579-1599, 2000.

[247] R. Codina, "Analysis of a stabilized finite element approximation of the Oseen equations using orthogonal subscales," *Applied Numerical Mathematics,* vol. 58, pp. 264-283, 2008.

[248] R. Codina, "Finite element approximation of the three field formulation of the Stokes problem using arbitrary interpolations," *Society for Industrial and Applied Mathematics Journal on Numerical Analysis,* vol. 47, pp. 699-718, 2009.

[249] S. Badia and R. Codina, "Unified stabilized finite element formulations for the Stokes and the Darcy problems," *SIAM Journal on Numerical Analysis,* vol. 47, pp. 1971-2000, 2009.

[250] S. Badia and R. Codina, "Stabilized continuous and discontinuous Galerkin techniques for Darcy flows," *Computer Methods in Applied Mechanics and Engineering,* vol. 199, no. 25-28, pp. 1654-1667, 2010.

[251] L. Benedetti, M. Cervera and M. Chiumenti, "Stress-accurate mixed FEM for soil failure under shallow foundations involving strain localization in plasticity," *Computers and Geotechnics,* vol. 64, pp. 32-47, 2015.

[252] E. Gdoutos, Problems of mixed mode crack propagation, in: Engineering Application of Fracture Mechanics, vol. II, Netherlands: Martinus Nijhoff, 1984.

[253] R. Spatschek, E. Brener and A. Karma, "Phase field modeling of crack propagation," *Philosophical Magazine,* vol. 91, pp. 75-95, 2011.

[254] M. Chiumenti, M. Cervera, C. Moreira and G. Barbat, "Stress, strain and dissipation accurate 3-field formulation for inelastic isochoric deformation," *Accepted in Finite Elements in Analysis and Design,* 2021.

[255] S. May, J. Vignollet and R. de Borst, "A numerical assessment of phase-field models for brittle and cohesive fracture: Γ-Convergence and stress oscillations," *European Journal of Mechanics and Solids,* vol. 52, pp. 72-84, 2015.

[256] R. de Borst and C. Verhoosel, "Gradient damage vs phase-field approaches for fracture: Similarities and differences," *Computer Methods in Applied Mechanics and Engineering,* vol. 312, pp. 78-94, 2016.

[257] C. Steinke, I. Zreid and M. Kaliske, "On the relation between phase-field crack approximation and gradient damage modelling," *Computational Mechanics,* vol. 59, pp. 717-735, 2017.

[258] T. Mandal, V. Nguyen and A. Heidarpour, "Phase field and gradient enhanced damage models for quasi-brittle failure: a numerical comparative study," *Engineering Fracture Mechanics,* vol. 207, pp. 48-67, 2019.

[259] J. Sargado, E. Keilegavlen, I. Berre and J. Nordbotten, "A combined finite element-finite volume framework for phase-field fracture," *Computer Methods in Applied Mechanics and Engineering,* vol. 373, art. 113474, 2021.

[260] J.-Y. Wu and Y. Huang, "Comprehensive implementations of phase-field damage models in Abaqus," *Theoretical and Applied Fracture Mechanics,* vol. 106, art. 102440, 2020.

[261] Y. Zhang, "Simulation methods for durability assessment of concrete structures: multifield framework and strong discontinuity embedded approach," Ph.D. Thesis, Viena University of Technology, 2013.

[262] M. Ambati, T. Gerasimov and L. De Lorenzis, "A review on phase-field models of brittle fracture and a new fast hybrid formulation," *Computational Mechanics,* vol. 55, pp. 383-405, 2015.

[263] H. Amor, J. Marigo and C. Maurini, "Regularized formulation of the variational brittle fracture with unilateral contact: numerical experiments," *Journal of the Mechanics and Physics of Solids,* vol. 57, no. 8, pp. 1209-1229, 2009.

[264] A. Muixi, S. Fernandez-Mendez and A. Rodriguez-Ferran, "Adaptive refinement for phase-field models of brittle fracture based on Nitsche's method," *Computational Mechanics,* vol. 66, pp. 69-85, 2020.

[265] B. Li, C. Peco, D. Millan, I. Arias and M. Arroyo, "Phase-field modeling and simulation of fracture in brittle materials with strongly anisotropic surface energy," *International Journal for Numerical Methods in Engineering,* vol. 102, no. 3-4, pp. 711-727, 2015.

[266] M. Ambati, T. Gerasimov and L. De Lorenzis, "Phase-field modeling of ductile fracture," *Computational Mechanics,* vol. 55, pp. 1017-1040, 2015.

[267] C. Kuhn, T. Noll and R. Muller, "On phase field modeling of ductile fracture," *GAMM-Mitteilungen,* vol. 39, no. 1, pp. 35-54, 2016.

[268] J.-Y. Wu and S.-L. Xu, "Reconsideration on the elastic damage/degradation theory for the modeling of microcrack closure-reopening (MCR) effects," *International Journal of Solids and Structures,* vol. 50, no. 5, pp. 795-805, 2013.

[269] J. Kiendl, M. Ambati, L. De Lorenzis, H. Gomez and A. Reali, "Phase-field description of brittle fracture in plates and shells," *Computer Methods in Applied Mechanics and Engineering,* vol. 312, pp. 374-394, 2016.

[270] S. Bhowmick and G.-R. Liu, "Three dimensional CS-FEM phase-field modeling technique for brittle fracture in elastic solids," *Applied Sciences,* vol. 8, no. 12, art. 2488, 2018.

[271] T. Nguyen, J. Yvonnet, Q.-Z. Zhu, M. Bornert and C. Chateau, "A phase field method to simulate crack nucleation and propagation in strongly heterogeneous materials from direct imaging of their microstructure," *Engineering Fracture Mechanics,* vol. 139, pp. 18-39, 2015.

[272] S. Zhou, X. Zhuang, H. Zhu and T. Rabczuk, "Phase field modelling of crack propagation, branching and coalescence in rocks," *Theoretical and Applied Fracture Mechanics,* vol. 96, pp. 174-192, 2018.

[273] S. Zhou, X. Zhuang and T. Rabczuk, "Phase field modeling of brittle compressive-shear fractures in rock-like materials: A new driving force and a hybrid formulation," *Computer Methods in Applied Mechanics and Engineering,* vol. 355, pp. 729-752, 2019.

[274] Hirshikesh, S. Natarajan, R. Annabattula and E. Martinez-Paneda, "Phase field modelling of crack propagation in functionally graded materials," *Composites Part B: Engineering,* vol. 169, pp. 239-248, 2019.

[275] T. Noll, C. Kuhn, D. Olesch and R. Muller, "3D phase field simulations of ductile fracture," *GAMM-Mitteilungen,* vol. 43, no. 2, art. e202000008, 2020.

[276] T. Heister, M. Wheeler and T. Wick, "A primal-dual active set method and predictor-corrector mesh adaptivity for computing fracture propagation using a phase-field approach," *Computer Methods in Applied Mechanics and Engineering,* vol. 290, pp. 466-495, 2015.

[277] S. Zhou and X. Zhuang, "Adaptive phase field simulation of quasi-static crack propagation in rocks," *Underground Space,* vol. 3, no. 3, pp. 190-205, 2018.

[278] N. Ferro, S. Micheletti and S. Perotto, "Anisotropic mesh adaptation for crack propagation induced by a thermal shock in 2D," *Computer Methods in Applied Mechanics and Engineering,* vol. 331, pp. 138-158, 2018.

[279] Hirshikesh, C. Jansari, K. Kannan, R. Annabattula and S. Natarajan, "Adaptive phase field method for quasi-static brittle fracture using a recovery based error indicator and quadtree decomposition," *Engineering Fracture Mechanics,* vol. 220, art. 106599, 2019.

[280] M. Cervera, C. Agelet de Saracibar and M. Chiumenti, "COMET: Coupled mechanical and thermal analysis. Data input manual, Version 5.0, Technical report IT-308. Available from http://www.cimne.upc.edu," 2002.

[281] A. Coll, R. Ribo, M. Pasenau, E. Escolano, J. Perez, A. Melendo, A. Monros and J. Garate, "GiD: the personal pre and post-processor User Manual," *CIMNE, Technical University of Catalonia,* <http://gid.cimne.upc.edu>, 2020.

[282] B. Trunk, "Einfluss der Bauteilgrösse auf die Bruchenergie von Beton," *Aedificatio publishers: Immentalstrasse 34, D-79104 Freiburg,* 2000.

[283] J. Chen, "A nonlocal damage model for elasto-plastic materials based on gradient plasticity theory," Ph.D. Thesis, Swiss Federal Institute of Technology, Zurich, 2001.

[284] J. Kim, "New finite elements with embedded strong discontinuities to model failure of three-dimensional continua," Ph.D. Thesis, University of California, Berkeley, 2013.

[285] J. Kim and F. Armero, "Three-dimensional finite elements with embedded strong discontinuities for the analysis of solids at failure in the finite deformation range," *Computer Methods in Applied Mechanics and Engineering,* vol. 317, pp. 890-926, 2017.

[286] X. Su, Z. Yang and G. Liu, "Finite element modelling of complex 3D static and dynamic crack propagation by embedding cohesive elements in Abaqus," *Acta Mechanica Solida Sinica,* vol. 23, no. 3, pp. 271-282, 2010.

[287] T. Ni, M. Zaccariotto, Q.-Z. Zhu and U. Galvanetto, "Coupling of FEM and ordinary state-based peridynamics for brittle failure analysis in 3D," *Mechanics of Advanced Materials and Structures,* p. 1-16, 2019. DOI: 10.1080/15376494.2019.1602237

[288] M. Arrea and A. Ingraffea, "Mixed-mode crack propagation in mortar and concrete," Report No. 81-13, Department of Structural Engineering, Cornell University, New York, 1982.

[289] J. Rots and R. de Borst, "Analysis of mixed-mode fracture in concrete," *Journal of Engineering Mechanics,* vol. 113, no. 11, pp. 1739-1758, 1987.

[290] W. Gerstle and M. Xie, "FEM modeling of fictitious crack propagation in concrete," *Journal of Engineering Mechanics,* vol. 118, no. 2, pp. 416-434, 1992.

[291] J. Galvez and D. Cendon, "Simulacion de la fractura del hormigon en modo mixto," *Revista Internacional de Metodos Numericos para Calculo y Diseno en Ingenieria,* vol. 18, no. 1, pp. 31-58, 2002.

[292] M. Jirasek and B. Patzak, "Consistent tangent stiffness for nonlocal damage models," *Computers and Structures,* vol. 80, pp. 1279-1293, 2002.

[293] C. Linder and F. Armero, "Finite elements with embedded strong discontinuities for the modeling of failure in solids," *International Journal for Numerical Methods in Engineering,* vol. 72, pp. 1391-1433, 2007.

[294] J. Galvez, J. Planas, J. Sancho, E. Reyes, D. Cendon and M. Casati, "An embedded cohesive crack model for finite element analysis of quasi-brittle materials," *Engineering Fracture Mechanics,* vol. 109, pp. 369-386, 2013.

[295] S. Bhattacharjee and P. Leger, "Application of NLFM models to predict cracking in concrete gravity dams," *Journal of Structural Engineering,* vol. 120, no. 4, pp. 1255-1271, 1994.

[296] T. Rabczuk and T. Belytschko, "Cracking particles: a simplified meshfree method for arbitrary evolving cracks," *International Journal for Numerical Methods in Engineering,* vol. 61, pp. 2316-2343, 2004.

[297] T. Rabczuk and T. Belytschko, "A three dimensional large deformation meshfree method for arbitrary evolving cracks," *Computer Methods in Applied Mechanics and Engineering,* vol. 196, no. 29-30, pp. 2777-2799, 2007.

[298] N. Monteiro Azevedo and J. Lemos, "Hybrid discrete element/finite element method for fracture analysis," *Computer Methods in Applied Mechanics and Engineering,* vol. 195, no. 33-36, pp. 4579-4593, 2006.

[299] S. Roth, P. Leger and A. Soulaimani, "A combined XFEM - damage mechanics approach for concrete crack propagation," *Computer Methods in Applied Mechanics and Engineering,* vol. 283, pp. 923-955, 2015.

[300] E. Schlangen, "Experimental and numerical analysis of fracture processes in concrete," *Heron,* vol. 38, no. 2, pp. 1-117, 1993.

[301] G. Wells and L. Sluys, "A new method for modelling cohesive cracks using finite elements," *International Journal for Numerical Methods in Engineering,* vol. 50, pp. 2667-2682, 2001.

[302] V. Garcia-Alvarez, R. Gettu and I. Carol, "Analysis of mixed-mode fracture in concrete using interface elements and a cohesive crack model," *Sadhana,* vol. 37, no. 1, pp. 187-205, 2012.

[303] A. Chopra and P. Chakrabarti, "The Koyna earthquake and the damage to Koyna dam," *Bulletin of the Seismological Society of America,* vol. 63, no. 2, pp. 381-397, 1973.

[304] S. Bhattacharjee and P. Leger, "Seismic cracking and energy dissipation in concrete gravity dams," *Earthquake Engineering and Structural Dynamics,* vol. 22, pp. 991-1007, 1993.

[305] M. Cervera, J. Oliver and R. Faria, "Seismic evaluation of concrete dams via continuum damage models," *Earthquake Engineering and Structural Dynamics,* vol. 24, no. 9, pp. 1225-1245, 1995.

[306] M. Cervera, J. Oliver and O. Manzoli, "A rate-dependent isotropic damage model for the seismic analysis of concrete dams," *Earthquake Engineering and Structural Dynamics,* vol. 25, no. 9, pp. 987-1010, 1996.

[307] H. Zhang and T. Ohmachi, "2 dimensional analysis of seismic cracking in concrete gravity dams," *Journal of Japan Society of Dam Engineers,* vol. 8, no. 2, pp. 93-101, 1998.

[308] J. Lee and G. Fenves, "A plastic-damage concrete model for earthquake analysis of dams," *Earthquake Engineering and Structural Dynamics,* vol. 27, pp. 937-956, 1998.

[309] Y. Calayir and M. Karaton, "Seismic fracture analysis of concrete gravity dams including dam–reservoir interaction," *Computers and Structures,* vol. 83, p. 1595–1606, 2005.

[310] J.-Y. Wu and J. Li, "Unified plastic-damage model for concrete and its applications to dynamic nonlinear analysis of structures," *Structural Engineering and Mechanics,* vol. 25, no. 5, pp. 519-540, 2007.

[311] R. Sarkar, D. Paul and L. Stempniewski, "Influence of reservoir and foundation on the nonlinear dynamic response of concrete gravity dams," *ISET Journal of Earthquake Technology,* vol. 44, no. 2, pp. 377-389, 2007.

[312] S. Zhang, G. Wang and W. Sa, "Damage evaluation of concrete gravity dams under mainshock–aftershock seismic sequences," *Soil Dynamics and Earthquake Engineering,* vol. 50, pp. 16-27, 2013.

[313] G. Wang, Y. Wang, W. Lu, C. Zhou, M. Chen and P. Yan, "XFEM based seismic potential failure mode analysis of concrete gravity dam-water-foundation systems through incremental dynamic analysis," *Engineering Structures,* vol. 98, pp. 81-94, 2015.

[314] J. Pan, C. Zhang, Y. Xu and F. Jin, "A comparative study of the different procedures for seismic cracking analysis of concrete dams," *Soil Dynamics and Earthquake Engineering,* vol. 31, no. 11, pp. 1594-1606, 2011.

[315] G. Gioia, Z. Bazant and B. Pohl, "Is no-tension dam design always safe? a numerical study," *Dam Engineering,* vol. 3, no. 1, pp. 23-34, 1992.

[316] F. Ghrib and R. Tinawi, "Nonlinear behavior of concrete dams using damage mechanics," *Journal of Engineering Mechanics,* vol. 121, no. 4, pp. 513-527, 1995.

[317] M. Shi, H. Zhong, E. Ooi, C. Zhang and C. Song, "Modelling of crack propagation of gravity dams by scaled boundary polygons and cohesive crack model," *International Journal of Fracture,* vol. 183, pp. 29-48, 2013.

[318] D. Santillan, J. Mosquera and L. Cueto-Felgueroso, "Phase-field model for brittle fracture. Validation with experimental results and extension to dam engineering problems," *Engineering Fracture Mechanics,* vol. 178, pp. 109-125, 2017.

[319] F.-G. Buchholz, A. Chergui and H. Richard, "Fracture analyses and experimental results of crack growth under general mixed mode loading conditions," *Engineering Fracture Mechanics,* vol. 71, pp. 455-468, 2004.

[320] F.-G. Buchholz, V. Just and H. Richard, "Computational simulation and experimental findings of three-dimensional fatigue crack growth in a single-edge notched specimen under torsion loading," *Fatigue and Fracture of Engineering Materials and Structures,* vol. 28, no. 1-2, pp. 127-134, 2005.

[321] V. Lazarus, F.-G. Buchholz, M. Fulland and J. Wiebesiek, "Comparison of predictions by mode II or mode III criteria on crack front twisting in three or four point bending experiments," *International Journal of Fracture,* vol. 153, pp. 141-151, 2008.

[322] R. Citarella and F.-G. Buchholz, "Comparison of crack growth simulation by DBEM and FEM for SEN-specimens undergoing torsion or bending loading," *Engineering Fracture Mechanics,* vol. 75, pp. 489-509, 2008.

[323] D. Colombo and P. Massin, "Fast and robust level set update for 3D non-planar X-FEM crack propagation modelling," *Computer Methods in Applied Mechanics and Engineering,* vol. 200, no. 25-28, pp. 2160-2180, 2011.

[324] S. Geniaut and E. Galenne, "A simple method for crack growth in mixed mode with X-FEM," *International Journal of Solids and Structures,* vol. 49, no. 15-16, pp. 2094-2106, 2012.

[325] G. Ferte, P. Massin and N. Moes, "3D crack propagation with cohesive elements in the extended finite element method," *Computer Methods in Applied Mechanics and Engineering,* vol. 300, pp. 347-374, 2016.

[326] A. Sadeghirad, D. Chopp, X. Ren, E. Fang and J. Lua, "A novel hybrid approach for level set characterization and tracking of non-planar 3D cracks in the extended finite element method," *Engineering Fracture Mechanics,* vol. 160, pp. 1-14, 2016.

[327] K. Agathos, G. Ventura, E. Chatzi and S. Bordas, "Stable 3D XFEM/vector level sets for non-planar 3D crack propagation and comparison of enrichment schemes," *International Journal for Numerical Methods in Engineering,* vol. 113, no. 2, pp. 252-276, 2018.

[328] A. Pandolfi and M. Ortiz, "An eigenerosion approach to brittle fracture," *International Journal for Numerical Methods in Engineering,* vol. 92, no. 8, pp. 694-714, 2012.

Publications included in the compendium

Finite element modelling of quasi-brittle cracks in 2D and 3D with enhanced strain accuracy

M. Cervera, G. B. Barbat and M. Chiumenti

Computational Mechanics

Vol. 60, issue 5, pp. 767-796, (2017)

https://doi.org/10.1007/s00466-017-1438-8

Finite element modeling of quasi-brittle cracks in 2D and 3D with enhanced strain accuracy

M. Cervera, G. B. Barbat and M. Chiumenti

International Center for Numerical Methods in Engineering (CIMNE)

Technical University of Catalonia – BarcelonaTECH

Edificio C1, Campus Norte, Jordi Girona 1-3

08034 Barcelona, Spain

miguel.cervera@upc.edu, gbarbat@cimne.upc.edu, michele@cimne.upc.edu

Abstract

This paper discusses the finite element modeling of cracking in quasi-brittle materials. The problem is addressed via a mixed strain/displacement finite element formulation and an isotropic damage constitutive model. The proposed mixed formulation is fully general and is applied in 2D and 3D. Also, it is independent of the specific finite element discretization considered; it can be equally used with triangles/tetrahedra, quadrilaterals/hexahedra and prisms.

The feasibility and accuracy of the method is assessed through extensive comparison with experimental evidence. The correlation with the experimental tests shows the capacity of the mixed formulation to reproduce the experimental crack path and the force-displacement curves with remarkable accuracy. Both 2D and 3D examples produce results consistent with the documented data.

Aspects related to the discrete solution, such as convergence regarding mesh resolution and mesh bias, as well as other related to the physical model, like structural size effect and the influence of Poisson's ratio, are also investigated.

The enhanced accuracy of the computed strain field leads to accurate results in terms of crack paths, failure mechanisms and force displacement curves. Spurious mesh dependency suffered by both continuous and discontinuous irreducible formulations is avoided by the mixed FE, without the need of auxiliary tracking techniques or other computational schemes that alter the continuum mechanical problem.

Keywords: Damage, Cracking, Mixed Finite Elements, Strain Localization, Structural Failure

1 Introduction

Modeling of cracking in quasi-brittle materials has been the object of intensive study in computational solid mechanics over the last five decades. In most of the studies carried out with standard irreducible elements, the attempts to predict the crack path fail because the obtained solution suffers from spurious bias mesh dependency. Several strategies have been developed for dealing with this obstacle.

Cracking problems have traditionally been tackled in two ways: through continuous and discontinuous approaches. In the continuous one, the failure process is modelled by the degradation of the material, at constitutive level. For this so-called *smeared crack approach*, classical methods were developed by [1-5]. More recently, nonlocal constitutive models [6], gradient enhanced [7, 8] and phase field techniques [8-12] have also been considered within the continuous approach.

In the discontinuous approach, an explicit crack representation is accounted for in the computed geometry and handled as a geometrical discontinuity [13, 14]. The kinematics of the finite element is enriched to capture the behavior near the propagating crack. Models developed with this approach include, but are not limited to, cohesive interface elements with or without remeshing [15-22], elements with embedded strong discontinuities [23-28], extended finite elements methods [29-34], and meshless and particle methods [35-39].

All these formulations have been proposed with the objective of solving the problems concerning lack of convergence when the mesh is refined and spurious mesh-dependency of the computed solution with standard irreducible elements. Despite all the proposed formulations, and their diverse level of success, these aspects still remained an issue.

The traditional smeared crack/deformation concept has the advantage of simplicity and is best suited for large-scale analyses. Most efficient from the computational point of view, it is the one favored by commercial FE codes and practitioners. Mesh-size dependency can be solved introducing the fracture energy concept and regularizing with respect the resolution of the FE mesh as proposed by [2].

The continuous approaches that use nonlocal, gradient enhanced or phase field schemes, alter the strong form of the governing equations embedding a length scale related to the width of the localization zone. A clear physical interpretation and direct link between the length parameter in the model and the characteristic length of the material is arguable [40]. An alternative geometrical interpretation has been proposed by [12].

Discontinuous approaches are often regarded as an improvement over the continuous ones, as it is considered that true separation can only be captured with discontinuous techniques. Discontinuous approaches almost invariably require the use of local or global crack tracking auxiliary techniques [41-44]. Those auxiliary techniques do not handle successfully cases that involve complex crack patterns such as multiple branching or intersecting cracks. Besides, they are usually applied only in one type of finite element and lack practical generality, as they require different implementations for each type of finite element.

In meshless and particle methods [35-39], these drawbacks are avoided through the definition of domains of influence rather than finite elements and the use of appropriate test and trial functions. Local and global remeshing techniques [15-18] also have been used in conjunction with both the continuous and discontinuous approaches.

A comprehensive coverage of all fracture strategies is far beyond the scope of this study that focuses on the application of a mixed FE formulation to the modeling of cracking in quasi-brittle materials. For more details, the reviews in references [45-47] are suggested.

Recently, mixed finite elements have been reexamined by [48-51] to deal with strain localization problems. Mixed finite element formulations have proved to be a remedy for spurious bias mesh dependency, allowing for the computation of strains and stresses with enhanced accuracy both in linear and nonlinear scenarios.

When using the standard finite element formulation, local convergence of the solution in terms of strains cannot be guaranteed in the quasi-singular stress or strain states that occur in the vicinity of the tip of propagating cracks. Even in linear elasticity, local convergence is not guaranteed in quasi-singular points. This lack of local convergence in the strain and stress leads to the spurious mesh bias dependence observed in problems of quasi-brittle crack propagation solved with the standard formulation, yielding incorrect solutions in many cases.

Mixed FE formulations for nonlinear solid mechanics problems guarantee an improvement over standard finite element formulations in terms of stress and strain accuracy. In mixed formulations, the strain is approximated independently from the displacement field, instead of being obtained from local discrete differentiation at element level. In this way, more accurate stress and strain fields are computed, resulting in a more precise computation of the solids nonlinear behavior, particularly for low order FE.

The more accurate stress and strain fields computed with the mixed formulation results in a significant betterment over the standard formulation, particularly in the prediction of the crack formation and propagation, where mesh-dependence issues are averted. This guarantees convergent results when computing crack trajectories, failure mechanisms and ultimate loads, producing practically mesh-independent solutions using both plasticity and damage constitutive laws.

The leverage of the mixed approach derives from the following strong points:

- It is fully variationally consistent [49, 50]
- It can be formulated for small or finite displacements or/and kinematics [52, 53]
- It applies equally to 2D and 3D problems [51]
- It is not restricted to a particular FE interpolation, it can be used with triangles/tetrahedra, quadrilaterals/hexahedra or prisms of any order [49-51]
- It is not dependent on the choice of the constitutive equation, it can be applied both for plasticity and/or damage models of any kind [51, 54]
- It can consider isotropic or directional inelastic behavior [55]
- It can address quasi-incompressible situations, including the incompressible limit [51, 56]
- It can accommodate rate-dependent viscid effects, linear or non-linear
- It can be extended to include inertial forces in dynamics, or multi-physics phenomena in coupled problems [53]

Also, and regarding cracking problems:

- It follows the classical local constitutive mechanics framework [50]
- It can model Mode I (extension), Mode II (shear) and Mode III (tearing) and mixed-mode fracture [51, 55]
- It can model structural size effect in quasi-brittle failure [54]
- It can accommodate orthotropic damage models with unilateral, crack-closing effects
- It does not require auxiliary crack tracking techniques [49-51]

With reference to the above mentioned alternatives for the computational modeling of quasi-brittle cracks, the mixed finite element formulation here presented fits into the continuous approach, as the crack is represented at constitutive level using a local stress vs. strain relationship. Therefore, the separation between the two opposite sides of the crack is modelled through continuous (linear) displacement and strain fields. No specific degrees of freedom are necessary to model the existing or evolving cracks. Instead, the kinematic enhancement provided by the independent interpolation of displacement and strains proves to be crucial in the numerical solution of strain localization problems.

Discontinuous resolution of the displacement jump across the crack and in conjunction with a traction vs. separation constitutive law, either via extended degrees of freedom or embedment, can be included in the mixed FE formulation as they are in the standard displacement-based one, but such developments are not addressed in the present paper. Without them, the formulation does not require apropos trial or test functions, or the use of specific quadrature rules in the modeling of the cracks. Local remeshing is also compatible with the mixed FE formulation, but is not considered in this paper.

In previous works by the authors, the mixed formulation has been derived and assessed through theoretical benchmark tests and capability demonstration cases, in order to highlight its advantages with regard to the standard form. However, aptness of the proposed model to replicate the behavior of engineering materials observed in experimental tests, specifically related to the crack behavior and propagation, remained open; mixed formulations for computing strain localization has not been adequately validated through correlation with experimental tests.

Therefore, the objectives of this paper are: (1) to present the mixed strain/displacement formulation in matrix notation, ready-to-use for implementation in finite element codes, (2) to demonstrate the application of this format in 2D and 3D applications, (3) to validate the proposed formulation with experimental results. To meet the last two objectives, an extensive comparison with experimental data observed from the literature is performed.

The outline of the paper is as follows. In Section 2, the mixed strain/displacement formulation for the solution of nonlinear solid mechanics problems is presented in matrix form, to be used in conjunction with an isotropic damage model summarized in Section 3. Section 4 presents numerical simulations performed in 2D and 3D using the proposed model. The computation results are compared to available data from experimental tests for validation purposes. Finally, conclusions and extensions for future work are presented.

2 Mixed strain/displacement formulation

In the following, the mixed strain-displacement formulation is laid out. Matrix and vector notation based on Voigt's convention for symmetric tensors is adopted, as customarily used in FE literature and in codes.

The formulation of the mixed solid mechanics problem in terms of the stress and displacement fields is classical and it has been used many times in the context of linear elasticity. Mixed FEM have been so derived from the Hellinger-Reissner Variational Principle [57, 58]. However, this is not the most convenient format for the material nonlinear problem. Most of the algorithms used for nonlinear constitutive models in solid mechanics have been derived for the irreducible formulation. This means that these procedures are usually strain driven, and they have a format in which the stress is computed in terms of the strain. Consequently, a mixed FE formulation in terms of the strains and displacement fields as the one used here can incorporate these procedures directly.

2.1 Variational form

In the following, the variational form of the nonlinear solid mechanics problem is cast in terms of the displacement $\boldsymbol{u}$ and strain $\boldsymbol{\varepsilon}$ fields. Writing the problem in matrix form, $\boldsymbol{u}$ and $\boldsymbol{\varepsilon}$ are expressed in Voigt's convention as vectors. For 2D analysis, plane stress and plane strain problems, $\boldsymbol{u} = (u, v)^T$ has 2 components and $\boldsymbol{\varepsilon} = \left(\varepsilon_x, \varepsilon_y, \gamma_{xy}\right)^T$ is a 3 component vector. In 3D analysis, $\boldsymbol{u} = (u, v, w)^T$ has 3 components and $\boldsymbol{\varepsilon} = \left(\varepsilon_x, \varepsilon_y, \varepsilon_z, \gamma_{xy}, \gamma_{yz}, \gamma_{xz}\right)^T$ has 6 components [59].

The strain and displacement fields are locally related through the compatibility equation

$$\boldsymbol{\varepsilon} = \boldsymbol{\mathcal{S}}\boldsymbol{u} \tag{1}$$

where $\boldsymbol{\mathcal{S}}$ is the differential symmetric gradient operator, defined as

$$\boldsymbol{\mathcal{S}}^T = \begin{bmatrix} \partial_x & 0 & 0 & \partial_y & 0 & \partial_z \\ 0 & \partial_y & 0 & \partial_x & \partial_z & 0 \\ 0 & 0 & \partial_z & 0 & \partial_y & \partial_x \end{bmatrix} \; in\, 3D \; ; \; \boldsymbol{\mathcal{S}}^T = \begin{bmatrix} \partial_x & 0 & \partial_y \\ 0 & \partial_y & \partial_x \end{bmatrix} \; in\, 2D \tag{2}$$

where $\boldsymbol{\partial} = \left(\partial_x, \partial_y, \partial_z\right)^T$ is the gradient operator in 3D and $\boldsymbol{\partial} = \left(\partial_x, \partial_y\right)^T$ in 2D.

Correspondingly, the stress $\boldsymbol{\sigma}$ is a vector with 3 components in 2D analysis, $\boldsymbol{\sigma} = \left(\sigma_x, \sigma_y, \tau_{xy}\right)^T$, and 6 in 3D analysis, $\boldsymbol{\sigma} = \left(\sigma_x, \sigma_y, \sigma_z, \tau_{xy}, \tau_{yz}, \tau_{xz}\right)^T$, whereas the body forces vector $\mathbf{f}$ has 2 in 2D, $\mathbf{f} = \left(\mathbf{f}_x, \mathbf{f}_y\right)^T$, and 3 components in 3D, $\mathbf{f} = \left(\mathbf{f}_x, \mathbf{f}_y, \mathbf{f}_z\right)^T$. Cauchy's equilibrium equation of a body written in matrix form is

$$\boldsymbol{\mathcal{S}}^T\boldsymbol{\sigma} + \mathbf{f} = \mathbf{0} \tag{3}$$

where $\boldsymbol{\mathcal{S}}^T$ is the differential divergence operator, adjoint to the $\boldsymbol{\mathcal{S}}$ in (1).

The stress vector $\boldsymbol{\sigma}$ and the strain vector $\boldsymbol{\varepsilon}$ are linked by the constitutive equation:

$$\boldsymbol{\sigma} = \mathbf{D}_s\boldsymbol{\varepsilon} \tag{4}$$

where $\mathbf{D}_s$ is the secant constitutive matrix. For the isotropic damage model laid out in Section 3, the constitutive equation is

$$\boldsymbol{\sigma} = (1 - d)\mathbf{D}_0\boldsymbol{\varepsilon} \tag{5}$$

Pre-multiplying equation (1) by the secant constitutive matrix $\mathbf{D}_s$ and introducing equation (4) into equation (3) results in

$$-\mathbf{D}_s\boldsymbol{\varepsilon} + \mathbf{D}_s\boldsymbol{\mathcal{S}}\boldsymbol{u} = \mathbf{0} \tag{6}$$

$$\boldsymbol{\mathcal{S}}^T(\mathbf{D}_s\boldsymbol{\varepsilon}) + \mathbf{f} = \mathbf{0} \tag{7}$$

The system of equations (6)-(7) is the strong form of the mixed $\boldsymbol{\varepsilon}/\boldsymbol{u}$ formulation, completed with the boundary conditions imposed on the boundary Γ of the body, partitioned in Γ_u and Γ_t, corresponding to the Dirichlet's and Newman's conditions, respectively, such that $\Gamma = \Gamma_u \cup \Gamma_t$ and $\{\emptyset\} = \Gamma_u \cap \Gamma_t$.

For the sake of conciseness, the prescribed displacements are assumed to vanish on the boundary Γ_u

$$\boldsymbol{u} = \mathbf{0} \quad in\, \Gamma_u \tag{8}$$

The nontrivial case, $\boldsymbol{u} = \bar{\boldsymbol{u}} \;\; in\, \Gamma_u$, can be accommodated following standard arguments. Additionally, the prescribed tractions on the boundary Γ_t are expressed as

$$\boldsymbol{t} = \bar{\boldsymbol{G}}^T \boldsymbol{\sigma} = \bar{\boldsymbol{t}} \quad in\, \Gamma_t \tag{9}$$

Where the projection matrix $\bar{\boldsymbol{G}}$ is defined in [59] as

$$\bar{\boldsymbol{G}}^T = \begin{bmatrix} n_x & 0 & 0 & n_y & 0 & n_z \\ 0 & n_y & 0 & n_x & n_z & 0 \\ 0 & 0 & n_z & 0 & n_y & n_z \end{bmatrix} \;\; in\, 3D;\; \bar{\boldsymbol{G}}^T = \begin{bmatrix} n_x & 0 & n_y \\ 0 & n_y & n_x \end{bmatrix} \;\; in\, 2D \tag{10}$$

where $\boldsymbol{n} = \left(n_x, n_y, n_z\right)^T$ is the outward normal vector at the boundary Γ_t.

The variational form of the problem is obtained as follows.

Firstly, equation (6) is premultiplied by an arbitrary virtual strain vector $\delta\boldsymbol{\varepsilon}$ and integrated over the spatial domain to obtain the weak form of the constitutive and compatibility relationships:

$$-\int_\Omega \delta\boldsymbol{\varepsilon}^T \mathbf{D}_s \boldsymbol{\varepsilon}\, \mathrm{d}\Omega + \int_\Omega \delta\boldsymbol{\varepsilon}^T \mathbf{D}_s \boldsymbol{\mathcal{S}}\boldsymbol{u}\, \mathrm{d}\Omega = 0 \quad \forall \delta\boldsymbol{\varepsilon} \tag{11}$$

Secondly, equation (7) is premultiplied by an arbitrary virtual displacement vector $\delta\boldsymbol{u}$ and integrated over the spatial domain

$$\int_\Omega \delta\boldsymbol{u}^T [\boldsymbol{\mathcal{S}}^T (\mathbf{D}_s \boldsymbol{\varepsilon})]\, \mathrm{d}\Omega + \int_\Omega \delta\boldsymbol{u}^T \mathbf{f}\, \mathrm{d}\Omega = 0 \quad \forall \delta\boldsymbol{u} \tag{12}$$

The virtual displacement $\delta\boldsymbol{u}$ complains with the boundary conditions, so that $\delta\boldsymbol{u} = \mathbf{0} \;\; in\, \Gamma_u$. Then, the Divergence Theorem is applied to the first term of equation (12):

$$\begin{aligned} \int_\Omega \delta\boldsymbol{u}^T [\boldsymbol{\mathcal{S}}^T (\mathbf{D}_s \boldsymbol{\varepsilon})]\, \mathrm{d}\Omega &= -\int_\Omega (\boldsymbol{\mathcal{S}}\delta\boldsymbol{u})^T (\mathbf{D}_s \boldsymbol{\varepsilon})\, \mathrm{d}\Omega + \int_\Gamma \delta\boldsymbol{u}^T (\bar{\boldsymbol{G}}^T \mathbf{D}_s \boldsymbol{\varepsilon})\, \mathrm{d}\Gamma \\ &= -\int_\Omega (\boldsymbol{\mathcal{S}}\delta\boldsymbol{u})^T (\mathbf{D}_s \boldsymbol{\varepsilon})\, \mathrm{d}\Omega + \underbrace{\int_{\Gamma_u} \delta\boldsymbol{u}^T (\bar{\boldsymbol{G}}^T \mathbf{D}_s \boldsymbol{\varepsilon})\, \mathrm{d}\Gamma}_{=0} + \int_{\Gamma_t} \delta\boldsymbol{u}^T \underbrace{(\bar{\boldsymbol{G}}^T \mathbf{D}_s \boldsymbol{\varepsilon})}_{=\bar{\boldsymbol{t}}}\, \mathrm{d}\Gamma \end{aligned} \tag{13}$$

In equation (13), the integral on the boundary is split in the boundaries Γ_u and Γ_t. The part corresponding to Γ_u is zero because the virtual displacement vanishes on that boundary. In Γ_t, equations (4) and (9) are used.

Therefore,

$$\int_\Omega (\boldsymbol{\mathcal{S}}\delta\boldsymbol{u})^T (\mathbf{D}_s \boldsymbol{\varepsilon})\, \mathrm{d}\Omega = \int_\Omega \delta\boldsymbol{u}^T \mathbf{f}\, \mathrm{d}\Omega + \int_{\Gamma_t} \delta\boldsymbol{u}^T \bar{\boldsymbol{t}}\, \mathrm{d}\Gamma \quad \forall \delta\boldsymbol{u} \tag{14}$$

which is the expression of the Virtual Work Principle, as the right hand side term $W(\delta\boldsymbol{u}) = \int_\Omega \delta\boldsymbol{u}^T \mathbf{f}\, \mathrm{d}\Omega + \int_{\Gamma_t} \delta\boldsymbol{u}^T \bar{\boldsymbol{t}}\, \mathrm{d}\Gamma$ represents the virtual work done by the tractions $\bar{\boldsymbol{t}}$ and body forces $\mathbf{f}$.

The resulting variational form of the mixed formulation is:

$$-\int_{\Omega} \delta\boldsymbol{\varepsilon}^T \mathbf{D}_s \boldsymbol{\varepsilon}\, \mathrm{d}\Omega + \int_{\Omega} \delta\boldsymbol{\varepsilon}^T \mathbf{D}_s \boldsymbol{\mathcal{S}}\boldsymbol{u}\, \mathrm{d}\Omega = 0 \quad \forall \delta\boldsymbol{\varepsilon} \tag{15}$$

$$\int_{\Omega} (\boldsymbol{\mathcal{S}}\delta\boldsymbol{u})^T (\mathbf{D}_s \boldsymbol{\varepsilon})\, \mathrm{d}\Omega = \int_{\Omega} \delta\boldsymbol{u}^T \mathbf{f}\, \mathrm{d}\Omega + \int_{\Gamma_t} \delta\boldsymbol{u}^T \bar{\mathbf{t}}\, \mathrm{d}\Gamma \quad \forall \delta\boldsymbol{u} \tag{16}$$

The mixed problem to be solved is to find the unknowns $\boldsymbol{u}$ and $\boldsymbol{\varepsilon}$ that verify the system of equations composed by (15) and (16) and that verify the boundary condition $\boldsymbol{u} = \mathbf{0}$ on Γ_u given the arbitrary virtual displacement $\delta\boldsymbol{u}$, which vanishes on Γ_u and arbitrary virtual strain $\delta\boldsymbol{\varepsilon}$. Note that this variational problem is symmetric if $\boldsymbol{D}_S$ is symmetric.

2.2 FE approximation

At this point, the FE discrete form of the problem is obtained by discretizing the domain in FE, so that $\Omega = \cup\, \Omega_e$, and substituting the displacement $\boldsymbol{u}$ and the strain $\boldsymbol{\varepsilon}$ with the FE discrete approximations $\hat{\boldsymbol{u}}$ and $\hat{\boldsymbol{\varepsilon}}$ defined element-wise as

$$\boldsymbol{u} \cong \hat{\boldsymbol{u}} = \boldsymbol{N}_u \boldsymbol{U} \tag{17}$$

$$\boldsymbol{\varepsilon} \cong \hat{\boldsymbol{\varepsilon}} = \boldsymbol{N}_\varepsilon \boldsymbol{E} \tag{18}$$

where $\boldsymbol{U}$ and $\boldsymbol{E}$ are vectors containing the values of the displacements and the strains at the nodes of the finite element mesh. $\boldsymbol{N}_u$ and $\boldsymbol{N}_\varepsilon$ are the matrices containing the interpolation functions adopted in the FE approximation.

In the Galerkin method, the same approximation is considered for the discrete virtual displacements and virtual strains so that

$$\delta\boldsymbol{u} \cong \delta\hat{\boldsymbol{u}} = \boldsymbol{N}_u \delta\boldsymbol{U} \tag{19}$$

$$\delta\boldsymbol{\varepsilon} \cong \delta\hat{\boldsymbol{\varepsilon}} = \boldsymbol{N}_\varepsilon \delta\boldsymbol{E} \tag{20}$$

The submatrices of $\boldsymbol{N}_u$ and $\boldsymbol{N}_\varepsilon$ are diagonal matrices and the corresponding components are $N_u^{(i)}$ and $N_\varepsilon^{(i)}$ interpolation functions, (i) being the node counter.

Introducing these approximations, equations (15) and (16) now become:

$$-\int_{\Omega} \delta\boldsymbol{E}^T \boldsymbol{N}_\varepsilon^T \mathbf{D}_s \boldsymbol{N}_\varepsilon \boldsymbol{E}\, \mathrm{d}\Omega + \int_{\Omega} \delta\boldsymbol{E}^T \boldsymbol{N}_\varepsilon^T \mathbf{D}_s \underbrace{\boldsymbol{\mathcal{S}}\boldsymbol{N}_u}_{=\boldsymbol{B}_u} \boldsymbol{U}\, \mathrm{d}\Omega = 0 \quad \forall \delta\boldsymbol{E} \tag{21}$$

$$\int_{\Omega} \underbrace{(\boldsymbol{\mathcal{S}}\boldsymbol{N}_u \delta\boldsymbol{U})^T}_{=\delta\boldsymbol{U}^T(\boldsymbol{\mathcal{S}}\boldsymbol{N}_u)^T = \delta\boldsymbol{U}^T\boldsymbol{B}_u^T} (\mathbf{D}_s \boldsymbol{N}_\varepsilon \boldsymbol{E})\, \mathrm{d}\Omega = \widehat{W}(\delta\boldsymbol{U}) \quad \forall \delta\boldsymbol{U} \tag{22}$$

where $\boldsymbol{B}_u$ is the discrete strain-displacement matrix defined as

$$\boldsymbol{B}_u = \boldsymbol{\mathcal{S}}\boldsymbol{N}_u \tag{23}$$

The submatrices of $\boldsymbol{B}_u$ have the structure corresponding to the $\boldsymbol{\mathcal{S}}$ operator in equation (2), and their components are the Cartesian derivatives of the $N_u^{(i)}$ and $N_\varepsilon^{(i)}$ interpolation functions $\left(\frac{\partial N^{(i)}}{\partial x}; \frac{\partial N^{(i)}}{\partial y}; \frac{\partial N^{(i)}}{\partial z}\right)$, (i) being the node counter.

In (22), $\widehat{W}(\delta\boldsymbol{U})$ is the work done by the tractions $\bar{\mathbf{t}}$ and body forces $\mathbf{f}$ defined as

$$\widehat{W}(\delta \boldsymbol{U}) = \int_{\Omega} \delta \boldsymbol{U}^T \boldsymbol{N}_u^T \mathbf{f} \, \mathrm{d}\Omega + \int_{\Gamma_t} \delta \boldsymbol{U}^T \boldsymbol{N}_u^T \bar{\boldsymbol{t}} \, \mathrm{d}\Gamma \tag{24}$$

In (21) and (22) and henceforth, integrals over the domain are understood as the sum of the integrals over the elements in the FE mesh

$$\int_{\Omega} (\cdot) \, \mathrm{d}\Omega = \sum_e \int_{\Omega_e} (\cdot) \, \mathrm{d}\Omega_e$$

Also, with some abuse of notation, $\boldsymbol{U}$ and $\boldsymbol{E}$ (and $\delta \boldsymbol{U}$ are $\boldsymbol{\delta E}$) are to be interpreted as the nodal values over the whole FE mesh. This implies the corresponding assembling operations for elemental matrices and vectors into global entities.

Note again that, if matrix $\mathbf{D}_s$ is symmetric, the discrete system (21)-(22) is symmetric but indefinite.

The virtual displacement $\delta \boldsymbol{U}$ and virtual strain $\delta \boldsymbol{E}$ nodal vectors that appear in equations (21)-(22) are arbitrary. Therefore, the system of equations for the mixed Galerkin method becomes

$$-\left(\int_{\Omega} \boldsymbol{N}_{\varepsilon}^T \mathbf{D}_s \boldsymbol{N}_{\varepsilon} \mathrm{d}\Omega \right) \boldsymbol{E} + \left(\int_{\Omega} \boldsymbol{N}_{\varepsilon}^T \mathbf{D}_s \boldsymbol{B}_u \, \mathrm{d}\Omega \right) \boldsymbol{U} = 0 \tag{25}$$

$$\left(\int_{\Omega} \boldsymbol{B}_u^T \mathbf{D}_s \boldsymbol{N}_{\varepsilon} \, \mathrm{d}\Omega \right) \boldsymbol{E} = \int_{\Omega} \boldsymbol{N}_u^T \mathbf{f} \, \mathrm{d}\Omega + \int_{\Gamma_t} \boldsymbol{N}_u^T \bar{\boldsymbol{t}} \, \mathrm{d}\Gamma \tag{26}$$

And the algebraic system of equations (25)-(26) can be written in matrix form as

$$\begin{bmatrix} -\boldsymbol{M} & \boldsymbol{G} \\ \boldsymbol{G}^T & \mathbf{0} \end{bmatrix} \begin{bmatrix} \boldsymbol{E} \\ \boldsymbol{U} \end{bmatrix} = \begin{bmatrix} \mathbf{0} \\ \boldsymbol{F} \end{bmatrix} \tag{27}$$

where $[\boldsymbol{E} \quad \boldsymbol{U}]^T$ is the array of nodal values of strains and displacements and

$$\boldsymbol{M} = \int_{\Omega} \boldsymbol{N}_{\varepsilon}^T \mathbf{D}_s \boldsymbol{N}_{\varepsilon} \, \mathrm{d}\Omega \tag{28}$$

$$\boldsymbol{G} = \int_{\Omega} \boldsymbol{N}_{\varepsilon}^T \mathbf{D}_s \boldsymbol{B}_u \, \mathrm{d}\Omega \tag{29}$$

$$\boldsymbol{F} = \int_{\Omega} \boldsymbol{N}_u^T \mathbf{f} \, \mathrm{d}\Omega + \int_{\Gamma_t} \boldsymbol{N}_u^T \bar{\boldsymbol{t}} \, \mathrm{d}\Gamma \tag{30}$$

$\boldsymbol{M}$ is a mass like projection matrix, $\boldsymbol{G}$ is the discrete gradient matrix and $\boldsymbol{F}$ is the vector of external nodal forces.

In the system (27), the nodal values $\boldsymbol{E}$ can be formally eliminated to write the solution in terms of the nodal displacements $\boldsymbol{U}$ only, as follows. From the first equation in (27), the nodal values for the strains $\boldsymbol{E}$ can be obtained as

$$\boldsymbol{E} = \boldsymbol{M}^{-1} \boldsymbol{G} \boldsymbol{U} \tag{31}$$

which can be substituted into the second equation to yield

$$\boldsymbol{U} = \left(\boldsymbol{G}^T \boldsymbol{M}^{-1} \boldsymbol{G} \right)^{-1} \boldsymbol{F} \tag{32}$$

where $\left(\boldsymbol{G}^T \boldsymbol{M}^{-1} \boldsymbol{G} \right)^{-1}$ is the Schur complement of $-\boldsymbol{M}$ in the system (27).

2.3 VMS stabilization

To ensure solvability (i.e. uniqueness) and stability of the solution in the algebraic system of equations (27), the interpolation functions in (17)-(18) must satisfy the Inf-Sup condition [60-62]. This condition is not verified if equal interpolations are used for strains and displacements. In that case, the solution is unstable, and uncontrollably spurious oscillations may appear in the computed displacement field. To be able to circumvent the strictness of the Inf-Sup condition and to use linear approximations in both interpolation functions, a stabilization procedure is necessary to provide the necessary stability to the mixed discrete formulation. The stabilization procedure consists in the modification of the discrete variational form using the Orthogonal Subscales Method, introduced in [63] within the framework of the Variational Multiscale Stabilization methods [64, 65], and adopted herein.

The basic idea of the stabilization procedure is to substitute the approximation of the discrete strain in equation (18) by the following stabilized discrete field

$$\boldsymbol{\varepsilon} \cong \hat{\boldsymbol{\varepsilon}} = \boldsymbol{N}_{\varepsilon}\boldsymbol{E} + \tau_{\varepsilon}(\boldsymbol{B}_{u}\boldsymbol{U} - \boldsymbol{N}_{\varepsilon}\boldsymbol{E}) = (1-\tau_{\varepsilon})\boldsymbol{N}_{\varepsilon}\boldsymbol{E} + \tau_{\varepsilon}\boldsymbol{B}_{u}\boldsymbol{U} \tag{33}$$

where τ_{ε} is a stabilization parameter with value $0 \leq \tau_{\varepsilon} \leq 1$. Note that for $\tau_{\varepsilon} = 1$, the strain interpolation of the standard irreducible formulation is recovered:

$$\boldsymbol{\varepsilon} \cong \hat{\boldsymbol{\varepsilon}} = \boldsymbol{B}_{u}\boldsymbol{U} \tag{34}$$

Making the corresponding substitution in equations (15) and (16), the final stabilized set of mixed FE equations is:

$$-(1-\tau_{\varepsilon})\int_{\Omega} \delta\boldsymbol{E}^{T}\boldsymbol{N}_{\varepsilon}^{T}\mathbf{D}_{s}\boldsymbol{N}_{\varepsilon}\boldsymbol{E}\,\mathrm{d}\Omega + (1-\tau_{\varepsilon})\int_{\Omega} \delta\boldsymbol{E}^{T}\boldsymbol{N}_{\varepsilon}^{T}\mathbf{D}_{s}\boldsymbol{B}_{u}\boldsymbol{U}\,\mathrm{d}\Omega = 0 \quad \forall\delta\boldsymbol{E} \tag{35}$$

$$(1-\tau_{\varepsilon})\int_{\Omega} \delta\boldsymbol{U}^{T}\boldsymbol{B}_{u}^{T}(\mathbf{D}_{s}\boldsymbol{N}_{\varepsilon}\boldsymbol{E})\,\mathrm{d}\Omega + \tau_{\varepsilon}\int_{\Omega} \delta\boldsymbol{U}^{T}\boldsymbol{B}_{u}^{T}\mathbf{D}_{s}\boldsymbol{B}_{u}\boldsymbol{U}\,\mathrm{d}\Omega = \widehat{W}(\delta\boldsymbol{U}) \quad ; \ \forall\delta\boldsymbol{U} \tag{36}$$

The stabilization used is variationally consistent: converging values of the unknowns $\boldsymbol{\varepsilon}$ and $\boldsymbol{u}$ which satisfy the Galerkin system (21)-(22) also satisfy the stabilized form (35)-(36). This is because residual-based stabilization procedures do not introduce any additional approximation nor any consistency error. For a converged solution, when the size of the element h tends to zero, $h \to 0$, $\boldsymbol{\varepsilon} \to \boldsymbol{N}_{\varepsilon}\boldsymbol{E} = \boldsymbol{B}_{u}\boldsymbol{U}$ and the stabilization term vanishes. For non-converged situation, the added terms $\tau_{\varepsilon}(\boldsymbol{B}_{u}\boldsymbol{U} - \boldsymbol{N}_{\varepsilon}\boldsymbol{E})$ are small, as they depend on the difference between two approximations of different order to the same quantity.

Therefore, for a given FE mesh, using different values of the stabilization procedure yields slightly different results. However, the consistency of the residual-based stabilization guarantees convergence to the unique solution. Using different stabilization parameters on the same mesh is akin to use different FE interpolations of the same order of convergence with the same nodal arrangement.

Moreover, note that optimal convergence rate in linear problems is obtained reducing the stabilization on mesh refinement [49], such that

$$\tau_{\varepsilon} = c_{\varepsilon}\frac{h}{L_{0}} \tag{37}$$

where c_ε is an arbitrary positive numbers, h is the finite element size and L_0 is the characteristic size of the problem. In nonlinear problems involving damage, the stabilization parameter is affected by the reduction of stiffness in the damaged elements, so that

$$\tau_\varepsilon = (1-d)c_\varepsilon \frac{h}{L_0} \tag{38}$$

When quasi-incompressible situations need to be modelled, additional consistent stabilization terms, equally based on residual considerations at discrete level, need to be added [51].

The stabilized system of equations is

$$\begin{bmatrix} -\boldsymbol{M_\tau} & \boldsymbol{G_\tau} \\ \boldsymbol{G_\tau^T} & \boldsymbol{K_\tau} \end{bmatrix} \begin{bmatrix} \boldsymbol{E} \\ \boldsymbol{U} \end{bmatrix} = \begin{bmatrix} \boldsymbol{0} \\ \boldsymbol{F} \end{bmatrix} \tag{39}$$

with $\boldsymbol{M_\tau} = (1-\tau_\varepsilon)\boldsymbol{M}$, $\boldsymbol{G_\tau} = (1-\tau_\varepsilon)\boldsymbol{G}$ and $\boldsymbol{K_\tau} = \tau_\varepsilon \boldsymbol{K}$ with

$$\boldsymbol{K} = \int_\Omega \boldsymbol{B}_u^T \mathbf{D}_s \boldsymbol{B}_u \, d\Omega \tag{40}$$

In the stabilized system (39), the nodal values $\boldsymbol{U}$ can be formally computed as

$$\boldsymbol{U} = \left(\boldsymbol{G_\tau^T M_\tau^{-1} G_\tau} + \boldsymbol{K_\tau}\right)^{-1} \boldsymbol{F} \tag{41}$$

where, now, the stabilization ensures definitiveness, uniqueness and stability of the solution if $\boldsymbol{K}$ is positive definite. Note again that for $\tau_\varepsilon = 1$, the stable solution of the standard form $\boldsymbol{U} = \boldsymbol{K^{-1}F}$ is recovered.

The discrete approximation in equation (33) is not to be interpreted point-wise, as in the VMS method only the variational effect of the stabilization is sought for. This means that the internal variables and secant matrix of the constitutive equations can be computed according to either of the alternative, discrete strain approximation (20) or (33).

2.4 Implementation and computational aspects

Nonlinear constitutive behavior such as the one considered in this work (see Section 3) requires an iterative procedure for solving the resulting nonlinear system of equations. In the present work, an iterative Picard's secant algorithm has been used. The problem is solved incrementally in a (pseudo) time step-by-step manner, solving the nonlinear system of equations at each step. Convergence at each time step is achieved when the ratio between the norm of residual forces and the norm of total external forces is lower than a certain imposed tolerance. Some of the analysis were performed under CMOD (crack mouth opening displacement) control in order to capture the complete post-peak behavior.

3 Isotropic damage model

For the evaluation of the stresses from the strains and the evaluation of the secant constitutive matrix $\mathbf{D}_s$, in equations (4) and (5), an isotropic damage model is used. The model adopted here, suitable for concrete, defines the effective equivalent stress through the Rankine and the Drucker-Prager criterions.

From equations (4) and (5)

$$\mathbf{D}_s = (1-d)\mathbf{D}_0 \tag{42}$$

where d is the internal damage index and $\mathbf{D}_0$ is the elastic constitutive matrix. The damage index d is an internal variable that measures the loss of stiffness of the material and it ranges $0 \leq d \leq 1$.

For the computation of the evolution of the internal damage index, the effective stress $\bar{\boldsymbol{\sigma}}$ is defined as $\bar{\boldsymbol{\sigma}} = \mathbf{D}_0\boldsymbol{\varepsilon}$. The corresponding equivalent effective stress σ_{eq} is defined through the damage criterion, $\sigma_{eq} = F(\bar{\boldsymbol{\sigma}})$. Tensile damage is modelled according to Rankine's criterion, so that

$$\sigma_{eq} = F(\bar{\boldsymbol{\sigma}}) = \langle \bar{\sigma}_1 \rangle \tag{43}$$

where $\bar{\sigma}_1$ is the major principal effective stress and $\langle \cdot \rangle$ are the Macaulay brackets, such that $\langle x \rangle = x \quad if \;\; x \geq 0, \quad 0 \quad if \;\; x < 0$. For mixed loading, a Drucker-Prager criterion is used, so that

$$\sigma_{eq} = F(\bar{\boldsymbol{\sigma}}) = \frac{3}{3 + \tan\phi}\left(\sqrt{3J_2} + \tan\phi \frac{I_1}{3}\right) \tag{44}$$

When I_1 and J_2 are the first and second effective stress invariants and ϕ is the internal friction angle of the material; this can be related to the uniaxial tensile and compressive strengths, f_t and f_c, as

$$\tan\phi = 3\frac{f_c - f_t}{f_c + f_t} \tag{45}$$

The damage criterion, $\mathbb{F}$, is defined as

$$\mathbb{F} = \sigma_{eq} - r(\bar{\boldsymbol{\sigma}}) \leq 0 \tag{46}$$

where r is the current stress-like damage threshold. Its initial value is the tensile strength of the material, $r_0 = f_t$. The current value of the damage threshold is explicitly updated as

$$r = \max\left(r_0, \max_{\hat{t}} \sigma_{eq}(\hat{t})\right) \quad \hat{t} \in [0, t] \tag{47}$$

This follows from the Kuhn-Tucker optimality and consistency conditions. It guarantees the irreversibility of damage and the positiveness of the dissipation.

The evolution of the internal damage variable is defined by

$$d = d(r) = 1 - \frac{r_0}{r}\exp\left(-2H_S\left(\frac{\langle r - r_0 \rangle}{r_0}\right)\right) \tag{48}$$

where H_S is the positive softening parameter, which controls the rate of material degradation.

In FE simulations of quasi-brittle failure, the softening parameter is linked to the material fracture energy G_f, which is a property of the material, in the following way:

$$H_S = \frac{\bar{H}_S b}{1 - \bar{H}_S b} \tag{49}$$

where b is the bandwidth of the smeared crack and $\bar{H}_S$ is

$$\bar{H}_S = \frac{(f_t)^2}{2EG_f} \tag{50}$$

f_t being the tensile strength and E the Young's modulus. In this work

$$b = (1 - \tau_\varepsilon)2h + \tau_\varepsilon h = (2 - \tau_\varepsilon)h \tag{51}$$

where h is the finite element size. This is coherent with the approximation adopted for the discrete strain field in equation (33).

4 Numerical simulations

In this section, six numerical simulations are performed using the mixed strain/displacement FE formulation laid out in the aforesaid. The numerical solutions are compared with the results of experimental tests reported in the literature. The simulations are:

1. An L-shaped panel subjected to a vertical load
2. A wedge-splitting test
3. Two mixed mode bending beam tests
4. Three notched beams with holes
5. Four-point bending test on a doubly-notched beam
6. Non-planar crack on a three-point bending test on skew notched beam

The examples have been solved using both 2D and 3D finite elements, using triangles or quadrilaterals for 2D and tetrahedra, hexahedra or prisms for the 3D simulations. All the problems are studied by means of a smeared crack approach. No tracking technique is used in any of the cases.

For this, calculations are performed with an enhanced version of the finite element program COMET [66]. Pre- and post-processing are done with GiD [67], developed at CIMNE (International Center for Numerical Methods in Engineering).

4.1 L-shaped panel

The numerical analysis of a concrete L-shaped panel subjected to vertical load is considered; corresponding experiments are reported in [68]. Other numerical solutions are reported in [41] and [42]. Reference [41] used embedded crack methods and crack tracking auxiliary techniques while reference [42] used extended finite elements for making their computations.

The geometry and loading is shown in Figure 1 and the material parameters are given in Table 1. The thickness of the panel is 0.1 m.

The load $\boldsymbol{F}$ is applied via increments of vertical displacement at the top left corner of the panel.

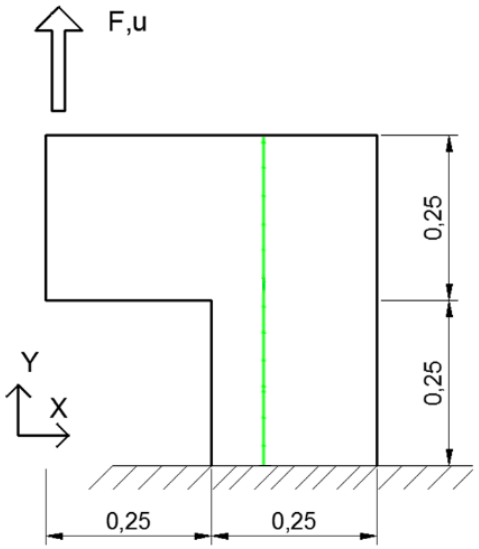

Figure 1. Geometry of the L-shaped panel (m) and vertical axis considered for line graphs

This example is solved with the mixed FEM using 2D quadrilateral and 3D hexahedral elements. The computational domain is discretized with fully structured meshes with elements of 8.33 mm, resulting in a mesh of 11,041 nodes for the 2D analysis and 44,164 nodes for the 3D analysis, shown in Figure 2. The 3D mesh is obtained by the out-of-plane extrusion of the 2D mesh. For the 2D analysis, plane stress conditions are assumed.

Young's Modulus	$25.85 \cdot 10^9$ Pa
Poisson's Ratio	0.18
Tensile Strength	$2.7 \cdot 10^6$ Pa
Fracture Energy	160 J/m^2

Table 1. Material parameters of the L-shaped panel

Figure 3 shows the computed tensile damage contour fills for an imposed vertical displacement of 1 mm obtained in the 2D and 3D analyses. Both results are identical, as the same mesh configuration is used in the XY plane of the panel in the 2D and 3D cases.

In the present FE formulation, the separation between the two opposite sides of the crack is modelled through continuous (linear) displacement and strain fields and the crack is accordingly smeared. The crack surface in the 3D analysis can be depicted as in Figure 4, plotted as an iso-level surface of the norm of displacements. It corresponds exactly with the crack path obtained in the 2D analysis.

These results are within the experimental range obtained by [68], as can be observed in Figure 5. In the FE-simulation, the crack propagates as expected from the experimental tests; no spurious mesh bias is observed, although no auxiliary local or global crack tracking techniques is used, nor any initial notch or flaw is imposed in the geometry of the panel to assure the correct crack path at the early stages of the crack formation, contrary to [41] and [42].

Figure 6 shows the computed load-imposed vertical displacement curve obtained in the 2D and 3D simulations, compared to the results from the tests in [68]. As shown, the numerical curves are almost overlapping, demonstrating the closeness of plane stress assumption in 2D. The results are inside the experimental range observed in the tests. It can be seen that the peak is accurately reproduced, as well as the general behavior of the curve.

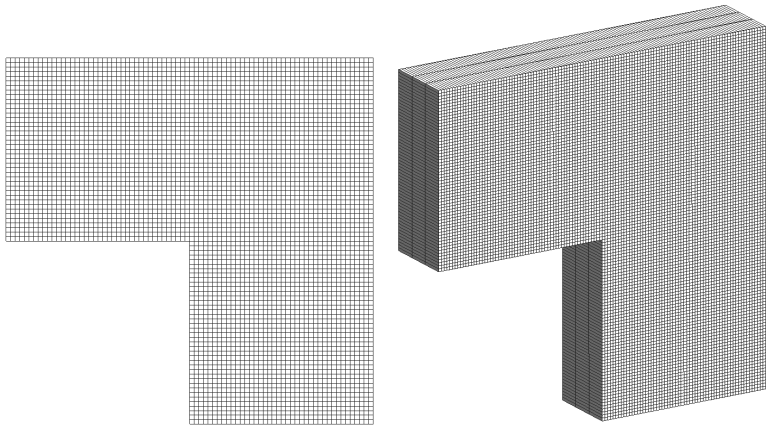

Figure 2. 2D and 3D meshes used for the analysis of the L-shaped panel

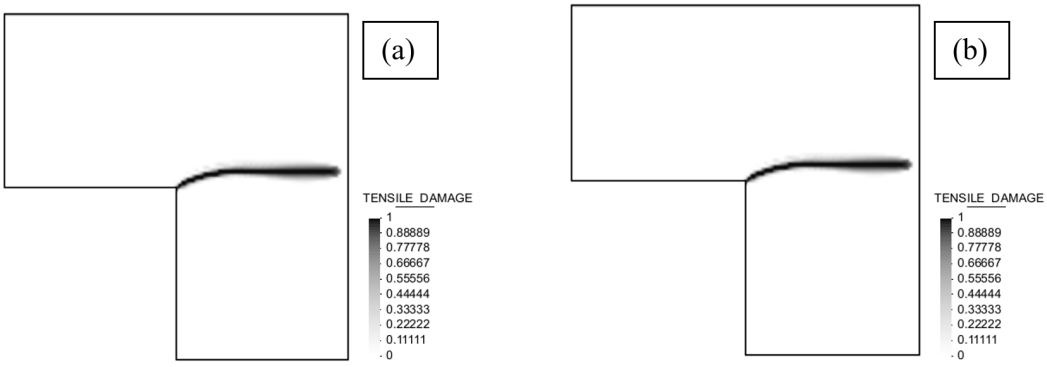

Figure 3. Tensile damage contour fills for the L-shaped panel, (a) 2D and (b) 3D solution

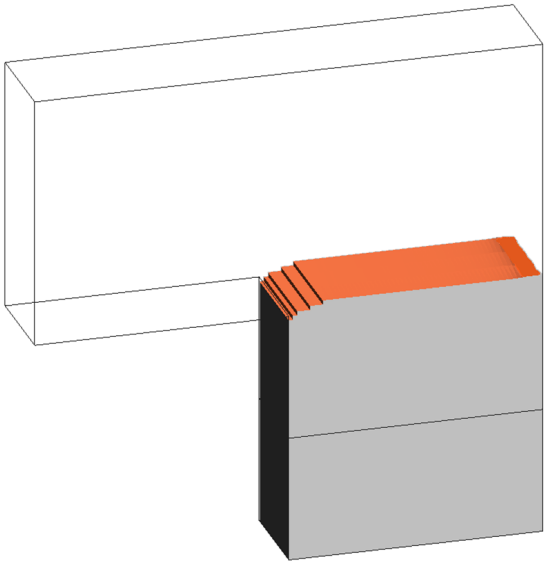

Figure 4. Crack Surface of the L-shaped panel

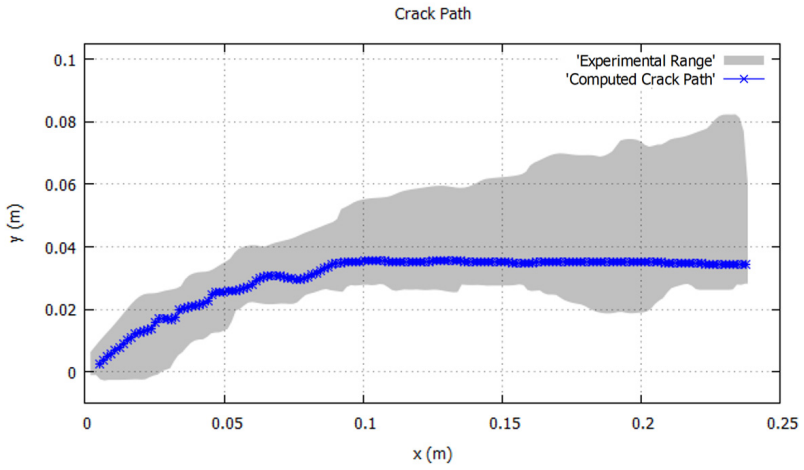

Figure 5. Crack path in the L-shaped panel compared to the experimental range reported in [68]

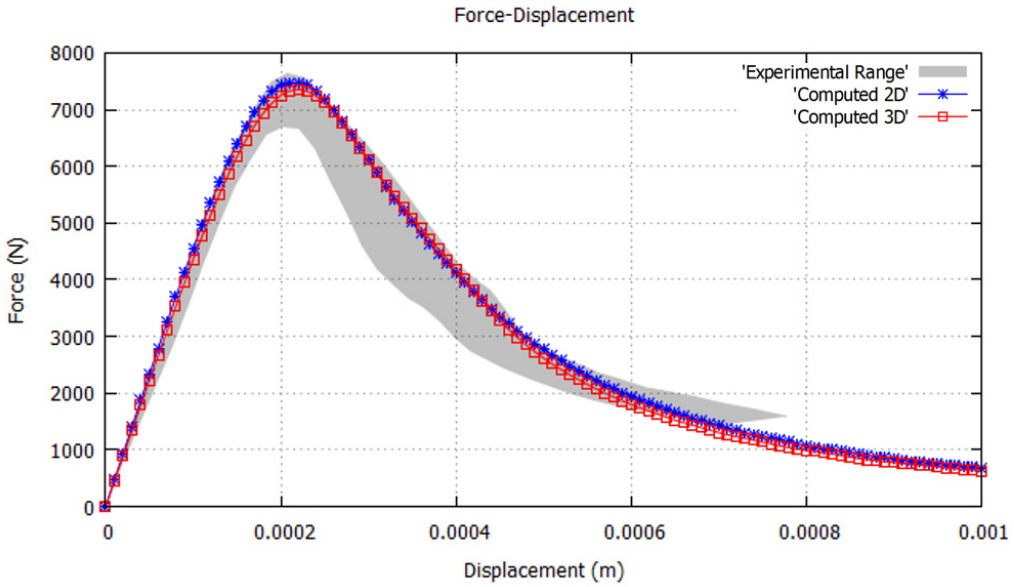

Figure 6. Force-displacement results for 2D and 3D analyses of the L-shaped panel

Independence of results with FE size

Thanks to the regularization procedure introduced in equation (49), the computed structural response is independent from the resolution of the FE mesh. This is shown in Figure 7, where the Force-Displacement curve obtained from grids of different sizes (h = 4, 8, 12 mm) are compared. The results obtained in the 3D analysis (h = 8 mm) are also shown. All the results are practically overlapping, demonstrating mesh-size independence.

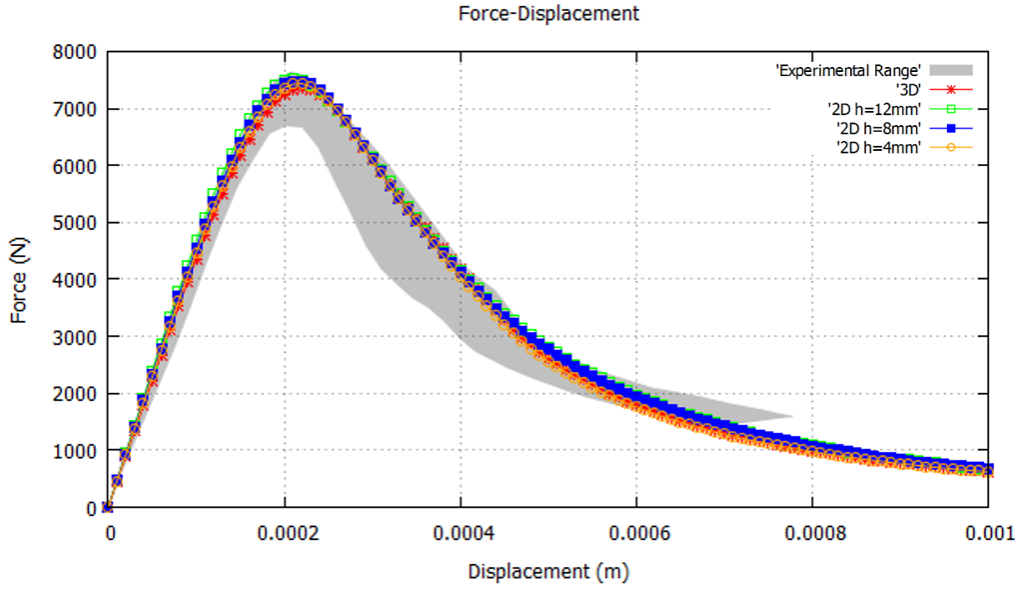

Figure 7. Force-displacement results for several mesh sizes

Convergence of displacement and strain fields

In order to illustrate the convergence of the displacement and strain fields provided by the smeared crack approach with mixed FE formulations, a vertical cut, shown in Figure 1, is considered.

Along this line, the profiles of vertical displacements and major principal strains are shown in Figure 8 for several load steps and in Figure 9 for different mesh sizes.

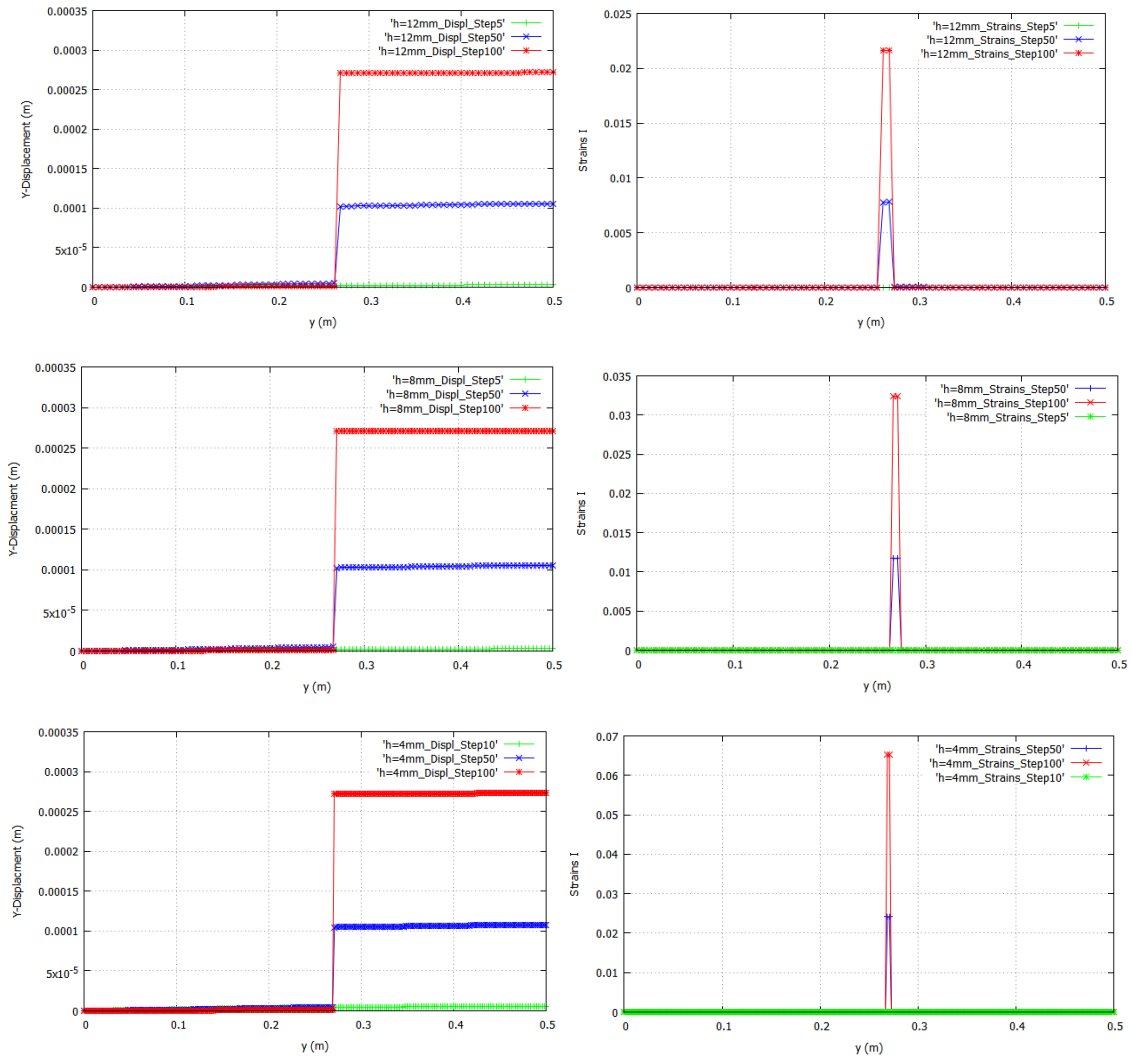

Figure 8. Vertical displacement and major principal strains along a vertical line for different load steps

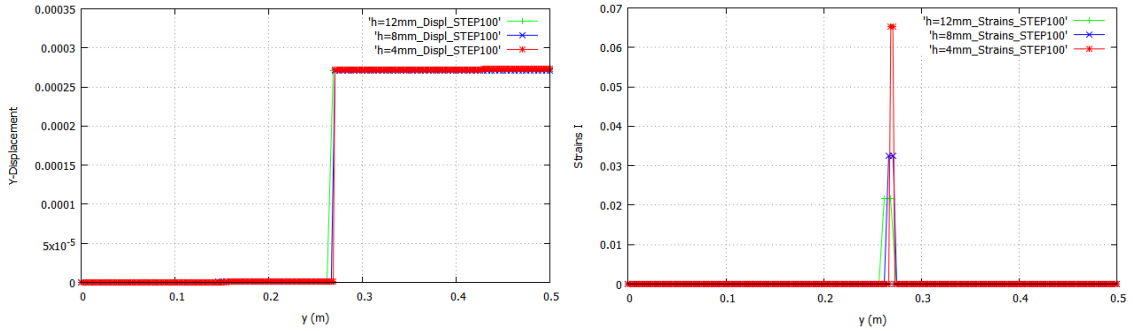

Figure 9. Vertical displacement and major principal strains along a vertical line for diferent sized meshes

Figure 8, left column, shows how the displacement jump across the crack (CMOD) evolves as the load increases; it can be observed that, in all the meshes, the displacement jump is smeared across

one element, an optimal representation of a strong discontinuity for the given mesh resolution. Figure 9, left, shows that the results practically overlap, demonstrating mesh size independence.

Figure 8, right column, shows the corresponding evolution of the strains as the load increases and the crack is formed. Note that: (a) the strain field is continuous, (b) the effective width of the strain localization band is 2h, (c) the value of the peak strain is inversely proportional to the mesh resolution, (d) the numerical solution approximates the Dirac's delta derivative of a discontinuous displacement field, as can be seen in Figure 9, right.

4.2 Wedge-Splitting test

In this second example, a wedge-splitting test of a concrete specimen is considered. The test was experimentally carried out by [69]. Reference [28] found similar results using embedded crack methods, as did reference [34] using XFEM. Reference [43] used embedded crack methods and crack tracking to compute a specimen with the same shape but in a reduced size.

The geometry is depicted in Figure 10 and the material properties are given in Table 2. The detail of the load application is shown in Figure 10. The thickness of the specimen is 0.4 m.

This problem is solved using 2D triangular and 3D prism elements. The 2D computational domain is discretized with an unstructured mesh with elements of 40 mm of size, resulting in 7,488 nodes for 2D. The numerical analysis is carried out under the hypothesis of plane stress. The 3D mesh is obtained by the out-of-plane extrusion of the 2D mesh resulting in a semi-structured mesh of 29,952 nodes.

Young's Modulus	$28.3 \cdot 10^9$ Pa
Poisson's Ratio	0.2
Tensile Strength	$2.27 \cdot 10^6$ Pa
Fracture Energy	420 J/m^2

Table 2. Material parameters of the wedge-splitting test

This problem is solved using an arc-length algorithm controlling the crack mouth opening displacement (CMOD) at the points of load application.

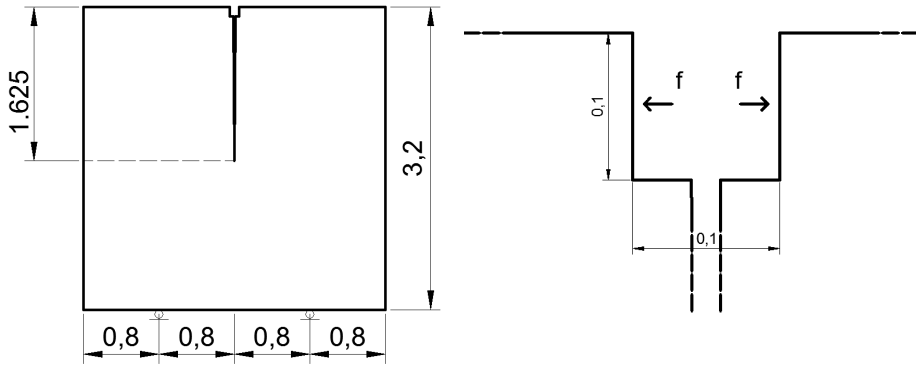

Figure 10. Geometry of the wedge-splitting test and detail of load application

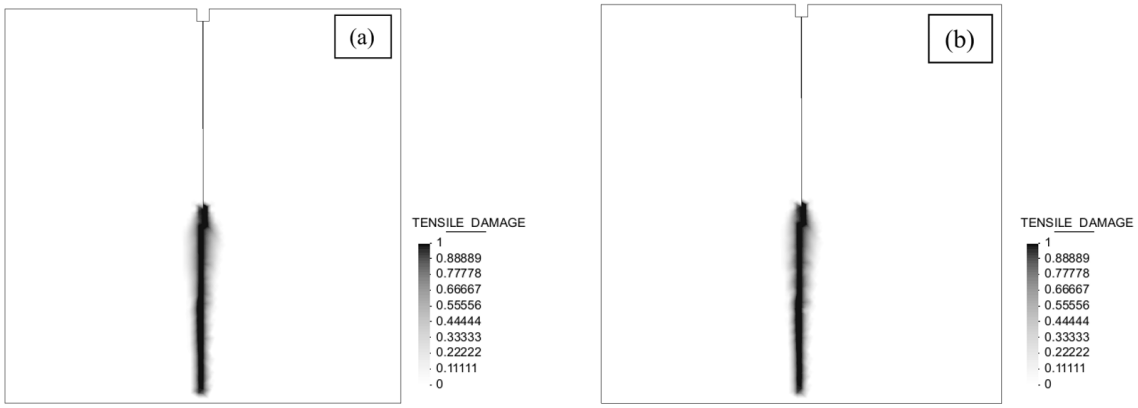

Figure 11. Tensile damage contour fills of the wedge-splitting test, (a) 2D and (b) 3D solution

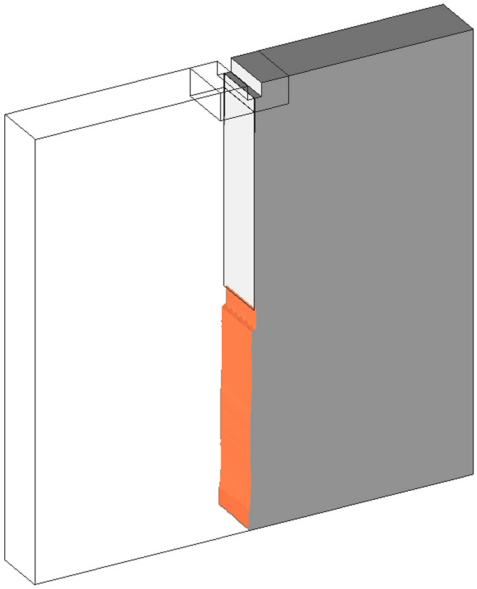

Figure 12. Crack surface of the modelled wedge-splitting test

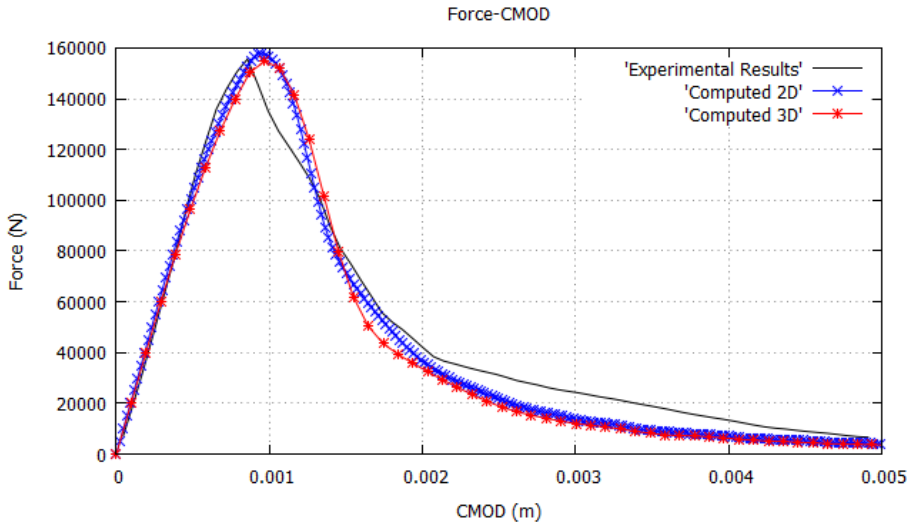

Figure 13. Force-CMOD results for 2D and 3D analysis.

Figure 11 shows the tensile damage distribution in the specimen for an imposed horizontal displacement of 5 mm obtained in the 2D and 3D analyses. Both results are identical because the same mesh configuration is used in the XY plane for the 2D and the 3D cases. These results agree with the experimental tests carried out by [69]. The crack path is vertical, as expected because of the symmetry of the geometry and the loading conditions. The crack surface obtained in the 3D analysis is shown in Figure 12, displayed as the level set surface of X-displacements. No auxiliary crack tracking technique has been used. No spurious mesh bias is observed.

Figure 13 shows the load vs. crack mouth opening displacement curve in the 2D and 3D cases, which are also compared to the results from the tests in [69]. Again, 2D and 3D results are almost overlapping. As can be seen, the results are very close to the experimental tests. They are also very close to the computational results of references [34], [28] and [43].

4.3 Three-point and four-point bending tests

In this section, beams subjected to three-point and four-point bending tests are considered. The experimental tests were carried out by [70]. Other numerical results are reported in [71] and [34], where crack tracking auxiliary techniques are used. In Figure 14 the geometry of the tested beams is shown. Two cases are considered. In the first one, the stiffness at the upper left support is assumed equal to zero (K=0), as in a three-point bending test, while in the second one it is considered infinite (K=∞), as in a four-point bending test. The thickness of the specimen is 0.05 m. The properties of the material are given in Table 3. For the 2D analysis, plane stress conditions are assumed.

Young's Modulus	$38.0 \cdot 10^9$ Pa
Poisson's Ratio	0.2
Tensile Strength	$3.0 \cdot 10^6$ Pa
Fracture Energy	69 J/m^2

Table 3. Material properties of the beams

The problem is solved using an arc-length algorithm controlling the crack mouth opening displacement (CMOD) at the notch.

For this example, 2D triangular and 3D tetrahedral elements are used. In the 2D analysis, the computational domain is discretized with a fully unstructured mesh with 2.5 mm elements, resulting in 18,738 nodes. For the 3D analysis, a fully unstructured tetrahedral mesh of 50,389 nodes and 2.5 mm element-size has been considered. Both meshes are shown in Figure 15.

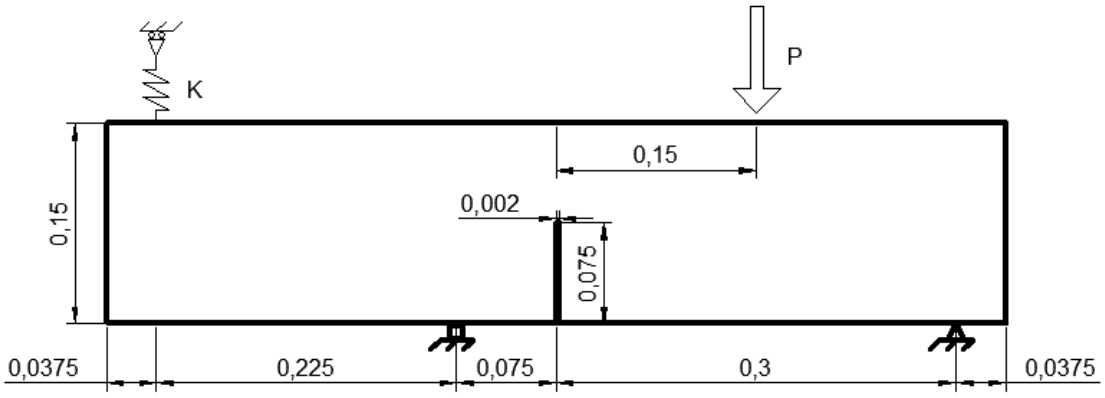

Figure 14. Geometry of the three-point and four-point beam (m)

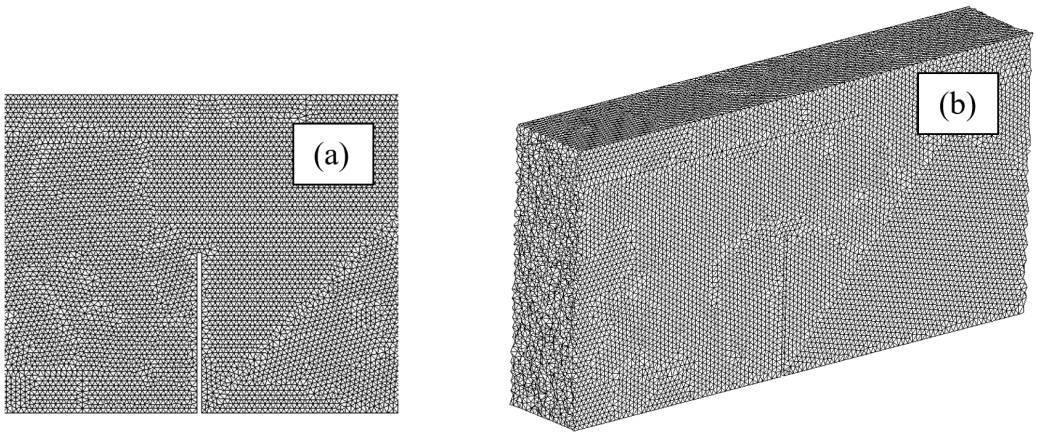

Figure 15. Meshes used for the (a) 2D and (b) 3D analyses of the three-point and the four-point bending tests

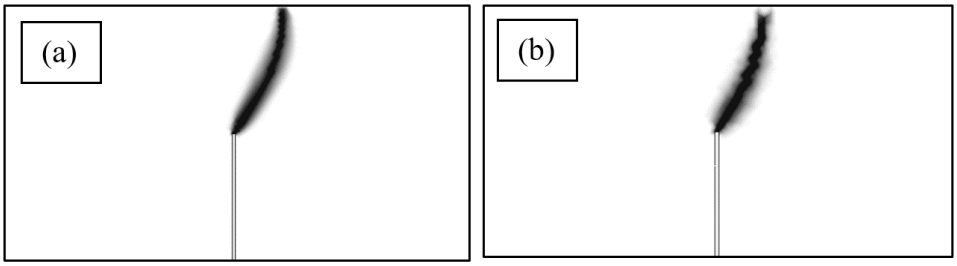

Figure 16. Tensile damage contour fills of the three-point bending test, (a) 2D solution, (b) 3D solution

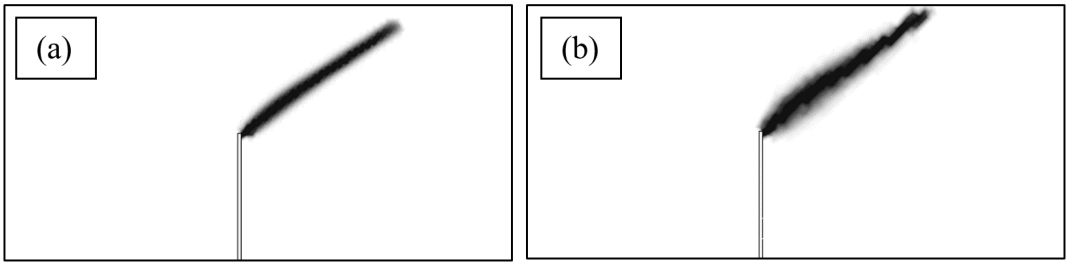

Figure 17. Tensile damage contour fill of the four-point bending test, (a) 2D solution, (b) 3D solution

Figures 16 and 17 show plots of the computed tensile damage index in the cases considered. It can be observed that the crack path changes significantly depending on the boundary conditions applied to the beam. The 2D and 3D results for each case are almost overlapping. In Figure 18 the crack surfaces in the 3D analyses are shown, plotted as an iso-level surface of the X-displacements. There can be seen the fully unstructured mesh used for the computation of the beams, which is fine enough to model the crack surface with precision. As can be seen in Figure 19, the numerical results agree with the experimental tests. References [71] reported very similar crack paths using a global tracking algorithm. Also, [34] found very similar results using XFEM and the same global tracking algorithm.

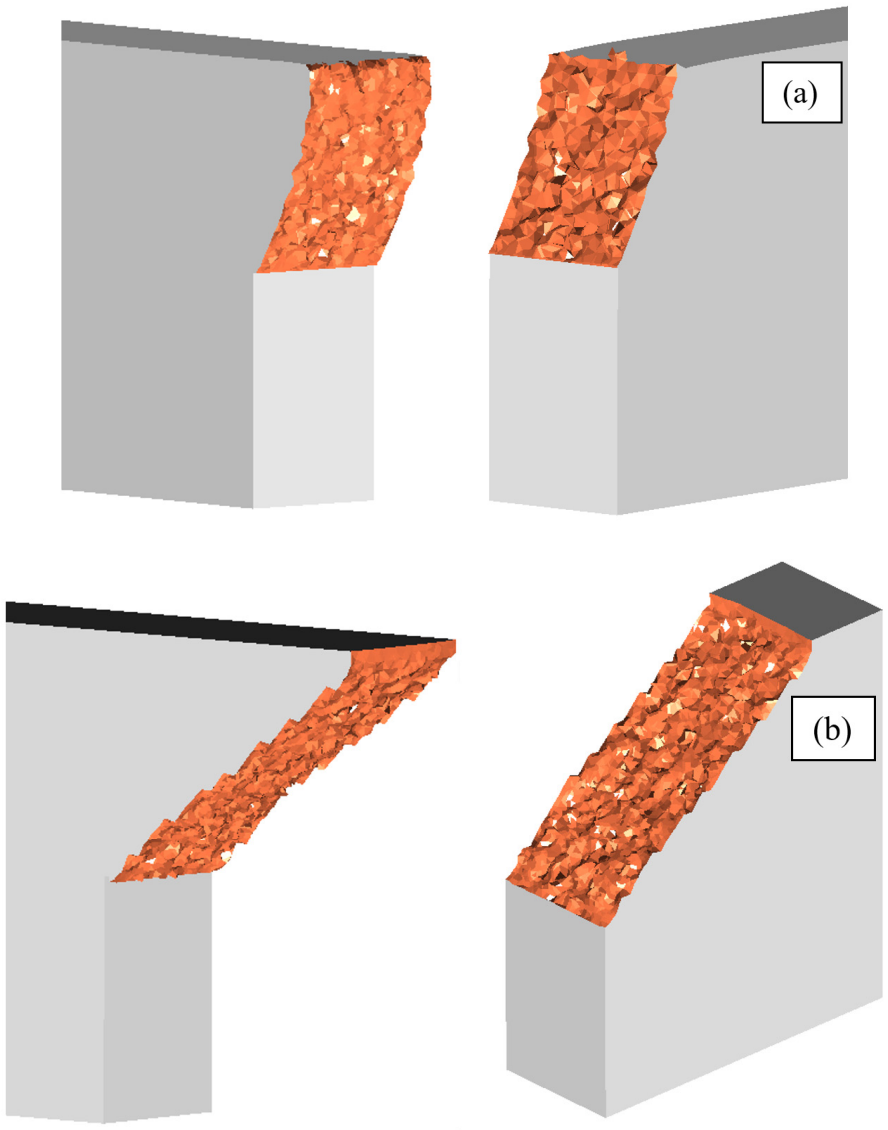

Figure 18. Modelled crack surfaces for the (a) three-point and (b) four-point bending cases

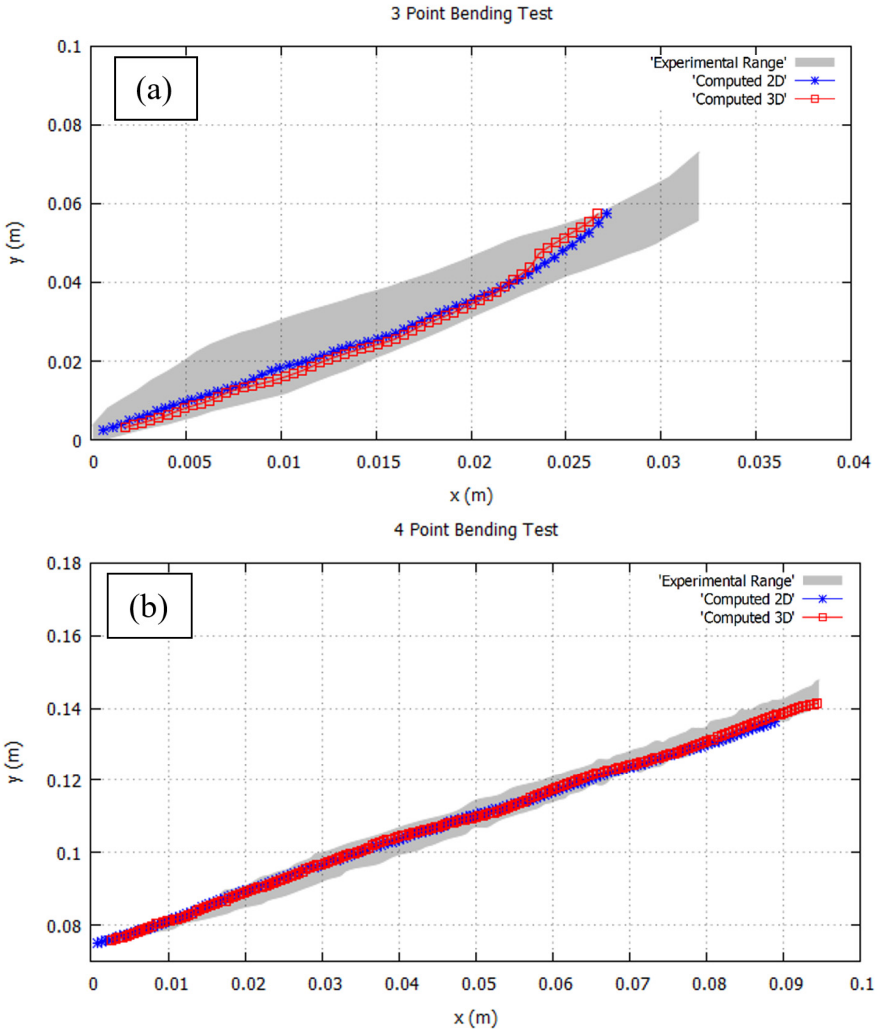

Figure 19. Computed crack paths compared to experimental results for (a) three-point and (b) four-point bending cases

Figure 20 shows the load-CMOD curves for both the 3 and 4 point bending tests. The results are similar to the ones obtained in references [71] and [34]. The three-point bending test shows very good agreement with the experimental results obtained by [70] both in the 2D and 3D analyses, even if at the last stages of the simulation the strength is slightly underestimated. The peak force is slightly lower in the 3D analysis. The four-point test has its peak slightly outside the experimental range of results. This occurs also in the numerical references [71] and [34].

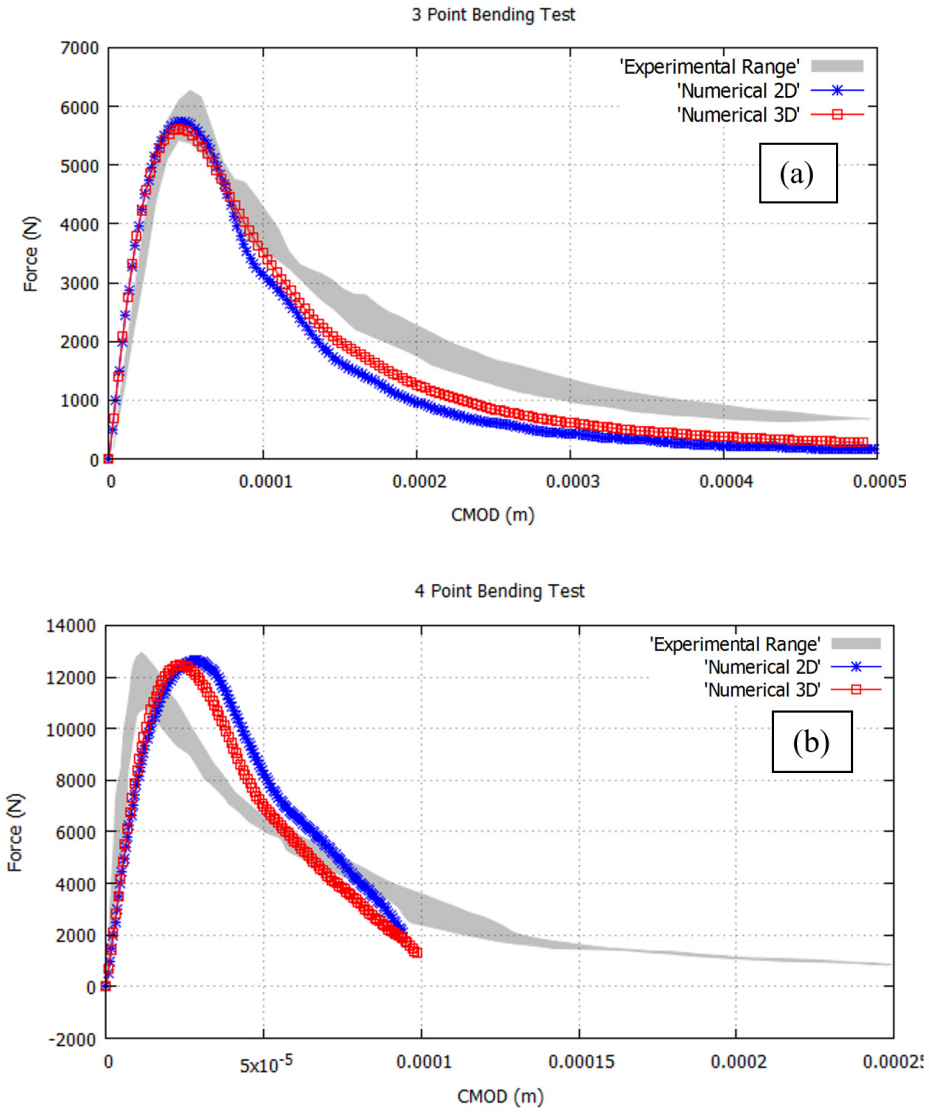

Figure 20. Load-CMOD curves for (a) the three-point and (b) four-point bending tests

Structural size effect

Structural size effect addresses the question of how the load capacity of geometrically similar structures varies when scaling up or down their relative sizes. Experimental evidence shows that, for a given structural problem, ductile behavior corresponds to the small scale limit (appropriate for small laboratory specimens), while brittle fracture occurs in the large scale limit (apt for structures of very large dimensions). Thus, it is of practical interest to develop analytical and numerical tools suitable to bridge the gap between perfectly ductile and perfectly brittle behavior, i.e. suitable for the range of quasi-brittle failure [54].

In quasi-brittle fracture, size effect does not only affect the load capacity (peak load), it also reflects on the post-peak behavior (ductility) of the structure. The capability of a quasi-brittle structure to absorb energy decreases, in relative terms, as the structure size increases [54].

In reference [70], structural size effect was investigated when testing the beams. For this, smaller specimens with half the original size, i.e. a height of D=75 mm, and double size, i.e. D=300 mm of height, where also experimentally tested. These cases have also been simulated computationally for the three-point beam and are reported in the following.

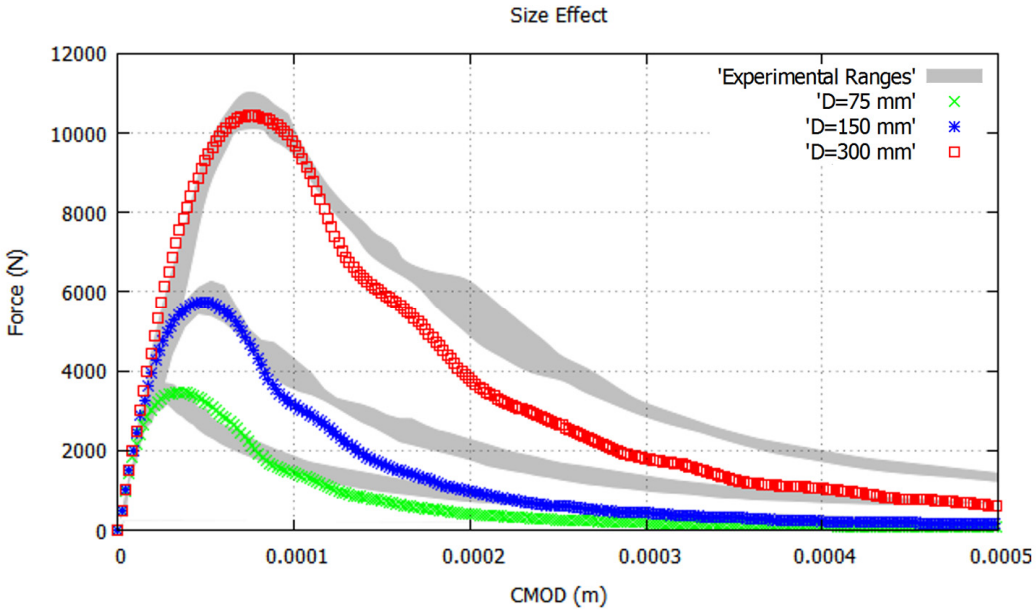

Figure 21. Force-CMOD curves for different beam sizes

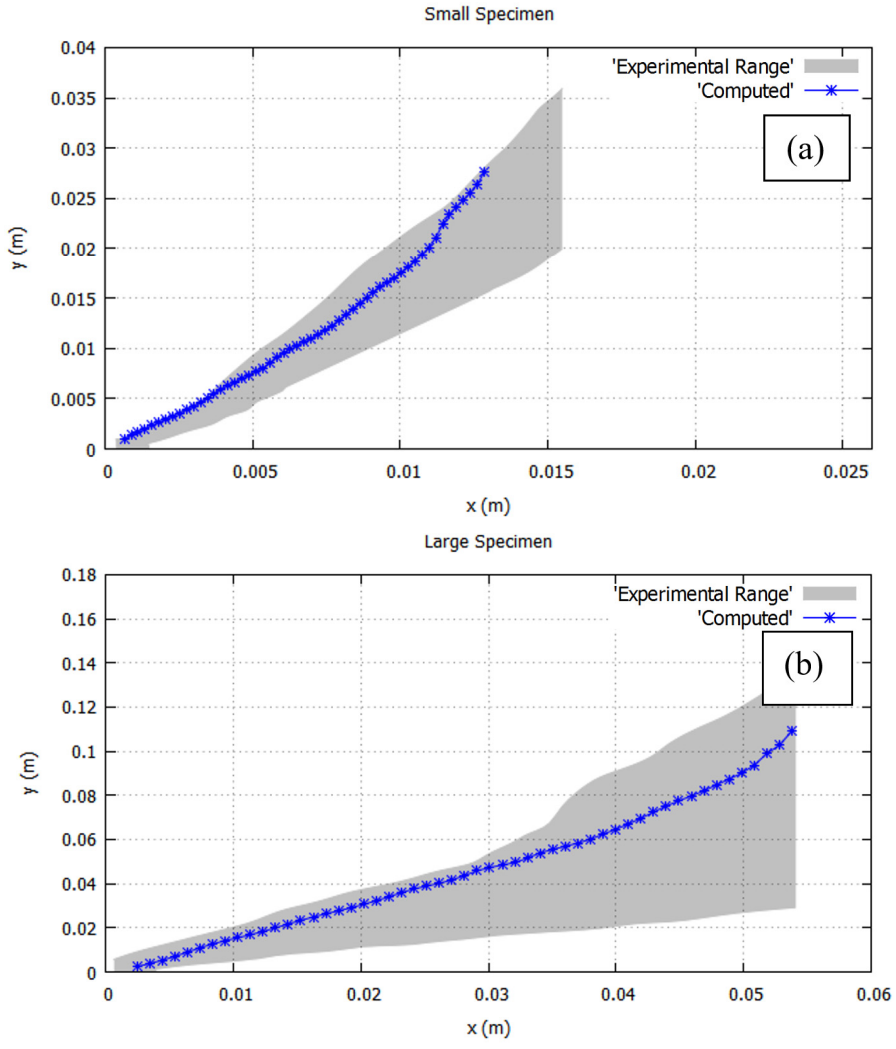

Figure 22. Crack path in (a) the small specimen and (b) the large specimen

In Figure 21, the Force-CMOD curves of the three considered cases, small (D=75 mm), medium (D=150 mm) and large (D=300 mm), are shown. The computed results show very good agreement with the experimental ones of reference [70], even if the dissipated energy is slightly underestimated. In Figure 22, the computed crack paths also show very good agreement with the experimental results for the small and large specimens.

Plane Strain vs Plane Stress

The plane stress hypothesis adopted in the 2D computation may be verified by comparing the results obtained against those obtained under plane strain assumptions. Figure 23 shows the force-CMOD results for both considerations. The 3D analysis is also included. All three cases are almost overlapping and equally close to the experiments. This indicates that the standard engineering practice of neglecting Poisson's effect in beam theory can be extended into the non-linear range.

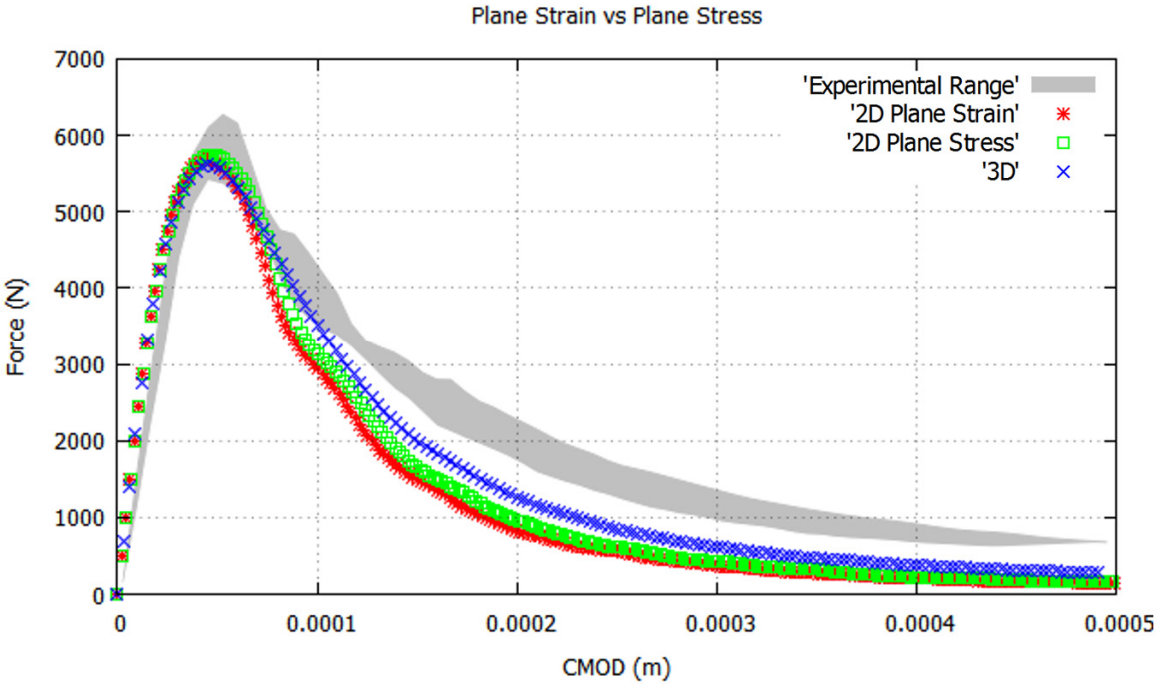

Figure 23. Comparison of 2D plane strain, 2D plane stress and 3D hypothesis

4.4 Notched beams with holes

A more involved example is considered in this section to explore the performance of the proposed finite element formulation. Here, a notched beam with holes, experimentally tested and numerically computed by [72], is considered. Other numerical solutions are reported in [41], [72] and [73]. Reference [41] modelled this example using crack tracking and embedded methods and [73] used fracture mechanics. Instead [72] used a probabilistic approach, where geometric and material uncertainties are considered when computing the crack path and load-displacement curves.

The tested beam is made of plexiglass; the properties used for the simulation are given in Table 4.

For comparison purposes, three different geometries regarding the position of the notch and the holes, shown in Figure 24, are studied. In the original experiment inches were used as units of length.

In the first case, the beam is notched but has no holes; the notch is 6'' from the center and 1'' long. In the second case, the beam has three holes of diameter 0.5'' at 4'' from the center and a notch identical to the previous case. In the third case, the hole layout is the same as in the second case and the notch is 4.5'' from the center and is 1.5'' long. The thickness of the beam is 0.5''. For the 2D analysis, plane stress conditions are assumed.

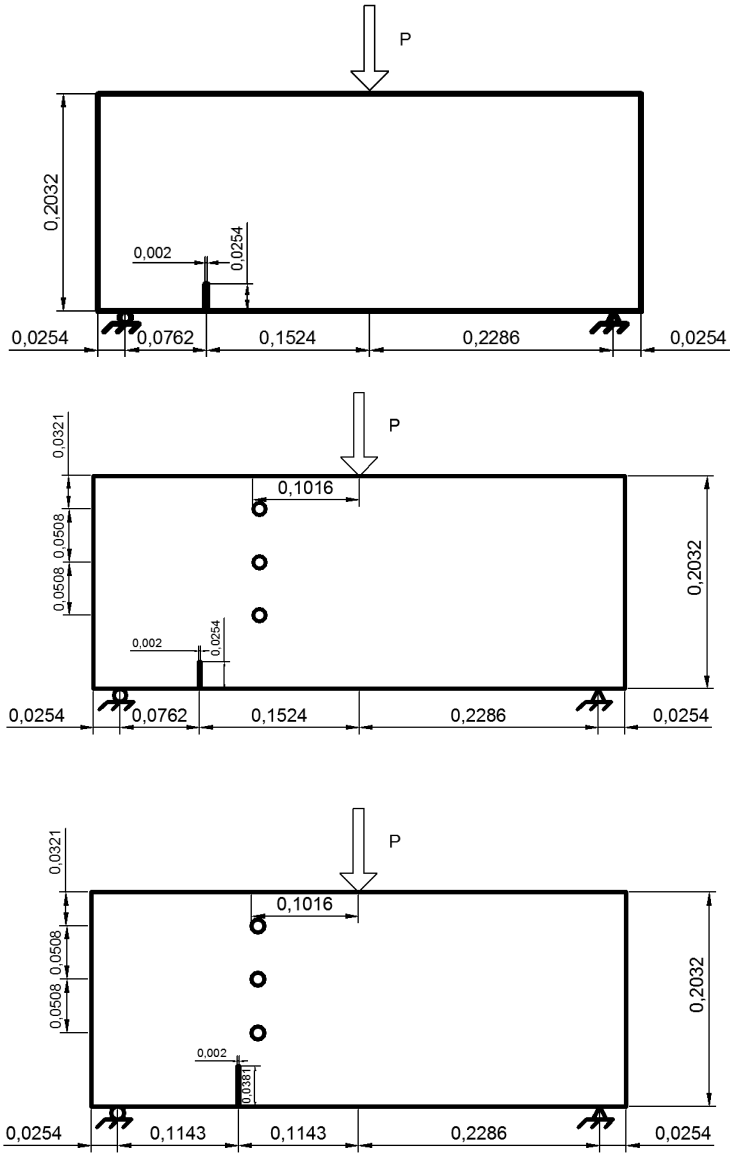

Figure 24. Geometry for the three notched beams (m)

Young's Modulus	$3.102 \cdot 10^9$ Pa
Poisson's Ratio	0.35
Tensile Strength	$7.0 \cdot 10^6$ Pa
Fracture Energy	500 J/m^2

Table 4. Material properties of the three holed notched beams

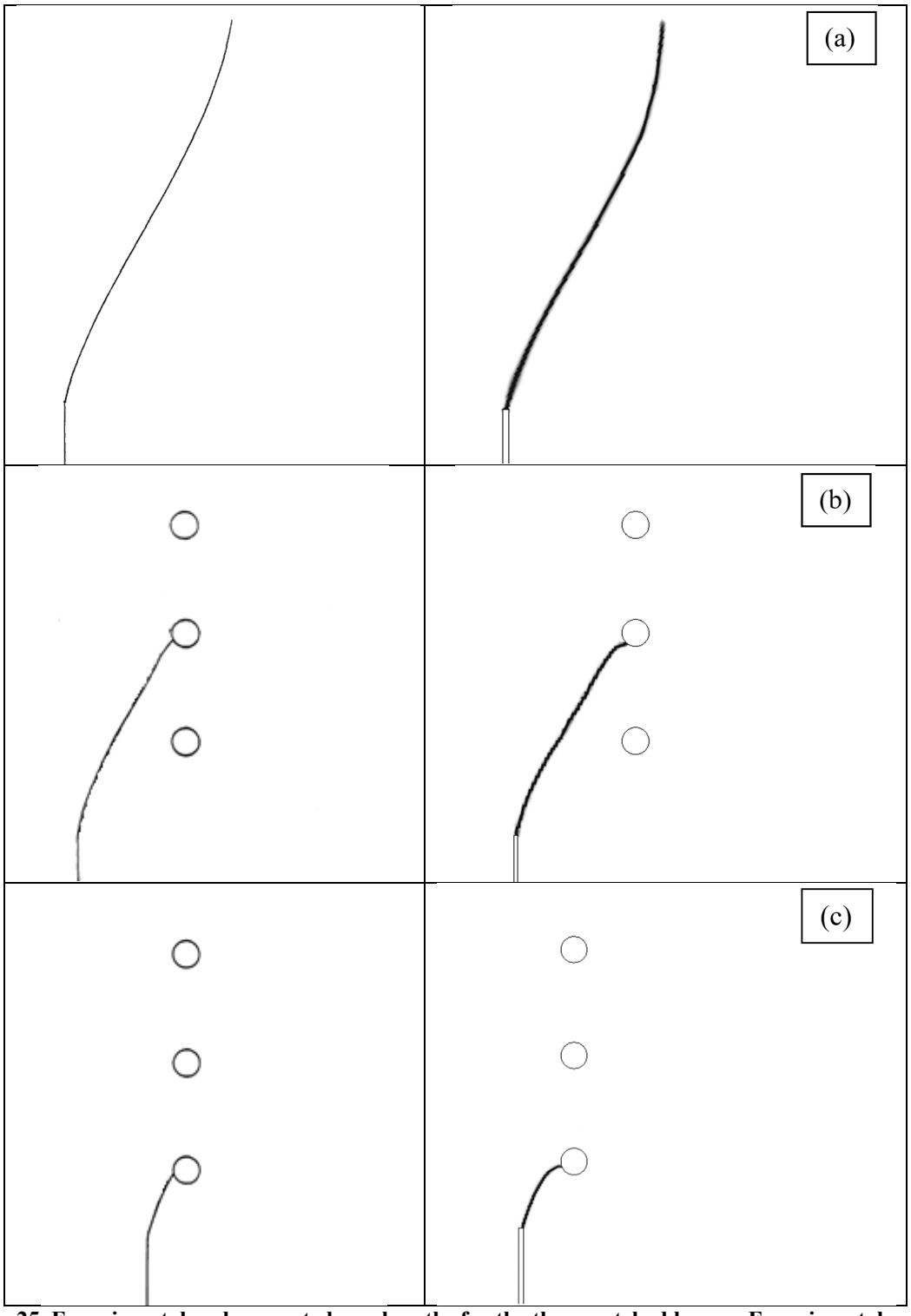

Figure 25. Experimental and computed crack paths for the three notched beams. Experimental results taken from [72]

In all cases, 2D triangular elements are used. The domain is discretized with unstructured meshes of 1 mm elements in the central part, where the crack forms, and of 2.54 mm in the rest of the beams, resulting in 44,956, 52,884 and 52,600 nodes, respectively.

The simulation is done using an arc-length algorithm controlling the crack mouth opening displacement (CMOD).

Figure 25 shows the computed crack paths next to the experimental results reported in [72]. It can be observed that the crack paths are different depending on the notch position and the presence of the holes. The crack path for the case without holes is almost identical to the experimental result. In the other two cases, the numerical results also show good agreement with tests. The present results are comparable to those obtained in [41], [72] and [73].

Figure 26 shows the load-CMOD curve for the case without holes, the only one reported in [72]. The computed results show good agreement with the ones obtained experimentally. In Figure 27 the force vs displacement curve at the point of load application is presented. The numerical results are stiffer than the experimental ones. This was also observed in the numerical results reported by [72]. Note that the local response at the point of load application is very dependent on the actual details of the experimental set-up. Nevertheless, the overall resemblance of the results is remarkable, in terms of peak values, snap-back response and dissipated energy.

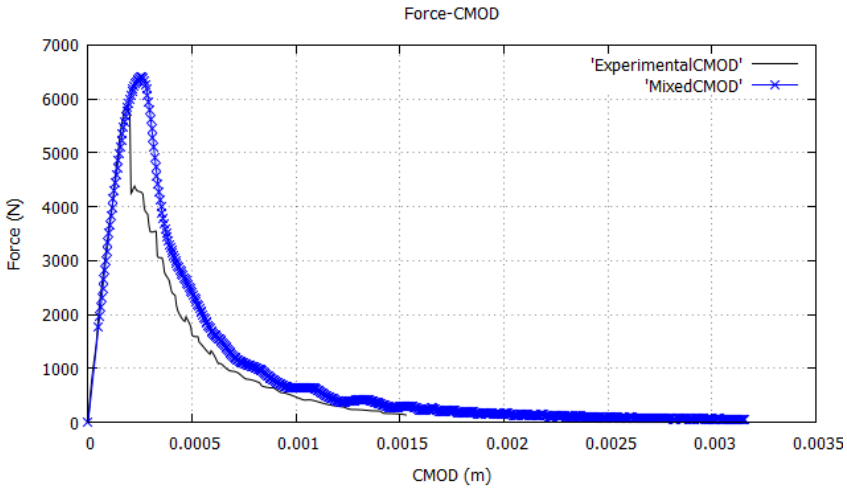

Figure 26. Force-CMOD curve for the notched beam without holes

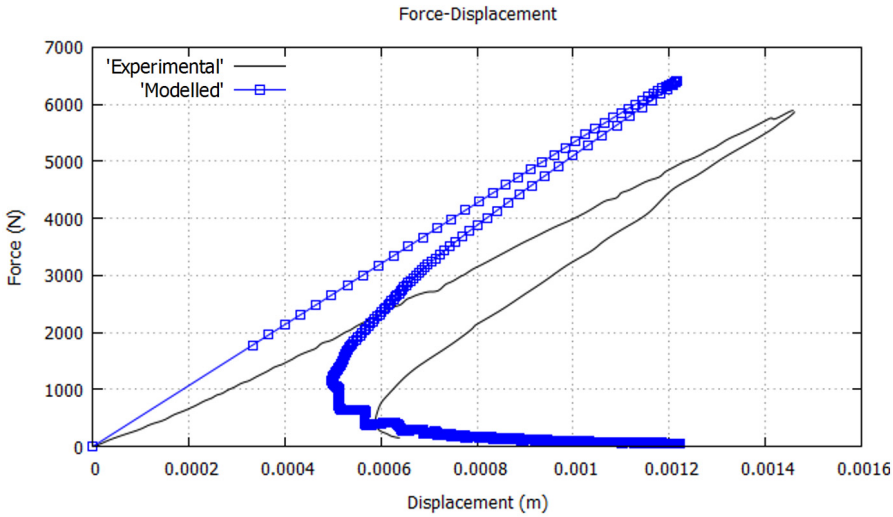

Figure 27. Force-displacement curve for the notched beam without holes

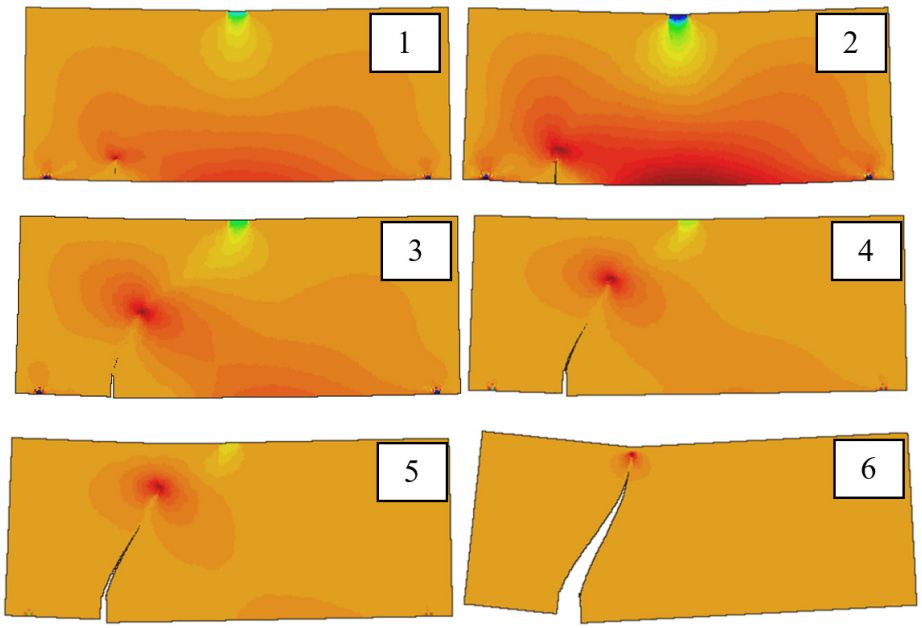

Figure 28. Crack propagation and evolution of major principal stresses in the notched beam without holes

Figure 28 shows the crack propagation and evolution of major principal stresses in the notched beam without holes. In the elastic range, stresses concentrate in the vicinity of the tip of the notch. This causes the crack to start and propagate through the height of the beam and towards the point of application of the load as also shown in Figure 25(a). The strain/displacement FE formulation is able to represent this progressive failure of the beam with noteworthy accuracy.

4.5 Four-point bending test on a doubly-notched beam

The numerical analysis of a four-point bending test on a doubly notched beam is considered next. The corresponding experiments are reported in [74]. Other numerical solutions are reported in [37, 75, 76]. In [37] an adaptive particle meshless method was used, while in [75] the boundary element method was employed. Reference [76] considers a localization limiter introduced to regularize the problem. All these simulations are in 2D.

The beam geometry and loading is shown in Figure 29 and the material parameters are given in Table 5. The thickness of the beam is 0.1 m. The structural problem presents polar-symmetry about the geometrical center. Thus, two symmetric cracks are expected to appear, starting from the top of the notches and propagating towards the opposite top and bottom faces of the beam. The cracks open and propagate under mixed Modes I and II (opening and shearing) loading. The ratio between the uniaxial compressive and tensile strengths is 15 [74].

In this section, the problem is analyzed in 2D, assuming plane stress conditions, and in 3D. The objective is to assess the performance of the proposed formulation when more than one crack appears.

The simulation is performed using an arc-length algorithm controlling the crack mouth opening displacement (CMOD) at the upper notch.

This example is solved using 2D quadrilateral elements and 3D hexahedra. In 2D the computational domain is discretized with a fully structured mesh of 1 mm size, resulting in a

54,021 node mesh. In 3D, the computational domain is partitioned using hexahedra elements of 1.5 mm size, ensuing a structured mesh of 53,998 nodes.

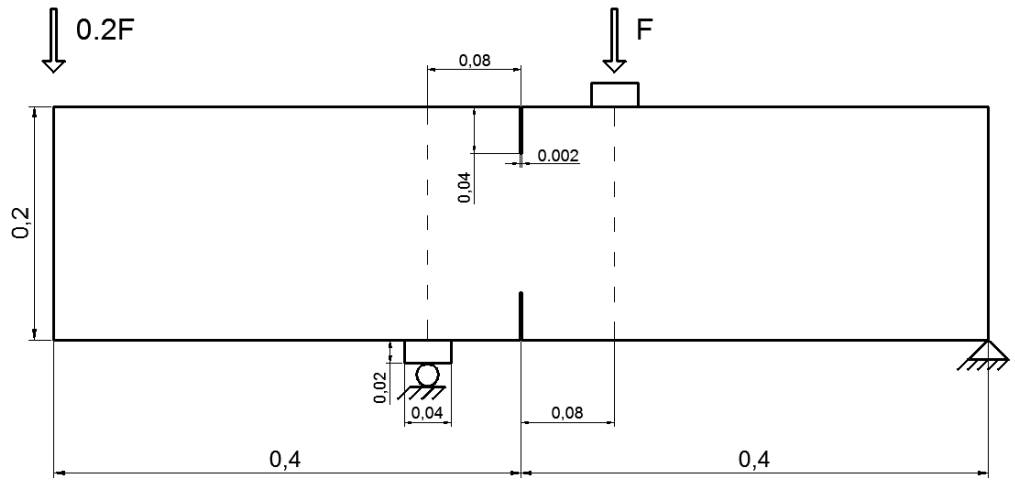

Figure 29. Geometry of the four-point bending test on a doubly-notched beam

Young's Modulus	$27 \cdot 10^9$ Pa
Poisson's Ratio	0.18
Tensile Strength	$2.0 \cdot 10^6$ Pa
Fracture Energy	100 J/m^2
Compressive Strength	$3.0 \cdot 10^7$ Pa

Table 5. Material parameters of the four-point bending test on a doubly-notched beam

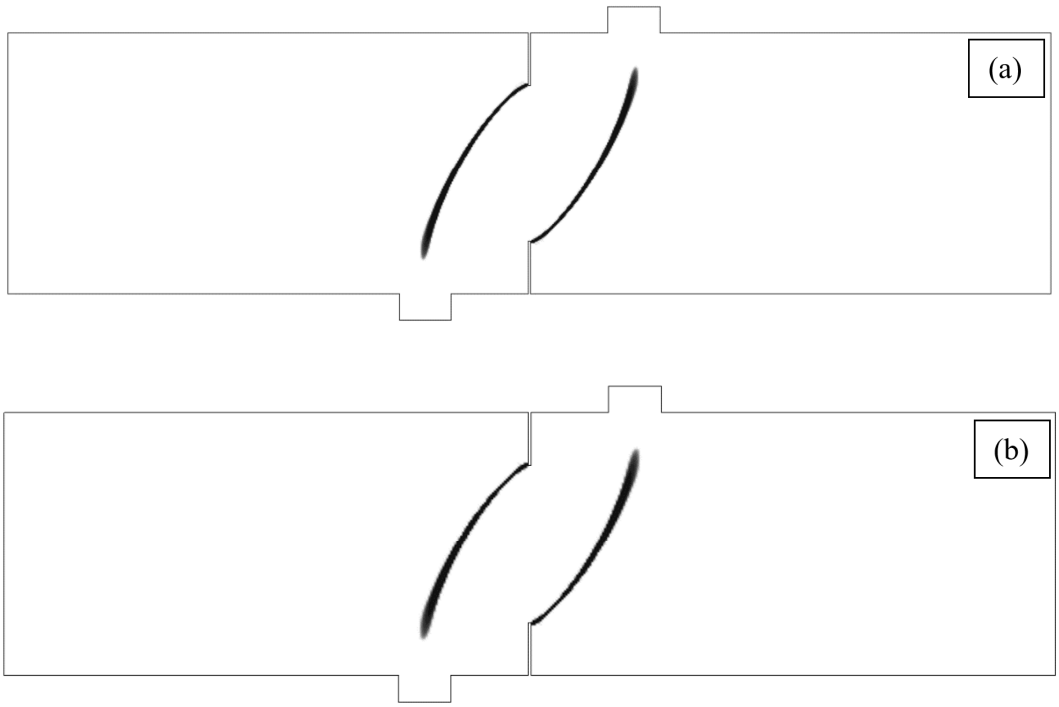

Figure 30. Tensile damage contour fills of the four-point bending test on a doubly notched beam for (a) the 2D and (b) the 3D computations

Figure 30 shows the tensile damage contour fills obtained in the 2D and 3D simulations. Due to the polar symmetry of the beam geometry and loading, two polar-symmetric cracks appear and propagate. These results are concordant with the ones observed in the experiments by [74]; the cracks propagate as expected. The computed 2D and 3D paths of both cracks are almost overlapping and are inside the experimental ranges obtained in the tests, as can be observed in Figure 31.

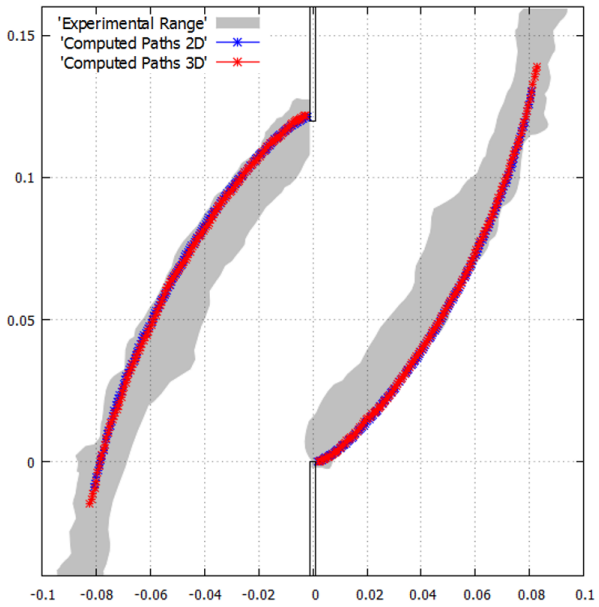

Figure 31. Crack path of the four-point bending test on a doubly notched beam

Also because of the polar symmetry of the problem, the central part of the beam rotates, with respect to the central point, as can be seen in Figure 32, where contour fills of the displacements are shown. The displacement "jump" across the cracks can also be observed neatly.

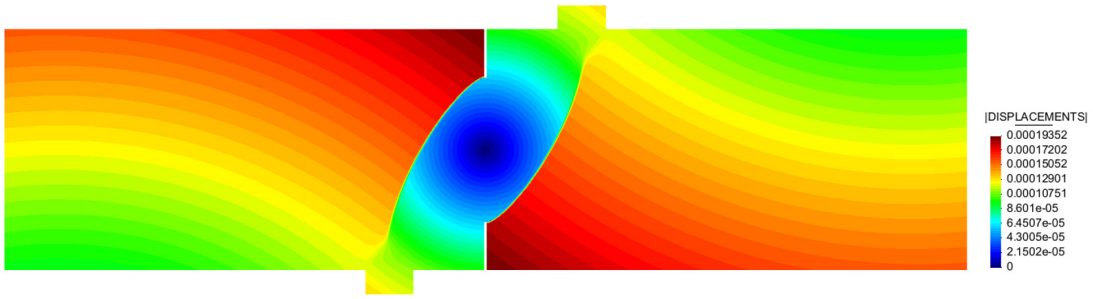

Figure 32. Displacements of the four-point bending test on a doubly notched beam

The crack surfaces in the 3D analysis are depicted in Figure 33, plotted as iso-level surfaces of the norm of displacements. In this way, the performed simulation allows to observe a 3D representation of the piece formed during the experiment. This case illustrates the performance of the proposed method to deal with several cracks propagating at the same time in 2D and 3D. As no auxiliary tracking technique is required, the present formulation can handle this situation, which does not represent an extra hindrance to the formulation.

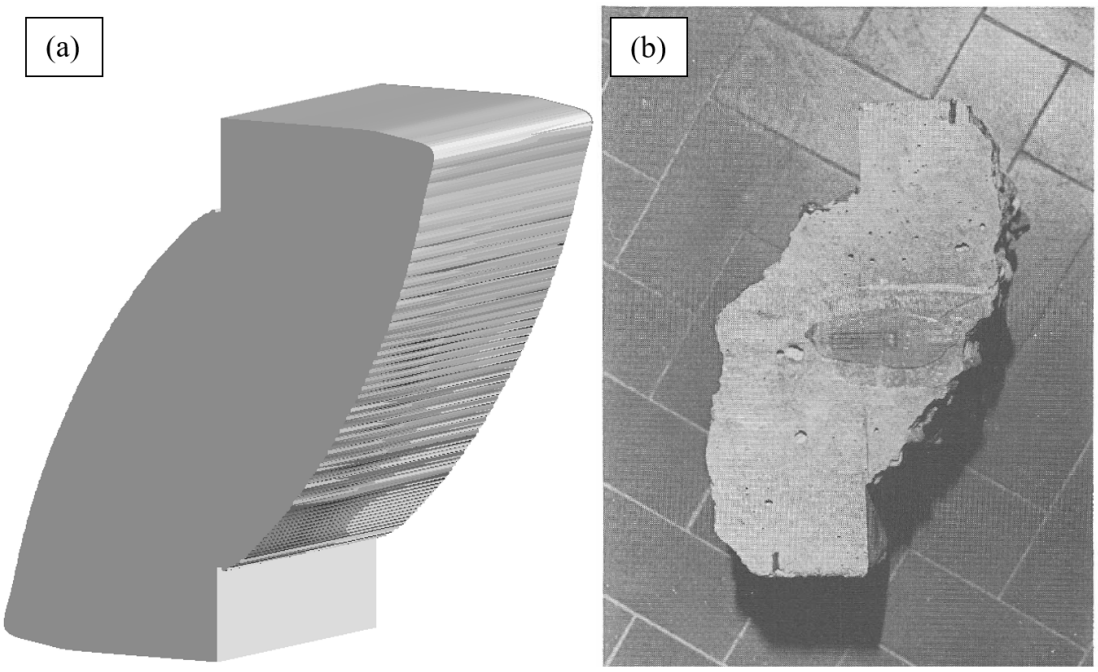

Figure 33. Central piece of (a) the modelled crack surfaces for the four-point bending test on a doubly notched beam and (b) a similar experiment [74]

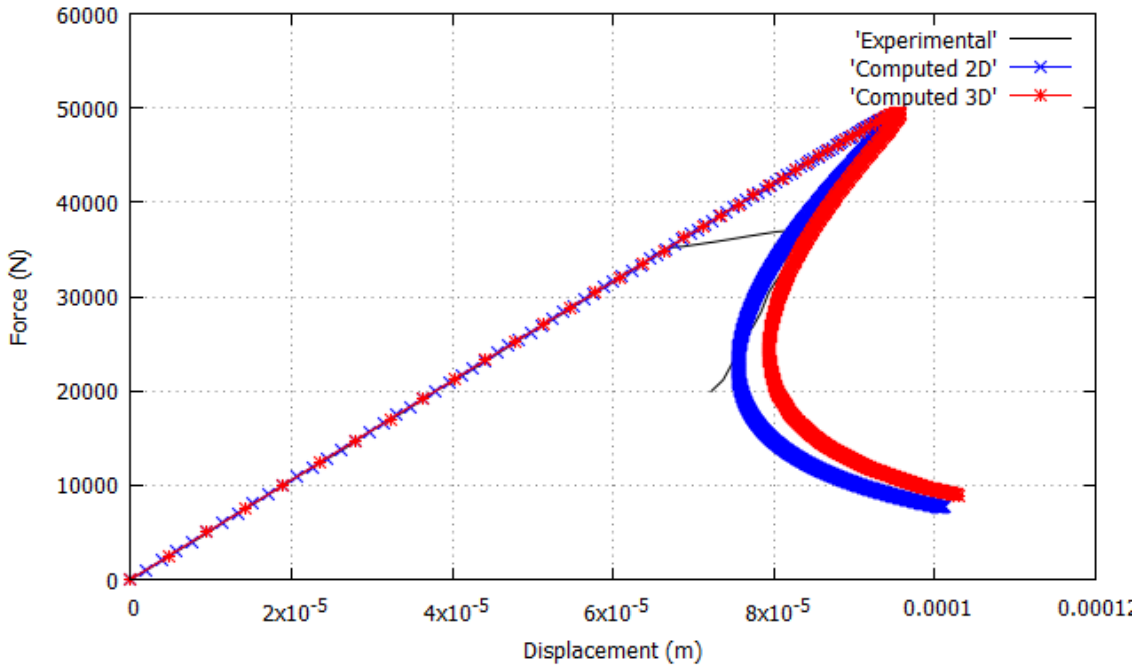

Figure 34. Force-displacement curve of the 2D and 3D simulations of the four-point bending test on a doubly notched beam

In Figure 34, the Force-displacement curve at the point of load application is shown for the 2D and 3D computations. The computed results show very good agreement with the experimental ones of reference [74], and also with the numerical results in [37, 76].

Figure 35 shows the crack propagation and evolution of major principal stresses in the doubly-notched beam. Again it can be seen how in the elastic range stresses concentrate at the vicinity of

the crack, causing its propagation through the height of the beam and towards the points of application of the loads, as seen in Figures 30, 31 and 34a. Note that the stress field is polar symmetric in the linear and in the nonlinear behavior.

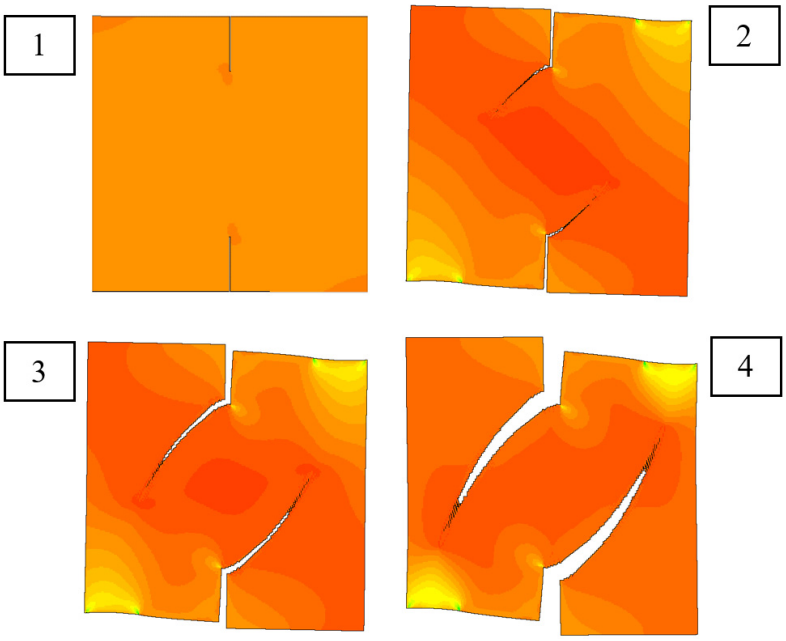

Figure 35. Crack propagation and evolution of major principal stresses in the four-point bending test on a doubly notched beam

4.6 Three-point bending test on a skew notched beam

In this section, a skew notched beam subjected to three-point bending is considered. The experimental tests were carried out by [77] using Plexiglass, to better reveal the evolution of the crack. Other numerical results are reported in [78], where a dual boundary element method (DBEM) was implemented and in [79], where the extended finite element method (XFEM) was used.

In Figure 36 the geometry of the tested beam is shown. The notch has a deviation of 45º with respect to the lateral faces of the beam. The thickness of the specimen is 0.01 m. The properties of the material are given in Table 6. The structural problem is skew-symmetric with respect to the vertical longitudinal and transversal mid-planes of the beam. Therefore, a non-planar crack is foreseen to materialize at the tip of the skew notch under mixed Mode I and Mode III loading and to propagate upwards while twisting around the vertical central axis until it is oriented normal to the longitudinal axis.

Due to the deviation of the notch, this example can only be solved in 3D. The load is applied imposing increments of displacement at the center of the top of the beam. 3D tetrahedral elements are used in a fully structured mesh of 21,516 nodes and 1.5 mm element size in the central area of interest. The elements of the structured mesh are laid out in a crisscross pattern. Another mesh, fully unstructured, of 14,709 nodes and 1 mm element size is also considered. Both meshes are shown in Figure 37.

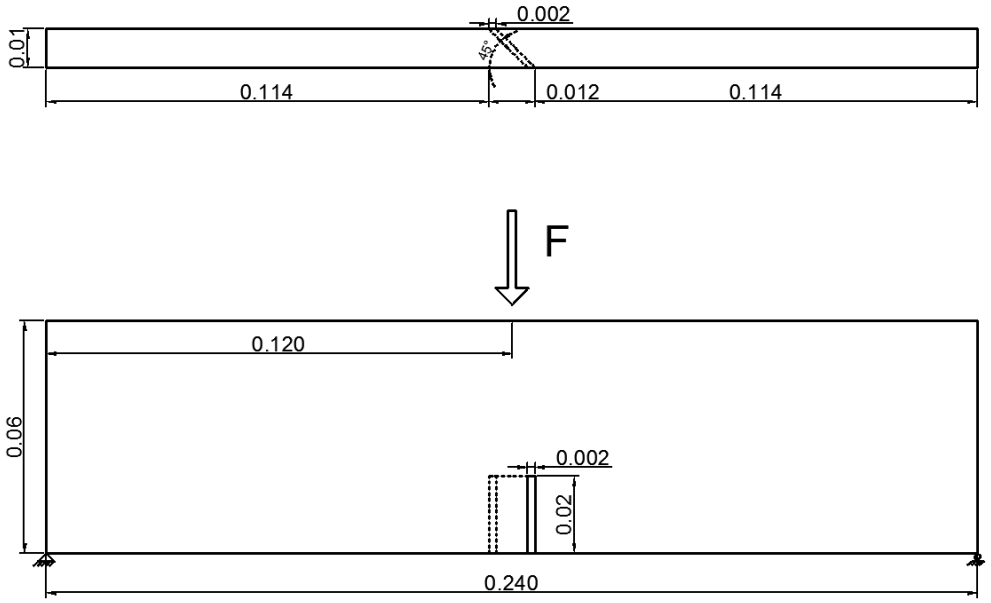

Figure 36. Geometry of the three-point bending test on a skew notched beam (m)

Young's Modulus	$28 \cdot 10^9$ Pa
Poisson's Ratio	0.38
Tensile Strength	$40.0 \cdot 10^6$ Pa
Fracture Energy	500 J/m^2

Table 6. Material properties of the three-point bending test on a skew notched beam

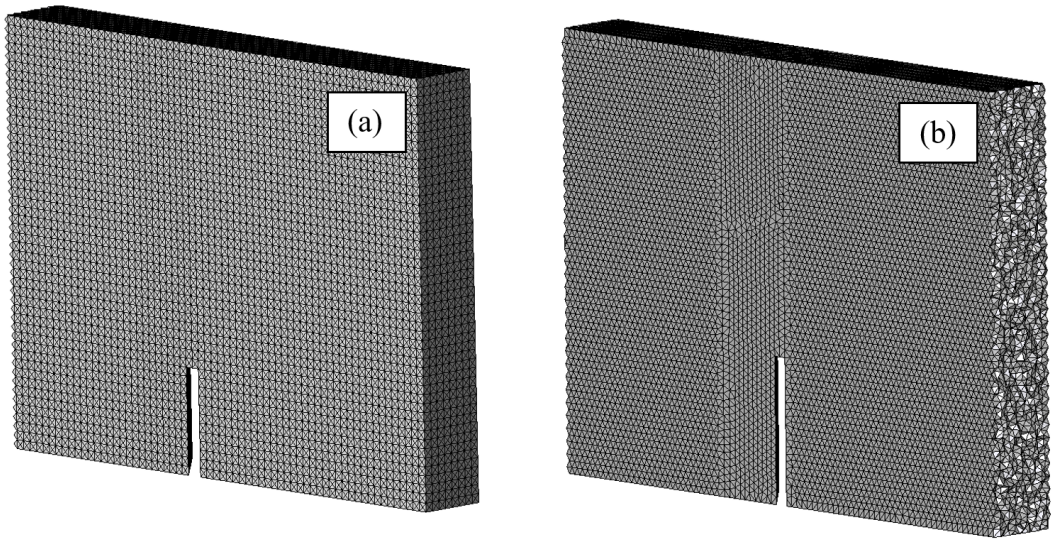

Figure 37. Meshes used for the (a) structured and (b) unstructured analyses of the three-point bending test on skew notched beam

In Figure 38 the crack surfaces are shown, plotted as an iso-level surface of the horizontal displacements along the axis of the beam. Both the structured and unstructured meshes used for the computation of the beam are fine enough to model the crack surface with precision. As can be seen in Figure 39, the numerical results agree well with the experimental results.

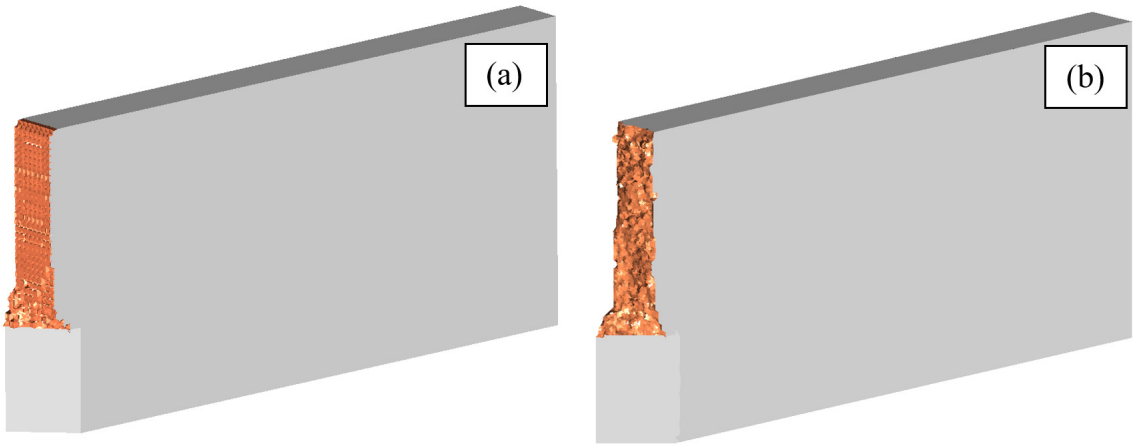

Figure 38. Crack surfaces of the three-point bending test on skew notched beam for (a) structured and (b) unstructured 3D tetrahedra mesh

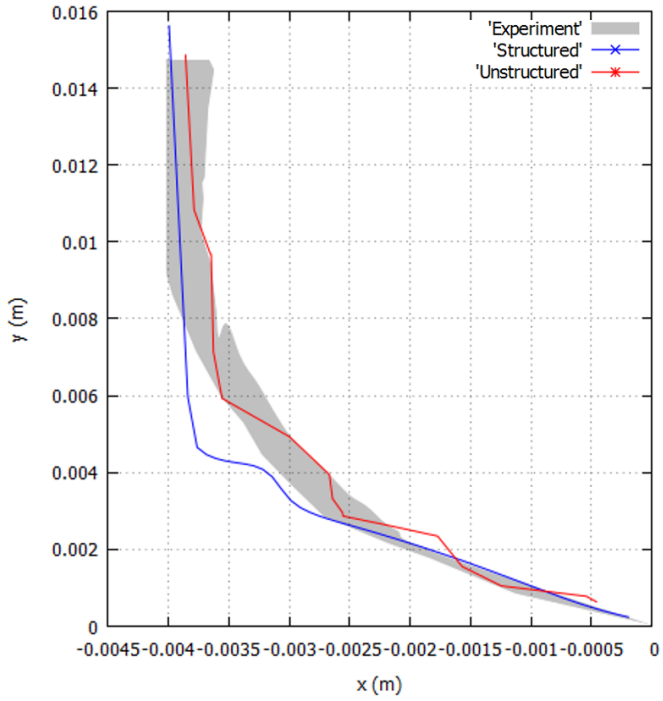

Figure 39. Crack paths of the three-point bending test on skew notched beam

In Figure 40, the crack surface computed in the simulations is compared to the one observed in the tests. The results are optimal within the spatial resolution of the considered meshes. Figure 38 to Figure 40 show that results with the structured and unstructured meshes are in good agreement with experiments as well as with the skew-symmetry conditions of the problem. Evolution of the crack surface is shown in Figure 41.

Detail of the evolution of the twist angle of the crack front with the height over the initial notch is shown in Figure 42. A distinct anti-symmetric crack trace along the straight crack front can be noticed. This is because of the combination of Mode I and the antisymmetric Mode III loading conditions along the initial notch. The initial crack plane is inclined 45º and ends at 90º and only Mode I along the final crack fronts.

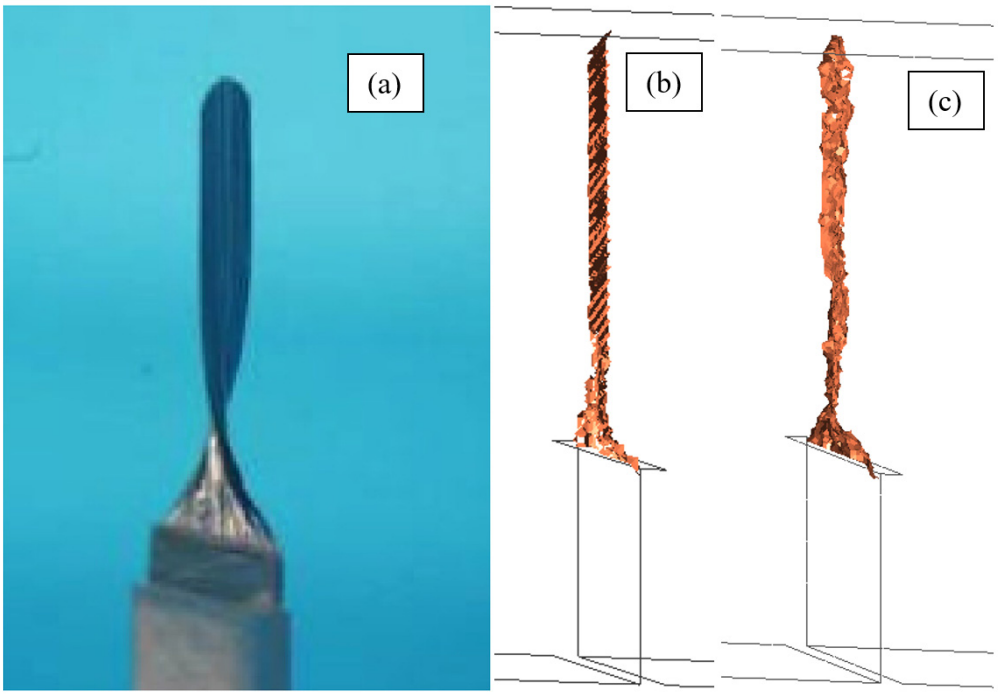

Figure 40. (a) Experimental [77] and computed crack surfaces with (b) structured and (c) unstructured meshes

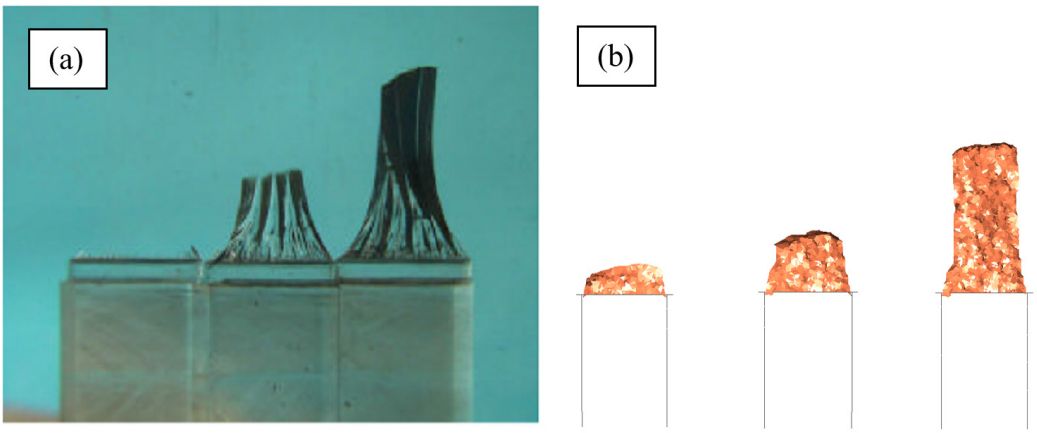

Figure 41. Evolution of the crack surface in (a) the experiment [77] and in (b) the present simulation

Figure 43 shows the crack propagation and evolution of major principal stresses in the skew notched beam. Once more, in the elastic range, stresses concentrate in the vicinity of the tip of the notch. This causes the crack to start and propagate through the height of the beam and towards the point of application of the load.

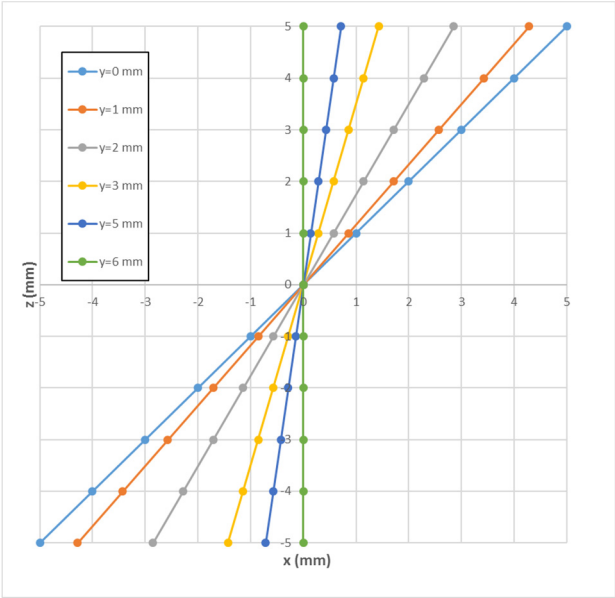

Figure 42. Computed evolution of the twist angle of the crack front with the height over the notch

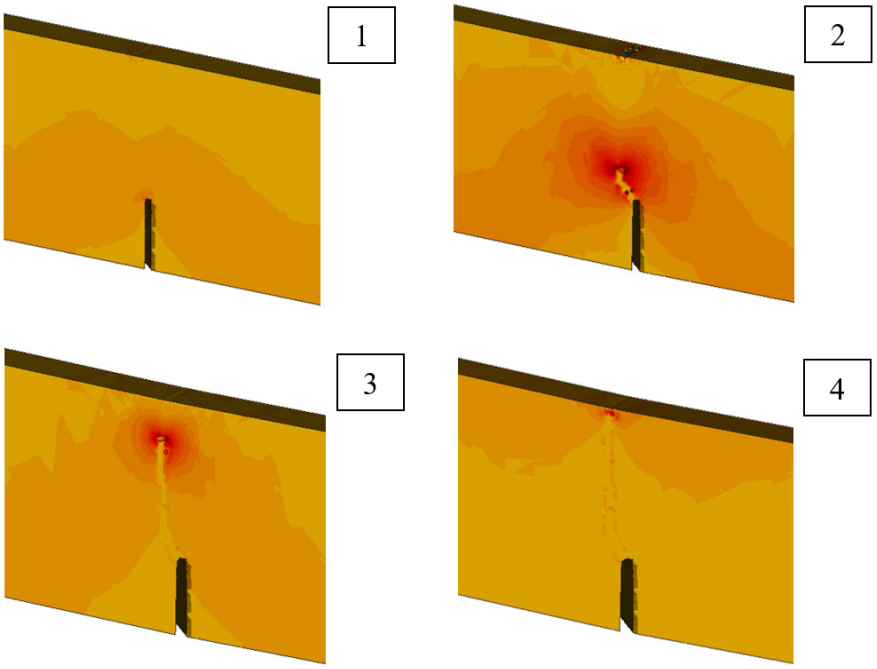

Figure 43. Crack propagation and evolution of major principal stresses in the three-point bending test on skew notched beam

5 Conclusions

In this work, the FE modeling of quasi-brittle cracks in 2D and 3D with enhanced strain accuracy is performed. To this end, a mixed strain/displacement formulation is presented, in a matrix and vector notation, based on Voigt's convention, in a ready-to-use format for its implementation in finite element codes. Then, experimental validation is performed by means of several simulations which are compared to experimental tests reported in the literature.

The proposed formulation is used in conjunction with an isotropic damage model suitable for the prediction of cracking in 2D and 3D applications. Finite element simulations using triangles, quadrilaterals, tetrahedra, hexahedra and prisms in structured, semi-structured and unstructured meshes are performed.

An extensive comparison with experimental data observed from the literature is carried out, to assess the capacity of the proposed formulation to model the behavior observed in the experimental tests. Several numerical simulations have been exhibited to illustrate the capacity of the formulation to solve strain localization problems in accordance to experimental results.

Problems involving propagation of single and multiple, straight and curved cracks in 2D and 3D, as well as non-planar cracks in 3D are addressed. Aspects related to the discrete solution, such as convergence regarding mesh resolution and mesh bias, as well as other related to the physical model, like structural size effect and the influence of Poisson's ratio, are also investigated.

The enhanced accuracy of the computed strain field leads to accurate results in terms of crack paths, failure mechanisms and force displacement curves. Spurious mesh dependency suffered by both continuous and discontinuous irreducible formulations is avoided by the mixed FE, without the need of auxiliary tracking techniques or other computational schemes that alter the continuum mechanical problem.

6 References

[1] Y. Rashid, "Ultimate strength analysis of prestressed concrete pressure vessels," *Nuclear Engineering and Design,* vol. 7, no. 4, pp. 334-344, 1968.

[2] Z. Bazant and B. Oh, "Crack band theory for fracture of concrete," *Matériaux et Constructions,* vol. 16, no. 3, pp. 155-177, 1983.

[3] J. Rots, P. Nauta and G. Kusters, "Variable reduction factor for the shear stiffness of cracked concrete," *Rep. BI-84-33, Institute TNO for Building Materials and Structures, Delft,* 1984.

[4] R. de Borst and P. Nauta, "Non-orthogonal cracks in a smeared finite element model," *Engineering. Computations,* vol. 2, pp. 35-46, 1985.

[5] R. de Borst, "Smeared cracking, plasticity, creep and thermal loading - a unified approach," *Computer Methods in Applied Mechanics and Engineering,* vol. 62, no. 99, pp. 89-110, 1987.

[6] Z. Bazant and G. Pijaudier-Cabot, "Nonlocal continum damage, localization instabilities and convergence," *Journal of Engineering Mechanics,* no. 55, pp. 287-293, 1988.

[7] R. Peerlings, R. de Borst, W. Brekelmans and J. de Wree, "Gradient enhanced damage for quasi brittle materials," *International Journal for Numerical Methods in Engineering,* vol. 39, pp. 3391-3403, 1996.

[8] R. de Borst and C. Verhoosel, "Gradient damage vs phase-field approaches for fracture: Similarities and differences.," *Computer Methods in Applied Mechanics and Engineering.,* p. doi: 10.1016/j.cma.2016.05.015, 2016.

[9] C. Miehe, F. Welschinger and M. Hofacker, "Thermodynamically consistent phase-field models of fracture: Variational principles and multi-field FE implementations," *International Journal for Numerical Methods in Engineering,* vol. 83, pp. 1273-1311, 2010.

[10] C. Miehe, L.-M. Schänzel and H. Ulmer, "Phase field modeling of fracture in multi-physics problems. Part I. Balance of cracks surface and failure criteria for brittle crack propagation in thermo-elastic solids," *Computer Methods in Applied Mechanics and Engineering,* vol. 294, pp. 449-485, 2015.

[11] J. Vignollet, S. May, R. de Borst and C. Verhoosel, "Phase-field model for brittle and cohesive fracture," *Meccanica,* vol. 49, pp. 2587-2601, 2014.

[12] J. Wu, "A unified phase-field theory for the mechanics of damage and quasi-brittle failure," *Journal of the Mechanics and Physics of Solids,* vol. 103, pp. 72-99, 2017.

[13] G. Barenblatt, "The mathematical theory of equilibrium cracks in brittle faillure," *Advanced Applied Mathematics,* vol. 7, pp. 55-129, 1962.

[14] D. Ngo and A. Scordelis, "Finite element analysis of reinforced concrete beams," *ACI Journal,* vol. 64, no. 14, pp. 152-163, 1967.

[15] P. Areias, M. Msekh and T. Rabczuk, "Damage and fracture algorithm using the screened Poisson equation and local remeshing," *Engineering Fracture Mechanics,* vol. 158, pp. 116-143, 2016.

[16] P. Areias and T. Rabczuk, "Finite strain fracture of plates and shells with configurational forces and edge rotations," *International Journal for Numerical Methods in Engineering,* vol. 94, pp. 1099-1122, 2013.

[17] P. Areias, T. Rabczuk and D. Dias-da-Costa, "Element-wise fracture algorithm based on rotation of edges," *Engineering fracture mechanics,* vol. 110, pp. 113-137, 2013.

[18] P. Areias, J. Reinoso, P. Camanho and T. Rabczuk, "A constitutive-based element-by-element crack propagation algorithm with local mesh refinement," *Computational Mechanics,* vol. 56, pp. 291-315, 2015.

[19] J. Schellekens, "A non-linear finite element approach for the analysis of mode-I free edge delamination in composites," *International Journal of Solids and Structures,* vol. 30, no. 9, pp. 1239-1253, 1993.

[20] O. Allix and P. Ladevèze, "Interlaminar interface modelling for the prediction of delamination," *Composite Structures,* vol. 22, no. 4, pp. 235-242, 1992.

[21] G. Bolzon and A. Corigliano, "A discrete formulation for elastic solids with damaging interfaces," *Computer Methods in Applied Mechanics and Engineering,* vol. 140, pp. 329-359, 1997.

[22] A. Pandolfi, P. Krysl and M. Ortiz, "Finite element simulation of ring expansion and fragmentation: The capturing of length and time scales through cohesive models of fracture," *International Journal of Fracture,* vol. 95, no. 1-4, pp. 279-297, 1999.

[23] E. Dvorkin, A. Cuitino and G. Gioia, "Finite elements with displacement interpolated embedded localization lines insensitive to mesh size and distorsions," *International Journal for Numerical Methods in Engineering,* vol. 30, pp. 541-564, 1990.

[24] J. Oliver, M. Cervera and O. Manzoli, "Strong discontinuities and continuum plasticity models: the strong discontinuity approach," *International Journal of Plasticity,* vol. 15, no. 3, pp. 319-351, 1999.

[25] T. Gasser and G. Holzapfel, "Geometrically non-linear and consistently linearized embedded strong discontinuity models for 3D problems with an application to the dissection analysis of soft biological tissues," *Computer Methods in Applied Mechanics and Engineering,* vol. 192, pp. 5059-5098, 2003.

[26] M. Motamedi, D. Weed and C. Foster, "Numerical simulation of mixed mode (I and II) fracture behaviour pf pre-cracked rock using the strong discontinuity approach," *International Journal of Solids and Structures,* Vols. 85-86, pp. 44-56, 2016.

[27] Y. Zhang, R. Lackner, M. Zeiml and H. Mang, "Strong discontinuity embedded approach with standard SOS formulation: Element formulation, energy-based crack tracking strategy, and validations," *Computer Methods in Applied Mechanics and Engineering,* vol. 287, pp. 335-366, 2015.

[28] X. Su, Z. Yang and G. Liu, "Finite element modelling of complex 3D static and dynamic crack propagation by embedding cohesive elements in Abaqus," *Acta Mecanica Solida Sinica,* vol. 23, no. 3, pp. 271-282, June 2010.

[29] N. Moes, J. Dolbow and T. Belytschko, "A finite element method for crack growth without remeshing," *International Journal for Numerical Methods in Engineering,* vol. 46, no. 1, pp. 131-150, 1999.

[30] T. Gasser and G. Holzapfel, "Modeling 3D crack propagation in unreinforced concrete using PUFEM," *Computer Methods in Applied Mechanics and Engineering,* vol. 194, pp. 2859-2896, 2005.

[31] M. Holl, T. Rogge, S. Loehnert, P. Wriggers and R. Rolfes, "3D multiscale crack propagation using the XFEM applied to a gas turbine blade," *Computational Mechanics,* vol. 53, pp. 173-188, 2014.

[32] G. Meschke and P. Dumstorff, "Energy-based modeling of cohesive and cohesion-less cracks via X-FEM," *Computer Methods in Applied Mechanics and Engineering,* vol. 196, pp. 2338-2357, 2007.

[33] J.-Y. Wu and F.-b. Li, "An improved stable X-FEM (Is-FEM) with a novel enrichment function for the computational modeling of cohesive cracks," *Computer Methods in Applied Mechanics and Engineering,* vol. 295, pp. 77-107, 2015.

[34] P. Areias and T. Belytschko, "Analysis of three-dimensional crack initiation and propagation using the extended finite element method," *International Journal for Numerical Methods in Engineering,* vol. 63, pp. 760-788, 2005.

[35] T. Rabczuk and T. Belytschko, "A three-dimensional large deformation meshfree method for arbitrary evolving cracks," *Computer Methods in Applied Mechanics and Engineering,* vol. 196, pp. 2777-2799, 2007.

[36] T. Rabczuk and T. Belytschko, "Adaptivity for structured meshfree particle methods in 2D and 3D," *International Journal for Numerical Methods in Engineering,* vol. 63, pp. 1559-1582, 2005.

[37] T. Rabczuk and T. Belytschko, "Cracking particles: a simplified meshfree method for arbitrary evolving cracks," *International Journal for Numerical Methods in Engineering,* vol. 61, pp. 2316-2343, 2004.

[38] X. Zhuang, C. Augarde and S. Bordas, "Accurate fracture modelling using meshless methods, the visibility criterion and level sets: Formulation and 2D modelling," *International Journal for Numerical Methods in Engineering,* vol. 86, pp. 249-268, 2011.

[39] X. Zhuang, C. Augarde and K. Mathisen, "Fracure modeling using meshless methods and level sets in 3D: framework and modeling," *International Journal for Numerical Methods in Engineering,* vol. 92, pp. 969-998, 2012.

[40] G. Nguyen, C. Nguyen, P. Nguyen, H. Bui and L. Shen, "A size-dependent constitutive modelling framework for localized faillure analysis," *Computational Mechanics,* vol. 58, pp. 257-280, DOI 10.1007/s00466-016-1293-z, 2016.

[41] C. Annavarapu, R. Settgast, E. Vitali and J. Morris, "A local crack-tracking strategy to model three-dimensional crack propagation with embedded methods," *Computer Methods in Applied Mechanics and Engineering,* vol. 311, pp. 815-837, 2016.

[42] P. Dumstorffz and G. Meschke, "Crack propagation criteria in the framework of X-FEM-based structural analysis," *International Journal for Numerical and Analytical Methods in Geomechanics,* vol. 31, pp. 239-259, 2007.

[43] J. Kim and F. Armero, "Three-dimensional finite elements with embedded strong discontinuities for the analysis of solids at faillure in the finite deformation range," *Computer Methods in Applied Mechanics and Engineering ,* no. http://dx.doi.org/10.1016/j.cma.2016.12.038, 2017.

[44] F. Riccardi, E. Kishta and B. Richard, "A step-by-step global crack-tracking approach in E-FEM simulations of quasi-brittle materials," *Engineering Fracture Mechanics,* vol. 170, pp. 44-58, 2017.

[45] D. Dias-da- Costa, J. Alfaiate, L. Sluys and Júlio E., "A comparative study on the modelling of discontinuous fracture by means of enriched nodal and element techniques and interface elements," *International Journal of Fracture,* vol. 161, no. 1, pp. 97-119, 2010.

[46] M. Jirasek, "Comparative study on finite elements with embedded discontinuities,". *Computer Methods in Applied Mechanics and Engineering,* vol. 188, pp. 307-330, 2000.

[47] T. Rabczuk, "Computational methods for fracture in brittle and quasi-brittle solids: state-of-the-art review and future perspectives," *ISRN Applied Mathematics,* p. DOI: 10.1155/2013/849231, 2013.

[48] M. Cervera, M. Chiumenti and R. Codina, "Mesh objective modelling of cracks using continuous linear strain and displacement interpolations," *International Journal for Numerical Methods in Engineering,* vol. 87, no. 10, pp. 962-987, 2011.

[49] M. Cervera, M. Chiumenti and R. Codina, "Mixed stabilized finite element methods in nonlinear solid mechanics. Part I: Formulation," *Computer Methods in Applied Mechanics and Engineering,* vol. 199, no. 37-40, pp. 2559-2570, 2010.

[50] M. Cervera, M. Chiumenti and R. Codina, "Mixed stabilized finite element methods in nonlinear solid mechanics. Part II: Strain localization," *Computer Methods in Applied Mechanics and Engineering,* vol. 199, no. 37-40, pp. 2571-2589, 2010.

[51] M. Cervera, M. Chiumenti, L. Benedetti and R. Codina, "Mixed stabilized finite element methods in nonlinear solid mechanics. Part III: Compressible and incompressible plasticity," *Computer Methods in Applied Mechanics and Engineering,* vol. 285, no. 0, pp. 752-775, 2015.

[52] A. Gil, C. Lee, J. Bonet and M. Aguirre, "A stabilized Petrov-Galerkin formulation for linear tetrahedral elements in compressible, nearly incompressible and truly incompressible fast dynamics," *Computer Methods in Applied Mechanics and Engineering,* vol. 276, pp. 659-690, 2014.

[53] N. Lafontaine, R. Rossi, M. Cervera and M. Chiumenti, "Explicit mixed strain-displacement finite element for dynamic geometrically non-linear solid mechanics," *Computational Mechanics,* vol. 55, pp. 543-559, 2015.

[54] M. Cervera and M. Chiumenti, "Size effect and localization in J2 plasticity," *International Journal of Solinds and Structures,* vol. 46, pp. 3301-3312, 2009.

[55] L. Benedetti, M. Cervera and M. Chiumenti, "3D modelling of twisting cracks under bending and torsion skew notched beams," *Engineering Fracture Mechanics,* vol. 176, pp. 235–256, 2017.

[56] M. Chiumenti, M. Cervera and R. Codina, "A mixed three-field FE formulation for stress accurate analysis including the incompressible limit," *Computer Methods in Applied Mechanics and Engineering,* vol. 283, pp. 1095-1116, 2014.

[57] E. Hellinger, "Die allegemeinen Ansätze der Mechanik der Kontinua, Art. 30," *Encyclopädie der Matematischen Wissenschaften, F. Klein and C. Muller (eds.), Leipzig, Teubner,* pp. 654-655, 1914.

[58] E. Reissner, "On variational principles of elasticity," *Proc. Symp. Appl. Math.,* vol. 8, pp. 1-6, 1958.

[59] O. Zienkiewicz, R. Taylor and Z. Zhu, "The finite element method, Vol. 1," *7th edition, Amsterdam, Elsevier Butterworth-Heinemann,* 1989.

[60] I. Babuska, "Error-bounds for finite element method," *Numerisch Mathematik,* vol. 16, pp. 322-333, 1971.

[61] D. Boffi, F. Brezzi and M. Fortin, "Mixed finite element methods and applications," *Springer,* 2013.

[62] F. Brezzi, "On the existence, uniqueness and approximation of saddle-point problems arising from lagrangian multipliers," *ESAIM: Mathematical Modelling and Numerical Analysis - Modélisation Mathématique et Analyse Numérique,* vol. 8, no. R2, pp. 129-151, 1974.

[63] R. Codina, "Stabilization of incompressibility and convection through orthogonal sub-scales in finite element methods," *Computer Methods in Applied Mechanics and Engineering ,* vol. 190, pp. 1579-1599, 2000.

[64] T. Hughes, G. Feijoo, L. Mazzei and J. Quincy, "The variational multiscale method - a paradigm for computational mechanics," *Computer Methods in Applied Mechanics and Engineering,* vol. 166, pp. 3-24, 1998.

[65] T. Hughes, L. Franca and M. Balestra, "A new finite element formulation for computational fluid dynamics: V. Circumventing the Babuska-Brezzi condition: A stable Petrov-Galerkin formulation of the stokes problem accomodating equal-order interpolations," *Computer Methods in Applied Mechanics and Engineering,* vol. 59, no. 1, pp. 85-99, 1986.

[66] M. Cervera, C. Agelet de Saracibar and M. Chiumenti, "COMET: Coupled mechanical and thermal analysis. Data input manuel, Version 5.0, Technical report IT-308. Available from http://www.cimne.upc.edu," 2002.

[67] "GiD: the personal pre and post-processor.," *CIMNE, Technical University of Catalonia,* p. <http://gid.cimne.upc.ed>, 2002.

[68] B. Winkler, "Traglastuntersuchungen von unbewehrten und bewerhrten Betonskrukturen auf der Grundlage eines objektiven Werkstoffgesetzes für Beton," Ph.D. Thesis, Universität Innsbruck*,* 2001.

[69] B. Trunk, "Einfluss der Bauteilgrösse auf die Bruchenergie von Beton," *Aedificatio publishers, Freiburg,* 2000.

[70] J. Gálvez, M. Elices, G. Guinea and J. Planas, "Mixed mode fracture of concrete under proportional and nonproportional loading," *International Journal of Fracture,* vol. 94, pp. 267-84, 1998.

[71] M. Cervera, L. Pela, R. Clemente and P. Roca, "A crack-tracking technique for localized damage in quasi-brittle materials," *Engineering Fracture Mechanics,* vol. 77, pp. 2431-2450, 2010.

[72] A. Ingraffea and M. Grigoriu, "Probabilistic fracture mechanics: A validation predictive capability," *Technical report, DTIC Document,* 1990.

[73] C. Miehe and E. Gürses, "A robust algorithm for the configurational-force-driven brittle crack propagation with R-adaptative mesh alignment," *International Journal for Numerical Methods in Engineering,* vol. 72, pp. 127-155, 2007.

[74] P. Bocca, A. Carpinteri and S. Valente, "Mixed mode fracture of concrete," *International Journal of Solids and Structures,* vol. 27, no. 9, pp. 1139-1153, 1991.

[75] A. Saleh and M. Aliabadi, "Crack growth analysis in concrete using boundary element method," *Engineering Fracture Mechanics,* vol. 51, no. 4, pp. 533-545, 1995.

[76] P. Areias, T. Rabczuk and J. César de Sá, "A novel two-stage discrete crack method based on the screened Poisson equation and local mesh refinement," *Computational Mechanics,* vol. 58, pp. 1003-1018, 2016.

[77] F. Buchholz, A. Chergui and H. Richard, "Fracture analyses and experimental results of crack growth under general mixed mode loading conditions," *Engineering Fracture Mechanics,* vol. 71, pp. 455-468, 2004.

[78] R. Citarella and F. Buchholz, "Comparison of crack growth simulation by DBEM and FEM for SEN-specimens undergoing torsion or bending loading," *Engineering Fracture Mechanics,* vol. 75, pp. 489-509, 2008.

[79] G. Ferte, P. Massin and N. Moës, "3D crack propagation with cohesive elements in the extended finite element method," *Computer Methods in Applied Mechanics and Engineering,* vol. 300, pp. 347-374, 2016.

Appraisement of planar, bending and twisting cracks in 3D with isotropic and orthotropic damage models

G. B. Barbat, M. Cervera and M. Chiumenti

International Journal of Fracture

Vol. 210, issue 1-2, pp. 45-79, (2018)

https://doi.org/10.1007/s10704-018-0261-3

Appraisement of planar, bending and twisting cracks in 3D with isotropic and orthotropic damage models

G. B. Barbat, M. Cervera and M. Chiumenti

International Center for Numerical Methods in Engineering (CIMNE)

Technical University of Catalonia – BarcelonaTECH

Edificio C1, Campus Norte, Jordi Girona 1-3

08034 Barcelona, Spain

gbarbat@cimne.upc.edu, miguel.cervera@upc.edu, michele@cimne.upc.edu

Abstract

This paper discusses the modeling of cracking in quasi-brittle materials using isotropic and orthotropic damage constitutive laws. A mixed strain/displacement finite element formulation is used, taking advantage of its enhanced precision and its enforced interelemental strain continuity. On the one hand, this formulation avoids the spurious mesh dependency of the computed solution associated to standard elements and does not require the use of tracking techniques. On the other hand, it greatly alleviates the spurious stress locking associated to the use of orthotropic models on standard finite elements.

The performance of several isotropic and orthotropic damage constitutive laws is assessed through an extensive comparison with analytical solutions, numerical tests and experimental evidence reported in the literature. The behavior of the different damage models in terms of crack surface, collapse mechanism and force displacement curves is investigated performing 3D analyses in several conditions including Mode I, Mixed Mode and Mode III fracture.

When performing the appraisement of planar, bending and twisting cracks, the enhanced accuracy of the mixed formulation allows for a distinct assessment of the several damage models considered. Aspects related to the behavior of damage models, such as the influence of Poisson's ratio, the shape of the damage surface and the adoption of isotropic and orthotropic models are investigated and noteworthy conclusions are drawn.

Keywords: Damage, Isotropy, Orthotropy, Constitutive law, Cracking, Mixed Finite Elements, Strain Localization

1 Introduction

Classical orthotropic crack models developed in the early 1970s for the modeling of cracking in concrete were largely abandoned in the late 1990s due, among others, to issues of spurious stress locking that made their use unreliable [1, 2]. Fixed Crack [3] and Rotating Crack Models [4, 5], as well as Multiple Fixed Crack [6, 7] and Microplane Models [8, 9], were proposed in the three in-between decades. For more details on those crack models the review of references [1, 10-15] is suggested. Spurious stress transfer brings in spurious energy dissipation and the associated stress locking during the cracking process and hamstrings the formation of realistic failure mechanisms. These serious hindrances are partly avoided by adopting isotropic damage models, where the inadequacy of the kinematical description of standard finite elements does not show in the stress field [2, 16-19]. Nowadays, isotropic damage has been adopted as a standard practice in the modeling of quasi-brittle materials.

Regretfully, the adoption of isotropic models is far from solving the problem of FE modeling of cracking. On the one hand, it is well established that the standard FE formulation produces mesh-biased results in many situations, due to its local lack of convergence in quasi-singular situations [20, 21]. On the other hand, an isotropic description of damage is not adequate for certain applications. For example, orthotropic models are needed in cyclic loading problems to take microcrack closure-reopening (MCR) effects into account [22].

Recently, mixed finite elements have been reexamined by [20, 21, 23-25] to deal with cracking problems. Mixed finite element formulations have proved to be a remedy for spurious mesh dependency and lack of convergence of the computed solution when using standard finite elements. The use of mixed FE formulations for solid mechanics problems results in an improvement over standard finite element formulations in terms of computed stress and strain fields accuracy both in linear and nonlinear scenarios. In mixed formulations, the strain is approximated independently from the displacement field, instead of being obtained from local discrete differentiation at element level. In this way, more accurate stress and strain fields are quantified, resulting in a more precise computation of the nonlinear behavior, particularly for low order FE. This is decisive in the numerical solution of strain localization problems, as mesh-bias independent outcomes are obtained without the need of auxiliary crack tracking techniques.

The mixed finite element technology has proved to be able to solve many of the problems related to standard elements. In [25], quasi-brittle cracks were modelled in 2D and 3D using several isotropic models. The use of an independent approximation for the strain field enforces the continuity of strains in the computed solution, whereas strains are inter-element discontinuous in standard FE. Strain continuity is crucial in alleviating the spurious stress locking that made the use of orthotropic models unpractical in the past decades. The enhanced accuracy of mixed finite elements allows now to reconsider the use of orthotropic damage constitutive laws in cracking models.

Therefore, the objectives of this paper are: (1) to assess the performance of several isotropic and orthotropic damage models to solve cracking problems in mode I, mixed mode and mode III loading, (2) to show that different models, and even the isotropic and orthotropic versions of the same model, produce different crack patterns for a given loading, (3) to demonstrate the capability of the mixed finite element formulation in successfully incorporating orthotropic damage models, as a consequence of their enforced strain continuity and enhanced accuracy. To attain these objectives, an exhaustive validation of the models is performed using theoretical results and experimental data from the literature.

The outline of this paper is as follows: in section 2, the isotropic and orthotropic damage constitutive laws considered in this article are presented, to be used in conjunction with the mixed

finite element formulation summarized in section 3. Section 4 presents numerical simulations performed in 3D where the performance of the constitutive laws is examined. Finally, the conclusions of the study are presented.

2 Isotropic and orthotropic constitutive damage models

In this section, the several constitutive damage models considered in this article are described. Using Voigt's convention, the strain and stress tensors, $\boldsymbol{\varepsilon}$ and $\boldsymbol{\sigma}$, are expressed as vectors [26]. In 3D analysis the strain vector $\boldsymbol{\varepsilon} = \left(\varepsilon_x, \varepsilon_y, \varepsilon_z, \gamma_{xy}, \gamma_{yz}, \gamma_{xz}\right)^T$ has 6 components. Correspondingly, the stress $\boldsymbol{\sigma}$ is also a vector with 6 components, $\boldsymbol{\sigma} = \left(\sigma_x, \sigma_y, \sigma_z, \tau_{xy}, \tau_{yz}, \tau_{xz}\right)^T$. The stress $\boldsymbol{\sigma}$ and the strain $\boldsymbol{\varepsilon}$ are linked through the constitutive equation:

$$\boldsymbol{\sigma} = \mathbf{D}_s \boldsymbol{\varepsilon} \tag{1}$$

where $\mathbf{D}_s$ is the secant constitutive matrix, which has to be symmetric and positive semidefinite from thermodynamic considerations. In damage models $\mathbf{D}_s$ is a function of a set of internal variables $\boldsymbol{d}$ that describe the degradation of the material such that

$$\mathbf{D}_s = \mathbf{D}_s(\boldsymbol{d}) \tag{2}$$

The material parameters of the damage models used in the paper are those standard for isotropic materials with tensile failure: undamaged Young's modulus E and Poisson's ratio ν, tensile strength f_t and fracture energy G_f. The Drucker-Prager criterion requires also the specification of the compressive strength f_c.

2.1 Isotropic damage models

In isotropic damage, the secant constitutive matrix $\mathbf{D}_s$ of equation (2) can be written as

$$\mathbf{D}_s = (1-d)\mathbf{D}_0 = (1-d)\begin{pmatrix} D_{11} & D_{12} & D_{13} & & & \\ D_{21} & D_{22} & D_{23} & & \mathbf{0} & \\ D_{31} & D_{32} & D_{33} & & & \\ & & & G_{12} & & \\ & \mathbf{0} & & & G_{13} & \\ & & & & & G_{23} \end{pmatrix} \tag{3}$$

where d is the internal damage index and $\mathbf{D}_0$ is the elastic constitutive matrix for homogeneous materials such that

$$\begin{aligned} D_{11} = D_{22} = D_{33} &= \frac{E(1-\nu)}{(1+\nu)(1-2\nu)} \\ D_{12} = D_{21} = D_{13} = D_{31} = D_{23} = D_{32} &= \frac{E\nu}{(1+\nu)(1-2\nu)} \\ G_{12} = G_{13} = G_{23} &= \frac{E}{2(1+\nu)} \end{aligned} \tag{4}$$

where E and ν are the undamaged elastic values of Young's modulus and Poisson's ratio respectively.

The damage index d is an internal variable that measures the loss of stiffness of the material and it ranges $0 \leq d \leq 1$.

From equations (1) and (3), the constitutive equation of an isotropic damage model can be written as

$$\boldsymbol{\sigma} = (1-d)\,\mathbf{D}_0\boldsymbol{\varepsilon} = (1-d)\,\overline{\boldsymbol{\sigma}} \tag{5}$$

where the effective stress $\overline{\boldsymbol{\sigma}}$ is introduced as $\overline{\boldsymbol{\sigma}} = \mathbf{D}_0\boldsymbol{\varepsilon}$, corresponding to the hypothesis of strain equivalence [21].

The damage criterion, $\mathbb{F}$, is defined as

$$\mathbb{F}\left(\sigma_{eq}, r\right) = \sigma_{eq}(\overline{\boldsymbol{\sigma}}) - r \leq 0 \tag{6}$$

where $\sigma_{eq}(\overline{\boldsymbol{\sigma}})$ is the equivalent effective stress, and r is the current stress-like damage threshold. For tensile cracking the initial value of the damage threshold is taken as the tensile strength of the material, $r_0 = f_t$.

From the Kuhn-Tucker optimality and consistency conditions, the current value of the damage threshold is explicitly updated as

$$r = \max\,\left(r_0, \max \sigma_{eq}(\hat{t})\right) \quad \hat{t} \in [0, t] \tag{7}$$

This guarantees the irreversibility of damage and the positiveness of the dissipation [21]. The evolution of the damage index is defined by the exponential function

$$d = d(r) = 1 - \frac{r_0}{r}\exp\left(-2H_S\left(\frac{\langle r - r_0\rangle}{r_0}\right)\right) \tag{8}$$

where H_S is the positive softening parameter, which controls the rate of material degradation.

In FE simulations of quasi-brittle failure [20, 24] following the smeared (or crack band) approach, the softening parameter is linked to the material fracture energy G_f, which is a property of the material, in the following way:

$$H_S = \frac{\overline{H}_S b}{1 - \overline{H}_S b} \tag{9}$$

where b is the bandwidth of the smeared crack and $\overline{H}_S$ is the inverse of the material length $\mathcal{L}$

$$\overline{H}_S{}^{-1} = \mathcal{L} = \frac{2EG_f}{(f_t)^2} \tag{10}$$

f_t being the tensile strength and E the Young's modulus. In this work, the bandwidth of the localized cracks is taken as

$$b = (1-\tau_\varepsilon)2h + \tau_\varepsilon h = (2-\tau_\varepsilon)h \tag{11}$$

where h is the finite element size and τ_ε is the stabilization parameter with value $0 \leq \tau_\varepsilon \leq 1$. This is consistent with the approximation adopted for the discrete strain field in the mixed formulation, see equation (38).

Damage criteria

This article centers in the assessment of the relative performance of several damage models. Consequently, the effective equivalent stress $\sigma_{eq}(\overline{\boldsymbol{\sigma}})$ is defined through different criteria. Specifically, the Beltrami, Modified Beltrami, Positive Beltrami, Rankine and Drucker-Prager criteria are considered.

- ***Beltrami***

$$\sigma_{eq}(\bar{\boldsymbol{\sigma}}) = \sqrt{(\bar{\sigma}_1)^2 + (\bar{\sigma}_2)^2 + (\bar{\sigma}_3)^2 - 2\nu(\bar{\sigma}_1\bar{\sigma}_2 + \bar{\sigma}_1\bar{\sigma}_3 + \bar{\sigma}_2\bar{\sigma}_3)} \tag{12}$$

where $\bar{\sigma}_1$, $\bar{\sigma}_2$ and $\bar{\sigma}_3$ are the major principal stresses and ν is the Poisson ratio.

The Beltrami criterion considers effective (ordered according to their value) tensile and compressive stresses equally; therefore, this criterion is adequate only for materials with similar tensile and compressive strength.

Beltrami's equivalent stress in equation (12) is the one used in the Simo and Ju damage model [27] and it is defined as $\sigma_{eq} = \sqrt{2\Psi_0} = \sqrt{\bar{\boldsymbol{\sigma}}\mathbf{D}_0^{-1}\bar{\boldsymbol{\sigma}}}$ where Ψ_0 is the Helmholtz free energy per unit of volume of the undamaged material.

The criterion is similar to the well-known Von Mises criterion, where

$$\sigma_{eq}(\bar{\boldsymbol{\sigma}}) = \sqrt{(\bar{\sigma}_1)^2 + (\bar{\sigma}_2)^2 + (\bar{\sigma}_3)^2 - (\bar{\sigma}_1\bar{\sigma}_2 + \bar{\sigma}_1\bar{\sigma}_3 + \bar{\sigma}_2\bar{\sigma}_3)} \tag{13}$$

but is not purely isochoric.

- ***Positive Beltrami***

$$\sigma_{eq}(\bar{\boldsymbol{\sigma}}) = \sqrt{(\langle\bar{\sigma}_1\rangle)^2 + (\langle\bar{\sigma}_2\rangle)^2 + (\langle\bar{\sigma}_3\rangle)^2 - 2\nu(\langle\bar{\sigma}_1\rangle\langle\bar{\sigma}_2\rangle + \langle\bar{\sigma}_1\rangle\langle\bar{\sigma}_3\rangle + \langle\bar{\sigma}_2\rangle\langle\bar{\sigma}_3\rangle)} \tag{14}$$

where $\langle\cdot\rangle$ are the Macaulay brackets, such that $\langle x\rangle = x \quad if \;\; x \geq 0, \quad 0 \quad if \;\; x < 0$.

This criterion is introduced to consider only damage under tensile (positive) stresses, so that damage is driven by the positive part of the Helmholtz free energy $\sigma_{eq} = \sqrt{2\Psi_0^+} = \sqrt{\bar{\boldsymbol{\sigma}}^+\mathbf{D}_0^{-1}\bar{\boldsymbol{\sigma}}^+}$ being $\bar{\boldsymbol{\sigma}}^+$ the vector that contains the positive part of the effective stresses, $\bar{\boldsymbol{\sigma}}^+ = (\langle\bar{\sigma}_1\rangle \quad \langle\bar{\sigma}_2\rangle \quad \langle\bar{\sigma}_3\rangle \quad 0 \quad 0 \quad 0)^{\boldsymbol{T}}$.

- ***Modified Beltrami***

A modification of the Beltrami model is considered in reference [28], in which Poisson's effect is accounted for differently in the evaluation of the equivalent stress and the computation of the constitutive matrix. The equivalent stress is

$$\sigma_{eq}(\bar{\boldsymbol{\sigma}}) = \sqrt{(\bar{\sigma}_1)^2 + (\bar{\sigma}_2)^2 + (\bar{\sigma}_3)^2} \tag{15}$$

The secant constitutive matrix is similar to that in equation (3):

$$D_{11} = D_{22} = D_{33} = \frac{E(1-\tilde{\nu})}{(1+\tilde{\nu})(1-2\tilde{\nu})}$$

$$D_{12} = D_{21} = D_{13} = D_{31} = D_{23} = D_{32} = \frac{E\tilde{\nu}}{(1+\tilde{\nu})(1-2\tilde{\nu})} \tag{16}$$

$$G_{12} = G_{13} = G_{23} = \frac{E}{2(1+\tilde{\nu})}$$

and the term $\tilde{\nu}$ is defined as $\tilde{\nu} = (1-d)\nu$.

A modified positive Beltrami criterion can also be defined.

- ***Rankine***

$$\sigma_{eq}(\bar{\boldsymbol{\sigma}}) = \langle\bar{\sigma}_1\rangle \tag{17}$$

where $\bar{\sigma}_1$ is the major principal effective stress. This criterion is also introduced with the objective of taking into account only tensile damage.

- ***Drucker-Prager***

$$\sigma_{eq}(\bar{\boldsymbol{\sigma}}) = \frac{3}{3+\tan\phi}\left(\sqrt{3J_2} + \tan\phi\,\frac{I_1}{3}\right) \tag{18}$$

where I_1 and J_2 are the first and second effective stress invariants, which are expressed in terms of the principal stresses as

$$\begin{aligned} I_1 &= (\bar{\sigma}_1 + \bar{\sigma}_2 + \bar{\sigma}_3) \\ J_2 &= \frac{1}{6}[(\bar{\sigma}_1 - \bar{\sigma}_2)^2 + (\bar{\sigma}_2 - \bar{\sigma}_3)^2 + (\bar{\sigma}_3 - \bar{\sigma}_1)^2] \end{aligned} \tag{19}$$

and ϕ is the internal friction angle of the material. The friction angle ϕ can be related to the uniaxial tensile and compressive strengths, f_t and f_c, as

$$\tan\phi = 3\,\frac{f_c - f_t}{f_c + f_t} \tag{20}$$

This criterion is appropriate for materials with different strengths for traction and compression and subjected to mixed mode loading.

2.2 Orthotropic damage models

In this article, orthotropic damage models with 3 independent damage indices, one for each principal direction of effective strain and stress, are also considered. Such symmetric orthotropic models are formulated using the hypothesis of energy equivalence [22, 29-31]. Equation (2) can be particularized for the orthotropic damage models as

$$\mathbf{D}_s = \mathbf{D}_s(\boldsymbol{d}) = \begin{pmatrix} D_{11}(d_1) & D_{12}(d_1,d_2) & D_{13}(d_1,d_3) & & & \\ D_{21}(d_1,d_2) & D_{22}(d_2) & D_{23}(d_2,d_3) & & \mathbf{0} & \\ D_{31}(d_1,d_3) & D_{32}(d_2,d_3) & D_{33}(d_3) & & & \\ & & & G_{12}(d_1,d_2) & & \\ & \mathbf{0} & & & G_{13}(d_1,d_3) & \\ & & & & & G_{23}(d_2,d_3) \end{pmatrix} \tag{21}$$

such that

$$\begin{aligned} D_{ii} &= (1-d_i)\frac{E(1-\nu)}{(1+\nu)(1-2\nu)} \quad ; \quad i = 1,3 \\ D_{ij} &= \sqrt{(1-d_i)(1-d_j)}\,\frac{E\nu}{(1+\nu)(1-2\nu)} \quad ; \quad i,j = 1,3 \quad i \neq j \\ G_{ij} &= \sqrt{(1-d_i)(1-d_j)}\,\frac{E}{2(1+\nu)} \quad ; \quad i,j = 1,3 \quad i \neq j \end{aligned} \tag{22}$$

where E and ν are the undamaged initial elastic values of Young's modulus and Poisson's ratio. Note that the secant matrix $\mathbf{D}_s$ is symmetric.

The damage indices d_1, d_2 and d_3 are linked to each of the principal directions of effective stress, $\bar{\sigma}_1$, $\bar{\sigma}_2$ and $\bar{\sigma}_3$, respectively. For evaluating the damage indices d_i; $i = 1,3$, damage threshold functions, r_i, and equivalent stresses $\sigma_{eq,i}$ are evaluated in each direction independently.

The damage criteria are

$$\mathbb{F}_i\left(\sigma_{eq,i}\,, r_i\right) = \sigma_{eq,i}(\bar{\boldsymbol{\sigma}}) - r_i \leq 0 \tag{23}$$

Damage thresholds are evaluated as

$$r_i = \max\,\left(r_0, \max \sigma_{eq,i}(\hat{t})\right) \quad \hat{t} \in [0, t] \tag{24}$$

similarly to equation (7). The corresponding damage indices d_i are calculated as

$$d_i = d_i(r_i) = 1 - \frac{r_0}{r_i}\exp\left(-2H_S\left(\frac{\langle r_i - r_0\rangle}{r_0}\right)\right) \tag{25}$$

where H_S is the parameter evaluated according to equations (9)-(11).

The orthotropic model laid out here falls within the rotating crack approach; “fixed” orthotropic damage models may also be considered [22].

The equivalent stress in each direction $\sigma_{eq,i}(\bar{\boldsymbol{\sigma}})$, according to the several criteria, are

- ***Beltrami***

$$\begin{aligned} \sigma_{eq,1} &= \sqrt{(\bar{\sigma}_1)^2 + (\bar{\sigma}_2)^2 + (\bar{\sigma}_3)^2 - 2\nu(\bar{\sigma}_1\bar{\sigma}_2 + \bar{\sigma}_1\bar{\sigma}_3 + \bar{\sigma}_2\bar{\sigma}_3)} \\ \sigma_{eq,2} &= 0 \\ \sigma_{eq,3} &= 0 \end{aligned} \tag{26}$$

so that damage affects only the direction of the maximum principal stress.

- ***Rankine***

$$\sigma_{eq,i} = \langle \bar{\sigma}_i \rangle \tag{27}$$

Like in its isotropic form, the orthotropic Rankine damage model is only sensitive to tensile stresses, but considers each principal direction indepently.

- ***Drucker-Prager***

$$\sigma_{eq,i} = \begin{cases} \dfrac{3}{3 + \tan\phi} \cdot \left(\sqrt{3J_2} + \tan\phi\,\dfrac{I_1}{3}\right) & if\ \bar{\sigma}_i \geq 0 \\ 0 & if\ \bar{\sigma}_i < 0 \end{cases} \tag{28}$$

In this criterion, damage only evolves in the directions where the corresponding principal stress is positive.

3 Mixed FE for strain localization

In this section, the adopted mixed finite element formulation is introduced. This formulation is presented in detail in reference [25]. For more details, references [20, 21, 24, 32] are suggested.

The mixed finite element formulation here presented fits into the continuous approach, as the crack is represented at constitutive level using the damage models detailed in Section 2. Therefore, the separation between the two opposite sides of the crack is modelled through continuous (linear) displacement and strain fields [25].

In the considered mixed FE formulation, the variational form of the nonlinear solid mechanics problem is cast in terms of the displacement $\boldsymbol{u}$ and the strain $\boldsymbol{\varepsilon}$ fields. Matrix and vector notation based on Voigt's convention for symmetric tensors is adopted, as customarily used in FE literature and in codes. Writing the problem in matrix form, $\boldsymbol{u}$ and $\boldsymbol{\varepsilon}$ are expressed in Voigt's convention as vectors. Details of the algebraic system of equations are given in [25].

The strain and displacement fields are locally related through the compatibility equation [26]

$$\boldsymbol{\varepsilon} = \boldsymbol{S}\boldsymbol{u} \tag{29}$$

where $\boldsymbol{S}$ is the differential symmetric gradient operator. Correspondingly, the stress vector $\boldsymbol{\sigma}$ and the body forces vector $\mathbf{f}$ are linked through Cauchy's equilibrium equation of a body, written in matrix form as

$$\boldsymbol{S}^T\boldsymbol{\sigma} + \mathbf{f} = \mathbf{0} \tag{30}$$

where $\boldsymbol{S}^T$ is the differential divergence operator, adjoint to the $\boldsymbol{S}$ in (29). The stress vector $\boldsymbol{\sigma}$ and the strain vector $\boldsymbol{\varepsilon}$ are linked by the constitutive equation:

$$\boldsymbol{\sigma} = \mathbf{D}_s\boldsymbol{\varepsilon} \tag{31}$$

where $\mathbf{D}_s$ is the secant constitutive matrix.

Pre-multiplying equation (29) by the secant constitutive matrix $\mathbf{D}_s$ and substituting equation (31) into equation (30) results in the mixed system of equations

$$-\mathbf{D}_s\boldsymbol{\varepsilon} + \mathbf{D}_s\boldsymbol{S}\boldsymbol{u} = \mathbf{0} \tag{32}$$

$$\boldsymbol{S}^T(\mathbf{D}_s\boldsymbol{\varepsilon}) + \mathbf{f} = \mathbf{0} \tag{33}$$

The system of equations (32)-(33) is the strong form of the mixed $\boldsymbol{\varepsilon}/\boldsymbol{u}$ formulation, completed with the proper boundary conditions.

The corresponding weak form in (34)-(35) is obtained by multiplying equation (32) by an arbitrary virtual strain $\delta\boldsymbol{\varepsilon}$ and multiplying equation (33) by an arbitrary displacement vector $\delta\boldsymbol{u}$. The system is then integrated over the spatial domain and the Divergence Theorem is used in the right hand side of the second integral operation. The resulting variational form is

$$-\int_\Omega \delta\boldsymbol{\varepsilon}^T\mathbf{D}_s\boldsymbol{\varepsilon}\,\mathrm{d}\Omega + \int_\Omega \delta\boldsymbol{\varepsilon}^T\mathbf{D}_s\delta\boldsymbol{u}\,\mathrm{d}\Omega = 0 \quad \forall\delta\boldsymbol{\varepsilon} \tag{34}$$

$$\int_\Omega (\boldsymbol{S}\delta\boldsymbol{u})^T(\mathbf{D}_s\boldsymbol{\varepsilon})\,\mathrm{d}\Omega = \int_\Omega \delta\boldsymbol{u}^T\mathbf{f}\,\mathrm{d}\Omega + \int_{\Gamma_t} \delta\boldsymbol{u}^T\bar{\boldsymbol{t}}\,\mathrm{d}\Gamma \quad \forall\delta\boldsymbol{u} \tag{35}$$

The mixed problem to be solved is to find the unknowns $\boldsymbol{u}$ and $\boldsymbol{\varepsilon}$ that verify the system of equations composed by (34) and (35) and that verify the boundary condition $\boldsymbol{u} = \mathbf{0}$ on Γ_u given the arbitrary virtual displacement $\delta\boldsymbol{u}$**,** which vanishes on the Dirichlet boundary Γ_u and arbitrary virtual strain $\delta\boldsymbol{\varepsilon}$. Note that this variational problem is symmetric if $\mathbf{D}_\mathbf{s}$ is symmetric.

The FE discrete form of the mixed problem is obtained by discretizing the domain in FE, so that $\Omega = \cup\,\Omega_e$, and substituting the displacement $\boldsymbol{u}$ and the strain $\boldsymbol{\varepsilon}$ with the FE discrete approximations $\widehat{\boldsymbol{u}}$ and $\hat{\boldsymbol{\varepsilon}}$ defined element-wise as

$$\boldsymbol{u} \cong \widehat{\boldsymbol{u}} = \boldsymbol{N}_u\boldsymbol{U} \tag{36}$$

$$\boldsymbol{\varepsilon} \cong \hat{\boldsymbol{\varepsilon}} = \boldsymbol{N}_\varepsilon\boldsymbol{E} \tag{37}$$

where $\boldsymbol{U}$ and $\boldsymbol{E}$ are vectors containing the values of the displacements and the strains at the nodes of the finite element mesh. $\boldsymbol{N}_u$ and $\boldsymbol{N}_\varepsilon$ are the matrices containing the interpolation functions adopted in the FE approximation.

To ensure solvability (i.e. uniqueness) and stability of the solution in the system of equations, the interpolation functions in (36)-(37) must satisfy the Inf-Sup condition. This requirement is not fulfilled if equal interpolations are used for strains and displacements. In such case, the solution is unstable, and spurious oscillations may appear in the discrete displacement field. To be able to circumvent the strictness of the Inf-Sup condition and to use linear approximations both for displacements and strains a stabilization procedure is necessary to provide stability to the mixed discrete formulation. The stabilization procedure consists in the modification of the discrete variational form using the Orthogonal Subscales Method, introduced within the framework of the Variational Multiscale Stabilization methods and adopted herein.

The basic idea of the stabilization procedure is to substitute the approximation of the discrete strain in equation (37) by the following stabilized discrete field

$$\boldsymbol{\varepsilon} \cong \hat{\boldsymbol{\varepsilon}} = \boldsymbol{N}_\varepsilon \boldsymbol{E} + \tau_\varepsilon (\boldsymbol{B}_u \boldsymbol{U} - \boldsymbol{N}_\varepsilon \boldsymbol{E}) = (1 - \tau_\varepsilon) \boldsymbol{N}_\varepsilon \boldsymbol{E} + \tau_\varepsilon \boldsymbol{B}_u \boldsymbol{U} \tag{38}$$

where τ_ε is a stabilization parameter with value $0 \leq \tau_\varepsilon \leq 1$. Note that for $\tau_\varepsilon = 1$, the strain interpolation of the standard irreducible formulation is recovered:

$$\boldsymbol{\varepsilon} \cong \hat{\boldsymbol{\varepsilon}} = \boldsymbol{B}_u \boldsymbol{U} \tag{39}$$

where $\boldsymbol{B}_u$ is the discrete strain-displacement matrix defined as $\boldsymbol{B}_u = \boldsymbol{S}\boldsymbol{N}_u$. For a given FE mesh, the use of different stabilization parameter values yields slightly different results. However, the consistency of the stabilization technique guarantees convergence to the unique solution upon mesh refinement. Additional details are given in reference [25].

The resulting algebraic system of equations reads:

$$\begin{bmatrix} -\boldsymbol{M}_{\boldsymbol{\tau}} & \boldsymbol{G}_{\boldsymbol{\tau}} \\ \boldsymbol{G}_{\boldsymbol{\tau}}^T & \boldsymbol{K}_{\boldsymbol{\tau}} \end{bmatrix} \begin{bmatrix} \boldsymbol{E} \\ \boldsymbol{U} \end{bmatrix} = \begin{bmatrix} \boldsymbol{0} \\ \boldsymbol{F} \end{bmatrix} \tag{40}$$

such that $\boldsymbol{M}_{\boldsymbol{\tau}} = (1 - \tau_\varepsilon)\boldsymbol{M}$, $\boldsymbol{G}_{\boldsymbol{\tau}} = (1 - \tau_\varepsilon)\boldsymbol{G}$ and $\boldsymbol{K}_{\boldsymbol{\tau}} = \tau_\varepsilon \boldsymbol{K}$ with

$$\boldsymbol{M} = \int_\Omega \boldsymbol{N}_\varepsilon^T \mathbf{D}_S \boldsymbol{N}_\varepsilon \, \mathrm{d}\Omega \tag{41}$$

$$\boldsymbol{G} = \int_\Omega \boldsymbol{N}_\varepsilon^T \mathbf{D}_S \boldsymbol{B}_u \, \mathrm{d}\Omega \tag{42}$$

$$\boldsymbol{K} = \int_\Omega \boldsymbol{B}_u^T \mathbf{D}_S \boldsymbol{B}_u \, \mathrm{d}\Omega \tag{43}$$

$$\boldsymbol{F} = \int_\Omega \boldsymbol{N}_u^T \mathbf{f} \, \mathrm{d}\Omega + \int_{\Gamma_t} \boldsymbol{N}_u^T \bar{\boldsymbol{t}} \, \mathrm{d}\Gamma \tag{44}$$

where $[\boldsymbol{E} \quad \boldsymbol{U}]^T$ is the array of nodal values of strains and displacements. $\boldsymbol{M}$ is a mass like projection matrix, $\boldsymbol{G}$ is the discrete gradient matrix, $\boldsymbol{K}$ is the standard stiffness matrix and $\boldsymbol{F}$ is the vector of external nodal forces.

In the system (40), the nodal values $\boldsymbol{E}$ can be formally eliminated to write the solution in terms of the nodal displacements $\boldsymbol{U}$ only, as follows. From the first equation in (40), the nodal values for the strains $\boldsymbol{E}$ can be obtained as

$$\boldsymbol{E} = \boldsymbol{M}^{-1}\boldsymbol{G}\boldsymbol{U} \tag{45}$$

which can be substituted into the second equation to yield

$$\boldsymbol{U} = \left(\boldsymbol{G}_{\boldsymbol{\tau}}^{T}\boldsymbol{M}_{\boldsymbol{\tau}}^{-1}\boldsymbol{G}_{\boldsymbol{\tau}} + \boldsymbol{K}_{\boldsymbol{\tau}}\right)^{-1}\boldsymbol{F} \tag{46}$$

This defines $\boldsymbol{K}^{mix} = \boldsymbol{G}_{\boldsymbol{\tau}}^{T}\boldsymbol{M}_{\boldsymbol{\tau}}^{-1}\boldsymbol{G}_{\boldsymbol{\tau}} + \boldsymbol{K}_{\boldsymbol{\tau}}$ as the stiffness matrix of the enhanced mixed FE formulation. Note that this definition is only formal, as $\boldsymbol{K}^{mix}$ cannot be assembled in an element-by-element fashion, nor it needs to be considered explicitly.

4 Numerical simulations

In this section, five sets of numerical simulations are performed using the isotropic and orthotropic damage models and the mixed FE formulation presented earlier. Numerical simulations are compared to theoretical or experimental solutions reported in the literature. The simulations are:

1. Willam's test
2. Traction tests on solid and hollow cylindrical specimens
3. Mixed mode bending tests
4. Mixed mode shearing-tension tests
5. Torsion test on a solid cylindrical specimen

Simulations 2 to 5 have been performed using 3D finite elements. No tracking technique is used in any of the cases. A stabilization parameter τ_{ε} = 0.1 is used in all the simulations.

Calculations are performed with an enhanced version of the finite element program COMET [33]. Pre- and post-processing are done with GiD [34], developed at CIMNE (International Center for Numerical Methods in Engineering).

4.1 Willam's Test

Willam's numerical test is used to highlight the difference between the isotropic and orthotropic damage models under shear loading. The test was proposed in reference [10] and it is regularly used to assess the performance of nonlinear damage constitutive laws [1, 31, 35-37].

The test examines the behavior of the isotropic and orthotropic damage models when the principal directions of strain rotate. The Rankine criterion is adopted in all cases.

The test is performed with a single quadrilateral 2D element in plane stress conditions. The material properties are shown in Table 1. The loading is applied in two stages via increments of displacements. In the first stage, a uniaxial displacement is imposed in the horizontal X direction; as a consequence, deformation occurs in the X and Y directions, due to Poisson's effect. This leads to strains with an incremental ratio of $\Delta\varepsilon_{xx}:\Delta\varepsilon_{yy}:\Delta\gamma_{xy} = 1:-\nu:0$. The first stage ends when the stress σ_{xx} reaches the value of the uniaxial tensile strength. In the second stage, displacements are imposed such that the incremental ratio of strains is $\Delta\varepsilon_{xx}:\Delta\varepsilon_{yy}:\Delta\gamma_{xy} = 1:1.5:1$ until the complete failure of the material. Note that in the second stage of the test the principal directions of strain change, as the ratio $\varepsilon_{xx}:\varepsilon_{yy}:\gamma_{xy}$ changes at each step.

A constitutive model is said to pass Willam's test if (a) the predicted maximum principal stress does not exceed the uniaxial tensile strength and (b) all computed stress components tend to zero asymptotically [35, 37].

Young's Modulus	$30 \cdot 10^9$ Pa
Poisson's Ratio	0.2
Tensile Strength	$3.0 \cdot 10^6$ Pa
Fracture Energy	200 J/m^2

Table 1. Material parameters of Willam's test

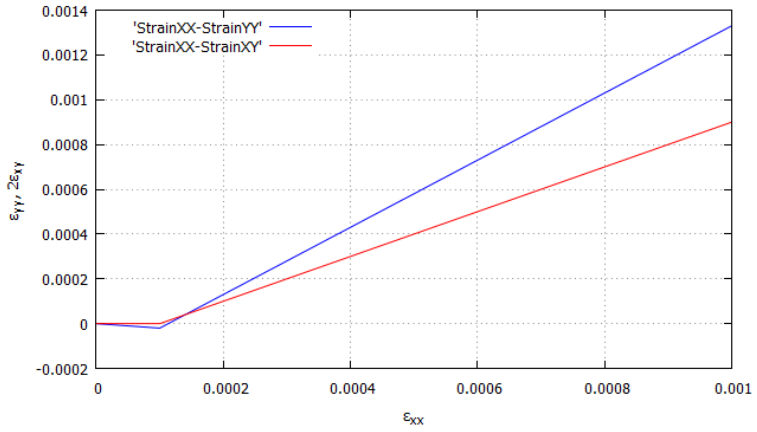

Figure 1. Imposed ε_{xx}, ε_{yy} and ε_{xy} during Willam's test

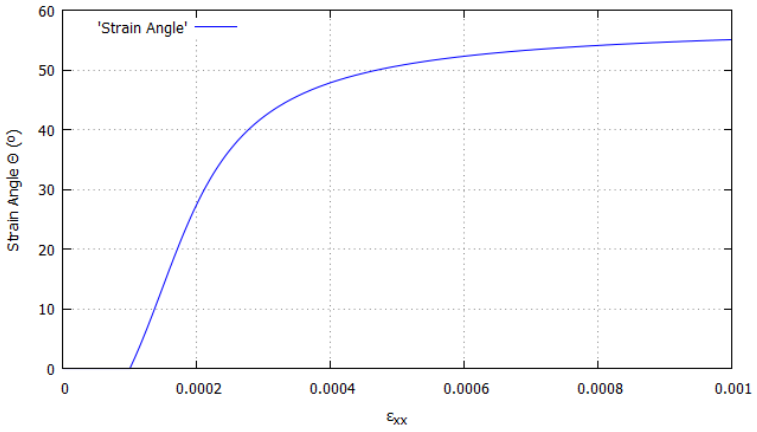

Figure 2. Evolution of the angle (degrees) of the maximum principal strain with respect to the X direction

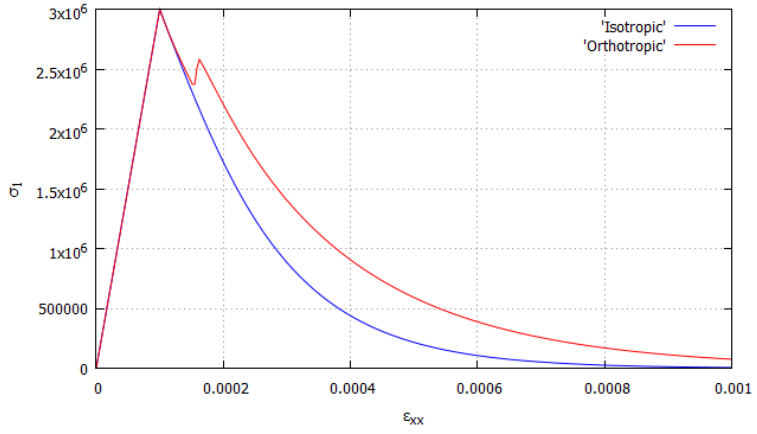

Figure 3. Computed maximum principal stress in Willam's test

Isotropic vs orthotropic damage

Figure 1 shows the evolution of strains during Willam's test. The two stages of the test can be easily identified. The rotation of the principal directions of strain that occurs during the process is depicted in Figure 2. In the first stage, the principal directions of strain are aligned with the axis of the element. In the second stage, strains rotate and the angle of the maximum principal strain with respect the X direction tends asymptotically to 58.28º, which corresponds to the limit case $\varepsilon_{xx}:\varepsilon_{yy}:\gamma_{xy} = 1:1.5:1$.

In Figure 3 the evolution of the maximum principal stress for the two constitutive laws is shown. In the isotropic case, the principal stress decreases asymptotically to zero after reaching the peak. In the orthotropic case, a second peak of stresses appears shortly after the occurrence of the first one. After that, the major principal stress also decreases asymptotically to zero.

In Figure 4, the evolution of the σ_{xx}, σ_{yy}, and τ_{xy} is depicted. For isotropic damage, there is a single damage index affecting the evolution of all the stresses components σ_{xx}, σ_{yy}, and τ_{xy}. On the contrary, with orthotropic damage, components σ_{xx} and σ_{yy} behave in a much more independent way, as each principal direction of stress is affected by a different damage index.

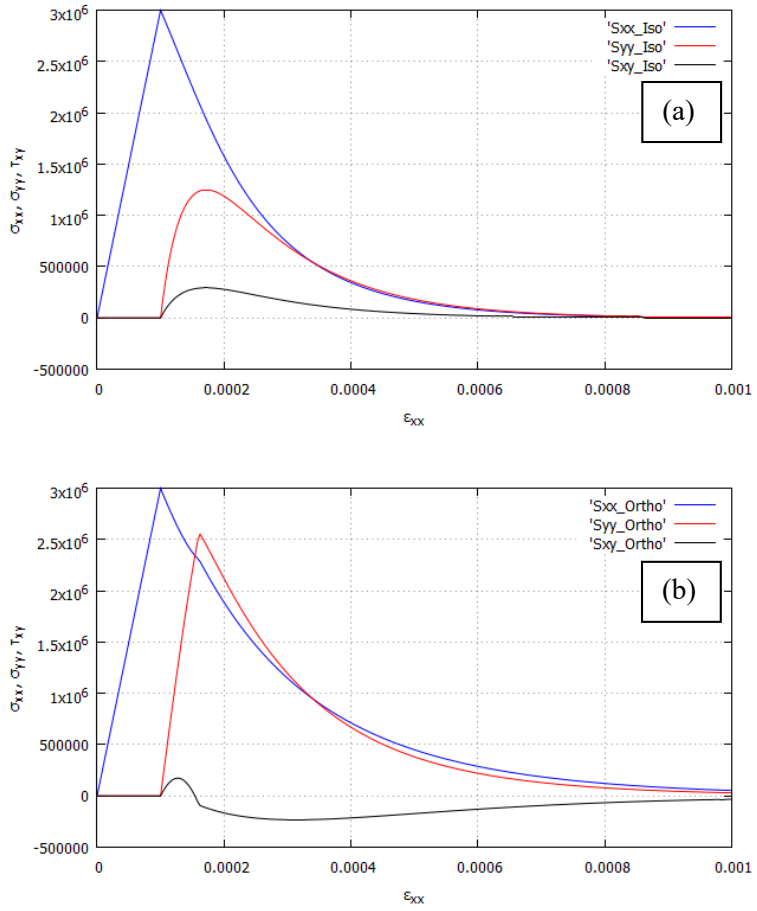

Figure 4. Evolution of σ_{xx}, σ_{yy} and τ_{xy} stresses in Willam's test for the (a) isotropic and (b) orthotropic models

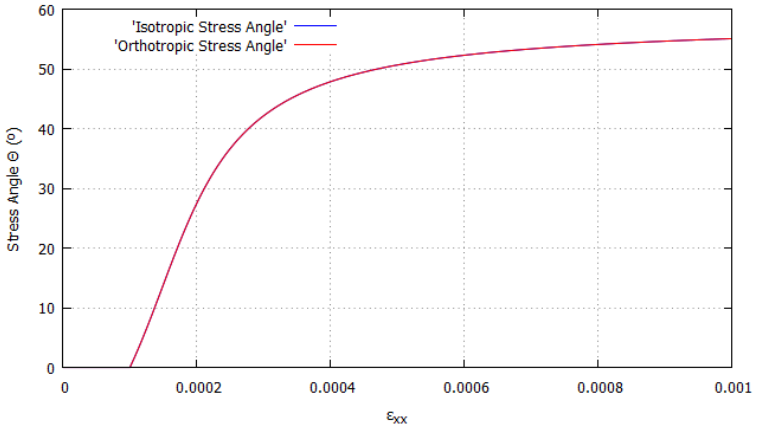

Figure 5. Evolution of the angle (degrees) of the maximum principal stress with respect to the X direction

Figure 4 also shows the rotation of principal directions of strain and stress. In the first stage, σ_{yy} and τ_{xy} are zero and the maximum principal stress σ_1 is in the direction of σ_{xx}. In the second stage, the ratio between σ_{xx}, σ_{yy}, and τ_{xy} is constantly changing, making the principal directions of stresses σ_1 and σ_2 to continuously rotate.

Figure 5 shows the evolution of the angle of the maximum principal stress with respect the X direction for the isotropic and orthotropic cases. As it can be observed, the two results are overlapping, demonstrating that in the two damage models the strains and stresses are coaxial. It should be noted that the angle of the maximum principal stress tends asymptotically to the same angle as the one corresponding to strains in Figure 2.

The two models pass the Willam's test according to the aforementioned criteria.

4.2 Traction test on solid and hollow cylindrical specimens

The numerical analysis of cylindrical concrete specimens subjected to axial straining is performed. The objective of this example is to test the behavior of several damage models with regard to their sensitivity to Poisson's ratio.

Computations are performed with the Beltrami and Modified Beltrami criteria. First, a comparison is performed between the isotropic versions of the models. Afterwards, the orthotropic Beltrami model is also employed.

Two cases are considered. In the first one, the cylinder is solid, and in the second one, the cylinder is hollow. The cylinder has a 50 mm radius and is 450 mm long in the solid case and 500 mm long in the hollow case. The thickness of the hollow specimen is 5 mm. A small hole of 5 mm radius has been introduced in the middle of the specimens to fix the occurrence of fracture. The material properties are shown in Table 2. Simulations are performed with different Poisson's ratio values. Opposite increments of vertical displacement are applied at the top and bottom surfaces of the specimen.

Case	Solid	Hollow
Young's Modulus	$38 \cdot 10^9$ Pa	$38 \cdot 10^9$ Pa
Tensile Strength	$2.3 \cdot 10^6$ Pa	$3.0 \cdot 10^6$ Pa
Fracture Energy	80 J/m^2	80 J/m^2

Table 2. Material parameters of the traction test

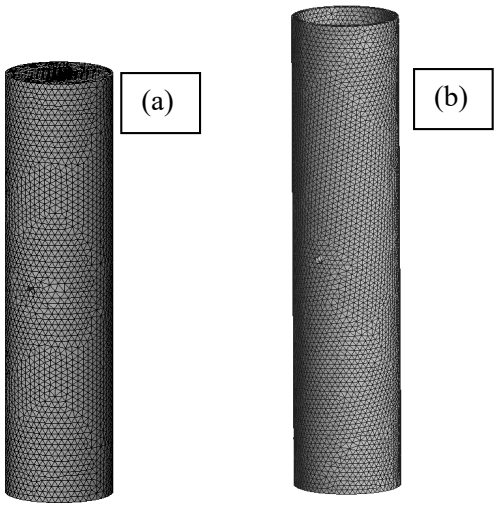

Figure 6. Meshes used for the analyses of the traction test for the (a) solid and (b) hollow specimens

In both cases, the specimens are discretized with fully unstructured meshes of tetrahedral elements, shown in Figure 6. For the solid specimen the elements have a size of 6 mm, resulting in a mesh of 21,986 nodes; in the hollow specimen, the elements are of 5 mm, ensuing a mesh of 15,823 nodes.

Influence of Poisson's ratio

Figure 7 shows the computed crack surfaces in the solid specimen obtained with the Beltrami criterion for different values of Poisson's ratio, plotted as the isolevel surface of the norm of vertical displacements. Corresponding results, also with the Beltrami criterion, are shown in Figure 8 for the hollow specimen.

It can be seen that different values of Poisson's ratio produce crack surfaces at different angles with the horizontal plane (orthogonal to the axial stress). This angle has been theoretically computed for Beltrami's criterion in reference [28] depending on the value of Poisson's ratio for plane stress and plane strain behavior. The solid specimen behaves closely to plane strain conditions while the hollow case behaves similarly to plane stress conditions. Table 3 compares the expected theoretical angles and the computed ones for each case. It can be seen that the computed results are very close to the expected theoretical solutions.

Figure 9 shows the force-displacement curves for both the solid and the hollow specimens computed with the Beltrami criterion for several Poisson's ratio values. It can be seen that the results in terms of dissipated energy depend on Poisson's ratio. Note that the load capacity of the specimens differs very little from the values corresponding to perfectly brittle failure (18.06 kN and 4.48 kN for the solid and hollow specimens, respectively) and are quite independent of Poisson's ratio. Contrariwise, the dissipated energy increases with the Poisson's ratio, as the failure mechanism and the corresponding crack surface varies.

The results computed with the Modified Beltrami criterion in Figure 10 are nearly identical for all values of Poisson's ratio, showing a horizontal crack surface. This result was also theoretically derived in reference [28]. It is to be expected as the influence of Poisson's ratio in the formulation of the modified model is very much reduced (see equations (15) and (16)).

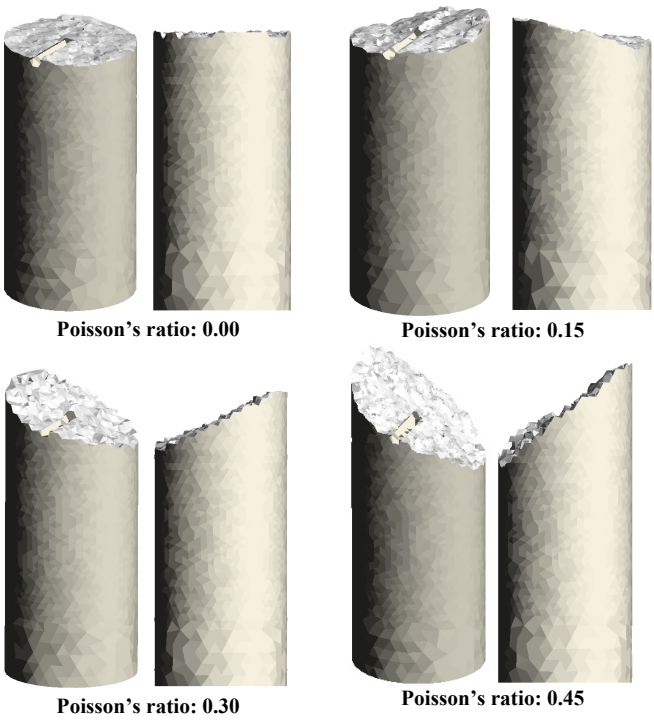

Figure 7. Crack surfaces of the traction test, solid specimen, with the Beltrami criterion for several Poisson's ratio values

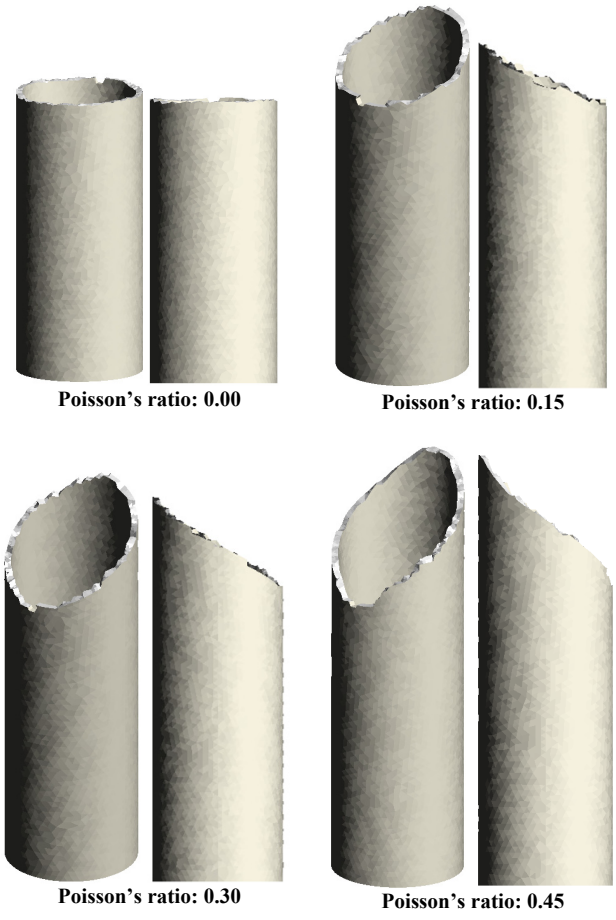

Figure 8. Crack surfaces of the traction test, hollow specimen, with the Beltrami criterion for several Poisson's ratio values

Poisson's ratio	Theoretical Angle Plane Strain	Computed Angle Solid Specimen	Error (%)	Theoretical Angle Plane Stress	Computed Angle Hollow Specimen	Error (%)
0.00	0.00°	0°	0.00	0.00°	0°	0.00
0.15	21.17°	19°	10.25	22.79°	23°	0.92
0.30	28.71°	29°	1.01	33.21°	33°	0.63
0.45	33.85°	34°	0.44	42.13°	40°	5.03

Table 3. Theoretical and computed angles of the crack surfaces in the traction test

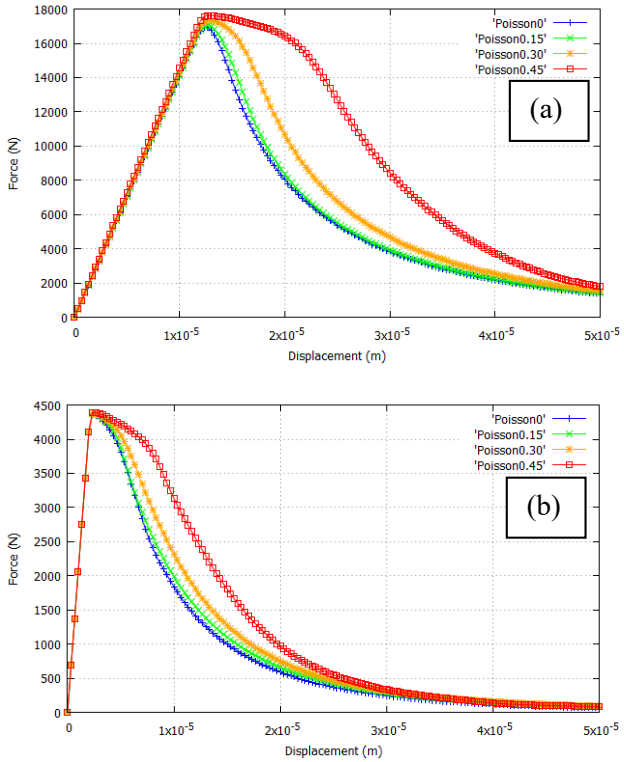

Figure 9. Force-displacement curves of the traction test computed with the Beltrami criterion for (a) the solid specimen and (b) the hollow specimen

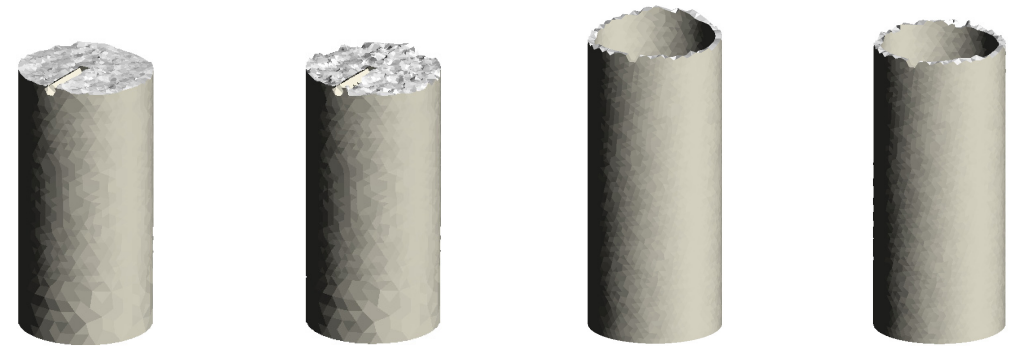

Figure 10. Crack surfaces of the traction test, with the Modified Beltrami criterion

Isotropic vs orthotropic models

In this section, the results obtained with the isotropic and orthotropic Beltrami models are compared. As it can be seen in the computed crack surfaces of Figures 11 and 12, and in Table 4, the crack surface angles are different. Compared to the isotropic results of Figures 7 and 8, the

orthotropic damage crack surfaces have an angle which is systematically and significantly smaller for the same Poisson's ratio value. Although no theoretical confirmation is available, this difference is attributed to the reduction of the effective Poisson's effect in orthotropic models.

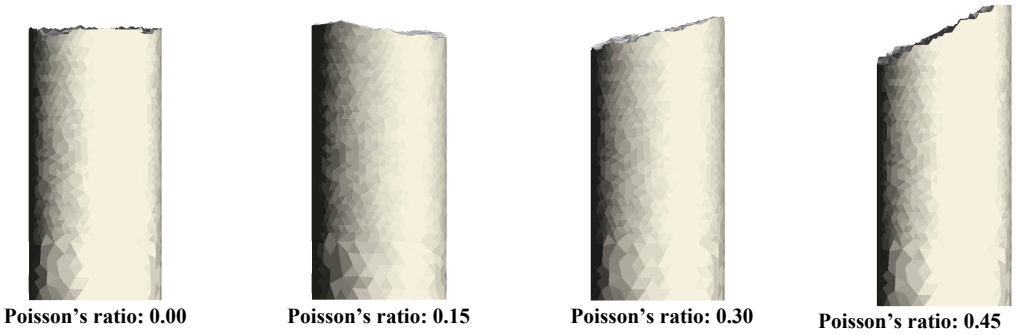

Figure 11. Crack surfaces of the traction test, solid specimen, computed with the orthotropic Beltrami criterion

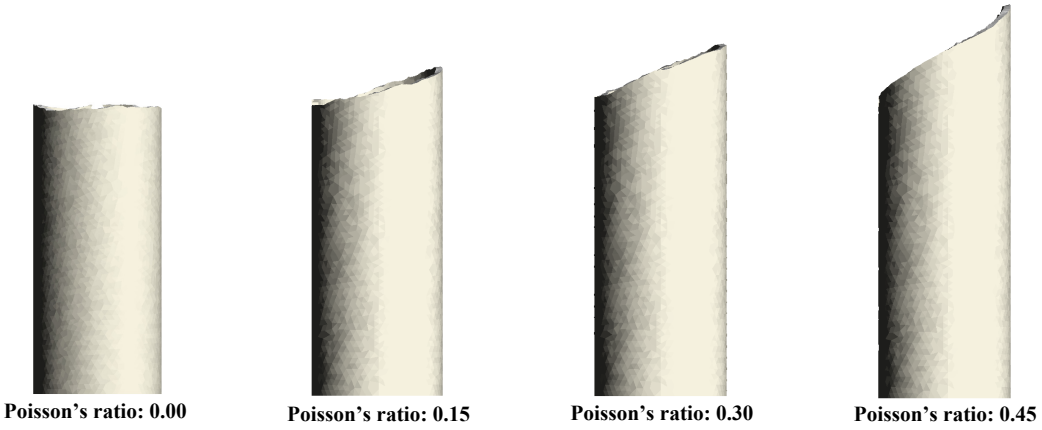

Figure 12. Crack surfaces of the traction test, hollow specimen, computed with the orthotropic Beltrami criterion

Poisson's ratio	Isotropic Beltrami Solid Specimen	Orthotropic Beltrami Solid Specimen	Isotropic Beltrami Hollow Specimen	Orthotropic Beltrami Hollow Specimen
0.00	0°	0°	0°	0°
0.15	19°	10°	23°	16°
0.30	29°	14°	33°	22º
0.45	34°	26°	40°	29º

Table 4. Computed angles of the crack surfaces for the isotropic and orthotropic Beltrami damage models in the traction test

4.3 Mixed mode bending test

In this section, a notched beam subjected to a mixed mode bending test is considered. The experimental tests were first carried out by Arrea and Ingraffea [38] and then repeated by Gálvez and Cendón [39]. Reference [39] also performed numerical simulations with a cohesive interface method. Other numerical results are reported in [40-43]. Reference [40] considers a localization limiter to regularize the problem. In [41] an adaptive particle meshless method was used, while in [42] the boundary element method was employed. In [43] an interface finite element approach was adopted.

This example is intended to assess the performance of the Rankine and Drucker-Prager criteria in mixed mode cracking situations. For comparison purposes, three different sets of beams with various geometries and properties were tested in [39]. The geometry of the three sets of beams is shown in Figure 13. In the A set, the beam thickness is 0.102 m and the notch a is 0.070 m long. In the B and C sets, the beam is 0.152 m thick and the notch a is 0.0824 m long. The different properties of the sets are shown in Table 5.

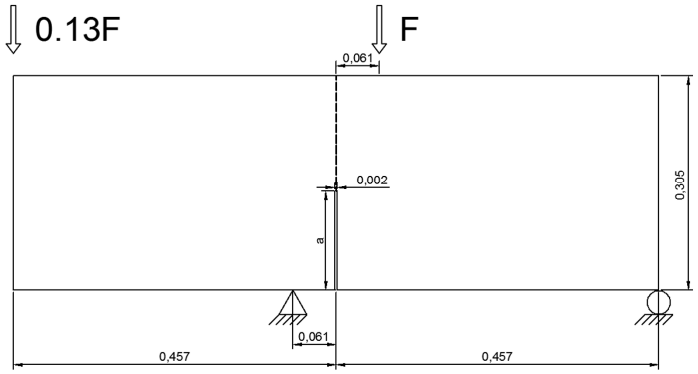

Figure 13. Geometry of the mixed mode bending test (m)

Set	A	B	C
Young's Modulus	$23.4 \cdot 10^9$ Pa	$24.8 \cdot 10^9$ Pa	$24.8 \cdot 10^9$ Pa
Poisson's Ratio	0.21	0.18	0.18
Tensile Strength	$4.6 \cdot 10^6$ Pa	$4.0 \cdot 10^6$ Pa	$3.7 \cdot 10^6$ Pa
Fracture Energy	75 J/m^2	125 J/m^2	130 J/m^2
Compressive Strength	$60.7 \cdot 10^6$ Pa	$45.5 \cdot 10^6$ Pa	$43.4 \cdot 10^6$ Pa

Table 5. Material properties of the mixed mode bending test

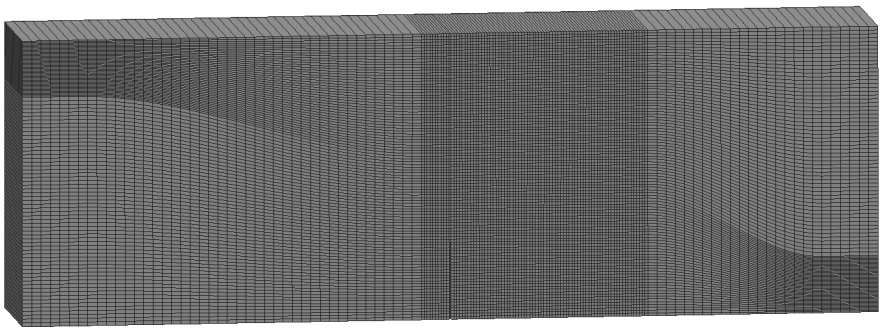

Figure 14. FE mesh used for the mixed mode bending test

The problem is solved using an arc-length algorithm controlling the crack mouth sliding displacement (CMSD) at the notch. For this example, 3D hexahedral elements are used, resulting in a fully structured mesh of 31,634 nodes and elements of 3 mm, shown in Figure 14.

First, a comparison between the isotropic and orthotropic Rankine models is performed to assess their ability to reproduce mixed mode I and II failure. Then, a comparison is made between the isotropic and orthotropic Drucker-Prager models. Finally, the relative performance of the mixed and standard FE formulations is addressed.

Rankine isotropic vs orthotropic models

Figure 15 shows damage contour fills for the sets A and C computed with the Rankine criterion. It can be seen that the results for the isotropic and orthotropic models are quite similar.

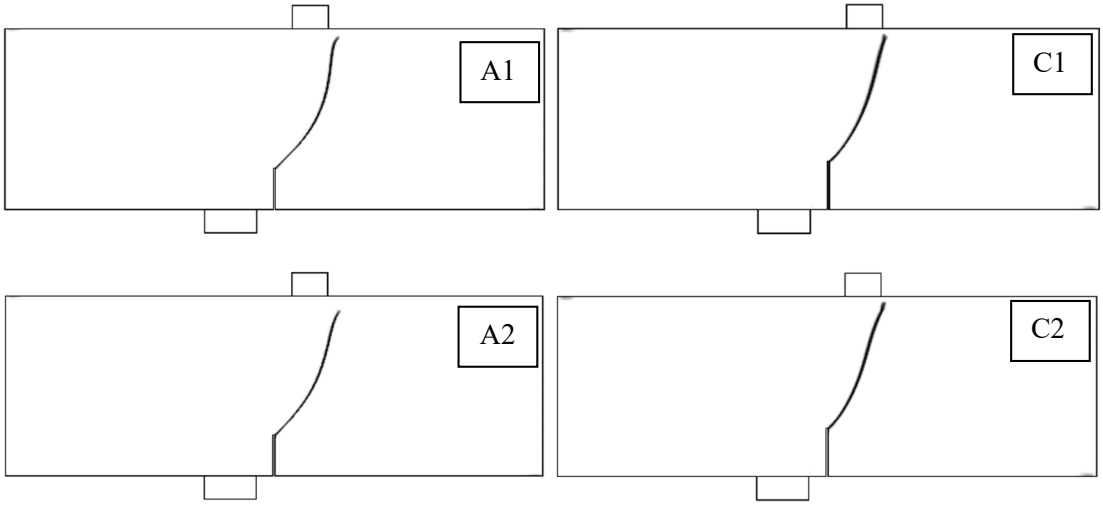

Figure 15. Damage contour fills of the mixed mode bending test, sets A and C, for the Rankine criterion with (1) isotropic damage and (2) orthotropic damage

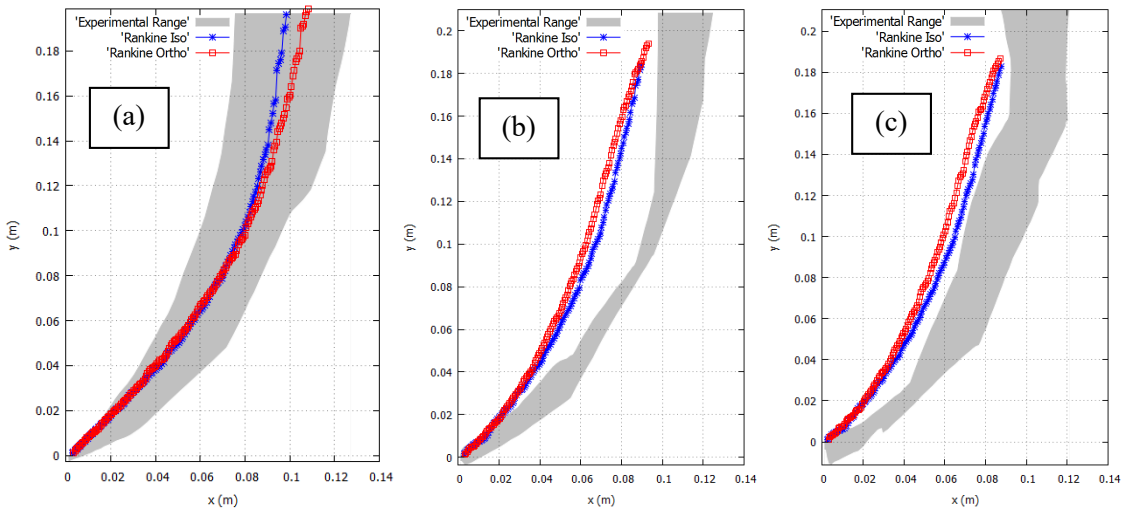

Figure 16. Crack paths compared to experimental results of the mixed mode bending test for the Rankine criterion (a) set A, (b) set B and (c) set C

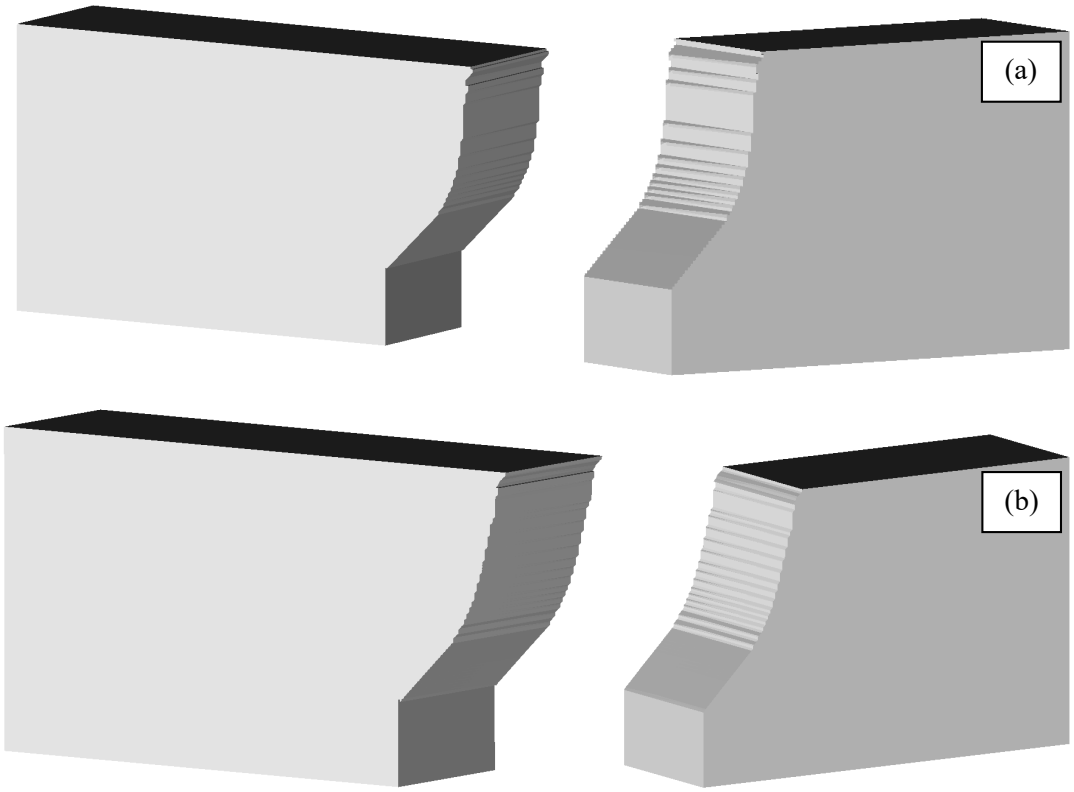

Figure 17. Crack surfaces of the mixed mode bending test, set C, for the Rankine criterion with (a) isotropic and (b) orthotropic damage

Crack trajectories are compared in detail in Figure 16 for all three sets. There, it can be seen that, for the A set, the computed crack paths with the different models are all very similar. In addition, they are all inside the experimental range of reference [39]. For the B and C sets, the results of the Rankine isotropic and orthotropic models are also very close, but none of them give results inside the experimental range.

The crack surface in the 3D analyses is depicted in Figure 17, plotted as an iso-level surface of the X-displacements. There, the crack surfaces of the different criteria considered for modeling set C can be observed.

In Figure 18, the force-CMSD curves are shown for each set. It can be seen that the isotropic and orthotropic models are very close and correlate very closely with the experiments.

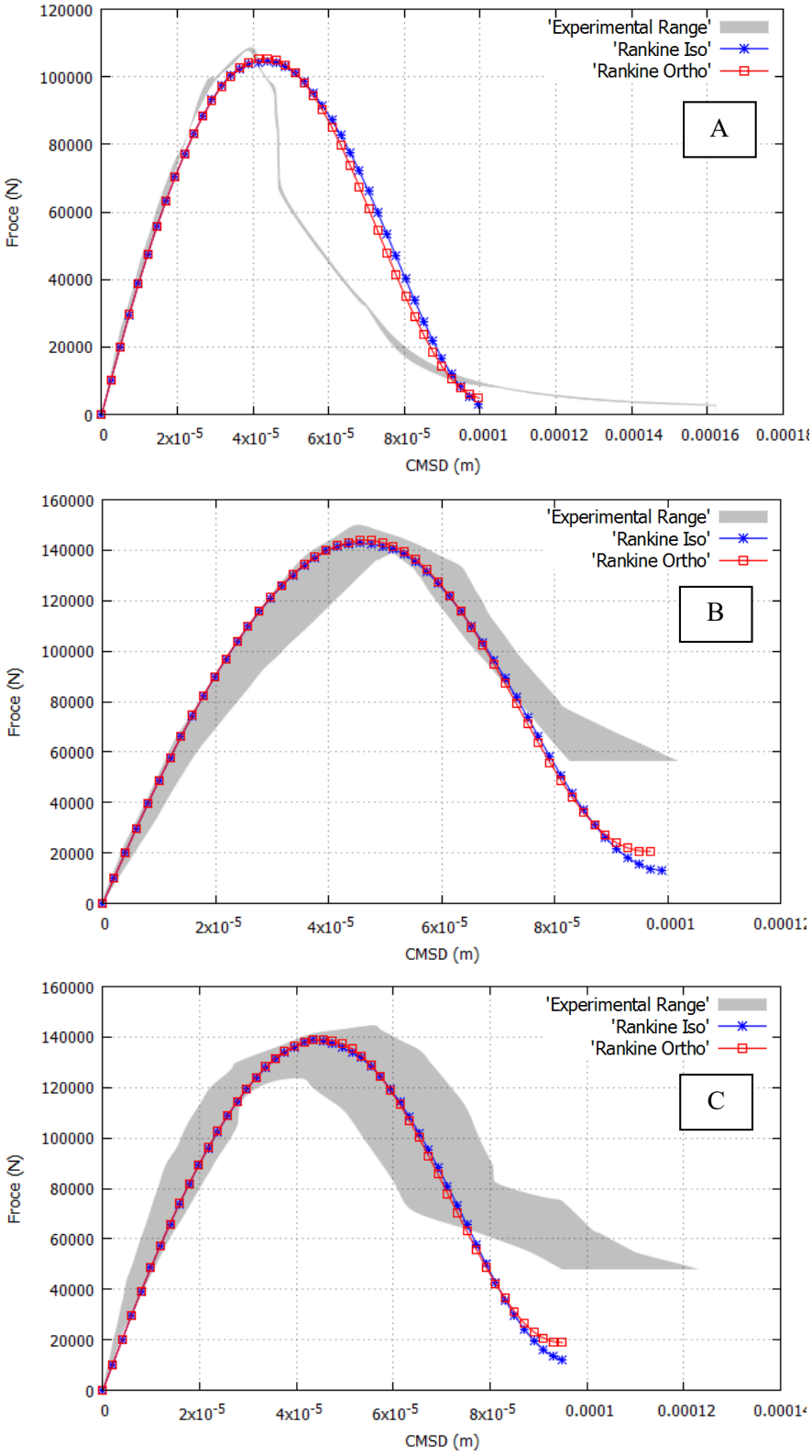

Figure 18. Force-CMSD curves of the mixed mode bending test for Rankine's model and sets A, B and C

Rankine vs Drucker-Prager damage criteria

In the following, the use of the Drucker-Prager damage criterion has been considered. The corresponding isotropic and orthotropic models are used, as detailed in Section 2. In the orthotropic Drucker-Prager laws, see equation (28), damage only evolves in the directions where the corresponding principal stress is positive.

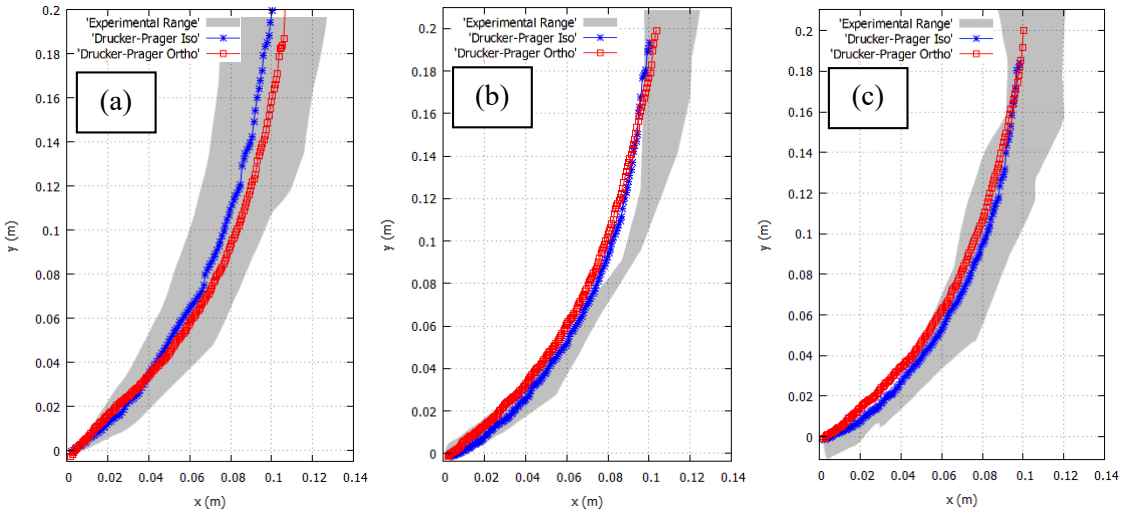

Figure 19. Crack paths compared to experimental results of the mixed mode bending test for the Drucker-Prager criterion (a) set A, (b) set B and (c) set C.

The crack paths of all three sets are included in Figure 19 for the isotropic and orthotropic Drucker-Prager models. It can be seen how isotropic and orthotropic models produce very similar results in terms of crack path. The crack surfaces are inside the experimental ranges for all three sets A, B, and C. Similar results were reported in the numerical simulations performed by [39], where a cohesive interface method was used.

In Figure 20 the computed crack surfaces of all three cases of unit C can be observed. The results captured with the Drucker-Prager orthotropic constitutive laws are very similar to the corresponding isotropic damage. Computed results show good agreement with the experimental surface reported in [38]. The Drucker-Prager criterion is also considered to perform better than Rankine's for mixed mode fracture in references [25, 32].

Figure 21 shows the force-CMSD curves of the three sets computed with the isotropic and orthotropic Drucker-Prager criteria. All the computed results are almost overlapping and in good agreement with the experiments.

In Figure 22 the evolution of the maximum principal stresses is depicted as the crack propagates in set A for the isotropic Rankine and Drucker-Prager models. Stresses concentrate at the tip of the crack making it to progress, following the path shown in Figure 19. Different damage criterions introduce different equivalent stresses and, therefore, they produce different crack paths. The Rankine and Drucker-Prager criterions produce similar but not identical crack trajectories, the crack corresponding to the latter being more curved. This is a direct consequence of the (slight) difference between the two different criteria for mixed stress states. The elastic principal stresses near the crack tip can be observed in Figure 23.

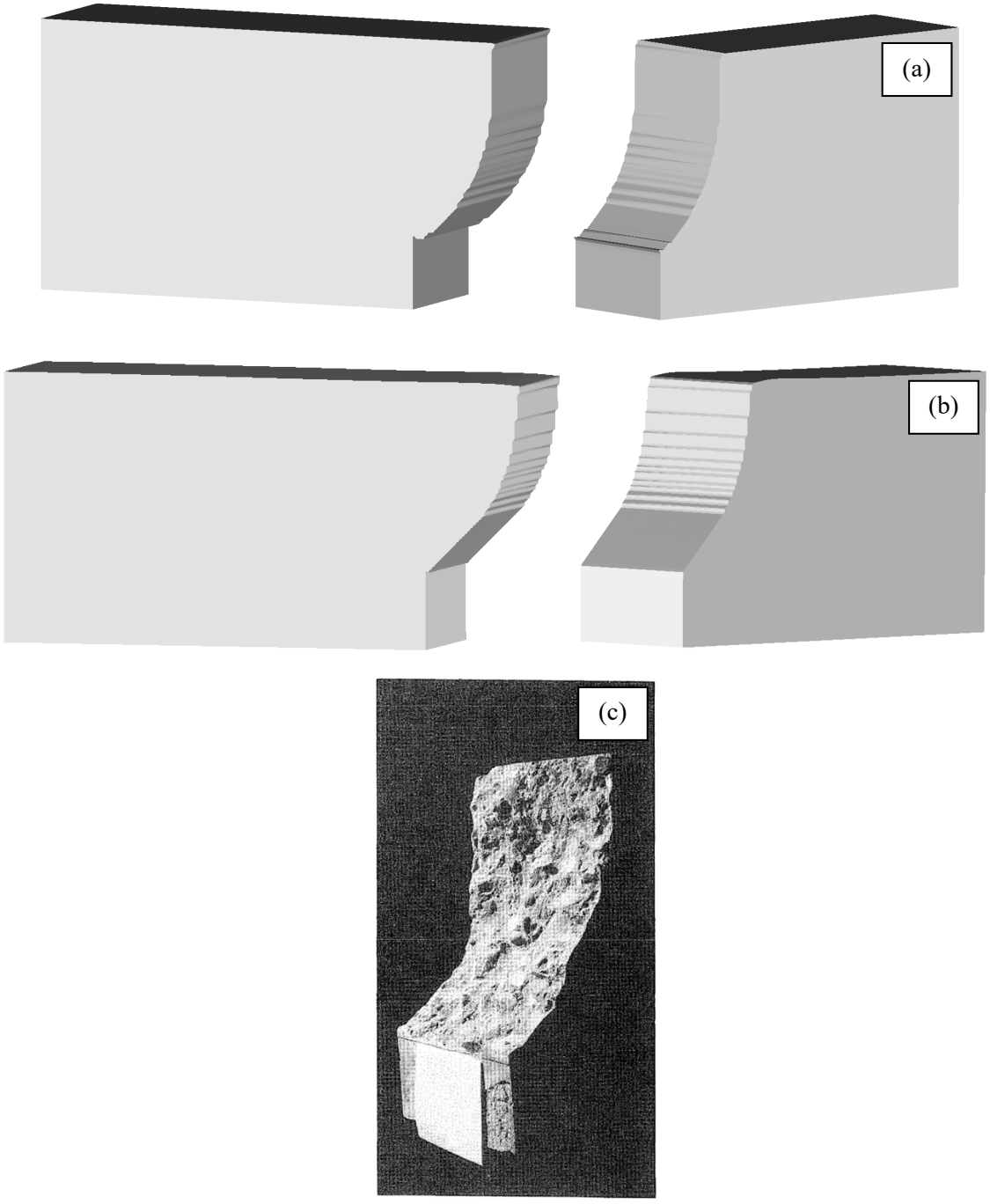

Figure 20. Crack surfaces, mixed mode bending test, set C, for the Drucker-Prager criterion with (a) isotropic (b) orthotropic damage and (c) a photo of the crack surface in the experiment of [38]

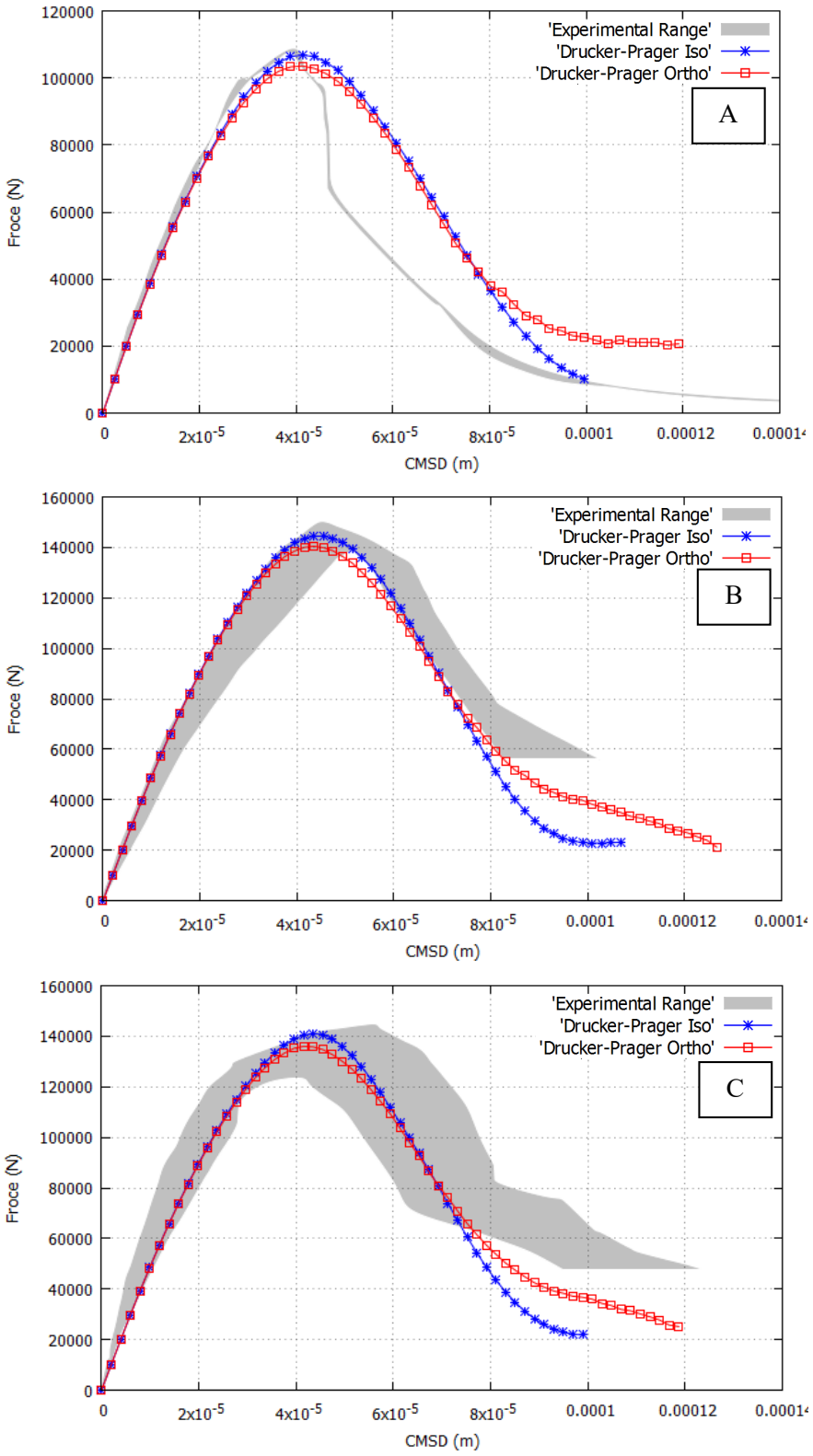

Figure 21. Force-CMSD curve of the mixed mode bending test for the Drucker-Prager model, sets A, B and C

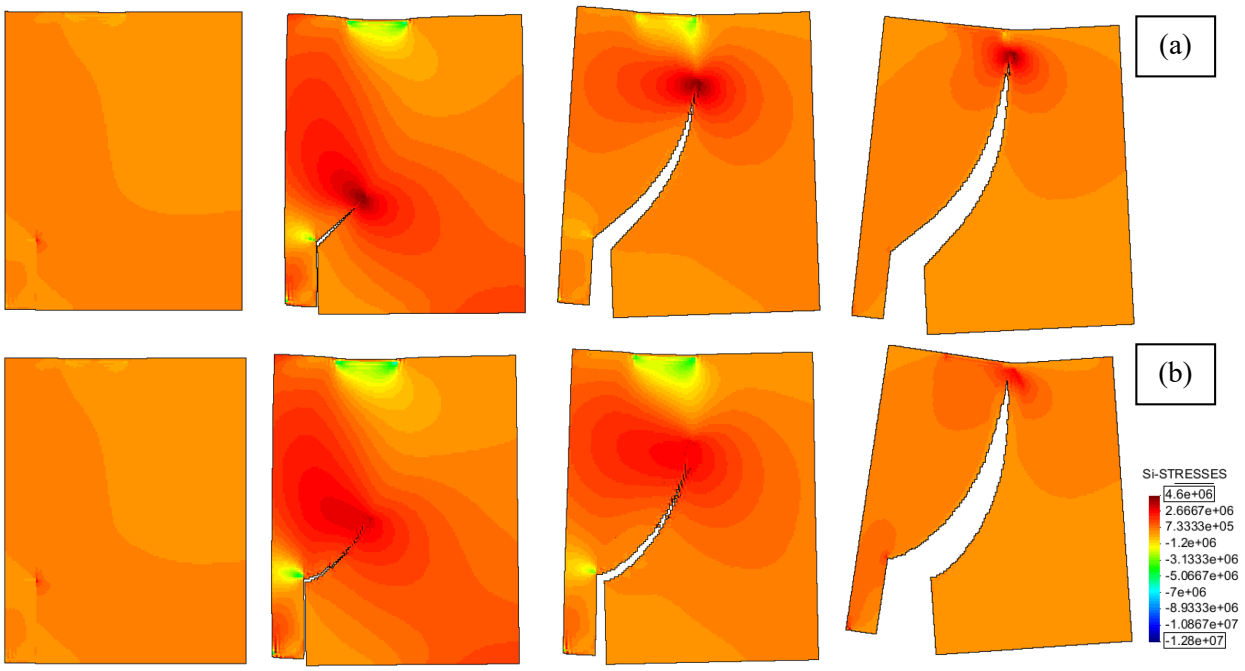

Figure 22. Stress evolution and crack propagation, in the set A, for the isotropic (a) Rankine and (b) Drucker-Prager models

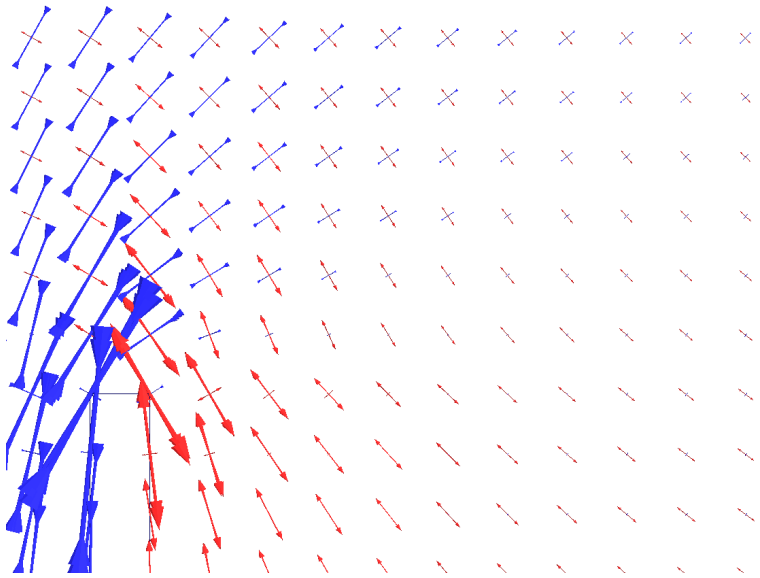

Figure 23. Elastic principal stresses near the crack tip

Comparison with standard FE

In this bending problem, isotropic and orthotropic models performed very similarly both for the Rankine and Drucker-Prager criteria. In this section, results for set C computed with standard finite elements are reported to show the relative improvement of the mixed formulation.

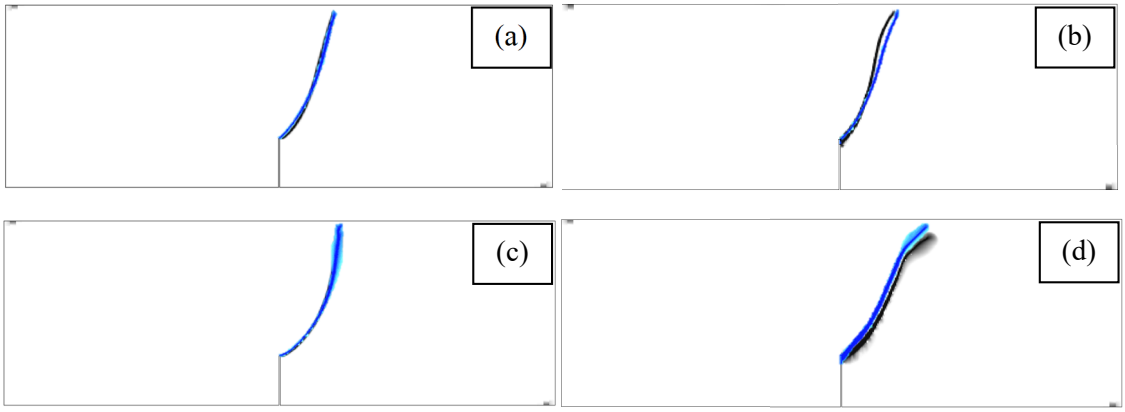

Figure 24. Damage contour fills of the mixed mode bending test, set C, computed with standard FE (black crack path) vs mixed FE (blue crack path) with (a) isotropic Rankine, (b) orthotropic Rankine, (c) isotropic Drucker-Prager and (d) orthotropic Drucker-Prager models

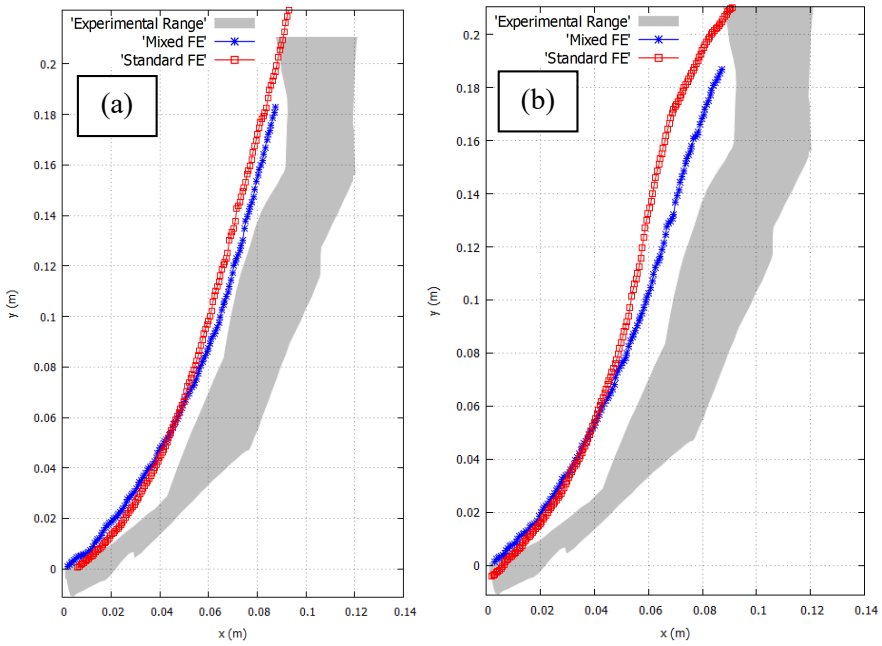

Figure 25. Crack paths compared to experimental results of the mixed mode bending test, set C, for (a) isotropic and (b) orthotropic Rankine models

In Figure 24 the damage contour fills computed with standard FE, for the Rankine and Drucker-Prager criteria, using isotropic and orthotropic damage, are compared to the results obtained with mixed FE. These are to be compared to Figure 15, where the corresponding results for the mixed formulation are given.

Details of the computed crack paths are given in Figures 25 and 26. It can be seen how the Rankine criterion also yields unsuitable results, outside the experimental range with standard FE. The mixed FE crack paths produce results slightly closer to the experiments. The Drucker-Prager model, on the other hand, results in crack paths which are also inside the experimental range when using standard finite elements. When using isotropic damage, the computed crack paths are very close, while when employing orthotropic models, they are different, especially in the last stages of the simulation.

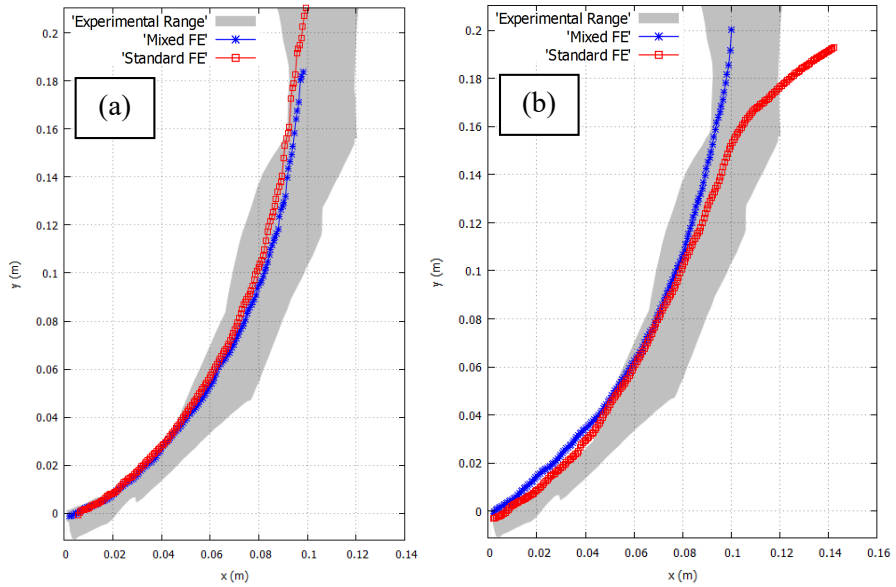

Figure 26. Crack paths compared to experimental results of the mixed mode bending test, set C, for (a) isotropic and (b) orthotropic Drucker-Prager models

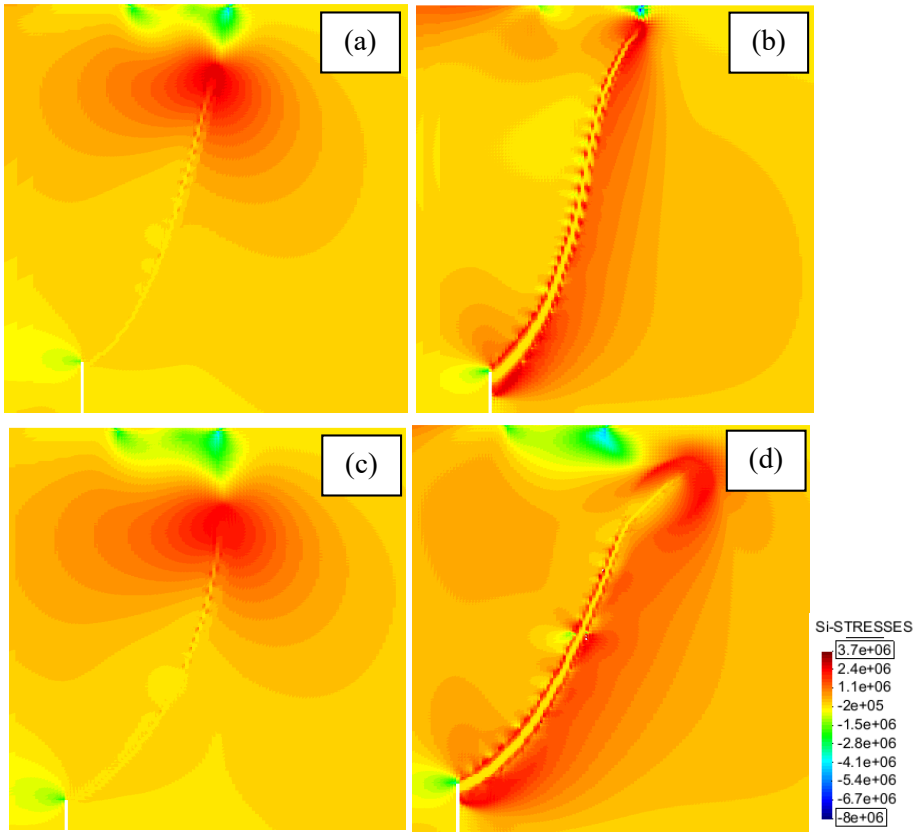

Figure 27. Maximum principal stress of the mixed mode bending test, set C, computed with standard FE with (a) isotropic Rankine, (b) orthotropic Rankine, (c) isotropic Drucker-Prager and (d) orthotropic Drucker-Prager

Figures 27 and 28 show the maximum principal stresses computed with standard and mixed FE, respectively. For isotropic damage, Figures 27a and 27c, stresses concentrate at the tip of the crack causing it to progress while the material unloads in the crack path as the material is damaged. With standard FE and orthotropic damage, Figures 27b and 27d, severe stress oscillations appear along the sides of the crack. With mixed FE, Figure 28 orthotropic models produce similar results to isotropic damage in terms of the stress field. No stress oscillations appear along the crack path. No trace of spurious stress transfer can be appreciated with the isotropic models, neither in the solution computed with standard or mixed FE, nor in the orthotropic solution computed with mixed FE. Contrariwise, severe spurious stresses are evident for the standard orthotropic damage along the crack path.

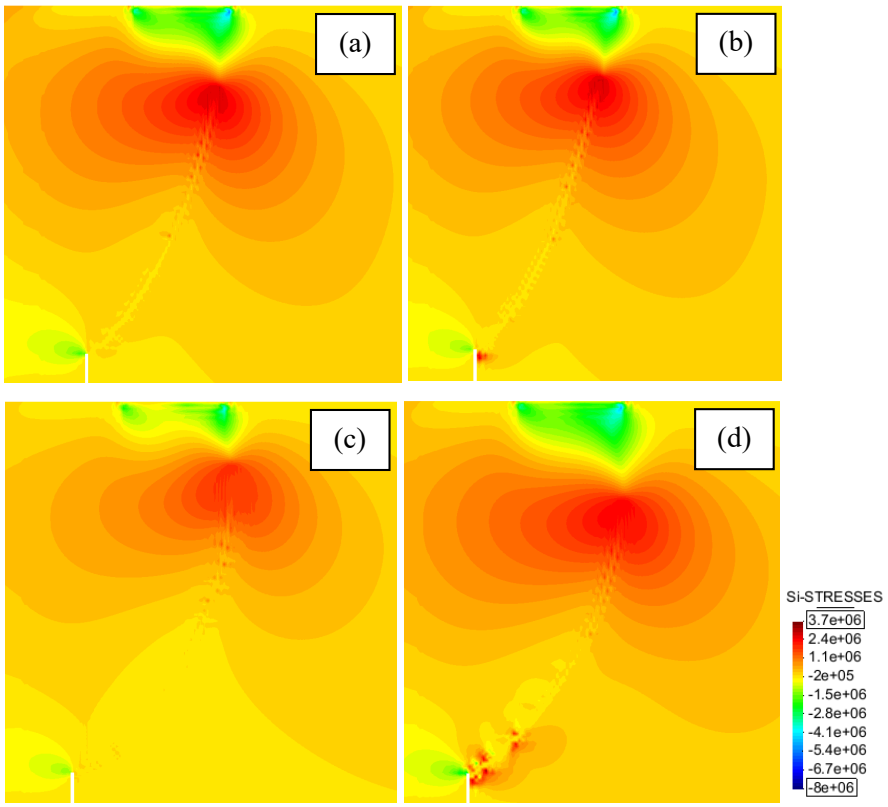

Figure 28. Maximum principal stress of the mixed mode bending test, set C, computed with mixed FE with (a) isotropic Rankine, (b) orthotropic Rankine, (c) isotropic Drucker-Prager and (d) orthotropic Drucker-Prager

For the mixed formulation, results are very similar regardless of whether isotropic or orthotropic models are used, both in terms of the computed crack paths (Figures 16 and 19) and force-CMSD curves (Figures 18 and 21). This does not happen with standard FE, as can be seen in the crack paths of Figures 25 and 26 or in the computed force-CMSD curves of Figures 29 and 30.

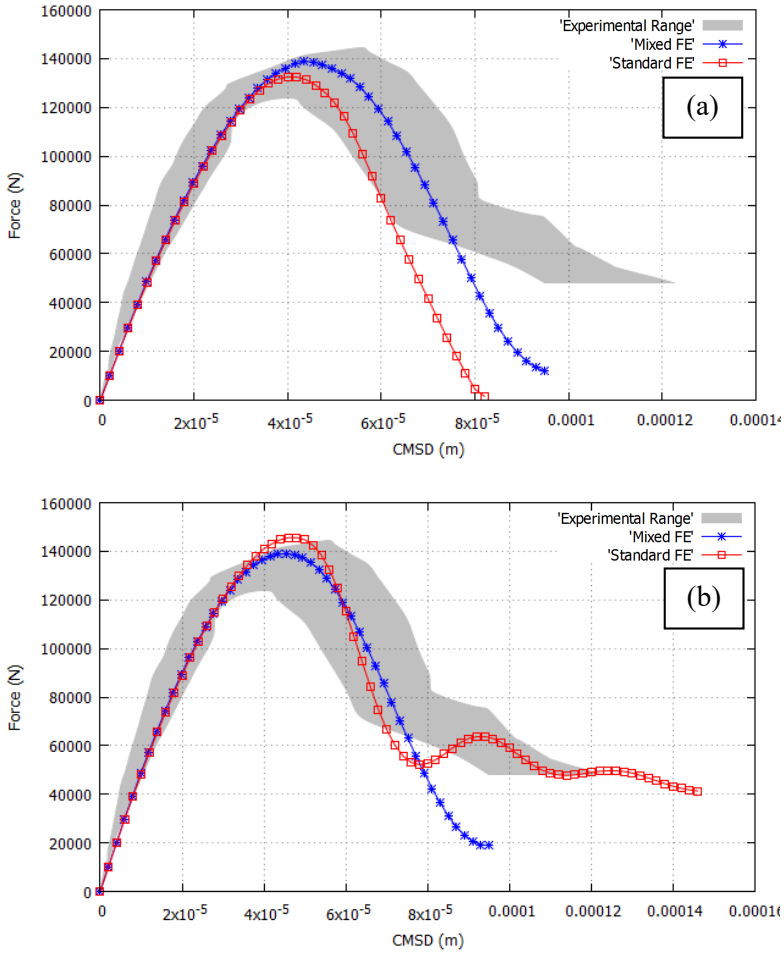

Figure 29. Force-CMSD curve of the mixed mode bending test for set C with (a) isotropic and (b) orthotropic Rankine models

Using isotropic damage models, the standard FE formulation is well-known to produce unrealistic mesh-biased results in many situations, so as to make it unreliable. Using orthotropic damage models, the discontinuous approximation of the strain field and the meagerness of the kinematic description of low order standard FE produces strain oscillations and spurious stresses that make their implementation unpractical.

The above problems are greatly alleviated by the enhanced kinematical description of the mixed $\boldsymbol{\varepsilon/u}$ finite elements.

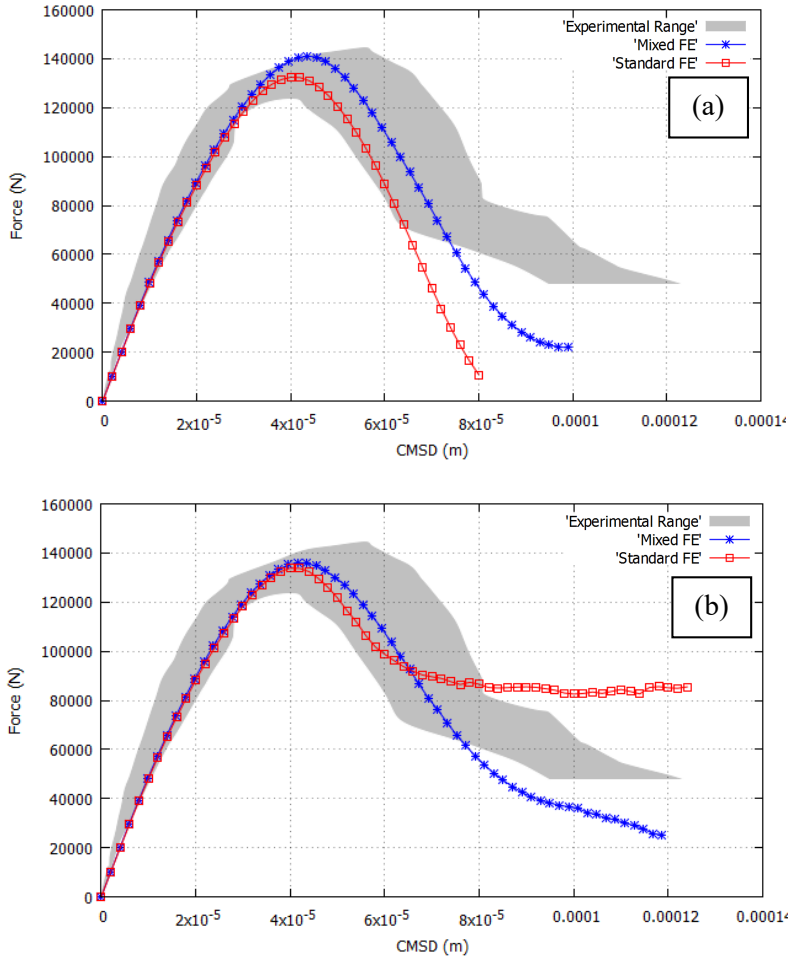

Figure 30. Force-CMSD curve of the mixed mode bending test for set C with (a) isotropic and (b) orthotropic Drucker-Prager models

4.4 Mixed mode shearing-tension test

The numerical analysis of a mixed mode shearing-tension test is considered. The specimen was experimentally tested by Nooru-Mohamed [44] and numerical simulations were made in references [45-50]. A tracking algorithm was considered in references [46-47, 49-50], while in [48] a sequentially linear analysis to non-proportional loading was done. In reference [45], the performance of several local and nonlocal models is addressed.

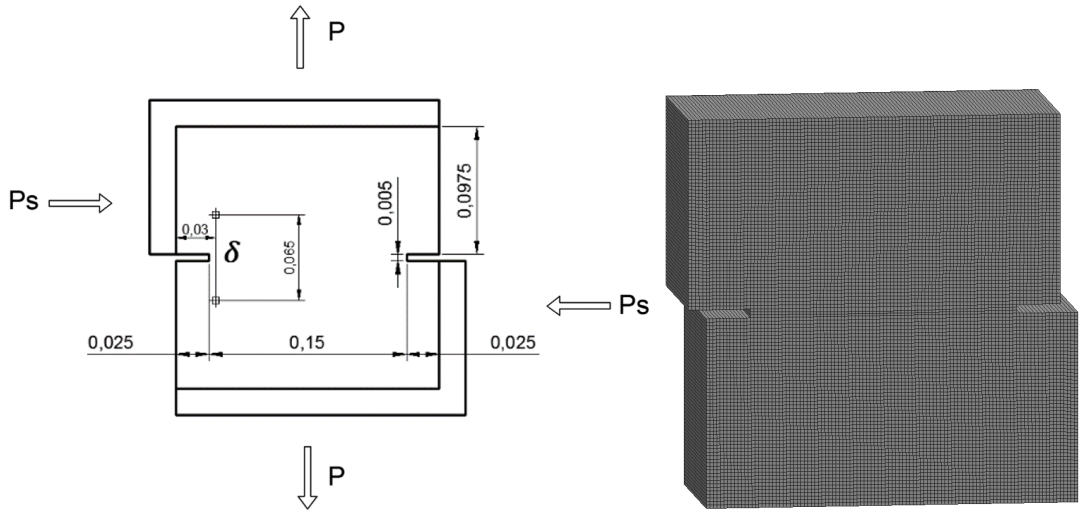

Figure 31. Geometry of the mixed mode shearing-tension test (m)

Young's Modulus	$30.0 \cdot 10^9$ Pa
Poisson's Ratio	0.2
Tensile Strength	$3.0 \cdot 10^6$ Pa
Fracture Energy	60 J/m^2
Compressive Strength	$6.0 \cdot 10^7$ Pa

Table 6. Material properties of the mixed mode shearing-tension test

The objective of this example is to assess the performance of the Drucker-Prager criterion in computing mixed mode cracking.

The geometry of the specimen is shown in Figure 31. The thickness of the specimen is 0.05 m. The loads are applied in two stages. In the first one, vertical tensile forces P are kept to zero while the horizontal shear forces P_s are incremented until a certain value. In the second stage, the loads P_s are kept constant and the loads P are incremented until failure occurs. The tests are performed under several loading conditions: in unit 4a, P_s reaches a value of 5 kN, in unit 4b P_s gets to 10 kN and in 4c, 27.5 kN. The load is applied in the specimen through contact with a rigid steel frame. In the numerical simulation, the load is applied in the first stage as horizontal forces and in the second stage via increments of vertical displacements to accurately capture the post-peak behavior.

The simulation is performed using the isotropic and orthotropic Drucker-Prager damage constitutive models. The material properties for the mixed mode shearing-tension test are shown in Table 6.

For this example, 3D hexahedral elements are used, resulting in a fully structured mesh of 23,748 nodes and elements of 2 mm, shown in Figure 31.

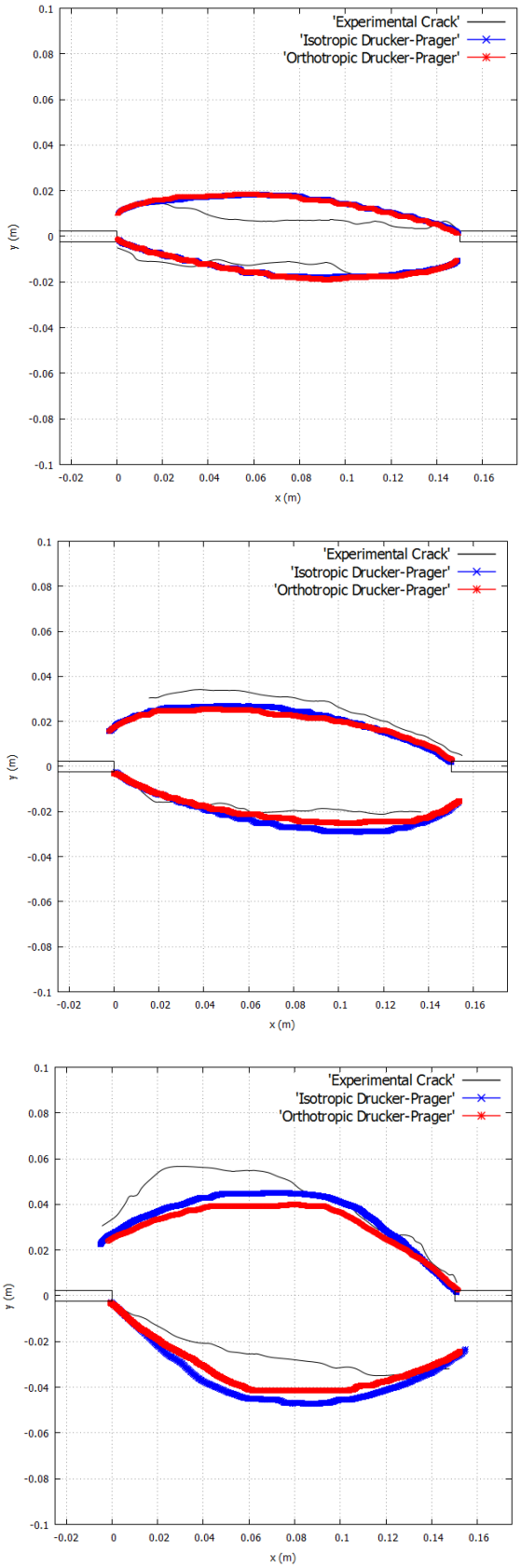

Figure 32. Crack trajectories of the mixed mode shearing-tension test, units 4a, 4b and 4c, for the isotropic and orthotropic Drucker-Prager models

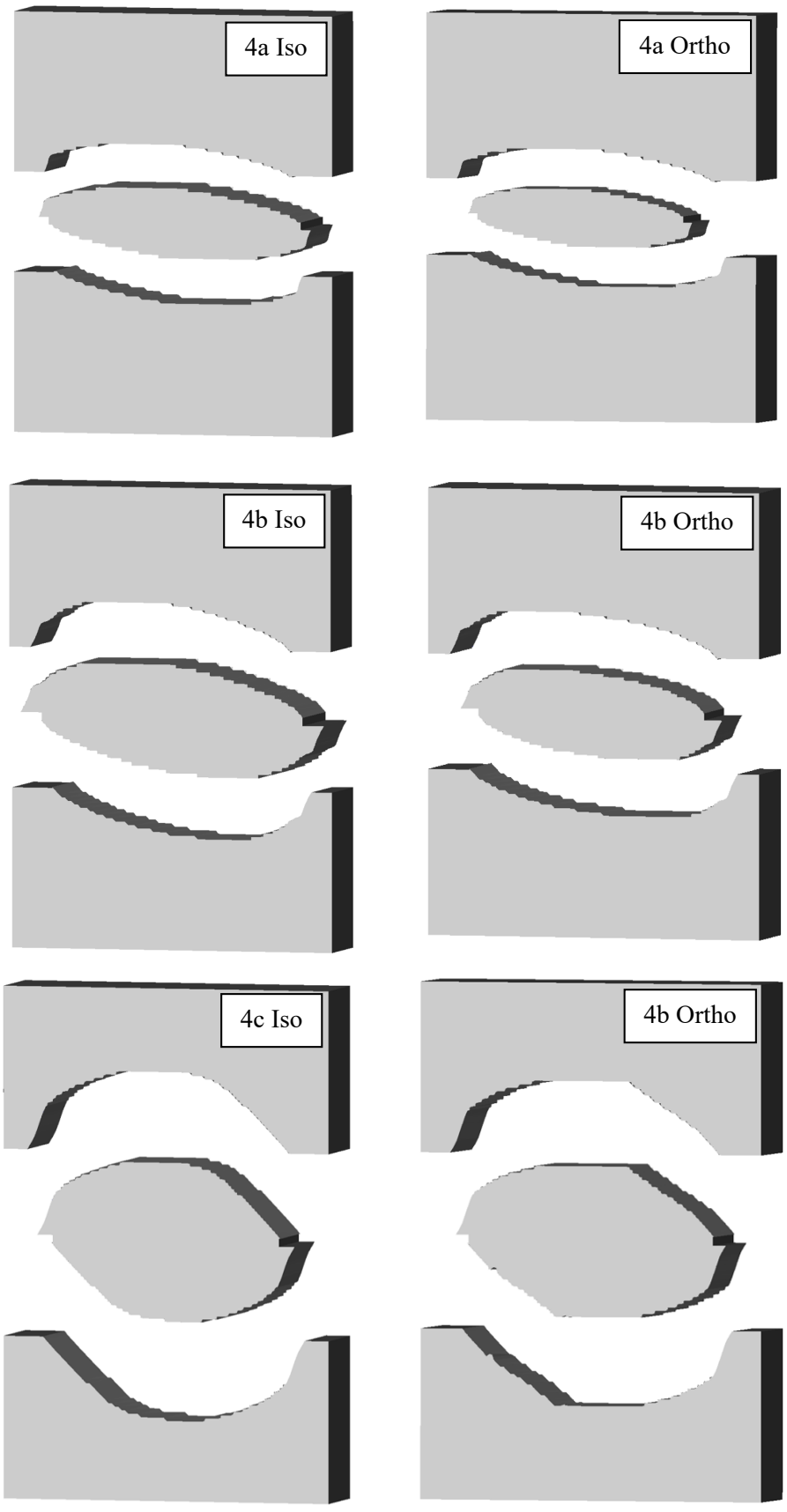

Figure 33. Crack surfaces of the mixed mode shearing-tension test, units 4a, 4b and 4c, for the isotropic and orthotropic Drucker-Prager models

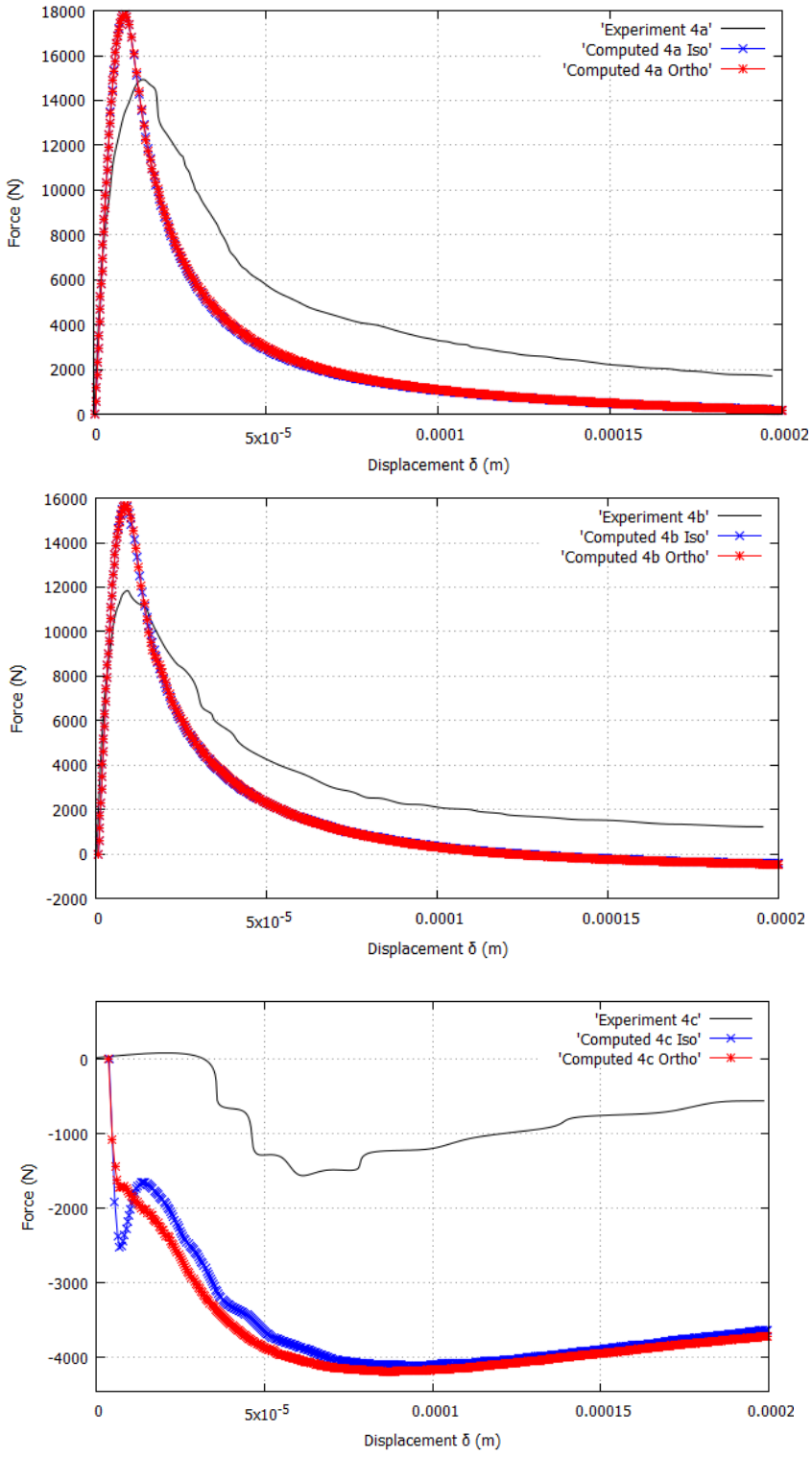

Figure 34. Force-displacement curves of the mixed mode shearing-tension test for units 4a, 4b and 4c

Isotropic and orthotropic Drucker-Prager models

Figure 32 shows the crack trajectories of the mixed mode shearing-tension test computed with the isotropic and orthotropic Drucker-Prager models for units 4a, 4b and 4c. The results computed with both the isotropic and orthotropic damage models are very similar. It can be seen that they are also rather resembling to the experiments for all the units. The computed results present the polar symmetric behavior expected for the intended loading and boundary conditions of the test. It should be noted that the experimental results lack this polar symmetry. There are several possible reasons for this, as it has been noted in [44]. Note that the computed crack paths are halfway between the upper and the lower cracks in the experiment.

Figure 33 also shows the crack surfaces resulting from the 3D analysis, with isotropic and orthotropic damage, plotted as an iso-level surface of the norm of displacements and the three pieces in which the specimen breaks. Both models produce lifelike crack surfaces.

Figure 34 shows the force-δ displacement curves for all three units. It can be seen that in all the specimens the experimental peak load is significantly lower than the computed one. This behavior has been systematically observed in all the solutions computed in references [47-50]. This may be due to the relative lack of symmetry of the experiment, resulting in slightly different crack paths and correspondingly different force-displacement curves. The isotropic and orthotropic models produce almost overlapping force-δ displacement curves.

In Scenario 4c, the axial force P reverses sign, turning rapidly to be negative, even if the applied axial displacement is positive, corresponding to pulling apart of the fixing frames. This behavior is peculiar and rather difficult to capture in a numerical simulation. References [47,50] are able to capture it, while [48,49] did not include this particular scenario. Figure 34 shows that the simulation captures the experimental behavior qualitatively, even if the quantitative difference is significant. Note that the value of the normal forces P involved in this case is much lower than the shear forces P_S.

4.5 Torsion test on a solid cylindrical specimen

In this section, the numerical analysis of a cylindrical concrete specimen subjected to a torsional load is performed. This example has been included to assess the performance of several isotropic and orthotropic damage models in Mode III tearing crack failure.

The specimen is a cylinder 450 mm long and with a 50 mm radius. A small hole of 5 mm radius has been introduced in the middle of the specimen to fix the occurrence of fracture. The material properties of the test are shown in Table 7. The load F inducing torsion is applied via increments of vertical displacements as shown in Figure 35.

Young's Modulus	$38 \cdot 10^9$ Pa
Poisson's Ratio	0.0
Tensile Strength	$2.3 \cdot 10^6$ Pa
Fracture Energy	80 J/m^2
Compressive Strength	$4.6 \cdot 10^7$ Pa

Table 7. Material parameters of the torsion test

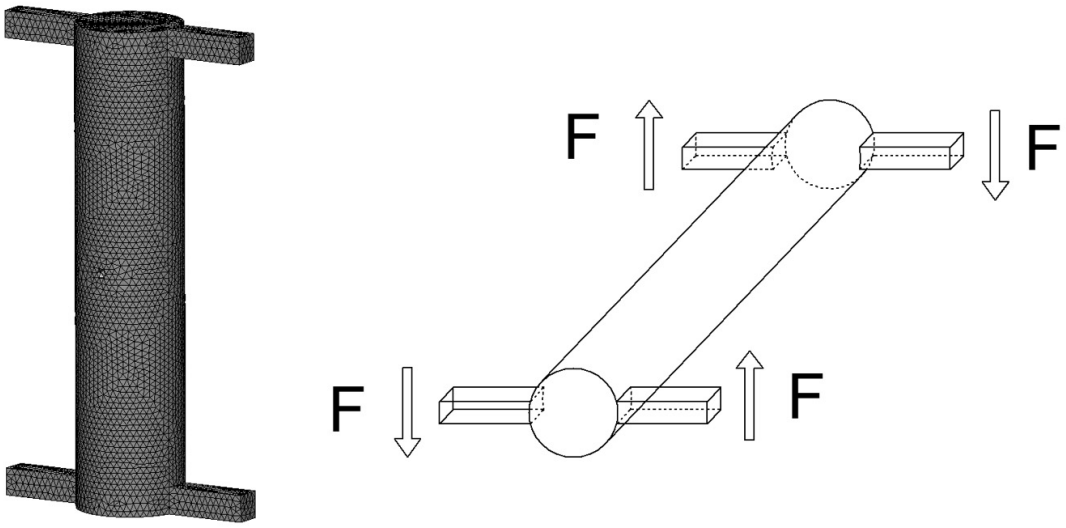

Figure 35. Geometry and loading of the torsion test (m)

To assess the performance of the different constitutive laws compared in this paper, the numerical results from the torsion test are compared to an analogous experiment, performed with a piece of chalk. The objective of this section is to accurately reproduce the twisting crack surface of the chalk shown in Figure 36, produced by pure torsional loading until failure.

Unlike for the case of uniaxial traction of section 4.2, the influence of Poisson's ratio in the solution of the three dimensional torsion test in terms of crack surface is negligible.

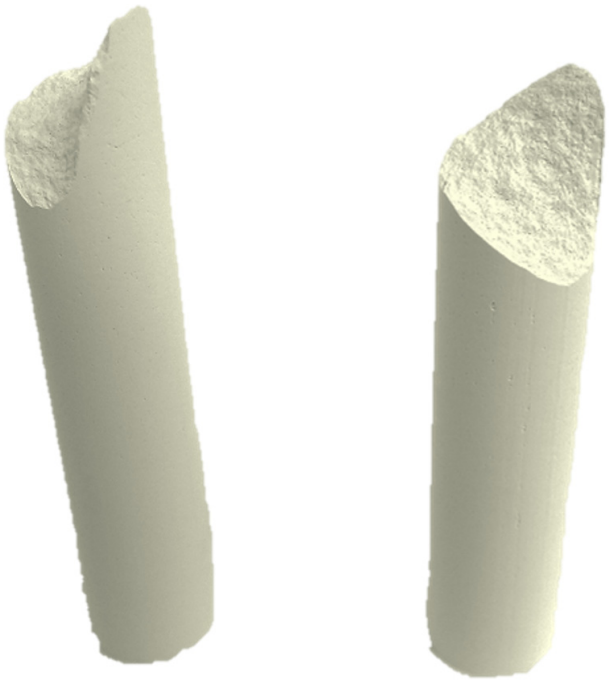

Figure 36. Analogous experiment of torsion test with a piece of chalk

This example is solved with the mixed FEM using 3D tetrahedral elements. The computational domain is discretized with fully unstructured meshes with elements of 6 mm, resulting in a mesh of 22,518 nodes, shown in Figure 35.

Isotropic models

Figure 37 (top) shows the computed crack surfaces in the specimen obtained with the isotropic Beltrami, Positive Beltrami, Rankine and Drucker-Prager criteria, plotted as the level set surface of the norm of displacements.

The Beltrami criterion produces a planar horizontal crack surface. This is accountable to the fact that, for pure torsion, this criterion coincides with the Von Mises criterion, that would yield exactly such a planar crack in the plane of maximum shear stress. Note that the Positive Beltrami and Rankine models produce very similar results, an helicoidal crack, which is explicable by their fairly similar formulation. As it has been explained in Section 2, these two criteria are only sensitive to tensile stress. Of all the isotropic models considered, the only one that is able to reproduce the helicoidal crack with 45º slope that occurs in the piece of chalk is the Drucker-Prager criterion.

Orthotropic models

Figure 37 (bottom) shows the computed crack surfaces obtained with the orthotropic Rankine and Drucker-Prager criteria. In this case, the isotropic and orthotropic Rankine models produce noticeably different results, even if they are driven by the same failure criteria. The reason for this is that the corresponding inelastic deformations are different. Only the orthotropic Rankine model produces the correct slope of 45º for the helicoidal crack. The orthotropic Drucker-Prager model performs similarly to its isotropic counterpart.

All these orthotropic criteria produce slightly different crack surfaces, all similar to the experiment, but the one that reproduces better the actual crack of the chalk in Figure 36 is the orthotropic Rankine constitutive law, as can be seen in detail in Figure 38. There, the similarities of the computed crack surface using this criterion and the test performed with the piece of chalk are highlighted.

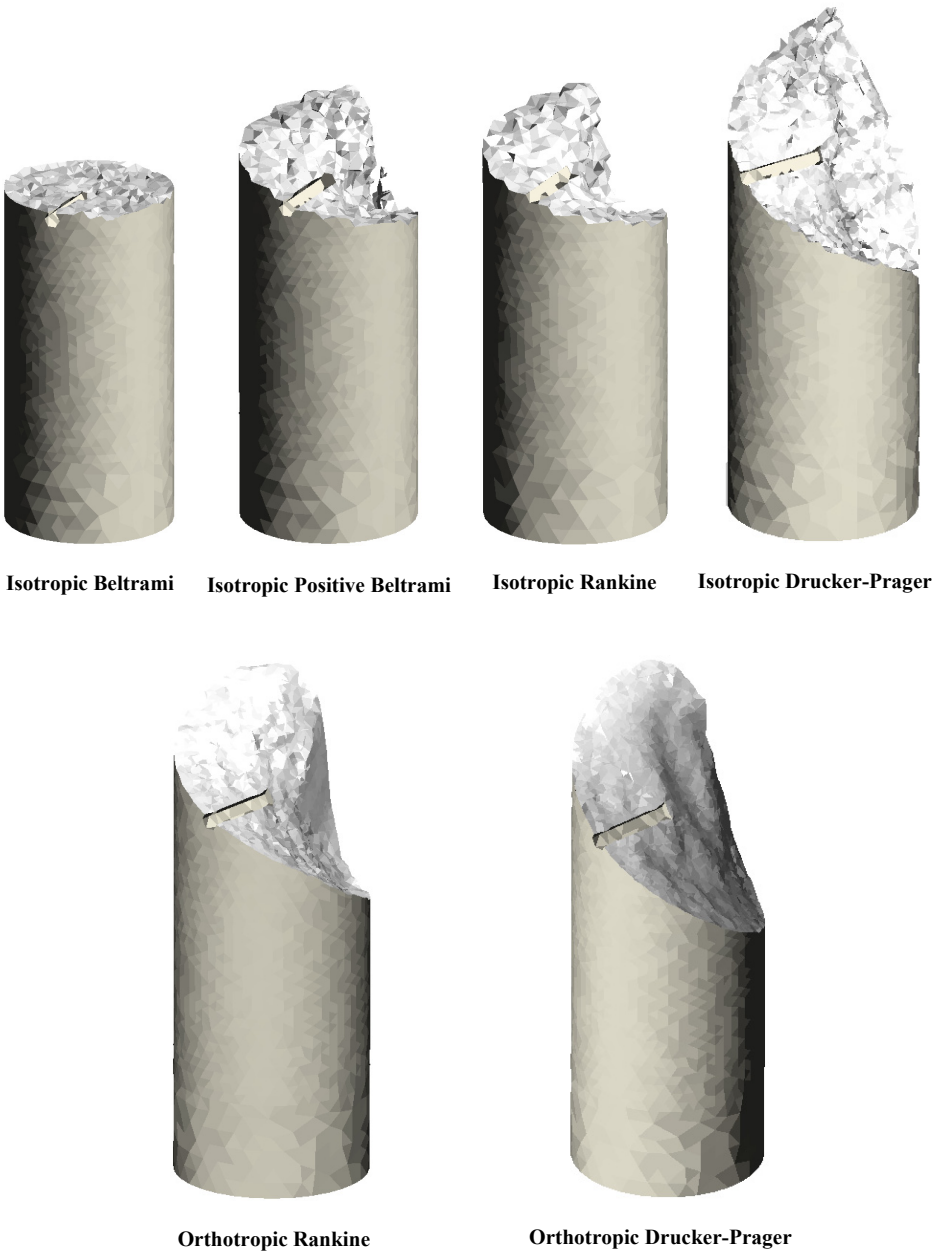

Figure 37. Crack surfaces of the torsion test, with several failure criteria

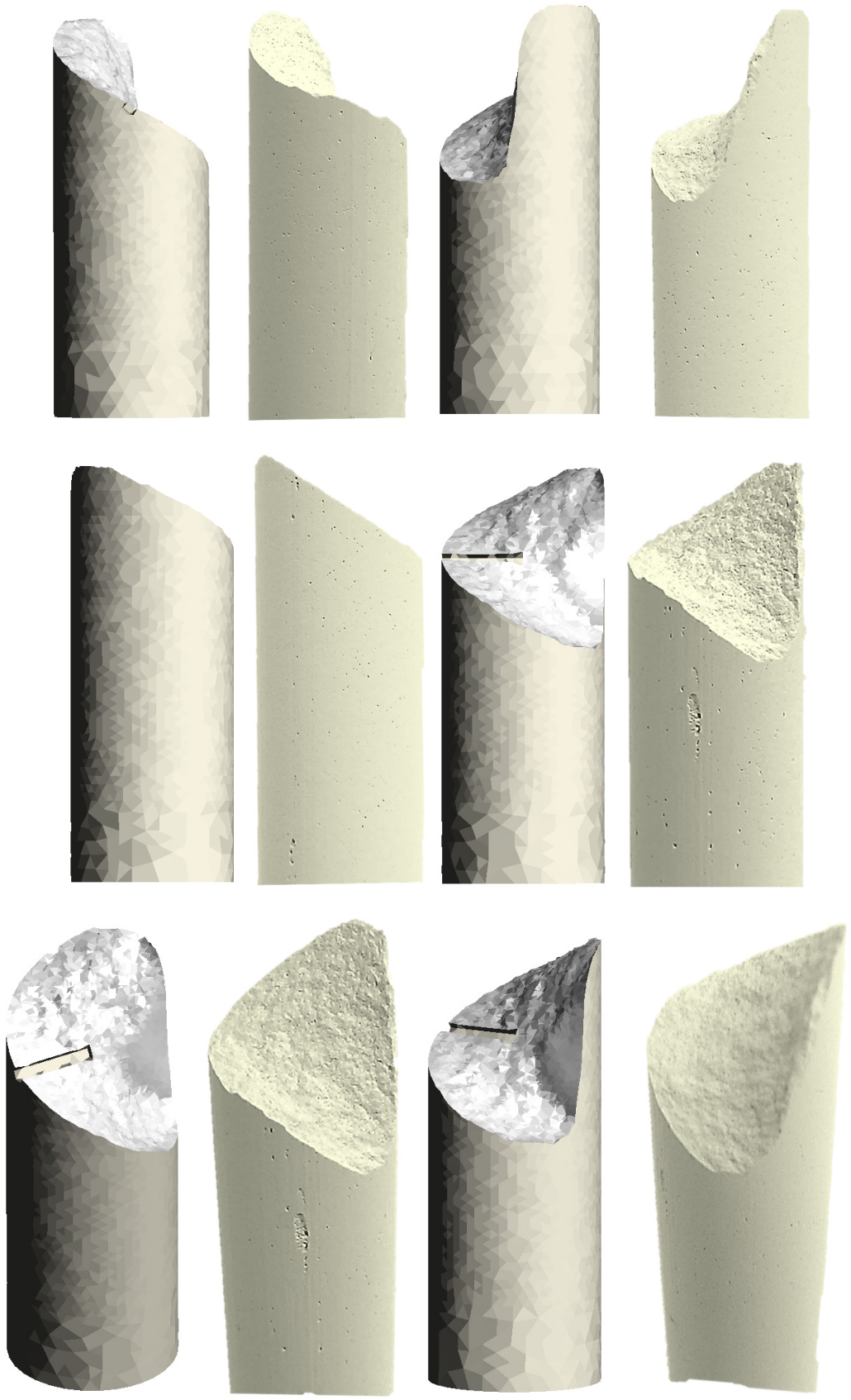

Figure 38. Different views of the crack surface obtained with the orthotropic Rankine damage model

5 Conclusions

In this work, the appraisement of planar, bending and twisting cracks in 3D is performed. To this end, a mixed finite element formulation is considered and the performance of several isotropic and orthotropic damage models is assessed. Several simulations are compared to theoretical and experimental results reported in the literature.

It is concluded that:

- The mixed finite element formulation is appropriate for solving the problem of quasi-brittle crack propagation without any mesh bias of the computed solution and without the need of any tracking technique.
- The enhanced accuracy of the mixed FE formulation allows for a transparent assessment of the several damage models considered without problems of spurious mesh bias associated to standard elements.
- The mixed FE formulation is fit to accommodate isotropic and orthotropic damage models.
- The enforcement of strain continuity in the mixed $\boldsymbol{\varepsilon/u}$ FE formulation practically vanishes the strain oscillations, and corresponding spurious stress transfer, in the crack and its vicinity, that pollute solutions obtained with the standard FE formulation.
- Isotropic and orthotropic damage models are able to compute planar, bending and twisting cracks with enhanced accuracy, producing solutions that match the analytical results and experiments.
- Different damage models produce different solutions in terms of crack surface and force-displacement curves to the same problem (geometry and loading).
- Differences between isotropic and orthotropic models depend on the actual problem. In some cases, significant variations are observed in terms of crack surfaces or force-displacement curves, while in other cases the models behave similarly.
- In mode I loading, differences between the isotropic and orthotropic models are caused by the Poisson effect.
- In problems of mixed mode I and II loading, the Drucker-Prager criterion produces excellent results in terms of computed crack path and load vs displacement curves. For this type of loading isotropic and orthotropic models produce very similar results.
- In mode III fracture, the Rankine criterion is remarkable when used in its orthotropic form. In this case, all the orthotropic damage models yield similar results.

From these, it is confirmed that the mixed FE formulation largely overcomes the difficulties associated both to isotropic and orthotropic damage models when using in the standard FE framework. Orthotropic models can be extended to include microcrack closure-reopening (MCR) effects, so that cyclic loading can be taken into account.

It is also noteworthy that all the examples in this paper are solved in 3D and that both tetrahedral and hexahedral FE are used. Prism elements can be similarly used, as the proposed FE formulation is not restricted to a particular FE integration.

6 References

[1] J. Rots, "Computational modeling of concrete fracture," Ph.D. Thesis, Delft University of Technology, 1988.

[2] M. Jirasek and T. Zimmermann, "Analysis of rotating crack model," *Journal of engineering mechanics,* vol. 124, no. 8, pp. 842-851, 1998.

[3] Y. Rashid, "Ultimate strength analysis of prestressed concrete pressure vessels," *Nuclear Engineering and Design,* vol. 7, no. 4, pp. 334-344, 1968.

[4] R. Cope, P. Rao, L. Clark and P. Norris, "Modelling of reinforced concrete behavior for finite element analysis of bridge slabs," *Numerical Methods for Nonlinear Problems, Pineridge Press, Swansey,* pp. 457-470, 1980.

[5] Z. Bazant, "Comment on orthotropic models for concrete and geomaterials," *Journal of Engineering Mechanics,* vol. 3, no. 109, pp. 849-865, 1983.

[6] R. Litton, "A contribution to the analysis of concrete structures under cyclic loading," Ph.D. Thesis, University of California, Berkeley, 1976.

[7] R. de Borst and P. Nauta, "Non-orthogonal cracks in a smeared finite element model," *Engineering Computations,* vol. 2, pp. 35-46, 1985.

[8] Z. Bazant, "Size effect in blunt fracture: concrete, rock, metal," *Journal of Engineering Mechanics,* vol. 4, no. 110, pp. 518-535, 1984.

[9] I. Carol and P. Prat, "A statically constrained microplane model for the smeared analysis of concrete cracking," *International Conference on Computer Aided Analysis and Design of Concrete Structures,* vol. 2, pp. 919-930, 1990.

[10] K. Willam, E. Pramono and S. Sture, "Fundamental issues of smeared crack models," *SEM/RILEM, International Conference on Fracture of Concrete and Rock,* pp. 142-153, 1987.

[11] P. Feenstra, "Computational aspects of biaxial stress in plain and reinforced concrete," Ph.D. Thesis, Delft University of Technology*,* 1993.

[12] S. Weihe and B. Kroplin, "Fictitious crack models: a classification approach," *Aedificatio publishers, Freiburg,* 1995.

[13] S. Weihe, B. Kroplin and R. De Borst, "Classification of smeared crack modles based on material and structural properties," *International Journal of Solids and Structures,* no. 12, pp. 1289-1308, 1998.

[14] R. Faria, J. Oliver and M. Cervera, "A strain-based plastic viscous-damage model for massive concrete structures," *International Journal of Solids and Structures,* vol. 35, no. 14, pp. 1533-1558, 1998.

[15] G. Hofstetter and G. Meschke, "Numerical modeling of concrete cracking," *Springer Science and Business Media,* vol. 532, 2011.

[16] J. Oliver, M. Cervera, S. Oller and J. Lubliner, "Isotropic damage models and smeared crack analysis of concrete," *II international conference on computer aided analysis and design of concrete,* 1990.

[17] M. Cervera, E. Hinton and O. Hassan, "Nonlinear analysis of reinforced concrete plate and shell structures using 20-noded isoparametric brick elements," *Computers and Structures,* vol. 25, no. 6, pp. 845-869, 1987.

[18] M. Cervera, "An orthotropic mesh corrected crack model," *Computer Methods and Applied Mechanics in Engineering,* vol. 197, no. 17-18, pp. 1603-1619, 2008.

[19] M. Cervera, "A smeared-embedded mesh-corrected damage model for tensile cracking," *International Journal for Numerical Methods in Engineering,* pp. 1930-1954, 2008.

[20] M. Cervera, M. Chiumenti and R. Codina, "Mixed stabilized finite element methods in nonlinear solid mechanics. Part I: Formulation," *Computer Methods in Applied Mechanics and Engineering,* vol. 199, no. 37-40, pp. 2559-2570, 2010.

[21] M. Cervera, M. Chiumenti and R. Codina, "Mixed stabilized finite element methods in nonlinear solid mechanics. Part II: Strain localization," *Computer Methods in Applied Mechanics and Engineering,* vol. 199, no. 37-40, pp. 2571-2589, 2010.

[22] M. Cervera and C. Tesei, "An energy-equivalent d+/d- damage model with enhanced microcrack closure-reopening capabilities for cohesive-frictional materials," *Materials,* vol. 10, no. 4, p. 433, 2017.

[23] M. Cervera, M. Chiumenti and R. Codina, "Mesh objective modelling of cracks using continuous linear strain and displacement interpolations," *International Journal for Numerical Methods in Engineering,* vol. 87, no. 10, pp. 962-987, 2011.

[24] M. Cervera, M. Chiumenti, L. Benedetti and R. Codina, "Mixed stabilized finite element methods in nonlinear solid mechanics. Part III: Compressible and incompressible plasticity," *Computer Methods in Applied Mechanics and Engineering,* vol. 285, no. 0, pp. 752-775, 2015.

[25] M. Cervera, G. Barbat and M. Chiumenti, "Finite element modelling of quasi-brittle cracks in 2D and 3D with enhanced strain accuracy," *Computational Mechanics,* vol. 60, no. 5, pp. 767-796, 2017.

[26] O. Zienkiewicz, R. Taylor and Z. Zhu, "The finite element method, Vol. 1," *7th edition, Amsterdam, Elsevier Butterworth-Heinemann,* 1989.

[27] J. Simo and J. Ju, "Strain- and stress-based continuum damage models. I: Formulation; II Compatational aspects.," *International Journal of Solids and Structures,* no. 23, pp. 821-869, 1987.

[28] J.-Y. Wu and M. Cervera, "Strain localization analysis of elastic-damaging frictional-cohesive materials: Analytical results and numerical verification," *Materials,* vol. 10, no. 4, 2017.

[29] G. Voyiadjis, Z. Taqieddin and P. Kattan, "Anisotropic damage-plasticity model for concrete," *International Journal of Plasticity,* vol. 24, pp. 1946-1965, 2008.

[30] J. Courdebois and F. Sidoroff, "Endommagement anisotrope en elasticité et plasticité," *Journal de Mecanique Theorique et Appliquee,* vol. Special Volume, pp. 45-60, 1982.

[31] I. Carol, E. Rizzi and K. Willam, "On the formulation of anisotropic elastic degradation. I: Theory based on pseudo-logarithmic damage tensor rate; II: Generalized pseudo-Rankine model for tensile damage," *International Journal of Solids and Structures,* vol. 38, no. 4, pp. 491-546, 2001.

[32] L. Benedetti, M. Cervera and M. Chiumenti, "3D modelling of twisting cracks under bending and torsion skew notched beams," *submitted to Engineering Fracture Mechanics,* 2017.

[33] M. Cervera, C. Agelet de Saracibar and M. Chiumenti, "COMET: Coupled mechanical and thermal analysis. Data input manuel, Version 5.0, Technical report IT-308. Available from http://www.cimne.upc.edu," 2002.

[34] "GiD: the personal pre and post-processor.," *CIMNE, Technical University of Catalonia,* p. <http://gid.cimne.upc.ed>, 2002.

[35] J.-Y. Wu and S.-L. Xu, "An augmented multicrack elastoplastic damage model for tensile cracking," *International Journal of Solids and Structures,* vol. 48, pp. 2511-2528, 2011.

[36] P. Feenstra and R. de Borst, "A plasticity model and algorithm for mode-I cracking in concrete," *International Journal for Numerical Methods in Engineering,* vol. 38, no. 5, pp. 2509-2529, 1995.

[37] P. Pivonka, J. Ozbolt, R. Lackner and H. Mang, "Comparative studies of 3D-constitutive models for concrete: application to mixed-mode fracture," *International Journal for Numerical Methods in Engineering,* vol. 60, pp. 549-570, 2004.

[38] M. Arrea and A. Ingraffea, "Mixed-mode crack propagation in mortar and concrete," *Report No. 81-13, Department of Structural Engineering, Cornell University, Ithaca, NY,* 1982.

[39] J. Galvez and D. Cendón, "Simulación de la fractura del hormigón en modo mixto," *Revista Internacional de Metodos Numericos para Calculo y Diseño en Ingenieria,* vol. 18, no. 1, pp. 31-58, 2002.

[40] P. Areias, T. Rabczuk and J. César de Sá, "A novel two-stage discrete crack method based on the screened Poisson equation and local mesh refinement," *Computational Mechanics,* vol. 58, pp. 1003-1018, 2016.

[41] T. Rabczuk and T. Belytschko, "Cracking particles: a simplified meshfree method for arbitrary evolving cracks," *International Journal for Numerical Methods in Engineering,* vol. 61, pp. 2316-2343, 2004.

[42] A. Saleh and M. Aliabadi, "Crack growth analysis in concrete using boundary element method," *Engineering Fracture Mechanics,* vol. 51, no. 4, pp. 533-545, 1995.

[43] W. Gerstle and M. Xie, "FEM modeling of fictitious crack propagation in concrete," *Journal of Engineering Mechanics,* vol. 118, no. 2, pp. 416-434, 1992.

[44] M. Nooru-Mohamed, "Mixed-mode fracture of concrete: an experimental approach," Ph.D. Thesis, Delft University of Technology, 1992.

[45] M. Di Prisco, L. Ferrara, F. Meftah, J. Pamin, R. De Borst, J. Mazars and J. Reynouard, "Mixed mode fracture in plain and reinforcement concrete: some results on benchmark tests," *International Journal of Fracture,* vol. 103, pp. 127-148, 2000.

[46] J. Oliver, A. Huespe, E. Samaniego and E. Chaves, "Continuum approach to the numerical simulation of material failure in concrete," *International Journal for Numerical and Analytical Methods in Geomechanics,* vol. 28, pp. 609-632, 2004.

[47] M. Cervera and M. Chiumenti, "Smeared crack approach: back to the original track," *International Journal for Numerical and Analytical Methods in Geomechanics,* vol. 30, pp. 1173-1199, 2006.

[48] M. Dejong, M. Hendriks and J. Rots, "Sequentially linear analysis of fracture under non-proportional loading," *Engineering Fracture Mechanics,* vol. 75, pp. 5042-5056, 2008.

[49] A. Slobbe, M. Hendriks and J. Rots, "Smoothing the propagation of smeared cracks," *Engineering Fracture Mechanics,* vol. 132, p. 147–168, 2014.

[50] S. Saloustros, L. Pela and M. Cervera, "A crack-tracking technique for localized cohesive-frictional damage," *Engineering Fracture Mechanics,* vol. 150, pp. 96-114, 2015.

Out-of-plane seismic response and failure mechanism of masonry structures using finite elements with enhanced strain accuracy

G. Vlachakis, M. Cervera, G. B. Barbat and S. Saloustros

Engineering Failure Analysis

Vol. 97, pp. 534-555, (2019)

https://doi.org/10.1016/j.engfailanal.2019.01.017

Out-of-plane seismic response and failure mechanism of masonry structures using finite elements with enhanced strain accuracy

G. Vlachakis[1], M. Cervera[1,2], G. B. Barbat[1], S. Saloustros[1]

[1] Department of Civil and Environmental Engineering, Universitat Politècnica de Catalunya, UPC-BarcelonaTech, Campus Nord UPC, Jordi Girona 1-3, 08034 Barcelona, Spain.

[2] CIMNE – International Center for Numerical Methods in Engineering, Campus Nord UPC, Gran Capità S/N, 08034 Barcelona, Spain

giorgovlachaki@gmail.com, miguel.cervera@upc.edu, gbarbat@cimne.upc.edu, savvas.saloustros@upc.edu

Abstract

The out-of-plane response is a complex and at the same time key aspect of the seismic vulnerability of masonry structures. It depends on several factors, some of which are the material properties, the quality of the walls, the geometry of the structure, the connections between structural elements and the stiffness of the diaphragms.

During the last years, a wide variety of numerical methods has been employed to assess the out-of-plane behaviour of unreinforced masonry structures. Finite element macro-modelling approaches are among the most famous as they allow modelling large structures at a reasonable computational cost. However, macro-modelling approaches may result in a non-realistic representation of localized cracks and a dependency of the numerical solution on the finite element mesh.

Mixed strain/displacement finite elements have been recently proposed as a remedy to the above numerical pathologies. Due to the independent interpolation of strains and displacements these finite element formulations are characterized by an enhanced accuracy in strain localization and crack propagation problems, being at the same time practically mesh independent. For these reasons, mixed finite elements are employed in this work for the out-of-plane assessment of unreinforced masonry structures, being at the same time their first real-scale application. A full-scale experimental campaign of two masonry structures, a stone and a brick one, subjected to shaking-table tests is chosen as reference benchmark. Their structural response under seismic actions is numerically assessed through nonlinear static analysis. The proposed approach is validated through the comparison of the numerical results with the experimental ones, as well as with the results obtained using standard irreducible finite elements.

Keywords: Masonry Structures, Out-of-plane loading, Pushover analysis, Cracking, Mixed Finite Elements

1 Introduction

Unreinforced masonry structures are one of the oldest structural typologies that are still worldwide inhabited and constitute the majority of the built cultural heritage. However, past seismic events have demonstrated that this type of structures is extremely vulnerable to horizontal loading (e.g. earthquakes of Umbria-Marche 1997, Kashmir 2005, Pisco 2007, L'Aquila 2009, Haiti 2010, Christchurch 2011, Lorca 2011, Emilia Romagna 2012, Nepal 2015, Central Italy 2016, Lesbos 2017, Mexico 2017). According to several post-earthquake surveys [1–7], out-of-plane mechanisms are undoubtedly the most crucial among the possible failures of unreinforced masonry structures under horizontal loading. Nevertheless, the out-of-plane behaviour is one of the most complex and yet inadequately addressed topics in the seismic analysis of masonry buildings [8,9]. The reason for this is the dependence of the out-of-plane response on several factors, such as the material properties, the quality of the walls, the geometry of the structure, the connections between structural elements and the stiffness of the horizontal diaphragms [10].

Engineering efforts towards the assessment of the out-of-plane response of unreinforced masonry structures have resulted in the development of several structural analysis methods and computational tools [11,12]. Although the available methods may significantly contribute to the estimation of the seismic safety of existing masonry structures, they still lack the capacity to predict realistic failure mechanisms and to give a reliable estimate of the seismic displacement demand [13].

From a methodological point of view, the different assessment techniques can be categorized in two main groups: analytical methods and numerical approaches. The former ones (e.g. [11,12,14-22]) are based on rigid body mechanics and are characterized by high efficiency and a low number of variables. Nevertheless, the identification and study of the possible collapse mechanisms depends highly on the expertise of the analyst. On the other hand, the advance of computational capabilities and methods in the last decades, has led to the development of a wide variety of numerical approaches [11,23–25]. The selection of an approach upon another is a complex issue, which depends on the field of application, the complexity and scale of the structure and the available resources.

One way to categorize the different numerical strategies is considering the level of the simulation scale. Today, there exist numerical approaches that model the distinct nature of the constituents of masonry (blocks and mortar), while other techniques consider masonry as a homogenous material with average properties. Within the first category of *direct numerical simulations*, the most common techniques used for the assessment of the out-of-plane response of masonry structures are the finite element micro-, meso- and multi-scale modelling (e.g. [26–29]), the discrete element method [30–32], and the combined finite-discrete element approach [33]. Although such techniques have proved to be very effective in simulating complex phenomena, the difficulties in obtaining the input parameters (i.e. exact geometry, large number of material and dynamic properties) and, most importantly, their high computational cost hamper their application to large-scale structures.

On the other hand, homogenization procedures are suitable for large-scale applications, as they allow computational modelling at a reasonable cost. A wide variety of homogenization techniques can be found in literature, mainly referring to numerical limit analysis [34–36], discrete macro-modelling [37] and finite element macro-modelling [38].

The finite element macro-modelling approach has been widely used in the last decades[23,24,39], and especially for large-scale structures [40–43]. Its main advantages are its capability to capture the complete loading history and mechanism formation of a structure and its compatibility with modern assessment concepts (displacement-based and energy based approaches).

Despite the aforementioned advantages, finite element techniques still encounter several challenges that hinder the assessment of the out-of-plane response of masonry structures. In particular, the reliable mesh-independent simulation of crack propagation in quasi-brittle materials, such as masonry, is still an open issue within the framework of finite element methods. In the last decades, numerous attempts have been made in order to confront this drawback, adopting mainly two different approaches for the crack simulation: continuous and discontinuous approaches. Within the continuous approach, the failure process is simulated by the degradation of the material at the constitutive level, while within the discontinuous approach, an explicit crack representation is considered and the crack is handled as a geometrical discontinuity. For a general overview of these methods, references [44–47] are recommended.

In the framework of the continuous approach, mixed finite elements have been recently employed as an alternative remedy to the problem of spurious mesh-dependency [48–52]. The main characteristic of the mixed formulation is the independent discrete approximation of main mechanical fields of interest. Particularly for the problem of strain localization, mixed finite elements are used to independently consider the strain field of the structure, in addition to the displacements. In this way, an enhanced accuracy for the strains (and consequently also for the stresses) is achieved, which is crucial for the quasi-singular points that lead the fracture and failure processes. This strategy allows mixed formulations to achieve local convergence, resulting in practically mesh-independent results.

The performance of the mixed strain/displacement formulation has been tested under several experimental and theoretical problems both in 2D and 3D including Mode I, Mode II, Mode III and mixed Mode fracture [49–54]. Mixed finite elements have shown to be capable of overcoming many of the challenges related to strain localization problems, providing accurate and practically mesh-independent solutions, without the need of auxiliary crack tracking techniques that are inherent in many discrete and continuous finite element crack approaches [47]. Another important advantage is the possibility to use mixed finite elements with any constitutive law (i.e. plasticity or damage) since their formulation follows the classical local constitutive mechanics framework.

The aim of this work is to explore the capabilities of the mixed strain/displacement FE formulation to assess the out-of-plane seismic response and failure mechanism of two real-scale masonry structures. The full-scale shaking table tests of two unreinforced masonry mock-ups carried out in reference [55] are chosen as benchmark, and the effect of the seismic action is simulated through non-linear static analyses. In order to evaluate the efficiency of the proposed approach, the results are compared with the experimental ones in terms of collapse mechanism and load capacity. The presented analyses are the first application of the mixed finite elements to the simulation of real-scale structures. The enhanced performance of the mixed formulation is validated through their comparison with the results obtained using standard irreducible finite elements.

The outline of the paper is as follows. Section 2 summarizes the mixed finite element formulation and Section 3 outlines the adopted isotropic damage constitutive model. Section 4 presents the numerical simulations of the masonry structures and their comparison with the experimental results and numerical analysis using standard irreducible finite elements. Section 5 includes a comparative study of mesh-dependence using standard and mixed finite elements for in-plane and out-of-plane loading. Finally, the conclusions of the study are summarized in Section 6.

2 Mixed Finite Elements

2.1 Formulation of the mixed finite elements

In this section, the matrix formulation of the mixed strain/displacement finite elements is briefly described, while a detailed presentation can be found in reference [53]. The matrix and vector notation adopts Voigt's convention for symmetric tensors.

2.1.1 Variational form

In a 3D problem, the displacements, the strains, the stresses and the body forces at a certain point can be noted as vectors: $\boldsymbol{u} = (u, v, w)^{\boldsymbol{T}}$, $\boldsymbol{\varepsilon} = \left(\varepsilon_x, \varepsilon_y, \varepsilon_z, \gamma_{xy}, \gamma_{yz}, \gamma_{xz}\right)^T$, $\boldsymbol{\sigma} = \left(\sigma_x, \sigma_y, \sigma_z, \tau_{xy}, \tau_{yz}, \tau_{xz}\right)^T$ and $\boldsymbol{f} = \left(f_x, f_y, f_z\right)^T$ respectively. The mechanical boundary value problem is defined in terms of these magnitudes, related through the compatibility, equilibrium and constitutive equations, as well as by the boundary conditions. Displacements and strains are locally related through the compatibility equations

$$\boldsymbol{\varepsilon} = \boldsymbol{\mathcal{S}}\boldsymbol{u} \tag{1}$$

where $\boldsymbol{\mathcal{S}}$ is the symmetric gradient operator.

The stresses and body forces are related through Cauchy's equilibrium equation

$$\boldsymbol{\mathcal{S}}^T\boldsymbol{\sigma} + \boldsymbol{f} = \boldsymbol{0} \tag{2}$$

where $\boldsymbol{\mathcal{S}}^T$ is the divergence operator. The stresses and the strains are associated through the constitutive equation

$$\boldsymbol{\sigma} = \boldsymbol{D}_S\boldsymbol{\varepsilon} \tag{3}$$

where $\boldsymbol{D}_S$ is the secant constitutive matrix.

In the mixed strain/displacement formulation presented herein, the strains are considered as unknowns in addition to the displacements. Therefore, the strong form can be obtained by pre-multiplying equation (1) with the secant constitutive matrix $\boldsymbol{D}_S$ and introducing equation (3) into (2)

$$-\boldsymbol{D}_S\boldsymbol{\varepsilon} + \boldsymbol{D}_S\boldsymbol{\mathcal{S}}\boldsymbol{u} = \boldsymbol{0} \tag{4}$$

$$\boldsymbol{\mathcal{S}}^T(\boldsymbol{D}_S\boldsymbol{\varepsilon}) + \boldsymbol{f} = \boldsymbol{0} \tag{5}$$

Equations (4) and (5), together with the proper boundary conditions of the problem compose the strong form of the mixed formulation. These are acting on the boundary Γ of the body, either as prescribed displacements Γ_u or as prescribed tractions Γ_t.

Note that further substitution of equation (4) into equation (5) would eliminate the strains as independent unknowns, and yield the standard formulation in terms of displacements only.

The variational form can be obtained in two steps. First, by pre-multiplying equation (4) with an arbitrary virtual strain vector $\delta\boldsymbol{\varepsilon}$ and integrating over the spatial domain Ω, and second, by pre-multiplying equation (5) with an arbitrary virtual displacement $\delta\boldsymbol{u}$ and integrating over the spatial domain Ω. Then, the Divergence Theorem is used in the later equation, while the boundary conditions on Γ_u are assumed, for simplicity, $\boldsymbol{u} = \boldsymbol{0}$. The nontrivial case $\boldsymbol{u} = \overline{\boldsymbol{u}}$ on Γ_u, can be accommodated following standard arguments. Thus, the variational form of the problem is

$$-\int_{\Omega} \delta\boldsymbol{\varepsilon}^T \boldsymbol{D}_S \boldsymbol{\varepsilon}\, \mathrm{d}\Omega + \int_{\Omega} \delta\boldsymbol{\varepsilon}^T \boldsymbol{D}_S \mathcal{S}\boldsymbol{u}\, \mathrm{d}\Omega = 0 \;\; \forall \delta\boldsymbol{\varepsilon} \tag{6}$$

$$\int_{\Omega} (\boldsymbol{\mathcal{S}}\delta\boldsymbol{u})^T (\boldsymbol{D}_S \boldsymbol{\varepsilon})\, \mathrm{d}\Omega = \int_{\Omega} \delta\boldsymbol{u}^T \boldsymbol{f}\, \mathrm{d}\Omega + \int_{\Gamma_t} \delta\boldsymbol{u}^T \bar{\boldsymbol{t}}\, \mathrm{d}\Gamma \;\; \forall \delta\boldsymbol{u} \tag{7}$$

Summarizing, the weak form of the mixed problem is to find the unknowns $\boldsymbol{u}$ and $\boldsymbol{\varepsilon}$ that verify the system of equations (6)-(7) and the boundary conditions imposed on Γ_u and Γ_t.

2.1.2 Finite element approximation and stabilization

In the discretized domain ($\Omega = \cup\Omega_e$) of the finite element approximation, displacements $\boldsymbol{u}$ and strains $\boldsymbol{\varepsilon}$ are approximated by

$$\boldsymbol{u} \cong \widehat{\boldsymbol{u}} = \boldsymbol{N}_u \boldsymbol{U} \tag{8}$$

$$\boldsymbol{\varepsilon} \cong \hat{\boldsymbol{\varepsilon}} = \boldsymbol{N}_\varepsilon \boldsymbol{E} \tag{9}$$

where $\boldsymbol{U}$ and $\boldsymbol{E}$ are the displacements and strains, respectively, at the nodes of the finite element mesh, while $\boldsymbol{N}_u$ and $\boldsymbol{N}_\varepsilon$ are the interpolation functions adopted in the finite elements.

If equal interpolations are considered for the strains and the displacements in equation (8) and (9) the solvability and the stability of the problem is not verified since the Inf-Sup condition [56] is not satisfied. Therefore, a stabilization technique is used in order to circumvent this problem, and ensure the necessary stability via the Orthogonal Subscales Method [48].

Specifically, this is achieved by substituting the approximated strains with the following form instead of using equation (9)

$$\boldsymbol{\varepsilon} \cong \hat{\boldsymbol{\varepsilon}} = \boldsymbol{N}_\varepsilon \boldsymbol{E} + \tau_\varepsilon (\boldsymbol{B}_u \boldsymbol{U} - \boldsymbol{N}_\varepsilon \boldsymbol{E}) = (1 - \tau_\varepsilon)\boldsymbol{N}_\varepsilon \boldsymbol{E} + \tau_\varepsilon \boldsymbol{B}_u \boldsymbol{U} \tag{10}$$

where $\boldsymbol{B}_u$ is defined as $\boldsymbol{B}_u = \boldsymbol{\mathcal{S}}\boldsymbol{N}_u$, and τ_ε is a stabilization parameter that ranges from 0 to 1. Note that this stabilization technique is fully consistent, as the stabilization form consists of the residual of equation (1). This means that the stabilization term $(\boldsymbol{B}_u \boldsymbol{U} - \boldsymbol{N}_\varepsilon \boldsymbol{E})$ tends to zero on mesh refinement. Observe that for $\tau_\varepsilon = 0$ the stabilization effect is lost, while for $\tau_\varepsilon = 1$ the standard irreducible formulation is recovered.

Intermediate values of the stabilization parameter represent alternative blending between the purely mixed and the irreducible FE forms.

Substituting equations (8) and (10) into the variational form of the problem, the system of equations of the stabilized mixed problem, written in matrix form, emerges as

$$\begin{bmatrix} -\boldsymbol{M}_{\boldsymbol{\tau}} & \boldsymbol{G}_{\boldsymbol{\tau}} \\ \boldsymbol{G}_{\boldsymbol{\tau}}^T & \boldsymbol{K}_{\boldsymbol{\tau}} \end{bmatrix} \begin{bmatrix} \boldsymbol{E} \\ \boldsymbol{U} \end{bmatrix} = \begin{bmatrix} \boldsymbol{0} \\ \boldsymbol{F} \end{bmatrix} \tag{11}$$

such that

$$\boldsymbol{M}_{\boldsymbol{\tau}} = (1 - \tau_\varepsilon) \int_{\Omega} \boldsymbol{N}_\varepsilon^T \boldsymbol{D}_S \boldsymbol{N}_\varepsilon\, \mathrm{d}\Omega \tag{12}$$

$$\boldsymbol{G}_{\boldsymbol{\tau}} = (1 - \tau_\varepsilon) \int_{\Omega} \boldsymbol{N}_\varepsilon^T \boldsymbol{D}_S \boldsymbol{B}_u\, \mathrm{d}\Omega \tag{13}$$

$$\boldsymbol{K}_{\boldsymbol{\tau}} = \tau_{\varepsilon} \int_{\Omega} \boldsymbol{B}_u^T \boldsymbol{D}_S \boldsymbol{B}_u \, \mathrm{d}\Omega \tag{14}$$

$$\boldsymbol{F} = \int_{\Omega} \boldsymbol{N}_u^T \mathbf{f} \, \mathrm{d}\Omega + \int_{\Gamma_t} \boldsymbol{N}_u^T \bar{\mathbf{t}} \, \mathrm{d}\Gamma \tag{15}$$

where $[\boldsymbol{E}\ \boldsymbol{U}]^T$ are the strains and displacements at the nodes of the mesh, the unknowns of the algebraic problem to be solved.

3 Continuum damage model

An isotropic continuum damage model is adopted [57] for modelling of the non-linear behaviour of the material.

In this model, an internal damage index d describes at constitutive level the material degradation. This scalar-type variable ranges from 0 for an intact material to 1 for a completely damaged one. The constitutive equation is described as

$$\boldsymbol{\sigma} = \boldsymbol{D}_S \boldsymbol{\varepsilon} = (1-d)\boldsymbol{D}_0 \boldsymbol{\varepsilon} = (1-d)\overline{\boldsymbol{\sigma}} \tag{16}$$

where the effective stress $\overline{\boldsymbol{\sigma}}$ is introduced as $\overline{\boldsymbol{\sigma}} = \boldsymbol{D}_0 \boldsymbol{\varepsilon}$, corresponding to the hypothesis of strain equivalence [58].

The damage criterion, F, is

$$\mathrm{F}\left(\sigma_{eq}, r\right) = \sigma_{eq}(\overline{\boldsymbol{\sigma}}) - r \leq 0 \tag{17}$$

where $\sigma_{eq}(\overline{\boldsymbol{\sigma}})$ is the equivalent effective stress defining the adopted failure surface, and r is the current stress-like threshold, described in the following.

A simple Rankine failure criterion is adopted in this study, triggering only tensile damage. The equivalent effective stress is then defined as

$$\sigma_{eq}(\overline{\boldsymbol{\sigma}}) = \langle \bar{\sigma}_1 \rangle \tag{18}$$

where $\bar{\sigma}_1$is the maximum principal effective stress, while $\langle \cdot \rangle$ stands for the Macaulay brackets ($\langle x \rangle = x$ if $x \geq 0$, $\langle x \rangle = 0$ if $x < 0$).

The initial value of the stress-like damage threshold r is equal to the tensile strength of the material $r_0 = f_t$, while it is explicitly updated at every step of the analysis $\hat{t}$ in order to consider the loading history and guarantee the irreversibility of damage

$$r = \max\left(r_0, \max\sigma_{eq}(\hat{t})\right) \qquad \hat{t} \in [0, t]. \tag{19}$$

An exponential softening law is adopted for describing the evolution of the damage index

$$d = d(r) = 1 - \frac{r_0}{r} exp\left(-2H_s \frac{r - r_0}{r_0}\right) \tag{20}$$

where $H_s \geq 0$ is the discrete softening parameter, taking into account the fracture energy of the material G_f and the characteristic finite element width b, ensuring mesh-size objective results according to the crack-band theory [59]. It is defined as

$$H_s = \frac{\overline{H}_s b}{1 - \overline{H}_s b} \tag{21}$$

where $\overline{H}_s$ is the inverse of the material length $\mathcal{L}$

$$\bar{H}_s^{-1} = \mathcal{L} = \frac{2EG_f}{(f_t)^2}. \tag{22}$$

4 Numerical simulation of two masonry structures

In this section, the mixed finite element formulation is applied for the first time to the analysis of two real-scale masonry structures, which were tested in an experimental campaign by Candeias et al. [55].

The experimental campaign was carried in the National Laboratory of Civil Engineering, in Lisbon, Portugal and included two masonry structures, a brick one and a stone one, subjected to shaking-table seismic motion. The mock-ups have a non-symmetric U-shape plan and are composed of three walls. These are the façade with a central opening facing east, and two transversal walls with the south one being blind and the north one having a window opening. A lime-based mortar was used for the construction for both mock-ups, while cement was added to the mortar used at the base, to ensure the connection of the structures with the shaking table. The detailed geometry of the two mock-ups is presented in Figure 1a,b, while the reader is referred to the original work for more information on the geometrical characteristics [55]. Both mock-ups were subjected to a sequence of unidirectional seismic loadings with increased Peak Ground Acceleration (PGA) (referred hereafter as TEST01-08) up to collapse, with a direction perpendicular to the façade.

Figure 2 presents the damage evolution at the end of some test sequences. Significant torsional effects, due to the asymmetric configuration of the openings, characterized the dynamic response of both structures. Concerning the brick structure, damage started developing at TEST05 and was already important at TEST07. The failure mechanism involved the out-of-plane collapse of the gable, together with the in-plane failure of the north return wall (both spandrel and piers). Additionally, the northern part of the gable experienced a local collapse. In the case of the stone structure, cracking initiated during the first two imposed seismic ground motion records (TEST01-02), and it consolidated during TEST03 and TEST05. The developed collapse mechanism involved a portion of the south part of the façade, the gable, the northeast corner, the spandrel of the window and the northwest pier. Especially for the stone structure, the high unit-to-structure size ratio and the big stones used as lintels played a decisive role to its structural behaviour, affecting both the local crack patterns and the developed collapse mechanisms. Finally, brick and stone structures experienced large displacements of 136.5 mm and 218.5 mm, respectively at the top of the gable, with a dominating rocking response after the failure mechanisms were formed.

The aforementioned experimental campaign is simulated in this work with the mixed strain/displacement finite element formulation. The numerical models aim to capture the structural response of the two mock-ups by means of nonlinear equivalent static analysis, while the nonlinear dynamic analysis of the tests will be addressed in a future work. Despite the known limitations of pushover analysis, such as the not consideration of the inertial phenomena and the cyclic nature of earthquake actions, it is widely regarded as a computationally efficient alternative to nonlinear dynamic analysis. For this reason, pushover analysis is included in several standards [60–62] and is commonly used for the estimation of the seismic response of masonry structures (e.g. [41,43,63–65]).

In the following, the load is applied perpendicular to the façade in both positive +X (referred to as the “Pulling” case hereafter) and negative –X (referred to as the “Pushing” case hereafter) directions (see Figure 3 for the +X direction). The effect of the seismic action is simulated as an “equivalent” mass-proportional horizontal body force, applied after the application of the self-

weight. The use of an isotropic damage model, described in Section 3 is justified by the monotonic nature of the applied loading and the absence of reported brick or stone crushing. The extension of this model to consider orthotropic induced damage and irreversible deformations in the case of cyclic and dynamic loading is feasible as described in Barbat et al. [54] and Saloustros et al. [66].

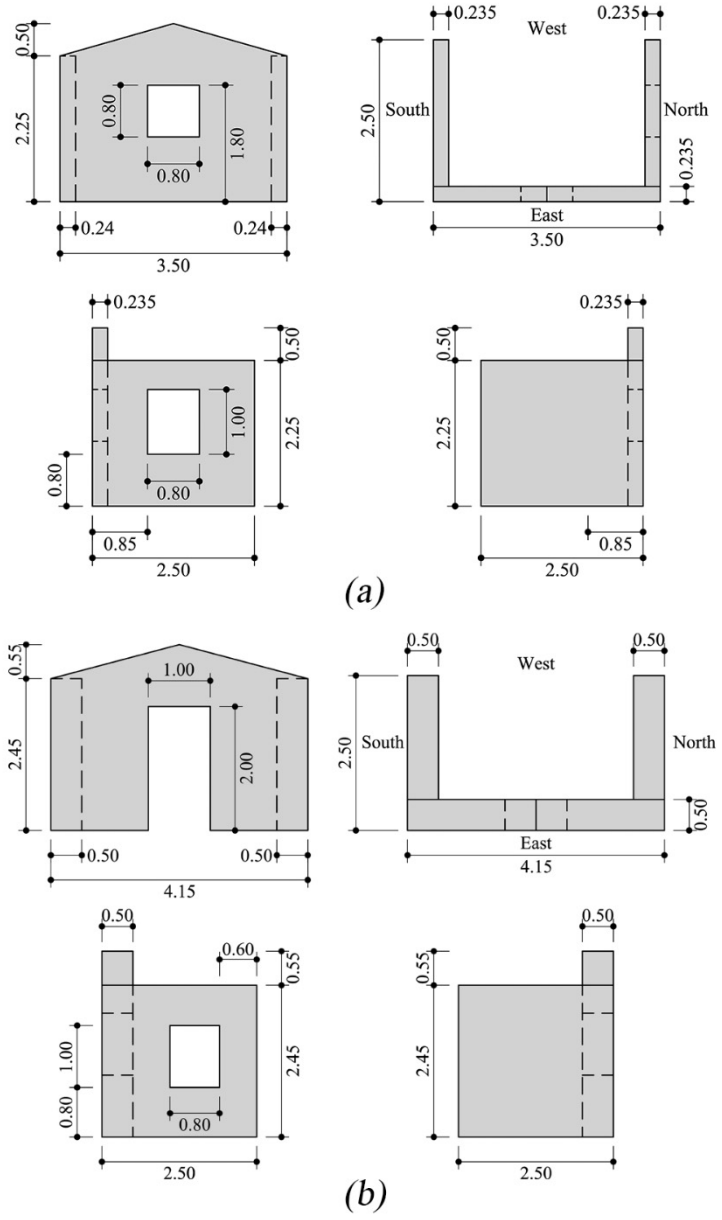

Figure 1. Geometry of (a) the brick structure and (b) the stone structure (Units in meters. Figure adapted from Candeias et al. [55]).

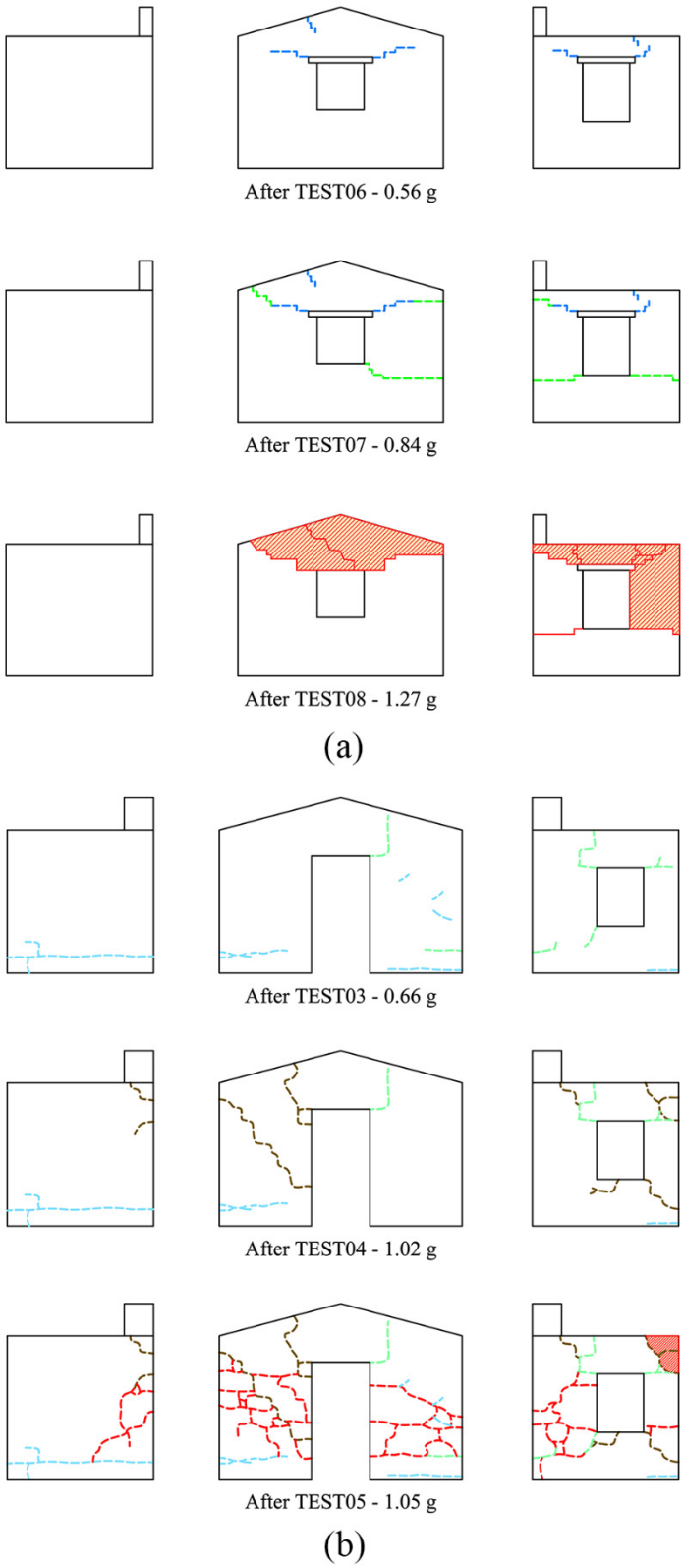

Figure 2. Damage evolution and collapse mechanism for (a) the brick structure, and (b) the stone structure (Figure adapted from Candeias et al. [55]).

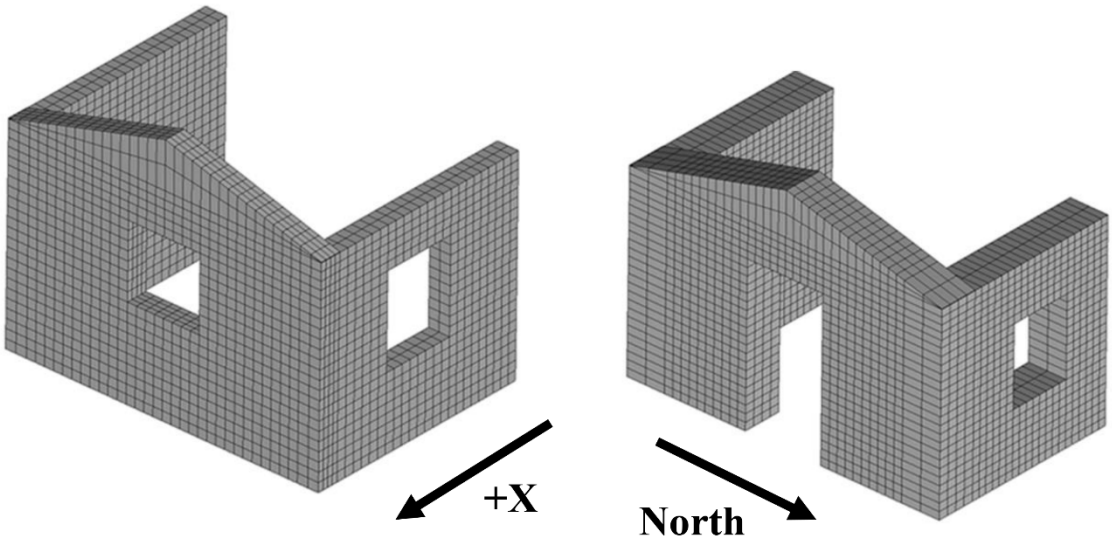

Figure 3. Adopted finite element meshes for the brick (left) and the stone (right) structures.

The material properties used in the simulations (shown in Table 1) are the ones provided by the experimental campaign [55], and were obtained by testing six wallets for each building, in vertical and diagonal compression. It should be noted that the fracture energy was not given by the experiment and values are adopted according to Lourenço [67], as in Chácara et al. [68] and Cannizzaro & Lourenço [69]. The calibration of the value of the fracture energy according to the experimental results using a reverse engineering approach is out of the scope of this work. The investigation of the capacity of the mixed FE formulation to predict the out-of-plane behaviour of masonry structures and to the correctly identify of the collapse mechanisms is carried out using typical values of fracture energy that are commonly adopted when experimental results are not available.

	Young's Modulus (GPa)	Specific Mass (kg/m^3)	Poisson's Ratio	Tensile Strength (MPa)	Tensile Fracture Energy (N/m)
Brick	5.17	1890	0.2	0.102	12
Stone	2.08	2360		0.224	48

Table 1. Mechanical Parameters for the brick and stone structures

3D hexahedra solid elements with linear/linear interpolations are used for the discretization of the structure, while the integration points are set at the nodes of the elements. A structured mesh is constructed consisting of approximately 0.1 x 0.1 m^2 elements over the plane of the walls, while 4 and 2 elements across their thickness are used in the façade and the return walls, respectively. This mesh size has been chosen after performing the proper sensitivity analysis of the results with respect to mesh refinement (see [70]). The difference in the number of elements per thickness of the façade and return walls is due to the fact that the first is subjected mainly to out-of-plane bending, which results in stresses and strains variation across the thickness. On the contrary, the two return walls are subjected mainly to in-plane loading that does not produce significant stresses and strains variation across the thickness of the wall. The final models are illustrated in Figure 3,

composed of 5100 and 4712 elements for the brick and the stone structure, respectively. A stabilization parameter $\tau_\varepsilon = 0.1$ is used in all the simulations. Finally, it should be noted that in the pushing cases of the analyses (-X), the first two layers of elements at the base are set to have a linear elastic behaviour. This choice intends to replicate the use of cement mortar at the base of the mock-ups, which aimed to prevent a possible sliding between the structure and the shake table [55].

Calculations are performed using the finite element program COMET [71,72], while the pre- and post-processing is done using GiD [73] both developed at CIMNE, Barcelona (International Centre for Numerical Methods in Engineering). The analyses are performed using an arc-length strategy in order to capture any possible snap-back response. Convergence of a load step increment is attained when the ratio between the norm of residual forces and the norm of the total external forces is lower than 10^{-2} (1%).

4.1 Brick Structure

4.1.1 Pushover analysis of the brick structure

Figure 4 presents the base shear force against the horizontal displacement at the top of the gable wall curve for the Pushing (-X) and the Pulling cases (+X). The structure presents a higher capacity when loaded towards -X direction (Pushing) than towards +X (Pulling). This is due to the beneficial effect of the return walls, which act as buttresses restraining the rotation of the façade during its pushing.

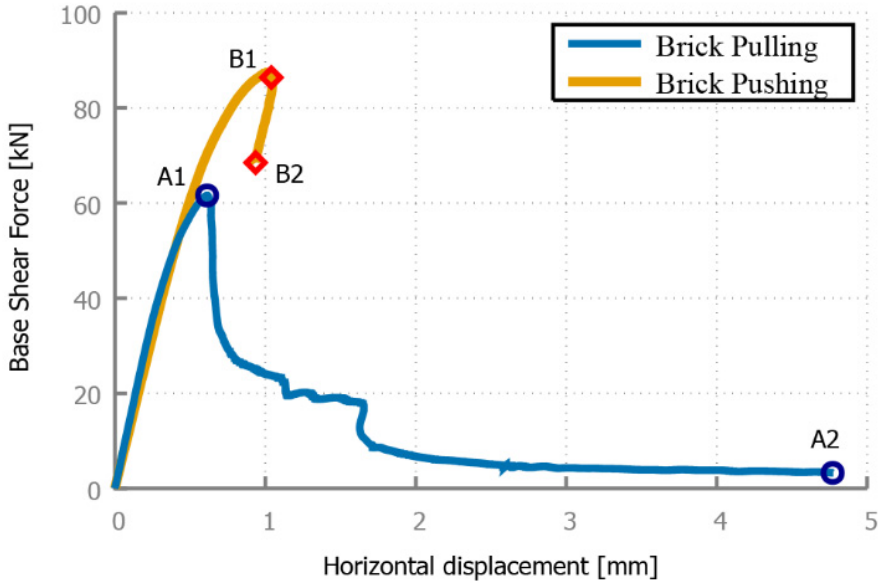

Figure 4. Base shear force against horizontal displacement at the top of the gable of the brick structure for both the Pulling (+X) and Pushing (-X) cases.

Figures 5a and 5b illustrate the strain localization process occurring during the Pulling (+X) of the brick structure at the peak load and at the end of the analysis, respectively. Initially, the structure responds almost elastically until reaching a value of the base shear of around 40 kN. At that point, damage develops and stiffness starts to decrease, until a peak load of around 60 kN. Figure 5a shows the open cracks (for elements with $\varepsilon_{max} \geq 1.97\ 10^{-5}$) at this stage of the analysis, through the contour of the maximum principal strain. At the façade, strain is localized at the west side of its base, which is caused by its vertical bending. A diffused strain field with high values also appears at the gable of the façade, without however showing any localization at

this stage of the analysis. The out-of-plane loading of the façade results in the initiation of two cracks at the connections with the return walls, especially at the top part. Regarding the return walls, both are slightly damaged at the west side of their base, due to their in-plane bending. Contrary to the south wall, the presence of a window opening in the north wall makes it more susceptible to damage. More specifically, diagonal shear cracks appear at the two corners of the window, whereas cracking exists at the top east side of the spandrel.

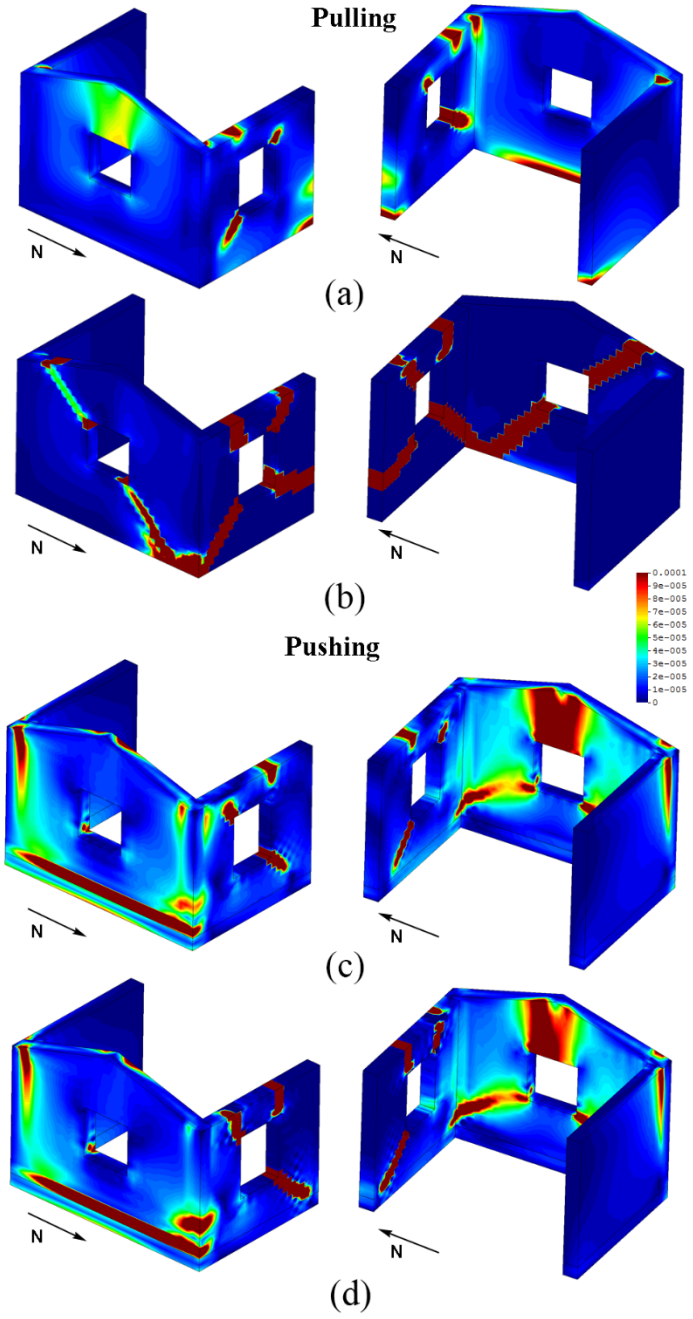

Figure 5. Contour of the maximum principal strains for the brick structure at different instances corresponding to the points of Figure 4: (a) A1 Pulling (+X), (b) A2 Pulling (+X), (c) B1 Pushing (-X) and (d) B2 Pushing (-X).

After reaching the peak load, the structure shows a very brittle response with significant loss of load capacity. This is due to the extension of the damage at the north return wall resulting in local

collapse mechanisms. More specifically, the spandrel is the first completely damaged element, with two cracks propagating at its two sides. At this point, the structure presents some residual strength, while the façade is bending horizontally as a cantilever due to the loss of its constraint at the north side. The northeast corner of the structure is weakly supported, as it has lost in succession the resistance of the spandrel, of the east pier in the north return wall (due to the diagonal crack) and finally, of its base, due to the flexural crack at the base of the façade. As a result, a second significant loss of load capacity appears for a displacement of 1.65 mm, which corresponds to the development of a diagonal crack that connects the north lower and south upper corners of the façade, crossing the window (Figure 5b). The complete development of this crack marks the formation of the collapse mechanism of the façade, and therefore, the top of the gable presents large displacements with very low resistance, until the crack propagates across the thickness of the façade and equilibrium is lost.

In the end of the analysis, the collapse mechanism of the structure is composed by three macro-elements. Namely the west pier of the north return wall, the spandrel of the north wall and the northeast corner, which includes the east pier of the north return wall and the upper north part of the façade (Figure 5b).

Regarding the Pushing (-X) case, the structure responds almost elastically up to a base shear force of 60 kN. From that stage of the analysis until the maximum capacity of 90 kN is reached, cracking develops simultaneously in several parts of the structure, as shown in Figure 5c. More specifically, the out-of-plane bending of the façade results in the first crack at its east base. As this crack develops, the return walls provide the only restriction to the out-of-plane movement of the facade. This beneficial action of the return walls changes the cracking pattern compared to the pulling case and results in vertical cracking at the gable above the window and at the corner connections of the façade with the return walls. Diagonal cracks also appear at the lower corners of the window. At the same time, significant in-plane damage occurs at the north return wall, due to the weakness introduced by the window. In particular, cracks at the both sides of the spandrel interrupt its connection with the piers, while a diagonal shear crack develops at the west lower corner of the window.

After the peak load, the propagation of the cracks at the spandrel and the west pier of the north wall produce a local failure (Figure 5d). The formation of this local collapse mechanism results in the loss of the equilibrium and marks the end of the analysis. Consequently, any further response at the softening region is not captured, due to lack of convergence of the equilibrium iterations.

4.1.2 Comparison with Experimental Results

The performance of the proposed approach is assessed in the following in terms of collapse mechanism and load capacity, through the comparison of the obtained numerical results with the results of the experimental campaign. Note that such a comparison is not straightforward for several reasons. First, as identified by [74], the characteristics of the ground motions, which are not considered in pushover analyses, may significantly influence the out-of-plane behaviour of the specimen. Second, the shaking table test provokes cyclic loading with dynamic effects taking place, while the non-linear static analysis is intrinsically monotonic and neglects inertial or damping effects. Third, the experimental procedure included a sequence of 8 steadily increasing excitations (TEST01-08) until the collapse of the structure. Therefore, damage was accumulated at every TEST, while the numerical analysis involves only one monotonic excitation until the loss of equilibrium.

In the following, the presentation of the experimental collapse mechanism is followed by its comparison with the numerical results.

The main failure mechanism of the brick mock-up involved a part of the gable wall and a big portion of the north return wall (Figure 2a), while a secondary local failure mechanism involved a part of the gable. More specifically, the main failure mechanism was already developed during the TEST07 as can be seen in Figure 2a, and involved four macro-elements: the northwest pier of the north return wall, the spandrel of the north return wall, the northeast corner and finally the gable of the façade. Consequently, during TEST08, the aforementioned mechanism was already formed and presented a rocking response. This rocking response, which was governed by torsional effects, was more intense at the north side, and therefore caused the formation of the secondary mechanism at the north part of the gable.

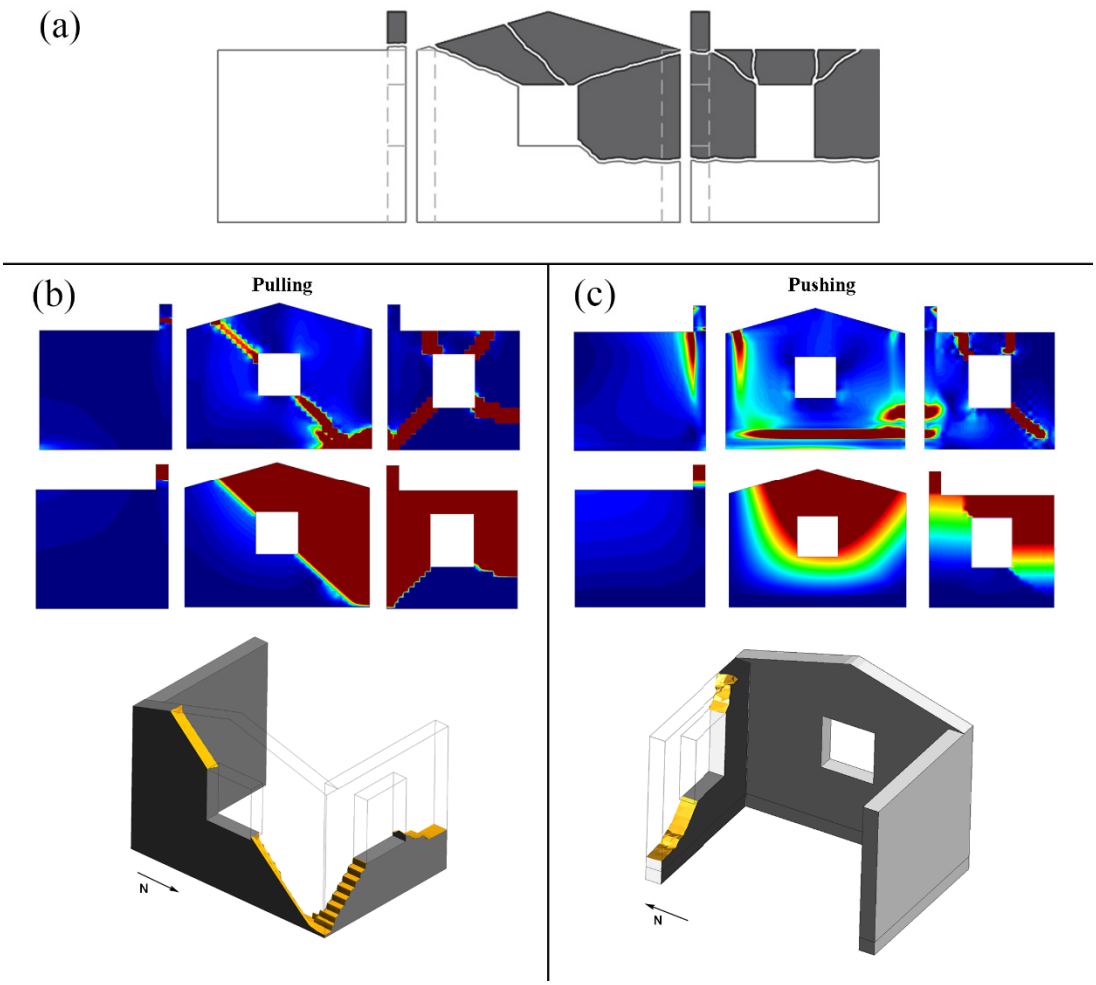

Figure 6. Comparison of the experimental collapse mechanism of the stone structure with the numerical one. (a) The experimental collapse mechanism (Figure adapted from Mendes et al. [76]), (b) maximum principal strains (top), displacements (middle) contour and crack surface (bottom) at point A2 of Figure 4, and (c) maximum principal strains (top), displacements contour (middle) and crack surface (bottom) at point B2 of Figure 4.

The mock-up appeared to be more vulnerable in the outward direction of the façade (+X), both before and after the complete formation of the mechanism [55], which is in agreement with the results of the proposed model, as discussed previously and shown in Figure 5. Figure 6 presents a comparison of the experimental mechanism [75] (shown in Figure 6a) and the results obtained for the pulling and pushing cases, respectively, with the proposed approach (shown in Figure 6b,c). The crack surface, shown in Figure 6, represents the location of the predominant cracks that divide the structure in different macroelements. This contour is obtained by plotting the

isosurface of the displacements for a selected at each case displacement threshold. In general, it can be appreciated that the obtained collapse mechanism is in good agreement with the experimental results. Regarding the north return wall, both analyses towards the ±X directions predict correctly the in-plane collapse mechanism and crack pattern. The numerical models capture also the out-of-plane failure of the top part of the façade and the northeast corner, with some differences that are discussed in the following.

Firstly, the numerical models do not predict the diagonal crack at the northern part above the window in the façade (see Figure 6a), which resulted in the collapse of the gable during the experiment. This cracking might have been provoked in the experiment by the presence of a wooden lintel above the window, which has not been considered in the numerical analyses. Secondly, there is a difference of the crack propagation at the northeast corner. The experimental structure develops a horizontal crack following the mortar joints and connecting the low corners of the two windows of the façade and the north wall, while the numerical model develops two diagonal cracks starting at the corners of the windows and joining at the lowest point of the corner. On the one hand, this difference may be due to the orthotropic behaviour of the brick masonry, which is not considered by the adopted isotropic elastic and damage models. In cases where the distinct linear and nonlinear directional properties of masonry are known, orthotropic damage models can be used to simulate the distinct response of masonry vertical and parallel to the mortar joints (e.g. [76,77]). On the other hand, the numerical results for the Pushing case (-X) could predict this horizontal crack (see Figure 5c,d). This implies that the experimentally obtained collapse mechanism is the result of the cumulative damage during the cyclic loading of the mock-up.

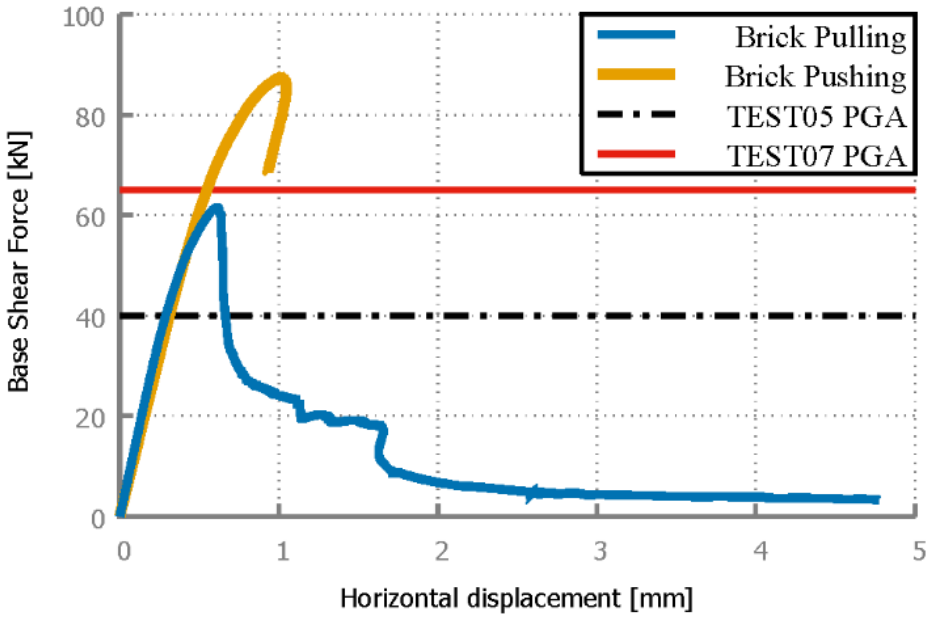

Figure 7. Comparison of base shear force against horizontal displacement at the top of the gable of the brick structure with the base shear values corresponding to the experimental PGAs of TEST05 and TEST07.

According to Candeias et al. [55], the collapse mechanism of the brick structure started to form at TEST05 and was completed at TEST07. The values of the base shear corresponding to the PGAs' of these two experimental tests have been plotted together with the pushover curves in Figure 7. The graphs show a good correlation between the experimental and the numerical results

for the Pulling case, with a collapse mechanism similar to the experimental one. For this case, the initiation of the collapse mechanism coincides with the beginning of the stiffness degradation and its completion with the peak load.

4.1.3 Comparison with Standard Finite Elements

This subsection investigates the enhanced accuracy of the proposed mixed formulation by comparing the results with the ones obtained using a standard irreducible finite element formulation, where displacements are the only unknowns of the finite element problem. Figure 8a compares the obtained capacity curves and Figure 8b the damage distribution at a specific step of the analysis with the use of mixed (top row) and standard (bottom row) finite element formulations.

The two capacity curves present differences in stiffness, load capacity and post-peak response. In particular, the standard finite element formulation predicts a higher stiffness of around 15% and 8%, and a higher load capacity of around 10% and 6% compared to the mixed formulation for the Pulling and the Pushing case, respectively. Additionally, the use of standard finite elements results in a higher residual strength at the post-peak region comparable to that obtained with the mixed formulation. Regarding the load predictions obtained from the most vulnerable Pulling case, the standard formulation predicts a higher capacity of 4.45% compared to the experimental one, while the mixed formulation gives a more conservative prediction of 5.21% lower than the maximum acceleration that the structure experiences during TEST05.

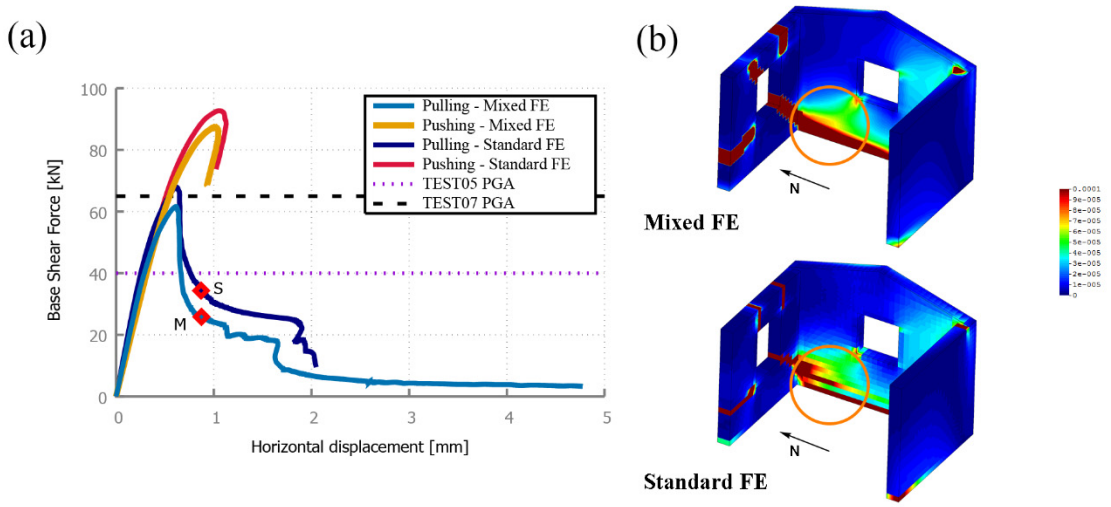

Figure 8. Comparison of results obtained with the mixed and standard formulation for the brick structure, in terms of (a) base shear force against horizontal displacement at the top of the gable, and (b) maximum principal strains contour at the numerical step depicted by the points on the graph for the mixed (top) and the standard (bottom) formulations for the Pulling case.

A closer look at the strain fields and crack propagation, shown in Figure 8b, highlights better the difference between the two finite element formulations. In the case of the standard FE formulation, the crack propagating from the low east corner of the window in the return wall cannot join the crack that has developed at the base of the façade. In particular, the crack direction at the northeast corner of the mock-up follows the mesh direction and spurious horizontal cracking appears at the third layer of elements from the base. This erroneous prediction of the crack direction hampers the evolution of the collapse mechanism and increases unrealistically the capacity and post-peak residual strength of the analysed structure. Mesh directionality biases the crack propagation also in the spandrel of the north wall, where the diagonal shear cracking is not

predicted by the standard finite element formulation. On the contrary, the results with the mixed formulation seem to be practically mesh-independent, avoiding the aforementioned incorrect predictions of the structural response and damage pattern.

4.2 Stone Structure

4.2.1 Pushover analysis of the stone structure

Figure 9 presents the structural response of the stone structure in terms of base shear force against horizontal displacement at the top of the cable. Similar to the brick mock-up, the structure appears to be more vulnerable in the +X direction (Pulling case).

Starting with the Pulling case (+X), the structure responds almost elastically until a base shear force of around 150 kN is reached. At that point, damage initiates and stiffness starts to decrease up to a peak load of around 230 kN. Figure 10a illustrates the open cracks (for elements with $\varepsilon_{max} \geq 1.07\ 10^{-4}$) at the peak load, through the contour of the maximum principal strain. Cracking exists at the base of the façade due to its vertical bending, while the tympanum presents a diffused high strain field. The out-of-plane loading of the façade results also in cracks at the connections with the return walls, especially at the top corners. Both return walls present some cracking at the west side of their base, due to their in-plane loading, while the north return wall is more vulnerable, with high concentration of strains around the window opening. More specifically, there is a crack starting at the low east corner of the window propagating diagonally towards the northeast corner. Moreover, a diagonal crack initiates at the northwest corner of the window. Finally, the spandrel presents significant strain concentration at its top east area.

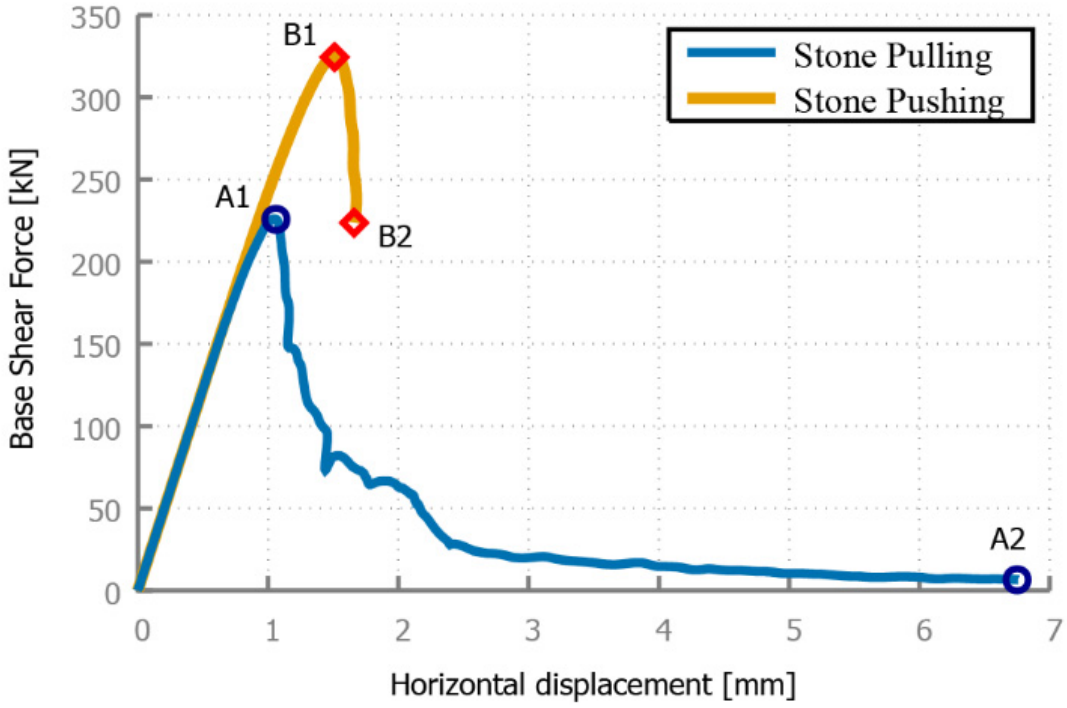

Figure 9. Base shear force against horizontal displacement at the top of the gable of the stone structure for both the Pulling (+X) and Pushing (-X) cases.

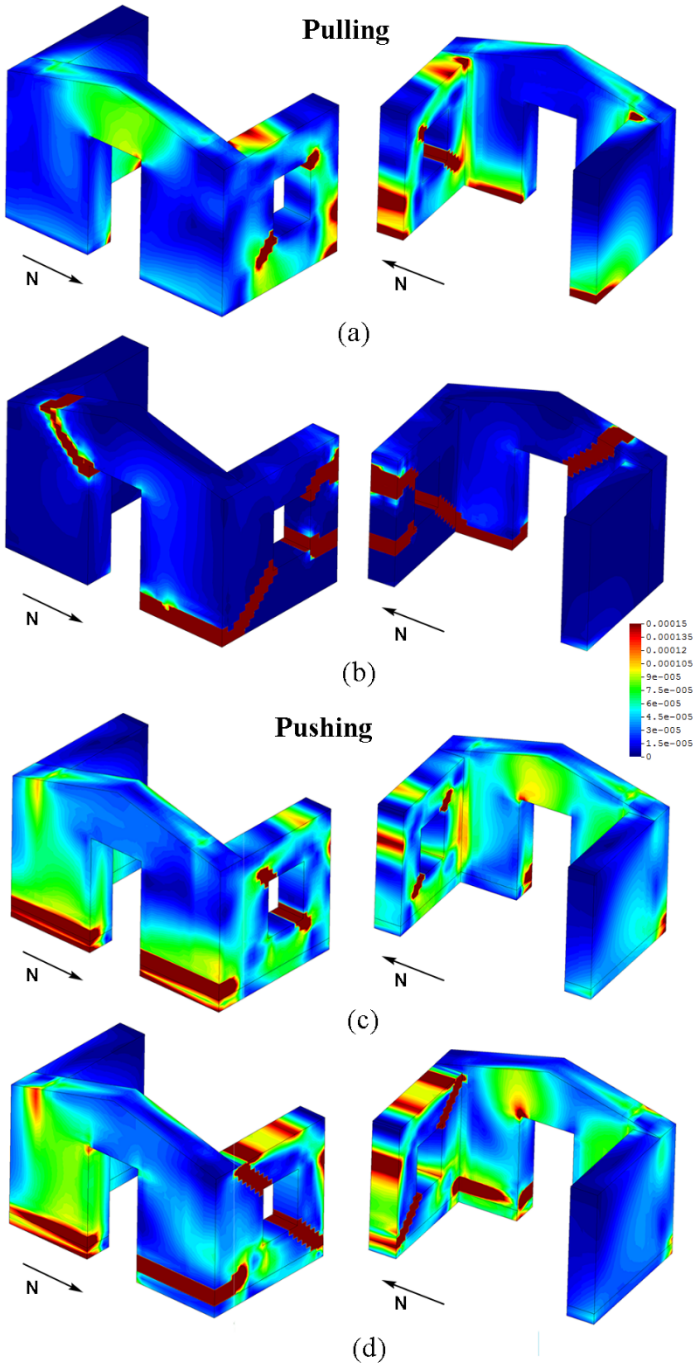

Figure 10. Contour of the maximum principal strains for the stone structure at different instances corresponding to the points of Figure 9: (a) A1 Pulling (+X), (b) A2 Pulling (+X), (c) B1 Pushing (-X) and (d) B2 Pushing (-X).

Following the peak load, damage occurs at several locations of the structure. In particular, a vertical crack initiates at the north corner of the door and the connection of the façade with the blind return wall presents significant strain concentration. Another critical area is the top east part of the spandrel. Finally, the west pier of the north return wall develops significant strains at both the base and the top leading to a brittle failure. Due to the brittle failure of the west pier caused by the propagation of two cracks, the structure notably loses its load capacity and significant stress redistribution occurs. The area of the spandrel at the north wall unloads and the whole structure presents an important torsional response. Moreover, the diagonal crack at the east pier of the north return wall advances significantly, meeting the crack at the base of the north part of the façade.

The above crack propagation provokes a local mechanism at the west pier, while a big portion of the northeast corner (including the spandrel, the east pier of the return wall and the north part of the facade) connects with the south part of the structure only through the gable of the façade. The increase of the displacements, amplifies the torsional response and a crack appears at the south top corner of the door and extends until the south top corner of the structure. Consequently, the northeast corner of the structure loses the connection with the south return wall. Figure 10b shows the open cracks at the end of the analysis (point A2 in Figure 9).

In the Pushing case (-X), the response is almost elastic until a base shear force of around 250 kN is attained, while the maximum capacity is of around 325 kN. During this part of the analysis, cracking develops simultaneously in two locations of the structure, in particular at the base of the façade due to its vertical bending, and at the north wall (Figure 10c). The post-peak response of the structure is determined by the propagation of two diagonal cracks at the north wall, causing a loss of load capacity and a brittle failure of the north-west corner, as shown in Figure 10d. At that point, the local collapse of the west part of the north return wall occurs and the local equilibrium is lost leading to the end of the analysis. Similar to the brick mock-up for the Pushing case, the analysis ends due to the loss of the stability of the west pier in the north wall and no further softening response is captured.

4.2.2 Comparison with Experimental Results

As with the brick structure, the performance of the proposed simulation is investigated by comparing the obtained results with the experimental ones in terms of collapse mechanisms and load capacity. Before this, a brief summary of the experimental response and failure is presented, in order to facilitate the comparison with the numerical results.

According to Candeias et al. [55], an initial damage state was observed in the structure before the initiation of the experiment. This was a horizontal crack along the mortar joints above the first course of stones at the south return wall up to the door of the façade and some additional minor cracks at the northern side of the façade, represented with the light blue line in Figure 2b. Besides that, the structure started developing cracks during TEST03 and TEST04, while TEST05 marked its ultimate state. Already at TEST04, the damage extended at the north return wall, with cracks starting from the corners of the window and developing diagonally towards the corners of the wall. Additionally, significant damage was observed at the façade, dividing it into four parts: north pier, spandrel and two parts in the south pier. The formation of the collapse mechanism during TEST05 is described in the following. First, the top west corner of the north wall detached due to the impulses of the lintel above the window. The corresponding pier presented a rocking in-plane response facilitated by a diagonal crack at its base and the failure of the top corner. The northeast corner rocked in-plane due to the propagation of a diagonal crack from the base of the window towards the northeast lower corner. Subsequently, it split into two parts by diagonal cracks. Finally, the façade presented an out-of-plane rocking behaviour with a diagonal crack at its south pier and an approximately horizontal crack near the base at its north pier. The middle part of the gable was also separated from the piers due to vertical cracking occurring at both sides of the lintel. The collapse of the structure is determined by its torsional response, due to the weak north side wall, the high unit-to-structure size ratio, and the significant impact of the big lintels, which either stabilized or ‘hammered’ parts of the structure.

Once more, the outwards (+X) direction appeared to be more vulnerable during the experiment [55] and this is correctly predicted by the numerical simulations as shown in Figure 9. Figure 11 presents a comparison of the experimental mechanism [75] (shown in Figure 11a) and the results obtained for the Pulling (Figure 11b) and Pushing (Figure 11c) cases with the proposed approach. Considering the results of both the Pulling and Pushing cases, the numerical model reproduces correctly the main aspects of the experimental collapse mechanism, while some differences exist

due to micro-scale phenomena. In the experiment, the effect of the lintel at the north return wall changed the initial mechanism at the northeast pier, by restraining the evolution of the crack at the lower corner of the window and inducing a diagonal crack that divided it in two parts. Moreover, the lintel of the door played also an important role, since it provoked two vertical cracks at its sides. Finally, the high unit size caused a distributed damage pattern at the façade, while the numerical model could only provide localized damage patterns.

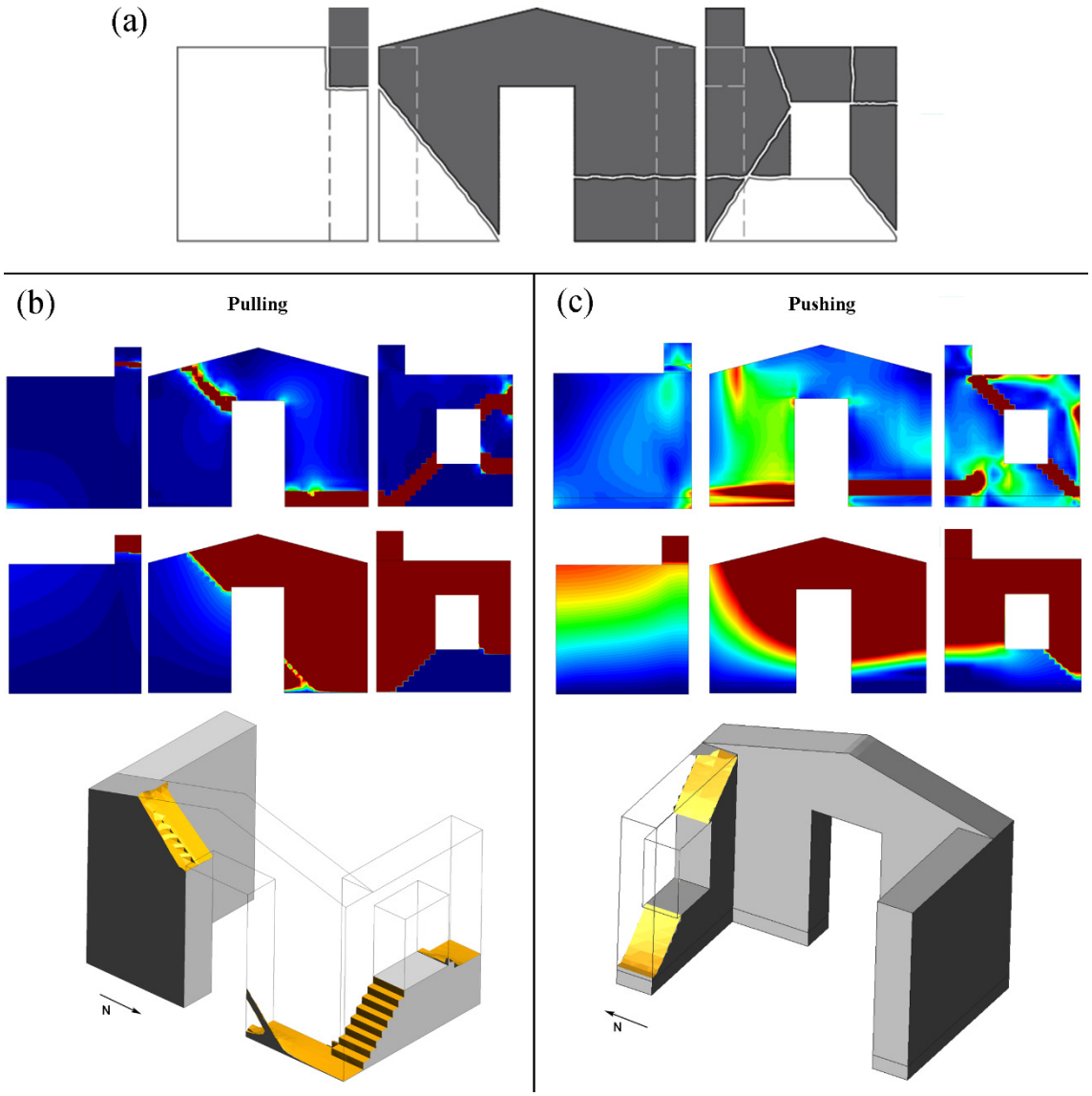

Figure 11. Comparison of the collapse mechanism formed for the stone structure with the numerical predicted one. (a) The experimental collapse mechanism (Figure adapted from Mendes et al. [76]), (b) maximum principal strains (top), displacements contour (middle) and crack surface (bottom) at point A2 of Figure 9, and (c) maximum principal strains (top), displacements contour (middle) and crack surface (bottom) at point B2 of Figure 9.

Candeias et al. [55] describe that the collapse mechanism of the stone structure started to form during TEST03, while TEST05 marked its completion. Similar to the brick mock-up structure, the base shear values corresponding to the PGAs of these two TESTs are reported together with the capacity curves of the numerical model in Figure 12. More specifically, the black dashed line corresponding to TEST03 highlights the damage initiation (stiffness degradation) of the structure,

while the red continuous one depicting TEST07 indicates the load peak at which the mechanism is formed. As for the brick structure, the experimental and numerical results correspond for the most vulnerable Pulling (+X) direction.

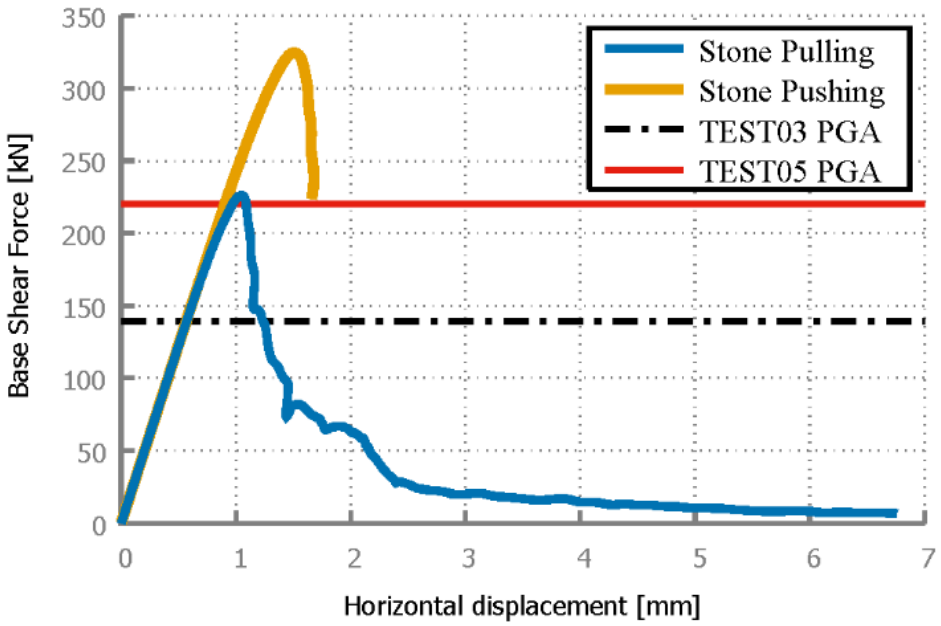

Figure 12. Comparison of base shear force against horizontal displacement at the top of the gable of the stone structure with the corresponding experimental PGAs of TEST03 and TEST05.

4.2.3 Comparison with Standard Finite Elements

Figure 13 shows the results of the mixed finite element formulation along with those obtained with the standard one. As for the brick mock-up, the standard formulation results in increased stiffness of around 8%, higher load capacity of around 13% and higher residual strength for the Pulling case (+X). In the Pushing case (-X), the increase of the stiffness given by the standard formulation is again 8%, while minor differences are observed in the base shear force against horizontal displacement graphs between the two formulations. Interestingly, and despite these similarities in the Pushing case, the two FE formulations predict a different final collapse mechanism, as shown in Figure 13b. In particular, in the standard irreducible formulation the mesh orientation biases the propagation of a crack along the whole base of the north return wall. In this case, the analysis stops due to a sliding failure at the base of the structure, while in the mixed FE formulation due to a local mechanism at the north return wall, as discussed in Section 4.2.1. The orientation of the finite element mesh erroneously affects the predictions regarding the collapse mechanism of the standard FE formulation. This case demonstrates again the directional mesh-bias dependency of standard finite elements and its effect in the prediction of inaccurate collapse mechanisms.

Similar to the results of the brick structure, the mixed formulation predicts also for this case a more conservative load capacity for the most vulnerable Pulling Case. This has a difference of 2.69% comparing to the experimental one, while the standard formulation predicts a higher load capacity of 15.90% compared to the maximum acceleration applied to the structure during TEST05.

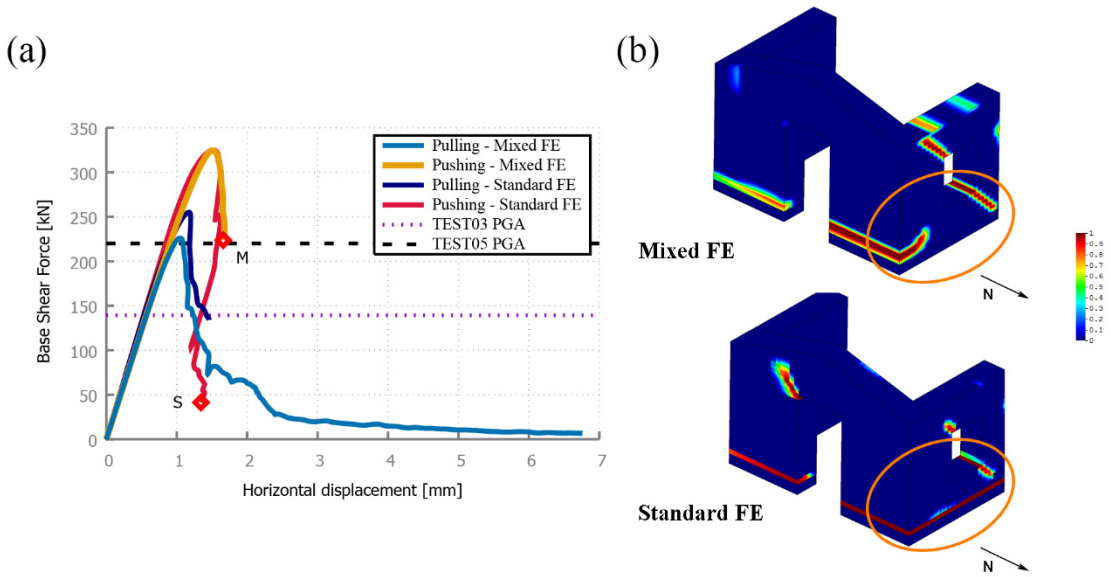

Figure 13. Comparison of results obtained with the mixed and standard formulation for the stone structure, in terms of (a) base shear force against horizontal displacement at the top of the gable, and (b) maximum principal strains contour at the numerical step depicted by the points on the graph for the mixed (top) and the standard (bottom) formulations for the Pushing case.

4.3 Computational Cost

The enhanced strain accuracy of the mixed formulation is the result of considering six strain components at each node as unknowns, additionally to the three displacement components that are considered in standard finite elements. The higher number of nodal variables increases the computational cost of each numerical iteration. On the other hand, the enhanced accuracy of the mixed formulation in high non-linear problems usually leads to less iterations for reaching equilibrium convergence compared with the standard formulation.

		Overhead using the mixed FE formulation (%)	
	Case	CPU	RAM
Brick Structure	Pulling (+X)	182.56	41.11
	Pushing (-X)	231.13	41.76
Stone Structure	Pulling (+X)	327.36	42.09
	Pushing(+X)	465.79	42.62

Table 2. Computational overhead in terms CPU and RAM requirements when using mixed finite elements over standard ones

Table 2 presents the computational overhead using the mixed formulation instead of the standard one in terms of CPU time and RAM memory requirements. Regarding the sizes of the models, the brick and the stone structure are composed by 7428 and 6931 nodes, respectively. The results show an average increase of 300 % for the CPU time and 42 % of RAM memory.

The computational efficiency is a key for the simulation of large-scale masonry structures. A way to reduce the computational cost of the mixed FE formulation is by taking advantage of the compatibility between mixed and standard finite elements as presented in Benedetti et al. [52]. In particular, mixed finite elements can be used only at zones where high stress gradients are expected, while the rest of the structure can be discretized using standard finite elements. Apart from this, the adaptive substitution of standard finite elements with mixed ones in areas with increasing strain gradients during the numerical analysis is feasible.

5 Comparative study of mesh-dependence using standard and mixed FE

This section investigates the mesh-dependency of the standard and mixed FE formulations under mixed Mode I and II in-plane (Section 5.1) and out-of-plane (Section 5.2) loading. This study complements the one presented in reference [49] where the relative performance of standard and mixed FE was analyzed for Mode I cracking.

5.1 In-plane loading

The simulation of a shear wall with dimensions of 1 *m* x 1 *m* x 0.1 *m* and a central opening of 0.2 *m* x 0.2 *m* under in-plane loading is considered. The base of the wall is completely constrained while the top is subjected to a simultaneous compressive vertical displacement and a horizontal shearing displacement. The applied incremental displacement ratio is $\Delta u_y : \Delta u_x = -1 : 0.74$ until collapse. The expected developing crack angle is different from 45º due to the combination of compression and shear. The mechanical parameters considered are Young's modulus $E = 7.5\ GPa$, Poisson's ratio $\nu = 0.0$, uniaxial tensile strength $f_t = 0.35\ MPa$ and fracture energy $G_f = 5\ N/m$. The wall is discretized with constant strain triangular finite elements of varying sizes and orientations. Analyses are performed with the standard and the mixed strain/displacement formulation.

Figure 14 illustrates the analysis results obtained with fully structured meshes and two different element sizes of 33 *mm* (top row in Figure 14) and 20 *mm* (middle row in Figure 14). Crack trajectories obtained with standard FE present a spurious mesh-dependency, as they are initially aligned with the vertical direction of the mesh close to the window corners and with the diagonal one far of them. The simulations with the mixed FE give in both cases cracks with the same direction, independently of the used mesh-pattern and element size. The last row of Figure 14 illustrates the deformation of the wall and the contour of the maximum principal strains obtained using the mixed FE formulation.

Figure 15 presents the analysis results using two unstructured meshes with element size of 30 *mm* (top row in Figure 15) and 20 *mm* (bottom row in Figure 15). As in the case of the structured meshes, the standard FE formulation predicts cracks that follow a path designated by the mesh orientation. On the contrary, the mixed formulation is able to predict in all the cases the same crack trajectory independently of the used mesh. Note that in the first mesh considered in Figure 15 (top row), with an element size of 30 *mm*, the computed upper-right crack path is similar in the standard and mixed FE formulations because the mesh is well oriented with respect to the developing crack. Contrariwise, the lower-left crack path is not identical because the unstructured mesh orientation is not favorable in that region.

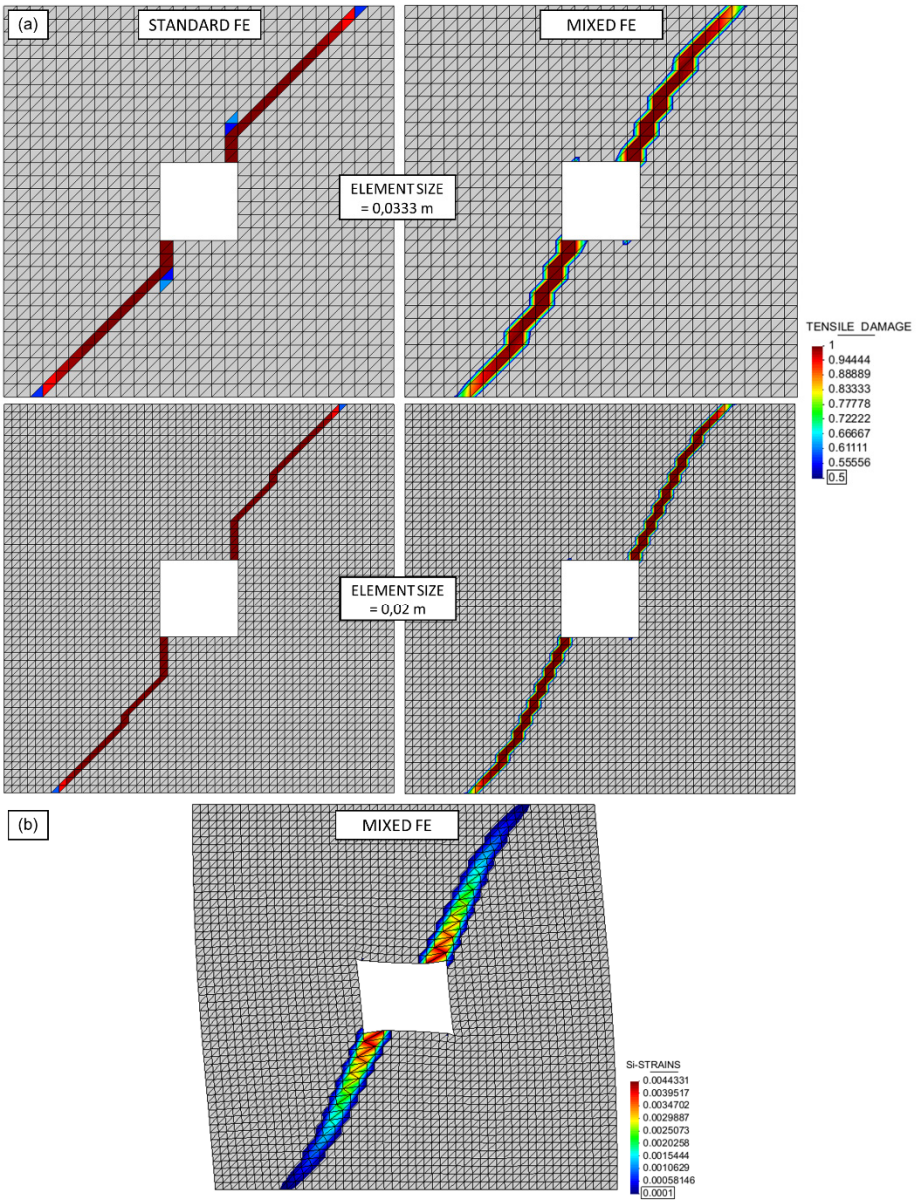

Figure 14. Mesh-dependence study for in-plane loading using structured meshes with varying element size: (a) damage contours using standard FE (left) and mixed FE (right) and (b) maximum principal strains using mixed FE (deformed shape x 300).

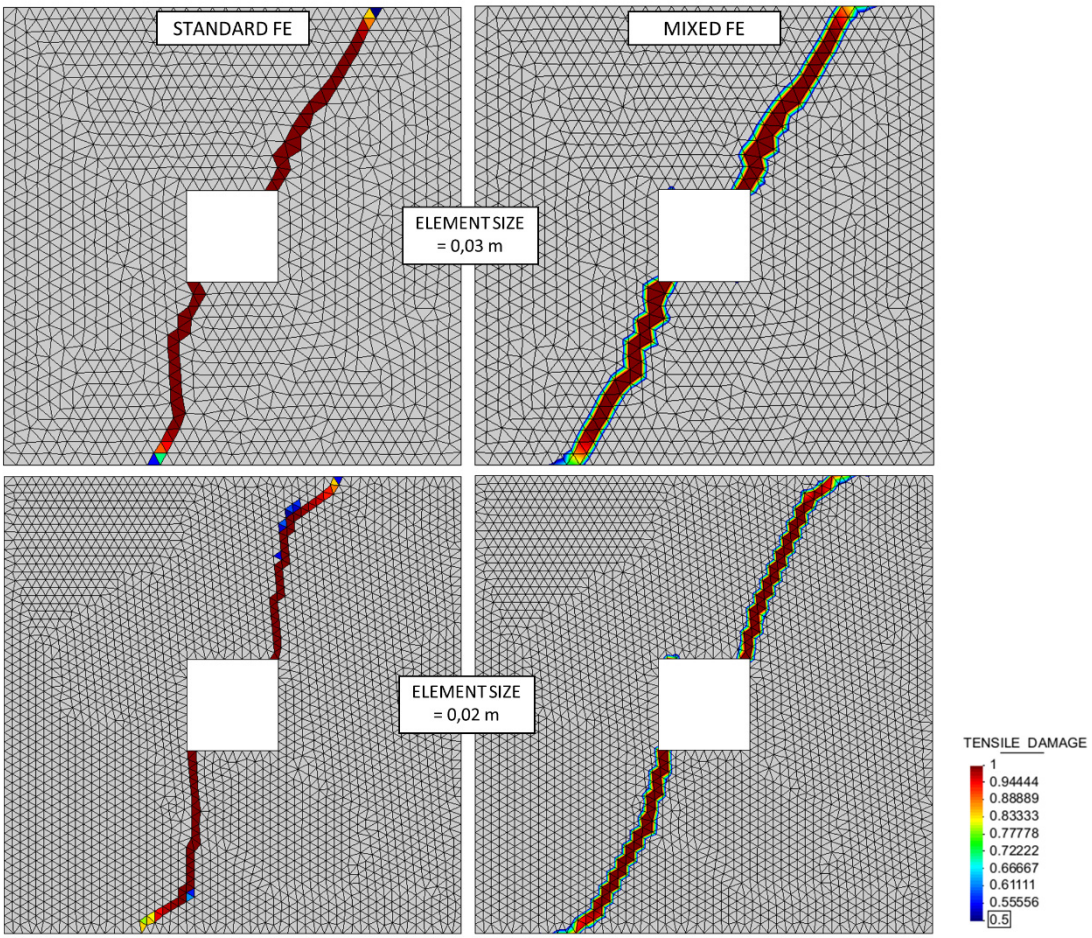

Figure 15. Mesh-dependence study for in-plane loading and unstructured meshes with varying element size: damage contours using standard FE (left) and mixed FE (right).

5.2 Out-of-plane loading

A wall with the same geometry and properties as the one in the previous section is subjected now to out-of-plane loading. A displacement in the out-of-plane direction of the wall of $5 \cdot 10^{-3}$ m is prescribed to at the top of the wall, while the base is fixed. For this case, no compressive vertical displacement is applied.

Simulations are performed using standard and mixed finite elements. Two different meshes of hexahedra of size 50 *mm* x 50 *mm* are considered, with 2 (top row of Figure 16) and 4 elements (middle row of Figure 16) across the thickness, respectively.

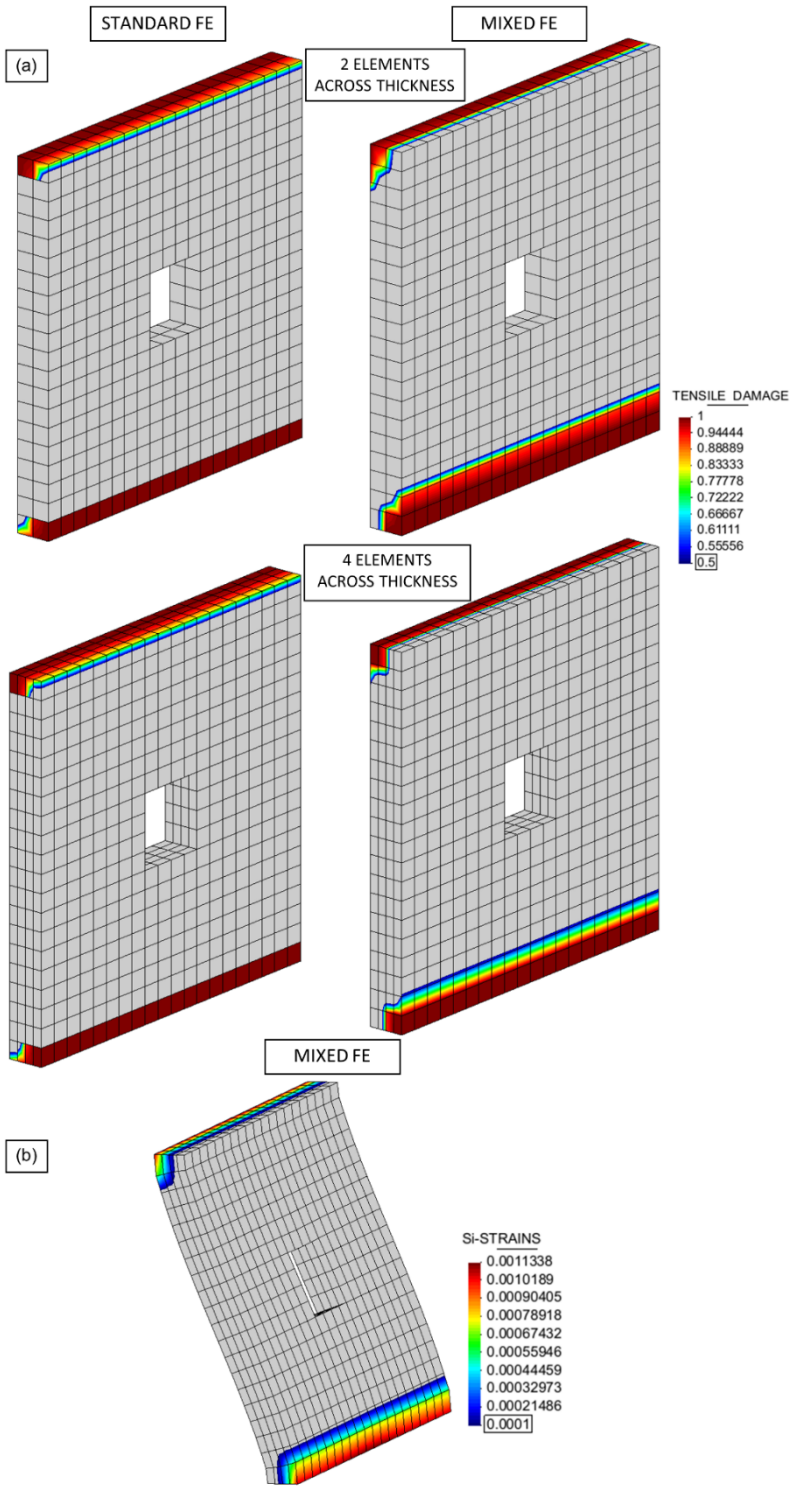

Figure 16. Mesh-dependence study for out-of-plane loading with varying element size per wall thickness: (a) damage contours using standard FE (left) and mixed FE (right) and (b) maximum principal strain using mixed FE (deformed shape x 300).

The computed results with standard FEs (left column of Figure 16) demonstrate that for both meshes cracking appears across the whole thickness at the top and bottom of the wall. For the same out-of-plane action, the mixed formulation gives a solution where damage does not cross yet the whole thickness of the wall. The enhanced strain accuracy given by the mixed FE formulation succeeds in simulating the expected tension-compression state at the top and bottom

parts of the wall induced by the out-of-plane bending. This situation, commonly encountered in masonry structures, cannot be accurately reproduced using standard finite elements. This is because with standard FE gives stiffer results than those obtained with the mixed FE and stiffer than the "true" solution (see [48]). Therefore, the computed effective stresses are greater with the standard FE and damage originates earlier. As shown in Figure 16, the over-stiffness of standard FE is not alleviated when refining the mesh only across the thickness. As a result, a failure condition that refers to sliding and not bending is predicted, which does not correspond to the analysed problem. The last row of Figure 16 illustrates the deformation of the wall and the contour of the maximum principal strains for the out-of-plane collapse mechanism using mixed FEs.

6 Conclusions

This work presents the application and assesses the performance of the mixed strain/displacement FE formulation on the out-of-plane response of two unreinforced masonry structures. The use of the mixed FE formulation aims to enhance the strain accuracy of the finite element solution and aid the mesh-independent strain localization in crack propagation problems.

A campaign of a brick and a stone structure subjected to shaking table tests is chosen as benchmark case, being one of the most challenging topics in the simulation of unreinforced masonry structures. The effect of the seismic action is considered in the numerical analysis through equivalent non-linear static analyses. The simulations are compared with the experimental outcomes in terms of collapse mechanism formation and load carrying capacity.

The results of the performed analyses are in good agreement with the experiments. The numerical simulations could capture the in-plane response and early failure of the weak return walls, the torsional effects associated with this failure and the out-of-plane collapse of the façades. Moreover, the damage pattern and collapse mechanism are also correctly predicted and a good agreement has been found for the load carrying capacity. Differences between the experimental and numerical outcomes are attributed either to micro-scale phenomena, or to the dynamic and accumulating nature of the experiment, which are neglected in the numerical simulations.

The enhanced accuracy of the mixed formulation is highlighted by comparing the results obtained with the standard irreducible FE formulation. The standard formulation presents higher stiffness and peak load strength, while significant residual strength is observed at the softening region, since some developing cracks are biased by the mesh orientation. Specifically for one of the investigated cases, the mesh-biased solution of the standard formulation results in the prediction of a different collapse mechanism than the experimental one. On the other hand, the results of the mixed formulation do not appear to suffer from any mesh dependency, justifying their benefits in crack propagation analysis of unreinforced masonry structures, albeit their higher computational cost.

The above superiority of the mixed formulation against the standard one in strain localization problems is corroborated through a mesh-dependence study using both the mixed and standard FE simulation on two benchmark in-plane and out-of-plane problems. The standard formulation predicts crack trajectories that are biased by the orientation of FE mesh for all the situations analyzed. On the other hand, mixed FE provide much more reliable results, which seem to be practically free of mesh-bias and avoid incorrect predictions of the structural response, the damage pattern and the collapse mechanism of the structure.

7 Acknowledgements

This research has received the financial support from the MINECO (Ministerio de Economia y Competitividad of the Spanish Government) through the MULTIMAS project (Multiscale

techniques for the experimental and numerical analysis of the reliability of masonry structures, ref. num. BIA2015-63882-P).

The support provided by the Spanish Ministry of Education for the Ph.D. research of Gabriel Barbat via an FPU grant is acknowledged.

This research was supported by the European Union within the framework of the Erasmus Mundus Advanced Master in Structural Analysis of Monuments and Historical Constructions (SAHC).

8 References

[1] M. Javed, A. Naeem, A. Penna and G. Magenes, "Behavior of masonry structures during the Kashmir 2005 earthquake," in: *First European Conference on Earthquake Engineering and Seismology*, Geneva, Switzerland, 2005.

[2] N. Augenti and F. Parisi, "Learning from construction failures due to the 2009 L'Aquila, Italy, earthquake," *Journal of Performance of Constructed Facilities,* vol. 24, pp. 536–555, 2010. doi:10.1061/(ASCE)CF.1943-5509.0000122.

[3] D. Dizhur, J. Centeno, C. Ventura, J. Leite, P. Lourenco, J. Ingham, L. Moon, M. Griffith, A. Schultz, I. Senaldi, G. Magenes, J. Dickie and S. Lissel, "Performance of masonry buildings and churches in the 22 February 2011 Christchurch earthquake," *Bulletin of the New Zealand Society for Earthquake Engineering,* vol. 44, pp. 279–296, 2011.

[4] D.F. D'Ayala and S. Paganoni, "Assessment and analysis of damage in L'Aquila historic city centre after 6th April 2009," *Bulletin of Earthquake Engineering*, 2011. doi:10.1007/s10518-010-9224-4.

[5] A. Penna, P. Morandi, M. Rota, C.F. Manzini, F. da Porto and G. Magenes, "Performance of masonry buildings during the Emilia 2012 earthquake," *Bulletin of Earthquake Engineering,* 2014. doi:10.1007/s10518-013-9496-6.

[6] H. Varum, R. Dumaru, A. Furtado, A.R. Barbosa, D. Gautam and H. Rodrigues, "Seismic performance of buildings in Nepal after the Gorkha earthquake," in: Impacts and insights of the Gorkha earthquake Nepal, 2018. doi:10.1016/B978-0-12-812808-4.00003-1.

[7] X. Romão, A.A. Costa, E. Paupério, H. Rodrigues, R. Vicente, H. Varum and A. Costa, "Field observations and interpretation of the structural performance of constructions after the 11 May 2011 Lorca earthquake," *Engineering Failure Analysis*, vol. 34, pp. 670-692, 2013. doi:10.1016/j.engfailanal.2013.01.040.

[8] A. Menon and G. Magenes, "Out-of-plane seismic response of unreinforced masonry : definition of seismic input," Rose School, IUSS Press, 2008.

[9] P.B. Lourenço, J.M. Leite, M.F. Paulo-Pereira, A. Campos-Costa, P.X. Candeias and N. Mendes, "Shaking table testing for masonry infill walls: unreinforced versus reinforced solutions," *Earthquake Engineering and Structural Dynamics*, vol. 45, pp. 2241–2260, 2016. doi:10.1002/eqe.2756.

[10] D.P. Abrams, O. AlShawa, P.B. Lourenço and L. Sorrentino, "Out-of-plane seismic response of unreinforced masonry walls: Conceptual discussion, research needs, and modeling issues," *International Journal of Architectural Heritage*, vol. 11, pp. 22-30, 2017. doi:10.1080/15583058.2016.1238977.

[11] T.M. Ferreira, A.A. Costa and A. Costa, "Analysis of the out-of-plane seismic behavior of unreinforced masonry: A literature review," *International Journal of Architectural Heritage*, vol. 9, pp. 949–972, 2015. doi:10.1080/15583058.2014.885996.

[12] L. Sorrentino, D. D'Ayala, G. de Felice, M.C. Griffith, S. Lagomarsino and G. Magenes, "Review of out-of-plane seismic assessment techniques applied to existing masonry buildings," *International Journal of Architectural Heritage*, vol. 11, pp. 2-21, 2017. doi:10.1080/15583058.2016.1237586.

[13] G. de Felice, S. De Santis, P.B. Lourenço and N. Mendes, "Methods and challenges for the seismic assessment of historic masonry structures," *International Journal of Architectural Heritage*, vol. 11, pp. 1-18, 2016. doi:10.1080/15583058.2016.1238976.

[14] J. Heyman, "The stone skeleton," *International Journal of Solids and Structures*, vol. 2, pp. 249-279, 1966. doi:10.1016/0020-7683(66)90018-7.

[15] D.P. Abrams, R. Angel and J. Uzarski, "Out-of-plane strength of unreinforced masonry infill panels," *Earthquake Spectra*, vol. 12, pp. 825–844, 1996. doi:10.1193/1.1585912.

[16] K. Doherty, "An investigation of the weak links in the seismic load path of unreinforced masonary buildings," University of Adelaide, 2000. doi:10.1155/2015/183712.

[17] M.C. Griffith, G. Magenes, G. Melis and L. Picchi, "Evaluation of out-of-plane stability of unreinforced masonry walls subjected to seismic excitation," *Journal of Earthquake Engineering*, 2003. doi:10.1080/13632460309350476.

[18] D. D'Ayala and E. Speranza, "Definition of collapse mechanisms and seismic vulnerability of historic masonry buildings," *Earthquake Spectra*, 2003. doi:10.1193/1.1599896.

[19] P. Block, T. Ciblac and J. Ochsendorf, "Real-time limit analysis of vaulted masonry buildings," *Computers and Structures*, vol. 84, pp. 1841-1852, 2006. doi:10.1016/j.compstruc.2006.08.002.

[20] M.J. DeJong, "Seismic assessment strategies for masonry structures," Ph.D thesis, Massachusets Institute of Technology, 2009.

[21] J. Vaculik, "Unreinforced masonry walls subjected to out-of-plane seismic actions," University of Adelaide, 2012.

[22] H. Derakhshan, M.C. Griffith and J.M. Ingham, "Airbag testing of multi-leaf unreinforced masonry walls subjected to one-way bending," *Engineering Structures,* vol. 57, pp. 512–522, 2013. doi:10.1016/j.engstruct.2013.10.006.

[23] P. Roca, M. Cervera, G. Gariup and L. Pelà, "Structural analysis of masonry historical constructions. Classical and advanced approaches," *Archives of Computational Methods in Engineering*, vol. 17, pp. 299–325, 2010. doi:10.1007/s11831-010-9046-1.

[24] D. Theodossopoulos and B. Sinha, "A review of analytical methods in the current design processes and assessment of performance of masonry structures," *Construction and Building Materials*, vol. 41, pp. 990–1001, 2013. doi:10.1016/j.conbuildmat.2012.07.095.

[25] D. Addessi, S. Marfia, E. Sacco and J. Toti, "Modeling approaches for masonry structures," *The Open Civil Engineering Journal,* vol. 8, pp. 288–300, 2014.

[26] L. Gambarotta and S. Lagomarsino, "Damage models for the seismic response of brick masonry shear walls. Part I: The mortar joint model and its applications," *Earthquake*

Engineering and Structural Dynamics, vol. 26, pp. 423–439, 1997. doi:10.1002/(SICI)1096-9845(199704)26:4<423::AID-EQE650>3.0.CO;2-%23.

[27] D. Addessi and E. Sacco, "A multi-scale enriched model for the analysis of masonry panels," *International Journal of Solids and Structures*, vol. 49, pp. 865–880, 2012. doi:10.1016/j.ijsolstr.2011.12.004.

[28] L. Macorini and B.A. Izzuddin, "A non-linear interface element for 3D mesoscale analysis of brick-masonry structures," *International Journal for Numerical Methods in Engineering,* vol. 85, pp. 1584–1608, 2011. doi:10.1002/nme.3046.

[29] M. Petracca, L. Pelà, R. Rossi, S. Oller, G. Camata and E. Spacone, "Multiscale computational first order homogenization of thick shells for the analysis of out-of-plane loaded masonry walls," *Computer Methods in Applied Mechanics and Engineering,* vol. 315, pp. 273–301, 2017. doi:10.1016/j.cma.2016.10.046.

[30] A.P. Alexandris, E. Protopapa and I. Psycharis, "Collapse mechanisms of masonry buildings drived by the distinct element method," *Proceedings of the 13th World Conference on Earthquake Engineering*, no.548, 2004.

[31] J. V. Lemos, "Discrete element modeling of masonry structures," *International Journal of Architectural Heritage*, vol. 1, pp. 190–213, 2007. doi:10.1080/15583050601176868.

[32] J. V. Lemos and A. Campos Costa, "Simulation of shake table tests on out-of-plane masonry buildings. Part (V): Discrete element approach," *International Journal of Architectural Heritage,* 2016. doi:10.1080/15583058.2016.1237587.

[33] O. AlShawa, L. Sorrentino and D. Liberatore, "Simulation of shake table tests on out-of-plane masonry buildings. Part (II): Combined finite-siscrete elements," *International Journal of Architectural Heritage,* vol. 11, pp. 1-15, 2016. doi:10.1080/15583058.2016.1237588.

[34] G. Milani, P.B. Lourenço and A. Tralli, "Homogenised limit analysis of masonry walls, Part I: Failure surfaces," *Computers and Structures,* vol. 84, pp. 166-180, 2006. doi:10.1016/j.compstruc.2005.09.005.

[35] G. Milani and G. Venturini, "Safety assessment of four masonry churches by a plate and shell FE non-linear approach," *Journal of Performance of Constructed Facilities*. doi:10.1061/(ASCE)CF.1943-5509.0000321.

[36] A. Chiozzi, G. Milani, N. Grillanda and A. Tralli, "A fast and general upper-bound limit analysis approach for out-of-plane loaded masonry walls," *Meccanica*, 2018. doi:10.1007/s11012-017-0637-x.

[37] L.C. Silva, P.B. Lourenço and G. Milani, "Nonlinear discrete homogenized model for out-of-plane loaded masonry walls," *Journal of Structural Engineering,* 2017. doi:10.1061/(ASCE)ST.1943-541X.0001831.

[38] A. Zucchini and P.B. Lourenço, "A micro-mechanical homogenisation model for masonry: Application to shear walls," *International Journal of Solids and Structures,* vol. 46, pp. 871–886, 2009. doi:10.1016/j.ijsolstr.2008.09.034.

[39] P.B. Lourenço, "Computations on historic masonry structures," *Progress in Structural Engineering and Materials,* vol. 4, pp. 301–319, 2002. doi:10.1002/pse.120.

[40] S. Saloustros, L. Pelà, M. Cervera and P. Roca, "An enhanced finite element macro-model for the realistic simulation of localized cracks in masonry structures: A large-scale

application," *International Journal of Architectural Heritage,* vol. 12, pp. 432–447, 2018. doi:10.1080/15583058.2017.1323245.

[41] F. Clementi, E. Quagliarini, F. Monni, E. Giordano and S. Lenci, "Cultural heritage and earthquake: The case study of "Santa Maria della Carità" in Ascoli Piceno," *The Open Civil Engineering Journal*, vol. 11, pp. 1079–1105, 2017. doi:10.2174/1874149501711011079.

[42] M.P. Ciocci, S. Sharma and P.B. Lourenço, "Engineering simulations of a super-complex cultural heritage building: Ica Cathedral in Peru," *Meccanica,* 2018. doi:10.1007/s11012-017-0720-3.

[43] J. Ortega, G. Vasconcelos, H. Rodrigues and M. Correia, "Assessment of the influence of horizontal diaphragms on the seismic performance of vernacular buildings," *Bulletin of. Earthquake Engineering*, 2018. doi:10.1007/s10518-018-0318-8.

[44] R. de Borst, "Fracture in quasi-brittle materials: A review of continuum damage-based approaches," *Engineering Fracture Mechanics*, vol. 69, pp.95-112, 2001. doi:10.1016/S0013-7944(01)00082-0.

[45] J. Mosler and G. Meschke, "Embedded crack vs. smeared crack models: a comparison of elementwise discontinuous crack path approaches with emphasis on mesh bias," *Computer Methods in Applied Mechanics and Engineering*, vol. 193, pp. 3351–3375, 2004. doi:10.1016/j.cma.2003.09.022.

[46] T. Rabczuk, "Computational methods for fracture in brittle and quasi-brittle solids : State-of-the-art review and future perspectives," *ISRN Applied Mathematics,* vol. 2013, pp. 1–61 2012. doi:10.1155/2013/849231.

[47] S. Saloustros, M. Cervera and L. Pelà, "Challenges, tools and applications of tracking algorithms in the numerical modelling of cracks in concrete and masonry structures," *Archives of Computational Methods in Engineering*, 2018. doi:10.1007/s11831-018-9274-3.

[48] M. Cervera, M. Chiumenti and R. Codina, "Mixed stabilized finite element methods in nonlinear solid mechanics. Part I: Formulation," *Computer Methods in Applied Mechanics and Engineering*, vol. 199, pp. 2559–2570, 2010. doi:10.1016/j.cma.2010.04.006.

[49] M. Cervera, M. Chiumenti and R. Codina, "Mixed stabilized finite element methods in nonlinear solid mechanics. Part II: Strain localization," *Computer Methods in Applied Mechanics and Engineering*, vol. 199, pp. 2571–2589, 2010. doi:10.1016/j.cma.2010.04.005.

[50] M. Cervera, M. Chiumenti and R. Codina, "Mesh objective modeling of cracks using continuous linear strain and displacement interpolations," *International Journal for Numerical Methods in Engineering*, 2011. doi:10.1002/nme.3148.

[51] M. Cervera, M. Chiumenti, L. Benedetti and R. Codina, "Mixed stabilized finite element methods in nonlinear solid mechanics. Part III: Compressible and incompressible plasticity," *Computer Methods in Applied Mechanics and Engineering,* vol. 285, pp. 752–775, 2015. doi:10.1016/j.cma.2014.11.040.

[52] L. Benedetti, M. Cervera and M. Chiumenti, "3D numerical modelling of twisting cracks under bending and torsion of skew notched beams," *Engineering Fracture Mechanics*, 2017. doi:10.1016/j.engfracmech.2017.03.025.

[53] M. Cervera, G.B. Barbat and M. Chiumenti, "Finite element modeling of quasi-brittle cracks in 2D and 3D with enhanced strain accuracy," *Computational Mechanics,* 2017. doi:10.1007/s00466-017-1438-8.

[54] G.B. Barbat, M. Cervera and M. Chiumenti, "Appraisement of planar, bending and twisting cracks in 3D with isotropic and orthotropic damage models," *International Journal of Fracture,* vol. 210, pp. 1–35, 2018. doi:10.1007/s10704-018-0261-3.

[55] P.X. Candeias, A.C. Costa, N. Mendes, A.A. Costa and P.B. Lourenço, "Experimental assessment of the out-of-plane performance of masonry buildings through shaking table tests," *International Journal of Architural Heritage,* vol. 11, pp. 1-28, 2016. doi:10.1080/15583058.2016.1238975.

[56] F. Brezzi, "On the existence, uniqueness and approximation of saddle-point problems arising from Lagrangian multipliers," *Revue Française d'Automatique, Informatique, Recherche Opérationnelle. Analyse Numerique.,* 1974. doi:10.1051/m2an/197408R201291.

[57] M. Cervera, "Viscoelasticity and rate-dependent continuum damage models," Monography N-79, CIMNE, Barcelona, 2003.

[58] J. Lemaitre and J.L. Chaboche, "Aspect phenomenologique de la rupture par endommagement," *Journal de Mécanique Appliquée.* vol. 2, 1978.

[59] Z.P. Bažant and B. Oh, "Crack band theory for fracture of concrete," Materials and Structures, vol. 16, pp. 155–177, 1983. doi:10.1007/BF02486267.

[60] EN 1998-1 (Eurocode 8), Design of structures for earthquake resistance, Part 1 General rules seismic actions and rules for buildings, 2003.

[61] FEMA - Federal Emergency Management Agency, FEMA 440 - Improvement of nonlinear static seismic analysis procedures, Washington DC, 2005.

[62] CNR-DT 212/213, Guide for the probabilistic assessment of the seismic safety of existing buildings, Rome, Italy, 2014.

[63] L. Pelà, A. Aprile and A. Benedetti, "Seismic assessment of masonry arch bridges," *Engineering Structures*, vol. 31, pp. 1777–1788, 2009. doi:10.1016/j.engstruct.2009.02.012.

[64] P.B. Lourenço, N. Mendes, L.F. Ramos and D. V. Oliveira, "Analysis of masonry structures without box behavior," *International Journal of Architectural Heritage,* vol. 5, pp. 369–382, 2011. doi:10.1080/15583058.2010.528824.

[65] Y. Endo, M.S. Llorens, P. Roca and L. Pelà, "Dynamic identification and static loading tests of timbrel vaults: Application to a modernist 20th century heritage structure," *International Journal of Architectural Heritage,* vol. 11, pp. 607–620, 2017. doi:10.1080/15583058.2016.1277566.

[66] S. Saloustros, M. Cervera and L. Pelà, "Tracking multi-directional intersecting cracks in numerical modelling of masonry shear walls under cyclic loading," *Meccanica,* vol. 53, pp. 1757–1776, 2018. doi:10.1007/s11012-017-0712-3.

[67] P.B. Lourenço, "Recent advances in masonry modelling: Micromodelling and homogenisation," in: Multiscale Modeling in Solid Mechanics: Computational Approaches, pp. 251–294, 2009. doi:10.1142/9781848163089_0006.

[68] C. Chácara, N. Mendes and P.B. Lourenço, "Simulation of shake table tests on out-of-plane masonry buildings. Part (IV): Macro and micro FEM based approaches," *International Journal of Architectural Heritage,* 2017. doi:10.1080/15583058.2016.1238972.

[69] F. Cannizzaro and P.B. Lourenço, "Simulation of shake table tests on out-of-plane masonry buildings. Part (VI): Discrete element approach," *International Journal of Architectural Heritage,* vol. 11, pp. 125–142, 2017. doi:10.1080/15583058.2016.1238973.

[70] G. Vlachakis, "Out-of-plane simulation of masonry structures using novel finite element techniques," MSc thesis Universitat Politècnica de Catalunya, UPC-BarcelonaTech, 2017.

[71] COMET, Coupled mechanical and thermal analysis, http://www.cimne.com/comet/, 2016.

[72] M. Cervera, C. Agelet de Saracibar and M. Chiumenti, COMET - data input manual version 5.0. Technical report IT-308, Barcelona, 2002.

[73] GiD v.13, The personal pre and post-processor, http://www.gidhome.com/, 2017.

[74] A.A. Costa, A. Arêde, A.C. Costa, A. Penna and A. Costa, "Out-of-plane behaviour of a full scale stone masonry façade. Part 2: shaking table tests," *Earthquake Engineering and Structural Dynamics,* vol. 42, pp. 2097-2111, 2013. doi:10.1002/eqe.2314.

[75] N. Mendes, A.A. Costa, P.B. Lourenço, R. Bento, K. Beyer, G. De Felice, M. Gams, M.C. Griffith, M. Jason, S. Lagomarsino, J. V Lemos, D. Liberatore, C. Modena, D. V. Oliveira, A. Penna and L. Sorrentino, "Methods and approaches for blind test predictions of out-of-plane behavior of masonry walls : A numerical comparative study," *International Journal of Architectural Heritage*, vol. 11, pp. 59–71, 2017. doi:10.1080/15583058.2016.1238974.

[76] P.B. Lourenço, J.G. Rots and J. Blaauwendraad, "Continuum model for masonry: Parameter estimation and validation," *Journal of Structural Engineering*, vol. 124, pp. 642–652, 1998. doi:10.1061/(ASCE)0733-9445(1998)124:6(642).

[77] L. Pelà, "Continuum damage model for nonlinear analysis of masonry structures, " PhD thesis, Universitat Politècnica de Catalunya (UPC-BarcelonaTech), 2009. http://eprints.unife.it/87/.

Architecture of a multi-crack model with full closing, reopening and sliding capabilities

M. Cervera, G. B. Barbat and M. Chiumenti

Computational Mechanics

Vol. 65, pp. 1593-1620, (2020)

https://doi.org/10.1007/s00466-020-01836-y

Architecture of a multi-crack model with full closing, reopening and sliding capabilities

M. Cervera, G. B. Barbat and M. Chiumenti

International Center for Numerical Methods in Engineering (CIMNE)

Technical University of Catalonia – BarcelonaTECH

Edificio C1, Campus Norte, Jordi Girona 1-3

08034 Barcelona, Spain

miguel.cervera@upc.edu, gbarbat@cimne.upc.edu, michele@cimne.upc.edu

Abstract

This paper discusses the finite element modeling of cracking of quasi-brittle materials under cyclic loading. A damage based crack model is proposed, which considers tensile and compressive damage, irreversible strains upon unloading in compression, as well as micro-crack closure-reopening effects (MCR) with special attention to the sliding of open cracks (MCRS). The model is implemented in conjunction with a mixed strain/displacement finite element formulation which provides enhanced accuracy and guarantees mesh size and bias independent results. Two distinct damage models are developed. The first one is based on the classical fixed orthotropic crack models and the second is an isotropic version. Both of them incorporate the necessary elements to furnish full MCRS capabilities. The model is demonstrated through several examples of application and comparison with experimental evidence, in mode I, mode II and mixed mode monotonic and cyclic loading.

Keywords: Cracking, Cyclic loading, Damage, Orthotropy, Mixed Finite Elements

1 Introduction

The numerical modelling of tensile cracking in concrete and other quasi brittle materials is a challenging problem that has been an active topic of research for the last 50 years. Springing from the pioneering work of [1] and [2] a broad supply of approaches has been developed for the modeling of cracks in solids. These range from the classical discrete and smeared crack models to the modern phase-field formulations.

In most of the abundant methods, procedures and techniques developed in these 5 decades attention has focused in proportional, monotonic loading and in cracking due to tensile straining. A Rankine-type criterion of admissible stress or strain has been commonly used. The topics of non-proportional, alternate loading and cracking due to shear straining have received far less attention, regardless of their interest in practical situations, e.g. for concrete structures subjected to seismic actions. These topics raise issues such as fixed material systems, stiffness recovery upon load reversal and simultaneous tensile and compressive damage, not present in standard crack models.

Up to date there is no general consensus for the realistic and efficient numerical analysis of failure in quasi-brittle materials [3]. On the contrary, at the same pace as the use of nonlinear numerical analysis became a common use of engineering practice, engineering researchers became growingly aware of the limitations of the ready to use models.

The crack models used in the vast majority of cases, both in practice and research, are those implemented in commercial codes; these are either classical fixed orthotropic models or some damage-based adaptation of those. The bane that this entails arises from two main causes: *shear locking* and *mesh bias dependence*. Let us consider them separately, although they are related.

Shear locking was identified as a problem of classical crack models almost from the start. The reasons for shear locking are twofold:

1. From the numerical standpoint, the lack of strain (or stress) continuity in-between adjacent elements in standard irreducible finite elements. In standard FE, the main variable, the displacement field, is approximated and interpolated by means of element-wise defined C^0 continuous functions, and strains are derived by discrete differentiation within each element from the nodal displacements. This results in an inter-elemental discontinuous discrete strain field and, through the constitutive equations, in a subsequent inter-elemental discontinuous discrete stress field.

   In (linear) problems and isotropic materials, this lack of continuity is frequently used as an error estimator of the numerical solution, as the inter-elemental discontinuity of strain and stress should be reduced on mesh refinement. In problems involving cracking, a severe (non-linear) orthotropic material behavior is induced, with large differences in the elastic moduli along different directions. In this situation, the discretization error occurring in the evaluation of the strain field is magnified, producing acute stress-locking.

2. From the physical point of view, a fixed orthogonal material system is a poor frame for a nonlinear secant constitutive model in situations in which the principal directions of strain change, e.g. non proportional loading. Material properties and constitutive relations between strain and stress in linear orthotropic materials are defined in fixed orthogonal systems. By analogy, the constitutive behavior of materials with nonlinear induced orthotropy due to cracking are often defined by secant relations in an orthogonal material system which needs to be defined.

Typically, the orientation of the material axes is defined by the directions of the components of the stress which causes the crack to firstly appear. This presents no difficulty if subsequent loading and unloading of the cracks occurs maintaining the same principal directions, but there are many practical situations in which this does not happen, e.g. non proportional loading; loss of co-axiality between strains and stresses aggravates the issue. Under cyclic loading and/or shear dominated situations, these limitations are unwieldy.

The numerical difficulties associated to shear locking in a fixed orthogonal material frame for cracks were soon identified, even for proportional, monotonic loading; the problem was firstly alleviated by the so-called rotating crack models and later by adopting isotropic damage models for tensile failure. The first ones maintained co-axiality of strains and stresses at the cost of rotating the material defects; shear locking was reduced, but not eliminated because of the mentioned lack of inter-element strain continuity in standard FEs. In isotropic damage models, remarkably simple to formulate and implement, shear locking is swiftly eradicated; for this reason, isotropic damage is at the core of phase-field formulations for cracks, despite the obvious locally directional nature of cracks.

The physical limitations of crack models are very clear under non-proportional and alternate loading. For non-proportional loading, the options are either rotating the material axes or allowing for multiple cracks; the first has been discussed above and the second was the motivation for some few multi-crack models [4, 5] and the micro-plane theory [6, 7]. For alternate loading, the features to be incorporated are stiffness recovery for crack closing (microcrack closure-reopening effects, MCR) and irrecoverable strains when unloading in compression. It needs to be understood that:

• Rotating crack and isotropic damage models cannot incorporate MCR effects, unless they are provided with some record of the directions in which damage occurred originally.

• In fixed crack models, stiffness recovery upon crack closure leads to unphysical jumps in the shear and transverse stresses if the sliding of the open crack is significant (MCRS effects).

• Irrecoverable strains can be readily incorporated to a crack model, but the formulation adopted may come in conflict with the strain-driven, explicit, secant form of crack models.

As explained, the remedies to the numerical issues raised in certain situations have obvious physical limitations and are often contradictory with the requirements for realistic modeling in some other cases. Reversely, some of the physically motivated requirements are not agreeable from the numerical point of view.

Mesh bias dependence has been a topic of great concern in computational mechanics for the last 30 years, and it has been addressed in a variety of approaches. In linear elasticity, the use of standard FEs cannot guarantee local convergence of the solution in terms of strains and stresses in quasi-singular points such as the re-entrant corners of the tip of a sharp crack. In cracking problems, such situations arise in the vicinity of the tip of propagating cracks, bringing in an incorrect evaluation of the strain and stress in these most critical locations. This lack of local convergence in the strain and stress leads to the spurious mesh bias dependence observed in problems of quasi-brittle crack propagation solved with the standard formulation, yielding incorrect solutions in many cases.

A mixed strain/displacement formulation, proposed and developed in references [8-13] resolves the strain independently from the displacement field, instead of being derived from it at element level as in standard FEs. This results in a kinematic enhancement and increase in the accuracy of the strain and stress fields. Seasonably, this enhanced accuracy has proved to eliminate the spurious mesh-dependency and lack of convergence of standard finite elements in problems

involving isotropic plasticity and damage models without the use of auxiliary tracking techniques and with mesh densities far smaller than those used in phase-field formulations.

In references [11, 12] the mixed finite element technology has been assessed for monotonic cracking problems using isotropic and orthotropic damage models in 2D and 3D. Remarkably, the enhancement of the inter-elemental continuity of the strain in mixed FEs alleviates to a large extent the spurious stress locking that used to make orthotropic models unpractical in conjunction with standard FEs. Also, the generality of the mixed finite element formulation allows using it jointly with orthotropic models developed for cyclic loading.

Therefore, the objectives of this paper are: (1) to define the elements of crack models with full MCRS capabilities, (2) to present the formulation of isotropic and orthotropic damage–based models integrating those elements, (3) to demonstrate the performance of the proposed models in situations involving tensile and compressive damage, irreversible strains, MCRS effects and multi-cracking, (4) to demonstrate the capability of the mixed FE formulation in successfully incorporating isotropic and orthotropic damage models subjected to cyclic loading without the numerical burdens associated to standard FEs.

The outline of this paper is as follows. In Section 2 the design requirements of crack models with full MCRS capabilities are given. In Section 3, isotropic and orthotropic fixed d+/d- damage-based crack models are presented; Section 4 incorporates irreversible strains under compression. Section 5 describes the specific treatment of MCR effects; Section 6 incorporates the irreversible strains corresponding to the change of open/closed crack status. Section 7 considers the generation of multi-crack systems for cracking under non-proportional loading. Section 8 demonstrates the performance of the model at local level. Section 9 summarizes the mixed FE formulation. Sections 10 and 11 present numerical simulations of a concrete beam and a metal specimen subjected to cyclic loading where the performance of the constitutive model is examined. Finally, some conclusions are given.

2 Architecture of crack models with full MCRS capabilities

The architecture of the multi-crack model with full close-reopening and sliding capabilities in this work consists of the assemblage of the following elements:

1. Strain-driven format.
2. Tensile damage, associated to tensile cracking.
3. Directionality of damage.
4. Irreversibility of damage and its directionality.
5. Secant form.
6. Compressive damage, associated to shear cracking and crushing.
7. Irreversible strains upon compressive unloading.
8. Stiffness recovery upon load reversal, MCR.
9. Stiffness recovery upon load reversal with significant sliding, MCRS.
10. Multi-cracks at local level.

Points 1 to **5** define a classical fixed crack model, and are common to later damage-based orthotropic models. Remarkably, the nowadays very much used isotropic damage models wave crack directionality aside, while rotating orthotropic models abandon its permanent character. Damage is assumed isotropic in phase-field formulations.

Points 6 and **7**, relative to the behavior under shear and compression, are present in several orthotropic damage models, based on the split of the tensile/compressive stress or strain tensors

[14-18], but not applied in fixed material systems. In this work, a completely new approach, based on the activation and deactivation of damage in a fixed material system is adopted.

Note that under shear loading, tensile and compressive stresses act simultaneously in orthogonal directions to each other. This implies that compressive damage needs to be contemplated in shear failure. On the one hand, tensile and compressive damage are not symmetrical; for instance, significant irreversible strains develop upon unloading under compression. On the other hand, compressive damage may be independent from tensile stresses (as in Rankine-type criteria) or related to them (as in Mohr-Coulomb and Drucker-Prager criteria).

Point 8 is necessary for alternate cyclic loading. Previous efforts [14, 15] are not applicable to shear dominated situations, unless some record on the directionality of damage at the moment of occurrence is kept, as demonstrated in [17, 18]. Regarding this, in the following, a full record of directionality is maintained, and the ensuing model is therefore "fixed". Stiffness recovery upon load reversal is here toggled through functions that define the status of the cracks as *open* or *closed*. The *active damage* is likewise defined.

Point 9 is closely associated to **Point 8**; as sliding of the open cracks occurs, stress continuity needs to be enhanced when the status of cracks, and their stiffness, changes. This is a novel feature of this work; irreversible "sealing" strains are introduced to ensure stress continuity in these situations.

Point 10 is also associated to non-proportional loading and the modification of the directions of straining. This concerned some classical multi-crack models [4, 5] and the micro-plane theory [6, 7]. Here, a multiplicity of material systems is allowed to develop, and the only one which is active at a current time is defined by the status of the cracks.

The procedures involved in Points **8**, **9** and **10** are simple and effective.

In the following Sections, the different parts of the assemblage are addressed, as well as the algorithms showing how they are implemented and integrated.

3 Isotropic and orthotropic d+/d- damage model with memory

In this section, the formulation of the isotropic and orthotropic damage models is presented in secant form. Tensile and compressive damage is considered.

Using Voigt's convention, the strain and stress tensors are expressed as vectors [19]. In 3D the strain vector is $\boldsymbol{\varepsilon} = \left(\varepsilon_x, \varepsilon_y, \varepsilon_z, \gamma_{xy}, \gamma_{xz}, \gamma_{yz}\right)^T$ and stress vector is $\boldsymbol{\sigma} = \left(\sigma_x, \sigma_y, \sigma_z, \tau_{xy}, \tau_{xz}, \tau_{yz}\right)^T$. In a secant damage model, $\boldsymbol{\varepsilon}$ and $\boldsymbol{\sigma}$ are linked through the constitutive equation:

$$\boldsymbol{\sigma} = \mathbf{D}(\boldsymbol{d}, \boldsymbol{\theta})\, \boldsymbol{\varepsilon} \tag{1}$$

where $\mathbf{D} = \mathbf{D}(\boldsymbol{d}, \boldsymbol{\theta})$ is the secant constitutive matrix, a function of a set of internal variables $\boldsymbol{d}$ that describe the degradation of the material and $\boldsymbol{\theta}$ which denotes the spatial directions in which damage occurs. Let be $\boldsymbol{d} = (d_1, d_2, d_3)^T$, with the scalar damage indices d_i, $i = 1{,}3$, associated to the 3 orthogonal spatial directions of $\boldsymbol{\theta}$.

In materials which are isotropic when undamaged, the orthotropic behavior induced by damage is generally associated to the principal directions of stress (and strain) at the inception of damage. In classical "fixed" crack models, the material system $\boldsymbol{\theta}$ was locked thereafter; in "rotating" crack models, the material axes were updated so that stress and strains remain coaxial. Visibly, the differences between both options are the treatment of crack sliding and shear transfer across cracks.

Regardless of the indisputable directional character of cracks, isotropic damage models were firstly proposed [20] and then broadly adopted as crack models as a way of avoiding the numerical issues that orthotropic models bear.

In the following, unless stated otherwise, the material axes $\boldsymbol{\theta}$ will be drawn on as in classical fixed models.

From thermodynamic considerations, the secant matrix needs to be symmetric and positive semidefinite. Symmetric orthotropic damage models may be effectively formulated from the hypothesis of energy equivalence [17, 21-23].

For an initially isotropy elastic material characterized by the Young's modulus E and the Poisson's ratio ν, the secant constitutive matrix may be expressed in the $\boldsymbol{\theta}$ material system as

$$\mathbf{D} = \mathbf{D}(\boldsymbol{d}) = \begin{pmatrix} D_{11}(d_1) & D_{12}(d_1,d_2) & D_{13}(d_1,d_3) & & & \\ D_{21}(d_1,d_2) & D_{22}(d_2) & D_{23}(d_2,d_3) & & \mathbf{0} & \\ D_{31}(d_1,d_3) & D_{32}(d_2,d_3) & D_{33}(d_3) & & & \\ & & & G_{12}(d_1,d_2) & & \\ & \mathbf{0} & & & G_{13}(d_1,d_3) & \\ & & & & & G_{23}(d_2,d_3) \end{pmatrix} \tag{2}$$

such that

$$\begin{aligned} D_{kk} &= (1-d_k)\, D_{kk}^0 \quad ; \quad k = 1,3 \\ D_{kl} &= \min[(1-d_k);(1-d_l)]\, D_{kl}^0 \quad ; \quad k,l = 1,3 \quad k \neq l \\ G_{kl} &= \min[(1-d_k);(1-d_l)]\, G_{kl}^0 \quad ; \quad k,l = 1,3 \quad k \neq l \end{aligned} \tag{3}$$

and

$$\begin{aligned} D_{kk}^0 &= \frac{E(1-\nu)}{(1+\nu)(1-2\nu)} \quad ; \quad k = 1,3 \\ D_{kl}^0 &= \frac{E\nu}{(1+\nu)(1-2\nu)} \quad ; \quad k,l = 1,3 \quad k \neq l \\ G_{kl}^0 &= \frac{E}{2(1+\nu)} \quad ; \quad k,l = 1,3 \quad k \neq l \end{aligned} \tag{4}$$

The isotropic version of the model is obtained by adopting $d_1 = d_2 = d_3 = d$, so that $\mathbf{D} = (1-d)\,\mathbf{D}_0$, where d is the single scalar internal damage index and $\mathbf{D}_0$ is the elastic constitutive matrix.

The effective stress is defined in terms of the elastic matrix as $\bar{\boldsymbol{\sigma}} = \mathbf{D}_0\,\boldsymbol{\varepsilon}$. Let $\bar{\sigma}_i,\ i = 1,3$, be the three normal stress components of the effective stress $\bar{\boldsymbol{\sigma}}$ in the material axes $\boldsymbol{\theta}$.

In isotropic models the equivalent effective stress, $\bar{\sigma}_{eq}$, depends on the effective stress $\bar{\boldsymbol{\sigma}}$ through the specific damage criterion F

$$\bar{\sigma}_{eq} = F(\bar{\boldsymbol{\sigma}}) \tag{5}$$

In orthotropic models, an equivalent effective stress is defined for each material direction, $\bar{\sigma}_{eq,i}$, depending on the specific damage criterion F and the material system $\boldsymbol{\theta}$:

$$\bar{\sigma}_{eq,i} = F_i(\bar{\boldsymbol{\sigma}}, \boldsymbol{\theta}), \quad i = 1,3 \tag{6}$$

In this work, Drucker-Prager and Rankine damage criteria are adopted as exemplary cases of isotropic and orthotropic models, respectively. Other criteria may be similarly considered.

The Drucker-Prager criterion depends on the first and second effective stress invariants I_1 and J_2 and the equivalent effective stress is defined as

$$\bar{\sigma}_{eq} = F(\bar{\boldsymbol{\sigma}}) = \frac{\left(\sqrt{3J_2} + \alpha I_1\right)}{1+\alpha} \tag{7}$$

with α being a function of the tensile and compressive strengths f_t and f_c

$$\alpha = \left(\frac{f_c}{f_t} - 1\right) \Big/ \left(\frac{f_c}{f_t} + 1\right) \tag{8}$$

The Rankine criterion depends on the normal effective stresses along the material axes, and the equivalent effective stresses are

$$\bar{\sigma}_{eq,i} = F_i(\bar{\boldsymbol{\sigma}}, \boldsymbol{\theta}) = \bar{\sigma}_i \qquad i = 1,3 \tag{9}$$

If tensile and compression damage are to be considered, two distinct failure surfaces $\mathbb{F}_i^{\pm}$ need to be explicitly defined, here noted with the + and – suffixes. For an orthotropic model, these surfaces are defined as

$$\mathbb{F}_i^{\pm}\left(\bar{\sigma}_{eq,i}^{\pm}, r_i^{\pm}\right) = \bar{\sigma}_{eq,i}^{\pm}(\bar{\boldsymbol{\sigma}}) - r_i^{\pm} = 0 \qquad i = 1,3 \tag{10}$$

where r_i^+ and r_i^- are the current tensile and compressive damage thresholds. From the Kuhn-Tucker optimality and consistency conditions, the current values of the damage threshold, defining the actual size of the damage surfaces, are explicitly updated at time t as

$$r_i^{\pm} = \max\left(r_0^{\pm}, \max \bar{\sigma}_{eq,i}(\hat{t})\right) \quad \hat{t} \in [0,t] \tag{11}$$

This guarantees the irreversibility of damage and the positiveness of the dissipation. Their initial values depend on the corresponding tensile and compressive uniaxial strengths of the material, $r_0^+ = f^+$ and $r_0^- = f^-$.

For example, for Rankine's criterion

$$\bar{\sigma}_{eq,i}^{\pm} = F_i(\bar{\boldsymbol{\sigma}}, \boldsymbol{\theta}) = \langle \pm \bar{\sigma}_i \rangle \qquad i = 1,3 \tag{12}$$

where $\langle \cdot \rangle$ are the Macaulay brackets, such that $\langle x \rangle = x \;\; if \;\; x \geq 0, \;\; 0 \;\; if \;\; x < 0$.

The evolution of the internal damage indices may be different for tension and compression in terms of their respective damage threshold internal variables. The requirements on the damage function defining this evolution are: it must be continuous, monotonically increasing from 0 to 1, and its derivative must be positive. These requirements ensure the continuous and positive dissipation of the strain energy and of the mechanical dissipation. In this work, they will follow a parabolic-exponential softening law

$$d_i^{\pm} = \begin{cases} 0 & if \quad r_i^{\pm} < f_0^{\pm} \\ A_d^{\pm} \dfrac{f^{\pm}}{r_i^{\pm}} \left(\dfrac{r_i^{\pm} - f_0^{\pm}}{f_p^{\pm} - f_0^{\pm}} \right) & if \quad f_0^{\pm} \leq r_i^{\pm} < f_p^{\pm} \\ 1 - \dfrac{f^{\pm}}{r_i^{\pm}} \exp\left[2H_d^{\pm} \left(\dfrac{f^{\pm} - r_i^{\pm}}{f^{\pm}} \right) \right] & if \quad r_i^{\pm} \geq f_p^{\pm} \end{cases} \tag{13}$$

where $f_0^{\pm} = \gamma_0^{\pm} f^{\pm}$ and $f_p^{\pm} = \gamma_p^{\pm} f^{\pm}$, as well as $0 \leq \gamma_0^{\pm} \leq 1$ and $\gamma_p^{\pm} \geq 1$, are material properties. Depending on these,

$$A_d^{\pm} = \frac{f_p^{\pm} - f^{\pm}}{f^{\pm}} \tag{14}$$

Note that for $\gamma_0 = \gamma_p = 1$ the softening law is purely exponential; the parabolic part vanishes.

Energy conservation considerations link the softening parameters, $H_d^{\pm}$, to the material fracture energies $G_f^{\pm}$ and to the width of the crack b in the following way [3]:

$$\frac{1}{H_d^{\pm}} = \frac{2E G_f^{\pm}}{(f^{\pm})^2} \frac{1}{b} - \frac{f_p^{\pm}}{f^{\pm}} - \bar{A}_d^{\pm} \tag{15}$$

with

$$\bar{A}_d^{\pm} = \frac{A_d^{\pm} \left[\left(f_p^{\pm} \right)^3 - 3 f_p^{\pm} \left(f_0^{\pm} \right)^2 + 2 \left(f_0^{\pm} \right)^3 \right]}{3 f^{\pm} \left(f_p^{\pm} - f_0^{\pm} \right)^2} \tag{16}$$

The details on the expression of the mechanical dissipation and the derivation of the softening parameters $H_d^{\pm}$ can be found in reference [3].

In this work, the bandwidth of the localized cracks is taken as $b = 2h$, h being the finite element size. This is consistent with the approximation adopted for the discrete strain field in the mixed formulation in Section 9.

For isotropic models, the effective stress is not defined for each material axis. Therefore, the i index is dropped in Eqs. (9), (10), (11), (12) and (13) for the isotropic version of the model. In this way, an isotropic Rankine criterion is defined by taking the maximum normal effective stress as the unique equivalent effective stress

$$\bar{\sigma}_{eq}^{\pm} = F(\bar{\boldsymbol{\sigma}}) = \langle \pm \bar{\sigma}_1 \rangle \tag{17}$$

For the Drucker-Prager criterion, we will adopt

$$\bar{\sigma}_{eq}^{\pm} = F(\bar{\boldsymbol{\sigma}}) = \left\langle \pm \frac{\bar{\sigma}_1}{|\bar{\sigma}_1|} \right\rangle \frac{\left(\sqrt{3J_2} + \alpha I_1 \right)}{1 + \alpha} \tag{18}$$

Other alternatives may be contemplated for the assignment of the tensile/compressive equivalent stresses in such a case.

The algorithm for the orthotropic d+/d- crack model is presented in Table 1. The isotropic version of the model is akin, but there is a unique driving equivalent effective stress $\bar{\sigma}_{eq}$.

Table 1 Algorithm for the orthotropic d+/d- crack models

1. Compute the effective stress $\overline{\boldsymbol{\sigma}} = \mathbf{D}_0\, \boldsymbol{\varepsilon}$
2. IF $\boldsymbol{d} = \mathbf{0}$ THEN
   Rotate $\overline{\boldsymbol{\sigma}}$ to its principal directions $\boldsymbol{\theta}$
   ELSE
   Rotate $\overline{\boldsymbol{\sigma}}$ to the material axes $\boldsymbol{\theta}$
   ENDIF
3. Compute the equivalent tensile/compressive effective stress $\bar{\sigma}_{eq,i}^{\pm} \quad i = 1,3$, with Eq. (6)
4. Update the tensile/compressive damage threshold $r_i^{\pm} \quad i = 1,3$, with Eq. (11)
5. Update the tensile/compressive damage index $d_i^{\pm} \quad i = 1,3$ with Eq. (13)
6. Compute the constitutive matrix $\mathbf{D}(\boldsymbol{d}, \boldsymbol{\theta})$ using Eq. (2)
7. Rotate the secant $\mathbf{D}$ matrix to the global axes
8. Compute $\boldsymbol{\sigma} = \mathbf{D}\, \boldsymbol{\varepsilon}$ with Eq. (1)

4 Irreversible strains

In this section, the orthotropic damage of the precedent Section is extended to incorporate the development of irrecoverable strains upon unloading. This is done by evolving an orthotropic version of the isotropic model used in [24]. Both models are explicitly strain-driven.

In the following, irreversible strains are driven by the compressive strains exclusively; tensile irreversible strains can be readily contemplated.

Let us consider the additive split of the total strain $\boldsymbol{\varepsilon}$ into its elastic $\boldsymbol{\varepsilon}^e$ and inelastic (irrecoverable) $\boldsymbol{\varepsilon}^i$ parts

$$\boldsymbol{\varepsilon} = \boldsymbol{\varepsilon}^e + \boldsymbol{\varepsilon}^i \tag{19}$$

so that the secant constitutive Eq. (1) is rewritten as

$$\boldsymbol{\sigma} = \mathbf{D}(\boldsymbol{d}, \boldsymbol{\theta})\, \boldsymbol{\varepsilon}^e \tag{20}$$

where $\mathbf{D}(\boldsymbol{d}, \boldsymbol{\theta})$ is the secant damage matrix from the previous Section and $\boldsymbol{\varepsilon}^e = \boldsymbol{\varepsilon} - \boldsymbol{\varepsilon}^i$. The effective stress is now redefined in terms of the elastic matrix and the elastic strain as $\overline{\boldsymbol{\sigma}} = \mathbf{D}_0 \boldsymbol{\varepsilon}^e$.

From the 3 directions of the material system $\boldsymbol{\theta}$, $i = 1,3$, direction k is selected, such that

$$r_k^- = \max_{i=1,3} \; (r_i^-) \tag{21}$$

The rate of (compression) irreversible strains is proportional to

- the current elastic strain and
- the increase of the distance to the (compression) damage surface (normalized with respect r, the actual size of the (compression) damage surface).

It is stated as:

$$\dot{\boldsymbol{\varepsilon}}^i = \frac{\beta}{1-\beta} \left[\frac{\dot{r}}{r}\right]_k^- \boldsymbol{\varepsilon}^e \tag{22}$$

where β, $0 \leq \beta \leq 1$, is a material parameter that controls the development of irreversible strains. The super and sub-indices $[\cdot]_k^-$ indicate both the directional and the compressive nature of the

argument. Note that the argument cannot be negative because the threshold r may not decrease, Eq. (11). This ensures positive dissipation when irreversible strains develop.

Note that in the limit case $\beta = 0$, no irreversible strains develop in the model. Contrariwise, for the limit case $\beta \to 1$, there is no evolution of the damage threshold r_k^-; in this case, the straining is fully irreversible.

The development of irreversible strain is dissipative. Under the assumption that the total dissipation of the damage model is not affected by the value of parameter β the softening modulus H_d^- is redefined as

$$\frac{1}{H_d^-} = (1-\beta)\left(\frac{2EG_f^-}{(f^-)^2}\frac{1}{b} - \frac{f_p^-}{f^-} - \bar{A}_d^- - \frac{\beta}{1-\beta}B_d^-\right) \tag{23}$$

where

$$B_d^- = \frac{\left(f_p^- - f_0^-\right)\left(3f_p^- - 2f^-\bar{A}_d^- + 3f_0^-\right)}{3(f^-)^2} \tag{24}$$

The supplementary details on the influence of the parameter β in the mechanical dissipation and the resulting renewed derivation of the softening parameters $H_d^{\pm}$ can be also found in reference [3].

The rate expression for the irreversible strain Eq. (22) may be integrated in time with an implicit backward Euler scheme. Let $\Delta t = t_{n+1} - t_n$ be a time increment between subsequent time steps n and $n+1$. In the following, let $\Delta(\cdot)$ indicate the increment of a specific quantity from step n to $n+1$.

The *trial effective stresses* at t_{n+1} are defined as the effective stresses that would occur without further development of irrecoverable strains,

$$\bar{\boldsymbol{\sigma}}_{n+1}^{tr} = \left(\bar{\boldsymbol{\sigma}}|_{\Delta\boldsymbol{\varepsilon}^i=0}\right)_{n+1} = \bar{\boldsymbol{\sigma}}_n + \mathbf{D}_0\,\Delta\boldsymbol{\varepsilon} \tag{25}$$

With some manipulation, it can be shown that

$$\Delta\boldsymbol{\varepsilon}^i = \frac{\beta}{1-\beta}\left[\frac{\Delta r}{r_{n+1}}\right]_k^-\boldsymbol{\varepsilon}_{n+1}^e = \frac{1-\lambda}{\lambda}\,\boldsymbol{\varepsilon}_{n+1}^e \tag{26}$$

with the scaling parameter λ

$$\lambda = 1 - \beta\left(1 - \left[\frac{r_n}{r_{n+1}^{tr}}\right]_k^-\right) \tag{27}$$

where $[r_{n+1}^{tr}]_k^-$ is evaluated with $\bar{\boldsymbol{\sigma}}_{n+1}^{tr}$. Note in Eq. (21) that the material parameter β defines the rate of the irreversible deformation by scaling the current increment of the equivalent stresses, and consequently the stress threshold. Therefore

$$[\Delta r]_k^- = (1-\beta)\left([r_{n+1}^{tr}]_k^- - [r_n]_k^-\right) \tag{28}$$

Due to the co-axiality of $\boldsymbol{\varepsilon}^e$ and $\Delta\boldsymbol{\varepsilon}^i$, it can be shown that $\bar{\boldsymbol{\sigma}}_{n+1}$are proportional to $\bar{\boldsymbol{\sigma}}_{n+1}^{tr}$, so that

$$\bar{\boldsymbol{\sigma}}_{n+1} = \lambda\,\bar{\boldsymbol{\sigma}}_{n+1}^{tr} \tag{29}$$

This allows taking into account the effect of the irreversible strains explicitly in the computation of the effective stresses prior to the update of the damage indices. The complete algorithm for updating stresses and internal variables is given in Table 2. Note that it is fully strain-driven.

Table 2. Algorithm for the evaluation of irreversible strains

1. Compute the increment of total strains $\Delta\boldsymbol{\varepsilon} = \boldsymbol{\varepsilon}_{n+1} - \boldsymbol{\varepsilon}_n$
2. Compute the trial effective stresses $\overline{\boldsymbol{\sigma}}_{n+1}^{tr}$ with Eq. (25)
3. Select direction k according to Eq. (21)
4. Compute $[r_{n+1}^{tr}]_k^-$ from Eq. (11) and λ from Eq. (27)
5. Compute the effective stress $\overline{\boldsymbol{\sigma}}_{n+1}$ from Eq. (29)
6. Compute $\Delta\boldsymbol{\varepsilon}^i$ from Eq. (26)
7. Update $\boldsymbol{\varepsilon}_{n+1}^i$ and $\boldsymbol{\varepsilon}_{n+1}^e$
8. Compute damage variables $\boldsymbol{d}$ and secant matrix $\mathbf{D}_{n+1}$ according to **Table 1**
9. Compute $\boldsymbol{\sigma}_{n+1} = \mathbf{D}_{n+1}\,\boldsymbol{\varepsilon}_{n+1}^e$ with Eq. (20)

5 Microcrack closure-reopening effects (MCR)

Cyclic straining requires the partial or total recovery of stiffness caused by crack closure and reopening to be resolved. For establishing the status of a crack as *active* (open) or *inactive* (closed), a set of step functions is associated to the tensile damage indices. In the orthotropic model, these functions are noted as H_i^+ and are defined for each of the directions $i = 1,3$, of the material axes $\boldsymbol{\theta}$ as

$$H_i^+ = \begin{cases} 0 & if\ \bar{\sigma}_i = 0 \\ \left\langle \dfrac{\bar{\sigma}_i}{|\bar{\sigma}_i|} \right\rangle & if\ \bar{\sigma}_i \neq 0 \end{cases} \tag{30}$$

where $\bar{\sigma}_i$ are the effective normal stresses along direction i. Therefore, the crack in direction i is *open* if $H_i^+ = 1$ and it is *closed* if $H_i^+ = 0$.

Associated to the H_i^+ functions that signal the current status of the crack in direction i, the discrete toggle functions $\mathcal{T}_i$ are defined as

$$\mathcal{T}_i = \begin{cases} 0 & if\ \Delta H_i^+ = 0 \\ 1 & if\ \Delta H_i^+ \neq 0 \end{cases} \tag{31}$$

where ΔH_i^+ is the increment of H_i^+ in the current time (or load) step.

The toggle functions signal if the status of the crack has changed, themselves activating the MCRS effects described in the next Section.

If compressive damage is also considered, an additional set of step functions H_i^- is defined as

$$H_i^- = \begin{cases} 0 & if\ \bar{\sigma}_i = 0 \\ 1 - H_i^+ & if\ \bar{\sigma}_i \neq 0 \end{cases} \tag{32}$$

The H_i^+ and H_i^- step functions are introduced to activate and deactivate the tensile and compressive damage indices in the secant constitutive matrix in each direction i. Note that H_i^+ and H_i^- are not equal to one concurrently; hence, tensile and compression damage are not active at the same time. The switch between tensile and compressive situations provides partial or total stiffness recovery when the corresponding effective stress flips sign.

Specifically, the active damage d_i used in Eq. (3) is posed as

$$d_i = H_i^+ d_i^+ + H_i^- d_i^- \tag{33}$$

In the isotropic model it is also necessary to determine if the tensile or compressive damage indices are active if MCR effects are to be elucidated. To this end, the material axes $\boldsymbol{\theta}$ are associated to the principal directions of stress (and strain) at the inception of damage and they are locked thereafter. The required step and toggle functions are defined by the first material axis, as it is the first to damage, so that

$$H^+ = H_1^+ \qquad H^- = H_1^- \qquad \mathcal{T} = \mathcal{T}_1 \tag{34}$$

Consequently, the active damage d is either $d = d^+$ if the crack is open or $d = d^-$ if it is closed:

$$d = H^+ d^+ + H^- d^- \tag{35}$$

In 3D, the orthotropic model needs to consider 3 damage variables in traction (one for each material direction) and 3 additional damage variables in compression. For isotropic damage, only 2 damage variables, one for tension and one for compression, are needed.

6 Microcrack closure-reopening effects with sliding (MCRS)

One of the serious drawbacks of classical fixed crack models is the transfer of shear stress due to sliding of the open cracks. This issue led firstly to the conception of the rotating crack models, which preserved co-axiality of strains and stress at all time at the expense of not fixing the direction of the material cracks, and secondly, to the adoption of isotropic damage models, which further enhanced co-axiality and disavowed directionality.

A secondary drawback of orthogonal crack models, fixed and rotating, was the evolution of Poisson's effect, which was usually discarded from the inception of cracking.

In any case, changes in the secant stiffness lead to discontinuities in the evolution of the stress under continuous straining, an objectionable feature for a constitutive model, burdensome in the numerical application. Note that isotropic damage models treat this issue in a remarkably straight-forward manner, one of the reasons for their broad adoption.

These concerns have a predominant role if cyclic straining with stiffness recovery from crack closure-reopening and sliding (MCRS) is considered. Changes in the secant stiffness due to the activation/deactivation of tensile/compressive damage in the material axes $\boldsymbol{\theta}$ are triggered by the individual normal effective stresses $\bar{\sigma}_i$, $i = 1,2,3$, but, once implemented, they interact both with the shear strains and with the normal strains in the other directions. If the stress field is to remain continuous in time under continuous straining, "sealing" irrecoverable strains need to be considered; they are associated to the shear and the transverse elastic strains that are present when damage flips occur. In the following, these strains are motivated and evaluated in correspondence with the previous Sections.

Let us consider the secant constitutive Eq. (20)

$$\boldsymbol{\sigma} = \mathbf{D}\, \boldsymbol{\varepsilon}^e \tag{36}$$

Differentiating with respect to time

$$\dot{\boldsymbol{\sigma}} = \mathbf{D}\, \dot{\boldsymbol{\varepsilon}}^e + \dot{\mathbf{D}}\, \boldsymbol{\varepsilon}^e \tag{37}$$

where the first term of the right hand side is due to the variation of the total and irrecoverable strains and the second term is due to the variation of the stiffness. In a continuous process in time, continuous strain rates drive continuous stiffness and stress rates. However, changes in stiffness associated to the closure-reopening of the cracks are not strain-driven, but motivated by the change in the *open/closed* status of the crack, signaled by the toggle functions $\mathcal{T}_i$. This means that if stress is to be continuous in time while a change of crack status occurs, there are irreversible strains that must take place concurrently. As in previous Sections, let n and $n+1$ be subsequent time steps, such that the closure or reopening of a crack takes place in the time increment in between. Let $\Delta(\cdot)$ indicate the increment of a specific quantity from step n to $n+1$, and $\Delta t = t_{n+1} - t_n$ be the time increment.

Making $\dot{\boldsymbol{\sigma}} = \mathbf{0}$ in Eq. (37) to ensure stress continuity regardless of the variation of stiffness, the incremental irreversible strains caused by crack closure are:

$$\Delta\boldsymbol{\varepsilon}^i = \mathcal{T}\ \mathbf{D}_{n+1}^{-1}\ \Delta\mathbf{D}\ \boldsymbol{\varepsilon}_n^e \tag{38}$$

where $\mathcal{T} = \max_{i=1,3}\ (\mathcal{T}_i)$. $\Delta\mathbf{D} = \mathbf{D}_{n+1} - \mathbf{D}_n$ corresponds to the variation of stiffness due to a change of the *open/closed* status of the crack. These additional irrecoverable strains guarantee stress continuity at t_n and are computed at t_{n+1}, added to those computed from Eq. (26).

The algorithm for the orthotropic crack model with irreversible strains and MCRS effects is given in Table 3. The isotropic version of the model is analogous, but there is a unique driving equivalent effective stress $\bar{\sigma}_{eq}$.

Table 3. Algorithm for the orthotropic crack model with irreversible strains and MCRS effects

1.	Compute the effective stress $\overline{\boldsymbol{\sigma}}^{tr}$ with Eq. (25)

2.	IF $\boldsymbol{d} = \mathbf{0}$ THEN
	Rotate $\overline{\boldsymbol{\sigma}}^{tr}$ to its principal directions $\boldsymbol{\theta}$
	ELSE
	Rotate $\overline{\boldsymbol{\sigma}}^{tr}$ to the material axes $\boldsymbol{\theta}$
	ENDIF

3.	Compute $\overline{\boldsymbol{\sigma}}$ according to Eq. (29)
4.	Compute irreversible strains $\boldsymbol{\varepsilon}^i$ following **Table 2**
5.	Compute the equivalent tensile/compressive effective stress $\bar{\sigma}_{eq,i}^{\pm}\ \ i = 1,3$, with Eq. (6)
6.	Update the tensile/compressive damage threshold $r_i^{\pm}\ \ i = 1,3$, with Eq. (11)
7.	Update the tensile/compressive damage index $d_i^{\pm}\ \ i = 1,3$, with Eq. (13)
8.	Compute the status and toggle functions $H_i^{\pm},\ \mathcal{T}_i\ \ i = 1,3$, with Eqs. (30), (31) and (32)
9.	Decide on active damage d, as in Eq. (33)
10.	Compute the constitutive matrix $\mathbf{D}(\boldsymbol{d}, \boldsymbol{\theta})$ using Eq. (2)
11.	Decide on changes on crack status $\mathcal{T} = \max_{i=1,3}\ (\mathcal{T}_i)$
12.	If crack status has changed, $\mathcal{T} \neq 0$, compute $\Delta\boldsymbol{\varepsilon}^i$ with Eq. (38)
13.	Rotate the secant matrix $\mathbf{D}$ and irreversible strains $\boldsymbol{\varepsilon}^i$ to the global axes
14.	Compute stress $\boldsymbol{\sigma} = \mathbf{D}\ \boldsymbol{\varepsilon}^e$ with Eq. (20)

7 Multi-crack model

Non-proportional loading may produce significant changes in the directions of the principal strains and this may cause multiple cracks in non-orthogonal directions. In cycling situations with pre-loading, these changes occur, inducing cyclic sliding and shearing in the existing cracks.

Fixed orthogonal damage models cannot contemplate the issue of non-orthogonal cracking locally. Rotating and isotropic damage models are even less apt, as they cannot detect so much as the swapping of the principal strain directions under load reversal that occurs under alternate pure shear loading. This concerned some classical multi-crack models [4, 5] and the micro-plane theory [6, 7].

The activation/deactivation scheme of tensile/compressive damage described in Section 5 allows the consideration of multi-cracks quite naturally. The proceedings are described in the following.

Let the secant constitutive Eq. (20) be

$$\boldsymbol{\sigma} = \mathbf{D}\left(\boldsymbol{d^I}, \boldsymbol{\theta^I}\right) \boldsymbol{\varepsilon}^e \tag{39}$$

where $\boldsymbol{d^I}$ is the set of damage parameters in the *active* material system $\boldsymbol{\theta^I}$. Note that only one set of material axes can be active at a given time.

Two questions need to be resolved to complete the multi-crack model:

1. The selection of the active material system $\boldsymbol{I}$,
2. The creation of a new material system.

Let $\boldsymbol{J = 1, N}$ be the number of standing material systems. For the selection of the active system $\boldsymbol{I}$, the step functions $[H_1^+]^J$ are evaluated. The active system $\boldsymbol{I}$ is the one such that

$$[H_1^+ d_1^+]^I = \max_J \; [H_1^+ d_1^+]^J \tag{40}$$

Systems are discarded if $[H_1^+]^J = 0$ because the corresponding crack is “closed”.

A new material system $\boldsymbol{\theta^{N+1}}$ may be considered if: (a) none of the existing ones is active, and (b) the maximum number of systems allowed is not reached. In this case, the new material system $\boldsymbol{\theta^{N+1}}$, coincides with the current principal directions of effective stress. The new system is locked once it becomes active because damage occurs in it.

In the proposed model the choice of the active crack system depends on tensile damage. If only compressive damage develops because of crushing, according to the criterion in Eq. (40), the activation of a second system does not take place. In such case, in the only existing system compressive damage is active if $H_i^- = 1$; otherwise elastic stiffness is recovered.

For the isotropic version of the multi-crack model, the procedure is analogous, the active system $\boldsymbol{I}$ is $[H^+ d^+]^I = \max_J \; [H^+ d^+]^J$.

The algorithm for the orthotropic multi-crack model is given in Table 4.

Table 4. Algorithm for the orthotropic multi-crack model

1. Compute the effective stress $\overline{\boldsymbol{\sigma}}^{tr}$ with Eq. (25)
2. DO for each of the standing material systems $\boldsymbol{J} = \boldsymbol{1}, \boldsymbol{N}$
   Perform steps **2**. to **8**. From **Table 3**
   ENDDO
3. Select the active material system $\boldsymbol{\theta^I}$ according to criterion (40)
4. If no system is active, check for the creation of a new material system $\boldsymbol{\theta^{N+1}}$
5. Check if system $\boldsymbol{\theta^{N+1}}$ is active, steps **2**. To **8**. From Table 3
6. Compute the constitutive matrix $\mathbf{D}\left(\boldsymbol{d^I}, \boldsymbol{\theta^I}\right)$ using Eq. (2)
7. Rotate the secant matrix **D** and irreversible strains $\boldsymbol{\varepsilon}^i$ to the global axes
8. Compute stress $\boldsymbol{\sigma} = \mathbf{D}\,\boldsymbol{\varepsilon}^e$ with Eq. (20)

As an explanatory remark, note that for alternate shear cyclic loading with an initial pre-compression (or pre-tension) in 2D, two material systems $\boldsymbol{\theta^1}$ and $\boldsymbol{\theta^2}$ are required. Their relative angles depend on the pre-loading as this determines how much the directions of the principal strains swing from the 90º corresponding to the pure shear case. The $\boldsymbol{\theta^2}$ system is activated by the alternate tension when system $\boldsymbol{\theta^1}$ is deactivated because axis x^1 is under compression.

8 Study of the model performance

The behavior of the proposed crack models is first assessed through several cyclic loading numerical tests. The performance of both the isotropic and the orthotropic models is examined. The Rankine criterion is adopted in all the cases. The material properties are shown in Table 5.

Young's Modulus	$1.5 \cdot 10^9$ Pa
Poisson's Ratio	0.0
Tensile Strength	$1.0 \cdot 10^6$ Pa
Tensile Fracture Energy	250 J/m^2
Compressive Strength	$3.0 \cdot 10^6$ Pa
Compressive Fracture Energy	500 J/m^2
γ_0^+ parameter	1.0
γ_0^- parameter	0.5
γ_p^+ parameter	1.0
γ_p^- parameter	1.5
β parameter for Irreversible Strains	0.0/0.2

Table 5. Material parameters of the tests

In the tests, the loading is applied via strain increments. Firstly, a vertical pre-tensile or pre-compressive strain is applied; secondly, four different cycles of shear loading with increasing amplitude are executed. For comparison purposes, the test is performed under three different values of initial vertical strain, noted as ε_v:

(a) Pure shear, $\varepsilon_v = 0.0$
(b) Pre-tension, $\varepsilon_v = 2.5 \cdot 10^{-4}$
(c) Pre-compression, $\varepsilon_v = -7.5 \cdot 10^{-4}$

In all the tests, four consecutive cycles of shear that have an amplitude of $\gamma_{xy} = 5.0 \cdot 10^{-3}$, $\gamma_{xy} = 1.0 \cdot 10^{-2}$, $\gamma_{xy} = 1.5 \cdot 10^{-2}$ and $\gamma_{xy} = 2.0 \cdot 10^{-2}$, respectively, are imposed.

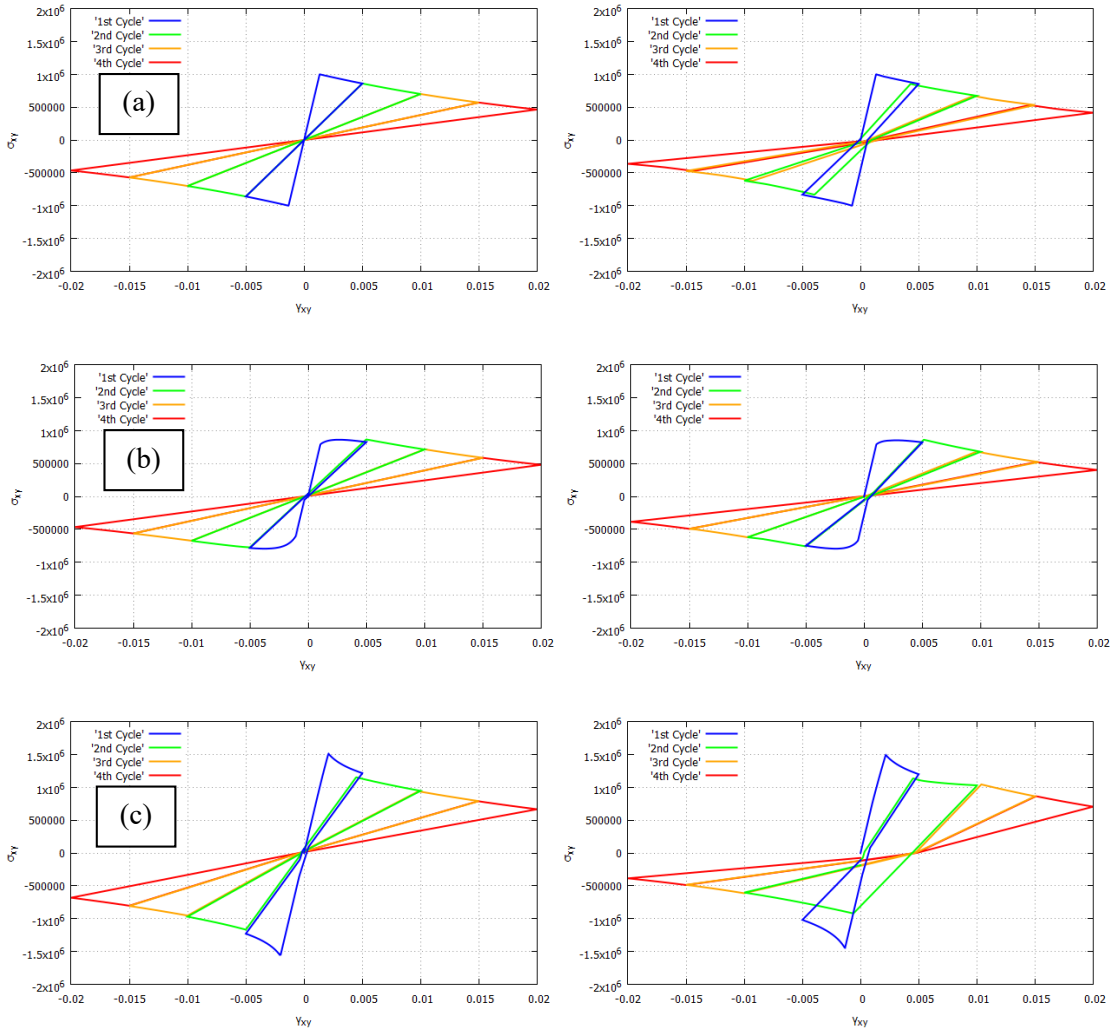

Figure 1. Stress (Pa) vs strain curves of the tests with (a) pure shear, (b) pre-tension and (c) pre-compression with the proposed isotropic model using β=0 (left) and β=0.2 (right)

The σ_{xy}-γ_{xy} curves obtained with the proposed *isotropic model* with each case are depicted in Figure 1 using a parameter for irreversible strains $\beta = 0.0$ (left) and $\beta = 0.2$ (right).

In all cases the stiffness is recovered properly during the cyclic process. Damage develops also when the load is reversed due to consideration in the model of multi-cracks as described in Section 7. For cases (a), proportional loading, pure shear, the principal strains swap directions, and the two cracks formed are orthogonal to each other. However, for cases (b), non-proportional loading, pre-tension, 2 crack systems are necessary, forming angles of 76.91º and 78.12º for $\beta = 0.0, 0.2,$ respectively; for cases (c), non-proportional loading, pre-compression, the 2 systems form angles of 61.36º and 62.77º for $\beta = 0.0, 0.2,$ respectively. Note that these values differ sensibly from what can be accomplished with a single orthogonal system.

The effect of the non-proportional pre-straining is clear comparing the three cases in the two columns. When pre-tension is applied, the peak shear stress is smaller than in pure shear; the opposite occurs with pre-compression. The first cycle of straining is most affected by the pre-load, but differences can be observed for all cycles. For $\beta = 0.2$, the differences between the three cases are very obvious, because the very asymmetric effect of the compressive irreversible strains is reduced in case (b) and enhanced in case (c).

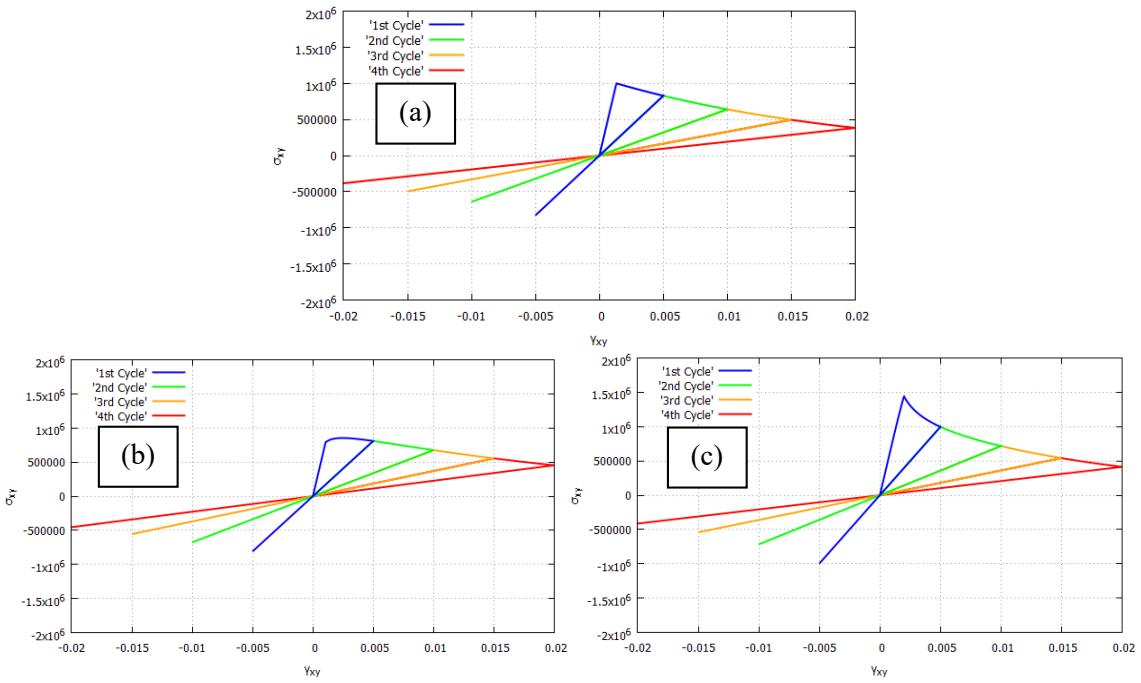

Figure 2. Stress (Pa) vs strain curves of the tests with (a) pure shear, (b) pre-tension and (c) pre-compression with a classical isotropic model

"Sealing" irreversible strains are considered according to the specifications of Section 6, even for the case $\beta = 0$, to guarantee the continuity of the stresses when cracks open and close.

Results can also be compared with the ones shown in Figure 2, where a standard (memoryless) isotropic model is used, which cannot reproduce either stiffness recovery or multi-cracking because it has no memory of the directions in which damage originated.

The σ_{xy}-γ_{xy} curves obtained with the proposed *orthotropic model* with each loading case are depicted in Figure 3 using a parameter for irreversible strains $\beta = 0.0$ (left) and $\beta = 0.2$ (right). Proper stiffness recovery takes place when cyclic loading is applied. For all cases, the two material systems form the same in-between angles as for the isotropic model, (a) 90º, (b) 76.91º and 78.12º, (c) 61.39º and 62.77º for $\beta = 0.0, 0.2$, respectively, as these values depend on the effective stresses and, therefore, on the applied straining. The departure from the 90º of a single material system is significant.

The effects of the pre-tension are opposite to those of the pre-compression, even more seemingly than for the isotropic model, and further evidenced by the asymmetry of the compressive irreversible strains.

Continuity of stresses is enforced at all times; the influence of the sealing strains is most noticeable in the first cycle. See that sealing strains of case (b) in Figure 3 are nearly canceled out by the irreversible strains.

In Figure 4 results corresponding to a classical rotating model are shown; there is no stiffness recovery, because the model has no record of the directions in which damage originated. Consequently, only a minor difference among the three cases is observable.

Figure 5 shows the resulting σ_{xy}-γ_{xy} curves in the pre-compression case when the sealing irreversible strains, detailed in Section 6, guaranteeing the continuity of the stresses are not considered. It is shown that in this situation the continuity of the stresses is lost when cracks open

or close and the stiffness changes accordingly. These results must be compared to the ones in Figure 1c and Figure 3c, where the stress continuity is enforced.

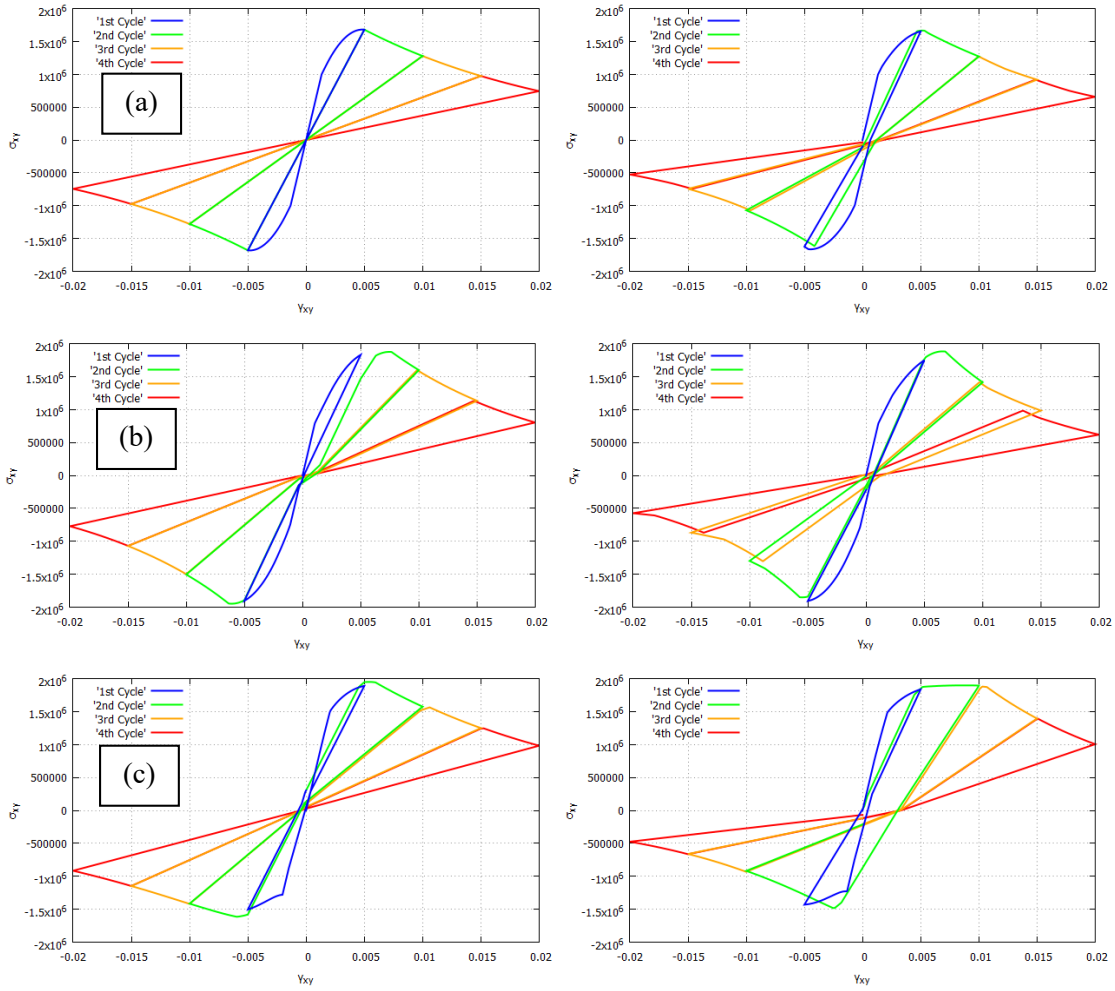

Figure 3. Stress (Pa) vs strain curves of the tests with (a) pure shear, (b) pre-tension and (c) pre-compression with the proposed orthotropic model using β=0 (left) and β=0.2 (right)

It is also important to note the comparative performance of the isotropic and orthotropic versions of the model, that is, Figure 1 vs Figure 3. The isotropic model is insensitive to the compressive strength, and damage is only due to the tensile stress that acts in one or the other direction, according to the alternate sign of the applied shear strain. Contrariwise, the orthotropic model responds simultaneously to the principal stresses (tensile and compressive) acting in at the same time. The response under shear of the orthotropic model is a blending of the behavior under pure tension and pure compression, both in terms of strength and dissipation.

The effect that the pre-tension and pre-compression have on the peak value of the stress in both models is as follows. On the one hand, for the isotropic model, for cases (a), in pure shear loading, the peak value of the σ_{xy} is 1 MPa, which is equal to the tensile strength of the material. However, for cases (b), in pre-tension, the peak value attained is lower than the tensile strength, while for cases (c), under pre-compression, the peak load is noticeably increased. On the other hand, in the orthotropic damage model, the effect of the pre-tension and the pre-compression on the alternate stress peak loads is asymmetrical.

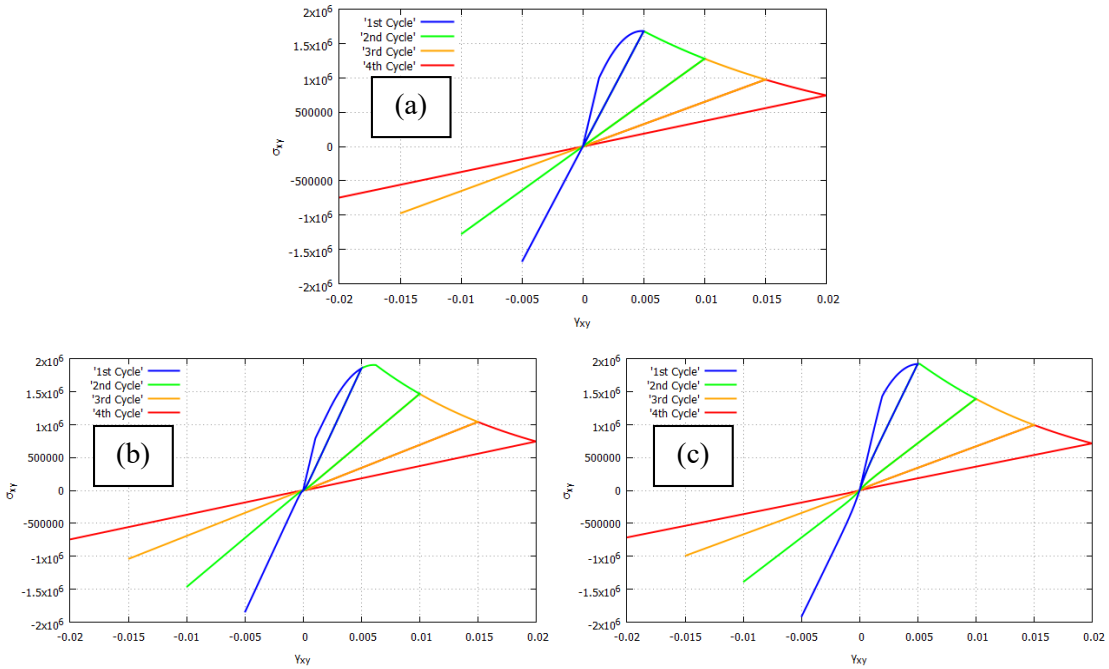

Figure 4. Stress (Pa) vs strain curves of the tests with (a) no pre-compression, (b) low pre-compression and (c) high pre-compression with a classical rotating model

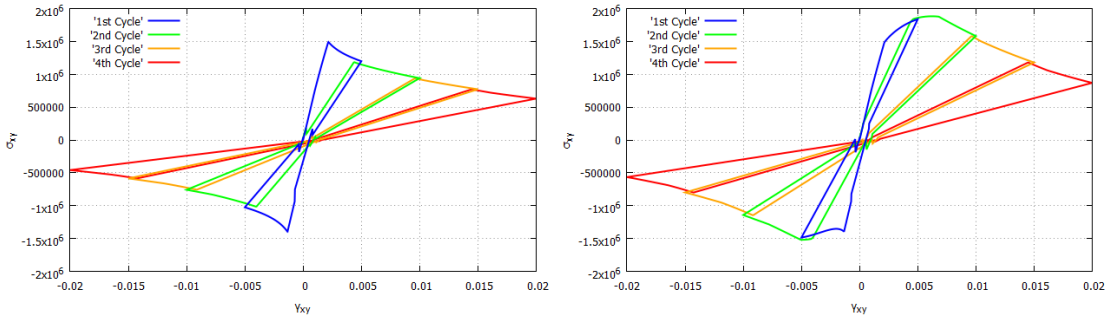

Figure 5. Stress (Pa) vs strain curves of the tests with pre-compression in the isotropic and orthotropic fixed models without irreversible strains of Section 6 guaranteeing stress continuity (β=0.2)

9 Mixed FE formulation

A mixed ε/u formulation is used to solve the problem with enhanced strain and stress accuracy and guarantee mesh-objective results. This formulation also helps avoiding the spurious stress oscillations which typically appear in orthotropic models when the standard formulation is used and that usually lead to severe stress locking [12]. In this section, the adopted mixed finite element formulation used to solve the problem is briefly introduced. The mixed FE formulation is described in reference [11]. For additional details on the formulation, references [8-10, 12, 25] are appropriate.

The model follows the local continuum mechanics framework. In the considered mixed FE formulation, the variational form of the nonlinear solid mechanics problem is computed in terms of the displacement $\boldsymbol{u}$ and the strain $\boldsymbol{\varepsilon}$ fields. Matrix and vector notation based on Voigt's

convention for symmetric tensors is adopted, as customarily used in FE literature and in most FE codes [19].

The compatibility equation links the strain and displacement fields

$$\boldsymbol{\varepsilon} = \mathbf{S}\,\boldsymbol{u} \tag{41}$$

where $\mathbf{S}$ is the differential symmetric gradient operator. Correspondingly, the stress vector $\boldsymbol{\sigma}$ and the body forces vector $\mathbf{f}$ are associated through Cauchy's equilibrium equation, written in matrix form as

$$\mathbf{S}^T\boldsymbol{\sigma} + \mathbf{f} = \mathbf{0} \tag{42}$$

where $\mathbf{S}^T$ is the differential divergence operator, adjoint to the $\mathbf{S}$ in Eq. (41). The constitutive equation relates the stress and strain vectors as

$$\boldsymbol{\sigma} = \mathbf{D}\left(\boldsymbol{\varepsilon} - \boldsymbol{\varepsilon}^i\right) \tag{43}$$

where $\mathbf{D}$ is the symmetric secant matrix.

A mixed system of equations is obtained pre-multiplying Eq. (41) by the secant matrix $\mathbf{D}$ and substituting Eq. (43) into Eq. (42)

$$-\mathbf{D}\boldsymbol{\varepsilon} + \mathbf{D}\mathbf{S}\boldsymbol{u} = \mathbf{0} \tag{44}$$

$$\mathbf{S}^T\left(\mathbf{D}\boldsymbol{\varepsilon} - \mathbf{D}\boldsymbol{\varepsilon}^i\right) + \mathbf{f} = \mathbf{0} \tag{45}$$

The strong form of the mixed $\boldsymbol{\varepsilon}/\boldsymbol{u}$ formulation is defined by the system of Eqs. (44)-(45) and the proper boundary conditions. Note that this differential problem is symmetric if $\mathbf{D}$ is symmetric.

The corresponding weak form is obtained by multiplying Eqs. (44) and (45) by the virtual strain $\delta\boldsymbol{\varepsilon}$ and displacement vector $\delta\boldsymbol{u}$ respectively. The system is then integrated over the spatial domain and the Divergence Theorem is used in the right hand side of the second integral operation. The following variational form results:

$$-\int_\Omega \delta\boldsymbol{\varepsilon}^T\mathbf{D}\boldsymbol{\varepsilon}\,\mathrm{d}\Omega + \int_\Omega \delta\boldsymbol{\varepsilon}^T\mathbf{D}\mathbf{S}\boldsymbol{u}\,\mathrm{d}\Omega = 0 \quad \forall\delta\boldsymbol{\varepsilon} \tag{46}$$

$$\int_\Omega (\mathbf{S}\delta\boldsymbol{u})^T(\mathbf{D}\boldsymbol{\varepsilon})\,\mathrm{d}\Omega = \int_\Omega \delta\boldsymbol{u}^T\mathbf{f}\,\mathrm{d}\Omega + \int_{\Gamma_t} \delta\boldsymbol{u}^T\bar{\boldsymbol{t}}\,\mathrm{d}\Gamma + \int_\Omega (\mathbf{S}\delta\boldsymbol{u})^T\left(\mathbf{D}\boldsymbol{\varepsilon}^i\right)\mathrm{d}\Omega \quad \forall\delta\boldsymbol{u} \tag{47}$$

The last term in the right hand side of Eq. (47) includes the effect of the irreversible strains in the equilibrium equation.

The mixed problem to be solved is to find the unknowns $\boldsymbol{u}$ and $\boldsymbol{\varepsilon}$ that verify the system of Eqs. (46) and (47) and that verify the boundary condition $\boldsymbol{u} = \mathbf{0}$ on Γ_u, for the arbitrary virtual displacements $\delta\boldsymbol{u}$, which vanish on Γ_u, and arbitrary virtual strains $\delta\boldsymbol{\varepsilon}$. Note that this variational problem is symmetric if $\mathbf{D}$ is symmetric.

The FE discrete form of the mixed problem is obtained by discretizing the domain in FE, so that $\Omega = \cup\,\Omega_e$, and substituting the displacement $\boldsymbol{u}$ and the strain $\boldsymbol{\varepsilon}$ with the FE discrete approximations $\widehat{\boldsymbol{u}}$ and $\hat{\boldsymbol{\varepsilon}}$ defined element-wise as

$$\boldsymbol{u} \cong \widehat{\boldsymbol{u}} = \boldsymbol{N}_u\boldsymbol{U} \tag{48}$$

$$\boldsymbol{\varepsilon} \cong \hat{\boldsymbol{\varepsilon}} = \boldsymbol{N}_\varepsilon\boldsymbol{E} \tag{49}$$

where $\boldsymbol{U}$ and $\boldsymbol{E}$ are vectors containing the values of the displacements and the strains at the nodes of the finite element mesh. $\boldsymbol{N}_u$ and $\boldsymbol{N}_\varepsilon$ are the matrices containing the interpolation functions adopted in the FE approximation.

The Inf-Sup condition is not verified if equal interpolation functions $\boldsymbol{N}_u$ and $\boldsymbol{N}_\varepsilon$ are used in Eqs. (48)-(49). In that case, the solvability, uniqueness and stability of the solution of the system of equations are ensured by using a stabilization procedure to provide the necessary stability to the mixed discrete formulation. The stabilization procedure consists in the modification of the discrete variational form using the Orthogonal Subscales Method, introduced within the framework of the Variational Multiscale Stabilization methods and adopted herein.

The stabilization procedure is simply to substitute the approximation of the discrete strain in Eq. (49) by the following stabilized discrete field

$$\boldsymbol{\varepsilon} \cong \hat{\boldsymbol{\varepsilon}} = \boldsymbol{N}_\varepsilon \boldsymbol{E} + \tau_\varepsilon(\boldsymbol{B}_u \boldsymbol{U} - \boldsymbol{N}_\varepsilon \boldsymbol{E}) = (1-\tau_\varepsilon)\boldsymbol{N}_\varepsilon \boldsymbol{E} + \tau_\varepsilon \boldsymbol{B}_u \boldsymbol{U} \tag{50}$$

where τ_ε is a stabilization parameter with value $0 \leq \tau_\varepsilon \leq 1$. Note that for $\tau_\varepsilon = 1$, the strain interpolation of the standard irreducible formulation is recovered:

$$\boldsymbol{\varepsilon} \cong \hat{\boldsymbol{\varepsilon}} = \boldsymbol{B}_u \boldsymbol{U} \tag{51}$$

where $\boldsymbol{B}_u$ is the discrete strain-displacement matrix defined as $\boldsymbol{B}_u = \boldsymbol{S}\boldsymbol{N}_u$

The resulting algebraic system of equations reads:

$$\begin{bmatrix} -\boldsymbol{M}_{\boldsymbol{\tau}} & \boldsymbol{G}_{\boldsymbol{\tau}} \\ \boldsymbol{G}_{\boldsymbol{\tau}}^T & \boldsymbol{K}_{\boldsymbol{\tau}} \end{bmatrix} \begin{bmatrix} \boldsymbol{E} \\ \boldsymbol{U} \end{bmatrix} = \begin{bmatrix} \boldsymbol{0} \\ \boldsymbol{F} \end{bmatrix} \tag{52}$$

where $[\boldsymbol{E} \quad \boldsymbol{U}]^T$ is the array of nodal values of strains and displacements, and $\boldsymbol{M}_{\boldsymbol{\tau}} = (1-\tau_\varepsilon)\boldsymbol{M}$, $\boldsymbol{G}_{\boldsymbol{\tau}} = (1-\tau_\varepsilon)\boldsymbol{G}$ and $\boldsymbol{K}_{\boldsymbol{\tau}} = \tau_\varepsilon \boldsymbol{K}$. $\boldsymbol{M}$ is a mass like projection matrix, $\boldsymbol{G}$ is the discrete gradient matrix, $\boldsymbol{K}$ is a stiffness like matrix and $\boldsymbol{F}$ is the vector of external nodal forces.

$$\boldsymbol{M} = \int_\Omega \boldsymbol{N}_\varepsilon^T \mathbf{D} \boldsymbol{N}_\varepsilon \, \mathrm{d}\Omega \tag{53}$$

$$\boldsymbol{G} = \int_\Omega \boldsymbol{N}_\varepsilon^T \mathbf{D} \boldsymbol{B}_u \, \mathrm{d}\Omega \tag{54}$$

$$\boldsymbol{K} = \int_\Omega \boldsymbol{B}_u^T \mathbf{D} \boldsymbol{B}_u \, \mathrm{d}\Omega \tag{55}$$

$$\boldsymbol{F} = \int_\Omega \boldsymbol{N}_u^T \mathbf{f} \, \mathrm{d}\Omega + \int_{\Gamma_t} \boldsymbol{N}_u^T \bar{\boldsymbol{t}} \, \mathrm{d}\Gamma + \int_\Omega \boldsymbol{B}_u^T \mathbf{D} \boldsymbol{\varepsilon}^i \, \mathrm{d}\Omega \tag{56}$$

In all the simulations shown in Sections 10 and 11, a stabilization parameter $\tau_\varepsilon = 0.1$ is used. Calculations are performed with an enhanced version of the finite element program COMET [26]. Pre- and post-processing are done with GID [27], developed at CIMNE (International Center for Numerical Methods in Engineering). Convergence of a load step increment is reached when the ratio between the norm of residual forces and the norm of the total external forces is lower than 10^{-3} %.

10 Concrete beam under cyclic loading

In this section, the numerical simulation of the test of a concrete beam under cyclic loading is presented. The beam was experimentally tested by [28], which also computed numerical simulations with their proposed constitutive model. Other numerical results are also reported in reference [29], where a non-local formulation is employed.

The objective of this example is to assess the performance of the proposed model with experimental evidence. The geometry of the beam is shown in Figure 6 and the material parameters are given in Table 6. The isotropic Drucker-Prager model is used. The thickness of the beam is 0.05 m. Loads are applied via increments of vertical displacements.

The example is solved under the plane stress hypothesis using two distinct 2D meshes: one of 1,998 quadrilateral elements of size h = 5 mm and a second one of 17,982 quadrilateral elements of size h = 1.66 mm. Both meshes are shown in Figure 7.

For comparison purposes, the beam in [28] is tested under monotonic and cyclic loading. For this reason, the simulations completed under cyclic loading are also compared with results obtained under a monotonically increasing load.

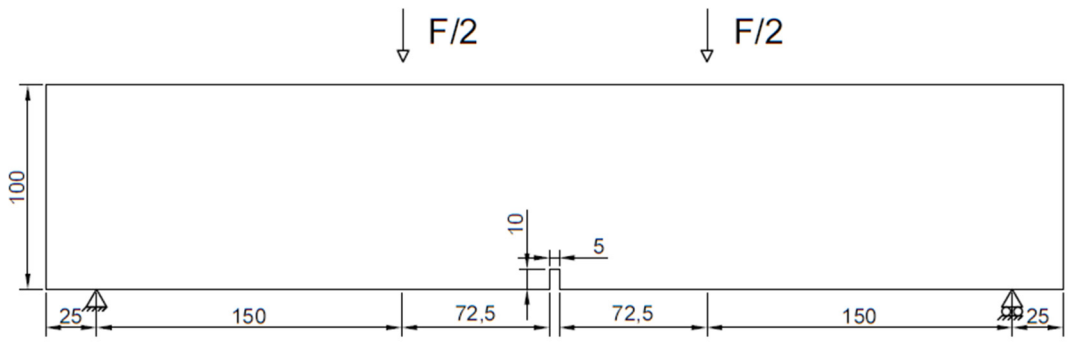

Figure 6. Geometry of the concrete beam under cyclic loading (mm)

Young's Modulus	$44.0 \cdot 10^9$ Pa
Poisson's Ratio	0.2
Tensile Strength	$2.35 \cdot 10^6$ Pa
Tensile Fracture Energy	85 J/m^2
Compressive Strength	$2.35 \cdot 10^7$ Pa
Compressive Fracture Energy	12000 J/m^2
$\gamma_0^{\pm}$ parameter	1.0
$\gamma_p^{\pm}$ parameter	1.0
β parameter for Irreversible Strains	0.7

Table 6. Material parameters of the concrete beam under cyclic loading

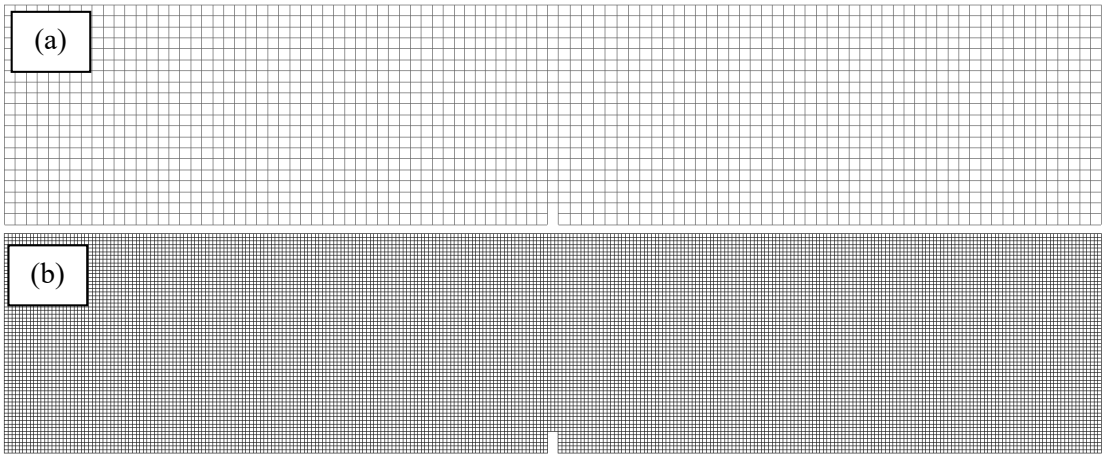

Figure 7. Meshes used for the concrete beam under cyclic loading, (a) h = 5 mm and (b) h = 1.66 mm

Figure 8 shows the maximum principal strain map of the computed beams under monotonic loading at the end of the simulation, for an imposed vertical displacement at the midpoint of $\delta = 0.7\ mm$ for both meshes used.

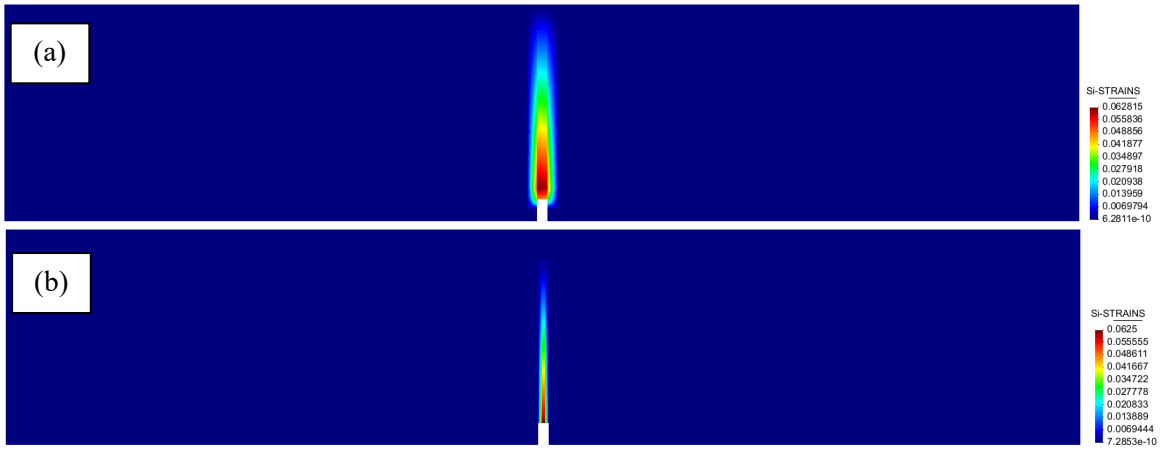

Figure 8. Maximum principal strain field for (a) h = 5mm and (b) h = 1.66 mm, for an imposed vertical displacement of δ = 0.7 mm, in the concrete beam under cyclic loading

Figure 9 shows the force-displacement curves obtained with both meshes. The computed results performed with both meshes are practically overlapping and are very similar to the experimental curves of Reference [28]. For both meshes, the results of the monotonic and the envelope of the cyclic simulations are overlapping.

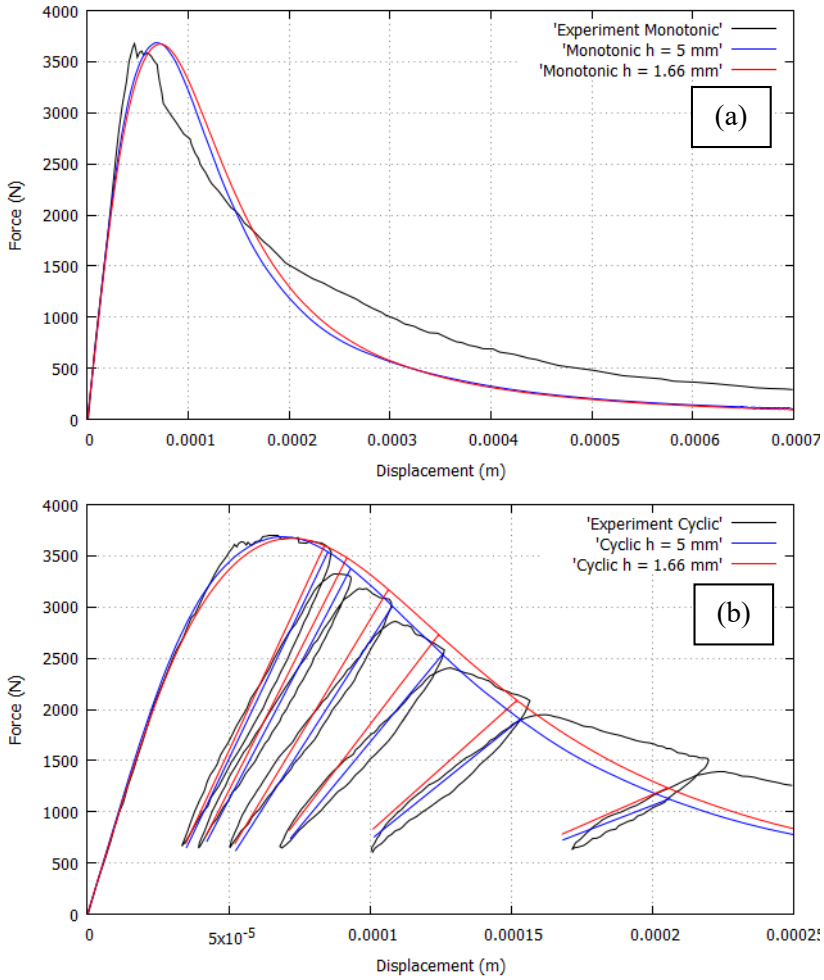

Figure 9. Converge analysis of the (a) monotonic and (b) cyclic simulations of the concrete beam under cyclic loading

11 Cubic metal specimen under shear cyclic loading

In this section the numerical simulation of a cubic metal specimen subjected to shear cyclic loading is considered. The objective is to assess the performance of the isotropic and orthotropic proposed models under shear cyclic conditions. For comparison, computations are done with the Rankine and Drucker Prager failure criteria and several different shear loading situations are considered.

The geometry and boundary conditions are shown in Figure 10. A cube metal of size 1 *mm* x 1 *mm* x 1 *mm* is subjected to monotonic and cyclic shear loading while different levels of pre-compression are applied. A small horizontal slit of 0.1 *mm* has been introduced in the center of the cube to fix the occurrence of fracture. The material properties are given in Table 7.

In the tests, the loading is applied via strain increments. Firstly, a pre-compressive strain is applied; secondly, several different cycles of shear loading with increasing amplitude are executed. For comparison purposes, the test is performed under different values of initial compressive strain.

The boundary conditions considered are the following. The base of the cube is fixed. The constant pre-compression is applied via a vertical displacement imposed at the top of the cube. The cyclic

shear load is applied through horizontal displacements also at the top. The vertical displacements of the lateral walls of the cube are prevented.

Many similar versions of this numerical benchmark have been reported for the testing of several crack models, mostly under monotonic conditions, e.g. in [30-32], where phase-field models are considered. In reference [33] a similar version of the test is used to assess the performance of a fatigue model developed also within the phase-field approach.

The example is solved assuming plane strain behavior and using a 2D structured mesh of 100 x 100 quadrilateral elements of size $h = 10^{-5}$ m.

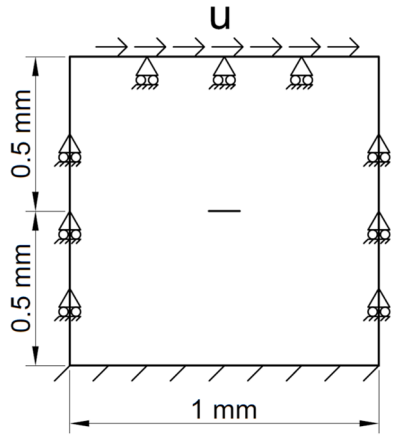

Figure 10. Geometry of the cubic metal specimen under shear cyclic loading

Young's Modulus	$21.0 \cdot 10^9$ Pa
Poisson's Ratio	0.3
Tensile Strength	10^9 Pa
Tensile Fracture Energy	30000 J/m^2
Compressive Strength	Various values are considered
Compressive Fracture Energy	30000 J/m^2
$\gamma_0^{\pm}$ parameter	1.0
$\gamma_p^{\pm}$ parameter	1.0
β parameter for Irreversible Strains	0.0/0.5

Table 7. Material parameters of the cubic metal specimen under shear cyclic loading

11.1 Isotropic Drucker Prager model with varying f_c/f_t ratio

The performance of the isotropic Drucker Prager model subjected to pure shear cyclic loading is addressed first. The simulation is done for varying ratios of compressive vs tensile strength. For this, the tensile strength is $f_t = 10^9$ Pa, while the ratio f_c/f_t = 1, 5, 8 and 100.

Figure 11 shows the computed crack trajectories for different ratios of compressive vs tensile strength under monotonic pure shear loading. It can be seen how for the case $f_c/f_t = 1$ the crack trajectory is a horizontal straight line, as is typical in metals for this type of loading and purely deviatoric behavior. For increasing values of f_c/f_t the crack turns and tends to a trajectory at an angle of 45º with respect the horizontal axis for the case $f_c/f_t = 1$, as would happen for cementitious materials.

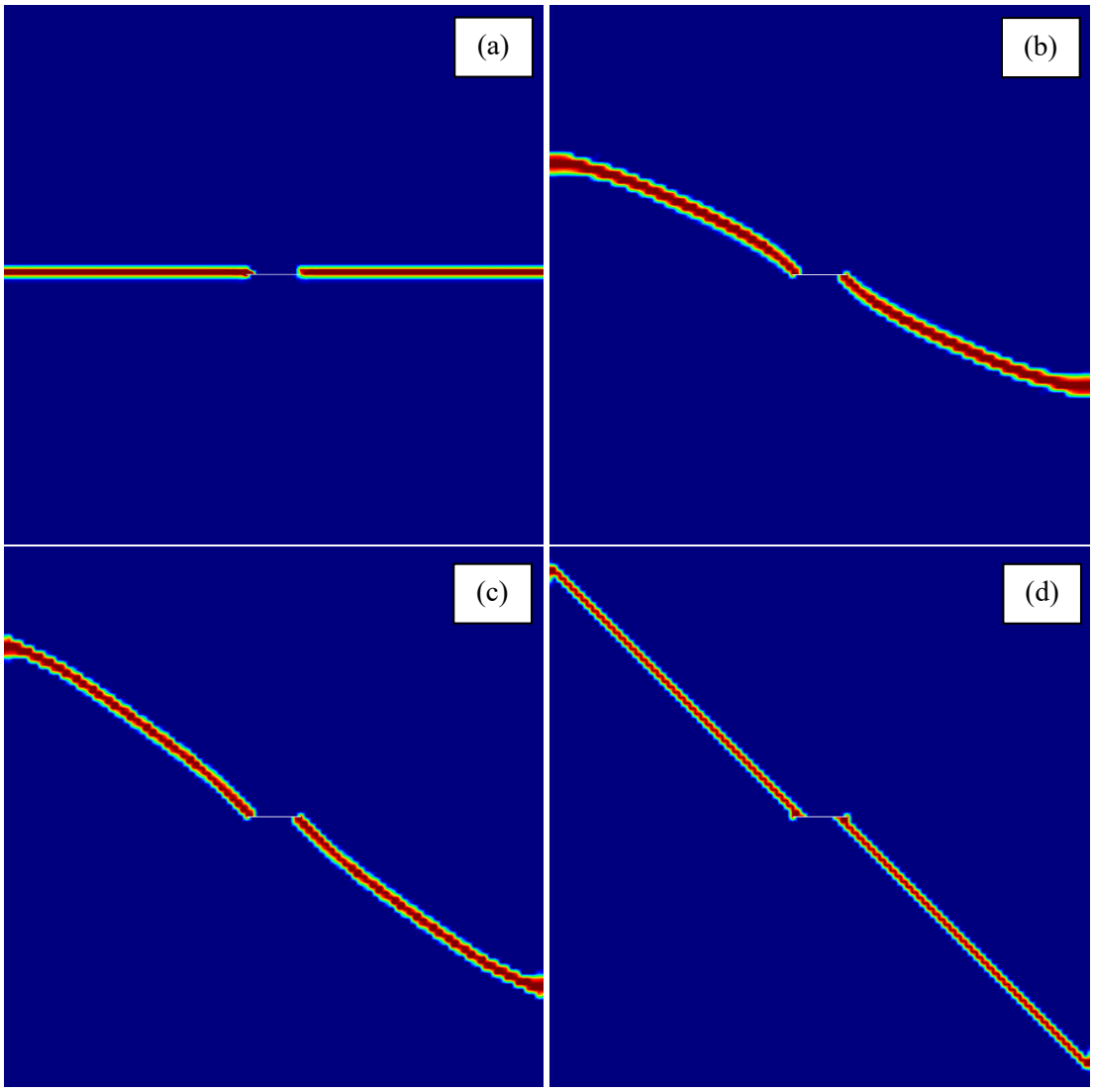

Figure 11. Isotropic Drucker Prager model damage contours for the cubic metal specimen under monotonic loading with (a) $f_c/f_t = 1$, (b) $f_c/f_t = 5$, (c) $f_c/f_t = 8$ and (d) $f_c/f_t = 100$

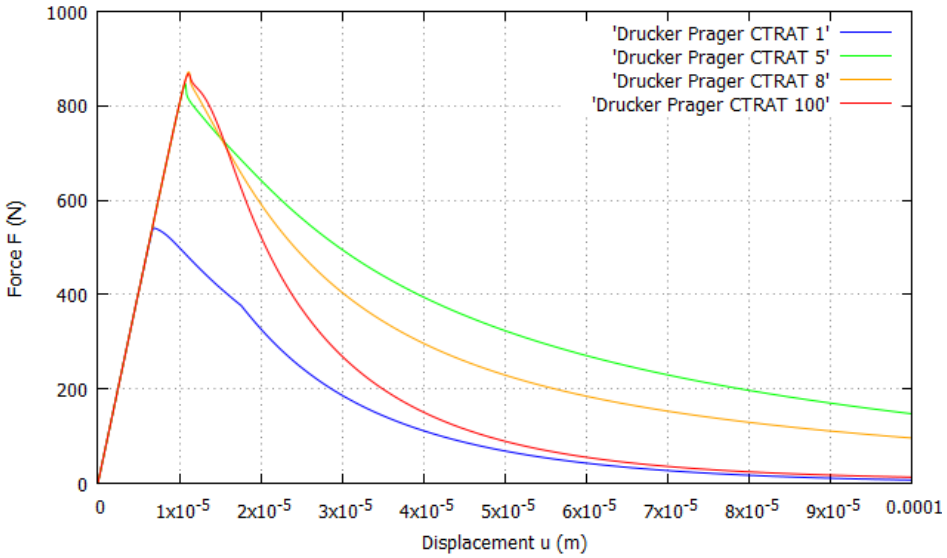

Figure 12. Isotropic Drucker-Prager model force-displacement curves for the different ratios of compressive vs tensile strength

It is to be noted that for the reciprocal ratios f_c/f_t = 1/5, 1/8 and 1/100, with the compressive strength smaller than the tensile one, the exact skew symmetric crack trajectories with respect the ones shown in Figure 11 develop.

In Figure 12 the force-displacement curves of the different situations are presented. It can be seen how the peak value of the force increases as the f_c/f_t ratio is increased, with the case $f_c/f_t = 1$ reaching a much lower peak value than the other cases. It can also be appreciated how the behavior of the material becomes more brittle as the f_c/f_t ratio increases.

Figure 13 shows the crack trajectories for different ratios of compressive vs tensile strength under monotonic (left) and cyclic (right) pure shear loading. It can be seen how the cracks under cyclic loading have central symmetry with respect the center of the sample and that cracks are nearly overlapping with the respective monotonic result. The observed differences in the trajectories between monotonic and cyclic results are of 1 element at the most, the resolution of the mesh.

In Figure 14 it can be seen how the force-displacement curves of the monotonic and cyclic simulations are overlapping in all the situations. It can also be seen how the stiffness is properly and completely recovered upon load reversal.

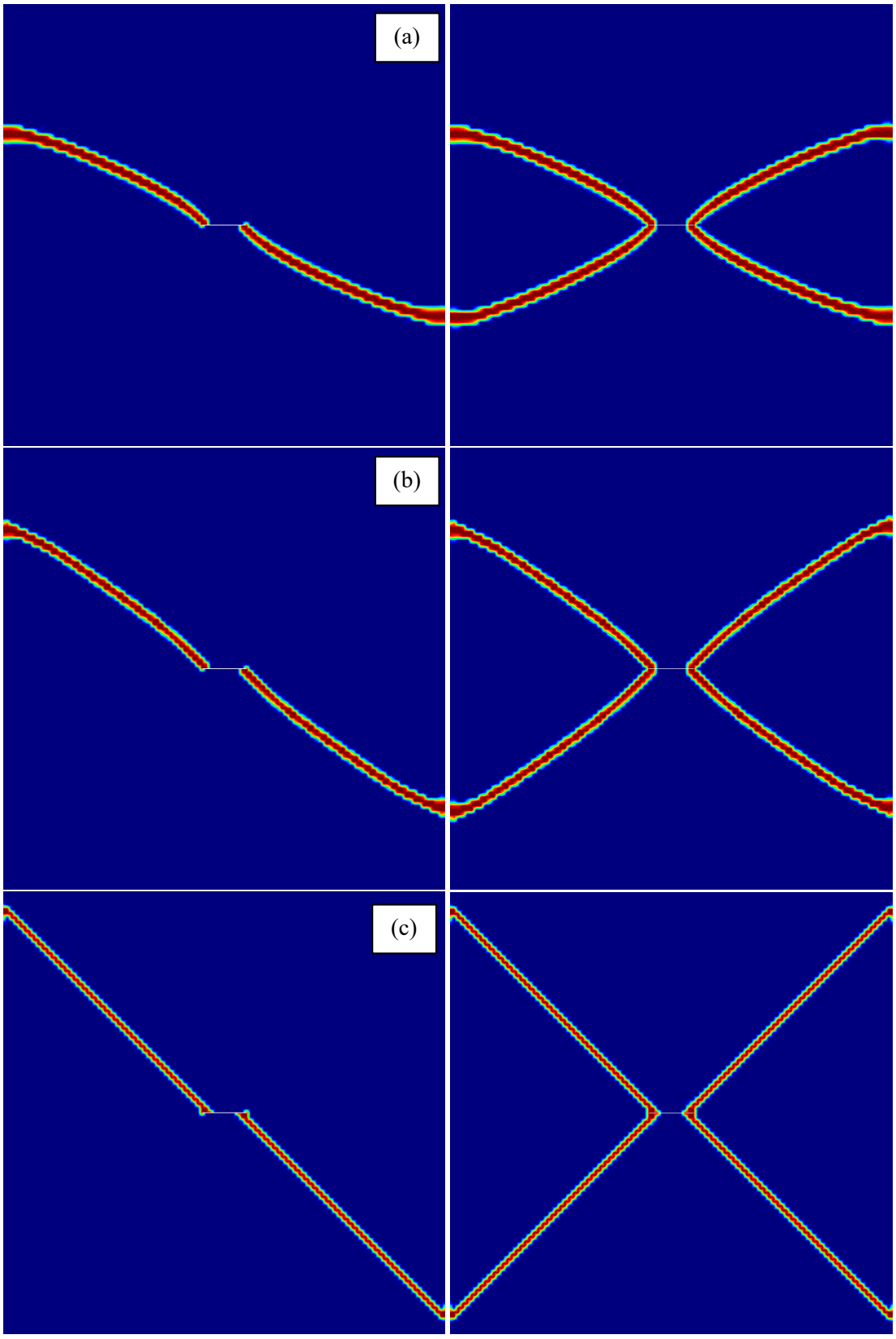

Figure 13. Isotropic Drucker-Prager model damage contours for the cubic metal specimen under monotonic (left) and cyclic (right) loading with (a) $f_c/f_t = 5$, (b) $f_c/f_t = 8$ and (c) $f_c/f_t = 100$

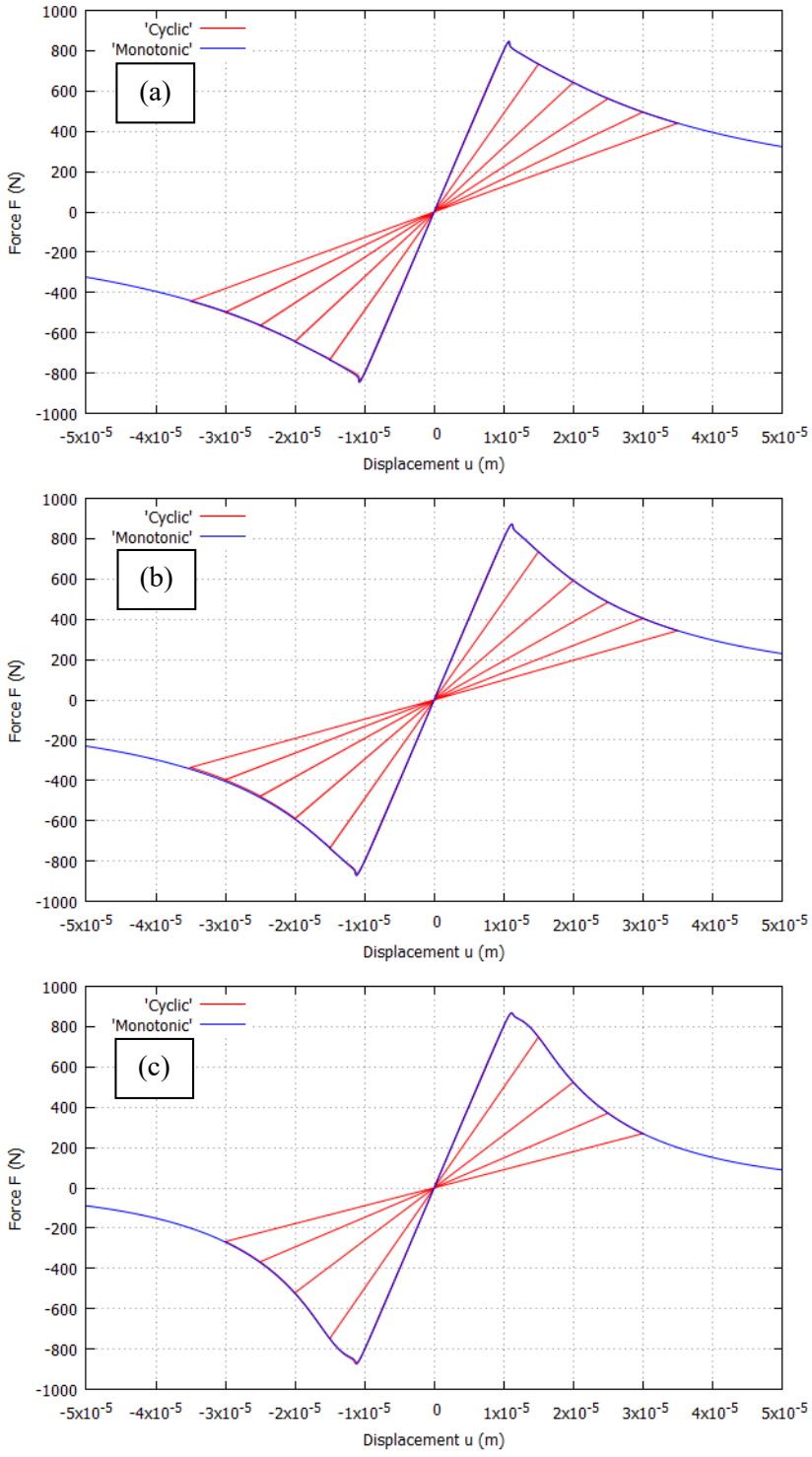

Figure 14. Isotropic Drucker Prager model force-displacement curves for the cubic metal specimen under monotonic and cyclic loading with (a) $f_c/f_t = 5$, (b) $f_c/f_t = 8$ and (c) $f_c/f_t = 100$

11.2 Isotropic vs Orthotropic Rankine model

The comparison of the isotropic and orthotropic Rankine models subjected to pure shear is now assessed. For the sake of clarity, $f_c/f_t = \infty$, and only tensile damage is considered. Figure 15 shows the crack trajectories for isotropic and orthotropic Rankine under monotonic (left) and cyclic (right) pure shear loading, demonstrating that crack trajectories are neatly different for isotropic and orthotropic damage. The force-displacement curves are depicted in Figure 16. It is remarkable that isotropic models may soften completely under shear loading, while orthotropic models fully retain their stiffness in the undamaged directions. Results are again overlapping in monotonic and cyclic loadings situations. The stiffness is properly recovered when cracks close and re-open.

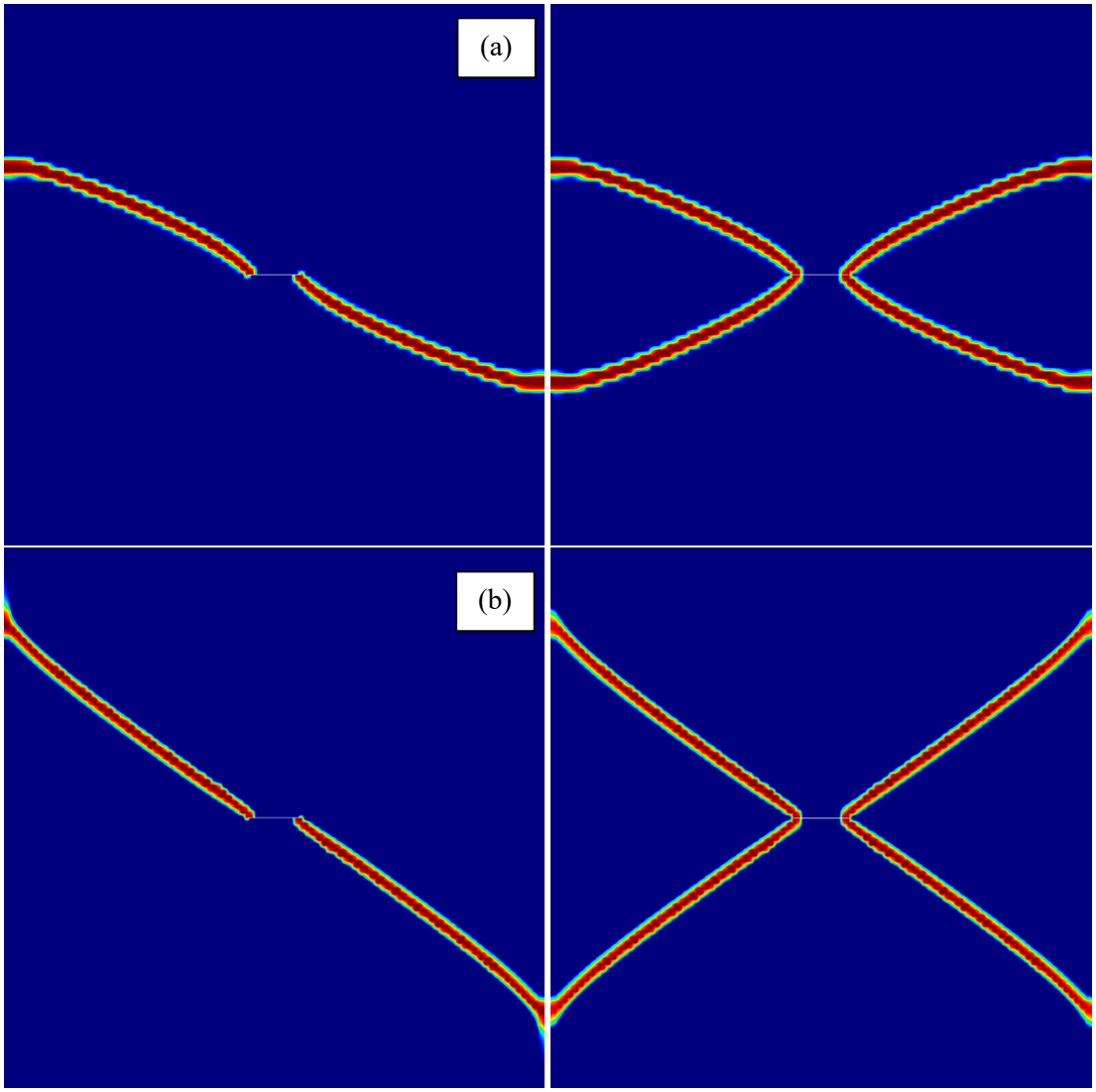

Figure 15. Rankine model damage contours of the (a) isotropic and (b) orthotropic version for the cubic metal specimen under monotonic (left) and cyclic (right) loading

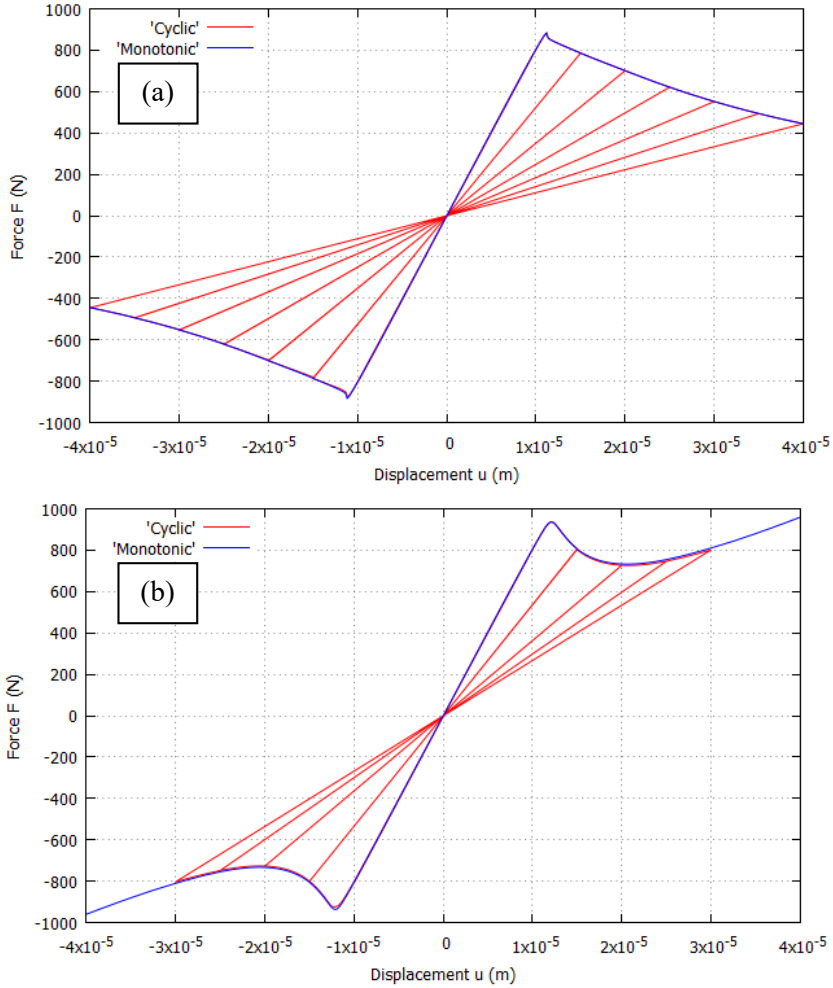

Figure 16. (a) Isotropic and (b) orthotropic Rankine model force-displacement curves for the cubic metal specimen under monotonic and cyclic loading

11.3 Effect of the pre-compression in the cyclic behavior

In this section, the performance of the model is assessed in situations in which the cubic metal specimen is first subjected to a level of pre-compression before the cycles of shear load of increasing amplitude are applied. The results obtained under three different values of pre-compressive strain, noted as ε_c, are compared:

- Pure shear cyclic loading test without compression, $\varepsilon_c = 0$
- Low compression, $\varepsilon_c = -2.0 \cdot 10^{-3}$
- High compression, $\varepsilon_c = -4.0 \cdot 10^{-3}$

The isotropic Rankine model is used, with $f_c/f_t = \infty$. Therefore, only tensile damage is considered.

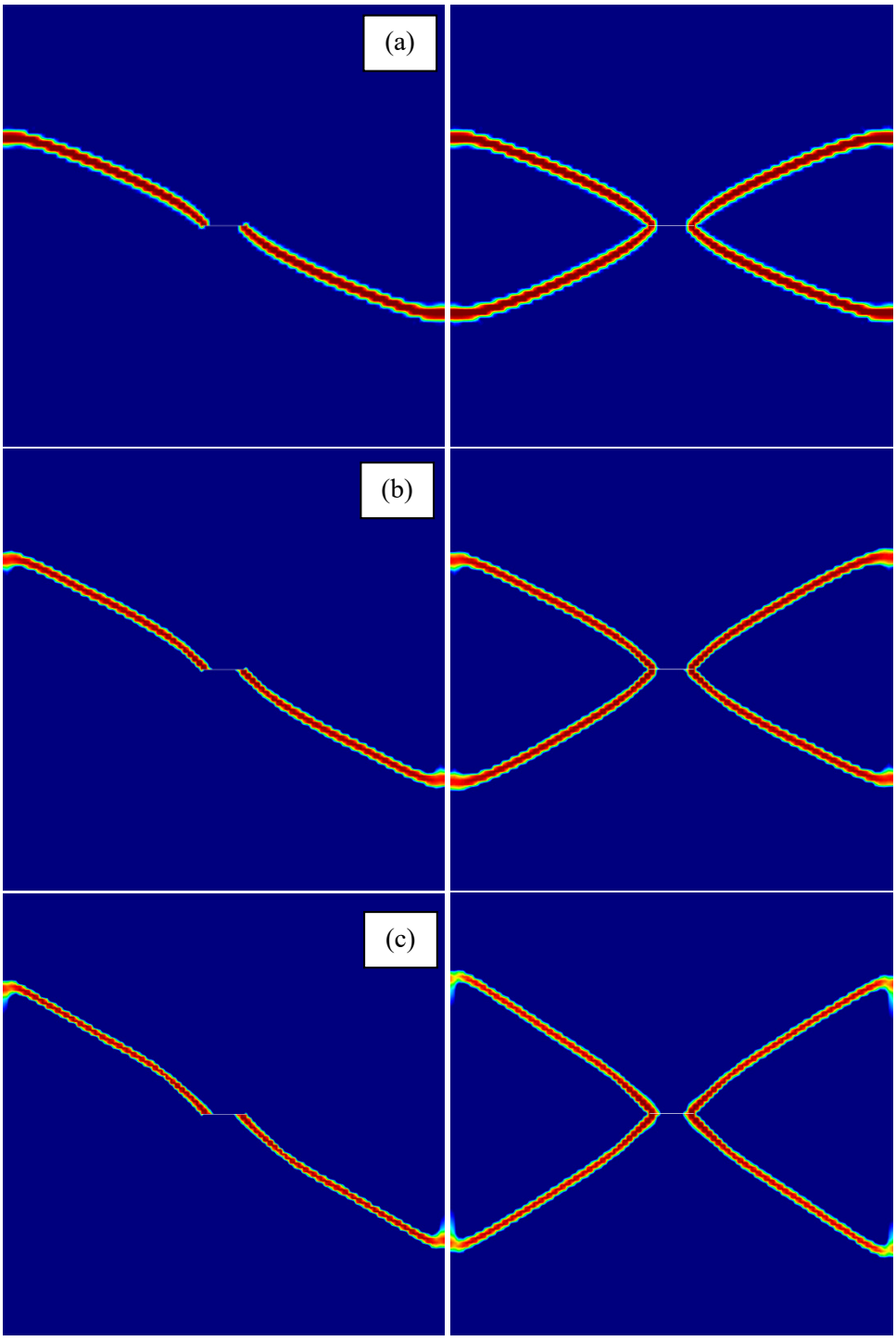

Figure 17. Isotropic Rankine model damage contours with (a) no compression, (b) low compression and (c) high compression for the cubic metal specimen under monotonic (left) and cyclic (right) loading

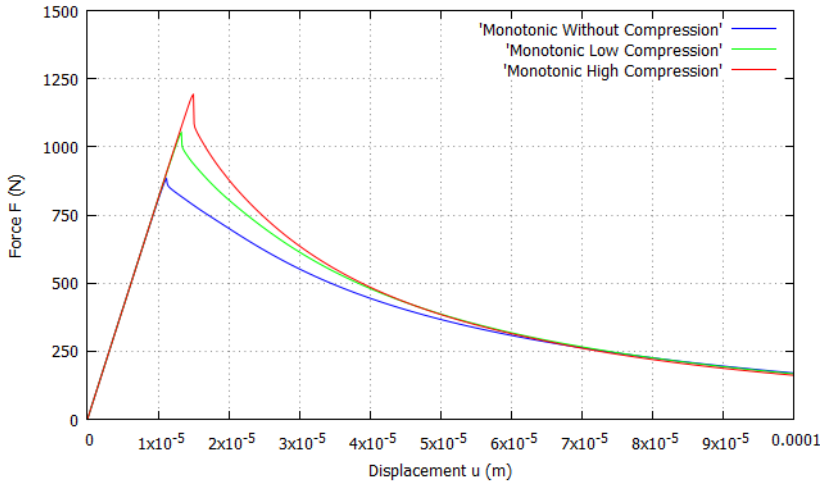

Figure 18. Isotropic Rankine model force-displacement curves with different pre-compression levels under monotonic loading in the cubic metal specimen

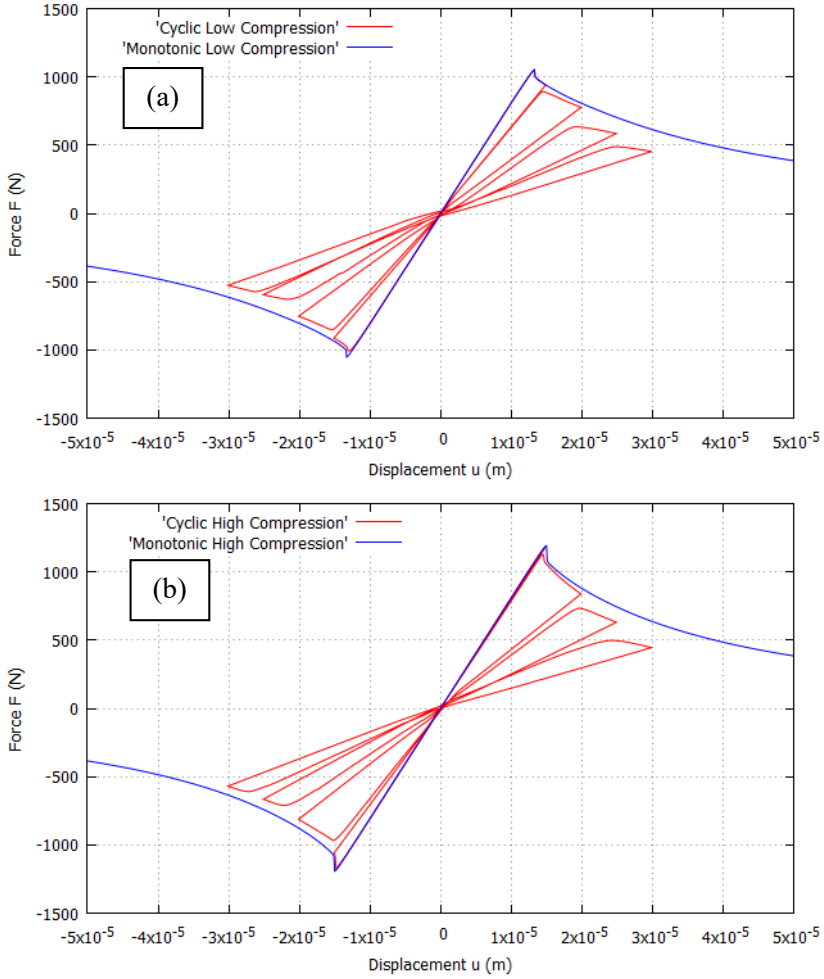

Figure 19. Isotropic Rankine model force-displacement curves for the cubic metal specimen under monotonic and cyclic loading in the (a) low compression and (b) high compression case

Figure 17 shows the crack trajectories obtained with different levels of pre-compression under monotonic (left) and cyclic (right) loading. It can be seen how the crack trajectories vary in function of the pre-compression applied to the cubic specimen. The in-between angle formed by the cracks increases with the pre-compression.

Figure 18 depicts the force-displacement curves under monotonic loading of the three cases considered. It can be seen how the peak load of the specimen increases when the pre-compression is increased.

In Figure 19, the monotonic and cyclic force-displacement curves are compared in the low and high pre-compression cases. It can be observed that stiffness is duly recovered when cracks close and reopen.

These results are to be compared with the curves of Figure 16a where no pre-compression is applied. It can be seen that the monotonic and cyclic curves no longer overlap when pre-compression is applied. This is caused by the development and accumulation of "sealing" strains when the cracks close or reopen. This causes a loss of symmetry in the force-displacement curves. The slight loss of symmetry caused by the "sealing" strains can also be observed in Figure 17 in the two cracks that develop in the body.

11.4 Effect of the irreversible strains

In this section, the effect of irreversible strains is included in the simulations. To this end, compressive damage is also considered in the isotropic Rankine model and a ratio $f_c/f_t = 3$ is used. The parameter $\beta = 0.5$ is used for irreversible strains. The same three loading cases with different pre-compression levels from the previous section are examined.

Figure 20 shows the crack trajectories obtained with different levels of pre-compression under monotonic (left) and cyclic (right) loading with the development of irreversible strains. The crack trajectories deviate in function of the level of pre-compression initially applied to the specimen. The results differ very slightly from those in Figure 17.

In Figure 21 the monotonic and cyclic force-displacement curves are depicted. It can be seen how in the cyclic results the development of irreversible strains under compression causes a noticeable loss of symmetry and the corresponding deviation with respect the monotonic computations.

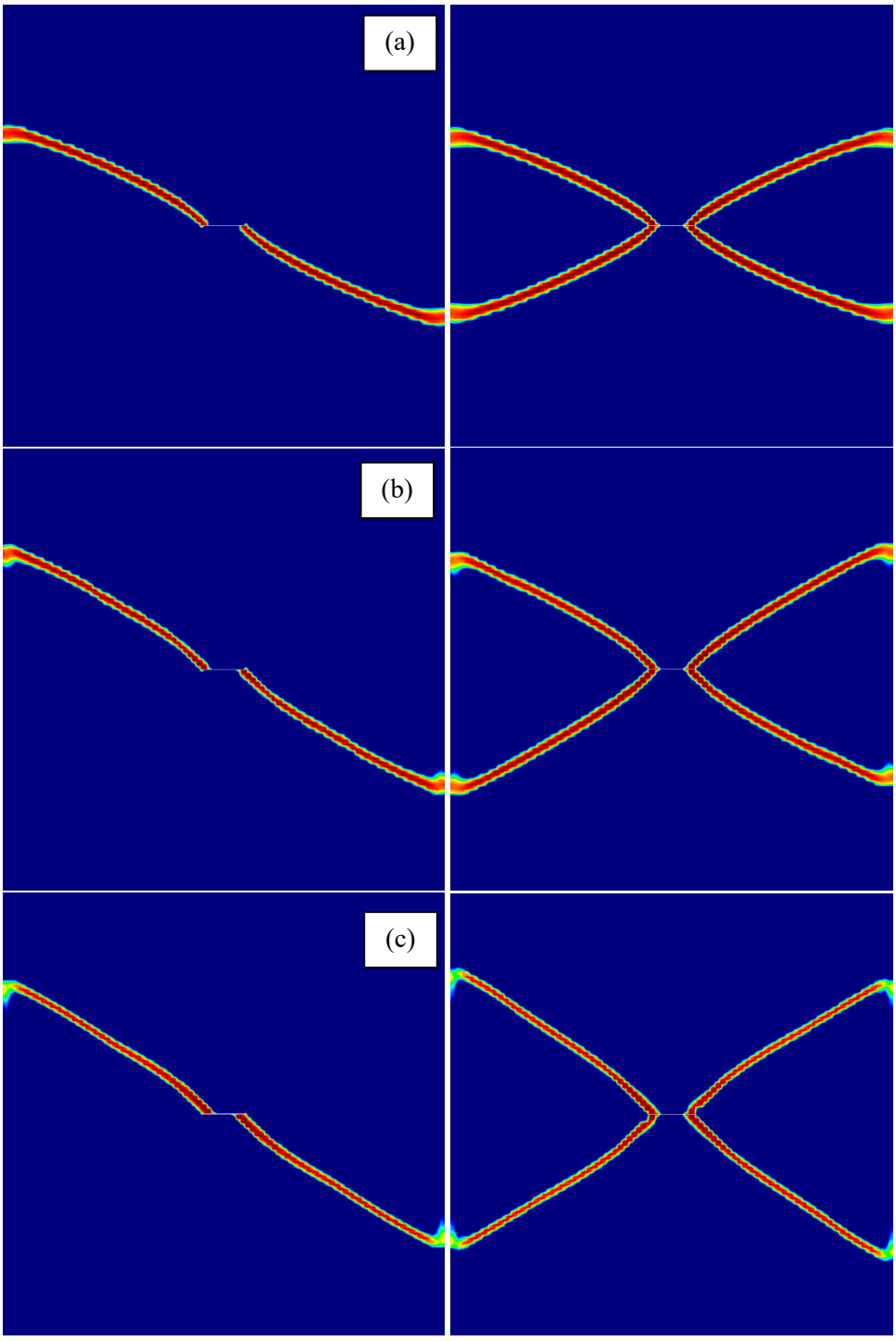

Figure 20. Isotropic Rankine model damage contours of the with irreversible strains (β=0.5) with (a) no compression, (b) low compression and (c) high compression for the cubic metal specimen under monotonic (left) and cyclic (right) loading

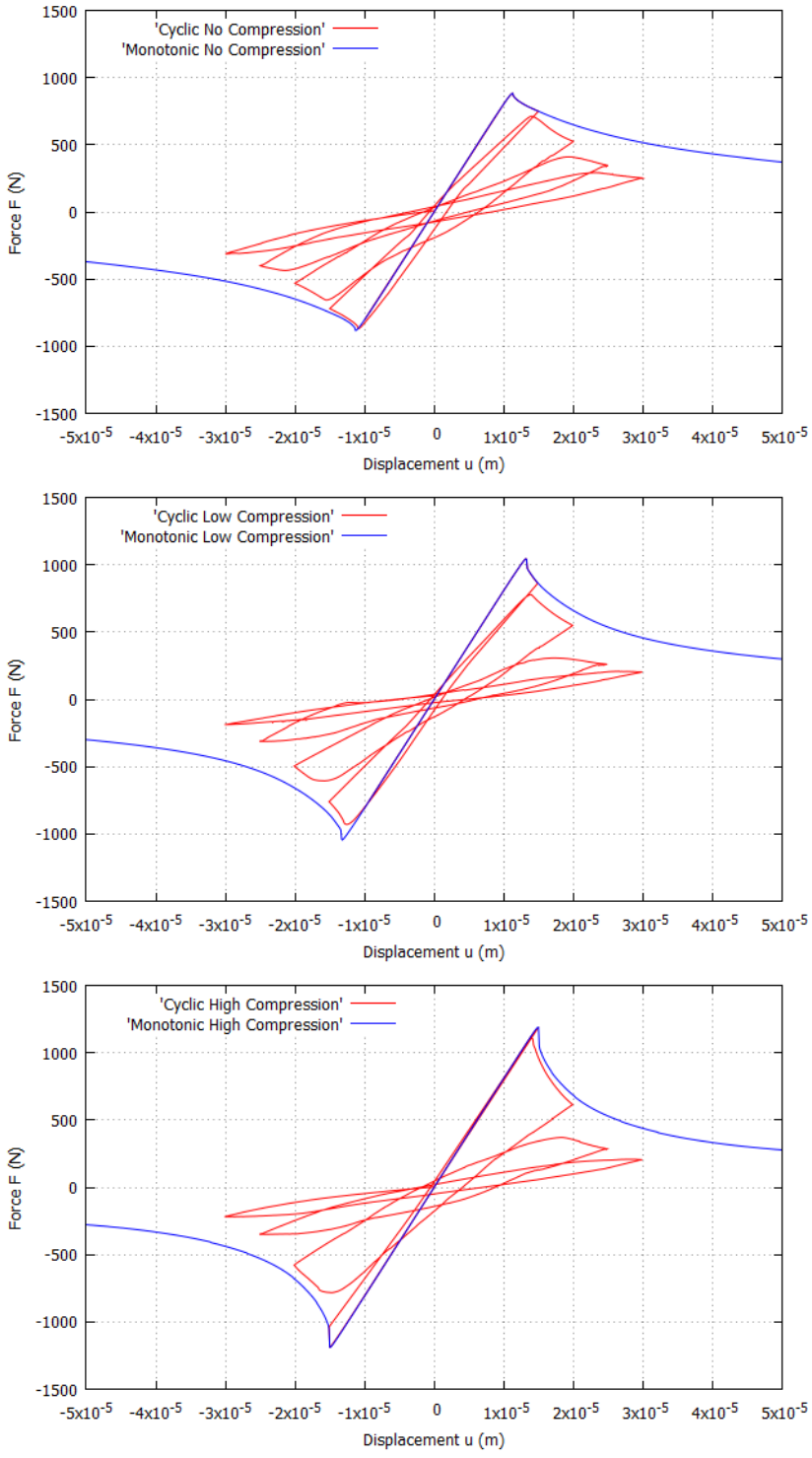

Figure 21. Isotropic Rankine model with irreversible strains (β=0.5) force-displacement curves for the cubic metal specimen under monotonic and cyclic loading in the (a) no compression, (b) low compression and (c) high compression case

12 Conclusions

In this work, a novel multi-crack model with full closing, reopening and sliding capabilities is proposed. The crack model is assembled from different features, some typical from classical orthogonal crack models, some others from up-to-date damage-based models, and some novel components. These are purposefully added to model micro-crack closure-reopening effects with significant sliding (MCRS). Two versions of the model, isotropic and orthotropic, are proposed, both provided with MCRS capabilities.

The model is used in conjunction with a mixed **ε/u** finite element formulation which provides enhanced accuracy and mesh-independent results in cracking problems.

Numerical benchmarks are used to demonstrate the performance of the model in Mode I, Mode II and Mixed Mode I and II cyclic loading situations.

It is observed that:

- The proposed damage constitutive models are fit for the numerical simulation of cracks in quasi-brittle materials with MCRS effects under cyclic loading situations.
- The phenomena of tensile and compressive damage, stiffness recovery and irreversible strains are properly reproduced.
- The model, used together with the mixed FE formulation is able to reproduce the behavior observed in experimental tests as well as to emulate complex crack patterns with MCRS effects.
- Results obtained are free from the spurious mesh bias and stress-locking typical of standard FEs.
- In mode I (traction) and in pure shear situations, monotonic and cyclic results obtained with the models are perfectly overlapping in terms of cracks trajectories and force-displacement curves.
- With pre-loading, monotonic and cyclic results are not overlapping, as irreversible strains develop and accumulate. This effect is very evident in force-displacement curves.
- Distinct results are obtained for different damage models. Hence, different damage criteria produce different crack trajectories and force-displacement curves.
- Likewise, isotropic and orthotropic versions of the same damage criterion also show very different results.

From these, it is concluded that the proposed isotropic and orthotropic constitutive damage models with memory, used in conjunction with the mixed finite element formulation, are capable of computing mode I, mode II and mixed mode I and II cracking problems taking into consideration MCRS effects and correctly computing stiffness recovery under cyclic loadings with shear sliding.

13 Acknowledgements

Financial support from the Spanish Ministry of Economy and Business via the ADaMANT (Computational Framework for Additive Manufacturing of Titanium Alloy) project (Proyectos de I + D (Excelencia) DPI2017-85998-P) is gratefully acknowledged. The support provided by the Spanish Ministry of Education to Mr. Gabriel Barbat via the FPU program is also acknowledged.

14 References

[1] D. Ngo and A. Scordelis, "Finite element analysis of reinforced concrete beams," *American Concrete Institute Journal,* vol. 64, no. 14, pp. 152-163, 1967.

[2] Y. Rashid, "Ultimate strength analysis of prestressed concrete pressure vessels," *Nuclear Engineering and Design,* vol. 7, no. 4, pp. 334-344, 1968.

[3] S. Saloustros, M. Cervera and L. Pelà, "Challenges, tools and applications of tracking algorithms in the numerical modelling of cracks in concrete and masonry structures," *Archives of Computational Methods in Engineering, https://doi.org/10.1007/s11831-018-9274-3,* 2018.

[4] R. Litton, "A contribution to the analysis of concrete structures under cyclic loading," Ph.D. Thesis, University of California, Berkeley, 1975.

[5] R. de Borst and P. Nauta, "Non-orthogonal cracks in a smeared finite element model," *Engineering Computations,* vol. 2, pp. 35-46, 1985.

[6] Z. Bazant and P. Gambarova, "Crack shear in concrete: Crack band microplane model," *Journal of Structural Engineering,* vol. 110, no. 9, pp. 2015-2036, 1984.

[7] I. Carol, P. Prat and Z. Bazant, "New explicit microplane model for concrete: theoretical aspects and numerical implementation," *International Journal of Solids and Structures,* vol. 29, no. 9, pp. 1173-1191, 1992.

[8] M. Cervera, M. Chiumenti and R. Codina, "Mixed stabilized finite element methods in nonlinear solid mechanics. Part I: Formulation," *Computer Methods in Applied Mechanics and Engineering,* vol. 199, no. 37-40, pp. 2559-2570, 2010.

[9] M. Cervera, M. Chiumenti and R. Codina, "Mixed stabilized finite element methods in nonlinear solid mechanics. Part II: Strain localization," *Computer Methods in Applied Mechanics and Engineering,* vol. 199, no. 37-40, pp. 2571-2589, 2010.

[10] M. Cervera, M. Chiumenti, L. Benedetti and R. Codina, "Mixed stabilized finite element methods in nonlinear solid mechanics. Part III: Compressible and incompressible plasticity," *Computer Methods in Applied Mechanics and Engineering,* vol. 285, pp. 752-775, 2015.

[11] M. Cervera, G. Barbat and M. Chiumenti, "Finite element modelling of quasi-brittle cracks in 2D and 3D with enhanced strain accuracy," *Computational Mechanics,* vol. 60, no. 5, pp. 767-796, 2017.

[12] G. Barbat, M. Cervera and M. Chiumenti, "Appraisement of planar, bending and twisting cracks in 3D with isotropic and orthotropic damage models," *International Journal of Fracture,* vol. 210, no. 1-2, pp. 45-79, 2018.

[13] G. Vlachakis, M. Cervera, G. Barbat and S. Saloustros, "Out-of-plane seismic response and faillure mechanism of masonry structures using finite elements with enhanced strain accuracy," *Engineering Faillure Analysis,* vol. 97, pp. 534-555, 2019.

[14] R. Faria, J. Oliver and M. Cervera, "A strain-based plastic viscous-damage model for massive concrete structures," *International Journal of Solids and Structures,* vol. 35, no. 14, pp. 1533-1558, 1998.

[15] C. Comi and U. Perego, "Fracture energy based bi-dissipative model for concrete," *International Journal of solids and structures,* vol. 38, no. 36-37, pp. 6427-6454, 2001.

[16] R. Faria, J. Oliver and M. Cervera, "Modeling material failure in concrete structures under cyclic actions," *Journal of Structural Engineering,* vol. 130, no. 12, pp. 1997-2005, 2004.

[17] M. Cervera and C. Tesei, "An energy-equivalent d+/d- damage model with enhanced microcrack closure-reopening capabilities for cohesive-frictional materials," *Materials,* vol. 10, no. 4, p. 433, 2017.

[18] M. Cervera, C. Tesei and G. Ventura, "Cracking of quasi-brittle structures under monotonic and cyclic loadings: a d+/d- damage model with stiffness recovery in shear," *International Journal of Solids and Structures,* vol. 135, pp. 148-171, 2017.

[19] O. Zienkiewicz, R. Taylor and Z. Zhu, "The finite element method, Vol. 1," *7th edition, Amsterdam, Elsevier Butterworth-Heinemann,* 1989.

[20] J. Oliver, M. Cervera, S. Oller and J. Lubliner, "Isotropic damage models and smeared crack analysis of concrete," *II international conference on computer aided analysis and design of concrete,* 1990.

[21] G. Voyiadjis, Z. Taqieddin and P. Kattan, "Anisotropic damage-plasticity model for concrete," *International Journal Plasticity,* vol. 24, pp. 1946-1965, 2008.

[22] J. Cordebois and F. Sidoroff, "Endommagement anisotrope en elasticité et plasticité," *Journal de Mecanique Theorique et Appliquee,* vol. Special Volume, pp. 45-60, 1982.

[23] I. Carol, E. Rizzi and K. Willam, "On the formulation of anisotropic elastic degradation. I: Theory based on pseudo-logarithmic damage tensor rate; II: Generalized pseudo-Rankine model for tensile damage," *International Journal of Solids and Structures,* vol. 38, no. 4, pp. 491-546, 2001.

[24] S. Saloustros, M. Cervera and L. Pela, "Tracking multi-directional intersecting cracks in numerical modelling of masonry shear walls under cyclic loading," *Meccanica, Special Issue on "New Trends in Mechanics of Masonry", http://dx.doi.org/10.1007/s11012-017-0712-3,* 2017.

[25] L. Benedetti, M. Cervera and M. Chiumenti, "3D numerical modelling of twisting cracks under bending and torsion skew notched beams," *Engineering Fracture Mechanics,* vol. 176, pp. 235-256, 2017.

[26] M. Cervera, C. Agelet de Saracibar and M. Chiumenti, "COMET: Coupled mechanical and thermal analysis. Data input manuel, Version 5.0, Technical report IT-308. Available from http://www.cimne.upc.edu," 2002.

[27] A. Coll, R. Ribo, M. Pasenau, E. Escolano, J. Perez, A. Melendo, A. Monros and J. Garate, "GiD: the personal pre and post-processor. User manual," *CIMNE, Technical University of Catalonia,* p. <http://gid.cimne.upc.ed>, 2016.

[28] D. A. Hordijk, "Local approach to fatigue of concrete, PhD Thesis," Delft University of Technology, 1991.

[29] I. Marzec and J. Tejchman, "Enhanced coupled elasto-plastic-damage models to describe concrete behaviour in cyclic laboratory tests: comparison and improvement," *Archives of Mechanics,* vol. 64, no. 3, pp. 227-259, 2012.

[30] B. Bourdin, G. Francfort and J.-J. Marigo, "Numerical experiments in revisited brittle fracture," *Journal of the mechanics and physics of solids,* vol. 48, no. 4, pp. 797-826, 2000.

[31] C. Miehe, M. Hofacker and F. Welschinger, "A phase field model for rate-independent crack propagation: robust algorithmic implementation based on operator splits," *Computer Methods in Applied Mechanics and Engineering,* vol. 199, pp. 2765-2778, 2010.

[32] J.-Y. Wu and V. Nguyen, "A length scale insensitive phase-field damage model for brittle fracture," *Journal of the Mechanics and Physics of Solids,* vol. 119, pp. 20-42, 2018.

[33] P. Carrara, M. Ambati, R. Alessi and L. De Lorenzis, "A novel framework to model the fatigue behavior of brittle materials based on a variational phase-field approach," *Submited to arXiv:1811.02244,* 2018.

Structural size effect: Experimental, theoretical and accurate computational assessment

G. B. Barbat, M. Cervera, M. Chiumenti and E. Espinoza

Engineering Structures

Vol. 213, Art. 110555, (2020)

https://doi.org/10.1016/j.engstruct.2020.110555

Structural size effect: Experimental, theoretical and accurate computational assessment

G. B. Barbat, M. Cervera, M. Chiumenti and E. Espinoza

International Center for Numerical Methods in Engineering (CIMNE)

Technical University of Catalonia – BarcelonaTECH

Edificio C1, Campus Norte, Jordi Girona 1-3

08034 Barcelona, Spain

gbarbat@cimne.upc.edu, miguel.cervera@upc.edu, michele@cimne.upc.edu, edu.espinoza.duran@gmail.com

Abstract

In this paper, experimental evidence, theoretical predictions and the finite element modelling of the structural size effect in cracking problems of quasi-brittle materials are discussed and assessed against each other. The fracture process is modelled through the crack band approach, using an isotropic damage constitutive law. The correct dissipation of the fracture energy, essential for modelling the phenomenon with precision, is introduced. An enhanced accuracy mixed finite element formulation is used to ensure mesh bias independent results. Several experimental campaigns where size effect is investigated are numerically reproduced in 2D and in 3D to assess the feasibility and the performance of the method. For this, mode I and mixed mode I and II fracture situations are considered in notched and unnotched beams. The correlation of the experimental results with the numerical simulations shows the capacity of the mixed FE formulation to reproduce crack paths, force-displacement curves and collapse mechanisms with precision for a wide range of structural sizes. The enhanced accuracy FE formulation eliminates the spurious mesh dependency that is characteristic of standard FE simulations. In addition, the model is able to follow Bazant's size effect law with precision. Results confirm that the energy release rate in the progressing fracture is the fundamental cause of size effect in quasi-brittle materials. This is additionally verified in a study of the relative influence of statistical and energetic size effect. Computations show that the essential requirements to suitably simulate the phenomenon are (1) a fracture model ensuring the correct energy dissipation at the crack and (2) a method guaranteeing mesh objective results.

Keywords: Cracking, Size Effect, Damage, Fracture Energy, Strain Localization, Mixed Finite Elements

1 Introduction

Structural size effect refers to the variation, motivated by a change of size, of the load capacity of a structure from estimations made using stress failure criteria [1]. The observed behavior of quasi-brittle specimens in laboratory tests does not correlate with the one perceived in real sized structures, because the latter are usually much bigger. This phenomenon has a profound impact in many practical applications such as in concrete structures, as evidenced by its incorporation into the 2019 version of the American Concrete Institute design norm for structural concrete [2], but also in geomechanics, composite materials or artic ice engineering among others [3, 4].

In order to take into consideration the physical phenomenon of size effect in engineering applications the use of numerical modelling is required. Both by academics and practitioners, the most widely used strategy to analyze fracture and structural failure with the finite element method is the smeared crack approach, introduced more than 50 years ago by Rashid [5] and adopted in this work. Within this approach, the fracture is modeled through the degradation of the material at the constitutive level.

Specifically, the crack band theory (CBT), introduced by Bazant in [6], is considered herein. CBT consists in regularizing, or "smearing", the displacement jump across a zero thickness crack into the corresponding nominal strains across a band of small, but finite, thickness. Consistency and, therefore, convergence, of the derived FE approach depends on two factors. On the one hand, the regularization of a discontinuous displacement field needs to be proved consistent at continuum level, before FE discretization is performed. This consistency is discussed in [7, 8], where, among other requirements, it is shown that to ensure correct energy dissipation when the cohesive crack opens it is necessary to relate, at continuum level, the cohesive behavior of the regularized crack, i.e. its softening behavior, to the actual width of the band. As will be discussed in detail in Section 2, achieving the proper energy dissipation when the crack is developing is an essential requirement for the correct assessment of the size effect phenomenon [4, 9-11]. On the other hand, the FE discrete problem needs to be consistent with the regularized continuum one. This requires from the FE formulation to relate the width of the crack to the size of the FE mesh. Therefore, the required adjustment of the softening behavior of the material with respect to the bandwidth of the regularized crack at continuum level, translates, when introducing the FE discretization, to its correction with respect to the FE size. This avoids spurious mesh size dependent results, as intended when the crack band theory was introduced in [6].

Notwithstanding the mesh size representation, the main difficulty posed by the smeared crack approach and the crack band theory, when applied with standard displacement-based FEs, is the spurious mesh dependency that it suffers when computing crack trajectories. However, mesh-bias independence is an indispensable requirement of the numerical model. Firstly, for a given structural size, the failure mechanism predicted by the numerical model must be the same independently of the FE mesh used in the analysis. Otherwise, the numerical solution is, in plain terms, useless. Secondly, and regarding size effect specifically, significant variations in the brittleness of the structural behavior caused by the changes in size may cause significant changes in the development of the collapse mechanism [11]. To overcome the lack of mesh-objectivity displayed by the smeared crack method in some situations, auxiliary crack tracking techniques have been proposed and successfully applied [12, 13].

Because of this drawback of the crack band theory, several alternative techniques have been proposed over the last decades to avoid mesh bias dependency in fracture problems. Gradient enhanced [14-16], nonlocal [17, 16] and phase-field models [15, 18-20] have been used to avoid spurious mesh-dependency of the computed results in terms of the crack path. However, these techniques use a localization limiter dependent on an internal length that governs the size of the crack band width. As it has been emphasized in [21], a clear physical interpretation and direct

link between the length parameter in the model and the characteristic length of the material is arguable. “Geometrically” regularized gradient-damage [22] and phase-field models [23-25] have been recently proposed. However, the practical use of all these methods is limited to specific situations and constitutive behaviors.

It has been shown in previous works [26, 27] that in cracking problems of quasi-brittle materials, the mesh dependency of the standard displacement-based FE formulation in solid mechanics is in fact caused by their lack of local convergence in the computed stress and strain fields. This is especially harmful because the trajectory is determined by the stresses and strains that develop in quasi-singular points near the tip of the propagating crack. The stress and strain at these points may be inaccurately computed, averting the correct computation of the crack trajectory.

In this work, the issue of spurious mesh-dependency is addressed through an enhanced-accuracy mixed strain/displacement FE formulation, proposed and developed in references [26-32]. In the mixed FE formulation, strains are additional nodal unknowns of the FE problem, as well as the nodal displacements. This provides an independent discrete interpolation of the strain field, instead of being computed at element level by discrete differentiation. This kinematic enhancement increases the rate of convergence of the strain and stress fields. Their local and global convergence is ensured in the quasi-singular situations that arise near the tip of the progressing crack. The spurious mesh dependency and lack of local convergence which hamstrings cracking problems solved with standard FE is prevented. In this way, it is possible to obtain accurate results in terms of fracture paths without the use of any crack tracking technique and with far coarser mesh densities than the ones required in phase-field formulations.

In previous works, the authors have demonstrated the use of mixed displacement/pressure FE to assess structural size effect in relation to mode II failure [11] and also shown the enhanced accuracy and mesh-objectivity achievable by the mixed strain/displacement FE in mode I and mixed mode fracture. Ensuingly, in this work, the strain/displacement mixed formulation is applied to assess structural size effect in mode I and mixed mode fracture situations.

A classical local damage constitutive law is employed to represent cracking in quasi-brittle materials. To model mode I and mixed mode I and II fracture, isotropic Rankine damage is considered. The nonlinear behavior of the material is characterized by two parameters: the (tensile) strength and the fracture energy. The capacity of the proposed constitutive law to reproduce size effect, including the perfectly ductile and perfectly brittle limits, is investigated. The bandwidth of the crack is set in function of the finite element size. It is determined by the resolution of the FE only, as required in the crack band method [6].

The objectives of this work are: (1) to establish the necessary and sufficient features required in a constitutive law for modelling the size effect phenomenon, (2) to show the performance of the proposed model in reproducing results consistent with documented data with regard collapse mechanisms, force-displacement curves and crack trajectories for a wide range of structural sizes, (3) to demonstrate the capability of the mixed FE formulation in producing precise and mesh independent results, (4) to show that the main and dominant influencing factor of size effect in quasi-brittle materials is the release of stored energy of the structure, (5) to demonstrate the performance of the model in accurately reproducing Bazant’s size effect law over a wide range of structural sizes.

The outline of this paper is as follows. In Section 2 structural size effect is introduced. In Section 3 the isotropic damage constitutive model used in this work is described. In Section 4 the mixed FE formulation employed to obtain mesh-bias independent results with enhanced accuracy is outlined. Section 5 presents the numerical simulations of several experimental campaigns where the capacity of the model in reproducing the size effect phenomenon is thoroughly analyzed. In

Section 6 a mesh-sensitivity study is performed to show the aptness of the model in producing results without spurious mesh dependence. In Section 7 the relative influence of the statistical variability of the mechanical properties of the material as a source of size effect is assessed. In Section 8 the ability of the model in reproducing Bazant's size effect law is investigated. Finally, some conclusions are given in Section 9.

2 Structural size effect

In this section, theoretical and practical considerations regarding structural size effect are given. According to Bazant [1, 3], several sources of structural size effect have been observed:

- Release of stored energy
- Statistical size effect
- Boundary layer effect
- Diffusion phenomena
- Hydration heat

However, not all these sources have the same influence in the phenomenon. Undoubtedly, the most important one is, by far, the release of stored energy. In quasi-brittle problems, the relative influence of statistical size effect is considered unimportant when compared to the effect that the release of the stored energy has in the overall phenomenon. The last three sources are deemed to have only a secondary impact and can be effectively neglected in laboratory tests where specimens have a constant thickness for all the sizes [1, 4].

Therefore, the study of the size effect phenomenon is principally related to energetic considerations [4, 9-11]. When the fracture develops the stored elastic energy in the structure is released into the crack front. This energy is dissipated and engaged into the process of the crack surface formation. The ratio between the elastic energy stored in the structure and the energy dissipated through the crack tip varies when size changes. This is the main cause for structural size effect. These energetic considerations also govern the relative extent of the fracture process zone within the structure. In plasticity theory, the size of the process zone is of the order of the structural size. The classical linear elastic fracture mechanics (LEFM) theory is developed under the hypothesis that the fracture process zone is negligible with respect to the structural size. For actual quasi-brittle materials, the extent of the fracture process zone cannot be neglected and it grows significantly when size decreases.

According to the dimensional analysis derived in reference [11], in situations involving materials with softening, the brittleness of the problem is governed by the brittleness number Π_B, the ratio D/L between the characteristic size of the structure D and the material characteristic length L, which depends only on the material properties. Irwin's characteristic length L is equal to

$$L = \frac{E G_f}{(f_t)^2} \tag{1}$$

where E is Young's modulus, f_t is the (tensile) strength and G_f is the fracture energy of the material, which is the energy dissipated per unit of area of the fracture surface. Thus, from energy considerations, the brittleness of the problem is size-dependent.

Consequently, collapse in smaller specimens occurs in a more ductile way while larger specimens fail in a more brittle manner. In the small limit case, the formation of a failure mechanism takes place as a result of the yielding of an extensive area. In the large scale limit, perfect brittle failure occurs. For intermediate sizes failure is due to the formation of a crack that gradually develops in

the structure while stress redistribution and the release of stored energy into the crack front takes place [1, 10].

From experimental observations and theoretical considerations [9] Bazant's size effect law has been proposed to represent the phenomenon. It describes the relationship between the load capacity of the structure and its characteristic size. It is defined in its simplest form as [1]:

$$\sigma_{N_u} = Bf_t\left(1+\frac{D}{D_0}\right)^{-\frac{1}{2}} \tag{2}$$

where σ_{N_u} is the nominal strength, defined as

$$\sigma_{N_u} = c_n\frac{P_u}{Db} \quad \text{(2D Scaling)}; \qquad \sigma_{N_u} = c_n\frac{P_u}{D^2} \quad \text{(3D Scaling)} \tag{3}$$

where D is the characteristic size of the structure, b is its thickness, P_u is the ultimate/failure load of the structure, f_t is the strength of the material and D_0 is a reference structural size; B is a dimensionless constant which depends on the shape and the loading of the structure but not on its size and c_n is a dimensionless constant that can be arbitrarily chosen. The law in Eq. (2) is only valid for quasi-brittle materials over a limited range of D. Modifications have been proposed in references [1, 33] to account for larger ranges of sizes and also for the particular case of unnotched structures. This law has been introduced in the 2019 version of the ACI code for structural concrete [2] for revising the strength of concrete in some situations through the inclusion of a size effect modification factor. In [2], which is intended for design purposes, D_0 for concrete is taken as $10\ in = 0.254\ m$.

Assuming that the reference structural size D_0 is linearly dependent with Irwin's characteristic length L, $D_0 = A^{-2}L$, A being a constant similar to B, allows to rewrite Bazant's law in Eq. (2) as

$$\begin{aligned}\sigma_{N_u} &= Bf_t\left(1+A^2\frac{D}{L}\right)^{-\frac{1}{2}}\\ &= Bf_t(1+A^2\Pi_B)^{-\frac{1}{2}}\end{aligned} \tag{4}$$

where $\Pi_B = D/L$ is the brittleness number defined in [11].

In Figure 1 the size effect behavior described by Bazant's law in Eq. (2) is shown, where the role of the reference size D_0 is appreciated. The law indicates how for small structures, when D/D_0 is much smaller than 1, $\Pi_B \to 0$, the structure collapses following the predictions of limit analysis, which does not contemplate size effect, as the nominal strength of the material is constant with size: $\sigma_{N_u}(\Pi_B \to 0) = Bf_t$. For large structures, when D/D_0 is much larger than 1, $\Pi_B \to \infty$, the structure fails following the LEFM theory, with the strongest possible size effect, the nominal strength being inversely proportional to the square root of the structural size [3]: $\sigma_{N_u}(\Pi_B \to \infty) = (B/A)\sqrt{EG_f}(D)^{-1/2}$. It can be seen that in large notched specimens, where stress singularities exist, a failure criterion expressed in terms of maximum stress is not adequate. In such cases, an energy failure criterion such as the one introduced in LEFM is applicable. For intermediate cases a gradual transition from one failure mode to the other takes place, as it typically happens in most applications involving quasi-brittle fracture [10].

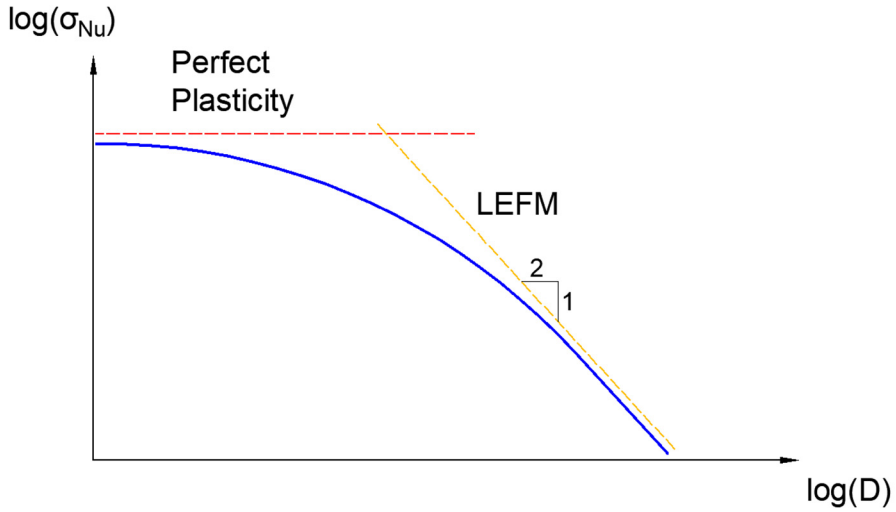

Figure 1. Bazant's size effect law

It is noteworthy that even though the size effect law is generally defined in terms of the nominal strength σ_{N_u}, this is in fact an indirect way of describing the peak load P_u sustainable by the structure in terms of its characteristic size. Therefore, the nominal stress is not a real stress but a load parameter, useful to depict in a clearer way the deviation from limit analysis due to size effect [4].

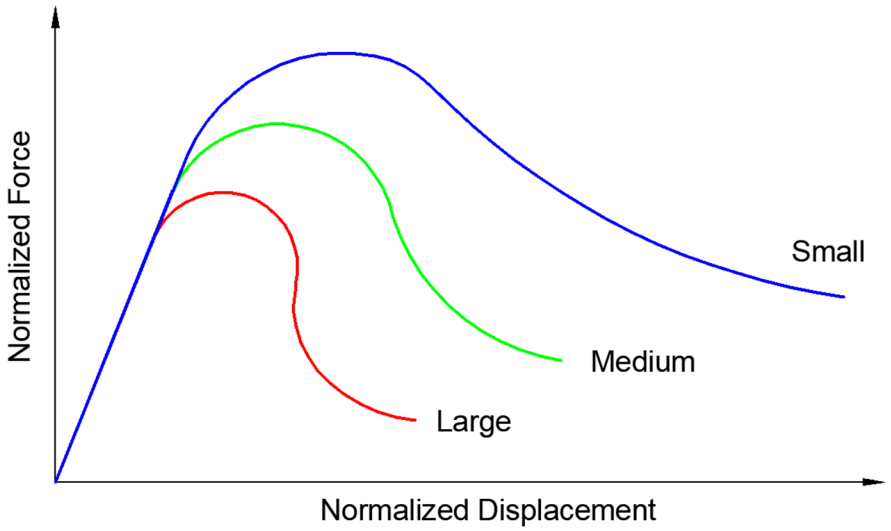

Figure 2. Force-displacement curves, normalized with size, of geometrically similar structures exhibiting size effect

Experimental evidence shows that, in addition to the consequences that it has on the structural load capacity, size effect also governs the ductility and post-peak behavior of the structure. For loading under displacement control, failure in larger sized structures occurs closer to the peak load [1, 3], as shown in Figure 2. The fact that the post-peak curves of large structures descend more steeply than in smaller ones [4, 10] is also due to the fact that, once properly normalized, the energy dissipated in the failure process is comparatively smaller in larger structures.

When considering the scaling of structures in general, several other factors do not scale geometrically apart from their brittleness. For example, in dynamic analysis, a big concern is the fact that the strain rate is influenced by the scaling factor, affecting the predictions of the stresses obtained from scaled models [34-36]. This issue, which requires specific attention, is not treated in this work which focusses on structural size effect under quasi-static loading. It should also be

noted that weight forces do not scale geometrically neither. Even if considering them in FE analysis is straightforward, they can be effectively neglected in laboratory tests of small concrete specimens. Regarding scale modelling, it should also be taken into consideration that in laboratory tests the possibilities of scaling the aggregate inside concrete are limited.

3 Isotropic damage model

In this section, the formulation of the isotropic damage constitutive law is presented. Employing Voigt's convention, the strain and stress tensors are represented as vectors. In 3D the strain vector is $\boldsymbol{\varepsilon} = \left(\varepsilon_x, \varepsilon_y, \varepsilon_z, \gamma_{xy}, \gamma_{xz}, \gamma_{yz}\right)^T$ and stress vector is $\boldsymbol{\sigma} = \left(\sigma_x, \sigma_y, \sigma_z, \tau_{xy}, \tau_{xz}, \tau_{yz}\right)^T$. In an isotropic damage model $\boldsymbol{\varepsilon}$ and $\boldsymbol{\sigma}$ are linked through the constitutive equation:

$$\boldsymbol{\sigma} = \mathbf{D}(d)\,\boldsymbol{\varepsilon} = (1-d)\mathbf{D}_0\,\boldsymbol{\varepsilon} \tag{5}$$

where $\mathbf{D} = \mathbf{D}(d)$ is the secant constitutive matrix, which is a function of the internal scalar damage variable d that describes the degradation of the material and $\mathbf{D}_0$ is the initial elastic constitutive matrix. From thermodynamic considerations, the secant constitutive matrix needs to be symmetric and positive semidefinite. In an initially isotropic elastic material, $\mathbf{D}_0$ is defined in function of the undamaged elastic values of Young's modulus E and Poisson's ratio ν.

In spite of the unquestionable directional character of cracks, isotropic damage models were firstly proposed [37] and then widely embraced as a way of circumventing the numerical issues related to orthotropic models. Orthotropic damage models have recently been re-assessed by the authors in relation with brittle failure in references [30, 32], but their use hereafter is not necessary for the objectives of this work.

The effective stress $\overline{\boldsymbol{\sigma}}$ is stipulated as $\overline{\boldsymbol{\sigma}} = \mathbf{D}_0\,\boldsymbol{\varepsilon}$, according to the hypothesis of strain equivalence. The damage criterion is introduced as $\mathbb{F}$

$$\mathbb{F}\left(\bar{\sigma}_{eq}, r\right) = \bar{\sigma}_{eq}(\overline{\boldsymbol{\sigma}}) - r = 0 \tag{6}$$

where $\bar{\sigma}_{eq}(\overline{\boldsymbol{\sigma}})$ is the equivalent effective stress and r is the current damage threshold. The initial value of the damage threshold is the tensile strength of the material f_t. In this work, only tensile damage is considered. The current value at time t of the damage threshold r is computed from the Kuhn-Tucker optimality and consistency conditions, guaranteeing the irreversibility of damage and the positiveness of the dissipation

$$r = \max\,\left(f_t, \max \bar{\sigma}_{eq}(\hat{t})\right) \quad \hat{t} \in [0, t] \tag{7}$$

The equivalent effective stress $\bar{\sigma}_{eq}$ is a function of the effective stress $\overline{\boldsymbol{\sigma}}$, defined through the Rankine damage surface

$$\bar{\sigma}_{eq}(\overline{\boldsymbol{\sigma}}) = \langle \bar{\sigma}_1 \rangle \tag{8}$$

where $\bar{\sigma}_1$ is the major principal effective stress and $\langle\cdot\rangle$ are the Macaulay brackets, such that $\langle x \rangle = x$ if $x \geq 0$ and $\langle x \rangle = 0$ if $x < 0$.

In this work, the evolution of the internal damage variable d follows an exponential softening law. Other functions can be alternatively contemplated if considered necessary. The only requirement for the damage function is that the evolution of d monotonically progresses from 0 to 1 as the damage threshold r varies from f_t to infinity. Therefore

$$d = 1 - \frac{f_t}{r}\exp\left(-2H_d\,\frac{\langle r - f_t \rangle}{f_t}\right) \tag{9}$$

where H_d is a softening parameter controlling the rate of degradation of the material. From energy conservation considerations, in the crack band theory H_d is linked to material properties through Irwin's characteristic length L in Eq. (1), and the width of the band of the crack b

$$H_d = \frac{b}{2L - b} \tag{10}$$

This approach allows to achieve independence of the results with respect to the size of the finite element mesh and to guarantee the correct energy dissipation during the fracture process. Note that the influence of the fracture energy of the material is taken into account through Irwin's characteristic length L. In the mixed formulation, the bandwidth of the cracks is taken as $b = 2h$, h being the finite element size. This is in accordance with the FE approximation of the strain field adopted, presented in Section 4.

Energy dissipation, size effect and FE meshes

Regarding energy dissipation, at the continuum level, when considering non-regularized cracks, the total energy dissipated during the fracture process is proportional to the area of the crack surface. However, when the regularization of the cracks is introduced, at continuum level, the total energy dissipation is proportional to the volume of the localization band [7, 8]. Therefore, for ensuring consistency between the regularized and non-regularized problems, the fracture energy per unit area G_f is substituted by $g_f = \mathrm{G}_f/b$ as the energy dissipated by unit volume, b being the width of the regularized crack. In such case, the same brittleness number as in the regularized problem holds

$$\Pi_B = \frac{D}{b} \cdot \frac{b}{L} = \frac{D}{L} \tag{11}$$

In the discrete FE problem, the crack bandwidth b is related to the FE size h ($b = \alpha h$, α being a constant, $\alpha = 1$ for standard FE, $\alpha = 2$ for mixed FE) and the same brittleness number is recovered

$$\Pi_B = \frac{D}{\alpha h} \cdot \frac{\alpha h}{L} = \frac{D}{L} \tag{12}$$

guaranteeing the consistency between the continuum and the discrete problems with respect to fracture energy dissipation and mesh-size objectivity.

Therefore, if structural size effect is investigated by increasing D while the ratio D/h fixed (that is, scaling the mesh with the structural size), brittleness is exactly expressed by the ratio h/L, where h increases in the same way as D.

Let $\Pi_0 = D_0/L$ be the brittleness of the reference size D_0 and the scale $s = D/D_0$. Then, for a size D

$$\Pi_B = \frac{D}{L} = \frac{D_0}{L} \cdot \frac{D}{D_0} = \Pi_0 \cdot s \tag{13}$$

When the ratio D/h is fixed, $D/h = D_0/h_0$ is constant, h_0 being the corresponding FE size when $D = D_0$, and

$$\Pi_B = \frac{D}{L} = \frac{D_0}{L} \cdot \frac{D}{D_0} = \frac{D_0}{L} \cdot \frac{h}{h_0} = \Pi_0 \cdot s \tag{14}$$

So, in such case, the scale s is determined by the actual size of the structure or the finite elements, as $s = D/D_0 = h/h_0$.

4 Mixed FE formulation

In this work a mixed **ε/u** formulation is adopted to solve the mechanical problem with enhanced accuracy. Apart from other strong points, this formulation avoids the spurious mesh dependency that is characteristic in fracture simulations of quasi-brittle materials. In this section, the mixed FE formulation used to compute all the simulations in this work is briefly presented. The formulation is fully described in reference [29]. For additional details, references [26-28, 30, 32, 38] are recommended.

In this technique, the variational form of the nonlinear solid mechanics problem is posed considering the displacements $\boldsymbol{u}$ and the strains $\boldsymbol{\varepsilon}$ as unknowns. Following Voigt's notation, the compatibility equation relates the strain and displacement fields

$$\boldsymbol{\varepsilon} = \mathbf{S}\,\boldsymbol{u} \tag{15}$$

where $\mathbf{S}$ is the differential symmetric gradient operator. In addition, the stress vector $\boldsymbol{\sigma}$ and the body forces vector $\mathbf{f}$ are linked through the Cauchy momentum equation, written in matrix form as

$$\mathbf{S}^T\boldsymbol{\sigma} + \mathbf{f} = \mathbf{0} \tag{16}$$

where $\mathbf{S}^T$ is the differential divergence operator, adjoint to the $\mathbf{S}$ in Eq. (15). The constitutive equation connects the stress and strain vectors

$$\boldsymbol{\sigma} = \mathbf{D}\,\boldsymbol{\varepsilon} \tag{17}$$

where $\mathbf{D}$ is the appropriate secant matrix. It is a thermodynamic requirement that $\mathbf{D}$ is symmetric.

By pre-multiplying Eq. (15) by the secant matrix $\mathbf{D}$ and substituting Eq. (17) into Eq. (16) a system of two equations is derived

$$-\mathbf{D}\boldsymbol{\varepsilon} + \mathbf{D}\mathbf{S}\boldsymbol{u} = \mathbf{0} \tag{18}$$

$$\mathbf{S}^T(\mathbf{D}\boldsymbol{\varepsilon}) + \mathbf{f} = \mathbf{0} \tag{19}$$

Eqs. (18)-(19) compose the strong form of the mixed $\boldsymbol{\varepsilon}/\boldsymbol{u}$ formulation together with the proper boundary conditions. The problem is symmetric.

The weak form of the problem is attained by multiplying Eqs. (18) and (19) by the virtual strain $\delta\boldsymbol{\varepsilon}$ and displacement vector $\delta\boldsymbol{u}$ respectively. Then the system is integrated over the spatial domain and the Divergence Theorem is utilized in the right hand side of the second integral operation. The variational form that ensues is

$$-\int_\Omega \delta\boldsymbol{\varepsilon}^T\mathbf{D}\boldsymbol{\varepsilon}\,\mathrm{d}\Omega + \int_\Omega \delta\boldsymbol{\varepsilon}^T\mathbf{D}\mathbf{S}\boldsymbol{u}\,\mathrm{d}\Omega = 0 \quad \forall\delta\boldsymbol{\varepsilon} \tag{20}$$

$$\int_\Omega (\mathbf{S}\delta\boldsymbol{u})^T(\mathbf{D}\boldsymbol{\varepsilon})\,\mathrm{d}\Omega = \int_\Omega \delta\boldsymbol{u}^T\mathbf{f}\,\mathrm{d}\Omega + \int_{\Gamma_t} \delta\boldsymbol{u}^T\bar{\mathbf{t}}\,\mathrm{d}\Gamma \quad \forall\delta\boldsymbol{u} \tag{21}$$

The variational form of the problem is to find the solutions $\boldsymbol{u}$ and $\boldsymbol{\varepsilon}$ that fulfill the system of Eqs. (20) and (21) and that comply with the boundary condition $\boldsymbol{u} = \mathbf{0}$ on Γ_u, for the arbitrary virtual displacements $\delta\boldsymbol{u}$, which becomes null on Γ_u, and the arbitrary virtual strains $\delta\boldsymbol{\varepsilon}$. This variational problem is symmetric.

To obtain the discrete form of the mixed problem the spatial domain Ω is discretized into nonoverlapping FE Ω_e, so that $\Omega = \cup\, \Omega_e$. The displacement $\boldsymbol{u}$ and the strain $\boldsymbol{\varepsilon}$ are replaced with the FE discrete approximations $\widehat{\boldsymbol{u}}$ and $\hat{\boldsymbol{\varepsilon}}$ defined element-wise as

$$\boldsymbol{u} \cong \widehat{\boldsymbol{u}} = \boldsymbol{N}_u \boldsymbol{U} \tag{22}$$

$$\boldsymbol{\varepsilon} \cong \hat{\boldsymbol{\varepsilon}} = \boldsymbol{N}_\varepsilon \boldsymbol{E} \tag{23}$$

where $\boldsymbol{U}$ and $\boldsymbol{E}$ are vectors incorporating the values of the displacements and the strains at the nodes of the finite element mesh. $\boldsymbol{N}_u$ and $\boldsymbol{N}_\varepsilon$ are the matrices incorporating the interpolation functions adopted in the FE approximation.

Using equal interpolation functions for $\boldsymbol{N}_u$ and $\boldsymbol{N}_\varepsilon$ does not conform with the Inf-Sup condition [39-41]. In this case a stabilization method becomes necessary to ensure the solvability, uniqueness and stability of the discrete mixed problem. The basis of the stabilization procedure is the modification of the discrete variational form using the Orthogonal Subscales Method, introduced within the framework of the Variational Multiscale Stabilization methods and adopted herein [42].

The stabilization strategy is solely to change the approximation of the discrete strain in Eq. (23) by the following discrete field

$$\boldsymbol{\varepsilon} \cong \hat{\boldsymbol{\varepsilon}} = \boldsymbol{N}_\varepsilon \boldsymbol{E} + \tau_\varepsilon (\boldsymbol{B}_u \boldsymbol{U} - \boldsymbol{N}_\varepsilon \boldsymbol{E}) = (1 - \tau_\varepsilon) \boldsymbol{N}_\varepsilon \boldsymbol{E} + \tau_\varepsilon \boldsymbol{B}_u \boldsymbol{U} \tag{24}$$

where τ_ε is a stabilization parameter with value $0 \leq \tau_\varepsilon \leq 1$. Note that for $\tau_\varepsilon = 1$, the strain interpolation of the standard irreducible formulation is regained:

$$\boldsymbol{\varepsilon} \cong \hat{\boldsymbol{\varepsilon}} = \boldsymbol{B}_u \boldsymbol{U} \tag{25}$$

where $\boldsymbol{B}_u$ is the discrete strain-displacement matrix defined as $\boldsymbol{B}_u = \boldsymbol{S}\boldsymbol{N}_u$.

The corresponding algebraic system of equations reads:

$$\begin{bmatrix} -\boldsymbol{M}_{\boldsymbol{\tau}} & \boldsymbol{G}_{\boldsymbol{\tau}} \\ \boldsymbol{G}_{\boldsymbol{\tau}}^T & \boldsymbol{K}_{\boldsymbol{\tau}} \end{bmatrix} \begin{bmatrix} \boldsymbol{E} \\ \boldsymbol{U} \end{bmatrix} = \begin{bmatrix} \boldsymbol{0} \\ \boldsymbol{F} \end{bmatrix} \tag{26}$$

where $[\boldsymbol{E} \quad \boldsymbol{U}]^T$ is the array of nodal values of strains and displacements, and $\boldsymbol{M}_{\boldsymbol{\tau}} = (1 - \tau_\varepsilon)\boldsymbol{M}$, $\boldsymbol{G}_{\boldsymbol{\tau}} = (1 - \tau_\varepsilon)\boldsymbol{G}$ and $\boldsymbol{K}_{\boldsymbol{\tau}} = \tau_\varepsilon \boldsymbol{K}$. $\boldsymbol{M}$ is a mass like projection matrix, $\boldsymbol{G}$ is the discrete gradient matrix, $\boldsymbol{K}$ is a stiffness like matrix and $\boldsymbol{F}$ is the vector of external nodal forces.

$$\boldsymbol{M} = \int_\Omega \boldsymbol{N}_\varepsilon^T \mathbf{D} \boldsymbol{N}_\varepsilon \, \mathrm{d}\Omega \tag{27}$$

$$\boldsymbol{G} = \int_\Omega \boldsymbol{N}_\varepsilon^T \mathbf{D} \boldsymbol{B}_u \, \mathrm{d}\Omega \tag{28}$$

$$\boldsymbol{K} = \int_\Omega \boldsymbol{B}_u^T \mathbf{D} \boldsymbol{B}_u \, \mathrm{d}\Omega \tag{29}$$

$$\boldsymbol{F} = \int_\Omega \boldsymbol{N}_u^T \mathbf{f} \, \mathrm{d}\Omega + \int_{\Gamma_t} \boldsymbol{N}_u^T \bar{\boldsymbol{t}} \, \mathrm{d}\Gamma \tag{30}$$

5 Numerical analysis of notched and unnotched concrete beams

In this section the experimental campaigns reported in references [43-45] are numerically investigated. In these laboratory experiments multiple series of geometrically similar notched and unnotched beams of varying sizes are tested. The objective of this section is to show the capacity of the proposed model in accurately reproducing the size effect phenomenon in quasi-brittle materials in mode I and mixed mode I and II fracture.

The simulations are conducted with an enhanced version of the finite element code COMET [46]. Pre- and post-processing are realized with GID [47], developed at CIMNE (International Center for Numerical Methods in Engineering). At each load step increment convergence is attained when the ratio between the norm of residual forces and the norm of total external forces is lower than 10^{-3} %. In all the simulations shown in this work, a stabilization parameter $\tau_\varepsilon = 0.1$ is used.

5.1 Analysis of the Grégoire tests: mode I fracture

In this section, the numerical simulation of the tests of the Grégoire concrete beams is presented. The experiments are reported in [43], which also computed numerical simulations with a non-local model. Other numerical results are also reported in reference [25], where a phase-field model is employed, in [48], where interface elements are used, in [49], where the beam-particle approach is applied, in [50], where the discrete element method is considered and in [51], where a gradient damage model is adopted.

Three-point bending tests of notched and unnotched beams were carried out. The experiments were performed for geometrically similar beams of varying depths D = 400 mm, 200 mm, 100 mm and 50 mm while the span-to-depth ratio was kept constant to 2.5. Several series of beams were tested, with different notch configurations. Specifically, beams with notch-to-depth ratios λ of 0.5 (half-notched), 0.2 (fifth-notched) and 0 (unnotched) were considered. All the beams had the same constant thickness of 50 mm for all the sizes. The details of the geometry of the beams are shown in Figure 3. The material parameters employed in the present simulations are given in Table 1. They have been calibrated by reverse fitting, and they are within a 10% variation to the values recorded from the experimental tests and the ones used in the corresponding reported numerical simulations in [25]. A vertical load is applied at the midpoint of the beams. The analyses are performed under CMOD (crack mouth opening displacement) control.

The case of notch-to-depth ratio of 0.5 is solved under the plane stress hypothesis using a structured mesh. Quadrilateral elements of a size of $1.25 \cdot 10^{-2} D$ are employed, resulting in a total of 22440 elements. The notch width is set equal to the width of one finite element, as shown in Figure 4. Note that this is the maximum mesh size fit to model the evolution of the fracture with the crack band approach. For the other notch configurations, the same FE size is fixed and similar meshes of 22464 and 22480 quadrilateral elements ensue.

Figure 5 shows the force-CMOD curves obtained. It can be seen how the peak load is very similar to the experimental results of [43] for all the sizes of the three series (the half-notched, fifth notched and unnotched beams). In addition, the computed post-peak softening behavior is also very close to the experimental envelopes in all the cases. The overall size effect phenomenon observed in the experiments is well captured by the model using the same material properties in all the simulations. In addition, the same set of material properties model reproduce well the behavior of the three series of beams with different notch-to-depth ratios.

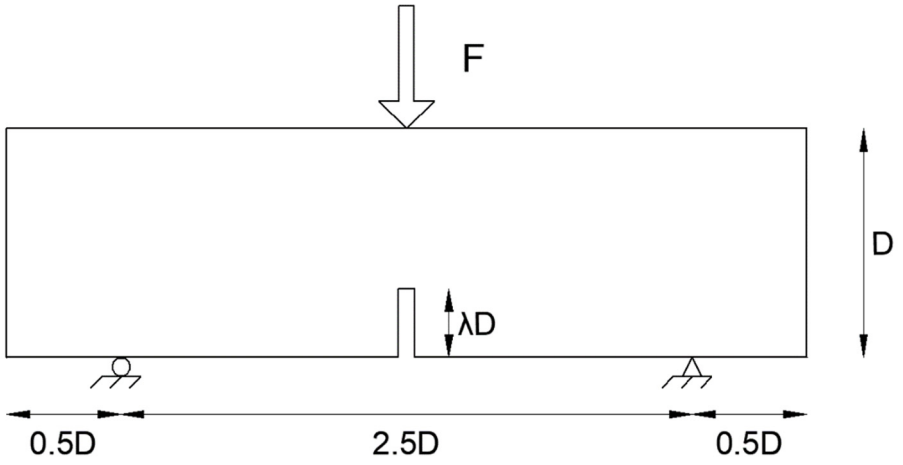

Figure 3. Geometry of the Grégoire experimental tests

Young's Modulus	$37.0 \cdot 10^9$ Pa
Poisson's Ratio	0.2
Tensile Strength	$3.5 \cdot 10^6$ Pa
Tensile Fracture Energy	90 J/m^2
Irwin's material length	0.2718 m

Table 1. Material parameters of the Grégoire tests

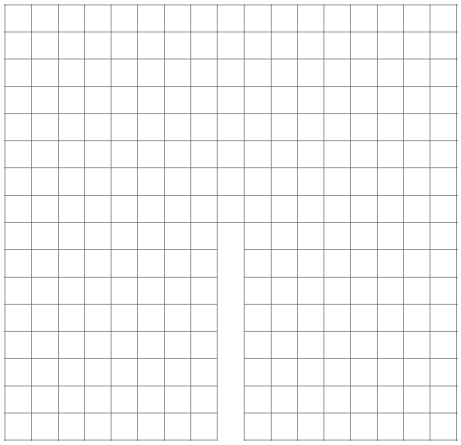

Figure 4. Detail of the mesh used for the Grégoire tests around the tip of the notch

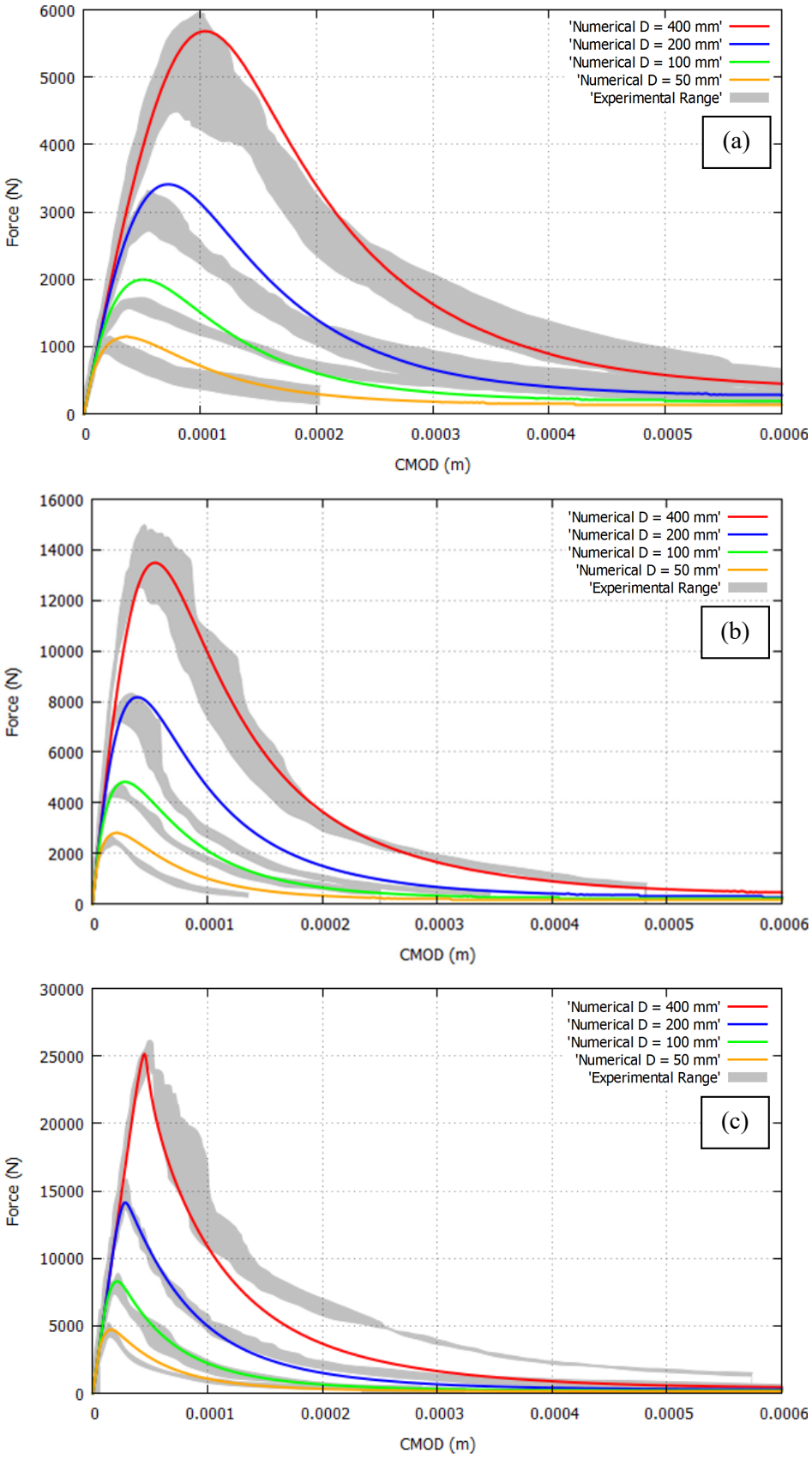

Figure 5. Force-CMOD curves of the Grégoire Tests for (a) the half-notched beams, (b) the fifth-notched beams and (c) the unnotched beams

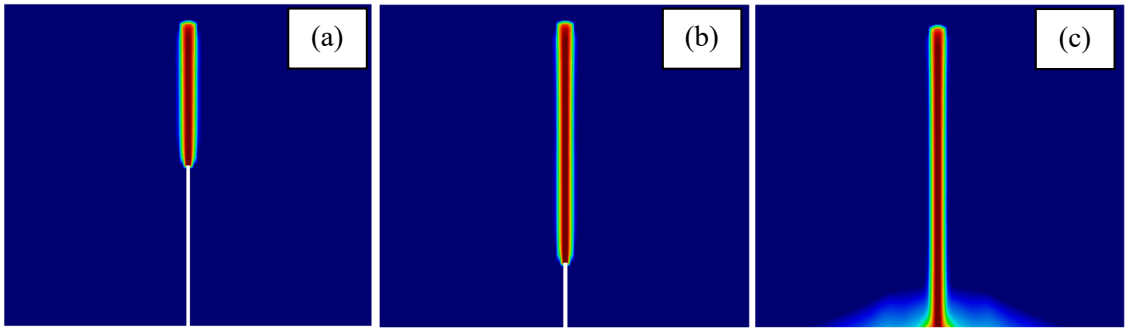

Figure 6. Damage contours of the Grégoire Tests in the 200 mm depth beams for (a) the half-notched case, (b) the fifth-notched case and (c) the unnotched case

Figure 6 shows the computed crack trajectories for the three different notch configurations of the beams with a depth of 200 mm. In all the beam sizes considered, the computed crack trajectory is a straight vertical line starting from the tip of the notch at the midpoint of the beam. For the unnotched series, an area of low value damage develops at the bottom midpoint of the beam prior to the strain localization.

5.2 Analysis of the Hoover tests: mode I fracture

In this second example, the numerical simulation of the beams of the Hoover experiments is considered. The tests are described in reference [44] and were repeated in reference [52]. Other numerical simulations of the tests can be found in references [25, 53-56]. To perform their computations, reference [25] used a phase-field model, references [53] and [54] considered nonlocal models, reference [55] employed a cohesive crack model and reference [56] compared the performance between a nonlocal model and the XFEM approach.

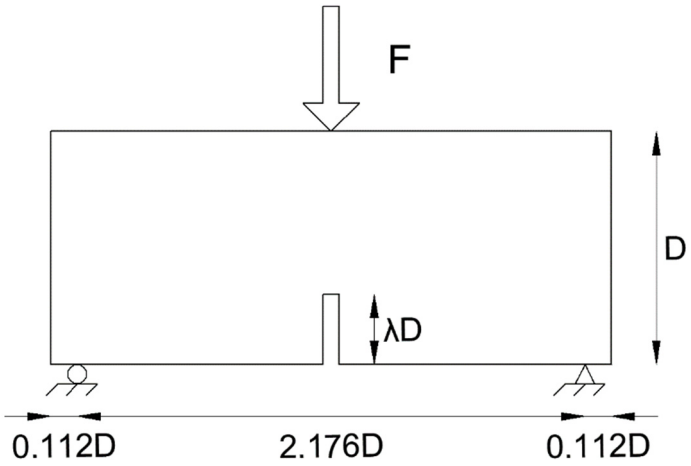

Figure 7. Geometry of the Hoover experimental tests

Young's Modulus	$41.0 \cdot 10^9$ Pa
Poisson's Ratio	0.17
Tensile Strength	$4.1 \cdot 10^6$ Pa
Tensile Fracture Energy	72.5 J/m^2
Irwin's material length	0.1768 m

Table 2. Material parameters of the Hoover tests

In the Hoover tests geometrically similar beams of varying sizes were subjected to three-point bending. The depths D of the tested units are 40 mm, 93 mm, 215 mm and 500 mm while the span-to-depth ratio was kept constant to 2.176. Five different notch-to-depth ratios λ were introduced: 0.3, 0.15, 0.075, 0.025 and 0.0 (unnotched). A constant thickness of 40 mm was kept for all the beam sizes. Details of the beam geometry are displayed in Figure 7. The beams are vertically loaded at the top midpoint. The simulations are done under CMOD control. Table 2 shows the material properties used for the Hoover tests. They are the same as the ones used for the numerical simulations reported in [25] and very close to the values recorded in the experiments.

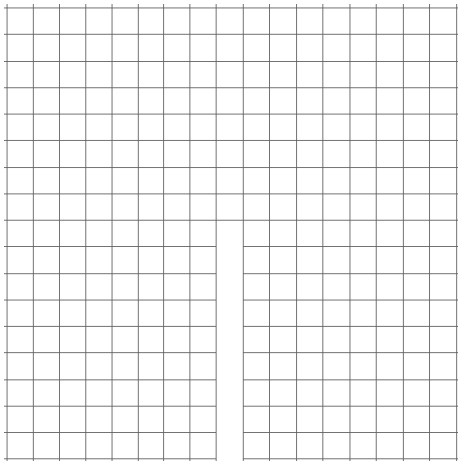

Figure 8. Detail of the mesh used for the Hoover tests around the tip of the notch

All the simulations are solved under the plane stress hypothesis using very similar structured meshes of 23970, 23985, 24092, 23898 and 23900 quadrilateral elements, depending on the notch configuration. The FE size is $10^{-2}D$, and the notch width is equal to the size of the element. In Figure 8, the detail of the mesh around the tip of the notch for the notch-to-depth ratio case of 0.3 is shown.

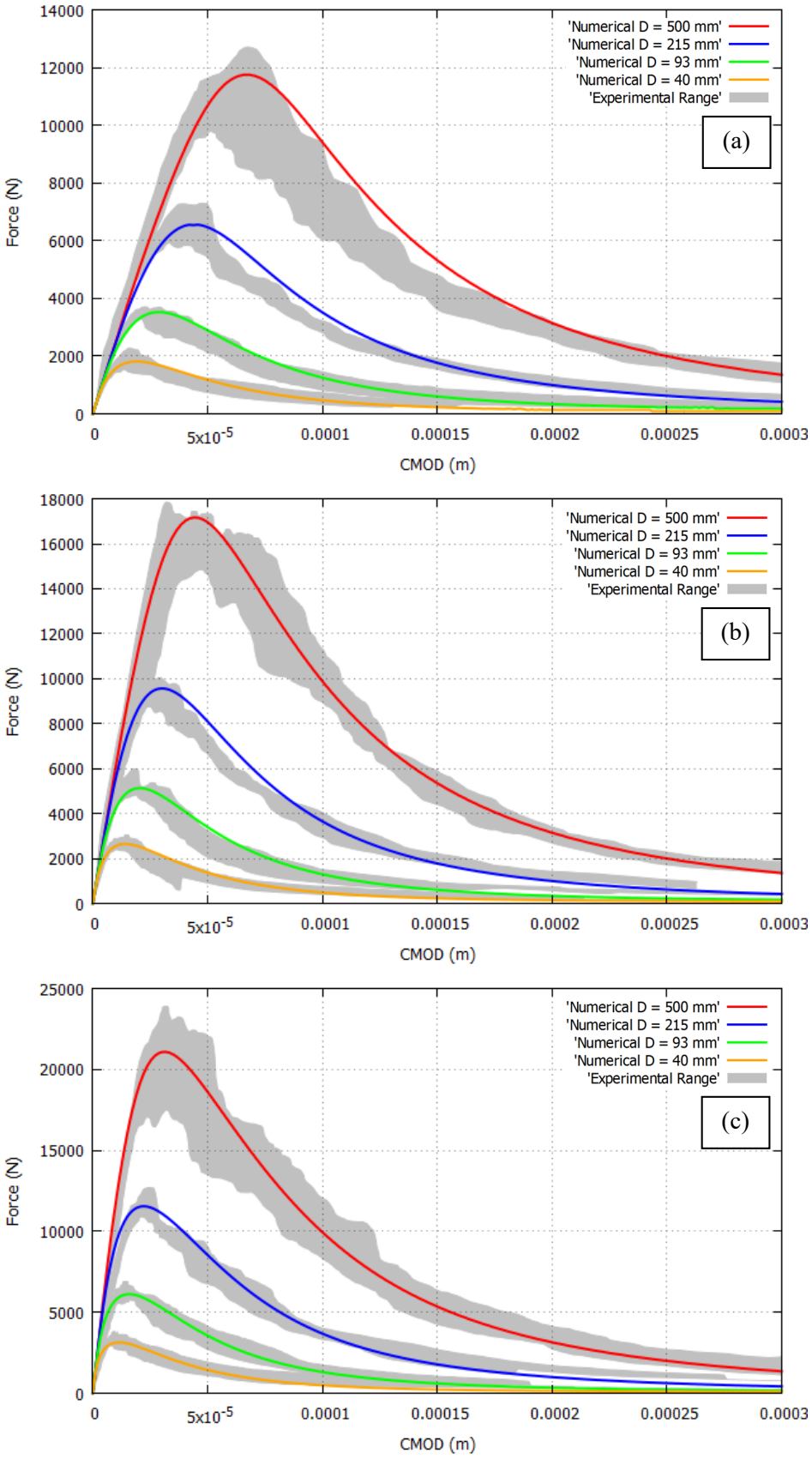

Figure 9. Force-CMOD curves of the Hoover Tests for notch to depth ratios of (a) 0.3, (b) 0.15 and (c) 0.075

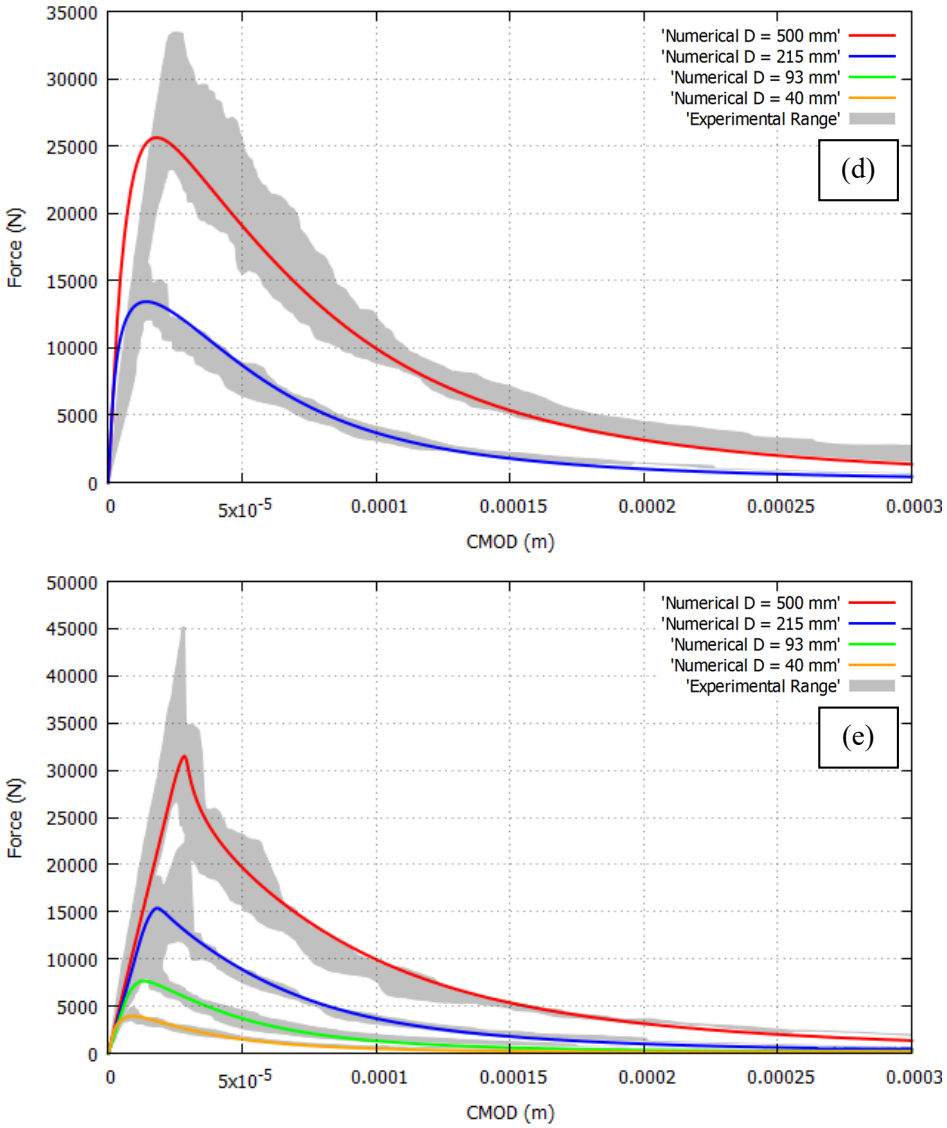

Figure 10. Force-CMOD curves of the Hoover Tests for notch to depth ratios of (d) 0.025 and (e) 0.0 (unnotched case)

Figures 9 and 10 display the obtained force-CMOD curves. It is shown how the computed peak loads are inside the experimental range reported in [44] for all the sizes and all the notch configurations. Furthermore, the calculated post-peak softening behavior is also inside the experimental envelopes in practically all the situations. Again, the computational model is able to reproduce the size effect behavior observed in the experiments using the same set of material properties for all the sizes and beams with different notch-to-depth ratios.

Figure 11 depicts the computed damage contours of the 40 mm depth beams for the different notch-to-depth ratios considered in the tests. The computed track trajectories form a straight vertical line for all the beam sizes. Cracks initiate at the tip of the notch in the notched specimens. Like in the Grégoire tests, an area of low value of damage develops at the bottom midpoint of the unnotched specimens prior to the development of the vertical crack.

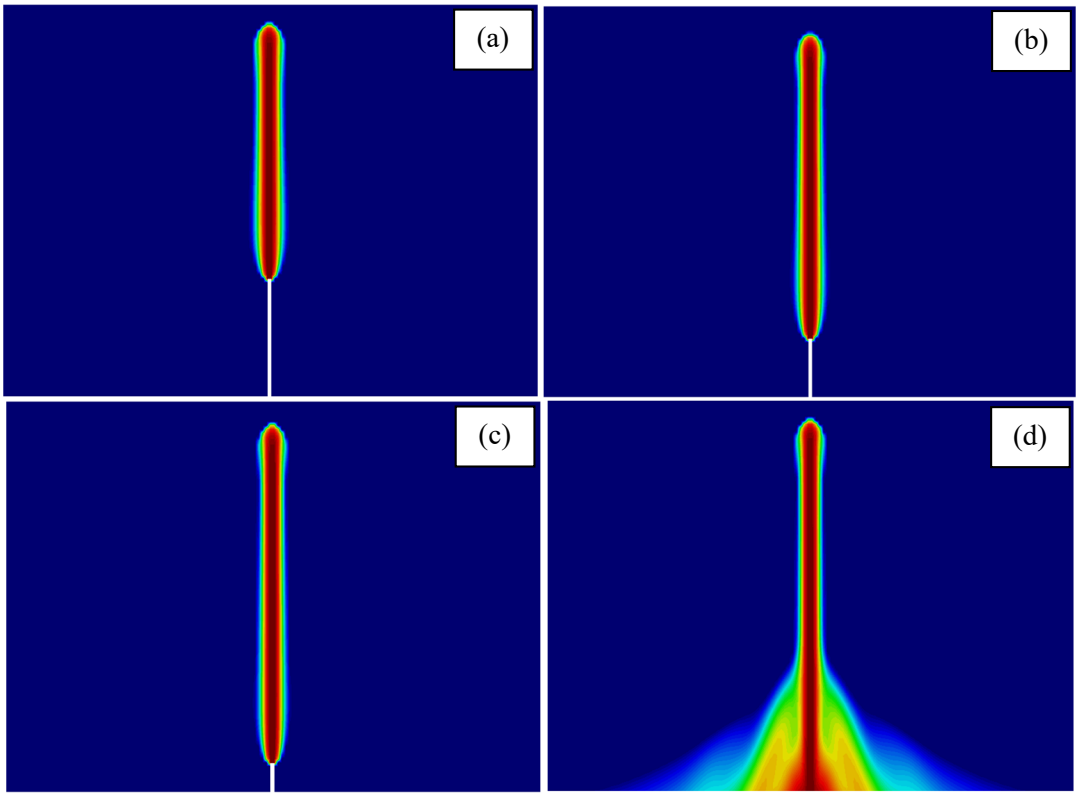

Figure 11. Damage contours of the Hoover Tests in the 40 mm depth beams for notch-to-depth ratios of (a) 0.3, (b) 0.15, (c) 0.075 and (d) 0.0 (unnotched case)

5.3 Analysis of the Garcia-Alvarez tests: mixed-mode fracture

In this section, the three-point bending tests performed by [45] are reproduced. In this case, an eccentricity of the notch was introduced in the beams, so that they are subjected to mixed-mode fracture. In [45] the experiments are also computationally modelled using interface elements. Other simulations of the results are reported in reference [25], where a phase-field approach is used.

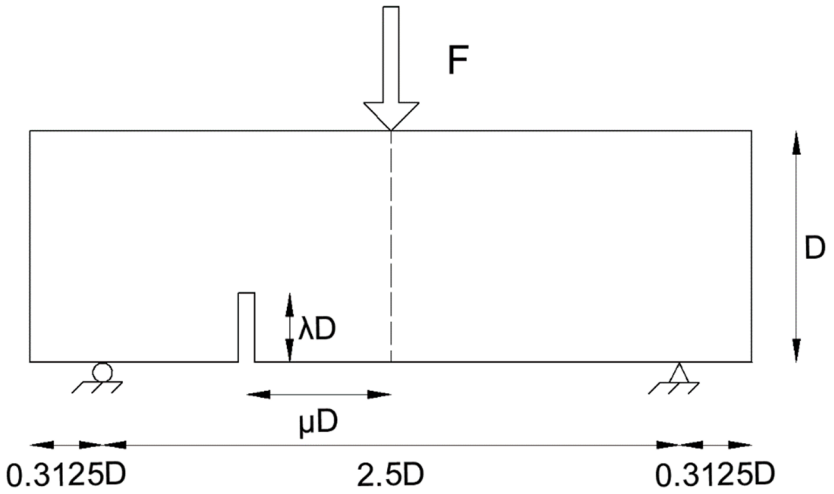

Figure 12. Geometry of the mixed-mode fractured beams

Young's Modulus	$33.8 \cdot 10^9$ Pa
Poisson's Ratio	0.2
Tensile Strength	$3.5 \cdot 10^6$ Pa
Tensile Fracture Energy	80 J/m^2
Irwin's material length	0.2207 m

Table 3. Material parameters for normal concrete strength in the mixed-mode fractured beams

Young's Modulus	$36.8 \cdot 10^9$ Pa
Poisson's Ratio	0.2
Tensile Strength	$6.0 \cdot 10^6$ Pa
Tensile Fracture Energy	120 J/m^2
Irwin's material length	0.1227 m

Table 4. Material parameters for high concrete strength in the mixed-mode fractured beams

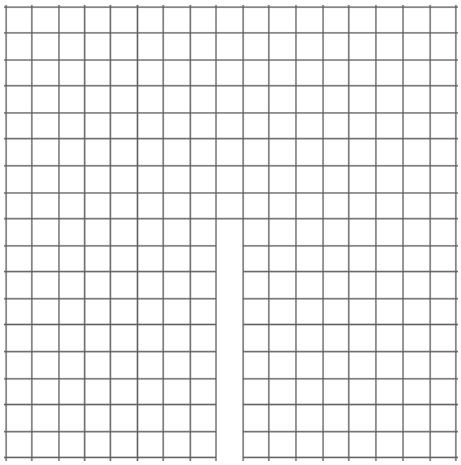

Figure 13. Detail of the mesh used for Garcia-Alvarez the mixed-mode fractured beams around the tip of the notch

Geometrically similar beams of depths D equal to 80 mm, 160 mm and 320 mm were tested while the span-to-depth ratio was kept constant to 2.5. Three different series were considered, where different notch eccentricities μD of $0.625D$, $0.3125D$ and $0.0D$ were introduced. The notch-to-depth ratio λ is 0.25 in all beams. The thickness of all the beams is 50 mm. The details of the geometry of the beams are shown in Figure 12. The material properties used in the present work are shown in Table 3. They are identical to the ones reported in [45] as well as the ones used in the corresponding numerical simulations in [25]. A vertical force is applied at the top midpoint of all the beams. The numerical simulations are performed under CMOD control.

In addition, a supplementary series of experiments is reported in [45], where high strength concrete was employed, instead of normal strength concrete. The beam depths were again 80 mm, 160 mm and 320 mm. In this case, no eccentricity was considered ($\mu = 0.0$) and the notch-to-depth ratio λ was 0.275. The material properties used to simulate the high concrete strength case, which are again the same as the ones reported in [45], are shown in Table 4.

All the simulations are solved under the plane stress hypothesis using very similar structured meshes of approximately 31000 quadrilateral elements, depending on the notch configuration. The size of the finite elements is $10^{-2}D$ and the width of the notch is set equal to the element size. In Figure 13, the detail around the tip of the notch of the mesh used for the case with an eccentricity of $0.625D$ is shown.

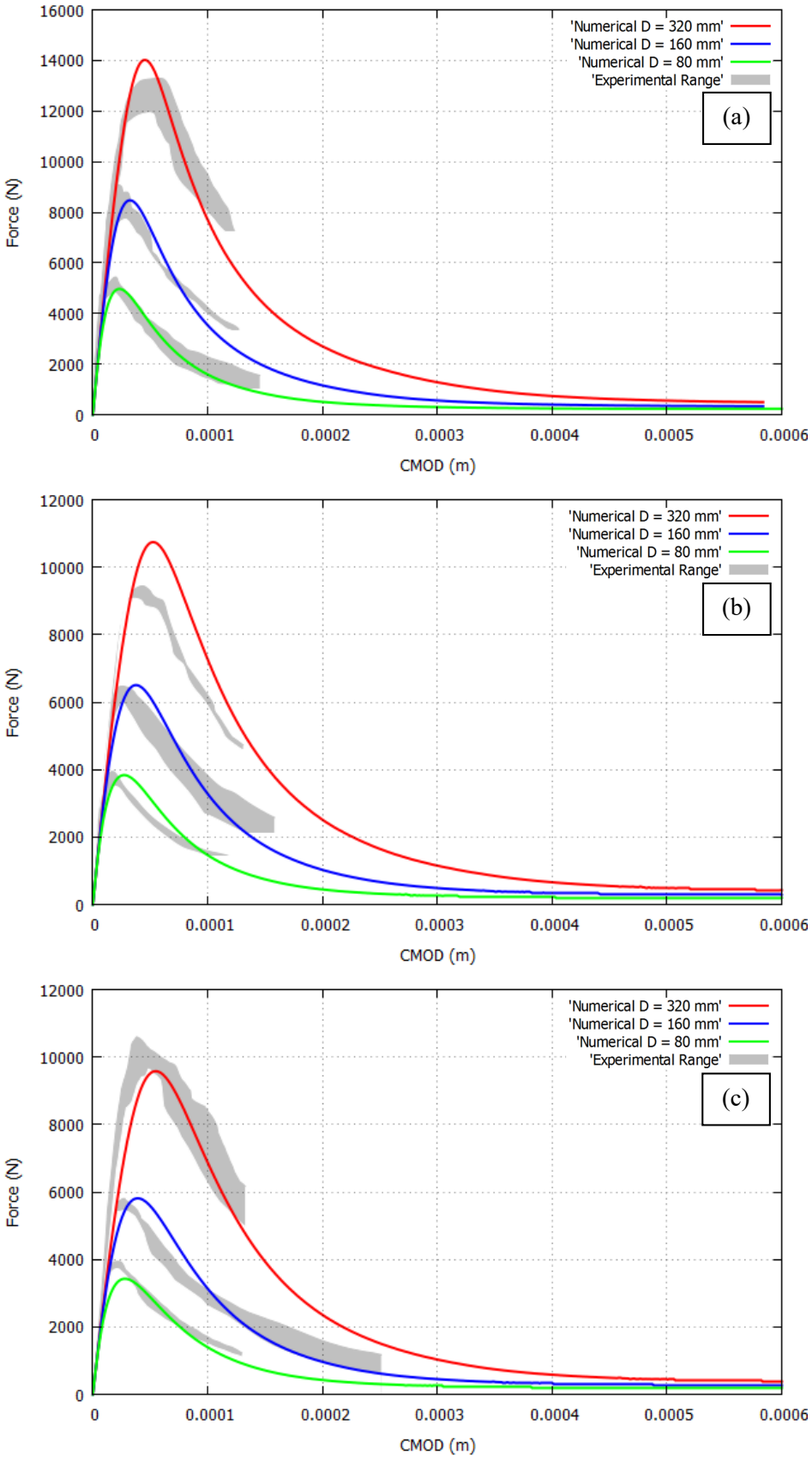

Figure 14. Force-CMOD curves of the mixed-mode fractured beams for the normal concrete strength specimens with eccentricities of (a) 0.625*D*, (b) 0.3125*D* and (c) 0.0*D*

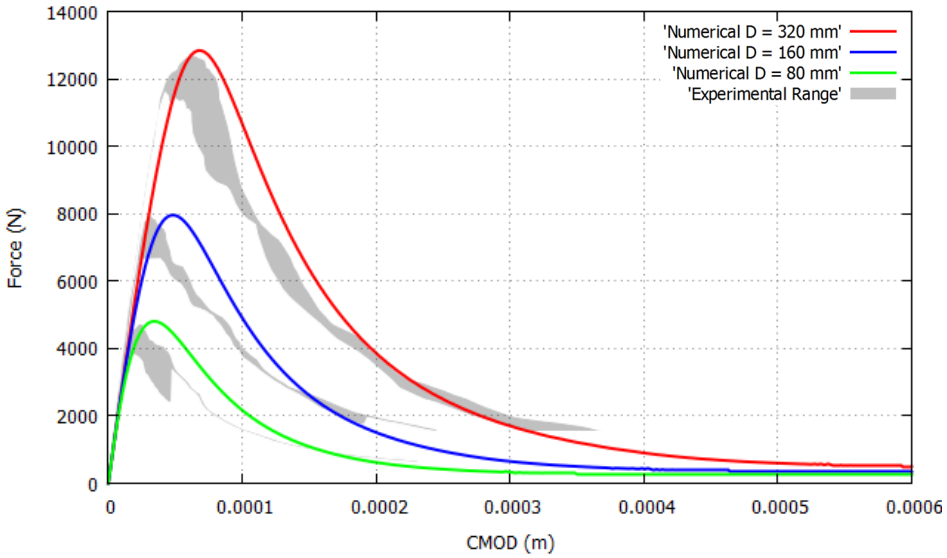

Figure 15. Force-CMOD curves of the mixed-mode fractured beams for the high concrete strength specimens

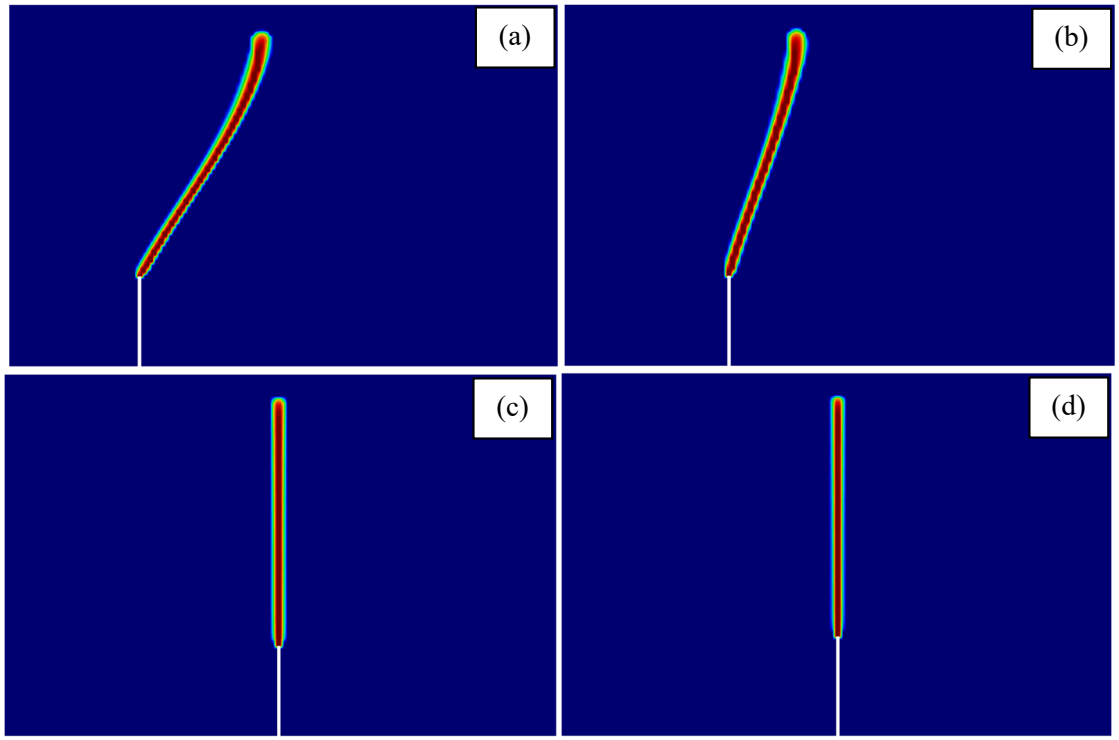

Figure 16. Damage contours of the mixed-mode fractured beams in the 320 mm depth case for the normal concrete strength specimens with eccentricities (a) 0.625*D*, (b) 0.3125*D* and (c) 0.0*D* and for (d) the high concrete strength specimens

Figures 14 and 15 show the force-CMOD curves obtained for the normal and high concrete specimens. Once more it can be seen that the results in terms of peak loads and post-peak softening curves are very similar to the experiments in all the cases. The agreement with the limited data documented from the tests is notable. The same set of material properties produce very reasonable simulations of the force-CMOD curves when compared with the narrow experimental range provided.

Figure 16 depicts the damage contours computed in the 320 mm depth beams for the different eccentricities contemplated in the tests for normal and high strength concretes. The cases with no eccentricity produce a vertical straight line for all the sizes. In the specimens with eccentricity the crack trajectories start at the tip of the notch and deviate towards the center of the beam where the vertical load is applied.

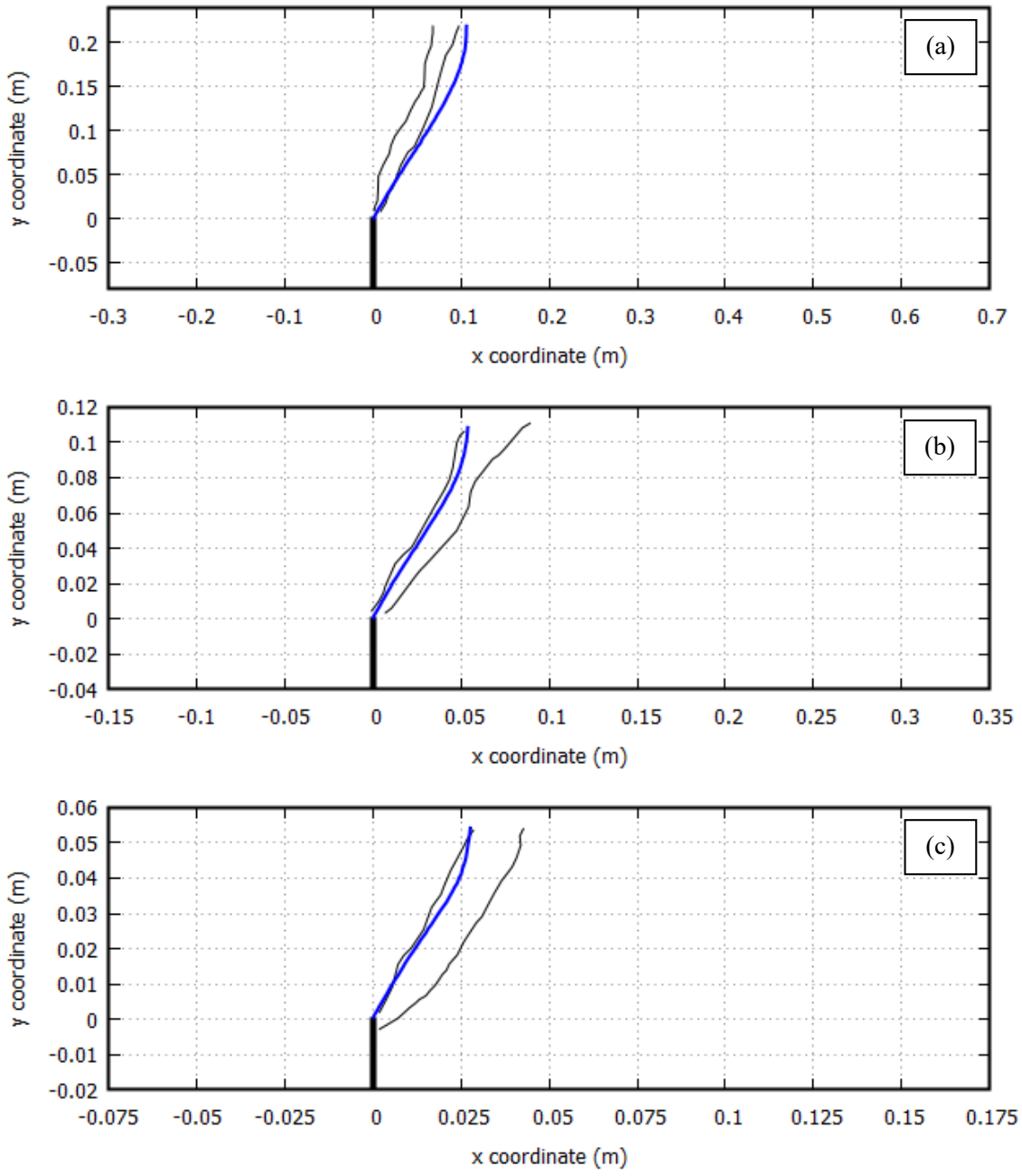

Figure 17. Computed crack paths compared to the experimental results of the mixed-mode fractured beams with a notch eccentricity of 0.625*D* for depths (a) 320 mm, (b) 160 mm and (c) 80 mm

The computed crack trajectories of the beams with eccentricities 0.625*D* and 0.3125*D* are compared in detail for all the sizes with the experimental results in Figures 17 and 18, respectively. It can be seen that the computed crack paths show very good agreement with the test results. In all the cases except the first one the crack is inside the experimental range. The overall

behavior of the model is considered very satisfactory given the limited data of the experiments provided and the simplicity of the material model considered, an isotropic damage model. The Drucker-Prager criterion is more suitable for mixed-mode cracking, as shown in reference [30]. However, for the numerical simulations of these experiments, the Rankine damage model produces satisfactory results in terms of crack trajectories and force-displacement curves when compared to the test results and is able to properly capture the observed size effect phenomenon.

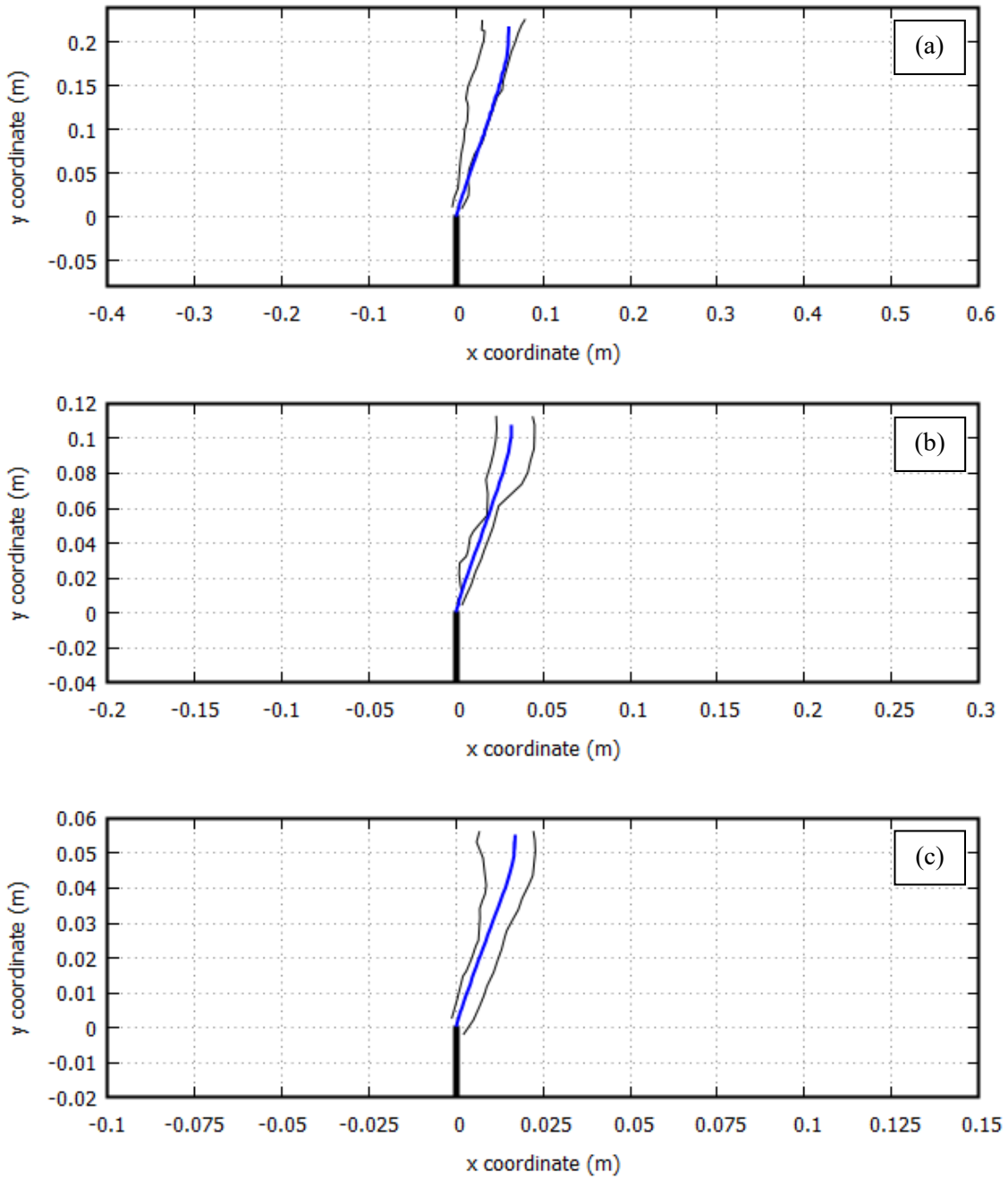

Figure 18. Computed crack paths compared to the experimental results of the mixed-mode fractured beams with a notch eccentricity of 0.3125*D* for depths (a) 320 mm, (b) 160 mm and (c) 80 mm

6 Mesh dependence study

In this section the performance of the mixed FE formulation is assessed. The sensitivity of the computed results with regard to the mesh used is analyzed. First, a comparison between 2D and 3D computations is considered. Then, solutions obtained with different mesh sizes and orientations are also contrasted. At the end of this section, a mesh independence study is also carried out comparing with standard irreducible linear and quadratic FE.

6.1 2D vs 3D simulations

In this section, the computed results obtained in 2D for the mixed-mode fractured beams in Section 5.3 are compared with corresponding 3D simulations. Specifically, the series with a notch eccentricity of $0.625D$ is taken into account for this study. The objective of this section is to show the capacity of the proposed model to accurately simulate the experiments in 3D and, reciprocally, to assess the plane stress hypothesis commonly used in beam analysis. The material properties of the simulation are the same as those used in 2D, shown in Table 3. The simulations of this section are performed with a mesh of 18475 hexahedral elements. The size of the FEs in the mesh used is $10^{-2}D$ in the central part where the crack forms and of $3.125 \cdot 10^{-2}D$ in the rest of the beam. The notch width is also equal to $10^{-2}D$.

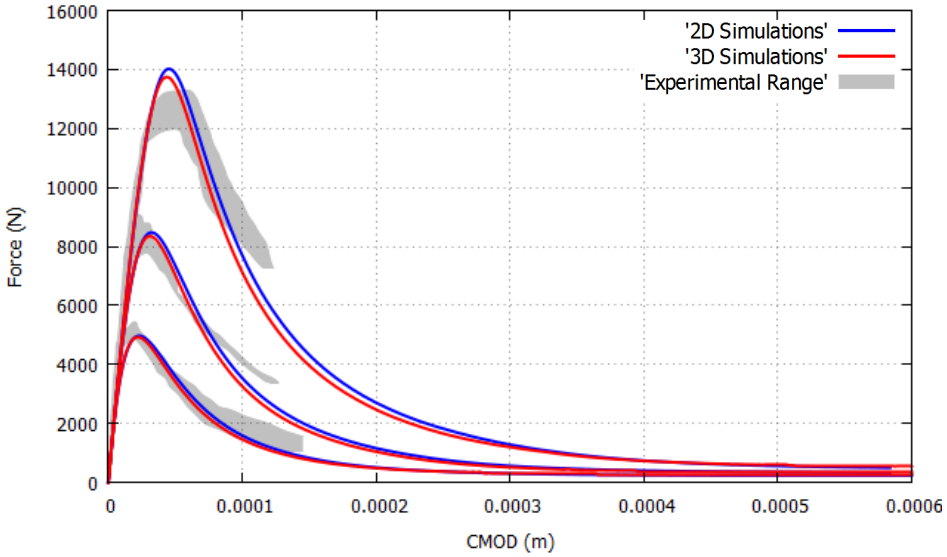

Figure 19. Force-CMOD curves of the mixed-mode fractured beams for the specimens with eccentricities of $0.625D$, in 2D and 3D

In the computed force-CMOD curves shown in Figure 19 the 2D and 3D results are almost overlapping and very close to the experimental range for all the sizes. The 2D numerical simulations produce a slightly larger peak load than in 3D. Force-displacement curves computed in 2D under the plane stress hypothesis are typically an upper bound to 3D results. The small difference is due to the disregardance of the out-of-plane stress components in the 2D simulation. In addition, the computed crack paths displayed in Figure 20 also show almost identical results and with good agreement with the test data. The crack surfaces obtained in the 3D analyses are depicted in Figure 21, showing the capacity of the model to accurately compute the 3D fracture surfaces that occur under mixed-mode fracture. This confirms that the plane stress hypothesis used to compute the results in 2D is appropriate for simulating the beam experiments.

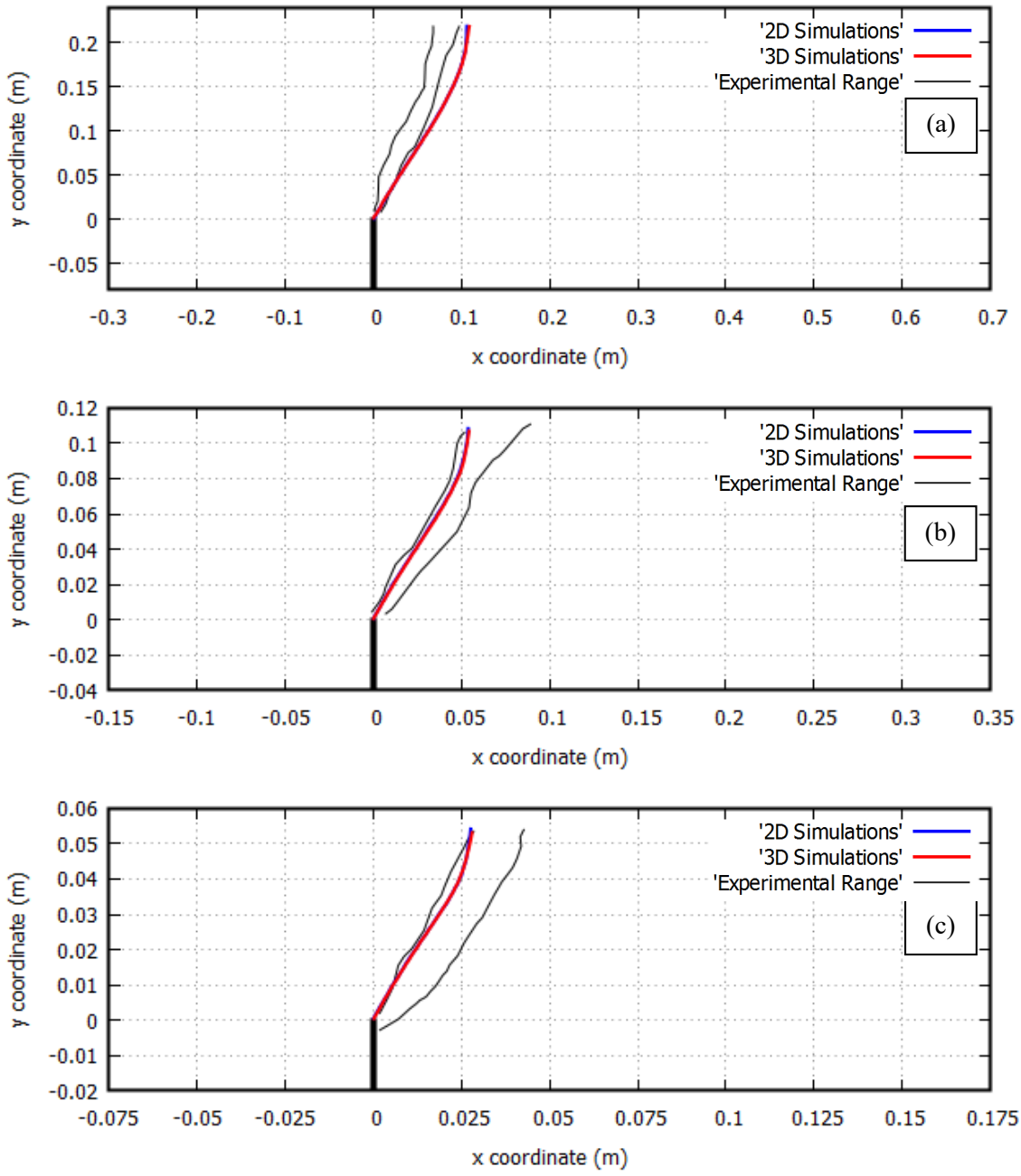

Figure 20. Computed crack paths in 2D and 3D of the mixed-mode fractured beams with a notch eccentricity of 0.625*D* for depths (a) 320 mm, (b) 160 mm and (c) 80 mm

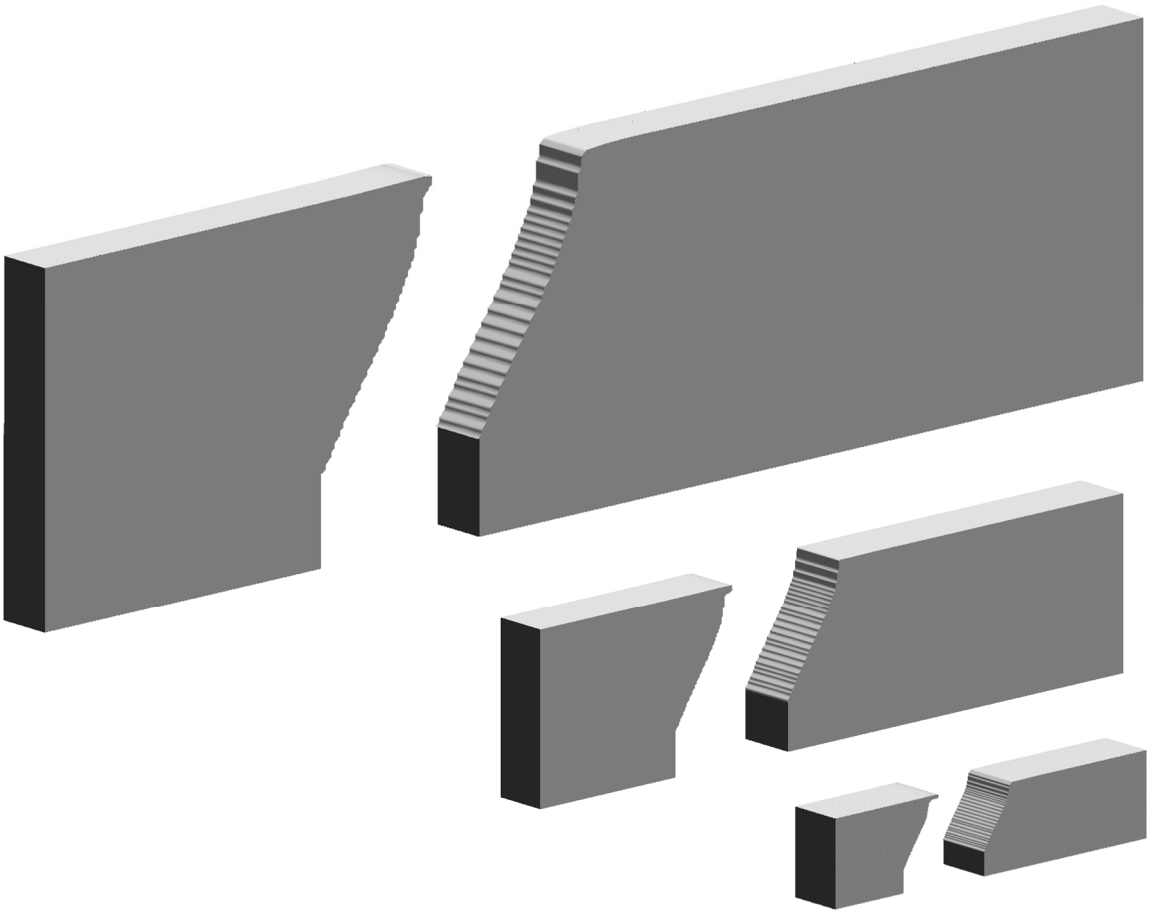

Figure 21. Computed crack surfaces of the mixed-mode fractured beams with eccentricity 0.625*D* for the three sizes of the series

6.2 Mesh independence study with mixed FE

The objective of the present section is to assess the capability of the mixed FE formulation of obtaining mesh-objective results with regard FE size and orientation. For this, the computation of the specimen with depth D of 80 mm and a notch eccentricity of $0.3125D$ of the mixed mode fracture tests reported in Section 5.3 is considered. Four different meshes are used for this study: (1) a 31175 quadrilateral element structured mesh already used in Section 5.3, (2) a 64700 quadrilateral element structured mesh, (3) a 36714 triangular element unstructured mesh and (4) a 126530 triangular element unstructured mesh. Meshes (1) and (3) have a FE size corresponding to $10^{-2}D$ in the center of the beam while in (2) and (4) the FE size is equal to $5\cdot10^{-3}D$ in the center of the beam. In all the cases, the width of the notch is equivalent to $10^{-2}D$. Different element orientations have been chosen for the triangular and quadrilateral meshes to test the mesh size and bias dependence of the computed results, as it can be seen in Figure 22.

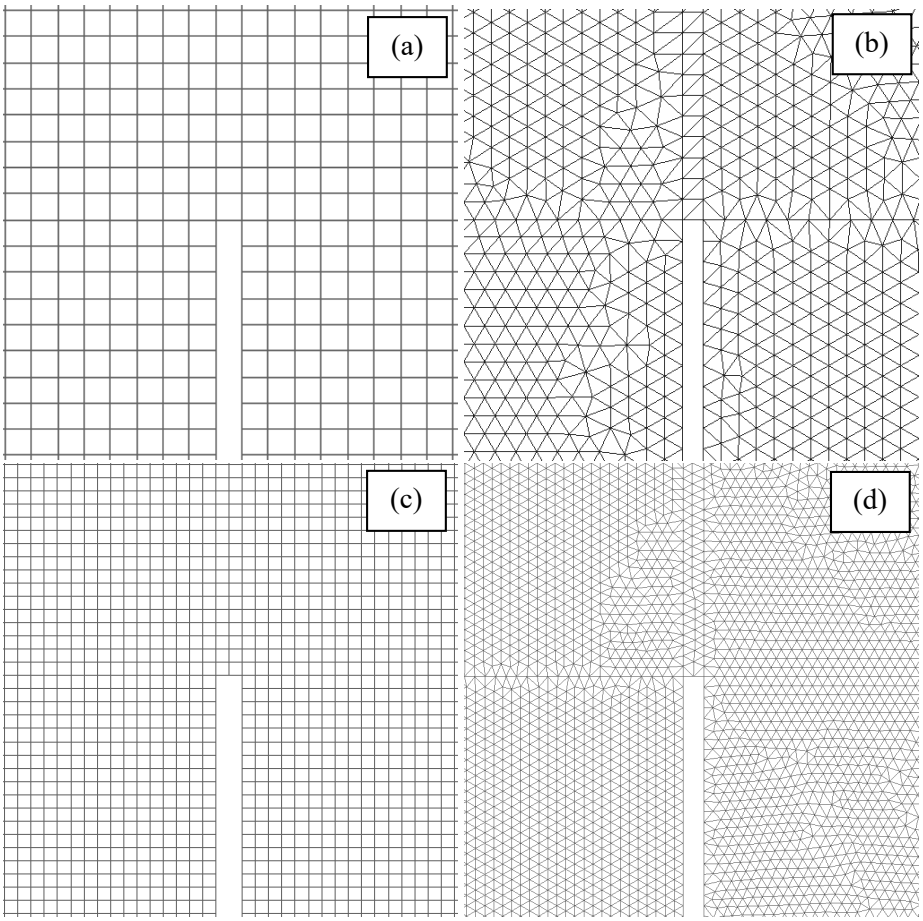

Figure 22. Detail of the mesh around the notch tip used for the mixed-mode fractured beams with (a) 31175 quadrilateral elements, (b) 36714 triangular elements, (c) 64700 quadrilateral elements and (d) 126530 triangular elements

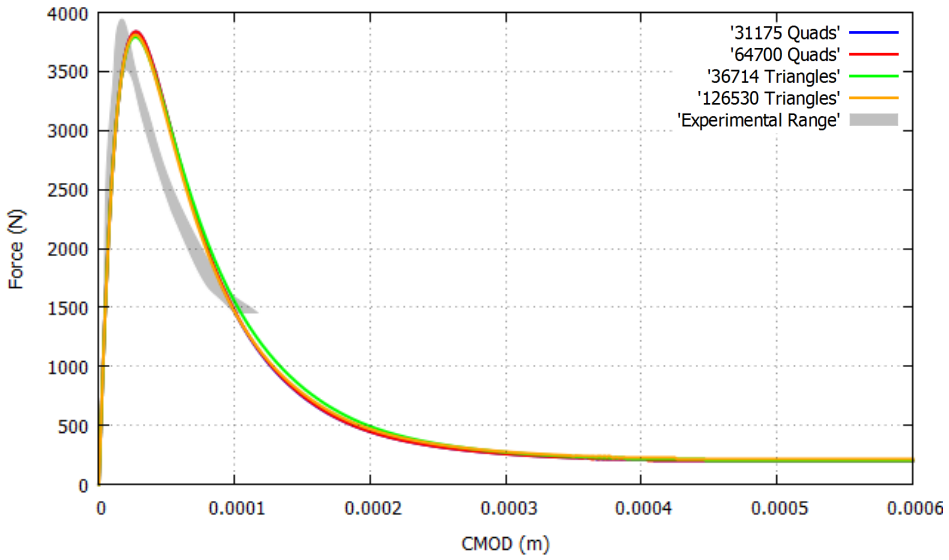

Figure 23. Force-CMOD curves of the mixed-mode fractured beams for the 80 mm depth specimen with 0.3125*D* eccentricity for the different meshes considered

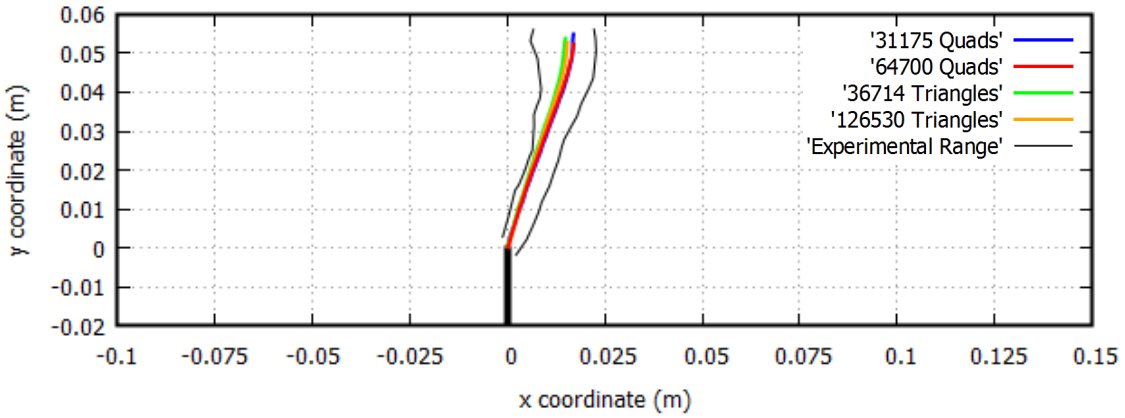

Figure 24. Computed crack paths of the mixed-mode fractured beams for the 80 mm depth specimen with 0.3125*D* eccentricity for the different meshes considered

Figure 23 shows the force-CMOD results obtained with the 4 different meshes. It can be seen that the results for all the meshes are almost overlapping and very close to the experimental result. The computed crack paths for the 4 meshes are depicted in Figure 24. They are all of them almost identical, the difference between each other being of the order of the FE size h.

Therefore, it can be concluded that: (1) the computed results are converged in terms of mesh size, (2) the mixed finite element formulation used is practically mesh-independent and does not show any spurious mesh-orientation bias.

6.3 Standard vs Mixed FE

In this section a comparison of the performance of standard and mixed FE is carried out. For this, the numerical simulation of the specimen with depth D of 80 mm and a notch eccentricity of $0.3125D$ of the mixed mode fracture tests of Section 5.3 is considered again. The computations using standard and mixed FE are compared for two different meshes: (1) the 31175 quadrilateral element mesh shown in Figure 22a and (2) the 36714 triangular element mesh depicted in Figure 22b.

In Figure 25 it can be seen that the force-CMOD computations for the standard and mixed FE are very close. This is significant because, as shown in Figure 26, the computed crack trajectories of the standard FE are completely off-mark, demonstrating the spurious mesh bias of this element while the paths obtained with mixed FE are inside the experimental range.

Finally, 3D simulations have been performed to further illustrate the spurious mesh dependence of standard FE. For this, considering the same specimen, an 18475 hexahedral element mesh has been used to assess the performance of standard tri-linear elements, standard tri-quadratic and mixed tri-linear FE. The size of the mesh is $10^{-2}D$ in the central part where the crack forms and of $3.125 \cdot 10^{-2}D$ in the rest of the beam. The notch width is also equal to $10^{-2}D$.

Figure 27 depicts the computed crack paths of the three simulations. On the one hand, it can be seen again how the linear standard formulation produces severely mesh dependent results. The results obtained with quadratic standard elements are closer to experimental range than the ones obtained with linear standard FE, but it is clearly visible that they suffer from spurious mesh dependence. On the other hand, the results computed with mixed FE are inside the experimental range. This can be seen in detail in Figure 28, where the computed 3D crack surfaces with the three elements are shown.

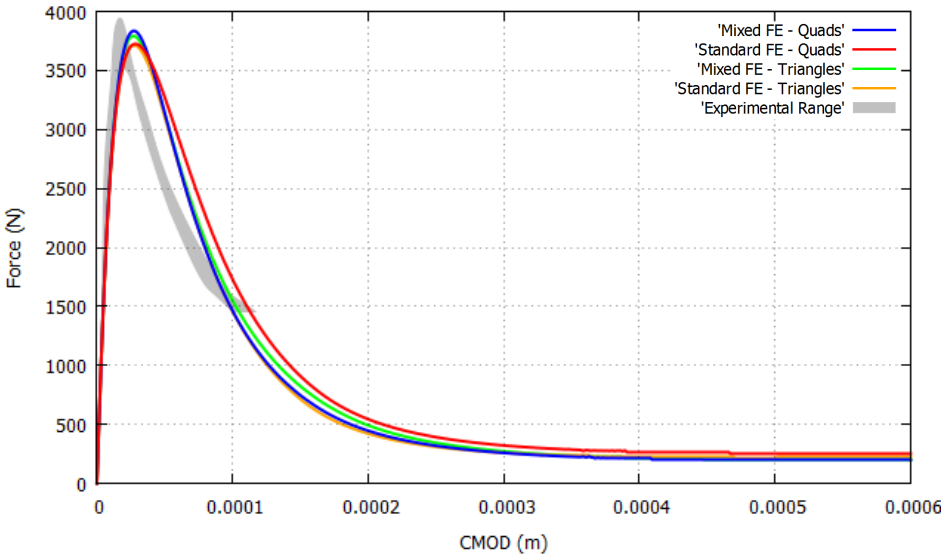

Figure 25. Force-CMOD curves of the mixed-mode fractured beams for the 80 mm depth specimen with 0.3125*D* eccentricity for standard and mixed FE

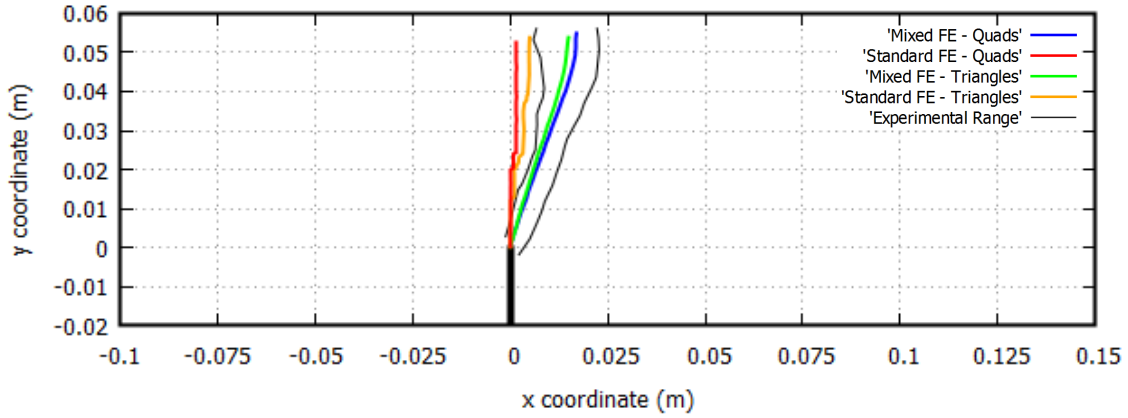

Figure 26. Computed crack paths of the mixed-mode fractured beams for the 80 mm depth specimen with 0.3125*D* eccentricity for standard and mixed FE

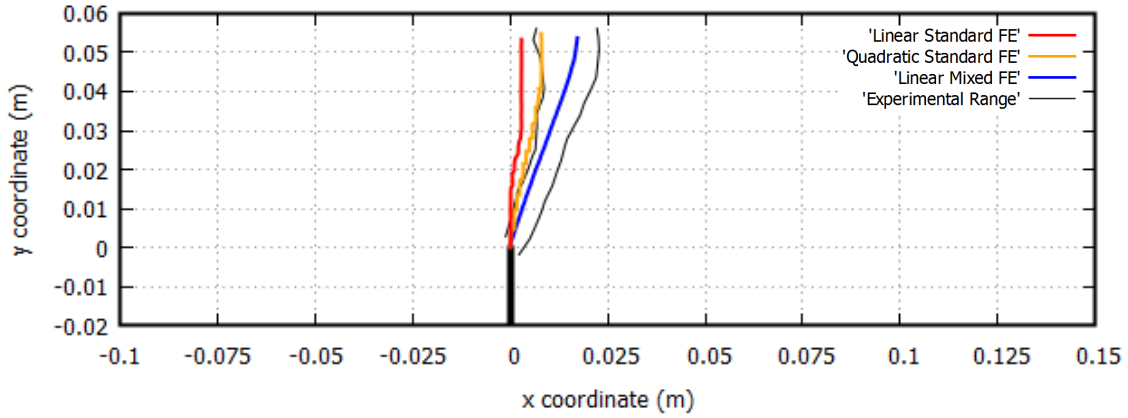

Figure 27. Computed crack paths of the mixed-mode fractured beams for the 80 mm depth specimen with 0.3125*D* eccentricity in 3D for standard and mixed FE

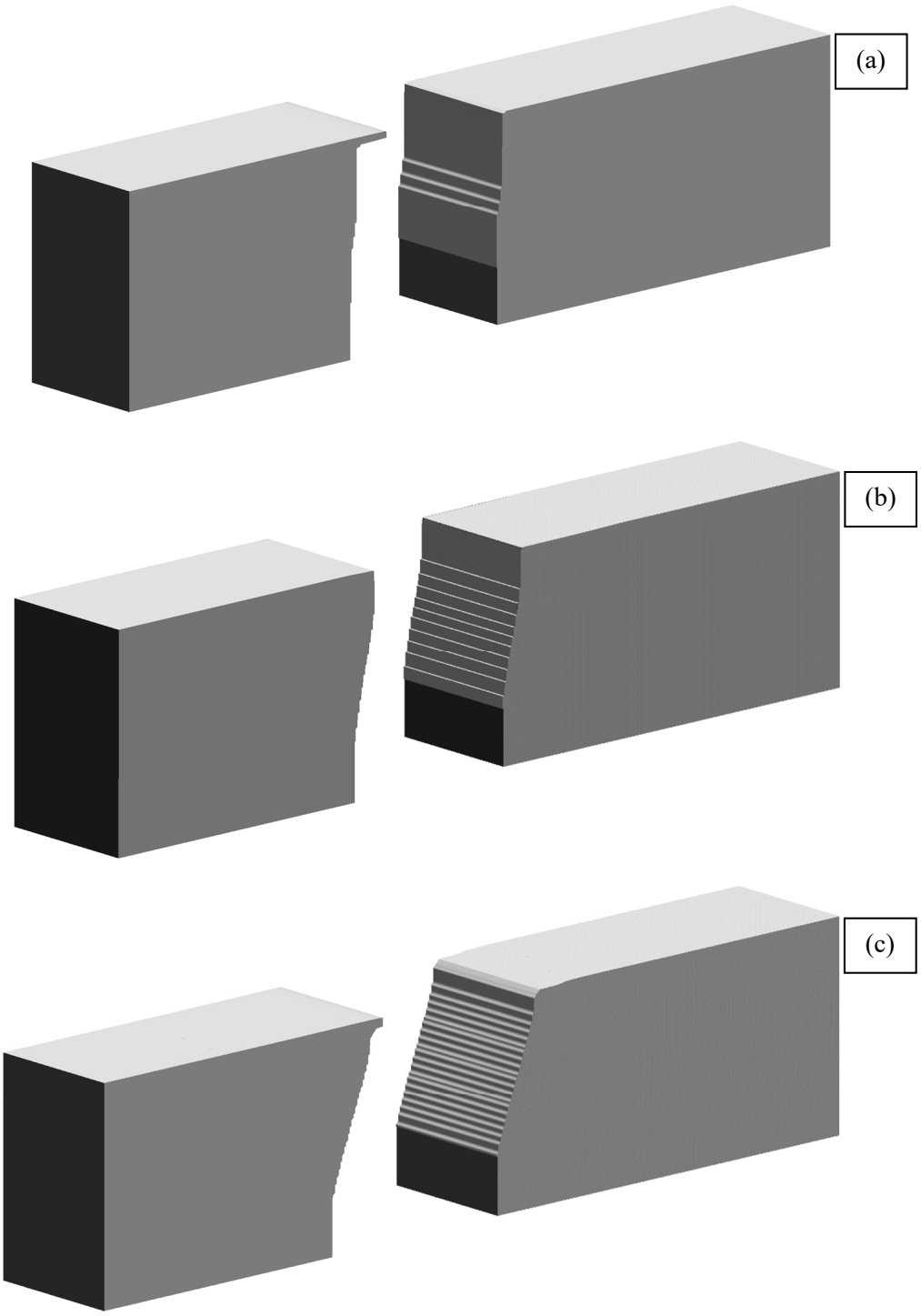

Figure 28. Computed crack surfaces of the mixed-mode fractured beams for the 80 mm depth specimen with 0.3125*D* eccentricity with (a) linear standard FE, (b) quadratic standard FE and (c) linear mixed FE

7 Influence of the statistical variability of the mechanical properties

The objective of this section is to analyse the influence of the statistical size effect compared to the impact that the release of stored energy has on the size effect phenomenon. It has been stated by Bazant and Planas in reference [1] that

> "*Statistical size effect ... is caused by the randomness of material strength and has traditionally been believed to explain most size effects in concrete structures. ... However, ... on closer scrutiny, this explanation is found to be inapplicable to most types of failures of reinforced concrete structures. ... Concrete structures fail only after a large stable growth of cracking zones or fractures. The stable crack growth causes large stress redistributions and a release of stored energy, which, in turn, causes a much stronger size effect, dominating over any possible statistical size effect. At the same time, the mechanics of failure restricts the possible locations of the decisive crack growth at the moment of failure to a very small zone. This causes the random strength values outside this zone to become irrelevant, thus suppressing the statistical size effect.* "

In the analysis of this section the beams of the Hoover series corresponding to the notch-to-depth ratio of 0.075 are computed considering the statistical variability of the mechanical properties of the material that was reported in [44, 52]. In the present study, only the variability of the Young modulus E, the tensile strength f_t and the fracture energy G_f are considered, as they are deemed to be the most influential in the structural response.

CV Young's Modulus	5%
CV Tensile Strength	3.5%
CV Tensile Fracture Energy	17%

Table 5. Coefficients of variation of the material parameters adopted for the Hoover tests

An accurate study of the relative influence of the deterministic and stochastic sources of size effect in quasi-brittle materials would necessarily include a certain number of numerical simulations where different material properties are randomly assigned to each finite element according to a probability density function and a spatial autocorrelation function.

R	Young's Modulus ($x10^{10}$ Pa)	Tensile Strength ($x10^{6}$ Pa)	Tensile Fracture Energy (J/m2)
1	4.1647	3.9172	68.219
2	4.2129	4.3060	77.698
3	3.8494	4.3789	88.638
4	4.3171	4.0705	75.954
5	4.1522	4.0352	84.161
6	3.9682	4.2678	56.885
7	4.4500	4.1607	82.345
8	4.0652	4.0529	58.623
9	3.7394	4.0908	81.015

Table 6. Sets of random properties generated for the Hoover tests

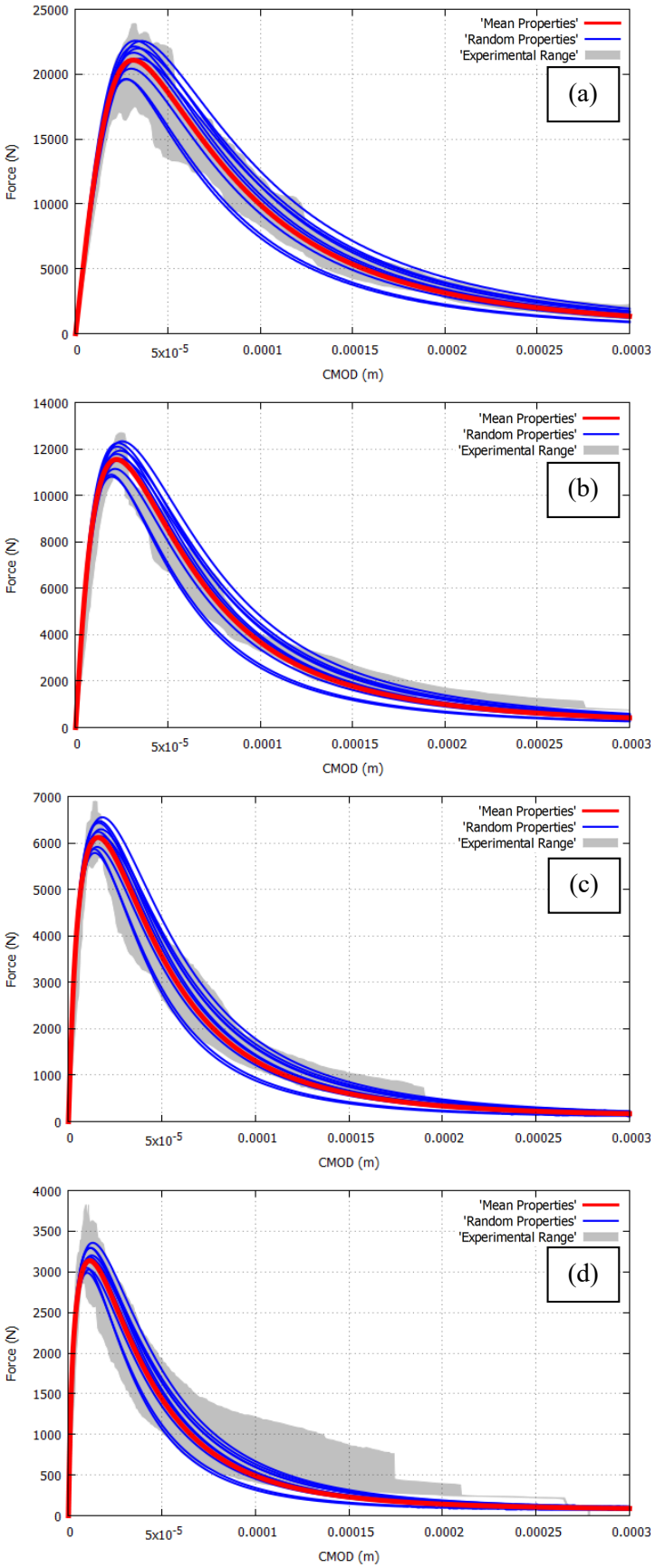

Figure 29. Force-CMOD curves of the Hoover Tests with the random properties generated, notch-to-depth ratio 0.075, for depths (a) 500 mm, (b) 215 mm, (c) 93 mm and (d) 40 mm

This process is here circumvented on the consideration that, even when the variability of the material is taken into account with the aforementioned method, for large enough specimens of quasi-brittle materials the crack is going to localize through a band of elements which represents a small percentage of the total number of elements. The behavior of the whole specimen is going to be determined by the material parameters of the very few elements located at the crack path. When considering as well the spatial correlation of the material properties, an effective and simpler way to tackle the issue is to assign to the whole body the same equivalent set of random parameters generated according to a certain probability density function.

Of course it is necessary to keep in mind the limitations of the present simplified approach to statistical size effect. On the one hand, in reference [57] it is shown that for small enough specimens, where the previous considerations are no longer acceptable, the influence of statistical size effect increases significantly. To consider that case, performing the simulations with varying properties in each element is mandatory. On the other hand, reference [33] states that for very large unnotched structures, where a very brittle failure takes place as soon as the fracture process starts, statistical size effect also becomes significant. However, for the sizes used in the Hoover tests the present simplified approach is deemed accurate enough.

For the computations of this section, it is assumed that the three material properties considered follow a Gaussian distribution. The mean values of the three properties are taken as the ones already used in the simulations of the present work in Table 2. The coefficients of variation adopted in this work (displayed in Table 5) are the ones reported in [44, 52]. With this data, 9 different sets of properties have been randomly generated, noted R1 to R9 and are shown in Table 6. These properties are used to simulate the four sizes of the Hoover beam series with a notch-to-depth ratio of 0.075.

The computed force-CMOD curves are shown in Figure 29. It can be seen how all the different randomly generated sets of properties produce results with good agreement with the experiments for all the sizes. In all the cases the values of the peak loads are inside the experimental range. The post-peak softening numerical result is very similar to the behavior observed in the tests. The ranges of numerical results generated overlap quite satisfactorily with the experimental envelopes. In this case the impact of statistical size effect is small and the size effect phenomenon can be sufficiently reproduced considering only the influence of the release of stored energy.

8 Size effect law predictions

It has been shown so far that the proposed model based on the mixed finite element formulation together with the proper constitutive law is able to reproduce with accuracy the size effect phenomena observed in experiments. The objective of this section is to perform a comprehensive analysis of the size effect phenomenon. For this, numerical simulations have been carried out for an extended range of sizes in notched and unnotched beams. The aptness of the model in reproducing the behavior theoretically expected is assessed in detail.

The Grégoire tests are considered for computing predictions of the behavior of notched and unnotched beams over a large interval of sizes. Specifically, the Grégoire series with a notch-to-depth ratio of 0.2 and 0.0 are contemplated. When taking the case with depth 400 mm as reference, computations with geometries scaled up to 10^2 times (and even more for the notched specimen) and 10^{-4} times smaller have been performed. In all the cases the same material properties from Table 1 are used and the thickness of the beam is kept constant to 50 mm.

Given the extensive range of sizes considered, there are several obvious factors that may alter the outcome of the extremely large and small tests that are not taken into consideration in the simulations performed in this section. In particular, the impact of the other sources of size effect

might increase. Considering the practical impossibility of performing the really big and really small scale tests in laboratory, the corresponding simulations presented are to be seen as a study of the limit cases for size effect.

In this section, the nominal strength σ_{N_u}, or peak nominal stress, is defined as

$$\sigma_{N_u} = \frac{P_u}{Db} \tag{31}$$

where P_u is the peak load, D is the depth of the beam and b is the thickness.

Unnotched beam size effect predictions

In Figure 30, the damage and maximum principal strain contour fills computed for a few cases are shown to demonstrate the change in the failure mode that happens when the size of the unnotched beam varies. The same mesh as the one used in the simulations of Section 5.1 is employed for all the scales. It can be seen that the mechanics of collapse are different for small and large size beams. When the beam is large enough, the structure fails as soon as the damage criterion is reached at the bottom midpoint of the beam and a vertical crack suddenly appears. When the size is small enough, damage develops over an extensive area before a collapse mechanism is formed and failure is due to the development in the center of the beam of a perfect hinge. As size increases, the observed mechanism tends from one limit case to the other. This is the source for structural size effect.

As it was observed in previous sections, in unnotched beams of medium sizes an area of low value damage develops at the bottom midsection of the beam prior to the strain localization. Note that this area is nonexistent in the larger beams and becomes bigger as size decreases. Note also that even though the damaged area can become large when size decreases, strain localization in a narrow band is properly taking place in the computed strain field for all the sizes. As the energy dissipated in the plastic limit is proportional to the inelastic strain developed, the correct strain localization pattern shows that energy is correctly dissipated even if the damaged zone is more extensive.

The peak load of both the small and large limit cases can be readily computed. Statics show that the maximum bending moment under three-point bending occurs at the midsection of the beam

$$M_{max} = \frac{1}{4} P_u \, 2.5D = \frac{5}{8} P_u D \tag{32}$$

In the small size limit, the peak load can be derived from the limit analysis of the beam. The structure fails when a hinge develops at the midsection of the beam. As only tensile damage is considered, the maximum bending moment that the cross section can sustain is attained when the entire section of the beam carries the tensile maximum stress f_t. With this stress distribution, the neutral axis is located at the top of the mid cross section and the bending moment of the beam at the midsection is

$$M_u = \frac{1}{2} D^2 b f_t \tag{33}$$

Therefore, equating (32) and (33), the peak load P_u of the beam for the small limit case is

$$P_u = \frac{4}{5} D b f_t \tag{34}$$

And the corresponding nominal strength σ_{N_u} is

$$\sigma_{N_u} = \frac{P_u}{Db} = \frac{4}{5} f_t \tag{35}$$

Notice that in the small limit case the peak load P_u is linear with respect the size D and the nominal strength σ_{N_u} is constant.

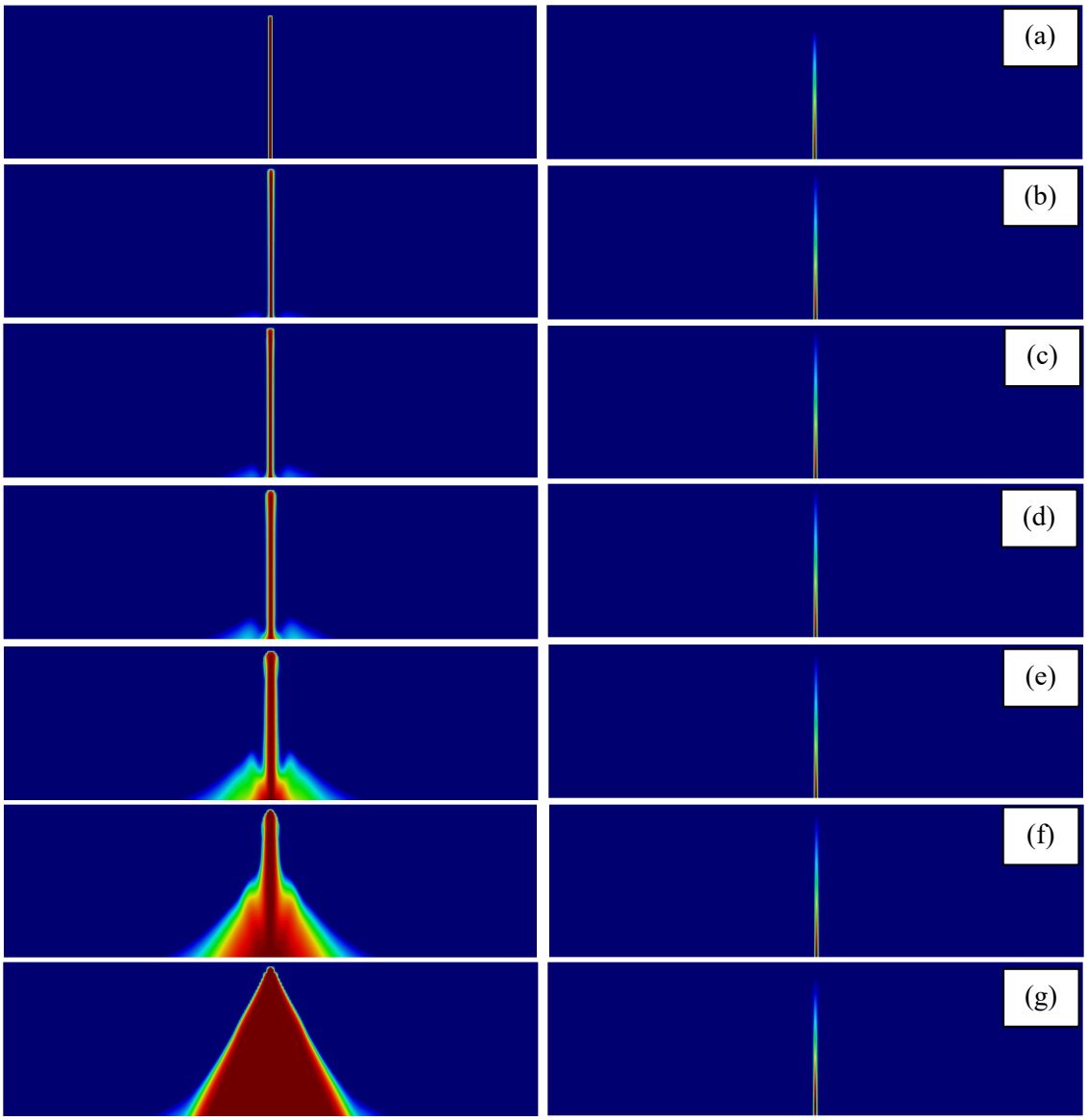

Figure 30. Variation of the (left) damage and (right) maximum principal strain contours of the unnotched beam for scales (a) 10, (b) 1, (c) 0.5, (d) 0.25, (e) 0.05, (f) 0.01 and (g) 10^{-4}

In the large size limit a perfectly brittle failure occurs and a linear elastic analysis of the beam can be considered. Considering the Euler-Bernoulli beam theory, a bending moment M acting on a D x b rectangular section produces a maximum tensile stress located at the bottom equal to

$$\sigma_{max} = 6 \frac{M}{D^2 b} \tag{36}$$

Therefore, for $M = M_{max}$ in Eq. (32)

$$\sigma_{max} = 3.75 \frac{P}{Db} \tag{37}$$

As structural failure occurs when $\sigma_{max} = f_t$, the peak load P_u of the beam in the large limit case is

$$P_u = \frac{4}{15} D b f_t \tag{38}$$

And the corresponding nominal strength σ_{N_u} is

$$\sigma_{N_u} = \frac{P_u}{Db} = \frac{4}{15} f_t \tag{39}$$

Notice that in the large limit case the peak load P_u is also linear with respect the size D and the nominal strength σ_{N_u} is constant.

Figure 31 shows the predictions of the nominal strength with respect the beam size that are obtained with the computational FE model. On the one hand, it can be seen that for small sizes the nominal strength tends towards the limit set by limit analysis. On the other hand, for big sizes the nominal strength reaches the value corresponding to perfectly brittle failure. Note that the large scale limit is not tending exactly to the limit predicted by the linear elastic analysis. This is because the beam has a span-to-depth ratio of 2.5, which is too small for the Euler-Bernoulli theory to be fully valid. Nonetheless, the large scale limit predicted with the Euler-Bernoulli assumptions is a good approximation (7% off).

In Figure 32 the computed ultimate load vs beam depth results are shown. As noted in the introduction, the nominal strength σ_{N_u} is in fact an indirect way of describing the peak load P_u reached by the structure. The phenomenon is described in a much clearer way using the nominal strength.

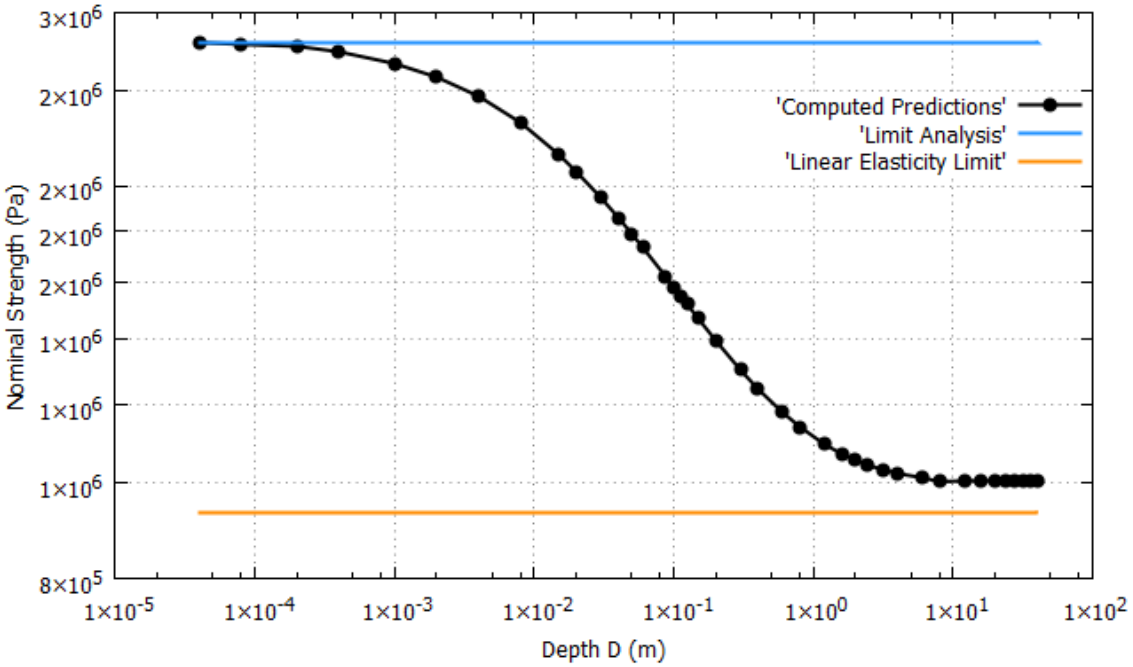

Figure 31. Computed predictions of the nominal strength vs beam depth for the unnotched beam

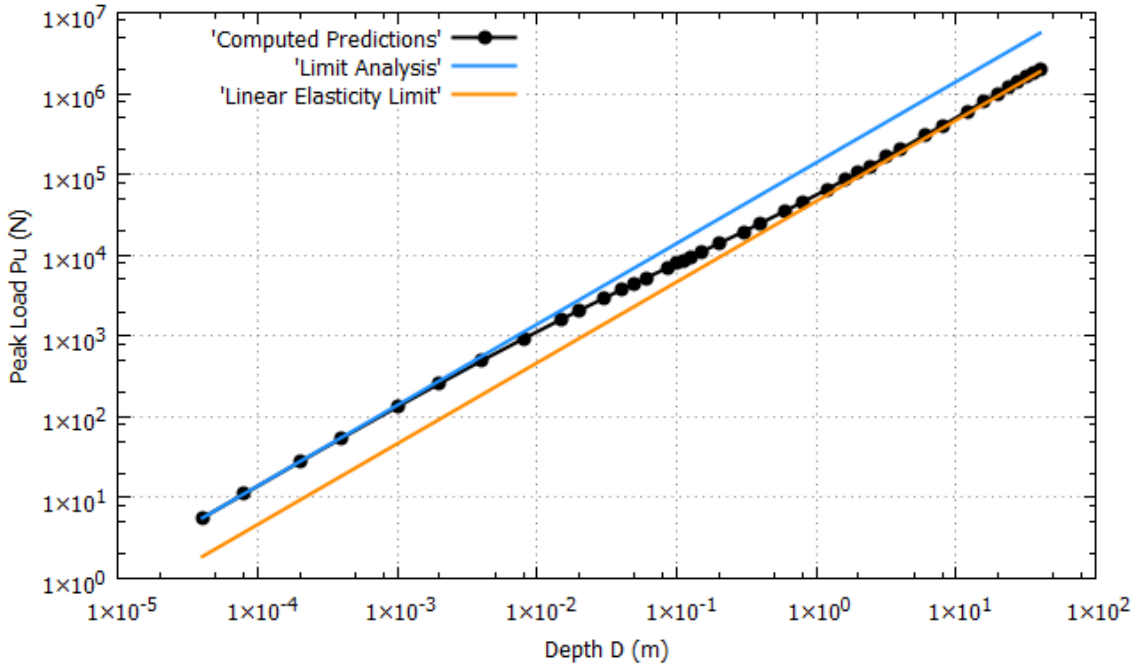

Figure 32. Computed predictions of the peak load vs beam depth for the unnotched beam

Notched beam size effect predictions

Figure 33 depicts damage and maximum principal strain contour fills obtained for several sizes of the notched beam. The same mesh as the one used in the simulations of Section 5.1, shown in Figure 34a, is employed for scales lower or equal than 20. For larger cases a finer mesh, detailed in Figure 34b, is used, where the FE size is $1.25 \cdot 10^{-4} D$ near the crack tip, resulting in a 121026 element mesh.

It can be seen that the extension of the area affected by damage grows as the size diminishes. It can be noticed once more that even though the damaged area becomes large for smaller sizes, strain localization in a narrow band is properly taking place in the computed strain field. For large beams a very brittle failure occurs, caused by a vertical crack starting at the tip of the notch. In that situation the structural failure is influenced in a determining way by the stresses concentrating around the notch, which need to be computed accurately. For this reason, a mesh refinement of the area near the tip of the notch is necessary for the larger cases. For small enough scales a perfect hinge is developed in the midsection of the beam, analogously to the unnotched case.

The peak load of the small limit case can be calculated from limit analysis using the same method as for the unnotched beam. The structure fails when a hinge develops at the midsection of the beam. Considering that the notch has a length of λD, the maximum bending moment at the midsection is

$$M_u = \frac{1}{2}(1-\lambda)^2 D^2 b f_t \tag{40}$$

Therefore, the peak load P_u of the beam for the small limit case is

$$P_u = \frac{4}{5}(1-\lambda)^2 D b f_t \tag{41}$$

And the corresponding nominal strength σ_{N_u} is

$$\sigma_{N_u} = \frac{P_u}{Db} = \frac{4}{5}(1-\lambda)^2 f_t \tag{42}$$

Notice that again the peak load P_u is linear with respect the size D and the nominal strength σ_{N_u} is constant.

The peak load of the large limit case cannot be correctly computed considering the Euler-Bernoulli beam theory as in the unnotched case because the effect of the stress concentration around the notch tip is not taken into account. In situations where stress singularities exist, a failure criterion expressed in terms of stress is not adequate. In such cases, an energy failure criterion such as the one introduced in LEFM becomes relevant.

In the LEFM approach the expected relation of the nominal strength for two sizes A and B is

$$\frac{\left(\sigma_{N_u}\right)_A}{\left(\sigma_{N_u}\right)_B} = \left(\frac{D_A}{D_B}\right)^{-\frac{1}{2}} \tag{43}$$

And the predicted relation of the corresponding peak loads is

$$\frac{(P_u)_A}{(P_u)_B} = \left(\frac{D_A}{D_B}\right)^{\frac{1}{2}} \tag{44}$$

In Figure 35 the computed predictions of the nominal strength with respect the beam size for the notched case are depicted. For small sizes the nominal strength reaches the limit set by limit analysis. It can be seen that for large sizes the nominal strength follows the behavior specified by LEFM theory.

In Figure 36 the computed predictions are shown in terms of peak load vs structural size. Once more the size effect phenomenon is revealed in a clearer way with the use of the nominal strength.

The aptness of the predictions computed with the model can be assessed by examining their fitting with respect Bazant's size effect law. To adjust the parameters of Bazant's law with the produced numerical data, a nonlinear least squares fitting procedure is performed. The result is shown in Figure 37.

Three different functions are considered for adjusting the data. First, Bazant's original law is considered

$$\sigma_{N_u} = B f_t \left[1 + \left(\frac{D}{D_0}\right)\right]^{-\frac{1}{2}} \tag{45}$$

The fitted parameters obtained are $B = 0.43987$ and $D_0 = 0.14895\, m$. It can be seen that Bazant's original law does not fit correctly the data for the whole range of depths; in particular, it does not fit well the regions corresponding to small and intermediate specimen sizes. This issue has already been discussed in reference [1] when considering a large range of sizes. As a remedy, Bazant's general law has been proposed

$$\sigma_{N_u} = B f_t \left[1 + \left(\frac{D}{D_0}\right)^r\right]^{-\frac{1}{2r}} \tag{46}$$

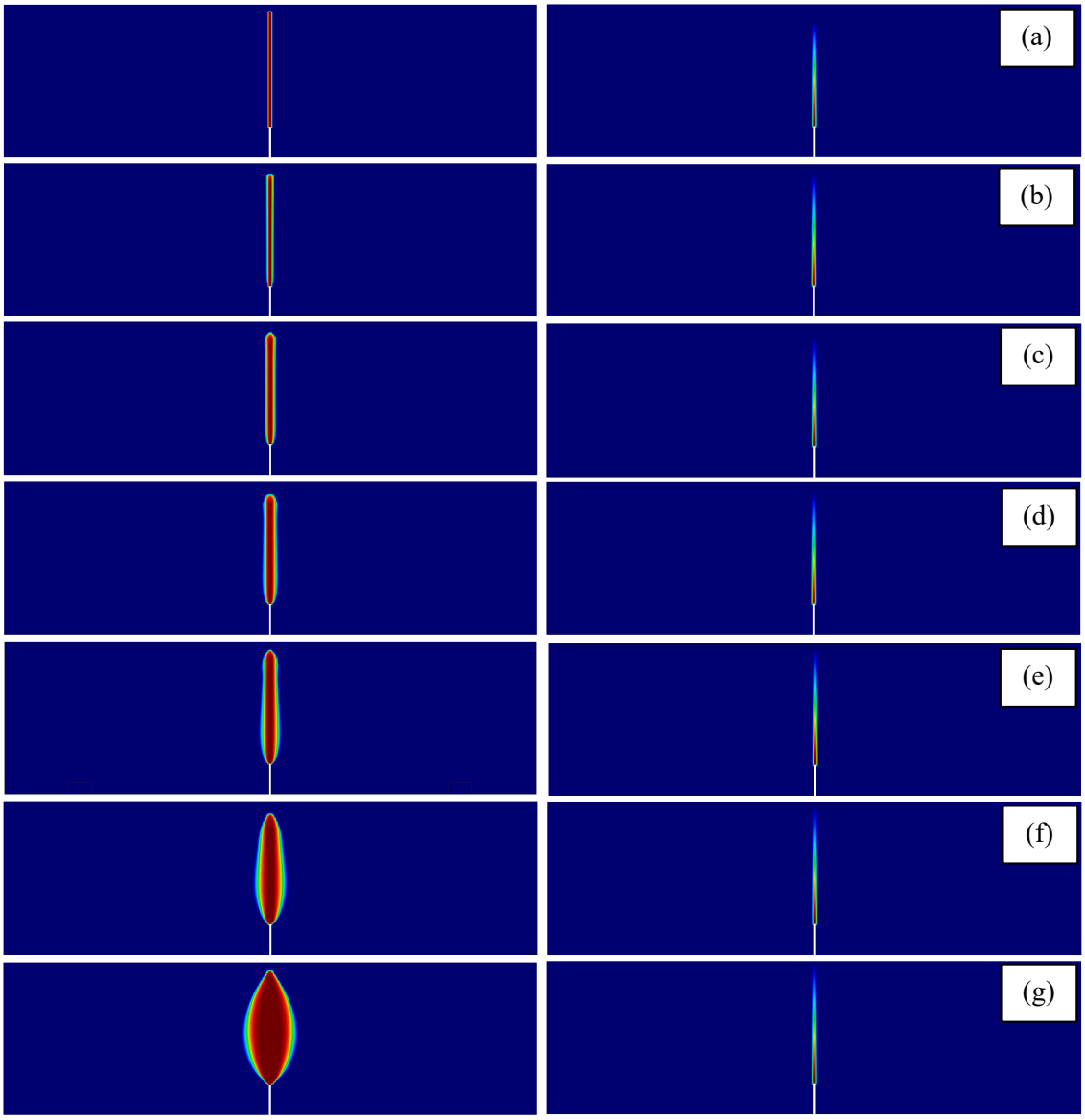

Figure 33. Variation of the (left) damage and (right) maximum principal strain contours of the notched beam for scales (a) 20, (b) 1, (c) 0,25, (d) 0.125, (e) 0.05, (f) 0.01 and (g) 10^{-4}

The fitted parameters obtained are $B = 0.51165$, $D_0 = 0.13819\, m$ and $r = 0.51318$. Note that $D_0 = 0.5084L$. It can be observed that Bazant's general law fits much better the computed predictions over the whole domain than the original law. The level of adjustment with the numerical predictions is notable as the size range considered here is very extensive, spreading over more than 6 orders of magnitude. In reference [1] it is already pointed out that parameters r close to 0.5 fit better data which is extended over a wide range of sizes.

Finally, let us consider the fitting of the computed predictions with the power law

$$\sigma_{N_u} = AD^m \tag{47}$$

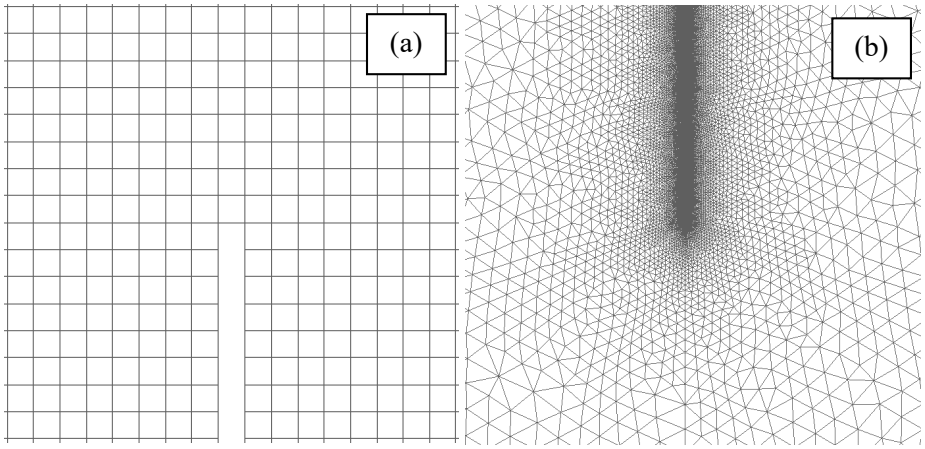

Figure 34. Detail of the mesh used for the notched beam size effect predictions around the tip of the notch with (a) 22464 quadrilateral elements and (b) 121026 triangular elements

The fitted parameters are $A = 322760.818$ and $m = -0.25189$ and the corresponding curve is also shown in Figure 37. It can be clearly seen that the power law fits very poorly the results. This clearly shows that, as it is stressed out in references [3, 4, 10], size effect cannot be modelled with the power law and that the phenomenon in fact involves a characteristic size D_0, related to the material characteristic length L.

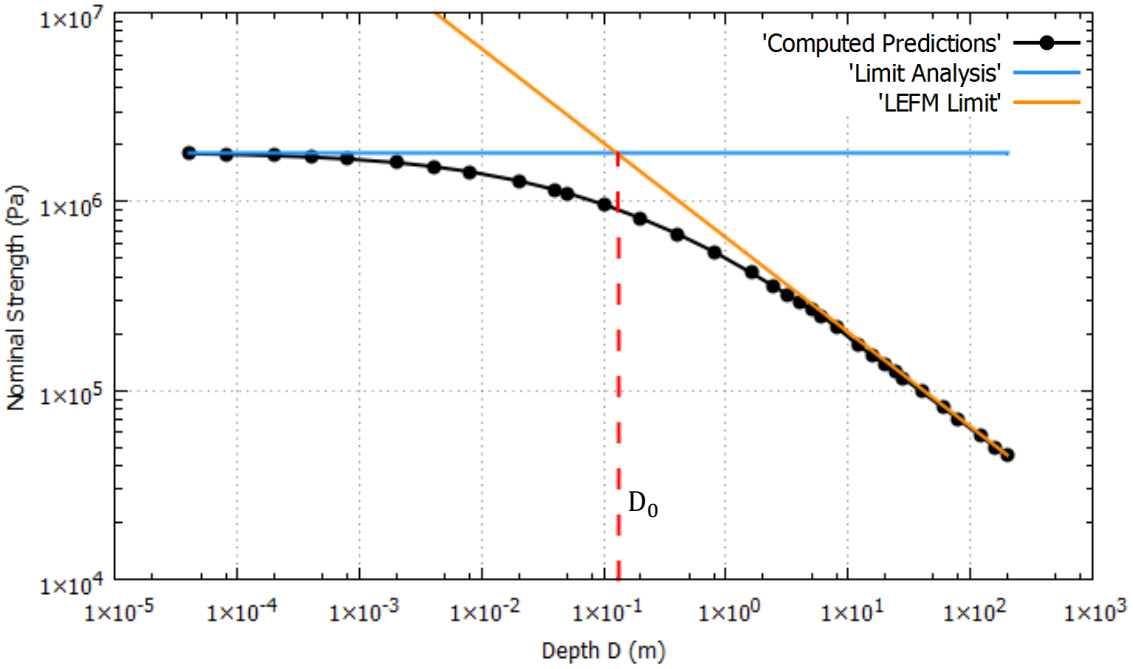

Figure 35. Computed predictions of the nominal strength vs beam depth for the notched beam

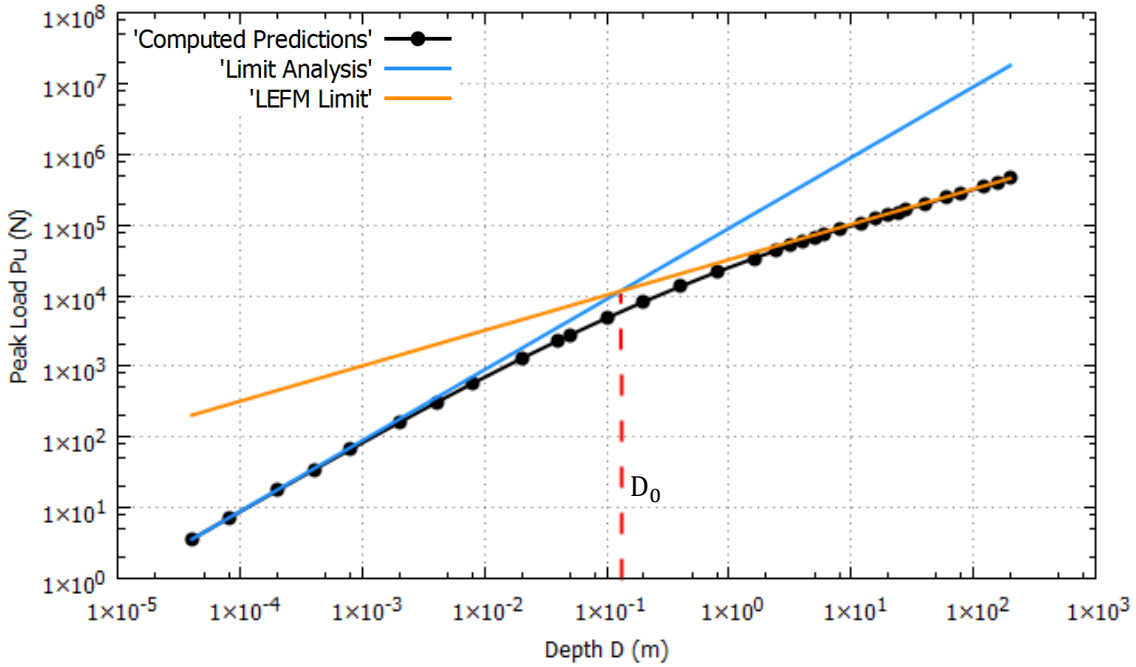

Figure 36. Computed predictions of the peak load vs beam depth for the notched beam

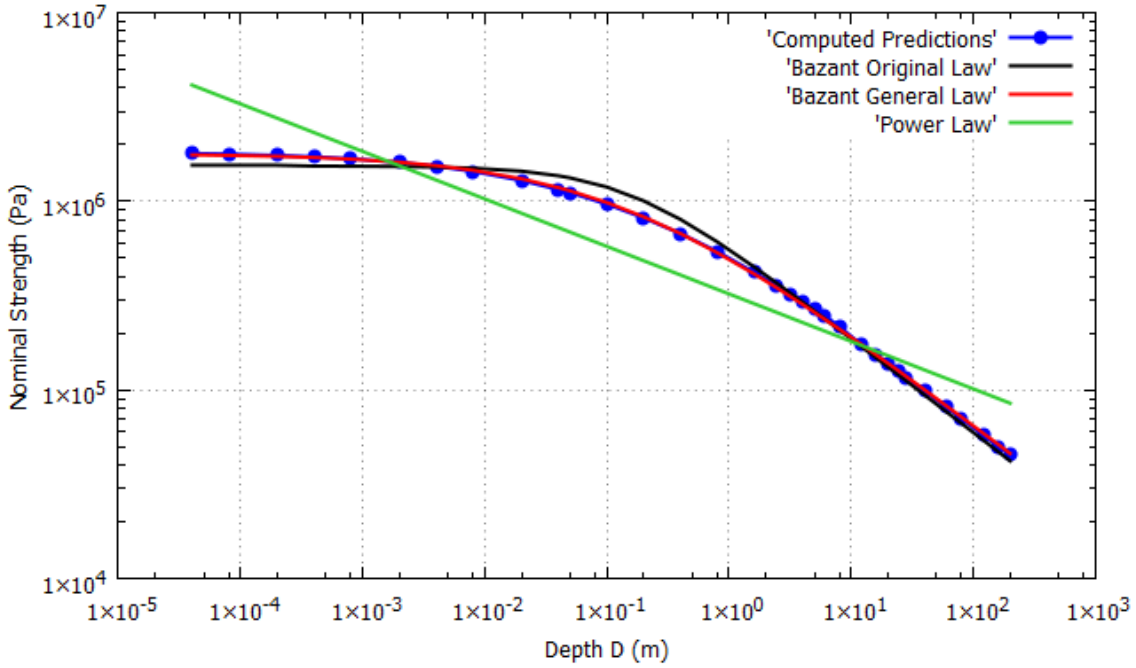

Figure 37. Fitting of the numerical predictions with respect Bazant's size effect law

The size effect phenomenon also involves a change in the ductility and the post-peak behavior of the specimens. Figure 38 shows the nominal stress vs normalized CMOD curve (nominal stress being also a measure of force normalized with respect structural size) of the simulations performed for the notched beams. It can be seen how the behavior of the beams changes from ductile to brittle when size increases. Once properly normalized, the peak load and the energy dissipated in the failure process is comparatively smaller in larger structures. The collapse in larger specimens happens closer to the peak load while in smaller ones the post-peak curve

descends much more slowly. It is observed that the nonlinear regime starts before the peak load is attained, particularly for more ductile behavior. Therefore, it is shown that, besides considering with accuracy the effect that the phenomenon has on load capacity, the computational model is also able of reproducing the ductility changes originated by variations in structural size.

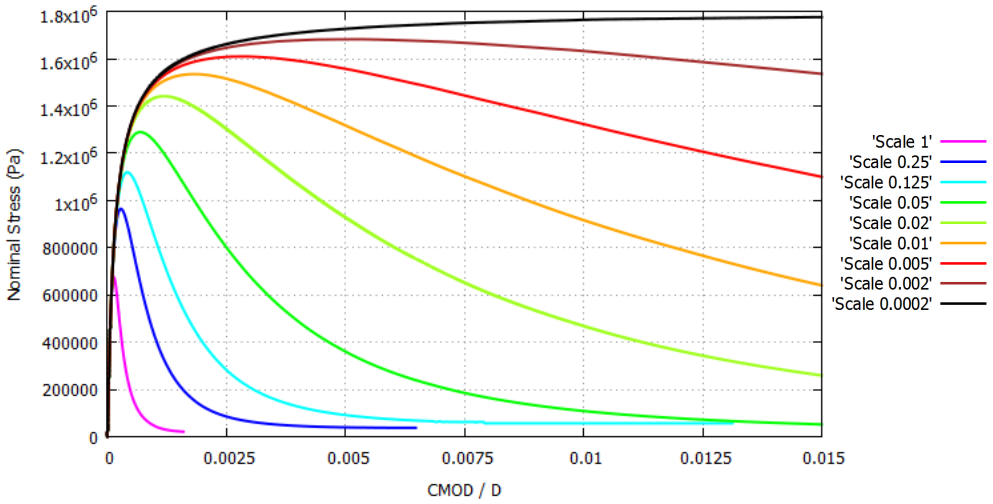

Figure 38. Normalized force-CMOD curves for various scales of the notched beam

9 Conclusions

In this work, the phenomenon of structural size effect is addressed, and experimental evidence, theoretical predictions and computational modelling using FEs are assessed against each other. Quasi-brittle failure is accurately modelled with a classical local isotropic Rankine damage constitutive law. The correct dissipation of fracture energy in the crack, fundamental to appropriately consider size effect, is enforced in conjunction with the crack band approach. The model is used together with an enhanced accuracy mixed **ε/u** finite element formulation to provide results without spurious mesh bias.

The simulation of several experimental campaigns, where the phenomenon is investigated in mode I and mixed mode I and II, is carried out. The performance of the model in modelling size effect is shown in notched and unnotched beams.

It is observed that:

- The proposed local isotropic damage constitutive model is fit for the numerical simulation of structural size effect.
- Results documented in several experimental campaigns where the phenomenon is carefully studied are accurately reproduced in 2D and 3D.
- The results obtained with the mixed FE formulation are free from the spurious mesh dependency in terms of computed crack trajectory which is typical of standard FEs.
- The dominant influence of size effect in quasi-brittle materials is the release of stored energy as the crack progresses in the structure
- Bazant's size effect law is followed with exactitude over a wide range using the proposed model.

From these, it is concluded that the proposed isotropic damage model, used together with the mixed finite element formulation, is suitable for reproducing size effect in quasi-brittle materials in mode I and mixed mode I and II loading with mesh objectivity and without the need of using auxiliary crack tracking techniques.

10 Acknowledgements

Financial support from the Spanish Ministry of Economy and Business via the ADaMANT (Computational Framework for Additive Manufacturing of Titanium Alloy) project (Proyectos de I + D (Excelencia) DPI2017-85998-P) is gratefully acknowledged. The support provided by the Spanish Ministry of Education to Mr. Gabriel Barbat via the FPU program is also acknowledged.

11 References

[1] Z. Bazant and J. Planas, Fracture and Size Effect in Concrete and Other Quasibrittle Materials, Boca Raton: CRC Press, 1998.

[2] ACI, Building Code Requirements for Structural Concrete (ACI 318-19), 2019.

[3] Z. Bazant, "Size effect," *International Journal of Solids and Structures,* vol. 37, pp. 69-80, 2000.

[4] Z. Bazant, "Size effect on structural strength: a review," *Archive of Applied Mechanics,* vol. 69, pp. 703-725, 1999.

[5] Y. Rashid, "Ultimate strength analysis of prestressed concrete pressure vessels," *Nuclear Engineering and Design,* vol. 7, no. 4, pp. 334-344, 1968.

[6] Z. Bazant and B. Oh, "Crack band theory for fracture of concrete," *Matériaux et Constructions,* vol. 16, no. 3, pp. 155-177, 1983.

[7] M. Cervera and J.-Y. Wu, "On the conformity of strong, regularized, embedded and smeared discontinuity approaches for the modelling of localized faillure in solids," *International Journal of Solids and Structures,* vol. 71, pp. 19-38, 2015.

[8] J. Wu and M. Cervera, "On the equivalence between traction- and stress-based approaches for the modeling of localized failure in solids," *Journal of the Mechanics and Physics of Solids,* vol. 82, pp. 137-163, 2015.

[9] Z. Bazant, "Fracture in concrete and reinforced concrete," in *Mechanics of Geomaterials*, 1985, pp. 259-303.

[10] Z. Bazant and E.-P. Chen, "Scaling of structural failure," Sandia Report SAND96-2948, Albuquerque, New Mexico, 1997.

[11] M. Cervera and M. Chiumenti, "Size effect and localization in J2 plasticity," *International Journal of Solids and Structures,* vol. 46, pp. 3301-3312, 2009.

[12] M. Cervera and M. Chiumenti, "Smeared crack approach: back to the original track," *International Journal for Numerical and Analytical Methods in Geomechancs,* vol. 30, pp. 1173-1199, 2006.

[13] M. Cervera and M. Chiumenti, "Mesh objective tensile cracking via a local continuum damage model and a crack tracking technique," *Computer Methods and Applied Mechanics in Engineering,* vol. 196, no. 1-3, pp. 304-320, 2006.

[14] R. Peerlings, R. de Borst, W. Brekelmans and J. de Wree, "Gradient enhanced damage for quasi brittle materials," *International Journal for Numerical Methods in Engineering,* vol. 39, pp. 3391-3403, 1996.

[15] R. de Borst and C. Verhoosel, "Gradient damage vs phase-field approaches for fracture: Similarities and differences.," *Computer Methods in Applied Mechanics and Engineering,* vol. 312, pp. 78-94, 2016.

[16] R. Peerlings, M. Geers, R. de Borst and W. Brekelmans, "A critical comparison of nonlocal and gradient-enhanced softening continua," *International Journal of Solids and Structures,* vol. 38, pp. 7723-7746, 2001.

[17] Z. Bazant and G. Pijaudier-Cabot, "Nonlocal continum damage, localization instabilities and convergence," *Journal of Engineering Mechanics ,* no. 55, pp. 287-293, 1988.

[18] C. Miehe, F. Welschinger and M. Hofacker, "Thermodynamically consistent phase-field models of fracture: Variational principles and multi-field FE implementations," *International Journal for Numerical Methods in Engineering,* vol. 83, pp. 1273-1311, 2010.

[19] C. Miehe, L.-M. Schänzel and H. Ulmer, "Phase field modeling of fracture in multi-physics problems. Part I. Balance of cracks surface and failure criteria for brittle crack propagation in thermo-elastic solids," *Computer Methods in Applied Mechanics and Engineering,* vol. 294, pp. 449-485, 2015.

[20] J. Vignollet, S. May, R. de Borst and C. Verhoosel, "Phase-field model for brittle and cohesive fracture," *Meccanica,* vol. 49, pp. 2587-2601, 2014.

[21] G. Nguyen, C. Nguyen, P. Nguyen, H. Bui and L. Shen, "A size-dependent constitutive modelling framework for localized faillure analysis," *Computational Mechanics,* vol. 58, pp. 257-280, DOI 10.1007/s00466-016-1293-z, 2016.

[22] J. Wu, "A geometrically regularized gradient-damage model with energetic equivalence," *Computer Methods in Applied Mechanics and Engineering,* vol. 328, pp. 612-637, 2018.

[23] J.-Y. Wu, "A unified phase-field theory for the mechanics of damage and quasi-brittle failure," *Journal of the Mechanics and Physics of Solids,* vol. 103, pp. 72-99, 2017.

[24] J.-Y. Wu and V. Nguyen, "A length scale insensitive phase-field damage model for brittle fracture," *Journal of the Mechanics and Physics of Solids,* vol. 119, pp. 20-42, 2018.

[25] D.-C. Feng and J.-Y. Wu, "Phase-field regularized cohesive zone model (CZM) and size effect of concrete," *Engineering Fracture Mechanics,* vol. 197, pp. 66-79, 2018.

[26] M. Cervera, M. Chiumenti and R. Codina, "Mixed stabilized finite element methods in nonlinear solid mechanics. Part I: Formulation," *Computer Methods in Applied Mechanics and Engineering,* vol. 199, no. 37-40, pp. 2559-2570, 2010.

[27] M. Cervera, M. Chiumenti and R. Codina, "Mixed stabilized finite element methods in nonlinear solid mechanics. Part II: Strain localization," *Computer Methods in Applied Mechanics and Engineering,* vol. 199, no. 37-40, pp. 2571-2589, 2010.

[28] M. Cervera, M. Chiumenti, L. Benedetti and R. Codina, "Mixed stabilized finite element methods in nonlinear solid mechanics. Part III: Compressible and incompressible

plasticity," *Computer Methods in Applied Mechanics and Engineering,* vol. 285, no. 0, pp. 752-775, 2015.

[29] M. Cervera, G. Barbat and M. Chiumenti, "Finite element modelling of quasi-brittle cracks in 2D and 3D with enhanced strain accuracy," *Computational Mechanics,* vol. 60, no. 5, pp. 767-796, 2017.

[30] G. Barbat, M. Cervera and M. Chiumenti, "Appraisement of planar, bending and twisting cracks in 3D with isotropic and orthotropic damage models," *International Journal of Fracture,* vol. 210, no. 1-2, pp. 45-79, 2018.

[31] G. Vlachakis, M. Cervera, G. Barbat and S. Saloustros, "Out-of-plane seismic response and faillure mechanism of masonry structures using finite elements with enhanced strain accuracy," *Engineering Faillure Analysis,* vol. 97, pp. 534-555, 2019.

[32] M. Cervera, G. Barbat and M. Chiumenti, "Architecture of a multi-crack model with full closing, reopening and sliding capabilities," *Computational Mechanics,* DOI:10.1007/s00466-020-01836-y , 2020.

[33] Z. Bazant and Q. Yu, "Universal size effect law and effect of crack depth on quasi-brittle structure strength," *Journal of Engineering Mechanics,* vol. 135, no. 2, pp. 78-84, 2009.

[34] N. Jones, Structural impact, Cambridge: Cambridge University Press, 1989.

[35] R. Oshiro and M. Alves, "Scaling impacted structures," *Archive of Applied Mechanics,* vol. 74, pp. 130-145, 2004.

[36] M. Alves, R. Oshiro, M. Calle and L. Mazzariol, "Scaling and structural impact," *Procedia Engineering,* vol. 173, pp. 391-396, 2017.

[37] J. Oliver, M. Cervera, S. Oller and J. Lubliner, "Isotropic damage models and smeared crack analysis of concrete," *II international conference on computer aided analysis and design of concrete,* 1990.

[38] L. Benedetti, M. Cervera and M. Chiumenti, "3D modelling of twisting cracks under bending and torsion skew notched beams," *Engineering Fracture Mechanics,* vol. 176, pp. 235-256, 2017.

[39] I. Babuska, "Error-bounds for finite element method," *Numerisch Mathematik,* vol. 16, pp. 322-333, 1971.

[40] D. Boffi, F. Brezzi and M. Fortin, "Mixed finite element methods and applications," *Springer,* 2013.

[41] F. Brezzi, "On the existence, uniqueness and approximation of saddle-point problems arising from lagrangian multipliers," *ESAIM: Mathematical Modelling and Numerical Analysis - Modélisation Mathématique et Analyse Numérique,* vol. 8, no. R2, pp. 129-151, 1974.

[42] R. Codina, "Stabilization of incompressibility and convection through orthogonal sub-scales in finite element methods," *Computer Methods in Applied Mechanics and Engineering ,* vol. 190, pp. 1579-1599, 2000.

[43] D. Grégoire, L. Rojas-Solano and G. Pijaudier-Cabot, "Faillure and size effect for notched and unnotched concrete beams," *International Journal for Numerical and Analytical Methods in Geomechanics,* vol. 37, pp. 1434-1452, 2013.

[44] C. Hoover, Z. Bazant, J. Vorel, R. Wendner and M. Hubler, "Comprehensive concrete fracture tests: Description and results," *Engineering Fracture Mechanics,* vol. 114, pp. 92-103, 2013.

[45] V. Garcia-Alvarez, R. Gettu and I. Carol, "Analysis of mixed-mode fracture in concrete using interface elements and a cohesive crack model," *Sadhana,* vol. 37, no. 1, pp. 187-205, 2012.

[46] M. Cervera, C. Agelet de Saracibar and M. Chiumenti, "COMET: Coupled mechanical and thermal analysis. Data input manuel, Version 5.0, Technical report IT-308. Available from http://www.cimne.upc.edu," 2002.

[47] A. Coll, R. Ribo, M. Pasenau, E. Escolano, J. S. Perez, A. Melendo, A. Monros and J. Garate, "GiD: the personal pre and post-processor User Manual," *CIMNE, Technical University of Catalonia,* p. <http://gid.cimne.upc.ed>, 2002.

[48] E. Rodrigues, O. Manzoli, L. Bitencourt and T. Bittencourt, "2D mesoscale model for concrete based on the use of interface element with a high aspect ratio," *International Journal of Solids and Structures,* Vols. 94-95, pp. 112-124, 2016.

[49] M. Vassaux, C. Oliver-Leblond, B. Richard and F. Ragueneau, "Beam-particle approach to model cracking and energy dissipation in concrete: Identification strategy and validation," *Cement and Concrete Composites,* vol. 70, pp. 1-14, 2016.

[50] J. Elias, "Boundary layer effect on behavior of discrete models," *Materials,* vol. 10, no. 2, p. 157, 2017.

[51] S. Seetharam, E. Laloy, A. Jivkov, L. Yu, Q. Phung, N. Pham, B. Kursten and F. Druyts, "A mesoscale framework for analysis of corrosion induced damage of concrete," *Construction and Building Materials,* vol. 216, pp. 347-361, 2019.

[52] R. Wendner, J. Vorel, J. Smith, C. Hoover, Z. Bazant and G. Cusatis, "Characterization of concrete failure behavior: a comprehensive experimental database for the calibration and validation of concrete models," *Materials and Structures,* vol. 48, pp. 3603-3626, 2015.

[53] P. Havlasek, P. Grassl and M. Jirasek, "Analysis of size effect on strength of quasi-brittle materials using integral-type nonlocal models," *Engineering Fracture Mechanics,* vol. 157, pp. 72-85, 2016.

[54] E. Lorentz, "A nonlocal damage model for plain concrete consistent with cohesive fracture," *International Journal of Fracture,* vol. 207, no. 2, pp. 123-159, 2017.

[55] J. Klon and V. Vesely, "Modelling of size and shape of damage zone in quasi-brittle notched specimens – analytical approach based on fracture-mechanical evaluation of loading curves," *Frattura ed Integrità Strutturale,* vol. 39, pp. 17-28, 2017.

[56] I. Marzec and J. Bobinski, "On some problems in determining tensile parameters of concrete model from size effect tests," *Polish Maritime Research,* vol. 102, no. 2, pp. 115-125, 2019.

[57] M. Gutierrez and R. De Borst, "Deterministic and stochastic analysis of size effects and damage evolution in quasi-brittle materials," *Archive of Applied Mechanics,* vol. 69, pp. 655-676, 1999.